

THE UNIVERSITY OF OKLAHOMA
GRADUATE COLLEGE

INTEGRATED GEOCHEMISTRY AND SEDIMENTOLOGY OF THE WOLFCAMP B3
AND B2 INTERVALS, MIDLAND BASIN, TX

A THESIS
SUBMITTED TO THE GRADUATE FACULTY
In partial fulfillment of the requirements for the
Degree of
MASTER OF SCIENCE

By
CECILIA LOPEZ-GAMUNDI
Norman, Oklahoma
2019

INTEGRATED GEOCHEMISTRY AND SEDIMENTOLOGY OF THE WOLFCAMP B3
AND B2 INTERVALS, MIDLAND BASIN, TX

A THESIS APPROVED FOR THE
CONOCOPHILLIPS SCHOOL OF GEOLOGY AND GEOPHYSICS

BY

Dr. Roger Slatt, Chair

Dr. R. Paul Philp

Dr. Gerilyn Soreghan

© Copyright by Cecilia Lopez-Gamundi 2019
All Rights Reserved.

*Dedicated to my parents,
who taught me that it's not about the shoes you fill,
but the shoes you make.*

Acknowledgments

This study would not have been possible without the core access allowed to by those at Pioneer Natural Resources. I would like to thank Bo Henk at Pioneer Natural Resources for believing in the value of this work after only a few short months of knowing me.

I owe a great deal of thanks my committee members Dr. Roger Slatt and Dr. Lynn Soreghan for their continuous geologic feedback and engraining in me that geologic models and generalizations always have exceptions. Furthermore, I would like to thank Dr. Pigott for never letting me forget the regional geologic context of my study area.

I would like to thank my colleagues in the organic geochemistry group who I am fortunate enough to consider friends: Damian Villalba, Lydia Jones, Yagmur Sumner, Ann Ojeda, Emilio Torres, and Andreina Laborias as well as to all my friends at The University of Oklahoma. I would also like to Dr. Silvana Barbanti for her support with HPLC calibration and Dr. Thanh Nguyen, Jon Allen, and Larry Hyde for help with lab procedure and technique.

Most importantly, I would like to thank Dr. Philp for his patience and support. This work would not have been possible without his guidance and mentorship. I am deeply honored and humbled that he took me on as one of his last students.

List of Tables

Table 1. Distribution of petrographic microfacies as a function of depth.	42
Table 2. Petrographic microfacies observed within specific lithofacies.	43
Table 3. Rock-Eval Pyrolysis data table. From left to right: core depth (ft.), TOC (wt. %), S1, S2, S3, T _{max} , HI, OI, S2/S3, ((S1/TOC)*100), RHP, and PI. Samples with asterisk (*) on far right indicate those samples that had further organic geochemical analysis performed on them. Note that some samples did not have sufficient TOC for further Rock-Eval data to be reported confidently by service company; these values are omitted.	85
Table 4. Biomarkers and chromatograms / fragmentograms analyzed.	100
Table 5. Terpane compound Identification (m/z 191)	118
Table 6. Selected terpane biomarker ratios for Wolfcamp B3 and B2 samples.	119
Table 7. Sterane compound identification (m/z 217)	151
Table 8. Selected sterane biomarker ratios for Wolfcamp B3 and B2 samples.	152

List of Figures

- Figure 1. Paleogeographic map of Permian-aged North America, roughly 275 Mya (Blakey, 2003) on left, Red rectangle indicates location of Permian Basin. Zoomed in view of the Permian Basin, focusing on major structural settings, modified from Atchley et al. (1999). Red star indicates approximate well location. 4
- Figure 2. Midland Basin depositional block diagram depicting various depositional mechanisms, including carbonate and siliciclastic sediment gravity flows (modified from Pioneer Natural Resources, 2015). Permian Basin structural setting location map (top left) indicating Midland Basin in green rectangle (modified from Atchley et al., 1999) Note rotated orientation of block diagram. Red star indicates approximate well location.7
- Figure 3. From left to right: Eustatic sea level curve, Midland Basin Stratigraphy, and global climate (icehouse-greenhouse) conditions from Pennsylvanian to Permian age and expanded regional sea level curve and Midland Wolfcamp Formation deposition with respective subintervals (Modified from Rygel et al., 2008). Please note that sea level curves are composite of second (blue solid and stippled lines) and third order cycles (filled-in blue curve). Red blocked area indicates cored Wolfcamp subintervals of interest, upper B3 and B2..... 9
- Figure 4. Representative examples of lithofacies. Lithofacies listed from left to right: black mudstone (9621.00 – 9621.17 ft), silty mudstone (9657.17 – 9657.33 ft.), massive gray mudstone (9660.67 – 9660.83 ft.), banded gray mudstone (9596.33 – 9596.50 ft), truncated packstone (9539.50 – 9539.66 ft.) blue line emphasizes contact and red arrows indicate truncated laminae, laminated packstone (9664.50 – 9664.67 ft.), massive packstone (9679.17 – 9679.33 ft.), coarse wackestone (9695.00 – 9695.17 ft.),

and heavily bioturbated (9565.00 – 9565.17 ft.) where green arrows show burrows. Note scale bar and associated facies color..... 19

Figure 5. Core description (left) and lithofacies assignment (right) every two inches showing upscaled features. Note the Wolfcamp B2 – B3 contact in red. Note core beak 9551-9565 ft. is not to scale. Lithofacies colors are corresponding to those delineated in Figure 4. Depth scales are to the left of each column. 24

Figure 6. Example of small calciturbidite (<1 ft) observed at 9670.50 ft. Massive carbonate base interpreted as a Bouma T_a. Planar laminations interpreted as a Bouma T_b. Faint climbing ripples followed by discontinuous laminations interpreted as T_c and T_d respectively. Textureless black mudstone interpreted as hemipelagic to pelagic background sedimentation or Bouma T_e. 27

Figure 7. Working sequence stratigraphic framework, including 2nd order FSST, LST, TST and mfz, HST, and potential nested 3rd order cycles. Stippled lines reflect a decrease confidence in interpretation. Stacked arrows reflect parasequence scale changes within and overall higher order systems tract. Note that moving forward only high confidence interpretation and lowest order sequence stratigraphic interpretation will be carried across to other geologic and geochemical interpretations..... 33

Figure 8. Examples of petrographic microfacies where number refers to petrographic microfacies and “a” and “b” refer to macroscopic and microscopic thin section images, respectively. 1) non-laminated black mudstone (9625.17 ft.), 1a) *chondrites* burrows visible, 1b) *Tasmanites* with organic matter infill; 2) poorly sorted coarse packstone (9697.17 ft.), 2a) matrix supported large lithoclast sand allochems 2b) red numbers indicate allochems as follows 1 large multichamber foram 2. shattered multi-chamber

foram 3. echinoderm spine fragment; (3) well sorted carbonate packstone (9690.84 ft.); 3b) cement infill and replacement 4) mixed carbonate siliciclastic wackestone (9594.66 ft.) 5) faintly laminated silty mudstone (9657.17 ft.); 6) bioturbated silty mudstone (9585.17 ft.) 5b) intense bioturbation only leaved OM rich discontinuous laminations.

Note scale bars and staining. Red indicates calcite and dark blue indicates ferroan dolomite..... 37

Figure 9. Schematic of observed trace fossils *Chondrites*, *Nereites*, *Phycosiphon*, *Planolites*, *Teichichnus*, and *Zoophycos*. Grayed out square represents visible 2D surface on core face (Bromley and Ekdale, 1984). 53

Figure 10. Schematic representation of idealized tiered community. Ichnofossils listed from top to bottom: *Phycosiphon*, *Planolites*, *Nereites*, *Chondrites* (large), *Zoophycos*, *Teichichnus*, and *Chondrites* (small) show increasing tolerance to low dissolved oxygen concentrations as distance increase from sediment water interface. 60

Figure 11. From left to right: Degree of total bioturbation (out of 100%), qualitative assessment (0 – 3) of presence of ichnofossils: *Phycosiphon*, *Planolites*, *Nereites*, *Zoophycos*, *Chondrites*; core description, observed lithofacies, and working sequence stratigraphic framework..... 64

Figure 12. Average major element composition (Si, Al, Ca, Fe, K, Mg, and S) of each lithofacies. 66

Figure 13. Paleoredox Proxies with Limited Detrital Influences: U, V, and Mo (ppm) concentration statistical distributions as a function of lithofacies. Minimum, Q1, median, Q3, and maximum shown. Note higher U maximums for black mudstone and laminated silt..... 71

Figure 14. Paleoredox Proxies with Strong Detrital Influences: Cr and Co (ppm) concentration statistical distributions as a function of lithofacies. Minimum, Q1, median, Q3, and maximum shown in box and whiskers plot. 77

Figure 15. Redox Sensitive Organometallic Trace Element Proxies: Ni, Cu, and Zn (ppm) concentration statistical distributions as a function of lithofacies. Minimum, Q1, median, Q3, and maximum shown. 80

Figure 16. Paleoproductivity and Nutrient Minor Element Proxies: Fe and P (wt %) abundance statistical distributions as a function of lithofacies. Minimum, Q1, median, Q3, and maximum shown. P maximum values are cropped. See appendix for raw values. 82

Figure 17. Pseudo van Krevelen Diagram showing HI (mg HC/ g TOC) versus TOC (wt.%) (top) and remain hydrocarbon potential (mg HC/ g rock) versus TOC (bottom) both indicating a mixed Type II – III kerogen. 89

Figure 18. Rock-Eval Maturity Assessment: HI (mg HC/ g TOC) versus Tmax (°C) (top) and PI (S1/(S1+S2)) versus Tmax (bottom). Tmax values indicate mature samples are in the late oil window. HI values support previous Type II-III kerogen interpretation while also accounting for hydrogen loss during thermal cracking. PI values relative to Tmax indicate little to no sample contamination. 90

Figure 19. Bulk organic geochemical data as a function of depth. From left to right: TOC, HC Potential, RHP, and OM Type are plotted as a function of depth next. Lithofacies and core description for reference. 93

Figure 20. Example GC trace of a saturate fraction. Taken from depth 9585.2 ft. Pr: pristine, Ph: phytane; n-C₁₇: C₁₇ normal alkane; n-C₁₈: C₁₈ normal alkane; n-C₃₀: C₃₀

normal alkane. Note unimodal distribution of *n*-alkanes, centered around *n*-C₁₆, and odd over even carbon number predominance..... 102

Figure 21. *N*-alkane biomarker ratios. From left to right: terrigenous aquatic ratio (TAR), carbon preference index (CPI), and odd even predominance (OEP). Arrows under depth plots indicate environmental, source material, and maturity factors thought to influence the *n*-alkane ratios. Stippled arrows indicate lower confidence interpretations of controls that exert less influence. Note higher matures CPI and OEP centered around 1.

Sequence stratigraphy on far right for reference. 105

Figure 22. Pristane/Phytane ratio (Pr/Ph) expressed as a function of depth with sequence stratigraphic framework on right for reference. Note intermediate Pr/Ph values indicating overall suboxic conditions. Fluctuations therein are considered relative.

Arrows indicate environmental factors to influence the Pr/Ph ratio and how. 109

Figure 23. Partial fragmentogram of *m/z* 123 showing sesquiterpene distribution.

Compounds are denoted on fragmentogram. Note absence of eudesmane. 114

Figure 24. Partial fragmentogram of *m/z* 191 ion showing terpane distributions for two different samples. Sample taken from 9609.00 – 9609.17 ft. (top) and 9645.00 – 9645.33 ft.). Peaks are identified in Table 3. Note 17 α (H), 21 β (H) Homohopane 22R coelutes with unknown tricyclic terpane 117

Figure 25. Tricyclic terpane depth plots. Ratios from left to right: C₁₉/C₂₃, C₂₀/C₂₃, and C₂₆/C₂₅ tricyclic terpanes and (C₂₈+C₂₉ tricyclic terpanes)/C₃₀ hopane. Arrows indicate environmental factors and source material precursors thought to influence the biomarker ratios and how. Stippled arrows indicate lower confidence interpretations of those controls that exert less influence on their respective biomarker ratios..... 122

Figure 26. Tetracyclic and pentacyclic terpane ratios plotted as a function of depth. From left to right: C_{30}^*/C_{29} Ts, C_{29}/C_{30} Hopane, C_{35}/C_{34} Homohopane, and the C_{24} Tetracyclic / C_{30} Hopane. Arrows below depth plot indicate controls on biomarker ratio and the direction it pulls the value. The sequence stratigraphic framework, including the lithofacies and core description are shown for reference. 139

Figure 27. Partial fragmentograms of m/z 217 showing differing sterane distributions in samples taken from 9633.00 – 9633.33 ft. (top) and 9653.00 – 9653.33 ft. (bottom). Identification of labelled peaks are listed in Table 7. 149

Figure 28. Ternary diagram for C_{27} , C_{28} , and C_{29} regular sterane distribution Based on original diagram produced by Huang and Meinschein, 1979 for sterol distributions from different depositional environments..... 154

Figure 29. Sterane depth plots. From left to right: $C_{30}/\Sigma C_{27-30}$ steranes indicating marine algae input, ΣC_{27-29} diacholestanes/ ΣC_{27-29} regular steranes, reflecting changes in clay content and redox conditions, and the sequence stratigraphic framework for reference. Arrows below biomarker depth plots indicate factors controlling ratios and how. 155

Figure 30. Half-foot averaged molybdenum (Mo) concentration cross plotted with corresponding TOC wt.% for the Wolfcamp B2 and B3 samples, segregated by 2nd order sequence stratigraphic position. From top to bottom, left to right: all samples; samples taken from the interpreted HST (marked in green); samples taken from the interpreted TST (marked in blue); and samples taken from the interpreted FSST and LST (marked in red and orange, respectively). Note varying correlation values. 161

Figure 31. Half-foot averaged molybdenum (Ni) concentration cross plotted with corresponding TOC wt.% for the Wolfcamp B2 and B3 samples, segregated by 2nd

order sequence stratigraphic position. From top to bottom, left to right: all samples; samples taken from the interpreted HST (marked in green); samples taken from the interpreted TST (marked in blue); and samples taken from the interpreted FSST and TST (marked in red and orange, respectively). Note varying correlation values and absolute ppm concentrations relative to Mo. 163

Figure 32. Inorganic and organic biogenic silica indicators. From left to right: Si / Al averaged over 0.5 ft., Zr / Si averaged over 0.5 ft. with axis reversed to indicate non-detrital Si, and (C₂₈ + C₂₉ tricyclic terpanes) / C₃₀ hopane, an organic geochemical indicator for the silica rich marine algae *Tasmanites*. Sequence stratigraphic framework on right for reference. 166

Figure 33. Organic and inorganic redox sensitive plant matter indicators. C₁₉ / C₂₃ tricyclic terpane ratio (left) compared to averaged Ni concentrations averaged over 0.5 ft. (ppm) (right). Controls on relative abundances indicated by arrows below respective depth plots, tenuous interpretations in stippled arrows. Sequence stratigraphic framework on far right for reference. 168

Figure 34. Inorganic and organic carbonate indicators. Calcium abundance averaged over 0.5 ft (w.t%) on the left and C₃₅ / C₃₄ homohopane ratio on right. Controls on relative abundances indicated by arrows below respective depth plots, with more minor controls in stippled arrows. Working sequence stratigraphic framework on far right for reference. 170

Figure 35. Summary figure showing changes in sedimentology, ichnology, inorganic geochemistry, and organic geochemistry in a sequence stratigraphic framework. From left to right: lithofacies log; core description; 2nd order sequence stratigraphic

interpretation; total bioturbation; *Zoophycus* ichnofossil; *Chondrites* ichnofossil; Pr/ Ph;
C₂₆/C₂₅ TT; Si / Al averaged over 0.5 ft.; (C₂₈ + C₂₉ TT) / C₃₀ hopane; C₁₉ / C₂₃ TT; and
Ni concentrations averaged over 0.5 ft..... 173

Table of Contents

Acknowledgments	iii
List of Tables	vi
List of Figures	vii
Abstract	xviii
1. Introduction	1
1.1. <i>Regional Geology</i>	2
1.2. <i>Permian Basin Evolution</i>	3
1.2.1. Lower Paleozoic ‘Passive Margin Phase’	3
1.2.2. Carboniferous ‘Collision Phase’	5
1.2.3. Permian ‘Basin Phase’	6
1.3. <i>Wolfcamp Stratigraphy</i>	8
1.4. <i>Objectives</i>	10
2. Methods	11
2.1. <i>Core Description</i>	11
2.2. <i>Petrography</i>	11
2.3. <i>Bioturbation and Ichnology</i>	11
2.4. <i>Inorganic Geochemistry</i>	12
2.5. <i>Organic Geochemistry</i>	13
2.5.1. Bulk Organic Geochemistry	13
2.5.2. Biomarker Analysis	13
2.5.2.1. Sample Selection	13
2.5.2.2. Sample Preparation	13
2.5.2.3. Soxhlet Extraction	14
2.5.2.4. Deasphalting	14
2.5.2.5. High Pressure Liquid Chromatography (HPLC) Separation	15
2.5.2.6. Molecular Sieving – Separation of Branched and Cyclics	16
2.5.2.7. Gas Chromatography (GC)	17
2.5.2.8. Gas Chromatography – Mass Spectrometry	17
3. Core Description	18
3.1. <i>Lithofacies</i>	18
3.1.1. Black mudstone	20
3.1.2. Laminated silty mudstone	20
3.1.3. Massive gray mudstone	21
3.1.4. Banded gray wackestone	21
3.1.5. Truncated packstone	21
3.1.6. Laminated packstone	22
3.1.7. Massive packstone	22
3.1.8. Coarse-grained wackestone	22
3.1.9. Heavily bioturbated	23
3.2. <i>Core Lithofacies Observations</i>	23

3.3.	<i>General Observed Stacking Patterns</i>	25
3.4.	<i>Lithofacies Association</i>	25
3.4.1.	<i>Sediment Gravity Flow Deposits</i>	26
3.4.1.1.	<i>Calciturbidite</i>	26
3.4.1.1.	<i>Transitional or Hybrid Flows</i>	28
3.4.1.1.	<i>Calcareous Debrite</i>	28
3.4.1.2.	<i>Distal Siliciclastic Turbidites</i>	29
3.4.2.	<i>Background Sedimentation</i>	29
3.4.2.1.	<i>Hemipelagic to Pelagic Sediments</i>	29
3.4.3.	<i>Potential Reworked Storm Deposits</i>	30
3.4.3.1.	<i>Contourites</i>	30
3.4.3.2.	<i>Tempestites</i>	31
3.5.	<i>Working Sequence Stratigraphic Framework</i>	32
4.	Petrography	36
4.1.	<i>Petrographic Microfacies</i>	36
4.1.1.	<i>Faintly laminated argillaceous silty mudstone</i>	38
4.1.2.	<i>Bioturbated silty mudstone</i>	38
4.1.3.	<i>Well sorted carbonate packstone</i>	39
4.1.4.	<i>Mixed carbonate siliciclastic wackestone</i>	39
4.1.5.	<i>Mudstone, non-laminated</i>	40
4.1.6.	<i>Poorly sorted coarse packstone</i>	40
4.2.	<i>Petrographic Environmental Associations</i>	41
5.	Bioturbation and Ichnology	51
5.1.	<i>Bioturbation and Oxygenation Assessment</i>	51
5.2.	<i>Observed Ichnogenera</i>	53
5.2.1.	<i>Chondrites</i>	53
5.2.2.	<i>Nereites</i>	54
5.2.3.	<i>Phycosiphon</i>	55
5.2.4.	<i>Planolites</i>	56
5.2.5.	<i>Zoophycos</i>	56
5.3.	<i>Ichnofacies</i>	57
5.3.1.	<i>Zoophycos Ichnofacies</i>	57
5.3.2.	<i>Nereites Ichnofacies</i>	58
5.4.	<i>Tiered Communities</i>	59
5.5.	<i>Bioturbation Observations and Interpretation</i>	59
6.	Inorganic Geochemistry	65
6.1.	<i>Lithofacies Major Elemental Distribution</i>	65
6.2.	<i>Lithofacies Minor and Trace Elemental Distribution</i>	68
6.3.	<i>Enrichment Factors and Caveats in Mixed Systems</i>	68
6.4.	<i>Trace Metal Paleoredox Proxies with Limited Detrital Influences</i>	69
6.5.	<i>Trace Metal Paleoredox Proxies with Strong Detrital Influences</i>	76
6.1.	<i>Redox Sensitive Organometallic Trace Element Proxies</i>	78
6.2.	<i>Paleoproductivity and Nutrient Minor Element Proxies</i>	81
7.	Organic Geochemistry	84
7.1.	<i>Bulk Organic Geochemistry</i>	84

7.1.1.	Overall Organic Matter Richness, Sources, and Maturity	84
7.1.2.	Changes in Organic Matter as a Function of Depth	92
7.2.	<i>Biomarkers</i>	100
7.2.1.	Acyclic Biomarkers	101
7.2.1.1.	n-Alkanes	101
7.2.1.2.	Pristane / Phytane	107
7.2.2.	Branched and Cyclics	113
7.2.2.1.	Sesquiterpanes	113
7.2.2.2.	Terpanes	115
7.2.2.2.1.	Tricyclic Terpanes	120
7.2.2.2.2.	Tetracyclic and Pentacyclic Terpanes	135
7.2.2.3.	Steranes	148
8.	Integrated Organic - Inorganic Geochemistry	159
8.1.	<i>Theoretical Refinement of Organic - Inorganic Geochemical Comparisons</i>	159
8.1.1.	Mo and Paleoredox Proxy - TOC Covariance	160
8.1.2.	Ni and Redox Sensitive Organometallic Proxy - TOC Covariance	162
8.2.	<i>Novel biomarker-elemental proxy correlations</i>	164
8.2.1.	Biogenic Silica and <i>Tasmanites</i> Biomarker Ratio	164
8.2.2.	Organometallic Trace Metal and Plant Matter Biomarker Ratios	167
8.2.3.	Ca Elemental Abundance and the Homohopane Index	169
9.	Conclusions	171
10.	Future Work	174
	References	176
	Appendix A. Core Photos, Core Description, and Lithofacies	198
	Appendix B. Petrography	219
	Appendix C. Inorganic Geochemistry	327
	Appendix D. Biomarker fractions, m/z 191 and 217 chromatograms	330

Abstract

The Permian-aged, hydrocarbon-rich, mixed carbonate-siliciclastic mudrocks of Midland Basin Wolfcamp B2 and B3 are highly heterogeneous, making paleoenvironmental reconstruction difficult. The high-frequency lithologic and geochemical variations in the examined core often fall below a 2-inch (~ 5 cm.) vertical resolution, warranting a novel inorganic geochemical interval averaging approach for geochemical comparisons. Conventional sedimentological techniques such as core description, petrography, and ichnology allowed for a localized application of a regionally accepted 2nd order sequence-stratigraphic framework. Inorganic and organic geochemical techniques were then applied to further corroborate the paleoredox and paleoproductivity interpretation established by more sedimentologically based techniques.

The influence of 2nd order eustatic sea-level fluctuations and sediment gravity flow events on paleoredox conditions was confirmed. Combined geochemical and ichnological evidence suggest that the Wolfcamp B3 and B2 mudrocks were deposited under suboxic conditions, with relatively more anoxic conditions during lowstand and progressively more oxic conditions during transgression and highstand, respectively.

1. Introduction

The Midland Basin, located in West Texas, spans approximately 3,740 mi² (9687 km³) area and has been a proven petroleum province since its initial conventional hydrocarbon discovery in 1920 in the Spraberry Trend. The Wolfcamp Formation produced 50 million barrels of oil in 2011 alone making it one of the largest unconventional plays in the United States (Gaswirth, 2017). The combination of high TOC values, established organic nanoporosity, sufficient thermal maturity, and relative brittleness of the Wolfcamp Formation make it an excellent source rock and unconventional reservoir (Baumgardner et al., 2014).

The Wolfcamp Formation is often subdivided into several subintervals. One of the most oil-rich intervals is the Wolfcamp B2. The Wolfcamp B2 is comprised of thin beds which commonly alternate lithology and rock properties at a 2-inch (~ 5 cm.) level, particularly in the more basinal sections (Murphy, 2015). These small-scale changes in lithofacies, petrographic microfacies, degree of bioturbation, major, minor, and trace metal chemical composition suggest high frequency changes in the depositional environment (Cortez III, 2012; Baumgardner et al., 2014). Trace metal - organic geochemical relationships remain relatively elusive and are thought to reflect the small fluctuations in intermediary redox conditions. Furthermore, the application of sequence stratigraphic models has been met with varying success given the complexity of the mixed carbonate system (Kendall and Schlager, 1981; Gianniny and Simo, 1996; McLaughlin et al., 2004; Zecchin and Catuneanu, 2017).

Generalized carbonate platform sequence stratigraphic models have been successful in predicting highstand carbonate platform shedding and dominantly

siliciclastic deposition during sea level lowstand (Wilson, 1967; Brown and Fisher, 1977; Sarg, 1988; Hine, 2001; Moore, 2002; Hemmesch et al., 2014). However, the interplay between updip reef building rates, relative sea level rise during transgression, and the overall effect on paleoredox and the depositional environment is not fully understood. Sediment gravity flows are pervasive, particularly in the base-of-slope setting. Deciphering these stacking patterns as a function of relative sea level fluctuations is important for paleoenvironmental reconstruction. Wolfcamp B2 and B3 deposition occurred during a transitional phase in global climate, from the Late Paleozoic Icehouse predictable glacial cyclothem deposits of the Lower Pennsylvanian (Waite et al., 2015), to the global anoxic ocean event and extreme arid conditions associated with an end of Permian mass extinction (Grice et al., 2005; Hays et al., 2007; Sur, 2009). This transition in global climate further occludes the sequence stratigraphic reconstruction (Salisbury, 2014). The interplay between organic and inorganic geochemistry coupled with a rigorous sedimentological analysis of a representative core could assist in teasing out the individual variables responsible for the high-frequency heterogeneity of the enigmatic Wolfcamp B2 and B3 intervals.

1.1. Regional Geology

The Permian Basin extends from west Texas to southeastern New Mexico and consists of three main basins or sub basins – the western Delaware Basin, the eastern Midland Basin, and the southeastern Val Verde Basin. The Central Basin Platform separates the Midland and Delaware Basins and the Ozona Arch separates the Midland and Val Verde Basins. The Diablo Platform and the Eastern Shelf define the western and eastern extent of the Permian Basin, respectively (Figure 1). The Northwestern Shelf, the

southern expression of the Perdernal Uplift, bounds the Permian Basin on the north. The Ouachita-Marathon Thrust Belt is locally expressed as the Southern Shelf, bounding it to the south. The Horseshoe Atoll is located north of the Midland Basin (Keller et al., 1980).

1.2. Permian Basin Evolution

The evolution of the Permian Basin until the late Permian can be subdivided into three major phases: (1) the Lower Paleozoic 'Passive Margin Phase' spanning the Late Precambrian to Mississippian or 850 – 310 Ma., (2) the 'Collision Phase' spanning the late Mississippian through the Pennsylvanian or 310-299 Ma., and (3) the Permian 'Basin Phase' spanning the entire Permian or 299-251 Ma (Adams, 1965; Muehlberger and Dickerson, 1989; Ainaji, 2013).

1.2.1. Lower Paleozoic 'Passive Margin Phase'

The collapse of a transcontinental arch that extended from southeastern New Mexico to west Texas during the Precambrian and Cambrian caused a slow subsidence of the area. This subsidence was too slow to produce a structural basin and instead created a flattened coastal plain by the Early Ordovician. The Ellenburger Sea transgressed towards the northwest, depositing shelf carbonates of the Ellenburger Formation over the underlying nearshore clastics derived from the weathering of the underlying Precambrian basement (Adams, 1965).

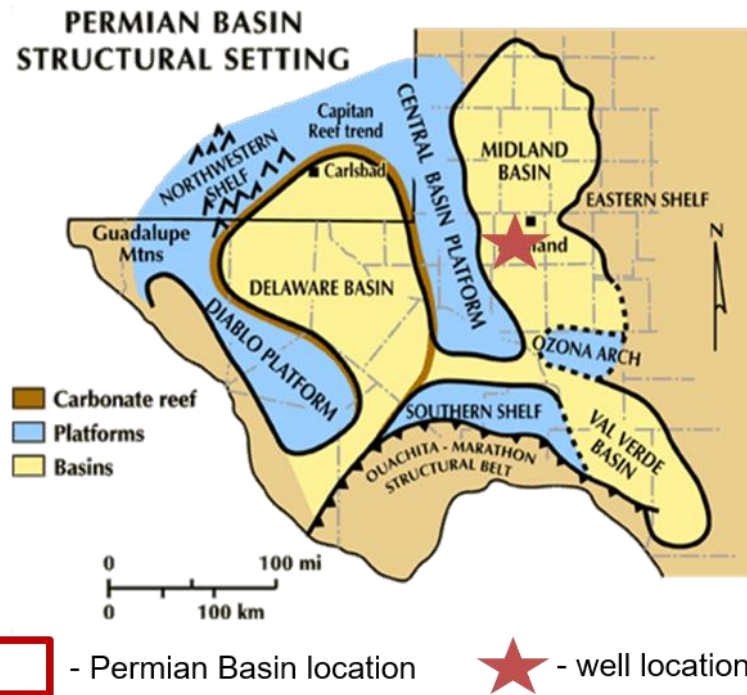
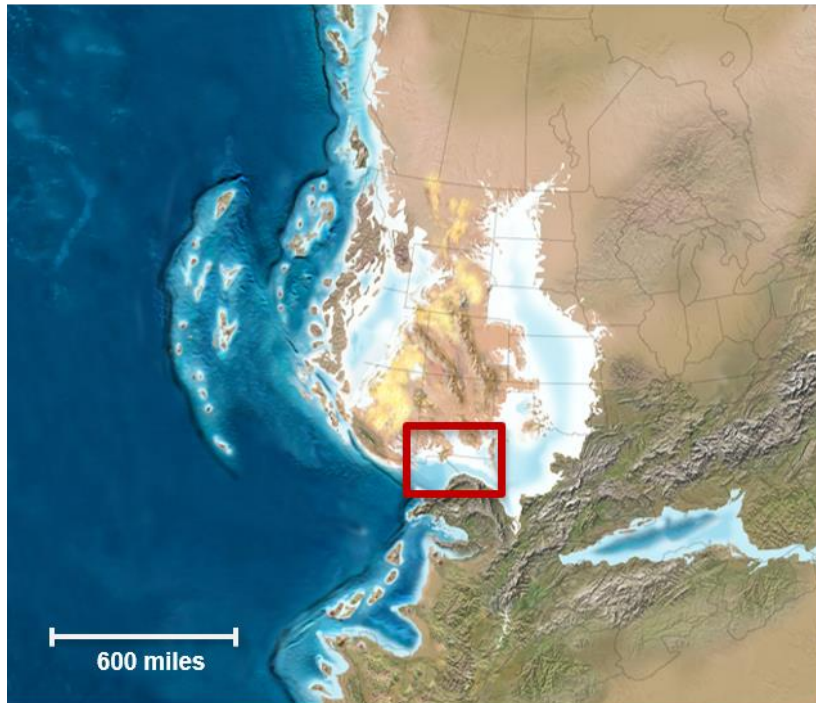


Figure 1. Paleogeographic map of Permian-aged North America, roughly 275 Mya (Blakey, 2003) on left, Red rectangle indicates location of Permian Basin. Zoomed in view of the Permian Basin, focusing on major structural settings, modified from Atchley et al. (1999). Red star indicates approximate well location.

Crustal warping divided the Lower Ordovician shelf into a series of sags and arches. During the mid-Ordovician, an approximately 350-mile (~ 563 km.) wide sag developed southwest of the North American Craton, gradually forming the shallow Tobosa Basin (Keller et al., 1980).

The second-order transgression continued throughout the middle Devonian depositing the Simpson, Montoya, Sylvan, and Fusselman formations successively. Sediment was shed from the surrounding Perdernal Massif and Texas Arch highs (Kottlowski and Stewart, 1970). An increase in the sediment supply during the mid-Ordovician caused the contemporaneous Simpson Formation to have significantly more clastic input compared to the later carbonate formations (Scotese et al., 1979). Although the Tobosa Basin was relatively deep by the late Ordovician, the more proximal areas were shallow, and well within the photic zone. This allowed for the extensive limestone deposition of the Montoya, Sylvan, and Fusselman carbonates up until the late Silurian (Adams, 1965). Over the course of these 35 million years, subsidence rates exceeded clastic sediment input and many areas of the basin were sediment starved. However, during the late Devonian and early Mississippian, sea level continued to rise, drowning out the shelf carbonate platform. This sea level rise deposited the regionally extensive, organic-rich Woodford Shale (Hemmesch et al., 2014).

1.2.2. Carboniferous 'Collision Phase'

Epeirogenic uplift deepened the eastern portion of the Delaware Basin and uplifted the Central Basin ridge during the Mississippian. Thick carbonates like the Kinderhook, Meramec-Osage, and Chester groups were deposited in the early and middle Mississippian. Although the Tobosa Basin began to deform in the Mississippian,

tectonism significantly increased in the Pennsylvanian with the collision of Gondwana and North America, known as the Marathon-Ouachita orogeny (Mazzullo, 1995). This collision formally subdivided the Tobosa Basin into the sub-basins known collectively as the Permian Basin. The subsequent formation of Pangea not only pushed the Permian Basin into an equatorial latitude ideal for carbonate production but increased clastic sediment input from newly eroding highlands. This dynamic tectonic setting allowed for the successive deposition of the complex lithologies of the Morrow, Atoka and Strawn formations. In general, these Pennsylvanian formations varied laterally from carbonate platforms on the basin edges to fine-grained siliciclastics in the deeper basin. The proximal late Pennsylvanian Canyon and Cisco Formations are time equivalent to the basinal Wolfcamp D formation, though their lithologies differ entirely (Algeo and Maynard, 2004; Waite et al., 2015).

1.2.3. Permian 'Basin Phase'

The early Permian was characterized by minimal tectonic activity, yet rapid basin subsidence. Thick sections of mudrock were deposited in the deeper parts of the basin due to the increase in accommodation space. These shales are often carbonate-rich, particularly in the later Leonardian series (Ewing, 2013). The three main carbonate platforms, the Central Basin Platform, the Northern Shelf, and the Eastern Shelf sourced the extensive debris flows and turbidites found throughout the Permian-aged Wolfcamp Formation, particularly in the Midland Basin (Figure 2). The Wolfcampian sedimentary sequence is the primary focus of this study.

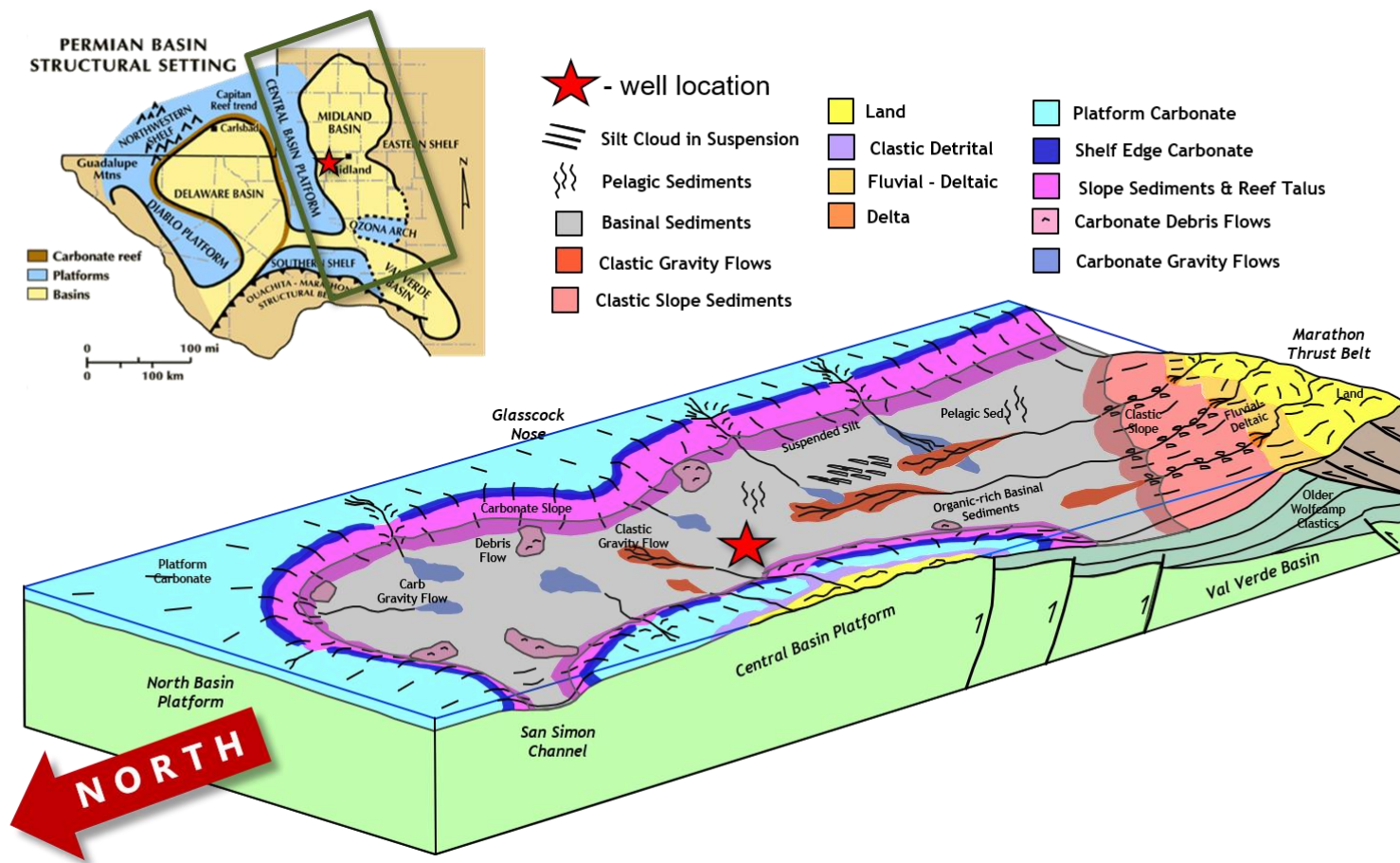


Figure 2. Midland Basin depositional block diagram depicting various depositional mechanisms, including carbonate and siliciclastic sediment gravity flows (modified from T. Reed, Pioneer Natural Resources, 2015). Permian Basin structural setting location map (top left) indicating Midland Basin in green rectangle (modified from Atchley et al., 1999) Note rotated orientation of block diagram. Red star indicates approximate well location.

1.3. **Wolfcamp Stratigraphy**

The Wolfcamp Formation can generally be subdivided into the Wolfcamp D, C, B, and A, from oldest to youngest. The more basinal portions of the Wolfcamp B within the Midland Basin consist of thinly bedded successions of alternating carbonate sediments and clastic mudstones (Fu, 2011; Baumgardner et al., 2014). Clastic input is primarily clay and silt sized grains, although coarser-grained siliciclastic deposits are found towards the Southern Shelf. The Wolfcamp Formation decreases in carbonate content away from the Central Basin Platform in a proximal-to-distal transect and generally thickening towards the east and south where clastic sediment input was greatest. The generalized stratigraphy and a hypothesized regional relative sea level curve are summarized in Figure 3. Within the understood regional sequence stratigraphic framework, the Wolfcamp B3 interval represents a relative 2nd order sea level fall and lowstand; whereas the Wolfcamp B2 is generally interpreted as a 2nd order transgressive systems tract transitioning to the highstand observed in the overlying B1 interval (Ross, 1963; Handford, 1981; Ross and Ross, 1995; Markello et al., 2011; Murphy, 2015). Smaller 3rd order sequences are thought to have occurred within the overall 2nd order Wolfcamp B2 transgression (Haq and Schutter, 2008; Rygel et al., 2008; Fu, 2011; Prochnow and Hinterlong, 2014). Although the regional context remains relatively well established, possibility that the observed sedimentological and geochemical changes within this single core represent a localized turbidite channel evulsion and a lateral shift in turbidite facies rather than a regional change in sea level and shore line trajectory cannot entirely be ruled out.

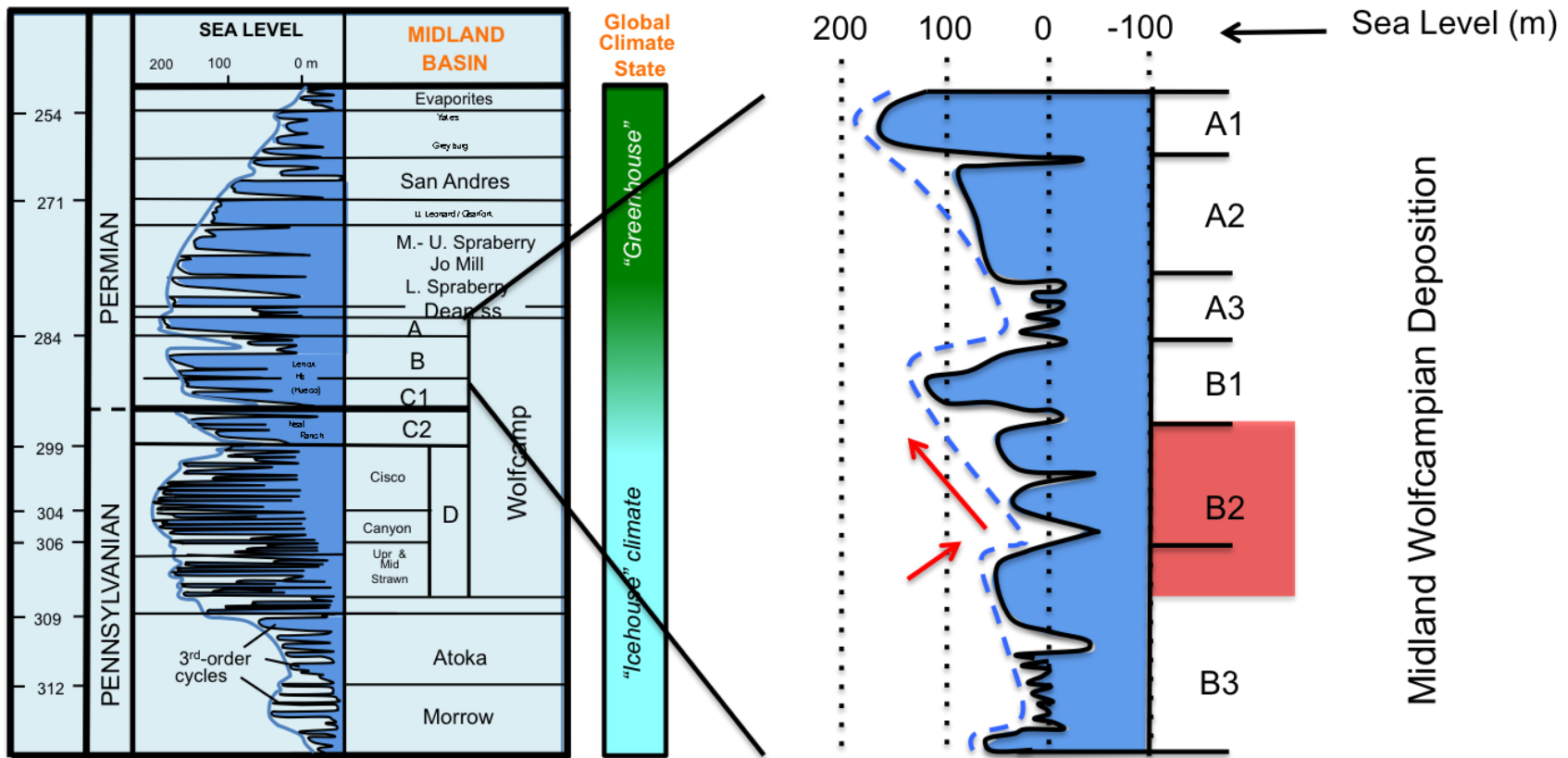


Figure 3. From left to right: Eustatic sea level curve, Midland Basin Stratigraphy, and global climate (icehouse-greenhouse) conditions from Pennsylvanian to Permian age and expanded regional sea level curve and Midland Wolfcamp Formation deposition with respective subintervals (Modified from Rygel et al., 2008). Please note that sea level curves are composite of second (blue solid and stippled lines) and third order cycles (filled-in blue curve). Red blocked area indicates cored Wolfcamp subintervals of interest, upper B3 and B2.

1.4. Objectives

The purpose of this study is to reconstruct the depositional environment within a sequence-stratigraphic framework from within an unnamed Wolfcamp B3 and B2 core, Midland County, Midland Basin, Texas utilizing a multidisciplinary approach of sedimentology, ichnology, petrography, and organic and inorganic geochemistry. Observed changes in water column conditions in the Wolfcampian Midland Basin played a critical role in the depositional history of the formation and the production and preservation potential of the organic matter. Continuous sedimentological characterization and trace fossil assemblage observations allowed for uninterrupted environmental reconstruction between geochemical sampling points. Organic geochemical biomarkers and inorganic trace metal composition per lithofacies were used to distinguish changes in the paleoredox conditions, water column structure, and organic source material.

Through an inorganic and organic geochemical comparison, this study attempts to resolve ambiguities surrounding the redox conditions and interplay between organic matter production versus preservation of the hydrocarbon rich Wolfcamp B3 and B2, and possibly narrow the productive interval with the B2. The geochemical effects and potential for bottom water re-oxygenation caused by the frequent turbidity currents were also investigated.

2. Methods

2.1. Core Description

Observed grain size, lithology, diagenetic alteration, and sedimentary features were used to develop a conventional core description. Then, six distinct lithofacies were identified and assigned to each preserved two-inch (~ 5 cm) interval of the core. Lithofacies were primarily characterized using the Dunham (1962) carbonate classification scheme. Both the conventional core description and the lithofacies stacking patterns were used to develop a working sequence stratigraphic model.

2.2. Petrography

Thin sections were prepared by TPS Enterprises. Samples were first impregnated with fluorescent blue epoxy resin using vacuum and high-pressure techniques. Specimens were then mounted to slides using a light cure adhesive, cut off, then ground to final thickness using water or oil as appropriate. Carbonates were ground to standard thickness, 30 μm , while mudstones were ground significantly thinner, (20 μm or less), to minimize grain overlap. Thin sections were either the smaller standard dimensions or oversized, depending on the amount of sampling available. Each thin section was stained with a 50:50 dual calcite (red) and ferroan dolomite (blue) stain.

2.3. Bioturbation and Ichnology

The degree of total bioturbation and destruction of the original sedimentary fabric was indicated by percentage from (0 – 100%). Furthermore, the qualitative abundance

of certain prevalent and environmentally diagnostic ichnofossils were denoted from 0 – 3, from absent to highly abundant respectively.

2.4. Inorganic Geochemistry

The non-destructive Bruker Tracer IV Hand-Held Energy Dispersive X-Ray Fluorescence (HH-ED-XRF) measures major elements heavier than sodium, but focuses primarily on those elements of geologic significance such as: Si, Al, Ca, Mg, Na, K, Fe, Mn, Ti, P, and S. Trace metals measured include Ba, V, Cr, Ni, Cu, Zn, Rb, Sr, Y, Zr, Nb, Mo, Th, and U. The Bruker Tracer IV HH-ED-XRF was set to emit rhodium x-rays at 40kV and 29 μ A over a span of 90 seconds. Major elements, which emit characteristic low energy K-shell x-rays between 1.25 – 7.06 kV, were measured with a vacuum pump filter allowing for the filtering of air between the silicon detector (SiPIN) and the sample window.

Trace elements, which have unique x-ray signatures between 6.92 and 19.80 kV, were measured with a corresponding high-energy setting. Major and trace elemental data was collected every 2 inches where possible along the slabbed core face from the depth interval 9700.84 - 9534.33 ft. (2956.82 – 2906.06 m.). The core face was thoroughly washed in order to ensure the removal of any salts or brines which would cause the Na peak to strongly coelute with the Ba (Ferret et al., 2003). The sample scan window is a 3 by 4 mm area. Visually observed major lithoclasts were avoided if possible. The core samples were stabilized face down on a plastic platform that ensures maximum surface area exposure with the detector, thus more accurate and consistent measurements. Beanbags were used to weigh down the core face flush on the detector.

2.5. Organic Geochemistry

2.5.1. Bulk Organic Geochemistry

Total organic content (TOC) and pyrolysis data, including S1, S2, S3, and Tmax, was collected by Weatherford Laboratories using standard LECO and Rock-Eval instrumentation, respectively. The core was sampled systematically every four feet for a total of 38 samples. Only a data table was provided. Pyrograms were not included.

2.5.2. Biomarker Analysis

2.5.2.1. Sample Selection

Nineteen samples were taken for biomarker analysis based primarily on two criteria: (1) each pre-described core facies is represented, TOC abundance permitting, and (2) an 8 ft. systematic sampling interval for every other TOC data point (every 4 ft.) to ensure that not only the high TOC intervals are analyzed in order to establish a more complete paleoceanographic record.

2.5.2.2. Sample Preparation

Samples of interest were slabbed off the back end of the viewing core using a wet saw located at in the Geological Sciences Department of Texas Christian University (TCU). A minimum of 30 grams for each sample was collected. Samples were then stored in sterile cloth bags and transported to the Organic Geochemistry Group Lab at The University of Oklahoma (OU) for sample preparation. Samples were photographed scrubbed using soap and water to ensure core orientation marks were removed, then

rinsed again with deionized water. Samples were then rinsed with methanol, then DCM, and left to dry for 24 hours prior to extraction. Samples were then crushed in a porcelain mortar and pestle and sieved to 40- mesh size (<355 um) and weighed.

2.5.2.3. Soxhlet Extraction

Soxhlet extraction requires that all glassware, cellulose thimbles, glass wool, boiling chips and acid activated copper are cycled for 24 hours with 1:1 (v:v) mixtures of CH₂Cl₂ (DCM) and CH₃OH (methanol) to ensure that they are free of organic contaminants. Samples were then placed in pre-extracted cellulose thimbles, packed with glass wool, and cycled with approximately 300 mL of a fresh 1:1 (v:v) mixture of DCM and methanol. Pre-extracted boiling chips were placed in 500 mL round bottom flasks to ensure continuous cycling of the solvent. Previously HCl activated copper balls were also placed in the round bottom flasks so that any sulfur in the crushed sample would complex to the surface as an oxide.

Extractions were performed for at least 48 hours or more depending on the mass and TOC of the sample. After the 48-hour cycling period, the sample extract was filtered through 150 mm filter paper to remove any fine sediment particles that may have cycled through the packed glass wool cellulose thimble during the extraction process. A rotary evaporator was used to evaporate the solvent from the sample extract. The potentially sulfide-complexed oxide copper balls were then removed.

2.5.2.4. Deasphalting

The extract was then separated into soluble and insoluble fractions, maltenes and asphaltenes, respectively. Total sample extracts exceeding 60 mg were subsampled, diluted with DCM, and transferred into their respective glass vials. The DCM was then

evaporated to ensure that none of the asphaltenes were in solution prior to the addition of the *n*-pentane (C₅H₁₂). The *n*-pentane was added to the extract by aliquot via a pasteur pipette at approximately 1:50 (m:m). Vials remained partly submerged in a sonicator to ensure the asphaltenes did not aggregate around the soluble organic material. The samples were then transferred to centrifuge tubes, then transferred to a freezer for a minimum of 12 hours. Samples were then centrifuged to ensure adequate separation of asphaltene and maltene fractions. Maltenes were transferred to 100 mL round bottoms where excess solvent was removed using a rotary evaporator. The maltenes were then transferred to empty pre-weighed 4mL vials where a nitrogen evaporator was used to remove the remaining *n*-pentane. Once sufficiently dried, the samples were weighed. Asphaltene fractions were transferred to pre-weighed 4 mL vials using DCM. Excess solvent was evaporated using a nitrogen evaporator and weighed.

2.5.2.5. High Pressure Liquid Chromatography (HPLC)

Separation

Maltene fractions exceeding 10 mg were diluted with *n*-hexane (C₅H₁₂) at a 10 mg/60 uL ratio for HPLC separation. Each sample injection is limited to the 60 uL at the previously specified dilution. Hexane, DCM, and a 98:2 (v:v) chloroform: methanol mixture were used to separate out the saturate, aromatic, and NSO polar compounds. The 46-minute HPLC method was adapted from by Dr. Nyguen as follows: 100% *n*-hexane flows at 4 mL/min for the first 4 minutes. From minute 4 to 5, the solvent composition progressively changes from 100% *n*-hexane to 70% *n*-hexane, 30% DCM. From minute 5 to 6, the flow rate progressively increases to 5 mL/min. From minute 12 to 13, the solvent composition progressively changes from 70% *n*-hexane, 30% DCM to 100%

DCM. From minute 14 to 16, the solvent composition progressively changes from 100% DCM to 100% 98:2 (v:v) chloroform methanol mixture. From minute 21 to 23, solvent composition progressively changes to 100% DCM. From minute 33 to 35, the solvent composition progressively changes to 100% n-hexane. From minute 44 to 46, the flow rate progressively slows back down to 4 mL/ min.

Fractions were collected in 100 mL round bottom flasks, which were manually switched out to collect fractions at their respective collection times. The saturate fraction was collected from the initial injection up until 4.7 min. The aromatic fraction was collected from 4.7 – 14.5 min. The NSO fraction was collected from 14.5 – 25.0 min. The remainder of the method (25.0 – 46.0 min) was used to clean the HPLC itself, particularly of polar compounds of the samples. Between sample runs, at least one blank run using the same method was executed to further ensure that the HPLC was clean and no cross contamination occurred. Sample fractions were then evaporated and weighed.

2.5.2.6. Molecular Sieving – Separation of Branched and Cyclics

Unweathered samples with maturity values less than an estimated vitrinite reflectance (Ro) of 1.0 tend to have saturate fractions dominated by n-alkanes. Molecular sieving techniques were employed in order to isolate the isoprenoids and cyclic saturate hydrocarbons for later analysis. Approximately half of the saturate fraction of each sample was sieved of the n-alkanes. A pasteur pipette was packed with pre-extracted glass wool and approximately 2 grams of activated HI-SiV 300. The packed molecular sieve column was then flushed 5 times with n-pentane with the aid of compressed air. Saturate fractions were diluted with n-pentane and transferred to the sieve column. The sieve column was then flushed with n-pentane repeatedly to ensure maximum recovery of branched and

cyclic saturates which were collected directly in a 4 mL vial. Excess solvent was evaporated with a nitrogen evaporator and the fraction weighed. The packed molecular sieve columns were stored and labeled in case the isolated n-alkane fraction was needed for analysis.

2.5.2.7. Gas Chromatography (GC)

Saturates were diluted with *n*-hexane (4 mg sample: 1 mL *n*-hexane) and run on a gas-chromatograph (Agilent 6890 series) with a split/splitless capillary injection system and equipped with a 30 m by 0.32 mm (i.d.) J&W scientific HP-5 Petro fused silica capillary column with a 0.25 µm film thickness. Samples were run using splitless injection mode with helium (He) as the carrier gas at a flow rate of 2 mL/min. Temperature was programmed and set at an initial temperature of 40°C with a 10-minute holding time; it increased to 300°C at a rate of 4°C/min and remained isothermal for 24 min with a detector temperature of 310°C.

2.5.2.8. Gas Chromatography – Mass Spectrometry

The branched and cyclic fractions were analyzed using gas chromatography-mass spectrometry (GC-MS; Agilent 7890A GC interfaced to a 5975C mass selective detector, MSD) on splitless injection mode. The capillary column of the GC was a 60 m by 0.25 mm J&W scientific DB-5MS with a 0.25 µm film thick coating. Specific ions for biomarker identification were analyzed using single ion monitoring (SIM). The temperature was programmed from an initial temperature of 40°C with 1.5-minute hold time; it increased to 300°C at a rate of 4°C/min and then remained isothermal for 34 minutes. Helium was used as the carrier gas with a 1.4 mL/min flow rate.

3. Core Description

A conventional core description, based on lithology, grain size, allochem assemblages, sedimentary structures, and boundary type was created in order to get a complete sedimentological record (see Appendix A). From this core description, distinct lithofacies were identified and are described in the following section. The stacking patterns of the lithofacies were then used to identify changes in the depositional environment, including inferred palaeoceanographic conditions. A continuous working sequence stratigraphic framework was created using the continuous core descriptions then cross-compared with other more intermittent, discontinuous, paleoenvironmental and palaeoceanographic data such as petrography, bioturbation, and inorganic and organic geochemistry.

3.1. Lithofacies

Nine discrete lithofacies were identified: black mudstone, laminated silty mudstone, massive gray mudstone, banded gray mudstone, truncated packstone, laminated packstone, massive packstone, coarse wackestone, and heavily bioturbated mudstone to packstone. Although there are parallel bioturbation indices, because of its paleoenvironmental significance, extensive bioturbated intervals were classified as their own facies. Observations for each lithofacies are summarized below with example images summarized in Figure 4. For additional core photographs and their associated lithofacies, see Appendix A. Lithofacies were assigned to every two inches of core for the interval 9539.00 - 9700.84 ft. (2907.49 - 2956.82 m.). The vertical resolution was matched by the XRF

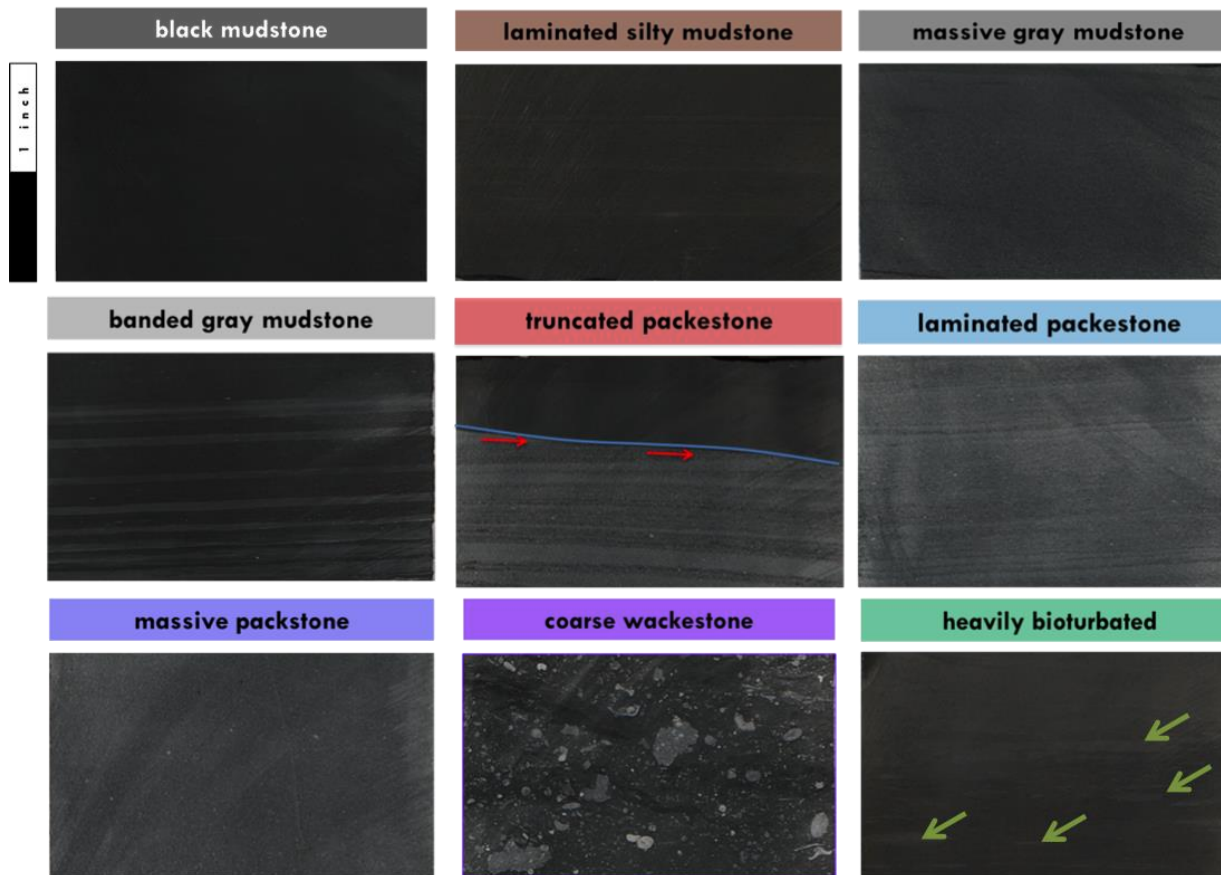


Figure 4. Representative examples of lithofacies. Lithofacies listed from left to right: black mudstone (9621.00 – 9621.17 ft), silty mudstone (9657.17 – 9657.33 ft.), massive gray mudstone (9660.67 – 9660.83 ft.), banded gray mudstone (9596.33 – 9596.50 ft), truncated packstone (9539.50 – 9539.66 ft.) blue line emphasizes contact and red arrows indicate truncated laminae, laminated packstone (9664.50 – 9664.67 ft.), massive packstone (9679.17 – 9679.33 ft.), coarse wackestone (9695.00 – 9695.17 ft.), and heavily bioturbated (9565.00 – 9565.17 ft.) where green arrows show burrows. Note scale bar and associated facies color

analysis for all 886 data points, which accounts for missing data points due to core breaks and uneven core face surfaces that impeded accurate XRF readings. Lithofacies were averaged over the two-inch interval rather than taken at the exact inorganic geochemical sample depth to have a more complete record of geologic time. Although this classification will allow for the lithofacies to more accurately reflect the holistic geology, the lithofacies may not accurately reflect the inorganic geochemical sample taken within the 2 by 4 mm scanning window, due to the high level of heterogeneity. The conventional Dunham classification scheme was used to describe this mixed siliciclastic carbonate system (Dunham, 1962). Siliciclastic grain sizes were almost exclusively clay to silt sized and hence categorized generically as a “mudstone” lithofacies.

3.1.1. Black mudstone

The massive, non-fissile, non-laminated, black mudstone is predominately composed of siliciclastic sediment, with little but variable carbonate mud. There is very little to no macroscopic bioturbation. No macroscopic sedimentary structures are visible. Secondary sedimentary structures include load features, flame structures, and other differential compaction structures. Dark reddish-brown ash beds are present but uncommon. Phosphatic nodules occur, although inconsistent and varied in abundance as a function of stratigraphic depth.

3.1.2. Laminated silty mudstone

The laminated silty mudstone is composed of clay- and silt-sized siliciclastic material. Silt sized grains are abundant within the planar to sub-horizontal laminae that are diagnostic of the lithofacies. Overall, the laminated mudstone is dark gray to dark

brown color and moderately well sorted. It often exhibits a sharp bottom contact with a sharp to diffuse top contact.

3.1.3. Massive gray mudstone

The well-sorted gray massive mudstone contains more carbonate mud and local carbonate shell fragments compared to both the black mudstone and the laminated silty mudstone. Heavy carbonate cementation is observed. There are no macroscopically visible sedimentary structures, aside from very faint planar laminations, and little to moderate bioturbation. Contact types vary from diffuse to sharp.

3.1.4. Banded gray wackestone

The banded gray wackestone is lithologically similar to massive mudstone but slightly coarser grained and more moderately sorted. Thin bands of massive light to medium gray carbonate wackestone frequently alternates with black mudstone and laminated dark gray mudstone within a 2-inch (~ 5 cm) interval. Bottom and top contacts are typically sharp. The banded gray wackestone appears to be heavily cemented. This lithofacies is rarely observed throughout the core, however since ash beds, which play a significant paleoproductivity role, have been other Wolfcamp B2 cores, they were given their own unique lithofacies (Murphy, 2015; Wickard, 2016).

3.1.5. Truncated packstone

The truncated packstone is lithologically similar to laminated packstone with the exception of a diagnostic sharp, typically angled, top contact that truncates the underlying laminations. Although this appears trivial, the truncating, erosive nature of the top contact

may have significant paleoenvironmental implications and warrants its own discrete lithofacies. Locally, opposing ripple directions are observed, indicating potential reworking. Phosphate nodules commonly overly the sharp contact.

3.1.6.Laminated packstone

The laminated packstone is light gray and almost entirely composed of .05 to 1 mm sized allochthonous carbonate skeletal fragments. Allochems are moderate to well sorted and include brachiopod, echinoderm, bivalve, and crinoid stem fragments. Allochems are deposited in laminar fashion. Planar to slightly inclined, continuous and discontinuous laminations occur. Small climbing ripples are rare. Common post-depositional features include contorted bedding, slumping, and differential loading.

3.1.7.Massive packstone

The massive packstone is similar to both the massive gray mudstone and the laminated packstone in texture and grain size, respectively. The massive packstone is coarser grained than the massive gray mudstone, however it has the same absence of primary sedimentary structures. The skeletal composition and grain size of the massive packstone is similar to that of the laminated packstone yet the allochems are slightly coarser and randomly orientated with no visible primary sedimentary structures. Heavy cementation is prevalent.

3.1.8.Coarse-grained wackestone

The coarse-grained wackestone is composed of large, mud-supported, poorly sorted, angular to subrounded, light gray lithoclasts and carbonate allochems. Allochems

include bivalves, brachiopods, bryozoan, and echinoderms. Small mm-scale carbonate allochems are chaotically mixed with cm scale lithoclasts. The large lithoclasts include eroded boundstone. Grains are predominantly randomly oriented with occasional subplanar orientation visible. Bottom contacts are undulate to sharp, erosive in nature, and exhibit differential loading. Top contacts are typically diffuse.

3.1.9. Heavily bioturbated

The heavily bioturbated lithofacies is similar in lithology and texture to massive gray mudstone but has faint color variation indicating burrowed and non-burrowed material. Burrow boundary definition varies from sharp in partial churned portions to diffuse in portions almost completely reworked. The majority of the primary sedimentary structures are destroyed. When distinguishable, the larger trace fossils, *zoophycos* and larger *chondrites* occur. Large discontinuous *zoophycos* burrows are parallel to subparallel to bedding, and often crosscut.

3.2. Core Lithofacies Observations

Important changes in thicknesses and observed lithofacies as a function of depth spanning from the base of the core at 9701 ft. to the top at 9539 ft. (approximately 2957 – 2907.5 m) are described in detail in the following section (3.3 General Observed Stacking Patterns) and summarized in Figure 5. These lithofacies stacking patterns play a critical role in interpreting the associated depositional environment and mechanisms that underpin the sequence stratigraphic framework.

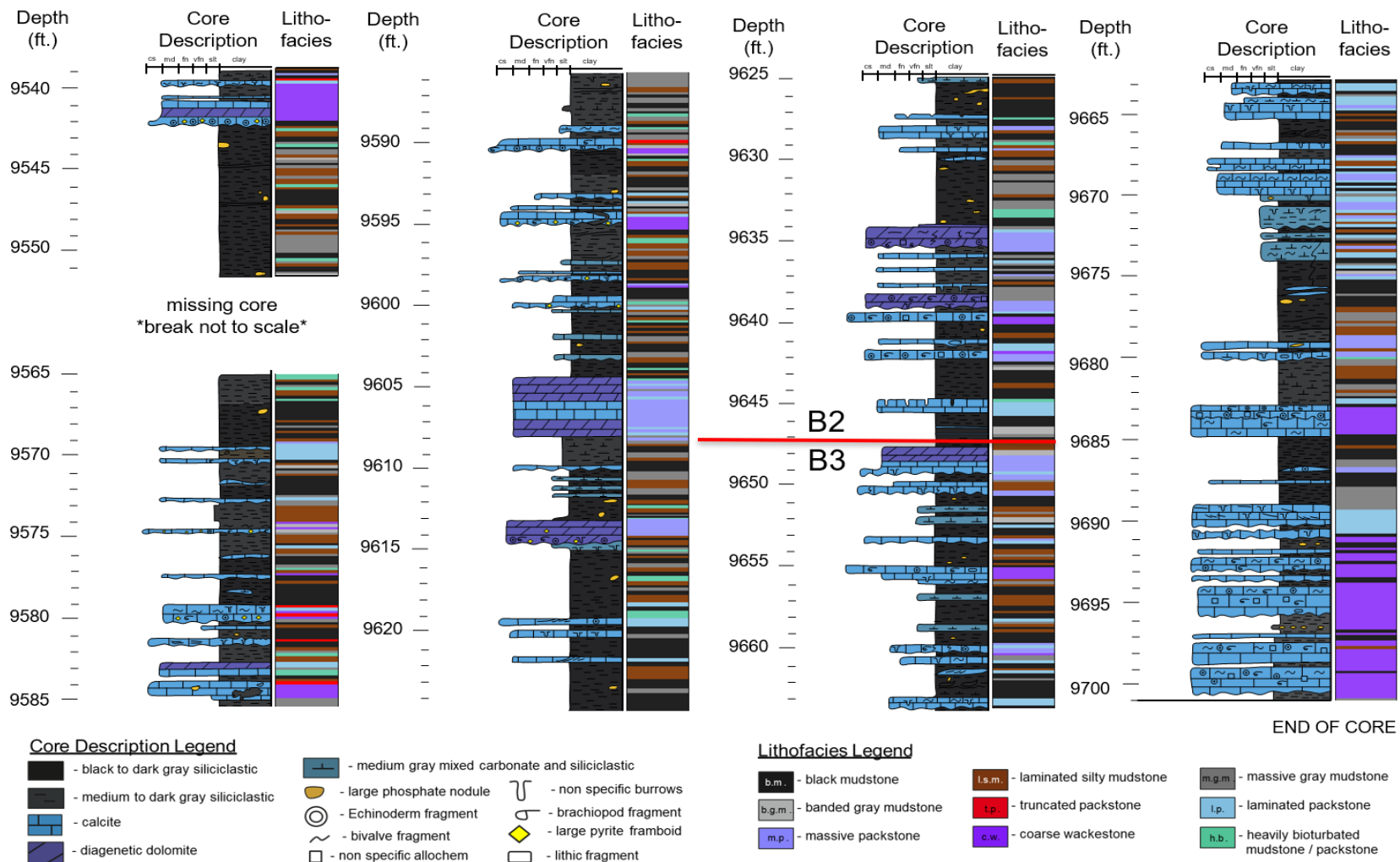


Figure 5. Core description (left) and lithofacies assignment (right) every two inches showing upscaled features. Note the Wolfcamp B2 – B3 contact in red. Note core break 9551-9565 ft. is not to scale. Lithofacies colors are corresponding to those delineated in Figure 4. Depth scales are to the left of each column.

3.3. General Observed Stacking Patterns

The thicker, coarse grained wackestone packages found towards the bottom of the core, mainly in the Wolfcamp B3 interval, were distinct from those further up section within the Wolfcamp B2. Lithoclasts range from 0.15–0.75 in. in diameter in the thicker packages compared to 0.01–0.10 in. in the thinner packages. The coarser wackestone packages are sparsely interbedded with mainly black mudstone.

Massive and laminated packstones were often found interbedded with each other, often interrupting the more siliciclastic deposition at random. Massive gray mudstones generally increased in frequency up section, and were densest between 9653–9585 ft., with a slight resurgence after the core break at 9551–9543 ft. These massive gray mudstones were mainly found interbedded with thin packages of laminated silty and bioturbated mudstones or overlying massive packstones.

The bioturbated lithofacies were often interbedded with the laminated silty and massive gray mudstones or directly overlying coarser carbonate packages, such as massive and laminated packstones. Banded gray wackestone was rarely observed but often found overlying the laminated packstones. The truncated packstones were only observed from 9590–9578 ft., usually overlying laminated and massive packstones as well as the finer grained, calcareous wackestones of the Wolfcamp B2.

3.4. Lithofacies Association

The observed stacking patterns expressed by many of the lithofacies can be associated with different depositional mechanisms within similar depositional environments. These lithofacies associations attempt to relate the descriptive lithofacies,

and to a lesser degree the petrographic microfacies later described, with genetic depositional mechanisms.

3.4.1. Sediment Gravity Flow Deposits

3.4.1.1. Calciturbidite

The massive and laminated packstones are interpreted as differing Bouma divisions of distal calcareous turbidites, or calciturbidites. Planar-laminated packstones are mainly considered part of the Bouma T_b unit. However, thin more clay-rich, yet carbonate grain supported, discontinuous planar-laminated packstones could be interpreted as Bouma T_e divisions. Laminations within the laminated packstone lithofacies can also be cross-laminated and even exhibit ripples. Observed ripples are both climbing and sediment starved, indicating both T_c and lower T_d Bouma divisions, respectively (Bouma, 1960). The banded gray mudstone is far more cryptic in terms of an associated depositional environment. However, when they are overly massive or laminated packstones, they can more confidently be interpreted as the upper flow regime settling out where the Bouma T_e is observed. This associated lithofacies interpreted as calciturbidites is summarized in Figure 6.

Discrete portions of the massive packstone, laminated packstone, or banded gray mudstone sometimes occur without the presence of the other lithofacies. This could be interpreted as differing portions of the flow regime being restricted to certain locations along a depositional transect. Facies reflecting the lower flow regime are commonly deposited in more proximal settings, whereas those facies reflecting the upper

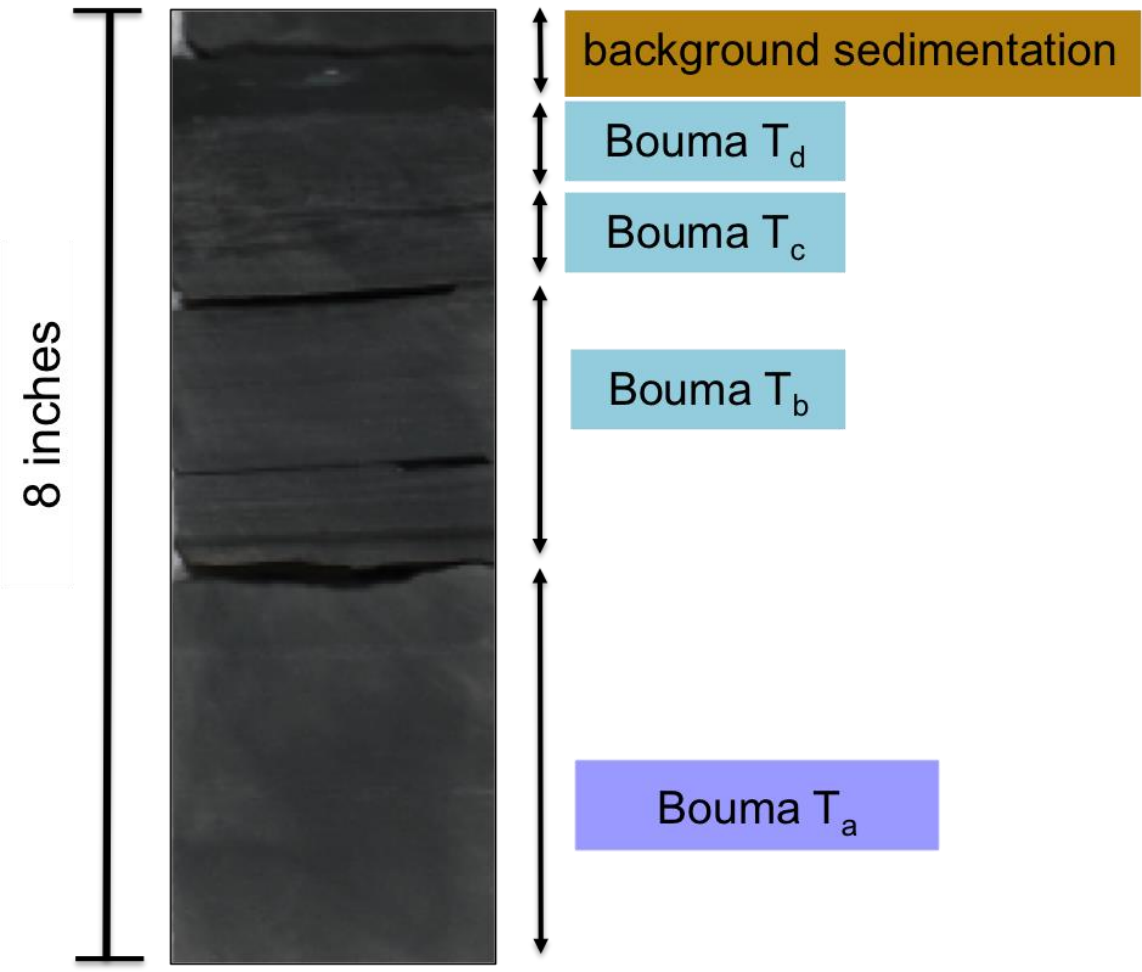


Figure 6. Example of small calciturbidite (<1 ft) observed at 9670.50 ft. Massive carbonate base interpreted as a Bouma T_a. Planar laminations interpreted as a Bouma T_b. Faint climbing ripples followed by discontinuous laminations interpreted as T_c and T_d respectively. Textureless black mudstone interpreted as hemipelagic to pelagic background sedimentation or Bouma T_e.

more distal setting, depending on the energy of the flow (Haughton et al., 2009). Therefore, interpretations can be made on the relative energy of flows if their point of origin remains constant (no shift in shoreline). Conversely, if isolated Bouma divisions and their relative frequencies are considered within the greater regional sequence stratigraphic framework, inferences can be made on shoreline shifts given the relative transport distances. Confidence in these interpretations generally decreases when individual lithofacies within the lithofacies assemblage are missing. Isolated carbonate beds may reflect deposit remobilization, not relative changes in flow energy or shifting shorelines

3.4.1.1. Transitional or Hybrid Flows

On rare occasions, the coarser massive packstones exhibit an irregular top contact, different from the more typical laminated packstone truncation observed towards the top of the B2 interval. These coarser, almost sand sized, massive packstones have so little clay that they border on being grainstones. The irregular top contact is draped by continuous black mudstone. The combination of very limited clay content, coarser and moderately well sorted, sand-sized carbonate lithoclasts, and non-reworked irregular top contact could be interpreted as a transitional sediment gravity flow, such as a grain flow (Haughton et al., 2009).

3.4.1.1. Calcareous Debrite

The majority of the coarse grained, poorly sorted wackestones are interpreted as higher-energy calcareous debrites, or “linked debrites” (Haughton et al., 2003). Higher confidence is placed in this interpretation for the thicker, coarser wackestone packages observed in the Wolfcamp B3 compared to the thinner, finer-grained, wackestones

observed in the Wolfcamp B2. Pebble sized, carbonate lithoclasts are interpreted as platform rip up clasts. Large, macroscopic allochems, such as bivalves, brachiopods, echinoderm, multichamber forams, and bryozoan fragments, suggest the carbonate material originated from a shallower, more proximal platform setting, which was later transported distally. The large size and high diversity of the allochem assemblage suggest that the platform they originated from was most likely a non-stressed environment with high biodiversity.

3.4.1.2. Distal Siliciclastic Turbidites

Laminated silty mudstone intervals are interpreted as distal siliciclastic turbidites. Ichnofossils *planolites* and *phycosiphon* were almost exclusively observed in the laminated silty mudstones and surrounding lithofacies, further indicating distal turbidite deposition (Follmi and Grimm, 1990; Algeo et al., 2004; Uchman et al., 2008). Faint laminations are composed of coarser grained silt-sized quartz grains, indicating a higher energy depositional mechanism than that of the black mudstone lithofacies. The laminated silty mudstones are generally interbedded with either a predominately siliciclastic lithofacies, such as black mudstone or the massive gray mudstone, suggesting an overall shift in sediment source.

3.4.2. Background Sedimentation

3.4.2.1. Hemipelagic to Pelagic Sediments

Uninterrupted deposition of black or massive gray mudstones are interpreted as hemipelagic to pelagic deposition, depending on the degree of biogenic input. However, without petrographic support, it is difficult to distinguish the biogenic contribution to the

sediment or the sediment transport mechanism, such as dilute hyperpycnal flows, hypopycnal hemipelagic, or pelagic deposition. Subtle detrital laminations only visible through thin section (explained in more detail later on) demonstrate a preference towards hemipelagic deposition interpretation (Garrison, 1990). Furthermore, many of these uninterrupted mudstones also contain phosphatic nodules. Phosphatic nodules high-nutrient conditions such as of upwelling systems and form at the oxic–anoxic boundary below the sediment water interface (Hatch and Leventhal, 1992). Although these uninterrupted mudstones may have been deposited via the same mechanisms, the background redox conditions during sedimentation may have been tied to larger sea level related redox conditions. As mentioned in the core description observations, a discrete interval within the B2 contains primarily black mudstone with relatively fewer phosphatic nodules than the black mudstone observed up section. Therefore, although certain meaningful associations between lithofacies and their depositional mechanism can be made, environmental conditions at the time of deposition aren't always the same.

3.4.3. Potential Reworked Storm Deposits

3.4.3.1. Contourites

The subplanar laminations of the truncated packstones are truncated by finer-grained, predominantly siliciclastic material. This irregular contact is unique in that usually erosive contacts have coarser grained material overlying them, indicative of a higher energy erosive mechanism. Finer grained sediments do not have the energy to scour underlying sediments – thus erosion must have occurred by other means. Contourites, or

bottom water contour current deposits, are a viable explanation. Persistent basin scale currents could have reworked the underlying calcareous turbidites and created this irregular top contact (Stanley, 1993). Phosphatic nodules commonly overly the truncated packstones, providing further evidence of bottom-water mobilization, such as the upwelling of deeper, more nutrient rich waters (Roe et al., 1982; Ece, 1990; Trela, 2008). These upwelling conditions are more indicative of transgression and high stand conditions, as a progressive sea level rise would enable better basin-wide circulation of previously more restricted waters. This progressive shift towards more highstand-like conditions agrees with the pre-established regional sequence stratigraphic framework previously mentioned (Algeo et al., 2004; Baumgardner et al., 2014).

3.4.3.2. Tempestites

An alternative depositional interpretation to the truncated packstones is that they are tempestites, or storm deposits. The low-angle, subplanar laminations could be interpreted as hummocky cross-stratification. Furthermore, the irregular top contact and truncated low-angle ripples and laminations may simply be wave reworked as energy from the event deposit dissipated (Einsele and Seilacher, 1982). Although this sedimentological distinction between a contourite and a tempestite may seem trivial, it has a significant impact on the sequence stratigraphic interpretation. While the contourite interpretation is in agreement with the large third order shift to progressive highstand conditions, the occurrence of tempestites could indirectly indicate the opposite, assuming there are no major changes in the sedimentary supply budget (Einsele, 1996). Since they first appear towards the top of the core, this may indicate a downward shift in the storm

wave base. A shift of that magnitude could indicate a drop in sea level, or lowstand conditions (Sageman, 1996; Molina et al., 1997). This drop in sea level may be reflect a more cryptic 3rd order sequence. Unfortunately, a large break in the core occurs just above of these truncated packstones, hindering a definitive interpretation. However, a relative drop in the storm weather wave base does not always imply a drop in sea level. As previously mentioned, Earth was starting to experience changes in global climate by the end of the early Permian. Storm intensification towards the end of icehouse conditions could cause progressively higher energy storm deposits to reach more distal parts of the Midland Basin (Ito et al., 2001).

3.5. Working Sequence Stratigraphic Framework

Given the observed stacking patterns of lithofacies, interpreted associated depositional environments, and the background knowledge of regional Wolfcamp B2 and B3 sequence stratigraphy in the Midland Basin, a working 2nd order sequence stratigraphic framework was created (Figure 7). The thick coarse-grained wackestone packages, interpreted as debrites, are more closely associated with a fall in sea level, or a falling stage systems track (FSST), which is delineated by red arrows. This definitively spans from the base of the core at 9700 ft. up to 9683 ft. (2956.5 - 2951.4 m). The overlying section from 9683 - 9647 ft. (2951.4 - 2940.4 m) is interpreted as a relative sea level low, or lowstand (LST), and is delineated in orange. The appearance of thicker laminated silty mudstone packages and lower energy calciturbidites is indicative of the reciprocal clastic sedimentation and relative decrease in energy, respectively, in a relatively more stagnant sea level low. An overall decrease in the amount of bioturbation towards the end of the LST suggests relatively more anoxic conditions towards the end

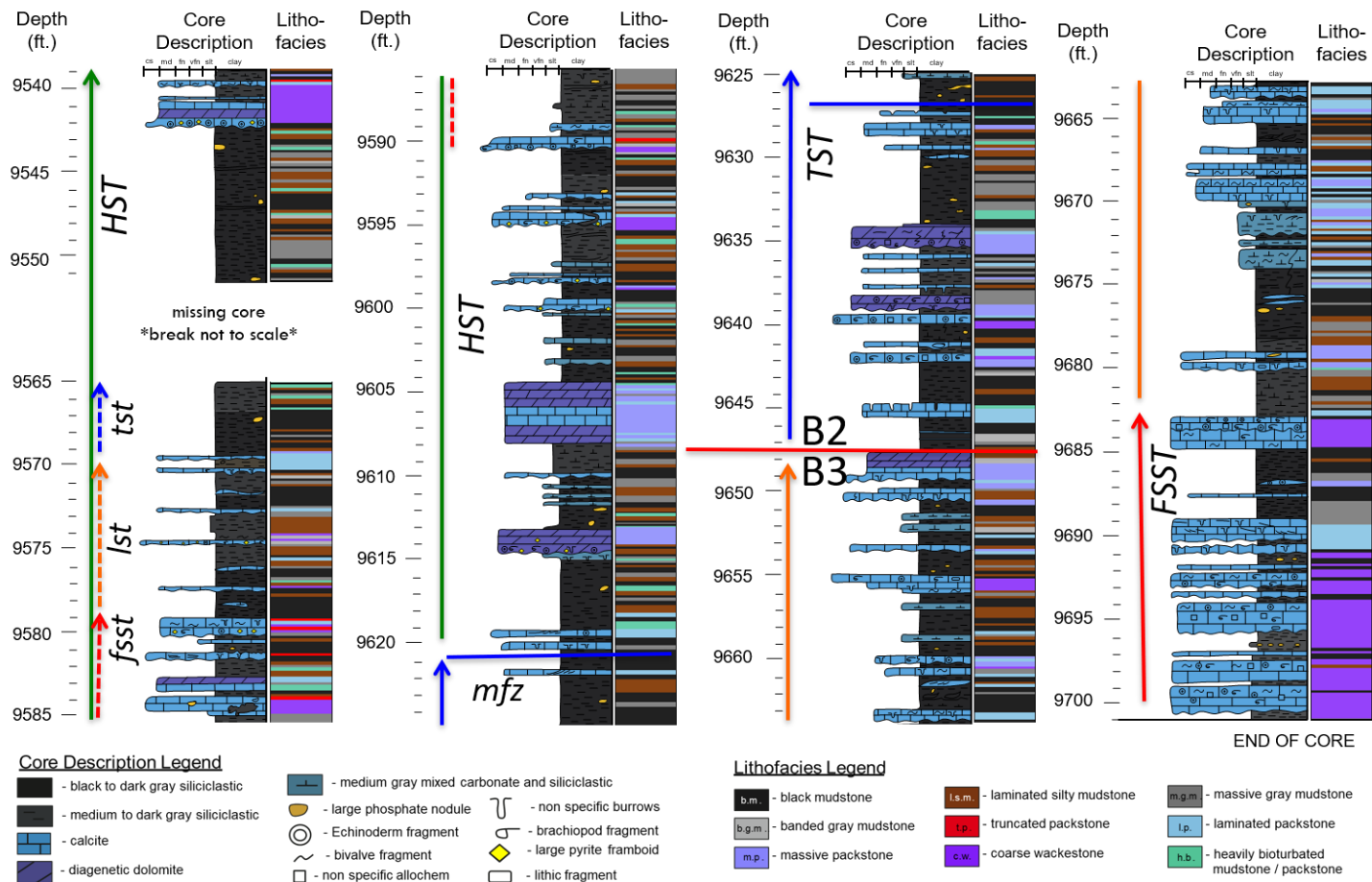


Figure 7. Working sequence stratigraphic framework, including 2nd order FSST, LST, TST and mfz, HST, and potential nested 3rd order cycles. Stippled lines reflect a decrease confidence in interpretation. Stacked arrows reflect parasequence scale changes within and overall higher order systems tract. Note that moving forward only high confidence interpretation and lowest order sequence stratigraphic interpretation will be carried across to other geologic and geochemical interpretations.

of the LST. The LST – TST (transgressive systems tract) transition is marked by a thick continuous calciturbidite package at 9648 ft. (2940.7 m) and is considered the contact between the Wolfcamp B3 and B2.

The onset of sea level rise, or transgression, is interpreted from the change in siliciclastic packages. Within the transgressive systems tract, calcareous and distal siliciclastic turbidites dominate the early and middle TST. These calciturbidites are progressively replaced by black, non-laminated mudstones, most likely representing hemipelagic or pelagic background sedimentation towards the end of the TST. Bioturbation is observed during the early and middle TST, indicating that there is an increase in oxygen after the LST. The ichnologically interpreted shift from relatively stagnant conditions to a progressively more open, well-circulated system with increased oxygen availability further supports the notion of sea level rise. The up section increase in the frequency of the black mudstone lithofacies coupled with a decrease in bioturbation is interpreted as yet another shift towards anoxic conditions and a sea level maximum. The six-foot zone, from 9627 – 9621 ft. (2934.3 - 2932.5 m), is the thickest most continuous package of interpreted pelagic or hemi pelagic deposition and is considered the maximum flooding zone, or *mfz*. The *mfz* is delineated by a blue arrow. Furthermore, the absence of potentially reoxygenating calciturbidites corroborates the paleoceanographic conditions of the interpreted sea level maximum. The decrease and then absence of the calciturbidites may indicate a progressively more distal basin setting associated with sea level rise and maxima, respectively.

An upsection increase in thin calciturbidites after the TST is indicative of highstand shedding from a productive carbonate platform that has caught up to sea level rise (Sarg,

1988). This interpreted high stand systems tract (HST) is delineated by a green arrow. These finer-grained HST calciturbidites are texturally distinct from the relatively coarser-grained LST calciturbidites (Vecsei and Sanders, 1997). However, the overall amount of carbonate decreases after the middle HST, creating an overall decrease in carbonate content throughout the core. Increased levels of bioturbation indicate potentially more oxygenating conditions associated with better ocean circulation related to highstand conditions.

The first occurrence of the truncated packstone at 9590 ft. (2923 m) could be interpreted in one of two ways. If the truncated packstones truly represent contourites and the development of strong, persistent bottom water contour currents, then this section would be considered continued highstand deposition. However, if the truncated packstones are interpreted as a series of tempestites, then a small, 3rd order sea level drop may be inferred. The presence of thick packages of distal siliciclastic turbidities overlying the potential tempestite packages further bolsters the argument for a 3rd order scale variation. A small fall in eustatic sea level would be followed by lowstand constituted by the primarily siliciclastic deposition observed from 9580 - 9570 ft. (2920 – 2917 m). The onset of parasequence scale transgression could then be marked by the resurgence in frequency of the heavily bioturbated facies. These parasequence scale variations are marked by the stippled lines of their respective colors on the inside of the HST sequence scale green arrow. Due to the overlying 14 ft. (~4.3 m) core break, it is extremely difficult to interpret the depositional environment, and hence relative sea level, for that part of geologic time. The increase in siliciclastic deposition coupled with a decrease in the frequency of thin calciturbidites, towards the end of the HST, particularly after the core

break, potentially suggesting a decrease in energy of system. However there heavily bioturbated lithofacies is frequently observed at the same interval, suggesting a continued oxygen rich environment. Due to this ambiguity surrounding a potential nested 3rd order sequence, the 2nd order sequence stratigraphic interpretation will be used moving forward. It will be used to contextualize data with a lower vertical sampling rate and resolution, such as petrographic and geochemical data.

4. Petrography

4.1. Petrographic Microfacies

Thin section sampling was limited to those samples with material remaining after organic geochemical analysis. Additional petrographic samples were taken from underrepresented lithofacies without Rock-Eval data, such as those that more calcareous and organic lean. Thin sections were either the smaller standard dimensions or oversized, depending on the amount of sampling available. Each thin section was stained with a 50:50 dual calcite (red) and ferroan dolomite (blue) stain. Due to the highly interbedded nature of the Wolfcamp Formation, multiple petrographic microfacies were commonly identified within a single thin section. Petrographic microfacies variation often fell below the 2 inch (~5 cm) vertical resolution of lithofacies assignment and inorganic geochemical analysis. Six major facies were identified from 21 thin sections. Representative samples of each petrographic microfacies are summarized in

Figure 8. See Appendix B. Petrography for additional micrographs.

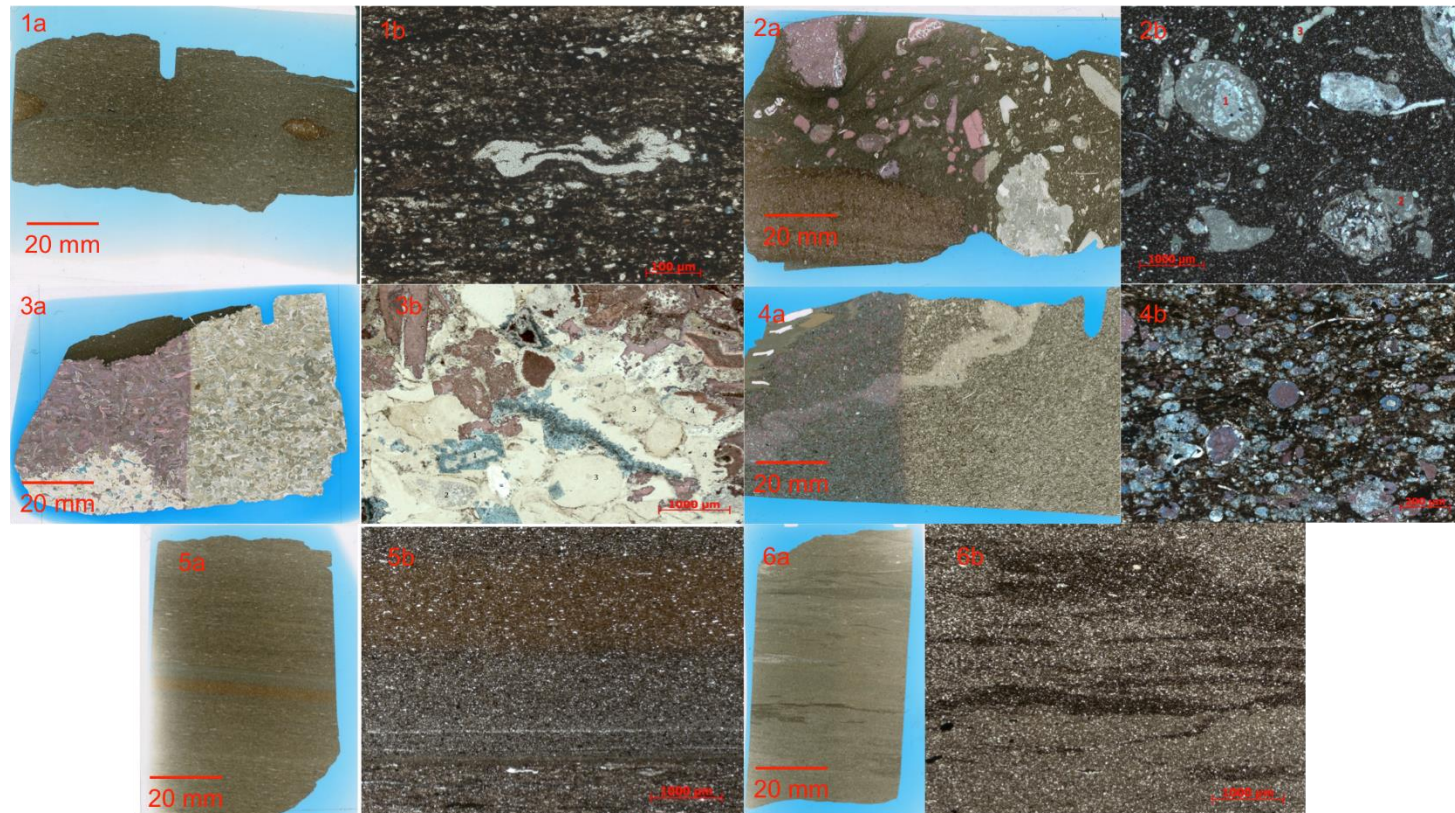


Figure 8. Examples of petrographic microfacies where number refers to petrographic microfacies and “a” and “b” refer to macroscopic and microscopic thin section images, respectively. 1) non-laminated black mudstone (9625.17 ft.), 1a) *chondrites* burrows visible, 1b) *Tasmanites* with organic matter infill; 2) poorly sorted coarse packstone (9697.17 ft.), 2a) matrix supported large lithoclast sand allochems 2b) red numbers indicate allochems as follows 1 large multichamber foram 2. shattered multi-chamber foram 3. echinoderm spine fragment; (3) well sorted carbonate packstone (9690.84 ft.); 3b) cement infill and replacement 4) mixed carbonate siliciclastic wackestone (9594.66 ft.) 5) faintly laminated silty mudstone (9657.17 ft.); 6) bioturbated silty mudstone (9585.17 ft.) 5b) intense bioturbation only leaved OM rich discontinuous laminations. Note scale bars and staining. Red indicates calcite and dark blue indicates ferroan dolomite.

4.1.1. Faintly laminated argillaceous silty mudstone

Faint laminations are usually visible from full thin section view and vary in thickness and color. Three laminations types were observed and are as follows: (1) cm thick faint bands of light tan or buff color, (2) mm thick white lamination of almost entirely detrital quartz and aligned silica rich agglutinated forams or *Tasmanites*, and (3) cm thick reddish-brown colored band, with less detrital quartz relative to the previous two lamination types. Bioturbation is typically limited to horizontal burrows and is relatively sparse so that the laminations and other sedimentary structures are still preserved. Agglutinated forams are generally more abundant than *Tasmanites*.

4.1.2. Bioturbated silty mudstone

Bioturbation ranges from moderate to heavy, with either discontinuous wavy laminations to complete churning of original sedimentary structures with no evident laminations or banding. Large (0.5 – 1.5 cm) horizontal burrows composed of cleaner coarser sediment typically truncate the discontinuous laminations. Agglutinated forams, and more rarely *Tasmanites* and radiolaria occur. Organic rich layers are commonly those most disrupted by horizontal burrows. Samples that are heavily bioturbated appear cleaner and devoid of organic material. Calcareous components are commonly restricted to diagenetic dolomite (non-ferroan and ferroan) replacement of non-carbonate material. Carbonate allochems compose less than 5% of the total matrix.

4.1.3. Well sorted carbonate packstone

Well-sorted carbonate allochems within the packstone exhibit varying degrees of abrasion. Mud constitutes up to 15% of the matrix but does not inhibit grain-to-grain contact with the majority of allochems. Mud was primarily observed in two main fabric types: (1) discrete organic rich clay rip ups often present as laminations and (2) individual pockets of partially micritized allochems. Heavy diagenetic alteration of replacive calcite, dolomite, and ferroan dolomite is commonly observed. The ferroan dolomite is commonly selectively zoned to clay rich laminations. Selective microcrystalline quartz, or chalcedony, recrystallization of certain allochems is present but limited. Oxides are abundant. Pyrite is visible as both small and large euhedral framboids, densely packed near lithologic contacts. Grain edge dissolution limited allochem identification. Allochems include: echinoderm spines, brachiopods, bivalves, multichamber forams, radiolara, sponge spicules, and to a minor extent, gastropods.

4.1.4. Mixed carbonate siliciclastic wackestone

The moderately well sorted carbonate allochems are matrix supported. The matrix is composed of argillaceous clays, micas, and minimal silt-sized detrital quartz. The percentage of matrix to the total sample ranges from 30% - 60%. Matrix grain size can range from clay to very fine silt. Allochem assemblages were less diverse relative to other carbonate dominant petrographic microfacies and restricted to a narrower grain size range of 50 to 250 um in length. Allochems include echinoderm spines, bivalve fragments, radiolara, and sponge spicules. Mutichamber forams are present, although not as abundant. Cement is typically observed as intragranular and replacive, with less common intergranular cement, usually limited to those allochems with grain-to-grain contact.

Macroscopically, a diagnostic stippled or salt and pepper fabric in the full thin section view identifies this petrographic microfacies. Grain boundary dissolution is relatively common, particularly with the more dolomitized allochems. Silty lithic fragments are present but uncommon. Oxides are present but infrequent.

4.1.5. Mudstone, non-laminated

The non-laminated organic rich mudstone has significantly less visible detrital quartz than the other siliciclastic dominant petrographic microfacies. No distinct laminations are observed, only the horizontal alignment of agglutinated forams. *Tasmanites* are partially compressed with varying amounts of organic matter infilled. Some of the agglutinated detrital quartz incorporated in forams is partially replaced by ferroan dolomite. Radiolaria are present. Small (300 μm) horizontal burrows are present but sparse. Burrows lack finer clays and organic matter. Elongate silt clasts are subangular and show evidence of shearing.

4.1.6. Poorly sorted coarse packstone

Relative to the other petrographic microfacies, the poorly sorted coarse-grained packstones has the most diverse allochem assemblage: large bryozoan, brachiopods, multichamber forams, echinoderm spines and shells, and bivalves. Notably, the petrographic microfacies lacks the smaller allochems abundant in other petrographic microfacies such as radiolaria, *Tasmanites*, and agglutinated forams. Aside from the diverse fossil assemblage, large lithoclasts comprised of previously lithified carbonate material are abundant. Mud content and degree of cementation within the lithoclasts varies. Lithoclast and allochem diameters are highly variable, ranging from 100 μm – 2

cm. Allochems and lithoclasts edges are typically abraded and sub-rounded to angular and with sharp clean edges. Macroscopically, differential compaction and deformation of underlying of clay rich material are frequently observed. The degree of grain-to-grain contact is variable, however, allochems and lithoclasts are generally mud supported. Ferroan dolomite cement is relatively sparse. Common silica replacement of internal carbonate allochem structure preserves original allochem texture or replaces is entirely. The matrix is comprised almost entirely of mud with silt-sized carbonate fragments and minimal detrital silt.

4.2. Petrographic Environmental Associations

The observed petrographic microfacies at their respective depths are listed in Table 1. Given the disparity in number of samples between petrographic microfacies and lithofacies identifications, it is difficult to definitively say that a single lithofacies can be truly petrographically characterized. Furthermore, given the number of thin sections, not all lithofacies were sampled. Hence the petrographic microfacies themselves are not used to further define the lithofacies themselves but rather generally compared to which lithofacies they were observed within Table 2. The depositional environment was also interpreted by utilizing the petrographic microfacies interpretations at the specific depths and comparing it to overall sedimentological interpretation based off the holistic core description, which will be discussed at length.

Table 1. Distribution of petrographic microfacies as a function of depth.

Petrographic microfacies						
Sample Depth (ft.)	Faintly laminated silty mudstone	Bioturbated silty mudstone	Well sorted carbonate packstone	Mixed carbonate siliciclastic wackestone	Non-laminated mudstone	Poorly sorted coarse packstone
9577.17	X		X			
9585.17		X				
9593.17	X		X	X		
9594.66				X		
9617.17	X					
9625.17					X	
9633.17		X				
9641.17				X	X	
9644.67			X	X		
9645.17			X			
9647.84		X				
9649.17			X			
9653.17	X		X	X		
9657.17	X					
9665.34	X					
9673.17	X			X		
9681.17	X			X		
9683.17						X
9689.17			X			
9690.84			X			
9697.17						X

Table 2. Petrographic microfacies observed within specific lithofacies.

Petrographic Microfacies	Black Mudstone	Laminated silty mudstone	Massive gray mudstone	Banded gray Mudstone	Truncated packstone	Laminated Packstone	Massive Packstone	Poorly sorted coarse packstone	Heavily bioturbated
Faintly laminated silty mudstone		6	1	1					
Bioturbated silty mudstone			1	1					1
Well sorted carbonate packstone				1		4	4		
Mixed carbonate siltstone / wackestone		1		1		1	2	1	
Non-laminated mudstone	1					1			
Poorly sorted coarse packstone								3	

Up to three individual petrographic microfacies were observed in certain thin sections, reemphasizing the difficulty in characterizing the small-scale (<2 inch) variation in the Wolfcamp B3 and B2. The core description, lithofacies, and working sequence stratigraphy aided in the petrographic environmental reconstruction. The bottom four thin sections representing the upper middle Wolfcamp B3, spanning core depths 9697.17 to 9683.17 ft. (2955.70 - 2951.43 m) are poorly sorted to well-sorted packstones. As previously mentioned, the Wolfcamp B3 is interpreted as a falling stage and relative lowstand, with abundant carbonate debris flows (Murphy, 2015). The poorly sorted, coarse packstone petrographic microfacies is often found in conjunction with the coarse-grained wackestone lithofacies and associated with these debrites. The well-sorted carbonate packstone petrographic microfacies is associated with more proximal or higher energy turbidites, relative to those represented by the mixed carbonate-siliciclastic wackestone. Coupled, these petrographic microfacies represent higher energy environments, indicative of the carving and shedding of the adjacent unstable carbonate platform during relative sea level fall (Grammer and Ginsburg, 1992; Vecsei and Sanders, 1997).

Further up section, faintly laminated silty mudstone and mixed carbonate and siliciclastic wackestone are present for two samples at depths 9681.17 and 9673.17 ft. (2950.82 and 2948.38 m), respectively. The change in petrographic microfacies suggests a relative decrease in the energy of the depositional environment. Finer carbonate grains / smaller allochem sizes and increased mud content in the carbonate dominate petrographic microfacies coupled with the first presence of a purely siliciclastic petrographic microfacies could be interpreted a transitional deposit and progressive shift

from a falling stage systems tract to a lowstand systems track (Hunt and Tucker, 1992). The lower energy associated with the transport of finer grain material relative to the underlying the debrites or the cleaner, high-energy turbidites may indicate sea level stabilization. Furthermore, the previous drop in sea level may have environmentally stressed the Central Basin Platform, reducing the carbonate sediment budget available for shedding (Murphy, 2015). The presence of the faintly laminated silty mudstone shows progressive increased siliciclastic input from the more clastic shelves.

In the upper Wolfcamp B3, for the depths 9665.34 and 9657.17 ft. (2946.00 and 2943.51 m), the faintly laminated silty mudstone petrographic microfacies is the only observed petrographic microfacies. The absence of significant carbonate sediment may indicate that the once stressed Central Basin Platform carbonate factory has now completely shut down. Therefore, the only sediment deposited is from siliciclastic sediment gravity flows sourced from the distant Eastern Shelf. Conventional carbonate platform models identify these siliciclastic packages in edge-of-slope and basinal tracts as reciprocal sedimentation during lowstand (Wilson, 1967; Sarg, 1988; Osleger and Montañez, 1996).

Three finer-grained petrographic microfacies, the faintly laminated silty mudstone, the well-sorted carbonate packstone, and the mixed carbonate siliciclastic wackestone, are observed at 9653.17 ft. (2942.29 m). This petrographic microfacies assemblage represents concurring flow events from mixed lithologic sources. These interbedded, mixed lithology, low-energy, distal to medial turbidites may be indicating the end of lowstand conditions and the onset of sea level rise. Allochthonous carbonate material may be shedding from the updip carbonate platform which, experiencing the onset of

relative sea level rise, may have begun to ramp up production (Crevello and Schlager, 1980; Andresen et al., 2003). The presence of faintly laminated silty mudstone however indicates that the distal siliciclastic turbidites remain the dominant mechanism for siliciclastic deposition to the basin. It is therefore interpreted that the degree of sediment bypass and subsequent siliciclastic deep-water deposition is less relative to earlier distinctly lowstand conditions (Murphy, 2015). The working sequence stratigraphic framework derived from the lithofacies stacking patterns sedimentologically corroborates this end of lowstand/ onset of transgression, petrographic interpretation. At the end of Wolfcamp B3 deposition, represented at the study area at a depth of 9649.17 ft. (2941.067 m), only the well sorted carbonate packstone petrographic microfacies is observed. As previously mentioned, the well-sorted packstone could be associated with a higher energy turbidity current shedding of the carbonate platform that has begun to catch up with the transgression (James and Macintyre, 1985).

During the onset of Wolfcamp B2 deposition, represented stratigraphically in the core at a depth 9647.84 ft. (2940.66 m), the first petrographically distinct bioturbated silty mudstone occurs. Although bioturbation is present in almost all siliciclastic petrographic microfacies, the extensive laminations and matrix fabric disruption defines this bioturbated petrographic microfacies. As previously mentioned, the Wolfcamp B2 has been interpreted as the onset of a transgressive systems tract (Murphy, 2015). This relative or eustatic increase in sea level could lead to localized oxygenation within the Midland Basin in three ways: (1) with a eustatic rise in sea level, oxygenated waters from the Panthalassa Ocean could re-enter the restricted basin, (2) a relative sea level rise could reinitiate localized basin scale currents in the previously stagnant lowstand Midland

Basin, or (3) eustatic or localized sea level rise increased platform shedding in the way of oxygen entrained-turbidity currents (Cortez III, 2012). Whether due to eustatic or localized, autogenic processes, relative oxygenation is inferred from evidence of newly established hospitable conditions for borrowing aerobic organisms (Wetzel, 1984; Follmi and Grimm, 1990; Kozur et al., 1996).

The transition from the observed underlying bioturbated silty mudstone petrographic microfacies at 9647.84 ft. (2940.66 m) to a well-sorted carbonate packstone petrographic microfacies at 9645.17 ft. (2939.85 m), during the independently sedimentologically identified early transgression, may indicate that updip carbonate production increased (Sarg, 1988). However, the subsequent coupled observance of the well-sorted carbonate packstone and mixed carbonate siliciclastic wackestone petrographic microfacies at 9644.67 ft. (2939.70 m) indicates more distal, lower energy, carbonate turbidity currents relative to previous well-sorted carbonate from edge of slope to basinal. Due to this shift in depositional setting and longer transport distance, finer grained suspended clays entrained in the carbonate dominated turbidity currents may settle out. This finer argillaceous material may have previously bypassed the base of slope setting (Sumner et al., 2012; Talling, 2014). However, a change in the rate of sea level rise could also have the same observed lithologic implication. The rate of sea level rise may have exceeded the rate of reef build up. A stressed reef updip would account for the observed decrease in carbonate material relative to siliciclastic material (Wilmsen, 2000). Whether due to a basinward shift of the study area, a drowning of the carbonate platform, or both, the trend in increasing siliciclastic material continued as the transgression progressed.

By depth 9641.17 ft. (2938.628 m), both the mixed carbonate and siliciclastic wackestone and non-laminated mudstone petrographic microfacies are observed. This is the first observance of the non-laminated mudstone petrographic microfacies indicating hemipelagic to pelagic deposition of clays (Garrison, 1990; Baumgardner et al., 2014). This coupled petrographic microfacies is depositionally interpreted as background sedimentation episodically punctuated by distal carbonate turbidites. The relatively more clay rich mudstone is overlain at depth 9633.17 ft. (2936.19 m) by bioturbated silty mudstone. Episodic distal turbidites have switched from a carbonate to siliciclastic further highlighting the lack of carbonate production during towards the end of transgression. The degree of bioturbation could indicate that either the episodic turbidity currents brought entrained oxygenated water and opportunistic burrowing organisms down to the basinal areas (Folmi and Grimm, 1990; Hallworth et al., 1993; Ozalas et al., 1994; Uchman et al., 2008) or sea level rise allowed oxygenating ocean currents to form (Ozalas et al., 1994).

The non-laminated mudstone petrographic microfacies, observed at 9625.17 ft., stratigraphically represents the inferred maximum flooding surface within the Wolfcamp B2 interval. The limited carbonate material and detrital silt, lack of continuous laminations, and absence of abundant bioturbation indicates pelagic or hemipelagic deposition in a relatively oxygen limited, lower energy, deep marine environment (Garrison, 1990). Observed *tasmanites* with organic infill and sparse radiolara indicate an increase in biogenic primary production, and thus slightly oxygenated water column conditions (Kidder and Erwin, 2001; Ikeda et al., 2016). However, the degree of terrigenous organic material remains unknown via petrographic analysis alone and requires geochemical

techniques to resolve the ambiguity. Therefore, the depositional mechanisms and dominant organic matter origin during the relative sea level maximum remains undetermined. The fine-grained sediment petrographically observed could have been deposited by suspension settling, by extremely dilute siliciclastic sediment gravity flows, or both. Given the argillaceous nature of the clays and the lack of interstitial micrite in the non-laminated mudstone petrographic microfacies, it can be inferred there was a decrease in the carbonate material budget. Carbonate platform growth may have been unable to keep up with the rate of sea level rise towards the end of sea level rise. The effectively drowned reef may have been unable to shed carbonate material to basinal areas (James and Macintyre, 1985; Wilmsen, 2000).

At 9617.17 ft. (2931.31 m), there is an observed shift to silty laminated mudstone indicating higher-energy siliciclastic deposition. This shift to a coarser, siliciclastic petrographic microfacies may reflect the transition to sea level highstand, before carbonate production had ramped up. After the 5 ft. (1.5 m) thick massive packstone package observed in the core beginning at 9608 ft. (2928.52 m), the petrographic microfacies observed include a distinctly fine-grained carbonate material mixed with silty mudstones. Mixed carbonate-siliciclastic wackestone, observed at 9594.67 ft. (2924.46 m), followed by combination of laminated silty mudstone, well sorted packstone, and mixed carbonate-siliciclastic wackestone, observed at 9593.17 ft. (2924 m), indicates an increase in progressively differently sourced concurrent turbidity flows (Osleger and Montañez, 1996). Furthermore, the progressively higher-frequency lithologic variability of the petrographic microfacies could indicate that both the Central Basin Platform and Eastern Shelf were both experiencing highstand conditions. Therefore, the hybrid

carbonate-siliciclastic platform model is preferred, rather than a pure carbonate model, in which significant siliciclastic material is deposited only as a function of reciprocal sedimentation during lowstands (Wilson, 1967),

The bioturbated silty mudstone petrographic microfacies, observed at 9585.17 ft. (2921.56 m), is well within the core interval exhibiting an increase in the frequency of the bioturbated lithofacies from 9580 - 9608 ft. (2920 - 2928.5 m). This congruence indicates a progressively more oxygenated environment and better ocean water circulation, typical of highstand conditions (Ozalas et al., 1994; Taylor et al., 2003). Towards the top of the Wolfcamp B2 section, at a depth of 9557.17 ft. (2913.03 m), the petrographic microfacies combination of laminated silty mudstone and well-sorted carbonate packstone occurs. The presence of the two relatively cleaner, lithologically different petrographic microfacies may indicate highstand sediment shedding from both the carbonate platform and siliciclastic shelves are matched.

Although the petrographic sampling was at a lower vertical resolution and more inconsistent relative to that of lithofacies and inorganic geochemistry, the three top-most samples did overlap with the potentially nested fourth order cycle (Figure 3). There was no definitive petrographic evidence of this higher order cycle; Only fine-grained carbonate and siliciclastic sediment was observed, limiting the possibility that a fourth order regression occurred. Furthermore, the bioturbated petrographic microfacies was observed within this ambiguous fourth order cycle, where prior to this point this petrographic microfacies, and its' lithofacies counterpart, was previously observed in the more well-constrained third-order transgression and highstand. Although this

inconsistency does not definitely eliminate the possibility of the nested fourth order cycle, it does indicate that a lower sampling density can occlude its interpreted presence.

5. Bioturbation and Ichnology

5.1. Bioturbation and Oxygenation Assessment

Ichnofossils are trace fossils, or burrows, created by organisms most suited for their environment. Assemblages of certain ichnofossils, or ichnofacies, have long been associated with distinct benthic depositional environments. The development of these benthic communities is controlled by several ecological limiting factors, such as: oxygen availability, salinity, substrate consistency, turbulence and bottom water energy, rate of deposition, and sometimes by disturbance events (such as storms, turbidity currents, ash falls) (Seilacher, 2007). A reduction in species diversity and individual trace fossil size indicates a reduction in endobenthic activity from these ecological stresses (Taylor et al., 2003). Hence, observations in ichnofossil diversity, abundance, and assemblage aid in paleoenvironmental reconstruction efforts. Each burrowing organisms' ability to handle varying degrees of oxygenation is of particular importance for sequence stratigraphic interpretation (Pemberton and MacEachern, 2005). A completely anoxic environment, devoid of all dissolved oxygen, is inhospitable to macroscopic borrowing organisms. However, degrees of dysoxia can be interpreted by the relative oxygen depletion each ichnogenera can endure (Savrda and Bottjer, 1986; Taylor et al., 2003). As in most geologic interpretations, the presence of one line of evidence, or singular burrow, is not enough to make a depositional environment or redox condition interpretation. It is best

practice to take into account the cumulative evidence of the diversity and assemble of various ichnofossils in conjunction with geochemical and sedimentological evidence (Schultz and Rimmer, 2004). There are inherent limitations and biases with an ichnological approach such as lack of lithologic color contrast, massive bedding or absence of preexisting sedimentological structures, and poor trace fossil preservation conditions. Erosive sediment gravity flows (and their corresponding core facies) create numerous biases in the ichnofossils and fabrics preserved in the rock record. Lower portions of tiered communities are preferentially preserved, which under-represent endobenthic communities that inhabit the sediment closer to the sediment – water interface. Furthermore, erosive flows can eliminate evidence of communities, and hence environmental conditions, during background (non-episodic) sedimentation. Lastly, given the comparative sedimentation rates of these flows and background hemipelagic fall out, sediment gravity flows will over-represent those ichnofauna suited for those conditions, regardless of the degree of erosion (Minter et al., 2016). Well-sorted, lithologically homogenous facies have very little color contrast which create a separate bias in ichnofauna identification. Without a disruption in linear features, such as laminations, or lithologic contrast (grain size and/ or color), burrows become increasingly difficult to identify. Therefore, lithologically homogeneous facies absent of sedimentary structures, such as massive portions of calcareous turbidites and non-laminated mudrock, have fewer recorded visible trace fossils. Petrographic methods are employed in attempts to mitigate these effects. Bioturbation was observed to varying degrees almost entirely throughout the core. Observed trace fossils included *Chondrites*, *Nereites*, *Phycosiphon*, *Planolites*, *Teichichnus*, and *Zoophycos* and are summarized in Figure 9.

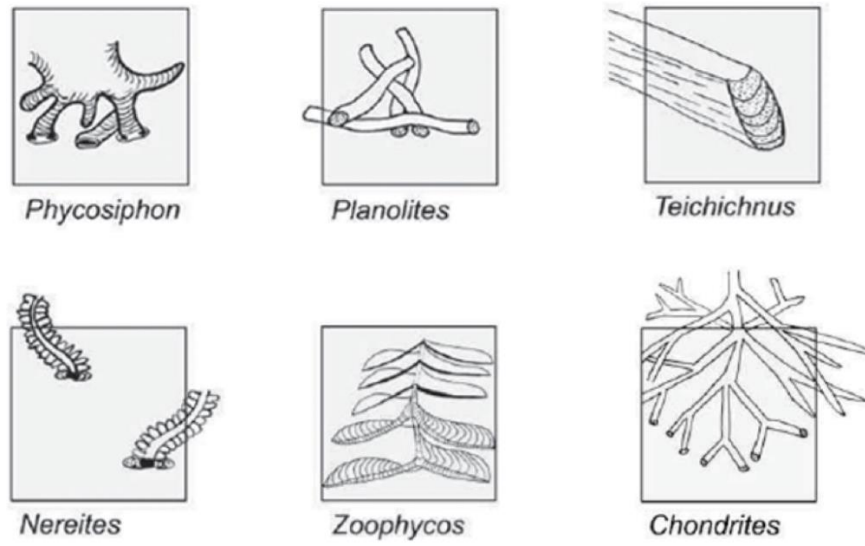


Figure 9. Schematic of observed trace fossils *Chondrites*, *Nereites*, *Phycosiphon*, *Planolites*, *Teichichnus*, and *Zoophycos*. Grayed out square represents visible 2D surface on core face (Bromley and Ekdale, 1984).

5.2. Observed Ichnogenera

5.2.1. *Chondrites*

These burrows are dendritic, equally sized, root-like tubes extending from a central shaft. Usually, only the branched tubes are cross cut, appearing like dark circles of equal diameters along bedding planes. The vertical shaft is locally cross cut in which the central tube is perpendicular to bedding, with branches oblique and parallel to bedding. These burrows are thought to have been created by deposit feeding organism in both anoxic and oxic environments (Bromley and Ekdale, 1984). In more oxygenated environments,

they comprise the lowest member of the tiered community, farthest away from the oxidizing pore waters near the sediment-water interface (Savrda and Bottjer, 1986). In more anoxic environments, *Chondrites* are found usually in low diversity communities with decreased burrow diameters. Although stressed, *Chondrites*, are more suited for dysaerobic environments compared to other ichnogenera, and hence indicative of anoxic environments (Bromley and Ekdale, 1984). These deposit-feeding organisms systematically mine a single location for unoxidized organic matter.

5.2.2. *Nereites*

Visually, *Nereites* are easily identified by the white halo of spreiten found around the edges of the oblong tubes. *Nereites* are differentiated from the *Phycosiphon* by the smaller burrow diameter. *Nereites* tube diameters range from 0.5 mm – 1.5 cm, roughly an order of magnitude larger than *Phycosiphon* (Ekdale et al., 1984). The meandering *Nereites* trace may be densely spaced and vary from circular to more oblong depending on the degree of compaction and the substrate consistency. They occur in a variety of settings, but more commonly on the top surface of thin turbidites at the base of slope and abyssal plain setting (Hu et al., 1998). Discussion surrounding the nature of *Nereites* as it pertains to turbidites and rapid sedimentation centered around two schools of thought: that these burrowing organisms were escaping the new sediment load (Kuenen, 1957) and that they were opportunistically inhabiting a temporary dysoxic environment (Seilacher, 1962). Overwhelming evidence has since favored the later interpretation. *Nereites* is one of the primary ichnogenus found in the *Nereites* Ichnofacies, which will be explained in greater detail further on.

5.2.3. *Phycosiphon*

Phycosiphon burrows are narrow U-shaped lobes arranged in an antler-like system extending from a central shaft (Wetzel, 1984; Wetzel and Uchman, 1998). In cross-section, these burrows are 0.8 – 1.5 mm in diameter with dark center and white spreiten halos. *Phycosiphon* are passively grazing organisms on the surface of the sea floor. *Phycosiphon* are adapted to a wide range of grain sizes and are normally absent in continuously accumulating fine-grained deep-sea sediment. This indicates that *Phycosiphon* is transported from the shelf or slope to deeper environments, potentially by sediment gravity flows (Wetzel, 1984). With higher dissolved oxygen content in these settings compared to of the ambient deep water, *Phycosiphon*, is thought to indicate a relative increase in bottom water oxygenation in a typically dysaerobic to anoxic setting (Seilacher, 1967).

Phycosiphon has a lower probability of appearance if turbidites are less frequent with long reoccurrence time. It is speculated that only two turbidity currents per 1000 years are necessary maintain the burrow forming exogenous fauna if background sedimentation does not exceed 50 cm/ 1000 years. More frequent turbidity currents (20-200/ 1000 years) would be necessary to establish a reproducing, formally exogenous, *Phycosiphon* community (Wetzel, 1984). Relative sediment rate fluctuations could be calculated given the presence of episodic versus long standing *Phycosiphon* burrows. The presence of *Phycosiphon* allows the identification of low density, distal, siliciclastic turbidites that are more difficult to identify without the aid of photomicrographs relative to their carbonate counterparts. Therefore, the persistence presence of *Phycosiphon* could indicate frequent yet faint, distal siliciclastic turbidites.

5.2.4. *Planolites*

Planolites are simple, unbranched cylindrical burrows infilled by a different lithology compared to the host rock. The burrows are straight or gently curved, roughly 1-5 mm long, and horizontal or oblique to bedding planes (Pemberton and Frey, 1982). Burrows often cross cut each other. Various invertebrate could be responsible these burrows which are typically found in shallow and deep marine environments. However, these burrows have been found in alluvial, lacustrine, and aeolian environments (Ekdale et al., 2007). In deep marine environments, the presence of *Planolites* indicates dysoxic to oxic conditions. *Planolites* have a lower tolerance for oxygen depletion relative to other traces such as *Chondrites*, *Teichichnus*, *Helminthopsis*, and sometimes *Zoophycos* (Savrda and Bottjer, 1986; Ekdale and Mason, 1988; Neal, 2015).

5.2.5. *Zoophycos*

Zoophycos burrows are spreiten-filled structures are comprised of numerous but small U- and J-shaped burrows that vary in length and orientation, depending on the stress on the system. Spreiten are arranged in a helix-like pattern in a circular shape around a central shaft. It is uncommon to find the central shaft in cross-section and burrows are generally lobate (Wetzel, 1984). The burrowing organisms responsible for *Zoophycos* live under dysoxic to anoxic conditions with consistent, non-episodic, background sedimentation rates (Olivero, 1996; Li et al., 2017). *Zoophycos* is found in both shallow and deep marine depositional settings, but is mainly associated with slope, base-of-slope, and basinal environments. *Zoophycos* is commonly associated with the appropriately named, *Zoophycos* ichnofacies however, it can be found within other

ichnofacies such as *Cruizana* and *Nereites*. Therefore, the presence of *Zoophycos* alone does not indicate the *Zoophycos* ichnofacies (MacEachern et al., 2012).

5.3. Ichnofacies

Ichnofacies are an assemblage of ichnofossils that are indicative of a certain depositional environment. There are a total of eight marine ichnofacies: *Trypanites*, *Teredolites*, *Glossifungites*, *Psilonichnus*, *Skolithos*, *Cruziana*, *Zoophycos*, and *Nereites* (Wetzel and Uchman, 1998; Taylor et al., 2003; Gingras et al., 2011). The *Zoophycos* and *Nereites* ichnofacies are the dominant ichnofacies present in the edge-of-slope and basinal environments and therefore are emphasized in this thesis.

5.3.1. Zoophycos Ichnofacies

Trace fossils commonly found in the *Zoophycos* ichnofacies include *Phycosiphon*, *Zoophycos*, *Chondrites*, and *Spirophyton*. These organisms tend to burrow in firmer substrates formed during slow hemipelagic to pelagic background sedimentation (Miller, 1991). Hence, the *Zoophycos* ichnofacies is associated with fine-grained, cohesive muddy to sandy substrates, with local variations in oxygen deficiency. Shallower tiers of the ichnofacies are found in soft grounds, whereas deeper tiers are found in stiff or hard grounds, depending on the depositional setting (Ekdale, 1985; MacEachern et al., 2012). The *Zoophycos* ichnofacies is usually found in low energy settings, below storm wave base, ranging from the shallow continental shelf to abyssal zone, but generally limited to the slope and abyssal plain settings (Seilacher, 1967; Frey and Seilacher, 1980; Frey et al., 1990). When found in the same depositional setting as the *Nereites* ichnofacies, the

Zoophycos ichnofacies is associated with slower sedimentation and less dissolved oxygenation relative to the *Nereites* Ichnofacies (Uchman and Wetzel, 2011).

5.3.2. *Nereites* Ichnofacies

Common trace fossils include *Helmenthoidia*, *Spiroraphe*, *Lorenzina*, *Chondrites*, *Paleodictyon*, *Nereites*, and *Cosmorhapse* (Seilacher, 2007). The main difference between the *Nereites* Ichnofacies and the *Zoophycos* Ichnofacies is the presence of organized grazing burrows with complex planar surface structures, or graphoglyptids (Ekdale, 1985; Uchman, 2003; MacEachern et al., 2012). Graphoglyptids have only been found in sediments directly after low-density distal turbidites in deep basins, and hence require a softer substrate and relatively more oxygenated conditions. Low-energy storm generated debris flows, or tempestites, are the shallow water shelf setting equivalent of these low energy turbidites (D'Alessandro et al., 1986). Given that these graphoglyptids are observed after event deposits sedimentologically sourced from proximal areas, it is hypothesized that the exogenous burrowing organisms originated in more proximal areas and were transported distally with the sediment gravity flows (Wetzel, 1984; Follmi and Grimm, 1990). Ichnosubfacies of the *Nereites* ichnofacies exist along a proximal to distal transect of turbiditic systems: *Ophiomorpha rudis*, *Paleodictyon*, and *Nereites* respectively (Uchman, 2009). To a lesser degree, this same relationship exists along a turbiditic lobe axis to fringe transect (Phillips et al., 2011; Monaco et al., 2012). Therefore, the distal assemblage of the *Zoophycos* Ichnofacies overlaps with the *Nereites* Ichnofacies in a very niche depositional environment: background sedimentation punctuated by episodic, distal turbidity currents occurring at the base of slope and abyssal plain settings.

5.4. Tiered Communities

Tiered communities are assemblages of ichnofossils that inhabit different depths at or away from the sediment water interface at the same instance geologic time. These organisms preferentially burrow at different depths according to their respective feeding mechanisms and tolerances to different environmental stresses (Taylor et al., 2003). Tier communities can also represent overlapping ichnofacies, particularly when turbidity currents oscillated the bottom water and interstitial pore water dissolved oxygen content; *Nereites* and *Zoophycos* ichnofacies often superimpose each other, with those ichnofossils more tolerant of depleted oxygen towards lower portions of the tier (Uchman and Wetzel, 2011; MacEachern et al., 2012). Deposit-feeding, exogenous fauna brought in by turbidity currents may inhabit the sediment at the sediment water interface where dissolved oxygen content is higher (i.e. *Nereites* ichnofacies). Further down, away from newly oxidizing shallow poor waters, ichnofossils of the *Zoophycos* ichnofacies dominate. At these depths, oxygen deficient conditions are similar to that during background sedimentation (Seilacher, 1962, 1977). As previously mentioned, selective preservation of lower tier communities is especially common in reoccurring erosive turbidites. Figure 10 is a schematic that summarizes the tiered communities observed in this study.

5.5. Bioturbation Observations and Interpretation

The relative abundances of each of the observed ichnofossils were given a qualitative value, ranging from 0 – 3, indicating absence, present, sparse, and abundant, in ascending order. Furthermore, if the overall degree of bioturbation within a 2-inch (5 cm) interval was greater than 30%, the degree of bioturbation was recorded, as well as which

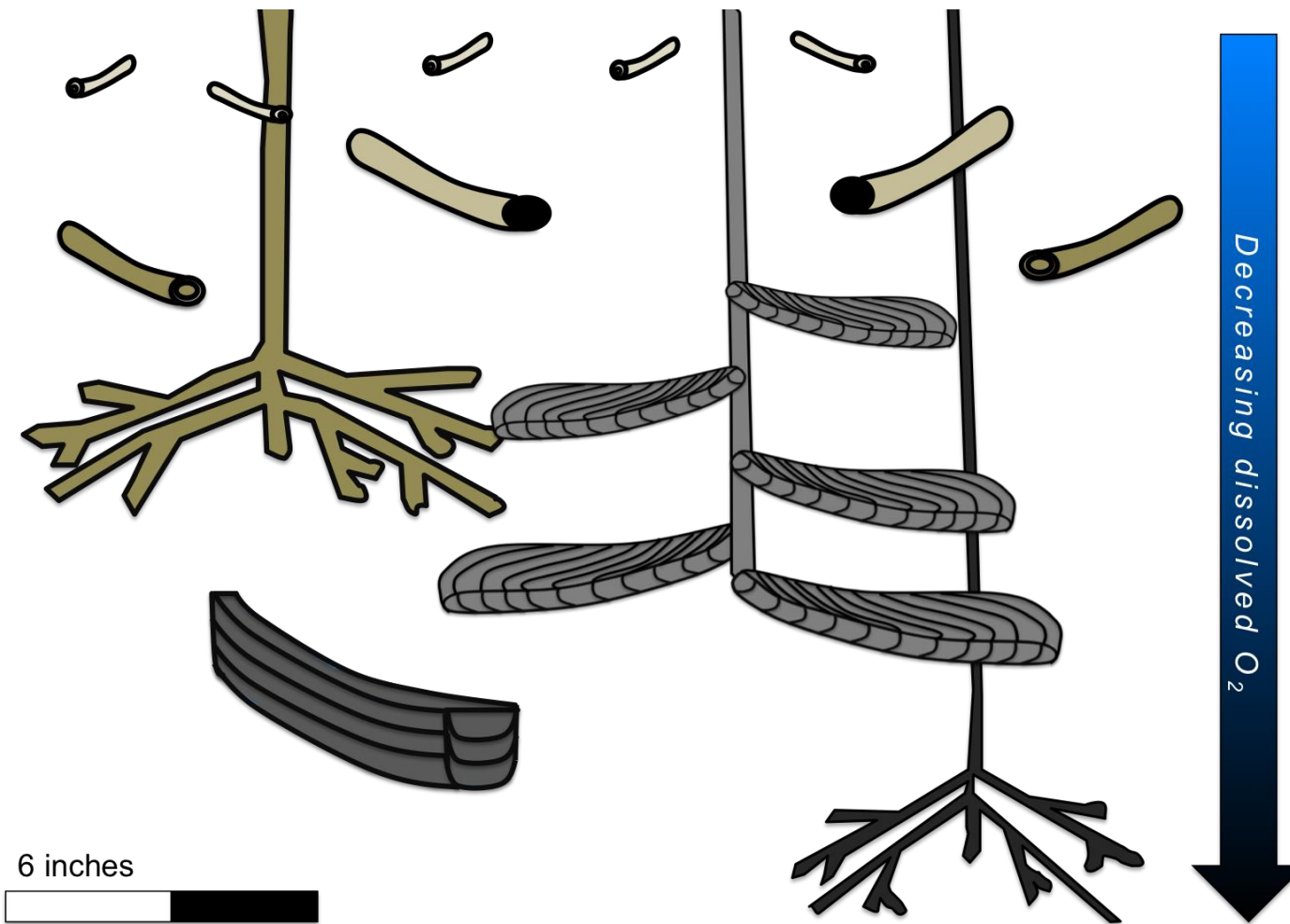


Figure 10. Schematic representation of idealized tiered community. Ichnofossils listed from top to bottom: *Phycosiphon*, *Planolites*, *Nereites*, *Chondrites* (large), *Zoophycos*, *Teichichnus*, and *Chondrites* (small) show increasing tolerance to low dissolved oxygen concentrations as distance increase from sediment water interface.

ichnofossils were observed. Large sections of zero values in the ichnofossil record reflect thick carbonate event deposits, the absence in bioturbation reflects the high energy of the sediment gravity flows, rather than limited oxygen availability.

Overall, there is an observed increase in the degree of bioturbation up section. The average degree of bioturbation remains below 10% from 9700 – 9680 ft. (~2957 - 2951 m), in the interpreted third-order FFST within the Wolfcamp B3. These low values most likely reflect the higher energy debris flows, which inhibit organisms from remaining on the eroded substrates. Total bioturbation remained relatively low during the lowstand (Wolfcamp B3) and transgression (Wolfcamp B2), with only three distinct deviations intervals at 9670 – 9665, 9647 – 9653, and 9628 – 9635 ft (~ 2947 - 2946, 2940 - 2942, 2935 - 2936.7 m). The 5 – 7 ft. (1.5 - 2 m) packages sedimentologically correspond to packages of thin, high frequency, fine-grained, increasingly more siliciclastic turbidites. Within these intervals, bioturbation values exceed 50%, indicating episodic increases in life-sustaining organic matter and dissolved oxygen. Beginning at approximately 9595 ft. (2924.5 m), bioturbation levels on average exceed 50%, consistent with the interpreted third-order onset of highstand conditions, with the exception of intermittent thicker, calcareous packages. This trend of increasing bioturbation levels continues throughout the highstand for approximately 35 ft. (~11 m), culminating in total bioturbation exceeding 80% around 9570 ft. (2917 m). This consistent, continuous increase in bioturbation, compared to the punctuated, episodic bioturbation cycles exhibited in the lowstand and transgression, indicates more persistent elevated oxygen levels. After the core break, bioturbation levels decreased to roughly an average of 40% from the churned bioturbated

fabrics of >80% exhibited earlier, suggesting a decrease in the available dissolved oxygen at the end of the HST.

Individual ichnofossils and their abundances were recorded. Those ichnofossils more strictly associated with sediment gravity flows, such as *Planolites* and *Phycosiphon*, were by far the most abundant throughout the core. *Planolites* and *Phycosiphon* burrowing intervals exhibiting consistent qualitative abundance levels >1 within the interpreted lowstand and transgression correspond to the three total bioturbation intervals exceeding 50% and sedimentologically to the 5-7 ft. (1.5 - 2 m) packages of thin high frequency turbidites. Their opportunistic yet short-lived presence indicates a subtle increase in dissolved oxygen concentrations associated with the small, dilute, yet high frequency distal sediment gravity flows. Oxygen levels would then later return to the dysoxic-anoxic equilibrium more commonly associated with eustatic sea level controlled oceanographic conditions during lowstand and transgression. *Planolites* and *Phycosiphon* burrows were most abundant during the interpreted third-order highstand, consistent with previously observed total bioturbation trends and theoretical highstand carbonate platform shedding by means of calciturbidites.

Chondrites, and to a lesser degree, *Zoophycos*, were the dominant ichnofossils observed between 9680 – 9650 ft. (~2951 – 2941 m), indicative of the *Zoophycos* ichnofacies, relatively consistent background sedimentation, and suppressed dissolved oxygen concentrations during Wolfcamp B3 deposition. Within this third-order lowstand, *Planolites* and *Phycosiphon* abundances mirrored *Zoophycos* abundances over the same previously mentioned 5 ft. (1.5 m) interval observed between 9670 – 9665 ft. (2947 -2946 m). This observation, coupled with the notable absence of abundant *Nereites* burrows,

is consistent with the *Zoophycos* ichnofacies interpretation. The presence of sediment gravity flow-dependent ichnofossils and the increase in burrow abundance of organisms more accustomed to elevated dissolved oxygen concentrations relative to *Chondrites* indicates that the dilute sediment gravity flows are only temporarily elevating oxygen levels during the lowstand.

During transgression and early highstand (9650 – 9590 ft.; 2941 – 2923 m), *Chondrites* abundance generally decreases, aside from several isolated instances. Towards the end of the transgression and throughout highstand conditions (9630 – 9540 ft; 2935 – 2908 m), *Nereites* and *Zoophycos* abundances closely track each other, except for an anomalous 10 ft. (3 m) interval (9605 – 9595 ft.; 2928 – 2925 m) towards the end of the early highstand, indicative of the *Nereites* ichnofacies, more oxygenated conditions, and dominantly turbiditic deposition. The overlap between the high abundances of *Nereites* and *Zoophycos* burrows and *Chondrites* burrows beginning at 9580 ft., is indicative of healthy, well-developed tiered communities, commonly associated with more oxygenated deep marine environments. However, the resurgence in abundant *Chondrites* burrows could also indicate a decrease in the overall dissolved oxygen concentrations. These potentially stressed, deoxygenated conditions could be attributed to a subtle fourth-order sea level fall nested within the third-order highstand, which was previously sedimentologically suggested. However, there is a notable increase in the overall *Zoophycos* burrow diameter during this same interval, favoring the well-developed tiered community interpretation during a third-order highstand. These findings are summarized in Figure 11.

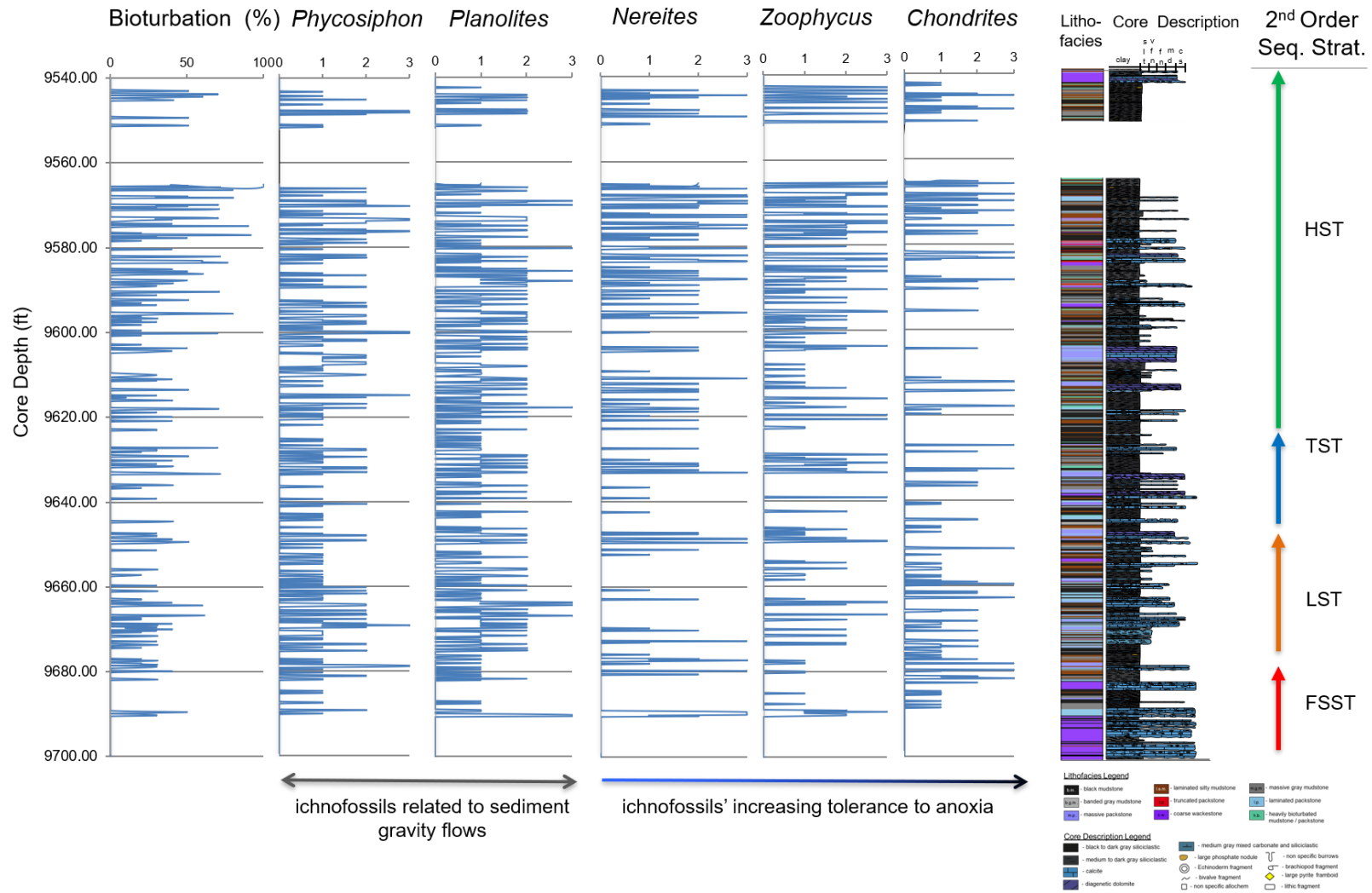


Figure 11. From left to right: Degree of total bioturbation (out of 100%), qualitative assessment (0 – 3) of presence of ichnofossils: *Phycosiphon*, *Planolites*, *Nereites*, *Zoophycos*, *Chondrites*; core description, observed lithofacies, and working sequence stratigraphic framework

6. Inorganic Geochemistry

6.1. Lithofacies Major Elemental Distribution

Major elements are defined as Si, Al, Ca, Mg, K, Fe, Mn, Ti, P, and S and are expressed as weight percentages (wt %). Mn, Ti, and P comprised < 2 wt% of each of the nine lithofacies and thus were excluded. Average major element compositions were then renormalized to Si, Al, Ca, Mg, K, Fe, and S. Average major element composition per lithofacies are summarized in Figure 12.

The texturally distinct black, non-laminated mudstone and laminated silty mudstones are identical in major element composition: 67% Si, 10% Al, 8% Ca, 5% Fe, 4% K, 2% Mg, and 4% S. The dark gray massive gray mudstone has slightly less Si and K and exhibits a 4% increase in Ca relative to the black and laminated silty mudstones. The even lighter gray, banded mudstone has a greater Ca percentage, slightly greater Mg and Fe percentages, and a smaller Si fraction compared to all the other individual mudstone lithofacies.

The truncated packstone has even more Ca than the mudstones, however, Si still remains the largest fraction with 50 wt. %. The large proportion of Si in the carbonate packstone is attributed diagenetic alteration and the Si incorporated in the clay matrix minerals observed above the contact (see Appendix A. Core Photos, Core Description, and Lithofacies and Appendix B. Petrography). Many of the XRF measurements were taken on the contact and hence reflect both the overlying mudstone as well as the underlying carbonate packstone (massive or laminated) in order to maintain the consistent 2-inch vertical sampling rate.

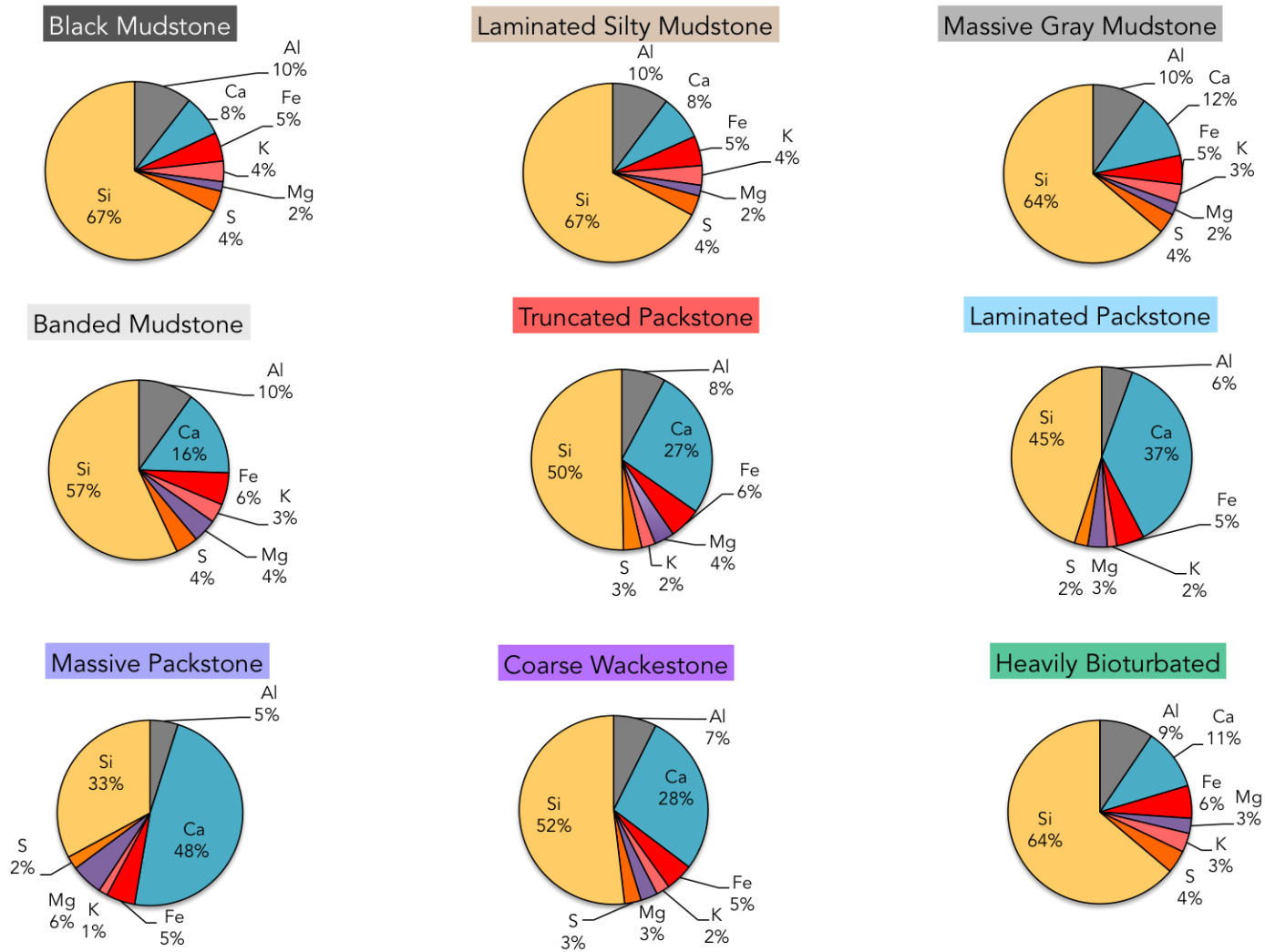


Figure 12. Average major element composition (Si, Al, Ca, Fe, K, Mg, and S) of each lithofacies.

The coarse wackestone major element distribution reflects the argillaceous supporting matrix rather than the coarse allochems: Si remains the dominant element (52%) with a larger, yet not dominant, Ca concentration of 28%. The progressively more carbonate rich lithofacies, such as the laminated packstone and massive packstone respectively, exhibit an expected progressive increase in Ca%. Silicon at 45%, remains the elemental contributor for the laminated packstone. This Si dominance within the laminated packstone, coupled with a higher Al% relative the massive packstone, may reflect the more siliciclastic/ clay rich laminations present within the former lithofacies. The laminated packstone may reflect the deposition of the upper flow regime of a turbidity current, which is relatively more diffuse, less dense, and hold more fine material in suspension than the lower flow regime, lithological represented by the massive packstone. This overall bulk incorporation of less dense clays, aside from the aligned clays represented in the laminations, may account for the Si dominance in the laminated packstone.

As previously mentioned, the massive packstone was cleaner and devoid of clay laminations. The massive packstone lithofacies is the only lithofacies with a dominant Ca fraction of 48 wt. %. This increase in Ca is coupled with a significant decrease in Si and to a lesser extent, Al and K. The massive packstone also exhibits a significant increase in the Mg fraction; nearly double that of the other calcareous lithofacies (laminated packstone and coarse wackestone). The increase in Mg is disproportionate to the increase in Ca, indicating that it is not solely attributed to an increase in Ca. This non-linear relationship between Ca and Mg may be indicating a relative increase in the amount

of dolomite. Overall, there is a subtle, progressive decrease in the average S%, from 4% to 2%, from the more argillaceous to the more calcareous lithofacies.

The heavily bioturbated lithofacies is independent of many of the lithologic constraints that defined the previous eight lithofacies. Although bioturbation occurred on average within finer-grained substrates, mineralogy does not play as large a role. This independent relationship between bioturbation and mineralogy is further supported by the major element composition of the lithofacies. The heavily bioturbated lithofacies elemental distribution fell between that of the black and silty laminated mudstones and the massive gray mudstone, indicating bioturbation occurred in substrates of a mix of both siliciclastic and calcareous lithologies.

6.2. Lithofacies Minor and Trace Elemental Distribution

Minor elements with a low relative wt.% (consistently <2 wt.% of the major element distribution for all lithofacies) and trace metals of paleo-environmental importance were more rigorously statistically analyzed. Median, first and third quartiles, and minimum and maximum values for each lithofacies were recorded.

6.3. Enrichment Factors and Caveats in Mixed Systems

Much of the trace metal literature often reports values as enrichment factors, Efs, which show the relative enrichment of major and trace elements relative to the Al fraction, (X/Al), which most directly represents the clay fraction. This enrichment factor methodology allows for the more accurate comparisons of trace metal concentrations (ppm) since their absolute concentrations change dramatically with only a small change

in the overall clay content. This enrichment factor methodology has been successful in predominantly siliciclastic, non-thinly bedded, paleo-environmental reconstruction (Algeo and Lyons, 2006; Scott and Lyons, 2012; Cheng et al., 2015; Turner, 2015; Turner and Slatt, 2016). However, mixed carbonate-siliciclastic environments pose a problem to the enrichment factor applications: relative enrichment of certain trace metals are dominantly controlled by low Al concentrations. Therefore, trace metal enrichment values express by large increases in the Ca fraction, rather than oceanographic, water column changes in redox conditions, or nutrient delivery. Preliminary application of the enrichment factor methodology to the Wolfcamp Formation core showed evidence of this Ca bias. Trace metals were reported in absolute concentrations and a simple quartile base statistical analysis was applied to show changes in trace metal composition as they relate to each lithofacies.

6.4. Trace Metal Paleoredox Proxies with Limited Detrital Influences

Trace elements molybdenum (Mo) and vanadium (V) are established paleoredox proxies (Tribovillard et al., 2006, 2008; Algeo et al., 2012; Gilleaudeau and Kah, 2013; Corn, 2017). The ionic species of Mo and V are found in extremely low concentrations in seawater relative to the clay minerals (Corn, 2017). They are predominately deposited in the sedimentary record at the redox boundary at or below the sediment water interface at the time of deposition or during early, shallow diagenesis. In particular, Mo and V complex with free S^{2-} in euxinic environments to form pyrite-like complexes (Vorlicek et al., 2004). Elevated values of Mo and V are widely used as indicators of anoxic and euxinia, that is,

anoxia with free H₂S in the water column (Algeo and Lyons, 2006). However, these pyrite-like complexes may be reflecting either the conditions of the overlying water column or that of the pore-waters below the sediment water interface. Paleoenvironmental reconstruction efforts of redox conditions can therefore remain relatively cryptic if these euxinic conditions are mutually exclusive. Without pyrite framboid dimensional analysis, the relative timing of pyrite formation, and therefore redox conditions, is unknown (Sweeney and Kaplan, 1973; Wilkin and Barnes, 1997). Furthermore, anoxic conditions with limited H₂S, but not enough to be euxinic, would lessen the degree of Mo and V sulfur-complexing (Schultz and Rimmer, 2004; Tribovillard et al., 2006). Uranium (U) also occurs predominantly as an ionic species in seawater and is enriched in the sediment. U (VI) reduction to U (IV) occurs in anoxic seawater, with pH conditions similar to those where Fe (III) reduction to Fe (II) occurs, and is theorized to be decoupled from abundance of free H₂S (Swanson, 1961; Tribovillard et al., 2012). Slow sedimentation rates allow for the downward diffusion of uranyl ions from the water column into the sediment. Furthermore, the presence of organic metallic ligands and humic acids accelerate U uptake into sediments (Crusius and Thomson, 2000). Uranium in a reduced state is therefore predominantly associated with non-sulfidic anoxia and limited oxygen penetration depth within the sediment. However, U is easily remobilized if oxygen does penetrate the sediment. Thus, bottom water oxygenation events, such as those created by turbidity currents, or reintroduction of oxygen into deeper sediments through burrowing and bioturbation, will remobilize U and decrease its concentration in the sedimentary record (McManus et al., 2005, 2006).

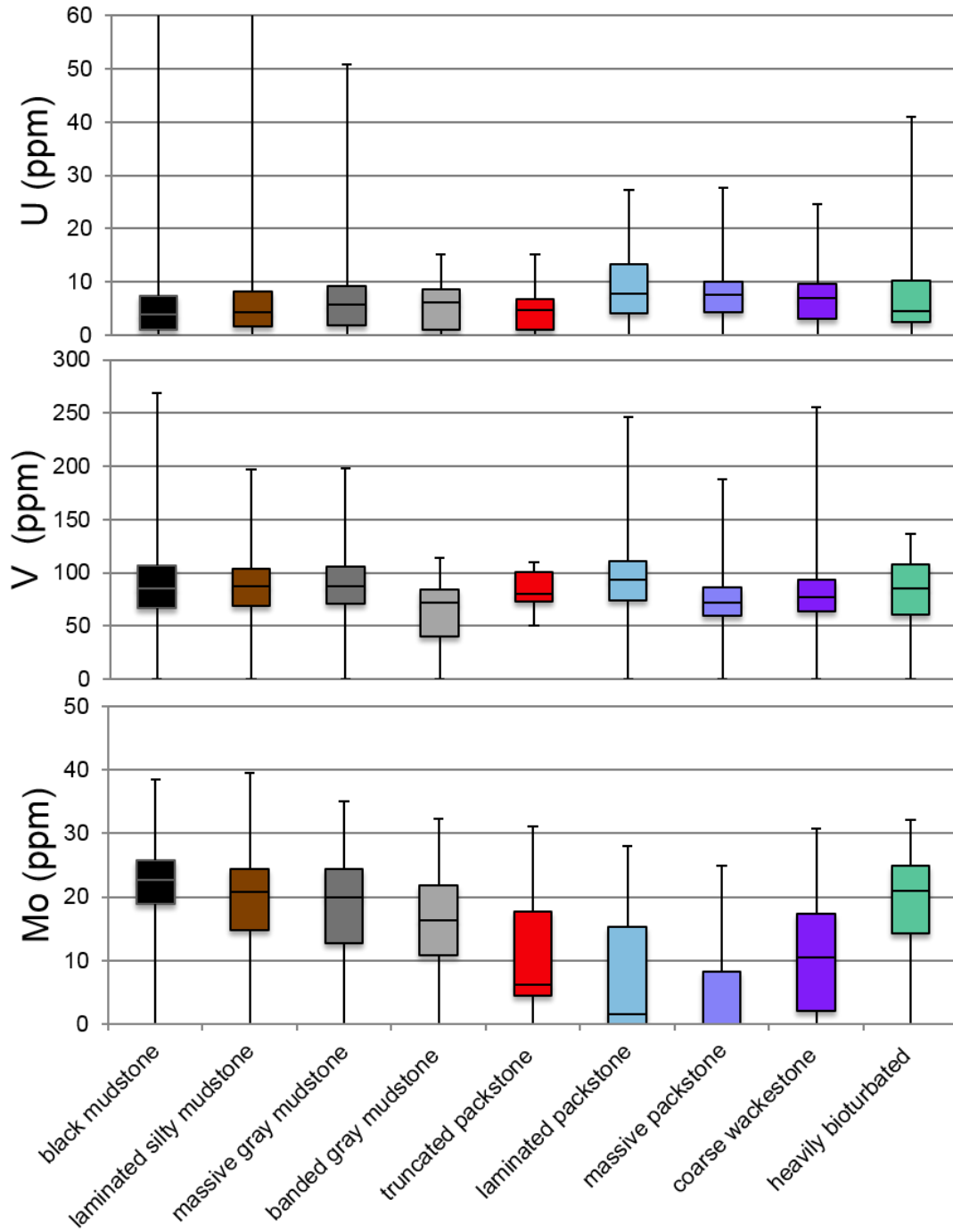


Figure 13. Paleoredox Proxies with Limited Detrital Influences: U, V, and Mo (ppm) concentration statistical distributions as a function of lithofacies. Minimum, Q1, median, Q3, and maximum shown. Note higher U maximums for black mudstone and laminated silt.

Mo, V, and U concentrations per lithofacies are summarized in Figure 13. Median U concentrations are low relative to many anoxic shale formations although maximum values are consistent with normal marine shale distributions, up to 250 ppm (Swanson, 1961). Maximum U values were left off Figure 13 to better show the main distribution of data and are as follows: 261 and 158 ppm for the black mudstone and laminated silty mudstone lithofacies, respectively. Median values for all lithofacies range from 2 – 5 ppm. Maximum U values are significantly smaller for the more calcareous lithofacies associated with sediment gravity flows as well as the heavily bioturbated intervals.

Vanadium concentrations are relatively consistent with expected lithofacies relationships. Those lithofacies associated with low energy depositional systems under relatively more anoxic conditions (black, laminated silty, and massive gray mudstones) show elevated V concentrations relative to those associated with higher energy, potentially more oxygenated, sediment gravity flows (banded gray mudstone and massive packstone). However, some calcareous lithofacies associated with the sediment gravity flow spectrum exhibit a higher V median (laminated packstone), larger maximum values (laminated packstone and coarse wackestone), or higher minimum values (truncated packstone). This discrepancy could be explained in two possible ways. As previously mentioned, Mo and V complex with S^{2-} to form pyrite-like complexes.

Therefore, the availability of reduced Fe plays a distinct role in the preferential formation of the Mo and V sulfide complexes (Breit and Wanty, 1991; Helz et al., 2014). Typically, there is an inverse relationship between Ca and Fe within a system. Iron is generally associated with the clay mineralogy and if the argillaceous clay content increases, it is usually at the expense of the calcareous content and vice versa (Breit and

Wanty, 1991). Although the major element distributions show a relatively consistent Fe% regardless of lithofacies, it is unknown where this elemental fraction mineralogically resides. Therefore, it is plausible that the less abundant, clay-related, reduced Fe (II) species during the carbonate deposition eliminated the kinetically preferable ionic competition for S²⁻ complexing (Tribovillard et al., 2004). The reduced ionic competition may have enabled for Mo and V sulfide complexes to form although the conditions may have been less anoxic than during potentially more anoxic, siliciclastic deposition. The other possible explanation is that V was preferentially incorporated into phosphate nodules rather than complexing with sulfide. Vanadium more readily incorporates into phosphate nodules compared to Mo (Breit and Wanty, 1991). This V - phosphate relationship had been observed in the phosphate nodules of the Woodford Shale (Turner, 2015). As previously mentioned, phosphate nodules were observed towards the top of the Wolfcamp B2 interval, where the truncated packstone lithofacies was exclusively found. The observed generalized stacking pattern of finer-grained coarse wackestone, laminated packstone, and truncated packstone observed towards the top of the core further supports the V – phosphate nodule incorporation argument. Although such small discrepancies amongst the lithofacies seems trivial, it plays an significant role in teasing out the fluctuating redox conditions and degrees of dysoxia during deposition since phosphate nodules are indicative of both upwelling, well circulated, oxygenated marine systems and upwelling induced and non-upwelling induced anoxia ones (Kupecz, 1974; Ece, 1990; Jarvis, 1992; Algeo et al., 1997; Ashckenazi-Polivoda et al., 2010).

Molybdenum concentrations per lithofacies are mostly consistent with associated depositional environment interpretations. Increases in carbonate content and increases

in depositional energy correspond with a progressive decrease in the Mo concentrations. Inversely, low energy hemipelagic to pelagic siliciclastic deposition, corresponding to laminated, silty mudstones and black mudstones respectively, show a progressive increase in Mo concentrations. The heavily bioturbated lithofacies shows lower Mo values relative to the black, laminated silty, and massive gray mudstones, but higher Mo values than those that represent sediment gravity flow deposition. This is consistent with the sedimentological interpretation that the heavily bioturbated intervals were relatively more oxygenated than the quiet, low-energy pelagic and hemipelagic mudstone deposits. The poorly sorted wackestone lithofacies shows slightly elevated Mo values relative to other lithofacies associated with different parts of the sediment gravity flow spectrum. This is particularly interesting since the coarse wackestone is associated with the highest energy facies – a debris flow. The anomalously high Mo values for the coarse, poorly sorted wackestone could be explained by three possible mechanisms: (1) decreased entrainment of oxygenated water, (2) different water column conditions during the time of deposition, or (3) allochthonous deposition of Mo-S complexes.

Debris flows (associated with the coarser, poorly sorted wackestone) entrain less water relative to turbidity currents (associated with the cleaner packstones). Given that these flows are sourced from the more proximal shelf environments, entrained waters tend to be more oxygenated than the deep basinal waters where the flows eventually deposit sediment. Debris flows are composed of approximately 50% entrained ambient water compared to the 90% of turbidity currents (Lowe, 1979; Lowe and Guy, 2000; Amy et al., 2005; Talling et al., 2012). Therefore, even though the debris flows are higher

energy, they entrain less oxygenated water. The oxygen content of the flow, rather than the energy of the flow, ultimately dictates redox conditions and hence Mo precipitation.

Although this relative decrease in the amount of entrained oxygenated water could explain the relative increase in Mo concentrations, it could also be attributed to more pervasive reducing water column conditions during debris flow deposition. As previously mentioned, the thickest continuous packages of coarse wackestone are found towards the bottom of the core, within the Wolfcamp B3 interval. It is widely accepted that the B3 interval was deposited during of period sea level fall and lowstand. In an epeiric sea, such as the one observed in the Permian Basin, a sea level fall could restrict the communication and re-entrance of sea water from the much larger Panthalassa Ocean and create a relatively more stagnant, anoxic conditions (Algeo et al., 2012; Tribovillard et al., 2012; Gilleaudeau and Kah, 2013). Given the lower stratigraphic position of these debris flows, their corresponding trace metal distributions may reflect the relatively more anoxic equilibrium redox conditions, regardless of the degree of entrained oxygenated water. Alternatively, much of the mud matrix within the coarse wackestone is comprised of rip up clasts, which may have mineralogically recorded the redox conditions of the more proximal location from which it was sourced. It is entirely plausible that the Mo-S complexes found in coarse wackestone are as allochthonous as the carbonate allochems (Sweetman and Insole, 2010). Ultimately, it is possible that the elevated Mo concentrations in the interpreted debris flows stem from a combination of all three mechanisms.

Lastly, the discrepancy between the Mo and V values for the truncated packstone lithofacies supports the V-phosphate nodule incorporation interpretation over the Fe ion

competition interpretation. Mo does not exhibit the same preferential enrichment in certain calcareous lithofacies found towards the top of the core and in closer proximity to observed phosphatic nodules as V does. This suggests that V was preferentially incorporated in phosphate nodules formed during certain oceanographic conditions rather than an ion species competition with the limited Fe in a carbonate system that would have expressed itself in elevated concentrations of both the Mo and V, consistent with the working sequence stratigraphic framework.

6.5. Trace Metal Paleoredox Proxies with Strong Detrital Influences

Chromium (Cr) and cobalt (Co) are trace metals used as paleoredox proxies that are strongly tied to detrital clastic sediments, thus limiting their use as pure paleoredox proxies (Tribovillard et al., 2006). Chromium is also found in clay and ferroan-magnesian minerals, regardless of seawater redox conditions. Chromium is not incorporated in pyrite-like sulfide complexes due to structural incompatibilities. However, reduced Cr species residing in anoxic sea water readily complexes with humic acids and adsorbs to Fe- and Mn- oxyhydroxides (Algeo and Maynard, 2004). Reduced Co complexes with humic acids and is found in clay minerals. Contrary to Cr, reduced Co forms sulfide complexes, although slow

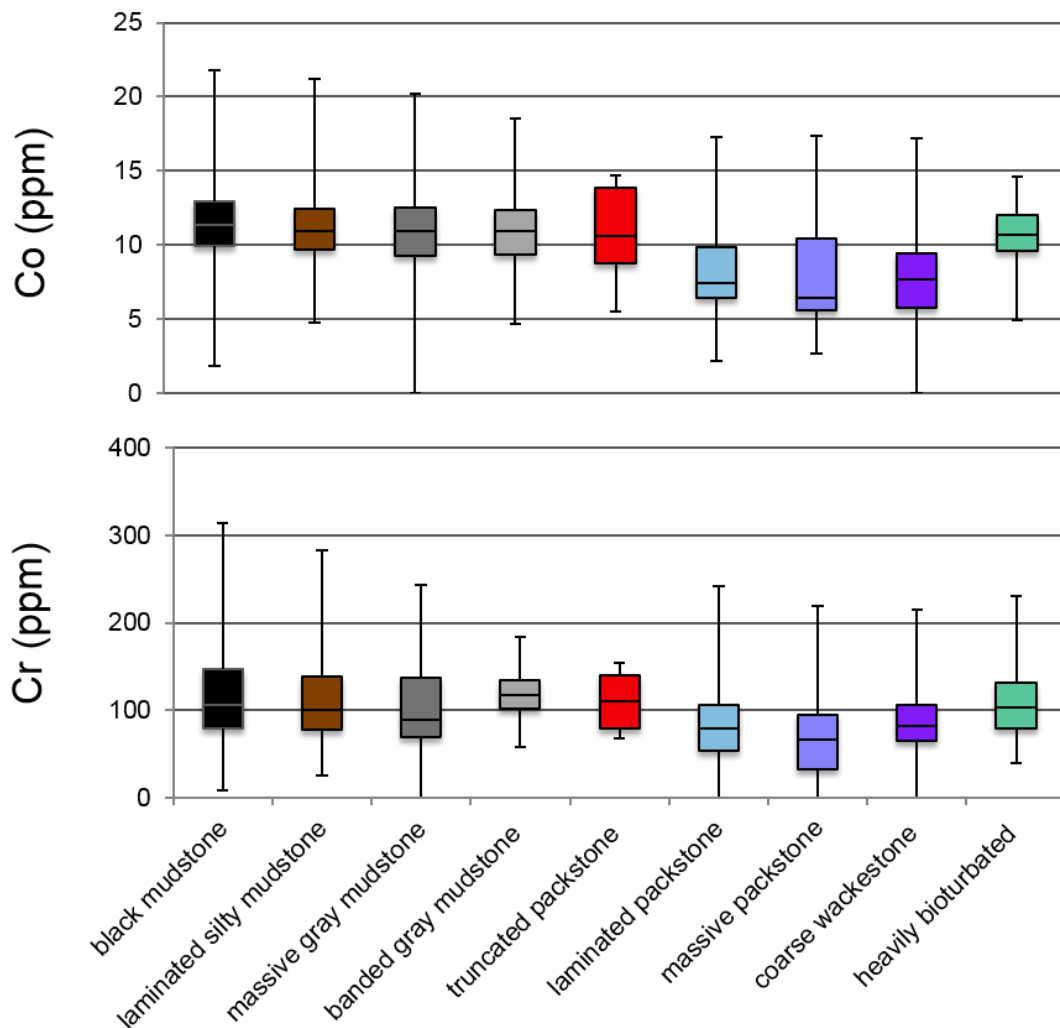


Figure 14. Paleoredox Proxies with Strong Detrital Influences: Cr and Co (ppm) concentration statistical distributions as a function of lithofacies. Minimum, Q1, median, Q3, and maximum shown in box and whiskers plot.

kinetics limits the extent of its incorporation (Achterberg et al., 1997; Morse and Luther, 1999). Hence, Co concentrations reflect both detrital input and redox conditions to a greater extent than Cr (Algeo and Maynard, 2004).

Figure 14 shows the distribution of Cr and Co concentrations per lithofacies and is relatively intuitive given their lithology. Overall, both Cr and Co have more similar distributions across the different lithofacies compare to the pure anoxia- euxinia proxies. Furthermore, the Cr and Co distributions for the truncated packstone lithofacies are more similar to their siliciclastic counterparts than anticipated for a calcareous package. This similar in distribution may reflect the clastics associated with the clay-rich, upper contact that defines the truncated packstone facies.

6.1. Redox Sensitive Organometallic Trace Element Proxies

In oxic marine conditions Ni, Cu, and Zn behave as micronutrients and are adsorbed onto humic and fulvic acids (Algeo and Maynard, 2004). Generally, humic acids are believed to be derived from plant matter (Swain, 1961; Flaig, 1966, 1972). Although their ubiquity in terrestrial and aquatic systems is thought to reflect hydrological dispersion (Schnitzer, 1977; Hatcher and Orem, 1986; Hedges et al., 1997), there is evidence of independent marine origins for some humic substrates (Nissenbaum and Kaplan, 1972; Hedges and Oades, 1997). In contrast, fulvic acids are thought to be derived from microbial degradation of organic matter (Schnitzer, 1977; Tissot and Welte, 1978; Hatcher and Orem, 1986). Ni, Cu, and Zn are scavenged by acids in the water column, to which they complex to, and upon OM deposition, are enriched in sediment (Calvert and Pedersen, 1993). Once the organic material decays, Ni, Cu, and Zn are mainly released

from the organometallic structure into the pore water, although can remain in a porphyrin structure under reducing conditions (Tribovillard et al., 2006). In a weakly anoxic (oxic-dysoxic) environment, much of the Ni, Cu, and Zn will be cycled from the sediment back to the overlying water column if there are no sulfides or oxides present. However, in relatively stronger anoxic conditions (dysoxic-intermittent anoxia / euxina),

Ni, Cu, and Zn complex with S^{2-} to form a pyrite like structures (Huerta-Diaz and Morse, 1992; Morse and Luther, 1999). Regardless of the slow kinetics in the sulfide complex formations, they are extremely insoluble and will remain in the sedimentary record, regardless of reoxygenation events. Nickel, Cu, and Zn's organic matter scavenging and organometallic complexing behavior make them a particularly useful redox sensitive plant and algae indicators (Racka et al., 2010). Figure 15 shows these redox-sensitive organometallic trace metal proxies' concentrations by lithofacies. Trace metal distributions are once again consistent with the associated depositional environment interpretation. Relatively more anoxic conditions, or the more oxygen-limited end member of dysoxia, persist during pelagic and hemipelagic deposition associated with the mudstones. Those more calcareous lithofacies associated with the sediment gravity spectrum show a progressive decrease in Ni, Cu, and Zn concentrations. The correlation between,

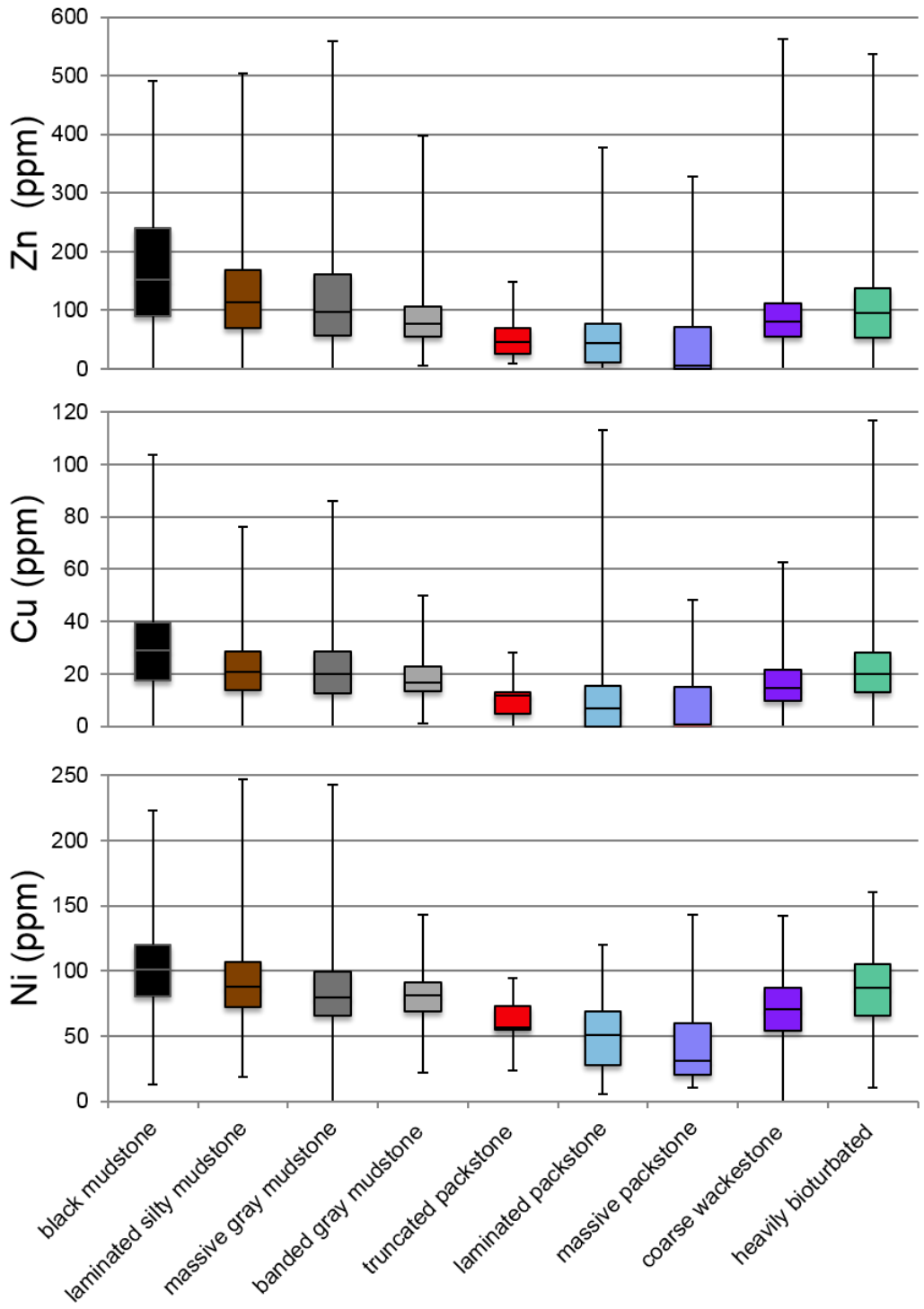


Figure 15. Redox Sensitive Organometallic Trace Element Proxies: Ni, Cu, and Zn (ppm) concentration statistical distributions as a function of lithofacies. Minimum, Q1, median, Q3, and maximum shown.

these redox-sensitive organometallic proxies and finer-grained, more clay-rich lithofacies further indicates that OM scavenging and organometallic settling occurred more consistently during the slower, more persistent pelagic, hemipelagic, and distal siliciclastic turbidite deposition rather than during the rapid sedimentation event deposits associated with the calcareous lithofacies. However, Ni concentrations are greater in the calcareous fractions relative to Cu and Zn. The more debritic lithofacies show an increase in the abundance of all trace metals, either reflecting their siliciclastic matrix or less entrained oxygenated water. Interestingly, the heavily bioturbated lithofacies shows greater trace metal concentrations relative to the more calcareous sediment gravity flows, and in some instances, such as Ni, more siliciclastic counterparts. This preferential enrichment may be reflecting trace metal complexing to fulvic acids produced by means or microbial aerobic degradation of OM. However, from trace metal analysis alone, it remains relatively unclear if the humic acids are of marine or terrestrial origin.

6.2. Paleoproductivity and Nutrient Minor Element Proxies

Iron is necessary for photosynthesis and is considered a limiting nutrient in marine systems given its insolubility in seawater. Potassium is necessary for all forms of life since it plays a fundamental role in many metabolic processes (Smith, 1984; Elser et al., 2007).

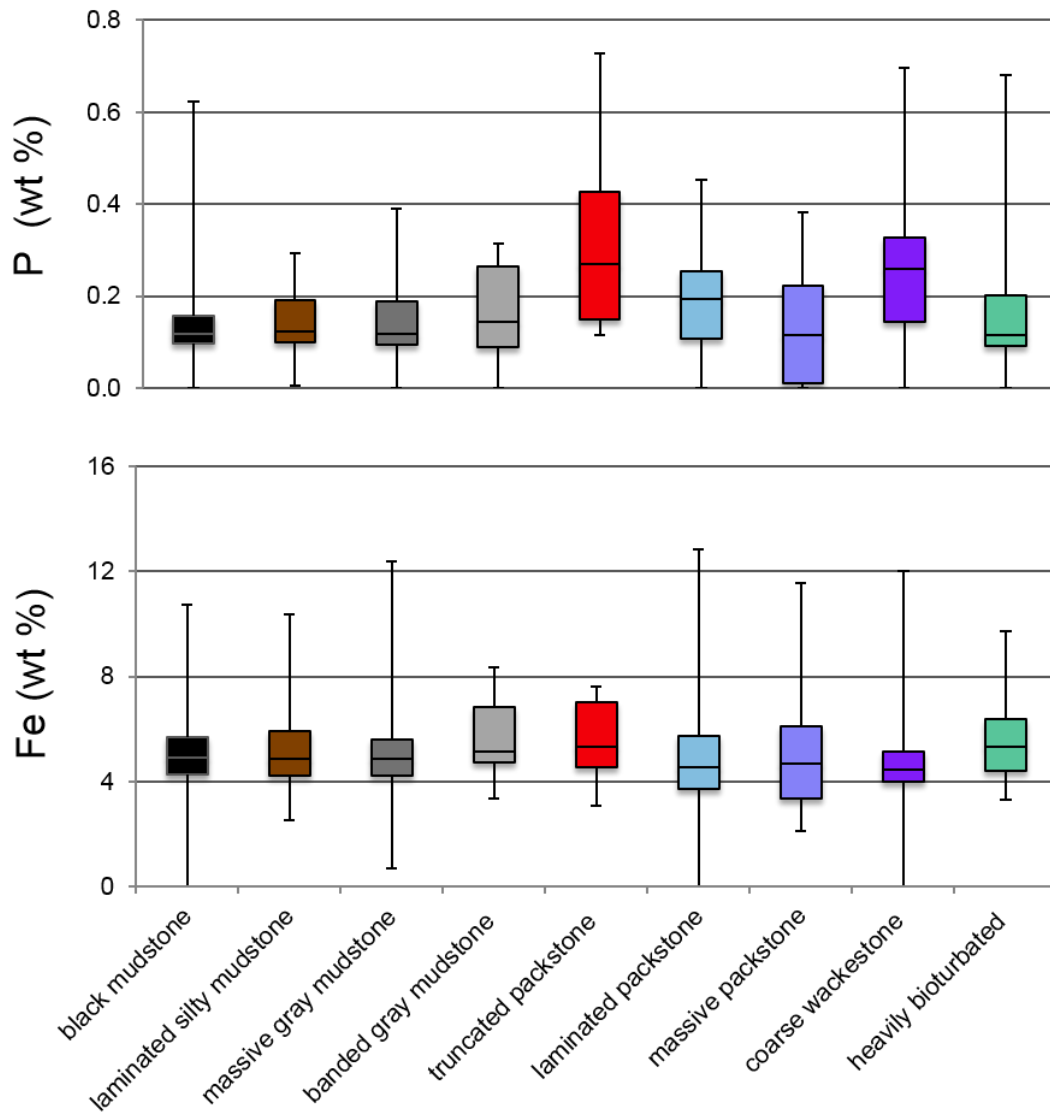


Figure 16. Paleoproductivity and Nutrient Minor Element Proxies: Fe and P (wt %) abundance statistical distributions as a function of lithofacies. Minimum, Q1, median, Q3, and maximum shown. P maximum values are cropped. See appendix for raw values.

corresponds to the anomalous V concentrations in the same lithofacies. The observed increase in phosphate nodules during Wolfcamp B2 deposition, towards Both Fe and P are considered limiting nutrients, and can be used as marine paleoproductivity indicators (Cullen and Tyrell, 1999; Okin et al., 2011). Furthermore, P is present in phosphate nodules that are commonly associated with highly productive upwelling systems. However, in low-productivity anoxic settings, P sorption onto iron-oxide coatings creates a Fe-P co-variation (Follmi, 1996). Figure 16 indicates relatively higher P wt % in the banded mudstone, truncated packstone, and coarse wackestone lithofacies, which the top of the section where the truncated packstones are exclusively observed, supports the notion that P – V co-variation may be indicating more relatively more oxic, upwelling conditions.

Furthermore, the greater increase in P concentrations relative to Fe in the coarse wackestone lithofacies, suggests an influx in nutrients. The increase in the frequency of the thinly bedded debrites around the same depth as the truncated packstones (upper HST) may be evidence of storm deposits, as previously hypothesized, which may contain P from storm runoff. The elevated Fe concentrations relative to P in the calcareous turbiditic flow lithofacies is thought to reflect allochthonous diagenetic ferroan dolomite from the platform rather than an increase in paleo-productivity, as suggested by the petrographic investigation.

7. Organic Geochemistry

7.1. Bulk Organic Geochemistry

General trends concerning organic matter richness, source, and maturity of the Wolfcamp B3 and B2 Formation were derived from LECO and Rock-Eval Pyrolysis data such as total organic content (TOC), S1, S2, S3, and Tmax. Calculated derivatives based of the original data, such as Hydrogen Index (HI), Oxygen Index (OI), Relative Hydrocarbon Potential (RHP), and Production Index (PI), provide addition information and are summarized in Table 3. Bulk organic geochemical data expressed as a function of depth furthers our understanding changes in the depositional environment though time and is the focus of the following section.

7.1.1. Overall Organic Matter Richness, Sources, and Maturity

The TOC expressed as mg of hydrocarbon (HC) per gram of rock (wt.%), of the cored Wolfcamp B3 and B2 intervals, from 9700 to 9534 ft., ranges from 0.38 to 4.10 wt.%, with an average of 2.57 wt.%, indicative of a good, but variable, source rock. The HI values range from 89 - 275 mg of HC₂/ g TOC, with an average of 193 mg of HC/ g TOC. The OI values range from 5– 44 mg of CO₂/ g TOC with an average of 16 mg of CO₂/ g TOC (Table 3).

The cross plot of the HI and OI sample values in a pseudo Van Krevlin Diagram indicate a mixed Type II–III kerogen, suggesting a mix of marine and terrestrially sourced organic matter, respectively (van Krevelen, 1961).

Table 3. Rock-Eval Pyrolysis data table. From left to right: core depth (ft.), TOC (wt. %), S1, S2, S3, T_{max}, HI, OI, S2/S3, ((S1/TOC)*100), RHP, and PI. Samples with asterisk (*) on far right indicate those samples that had further organic geochemical analysis performed on them. Note that some samples did not have sufficient TOC for further Rock-Eval data to be reported confidently by service company; these values are omitted.

Core Depth (ft.)	TOC (wt. %)	S1 (mg HC/g)	S2 (mg HC/g)	S3 (mg CO ₂ /g)	T _{max} (°C)	HI ((S2*100)/TOC)	OI ((S2*100)/TOC)	S2/S3	((S1/TOC)*100)	S2/TOC	RHP ((S1+S2)/TOC)	PI (S1/(S1+S2))	
9534.30	4.10	4.20	10.29	0.35	451	250.73	8.53	29.40	102.34	2.51	3.53	0.29	*
9539.10	2.45	2.13	5.42	0.35	450	221.13	14.28	15.49	86.90	2.21	3.08	0.28	
9543.10	2.84	3.41	7.24	0.24	449	255.02	8.45	30.17	120.11	2.55	3.75	0.32	
9547.25	3.48	4.60	9.34	0.19	451	268.47	5.46	49.16	132.22	2.68	4.01	0.33	
9551.10	3.79	2.03	3.42	0.44	445	90.29	11.62	7.77	53.59	0.90	1.44	0.37	
9565.10	3.80	2.32	3.37	0.31	445	88.61	8.15	10.87	61.00	0.89	1.50	0.41	
9569.50	3.83	3.22	8.40	0.50	450	219.21	13.05	16.80	84.03	2.19	3.03	0.28	*
9573.10	1.76	1.79	3.58	0.39	448	203.06	22.12	9.18	101.53	2.03	3.05	0.33	
9577.10	2.69	2.22	4.53	0.33	449	168.40	12.27	13.73	82.53	1.68	2.51	0.33	*
9581.10	3.43	4.70	9.43	0.28	450	275.33	8.18	33.68	137.23	2.75	4.13	0.33	
9585.15	2.09	1.68	3.59	0.41	445	171.85	19.63	8.76	80.42	1.72	2.52	0.32	*
9589.10	1.99	2.70	6.27	0.36	450	314.92	18.08	17.42	135.61	3.15	4.51	0.30	
9593.15	3.29	2.08	5.69	0.30	452	172.74	9.11	18.97	63.15	1.73	2.36	0.27	*
9597.10	3.25	1.56	3.23	0.30	447	99.26	9.22	10.77	47.94	0.99	1.47	0.33	
9601.35	3.24	3.43	7.34	0.18	453	226.54	5.56	40.78	105.86	2.27	3.32	0.32	*
9605.10	1.02	1.00	1.86	0.45	445	183.07	44.29	4.13	98.43	1.83	2.81	0.35	
9609.10	3.02	2.35	6.47	0.52	451	214.24	17.22	12.44	77.81	2.14	2.92	0.27	*
9613.15	3.32	2.66	7.60	0.70	451	229.12	21.10	10.86	80.19	2.29	3.09	0.26	
9617.10	2.24	1.86	3.94	0.31	449	175.81	13.83	12.71	83.00	1.76	2.59	0.32	*
9621.10	0.64												
9625.10	2.47	2.00	4.73	0.32	449	191.89	12.98	14.78	81.14	1.92	2.73	0.30	*
9629.10	1.39	0.94	1.73	0.39	448	124.10	27.98	4.44	67.43	1.24	1.92	0.35	
9633.10	1.81	1.03	2.45	0.37	449	135.43	20.45	6.62	56.94	1.35	1.92	0.30	*

Table 2 (continued). Rock-Eval Pyrolysis data table. From left to right: core depth (ft.), TOC (wt. %), S1, S2, S3, Tmax, HI, OI, S2/S3, ((S1/TOC)*100), RHP, and PI. Samples with asterisk (*) on far right indicate those samples that had further organic geochemical analysis performed on them. Note that some samples did not have sufficient TOC for further Rock-Eval data to be reported confidently by service company; these values are omitted.

Core Depth (ft.)	TOC (wt. %)	S1 (mg HC/g)	S2 (mg HC/g)	S3 (mg CO ₂ /g)	Tmax (°C)	HI ((S2*100)/TOC)	OI ((S2*100)/TOC)	S2/S3	(S1/TOC)*100	S2/TOC	RHP ((S1+S2)/TOC)	PI (S1/(S1+S2))	
9637.30	3.13	1.63	4.67	0.55	451	149.11	17.56	8.49	52.04	1.49	2.01	0.26	
9641.10	3.76	3.34	9.29	0.24	453	247.40	6.39	38.71	88.95	2.47	3.36	0.26	*
9645.20	0.46												*
9649.10	0.38												
9653.25	1.16	0.88	1.73	0.23	450	149.27	19.84	7.52	75.93	1.49	2.25	0.34	*
9657.15	3.53	2.59	6.23	0.32	452	176.59	9.07	19.47	73.41	1.77	2.50	0.29	*
9661.10	2.64	2.28	5.52	0.19	452	208.77	7.19	29.05	86.23	2.09	2.95	0.29	
9665.30	2.60	1.63	3.94	0.55	450	151.83	21.19	7.16	62.81	1.52	2.15	0.29	*
9669.05	1.40	1.14	2.28	0.35	449	163.21	25.05	6.51	81.60	1.63	2.45	0.33	
9673.15	2.76	2.10	5.30	0.39	449	191.82	14.12	13.59	76.00	1.92	2.68	0.28	*
9677.10	3.40	3.02	8.12	0.38	451	239.10	11.19	21.37	88.93	2.39	3.28	0.27	
9681.10	3.22	2.83	8.39	0.44	448	260.88	13.68	19.07	88.00	2.61	3.49	0.25	*
9685.20	2.69	2.27	6.55	0.47	450	243.95	17.50	13.94	84.54	2.44	3.28	0.26	
9689.10	2.68	1.73	4.54	0.58	453	169.47	21.65	7.83	64.58	1.69	2.34	0.28	*
9693.10	2.24	1.86	3.85	0.38	449	172.11	16.99	10.13	83.15	1.72	2.55	0.33	
9697.20	2.50	2.09	4.15	0.56	445	165.80	22.37	7.41	83.50	1.66	2.49	0.33	*
9701.10	2.18	1.85	3.87	0.42	450	177.20	19.23	9.21	84.71	1.77	2.62	0.32	

A cross plot comparing the remaining hydrocarbon potential (S_2 , mg HC / g rock) versus TOC agrees with the mixed kerogen type interpretation (Figure 17). Although the distal depositional settings would typically lend itself to more marine prone organic material, abundant sediment gravity flow deposits were observed throughout the core. These flows are thought to have transported more proximally sourced sediments, and plausibly terrestrial organic matter within, to distal portions of the Midland Basin. This hypothesized mechanism by which terrestrial organic matter was deposited in a base-of-slope setting be further investigated by comparing changes in HI and biomarker ratio values to the sedimentology as a function of depth in later sections. However, the relationship between decreasing HI with increasing maturity is well established (van Krevelen, 1961; Banerjee et al., 1998; Okiongbo et al., 2005). Increased maturity, particularly around peak oil generation, will cause hydrogen loss due to thermal cracking. This in turn produces lower S_2 , and subsequently HI, values, erroneously decreasing the interpreted amount Type II kerogen and increasing the amount of Type III kerogen. This could lead to the incorrect interpretation that the high-maturity samples are more terrestrial in origin, rather than marine organic matter that has lost significant amounts of hydrogen. Therefore, Tmax data does not only provide useful information on the estimated maturity of the rock, but also plays an important role in contextualizing HI data as it pertains to organic matter source interpretations. The measured Rock Eval Tmax values ranged from 445 – 453 °C throughout the core, with an average of 449°C, indicative of a mature, although potentially somewhat variable, source rock (+/- 5°C). This unusual variability over a 170 ft. core is investigated in detail later. At this maturity level,

some biomarkers useful for paleo-environmental reconstruction begin to thermally degrade

..

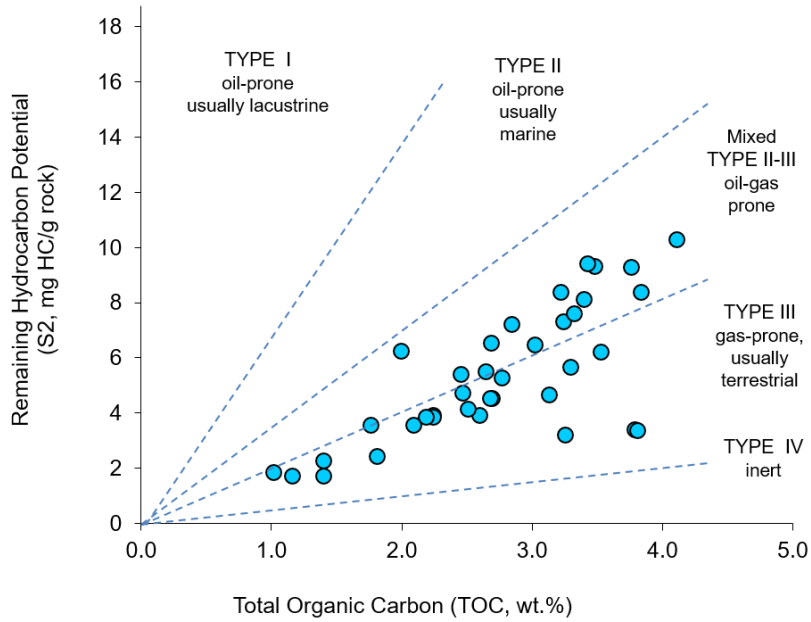
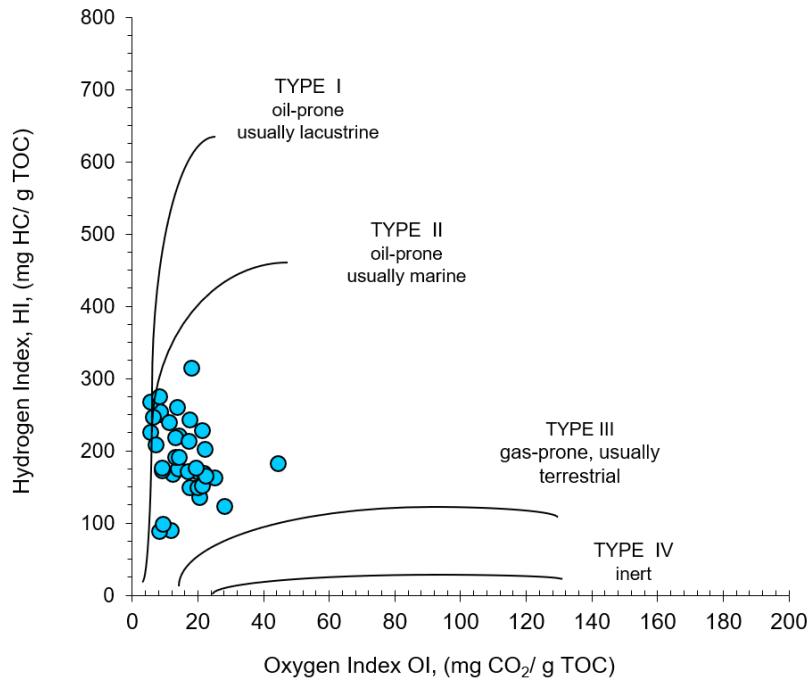


Figure 17. Pseudo van Krevelen Diagram showing HI (mg HC/ g TOC) versus TOC (wt.%) (top) and remain hydrocarbon potential (mg HC/ g rock) versus TOC (bottom) both indicating a mixed Type II – III kerogen.

Overall, these Tmax values are consistent with peak oil generation and, more specifically, early entrance in to the late oil window and peak oil generation (Table 3, Figure 18). The cross plot of HI versus Tmax also indicates a mature source rock, with a mixed Type II-III kerogen (Figure 18). This increases confidence in the previous Pseudo Van Krevelin interpretation while still accounting for decreases in HI due to cracking during this critical stage in maturation. Production Index (PI, $S_1/(S_1+S_2)$) values range from 0.25-0.41 with an average of 0.31, further supporting the notion of a mature source rock in the late oil window (Table 3, Figure 18). By cross plotting PI and Tmax values and comparing the data to a known theoretical kerogen to hydrocarbon conversion curve, it can further be established that these mature samples were not contaminated by non-indigenous hydrocarbons. Although this is often the case with nano-porous source rock, ruling out even the slightest source of contamination is important, particularly when utilizing small changes in biomarker ratios to determine changes in the depositional environment over time. Furthermore, ruling out contamination from less mature, non-indigenous hydrocarbons helps constrain the interpreted maturity of the core. Although theoretically a 170 ft. (52 m) section of core should be the same maturity, the measured Tmax varies frequently (<10 ft. / 10 m) and significantly (> +/- 2°C) as a function of depth. This Tmax variation over a short distance is highly unusual and the possible geologic processes that may cause it are highly limited and usually restricted to the exotic metamorphic regimes or igneous intrusions. The Tmax data is compared several geochemical parameters to investigate if they reflect maturity.

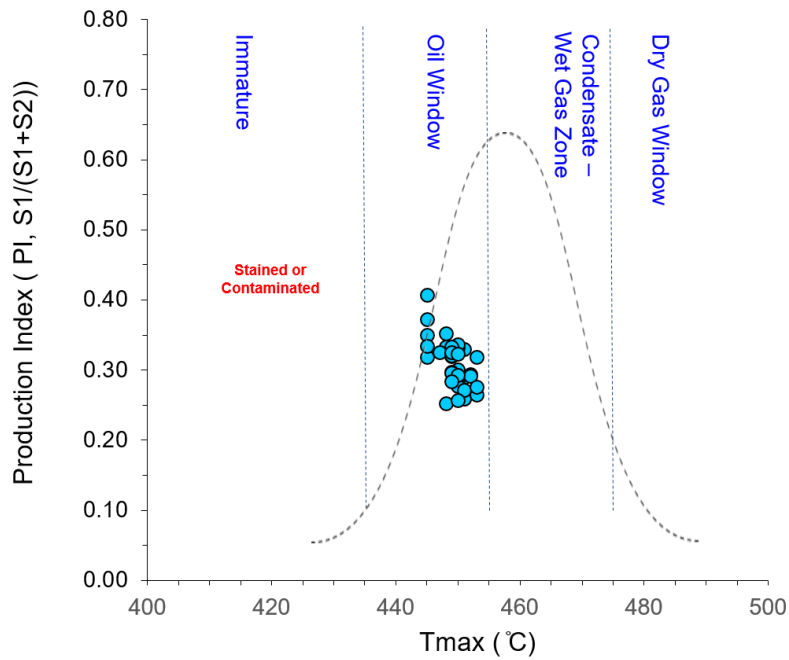
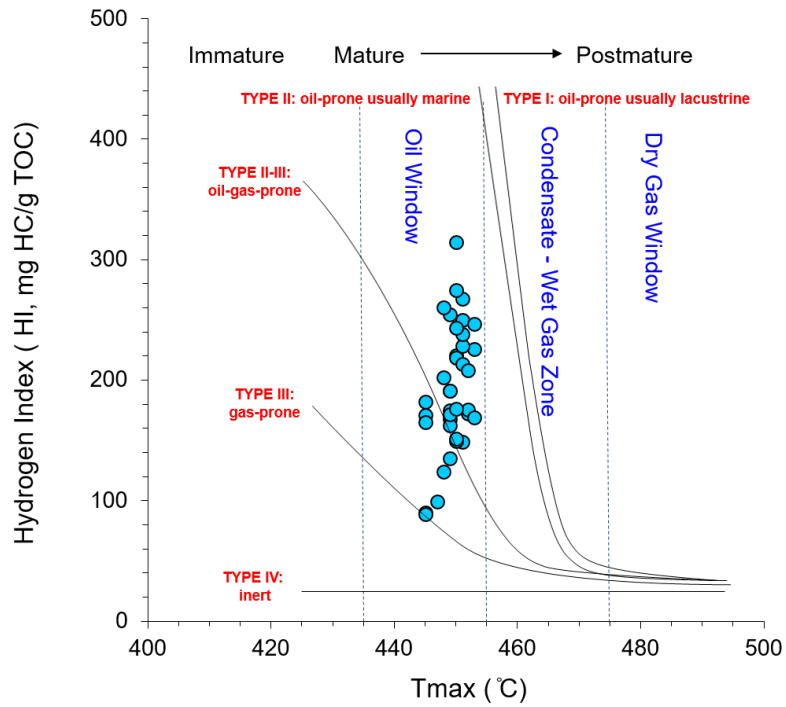


Figure 18. Rock-Eval Maturity Assessment: HI (mg HC/ g TOC) versus Tmax (°C) (top) and PI (S1/(S1+S2)) versus Tmax (bottom). Tmax values indicate mature samples are in the late oil window. HI values support previous Type II-III kerogen interpretation while

also accounting for hydrogen loss during thermal cracking. PI values relative to Tmax indicate little to no sample contamination.

No statistical relationship between Tmax and S2 or HI was observed, suggesting that differential thermal cracking of H-C bonds over the small depth interval did not occur. Furthermore, no statistical relationship between Tmax and OI was observed, suggesting that oxidation events that may have left behind more thermally stable bitumen, in turn elevating the measured Tmax, did not occur. Finally, no statistically meaningful relationship between Tmax and elemental S was identified, suggesting that the potential thermal degradation of weaker C-S bonds broken down earlier during early oil generation did not cause an elevation in the measured Tmax of the remaining more thermally stable bitumen (Gentzis et al., 1993; Snowdon, 1995; Werne et al., 2004). Hence, although no pyrograms were provided by the service company, it can be said with a fair degree of confidence that the Tmax variability most likely does not reflect actual maturity variability but rather an analytical or interpretive limitation. Hence, for the purposes of this investigation, the core is considered iso-mature and biomarker ratio changes truly reflect changes in the depositional environment and source material.

Regardless of the cause of the measured Tmax variability, it can be assumed that the 170 ft. section of core entered the late oil generation window. However, many organic compounds such as monoaromatic steroids and dibenzothiophene (DBT) used for source material and anoxic to sulfidic redox condition assessment, respectively, begin to thermally degrade at the onset of oil generation. Monoaromatic steranes begin to aromatize to triaromatic steranes and DBT begins to form methylated derivatives (Abbott and Maxwell, 1988; Dartiguelongue et al., 2005; Li et al., 2012). Although euxinic conditions are not anticipated from the earlier inorganic geochemical paleoredox proxy

investigation, the absence of DBT and methylated derivatives from preliminary aromatic screenings could be attributed to the thermal maturity of the samples. Biomarker maturity parameters used further constrain the overall Tmax interpreted maturity of the core.

7.1.2.Changes in Organic Matter as a Function of Depth

To investigate how the organic matter type and origin changed over time, TOC, HC Potential, RHP, and OM Type are plotted as a function of depth next to the working sequence stratigraphic model for reference (Figure 19). As previously mentioned, breaks in the line plots indicate values that were too low to report. The HC Potential and OM Type plots are both based on the S2 values from Rock Eval data and therefore are expected to track each other. The RHP ratio is used to assess the redox conditions. Lower RHP values suggest that the total amount of S1 and S2 decreased because the organic matter present was oxidized, and potentially deposited under oxic conditions. Conversely, higher RHP values are thought to represent more anoxic conditions. These fluctuations in redox conditions have been attributed to eustatic sea level fluctuations and aided in the identification of parasequences in other formations, such as the Woodford and Eagleford Shales (Romero and Philp, 2012; Miceli Romero et al., 2018).

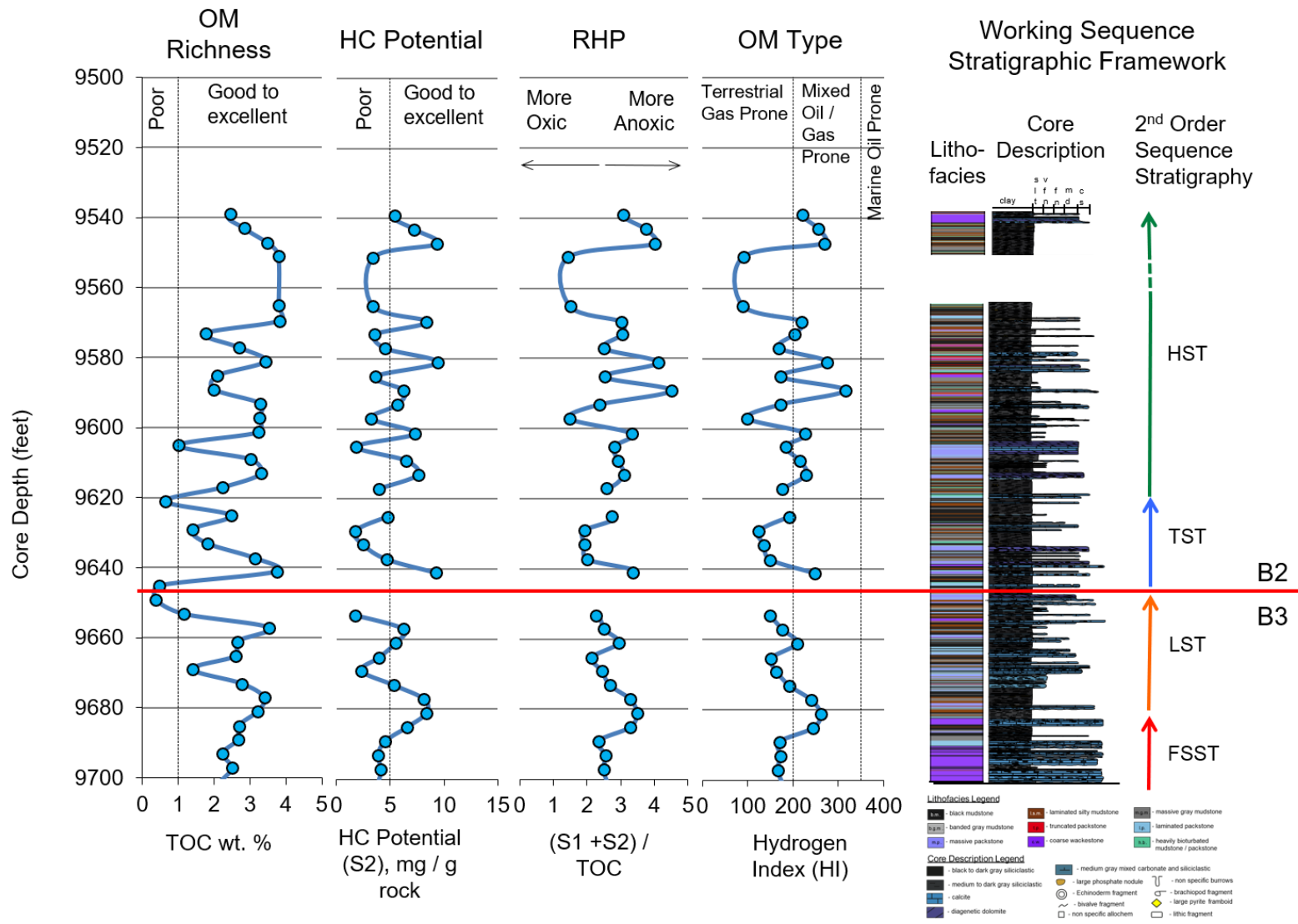


Figure 19. Bulk organic geochemical data as a function of depth. From left to right: TOC, HC Potential, RHP, and OM Type are plotted as a function of depth next. Lithofacies and core description for reference.

Generally, dramatic decreases in TOC correlate to the lithofacies associated fine-grained calcareous turbidites (Figure 19). Higher energy calcareous turbidites with entrained oxygenated water could be oxidizing preexisting organic material and occasionally derived shelf terrestrial organic material. The calcareous turbidites are generally more organic lean relative to their more argillaceous counterparts. This inverse relationship between carbonate material and TOC has been observed in the Midland Basin before (Salisbury, 2014) and is somewhat intuitive. This trend can be observed in both thicker, singular calcareous turbidite event deposits, such as those observed around 9650 ft. and 9605 ft. (2941.3 and 2927.6 m), and thinner, high-frequency calcareous turbidites throughout the interpreted highstand. However, the thick coarse wackestone packages in the Wolfcamp B3 interval do not cause major changes in the TOC richness and relative hydrocarbon potential that thinner, cleaner calcareous packstone packages up section do. The inability of these associated debris flows to change the redox conditions as dramatically as turbidity currents reflects their relative inability to entrain oxygenating water. Sediment gravity flows thus play a large role in the redox conditions recorded in the sedimentary record. Therefore, it is important to understand the causes, effects, and frequencies of these sediment gravity flows and not simply attribute fluctuation in RHP and redox values to changes in the eustatic sea level. Episodic sediment gravity flows causing punctuated disturbances in an overall eustatically driven paleoredox trend should not be over interpreted. Rather, lithofacies frequency and a multi-proxy approach to paleoredox reconstruction could help discern isolated sediment gravity flows from those associated within a larger mixed siliciclastic carbonate sequence stratigraphic model.

Beginning at 9700 ft. (2956.6 m), all the bulk organic matter parameter values increase up until around 9681 ft. (2950.8 m), equivalent to the FSST-LST boundary. The increase in RHP, HI, and TOC values suggest increasingly more anoxic conditions are responsible for marine organic matter accumulation, respectively, during the FSST. The lack of terrestrial material around this FSST-LST boundary may suggest that pelagic, rather than hyperpycnal siliciclastic flows, are the dominant mechanism for siliciclastic deposition at this time. Although the decrease in the terrestrial organic matter observed during sea level fall appears to counter traditional carbonate platform clastic reciprocal sedimentation models, there is a steady increase in the interpreted terrestrial organic matter as the LST progresses. All bulk organic matter parameter values begin to decrease from 9681 ft. (2950.8 m) to roughly 9669 ft. (2947.1 m), equivalent to the middle LST. These bulk geochemical decreases suggest an overall decrease in organic matter accumulation and a transition to more terrestrial prone OM and / or more oxic conditions. The transition from terrestrial marine prone OM during the early LST to terrestrial prone OM by the middle LST suggests a lag time between the initial arrival of the clastic sediments and the associated terrestrial organic material over this sequence stratigraphic interval. By the end of the middle LST (9669 ft.; 2947.1 m), all bulk organic geochemical parameters generally begin to decrease, suggesting a shift to slightly more marine derived OM accumulation under relatively more anoxic condition. All bulk organic geochemical parameters begin to decrease at around 9661.1 ft. (2944.7 m) up until 9653.25 ft. (2942.3 m), equivalent to the end of the middle LST and the end of the LST, respectively. The decrease in HI, TOC, and RHP values suggest a shift to more terrestrially derived OM accumulation under relatively more oxic conditions.

Coincidentally, calcareous turbidite deposition increases during the middle LST, suggesting that the calcareous turbidites may be bringing in more terrestrial material than their dilute siliciclastic counterparts. Furthermore,

A thick, organic-lean calcareous turbidite (9653 - 9645 ft.; 2942.2 - 2939.8 m) marks the transition between the Wolfcamp B3 and B2. The absence of HC Potential and OM Type data points at the depths 9649.1 ft. and 9645.2 ft. (2941 & 2939.9 m) reflects the non-reported S1 and S2 values due to the low TOC values. Overlying this thick calcareous package are thin beds of silty laminated mudstone, progressively interbedded at a higher frequency with thin massive laminated calcareous packstone packages, up until 9629 ft. (2934.9 m). The initial increase in TOC after the thick calcareous turbidite progressively decreases throughout the TST, from 9641.1 - 9629.1 ft. (2938.6 - 2934.9 m), most likely reflecting the increase in thin calcareous packages. The decrease in HC Potential over the early and middle TST suggests that the organic matter may have been oxidized by the frequent calcareous sediment gravity flows. After the initial increase in RHP values at the onset of the TST, values then decreased. However, RHP values remain relatively constant (RHP = 1.92 - 2.01) until 9629.1 ft. (2934.9 m), indicating a shift to more persistently oxic water column conditions.

The onset of transgression could create a more well-circulated, and therefore more oxygenated, system. Furthermore, the aggregate of high-frequency turbidity currents could shift the water column conditions from episodically oxygenated to semi-persistently oxygenated. The low HI values over the same interval supports this interpretation and may also indicate a shift to more terrestrially derived OM. It isn't until the end of the interpreted TST, within the maximum flooding zone (*mfz*), at 9625.1 ft. (2933.7 m), that

an increase in all bulk organic geochemical parameters is observed, indicating a more organic-rich, marine, anoxic setting. However, by the very end of the *mfz* at a depth of 9621.1 ft. (2932.5 m), the TOC drops dramatically to 0.64 wt.%. Unfortunately, other bulk organic geochemical parameters are not reported for TOC values less than 1 wt. %. Therefore, it remains unclear if the anomalously low TOC of the black mudstone samples is indicative of an *mfz* with low preservation or low productivity potential. Overall the *mfz* contains the most continuous segment non-laminated black mudstone, yet it is neither the most anoxic nor the most marine prone organic matter.

The TOC progressively increases to about 3.32 wt.% at a depth of 9613.15 ft. (2930.1 m), interpreted as the onset of the HST. Over the same interval, the RHP values remain to be relatively stable, suggesting little variability in the degree of oxygenation, somewhat countering the sedimentological and ichnological derived oxygenation interpretations of the early HST. However, HI values remain greater than 200, suggesting more marine derived organic matter, consistent with the early HST interpretation. Interestingly, the thick, TOC lean (~1 wt.%) massive packstone around 9605.1 ft. did not affect RHP or HI values, suggesting that the thick calcareous package was most likely formed by a single event which quickly equilibrated to background redox conditions. These elevated RHP and HI values are at odds with the highstand sedimentological interpretation and indicate water column conditions and organic matter contribution more similar to that which is observed at the end of the transgression. This decoupling of the sedimentological and associated geochemical conditions is similar to that which was observed at the beginning the lowstand (9680 – 9650 ft.; 2950.5 - 2941.3 m) and may

also reflect lag times between physical sedimentological processes and chemical oceanographic conditions due to sea level fluctuations.

All the bulk organic geochemical parameters suggest that the depositional environment became increasingly dynamic in the middle HST (9601.35 – 9569.5 ft.; 2926.5 - 2916.8 m) compared to steadier redox conditions and OM type input during the early HST. Sedimentologically, the middle HST is characterized by the occurrence of the truncated packstones and the finer grained end members of the coarse grained wackestone. Unfortunately, these bulk geochemical shifts do little to resolve the contour-current versus storm-derived hyperpycnal flow depositional mechanism ambiguity. Both mechanisms could create the observed oscillations in the productivity and redox conditions in the inorganic and bulk organic geochemical data. Furthermore, it remains unclear if this sedimentological and geochemical ambiguity within the middle 2nd order HST reflects a nested 3rd order sequence. Regardless, the variations in HI and RHP values that define the early middle HST progressively decrease in magnitude towards the end of the middle HST. The TOC values over the same interval (9601.35 – 9569.5 ft.; 2926.5 - 2916.8 m) do not show a qualitative relationship with HI or RHP variability as a function of depth, suggesting the interpreted redox conditions are not the dominant control on the amount of TOC present in the middle HST.

Bulk geochemical interpretations of the early late HST within a sedimentological context are difficult due to the core gap from 9565 – 9552 ft. (2915.4 - 2911.4 m). The TOC values remain relatively high (~ 3.8 wt.%) from 9565 – 9551 ft. (2915.4 - 2911.1 m), while both HI and RHP values shift to some of the lowest observed throughout the core (~ 90 and 1.5, respectively). Furthermore, both early late HST samples sedimentologically

correspond to highly bioturbated flow deposits which, combined with the bulk geochemical data, suggest more oxygenated conditions and influxes of terrestrial plant matter. However, little confidence can be placed in such a depositional interpretation since the cause of the core break is unknown and post-depositional or anthropogenic causes for organic matter oxidation cannot be ruled out.

The three remaining samples thereafter, beginning at 9547.25 ft. (2910 m), are thought to be representative of the deposition environment in the late HST and unaffected by the core break. The TOC, HI, and RHP values all gradually decrease for remainder from 9547.25 to 9539.1 ft. (2910 - 2907.5 m), indicating a progressive shift to more terrestrial organic matter and a more oxic environment. An increase in the frequency of laminated mudstone lithofacies is also observed over the same interval, suggesting more oxygenating distal siliciclastic turbidity currents may be responsible for the influx of terrestrial organic matter. Furthermore, the only carbonate sediment gravity flow deposit observed over this interval is believed to be from a more dilute debris flow, carrying with it less entrained oxygenating water than the calcareous turbidity current counterparts. These sedimentological processes are thought to be working in conjunction with preexisting oxygenated oceanographic conditions typical during the HST. The constructive oxygenation signal interference would create a gradual overall geochemical shift compared to the punctuated, event deposit controlled redox changes observed earlier in the HST. Overall, the system appears more dynamic and oxygenated during the HST relative to other sequence stratigraphic intervals.

7.2. Biomarkers

Biomarkers are molecular fossils of precursor biological organisms which have undergone alteration under the presence of certain lithologies, redox conditions, and/or thermal stresses. Although many of these pathways form through a combination non-unique conditions, biomarkers remain useful in paleo-environmental reconstructions. Biomarkers were analyzed using GC and GC-MS techniques. Table 4 below summarizes the specific biomarkers analyzed in this investigation.

Table 4. Biomarkers and chromatograms / fragmentograms analyzed.

Biomarker	Chromatogram / Fragmentograms
<i>n</i> -alkanes	Saturate fraction chromatogram
Pristane and Phytane	Saturate fraction chromatogram
Sesquiterpanes	Branched / cyclic; <i>m/z</i> 123
Terpanes / Hopanes	Branched / cyclic; <i>m/z</i> 191
Steranes	Branched / cyclic; <i>m/z</i> 217

7.2.1. Acyclic Biomarkers

7.2.1.1. *n*-Alkanes

Since samples were taken from a thermally mature, unweathered core, *n*-alkanes are the dominant compounds observed in the saturate fractions. Overall, the chromatograms' fingerprints did not vary widely between samples as a function of depth, suggesting overall stable environmental conditions through time. *n*-Alkane distributions were predominately unimodal and centered around the lower carbon numbers ($<n\text{-C}_{24}$) with a maximum at *n*-C₁₆ (Figure 20). This distribution indicates mainly marine algae and phytoplankton contributions to the organic matter (Tissot and Welte, 1978; Jacobson et al., 1988; Wang and Philp, 1997). However, this marine organic matter interpretation partially conflicts with mixed marine / terrestrial kerogen (Type II / III) indicated by the modified van Krevelen plot. Cracking of the longer chained *n*-alkanes, possibly derived from more terrigenous material, during oil generation could cause a shift to lower carbon numbers. Therefore, the *n*-alkane unimodal distribution centered around *n*-C₁₆₋₁₈ may be reflecting thermal maturity as well as a marine organic matter contribution. However, some samples showed a slight predominance of odd carbon over even numbered *n*-alkanes, suggesting a higher plant matter contribution to the organic matter (Tissot and Welte, 1978). Alternatively, the predominance of even over odd is thought to reflect carbonate deposition under more reducing conditions (Moldowan et al., 1985; Wang and Philp, 1997). However, increasing maturity tends to decrease the predominance of one over another, producing values close to 1 (Wang and Philp, 1997).

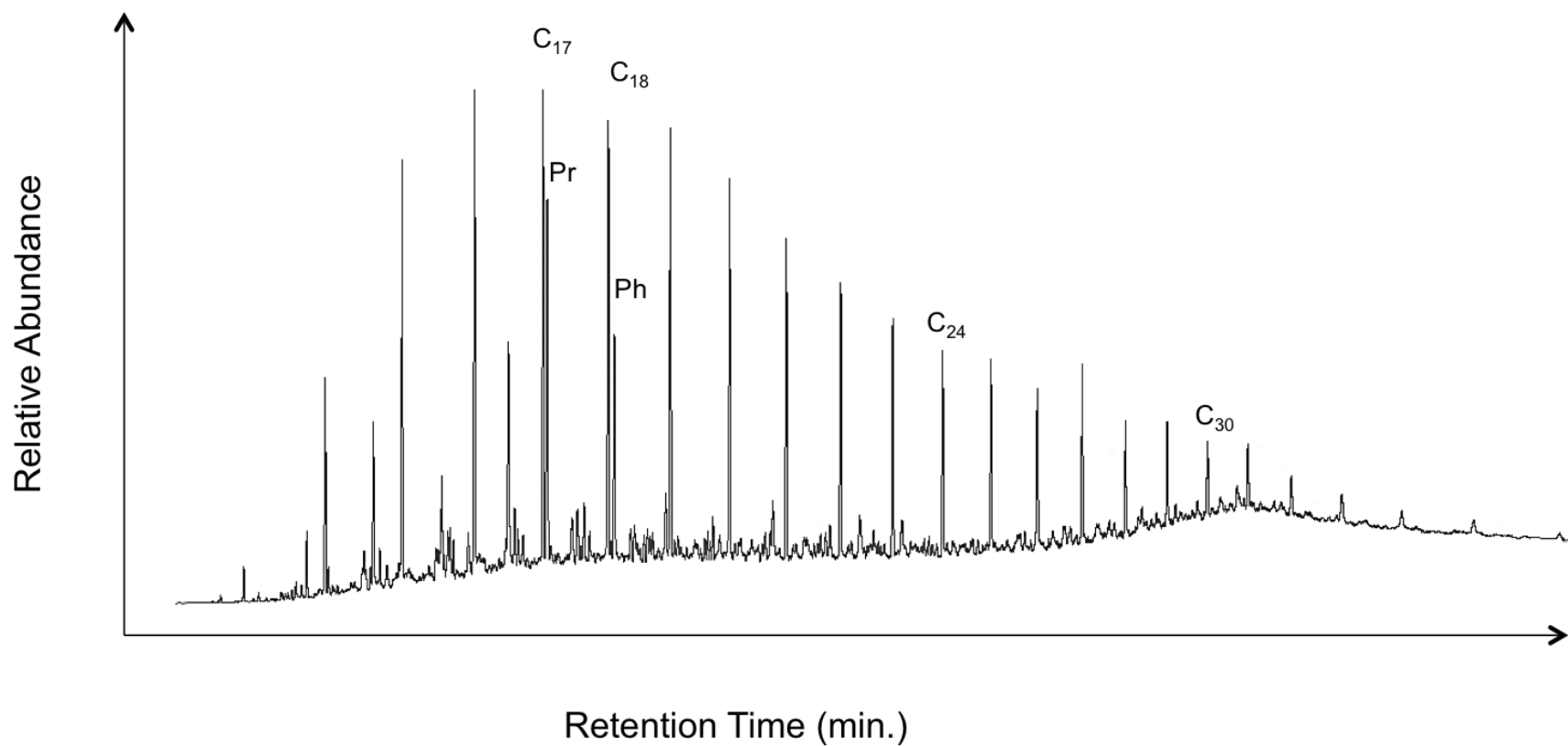


Figure 20. Example GC trace of a saturate fraction. Taken from depth 9585.2 ft. Pr: pristine, Ph: phytane; n-C₁₇: C₁₇ normal alkane; n-C₁₈: C₁₈ normal alkane; n-C₃₀: C₃₀ normal alkane. Note unimodal distribution of n-alkanes, centered around n-C₁₆, and odd over even carbon number predominance.

Bray and Evans (1961) originally proposed using the Carbon Preference Index (CPI) to numerically reflect the relative predominance of odd versus even carbon numbered *n*-alkanes. A modified version of the original formula is used in this study and is as follows (Marzi et al., 1993):

$$CPI = \left[\frac{C_{23} + C_{25} + C_{27}}{C_{24} + C_{26} + C_{28}} \right] + \left[\frac{C_{25} + C_{27} + C_{29}}{C_{24} + C_{26} + C_{28}} \right] \times \frac{1}{2}$$

Scalan and Smith (1970) proposed an alternative equation, Odd Even Predominance (OEP), which considered changes in the average carbon length. However, a simpler version of the moving average equation was later adopted and is as follows (Peters et al., 2005):

$$OEP = \left[\frac{C_{21} + 6C_{23} + C_{25}}{4C_{22} + 4C_{24}} \right]$$

The terrigenous/ aquatic ratio (TAR) provides insight on the relative amount of organic matter from terrigenous input (Bourbonniere and Meyers, 1996). TAR was calculated from *n*-alkanes on the GC traces of the saturate with the following equation (Peters et al., 2005):

$$TAR = \left[\frac{C_{27} + C_{29} + C_{31}}{C_{15} + C_{17} + C_{19}} \right]$$

The CPI, OEP, and TAR values are all plotted as a function of depth with the sequence stratigraphic framework for reference in Figure 21. TAR values range from 0.19 - 0.68 with an average of 0.33. Terrigenous land plants contribute to high-end *n*-alkanes (>*n*-C₂₇) and result in higher TAR values (Eglinton and Hamilton, 1967; Cranwell, 1973). Conversely, algal matter is thought to contribute to the low-end *n*-alkanes (<*n*-C₁₉) and results in lower TAR value (Blumer et al., 1971; Giger et al., 1980; Cranwell et al., 1987). However, the unimodal distribution of the lower end member may reflect thermal maturation effects (Sofer, 1984; Tegelaar et al., 1989). Given that samples were taken from a core and uniform maturity is assumed, TAR is a relatively useful parameter for showing changes in organic matter input over time (Meyers, 1997).

Beginning at a depth of 9700 ft., TAR values progressively increase from 0.32 to 0.51 at a depth of 9681 ft. This increase in TAR values suggests an increase in terrestrial plant matter as the FSST progresses, reaching a localized maximum at the FSST – LST transition. This influx of terrestrial material at this sequence stratigraphic transition is expected as carbonate debris flows due to shelf instability cease and siliciclastic deposition begins. However, as the LST progresses, TAR values decrease, suggesting a decrease in terrestrial plant matter input and, conversely, an increase in the amount of aquatic organic material. This contradicts the HI derived organic matter type interpretation throughout the LST (Figure 19). However, the positive HI value excursion at the FSST – LST transition may be reflecting more reducing conditions rather than a shift to more marine derived organic matter, consistent with the sequence strat-

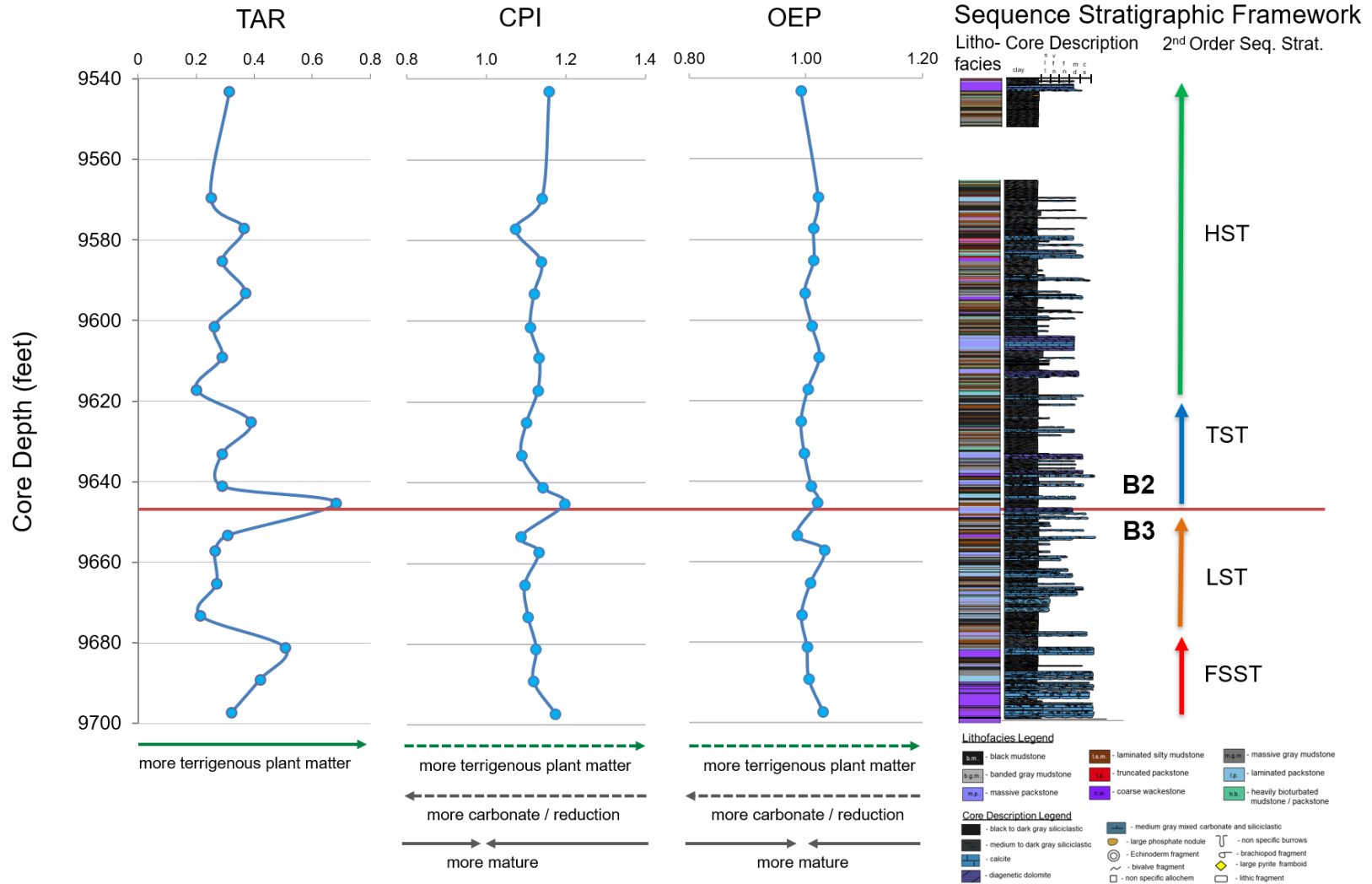


Figure 21. *N*-alkane biomarker ratios. From left to right: terrigenous aquatic ratio (TAR), carbon preference index (CPI), and odd even predominance (OEP). Arrows under depth plots indicate environmental, source material, and maturity factors thought to influence the *n*-alkane ratios. Stippled arrows indicate lower confidence interpretations of controls that exert less influence. Note higher matures CPI and OEP centered around 1. Sequence stratigraphy on far right for reference.

graphic redox interpretation. Although classic carbonate reciprocal sedimentation would lead us to believe that there would be more terrigenous material deposited during the LST, relatively low TAR values (< 0.3) suggest consistently little terrigenous input during this time.

The TAR value then increases to 0.68 by 9653.3 ft., suggesting a sharp increase in the amount of terrigenous material at the LST – TST, and Wolfcamp B3 – B2, transition. Interestingly, the largest TAR value observed throughout the entire core comes from a laminated packstone sample within a calciturbidite, suggesting that the calcareous turbidity currents, rather than their more dilute siliciclastic counterparts, may be the dominant mechanism by which terrigenous plant matter was transported to deeper parts of the basin. The TAR values remain relatively low and consistent (~ 0.3 , $\Delta\text{TAR} < 0.1$) throughout the core consistent with mainly marine organic matter input and only small, episodic inputs of terrestrial organic matter during the sea level high (HST).

Both the CPI and OEP values vary very little and are centered around one, reflecting the samples' maturity within the middle to late oil generation window. The CPI values ranged from 1.07 – 1.20 with an average of 1.12., while OEP values range from 0.98 to 1.03 with an average of 1.01. Generally, CPI and OEP values track each other well as a function of depth. However, numerically the CPI values are all elevated relative to OEP values due to the lower carbon numbers within the OEP denominator and the samples' lower carbon number ($< n\text{-C}_{24}$) centered *n*-alkane distribution. Small oscillations in CPI and OEP values may reflect changes in organic matter contribution or preferential oxidation or preservation of shorter chained *n*-alkanes.

7.2.1.2. *Pristane / Phytane*

Pristane (Pr) and phytane (Ph) are acyclic isoprenoids commonly used to evaluate redox conditions during deposition (Tissot and Welte, 1978; Peters et al., 2005). They are believed to be derived from different redox pathways from the same phytol chain of chlorophyll *a* (Brooks et al., 1969). The more oxidizing redox pathway is thought to form Pr while the more reducing pathway is thought to form Ph. Therefore, low Pr/Ph values (<1) indicate anoxic conditions whereas high Pr/Ph (>3) values indicate oxic conditions (Powell and McKirdy, 1973; Didyk et al., 1978). However, increasing maturity, particularly around peak oil generation, is known to elevate overall Pr/Ph values (Connan, 1974; Albrecht et al., 1975; Connan and Cassou, 1980). Furthermore, other pristane and phytane precursors, such as archaeobacterial lipids, tocopherols, and zooplankton, have been proposed (Blumer et al., 1963; Blumer and Snyder, 1965; Goossens et al., 1984; Risatti et al., 1984; Volkman and Maxwell, 1986). Both the uncertainty surrounding the precursors and the effects of maturity occlude Pr/Ph paleoredox interpretations. Therefore, it is imperative to consider all geochemical and sedimentological data, particular for Pr/Ph values between 0.8 and 3, before making a paleoredox assessment (Peters et al., 2005). All samples within the core are the same maturity and therefore relative changes in Pr/Ph values are thought to reflect changes in the paleoredox conditions. However, given the samples' intermediary Pr/Ph values and relatively small fluctuations, and the samples elevated maturity, the following Pr/Ph paleoredox interpretation is contextualized with previous sedimentological and geochemical findings.

The Ph / Ph values are displayed as a function of depth with the sequence stratigraphic framework for reference in Figure 22. Overall, Pr/Ph values have a narrow

range from 1.28 – 1.59, indicating a form of suboxia or dysoxia. These intermediate values are consistent with the low concentrations of redox dependent trace metals throughout the core. Although the Pr/Ph values consistently lie well within in the interpreted suboxia range, relative fluctuations may indicate subtle changes in redox conditions associated not only with eustatic sea level fluctuations but episodic sediment gravity flows. The Pr/Ph values vary most (Δ Pr/Ph = 0.31) over the first 30 ft. of core, spanning the interpreted FSST and the beginning of the LST in the Wolfcamp B3. Beginning at 9697 ft., the initial Pr/Ph of 1.47 decreases to 1.28 by 9681 ft. The initial elevated Pr/Ph values coincide with first debris flow and suggests a small oxygenation event which may have preequilibrated with the background, relatively more anoxic redox conditions. The overlying fine-grained section observed at 9681 ft. has the lowest measured Pr/ Ph value measured throughout the entire core and is interpreted to represent background sedimentation redox conditions. This lowest value also coincides with the FSST-LST boundary further suggesting that the most oxygen limited conditions occurred during the onset of the LST, which is corroborated by ichnological data. Interestingly, this lowest value observed in the entire core is preceded by the highest value (Pr/Ph = 1.59) observed throughout the core, at a depth of 9673 ft.

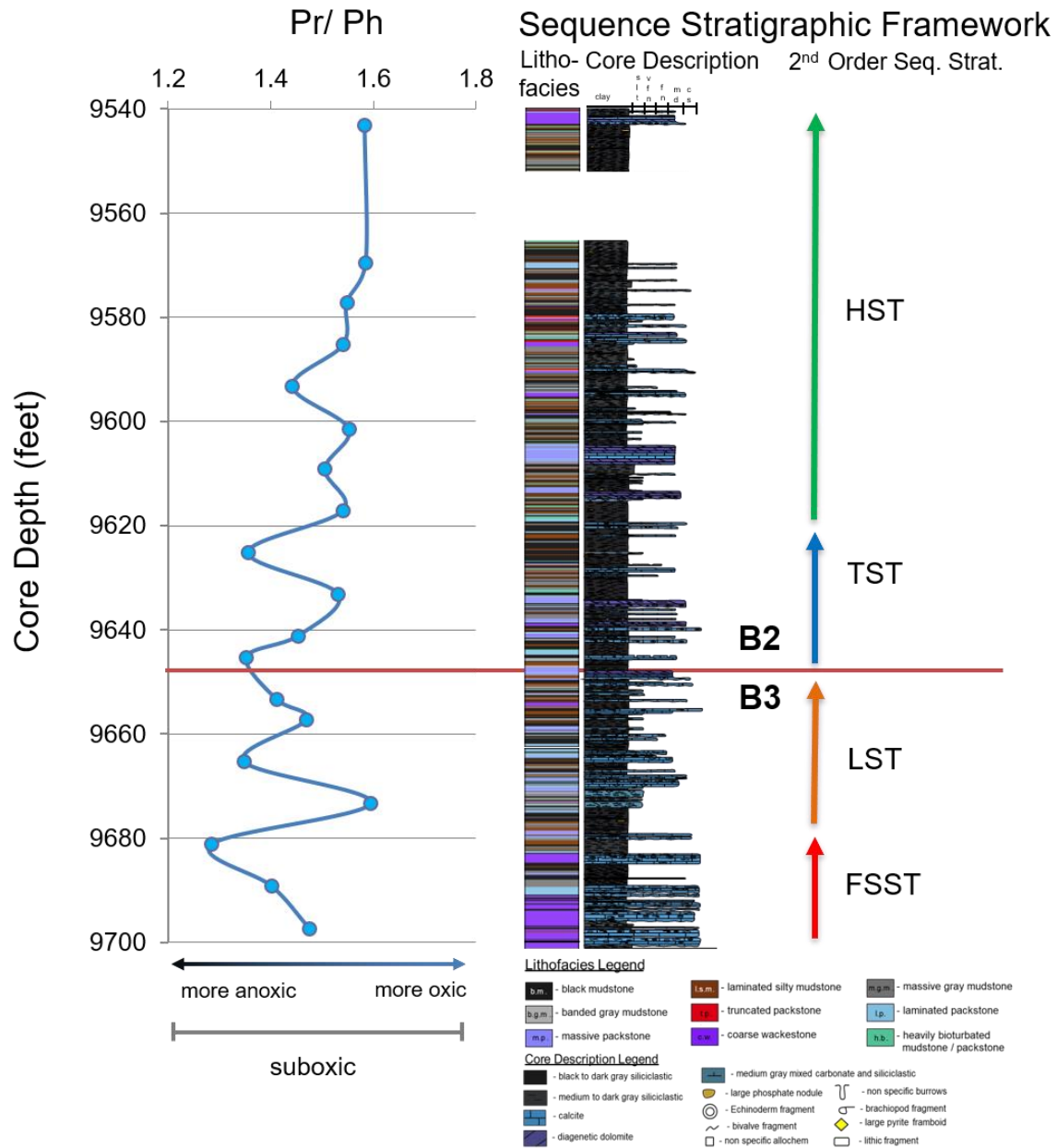


Figure 22. Pristane/Phytane ratio (Pr/Ph) expressed as a function of depth with sequence stratigraphic framework on right for reference. Note intermediate Pr/Ph values indicating overall suboxic conditions. Fluctuations therein are considered relative. Arrows indicate environmental factors to influence the Pr/Ph ratio and how.

This depth coincides with the first high frequency calciturbidites in the middle LST. The relatively large change (although in absolute terms, quite small) emphasizes the ability of turbulent flows, with a significantly higher proportions of entrained water relative to their more debritic counterparts, to temporarily oxygenate a system. By 9665 ft., the Pr/ Ph values return a background sedimentation value of approximately 1.35, indicating a return to relatively more anoxic conditions, although not to the same degree as which was observed at the FSST-LST transition. Over the next 20 ft. (9665 – 9645 ft.), there is another Pr/Ph high-low cycle, potentially indicative of another reoxygenation sequence. Lower confidence is placed in this redox interpretation due to small magnitude of the change and its apparent contradiction to other geochemical and ichnological data, which suggest more anoxic conditions towards the end of the LST. Elevated Pr/Ph values may reflect a later oxidizing diagenetic fluid, as suggested by the heavily dolomitization observed over 9657 – 9659 ft. (ten Haven et al., 1987) (see Appendix C. Inorganic Geochemistry).

Although there is no significant Pr/Ph oxygenation marker signifying the onset of the TST at 9645 ft., Pr/Ph values gradually increase over the next 12 ft., maxing out at 1.53, before sharply decreasing at the very end of the TST, or *mfz*. This is interpreted as a gradual oxygenation due to increased sea water circulation during sea level rise, but more stagnant, reducing water column conditions during the sea level maximum. However, the degree to which sediment gravity flows effected the paleoredox redox record over the TST is unknown. Since the early TST contains more high-frequency calcareous turbidites than the *mfz*, it remains somewhat unclear if the sharp decrease in Pr/Ph values within the *mfz* reflects a sharp change from more constantly oxygenated

conditions to less oxygenated or rather that the oxygenation events finally re-equilibrated to the background anoxic conditions, similar to the re-equilibration observed during the FSST. Whatever the case may be, the Pr/Ph values suggest the early LST was relatively more anoxic than the end of the TST, a notion previously supported by inorganic geochemical, ichnological, and sedimentological data.

The Pr/Ph values remain relatively constant ($\text{Pr/Ph} \approx 1.6$; $\Delta \text{Pr/Ph} < 0.1$) over the interpreted HST (9617 – 9543 ft.) with a minor exception around 9593 ft. At this depth, the Pr/Ph value decreases to 1.44, suggesting a slight shift to more anoxic conditions during an otherwise more oxygenated time. Notably, this shift in Pr/Ph values coincides with the first occurrence of the phosphorus-rich truncated packstone facies. This decrease in the Pr/Ph value is also mirrored by the rapid increase in RHP values around the same depth, further supporting the notion of a strengthening, yet still in absolute terms, weak, chemocline. However, RHP values, which have a higher sampling density (every 4 ft. compared to every 8 ft. for biomarker data sampling) suggest that the chemocline may have been erratic and unstable around the same time. Although not purely controlled by redox conditions, the oscillating RHP values may be shedding light on redox cycles that occurred at too high of a frequency to be captured by Pr/Ph alone, which may be relatively insensitive rapid changes in palaeoceanographic conditions. However, it remains unclear if this shift to relatively more anoxic conditions during the HST is indicating the evolution of upwelling currents and anoxic bottom waters, an influx of nutrient rich waters from hyperpycnal flows, and a subsequent algal bloom and die off cycle resulting in an anoxic episode, or a nested 4th order parasequence within the overall 3rd order HST. This elusive depositional mechanism will be elaborated on in the 7.2.2.2.1

Tricyclic Terpanes section. Generally, however, Pr/Ph values remain elevated (~1.58) throughout the HST, signifying more oxic conditions at this time than at any other point during deposition, an interpretation supported by all the sedimentological, ichnological, and geochemical data.

Overall, the intermediate Pr/Ph values suggest that the upper portion of the Wolfcamp B3 and the entirety of the Wolfcamp B2 were deposited under predominately suboxic conditions. Furthermore, the system became progressively more oxygenated as time progressed, with more anoxic conditions during the FSST and LST, and more oxic conditions during the TST and HST. Oscillations in Pr/Ph values decrease in magnitude as a function of time, suggesting the development of relatively more stable and oxygenated palaeoceanographic conditions. Whether this perceived redox stability is an artifact of lower sampling density the relative insensitivity of Pr/Ph to higher frequency changes in redox conditions, or due to pervasive turbidity flows during highstand shedding or better overall palaeoceanographic circulation remains unclear. Rapid increases in Pr/Ph values are thought to be linked to sediment gravity flows along a fluid entrainment spectrum. Smaller magnitude shifts are believed to be associated with debritic, weakly oxygenated flow events or overprinted by differing diagenetic conditions. Conversely, larger magnitude shifts are believed to be associated with the clustering of more turbulent oxygenated flow events. Low Pr/Ph values correlate with elevated TAR values and high RHP values indicating the input of terrigenous material is associated with more anoxic conditions. Furthermore, the thicker packages of the heavily bioturbated lithofacies correlate with higher Pr/Ph values and relatively more oxic conditions.

7.2.2. Branched and Cyclics

7.2.2.1. Sesquiterpanes

Bicyclic sesquiterpanes (m/z 123) are biomarkers that can be used to determine the extent of terrigenous input into the organic matter as well as microbial reworking of organic matter (Philp et al., 1981; Alexander et al., 1983; Philp and Gilbert, 1986). 8β (H)-Drimane is believed to be related to bacterial contribution of organic matter through the degradation of hopanoids (Alexander et al., 1983). 4β -Eudesmane is derived from higher plant matter (Weston et al., 1989).

A series of sesquiterpanes were identified in the Wolfcamp samples in varying abundance, however, 4β -eudesmane was not detected (Figure 23). Philp and Gilbert (1986) noted the low abundance of 4β -eudesmane in oils that largely originated from terrigenous material (Philp and Gilbert, 1986). More specific to this study, Salisbury noted the absence of 4β -eudesmane altogether in Wolfcampian source rock extracts from a neighboring county in the Midland Basin in 2014, even though other inorganic geochemical and biomarker ratios suggested plant matter input. Palynological research suggests that west Texas and New Mexico were marked by low diversity, spatially patchy vegetation during the Early Permian (DiMichele et al., 2007). Therefore, although higher plant matter was available during the Wolfcampian, low biodiversity, sparse availability, and long transport distances may have greatly reduced the amount of plant material available in distal marine settings. Thus, it is likely that plant matter was not present in sufficient quantities for 4β -eudesmane detection.

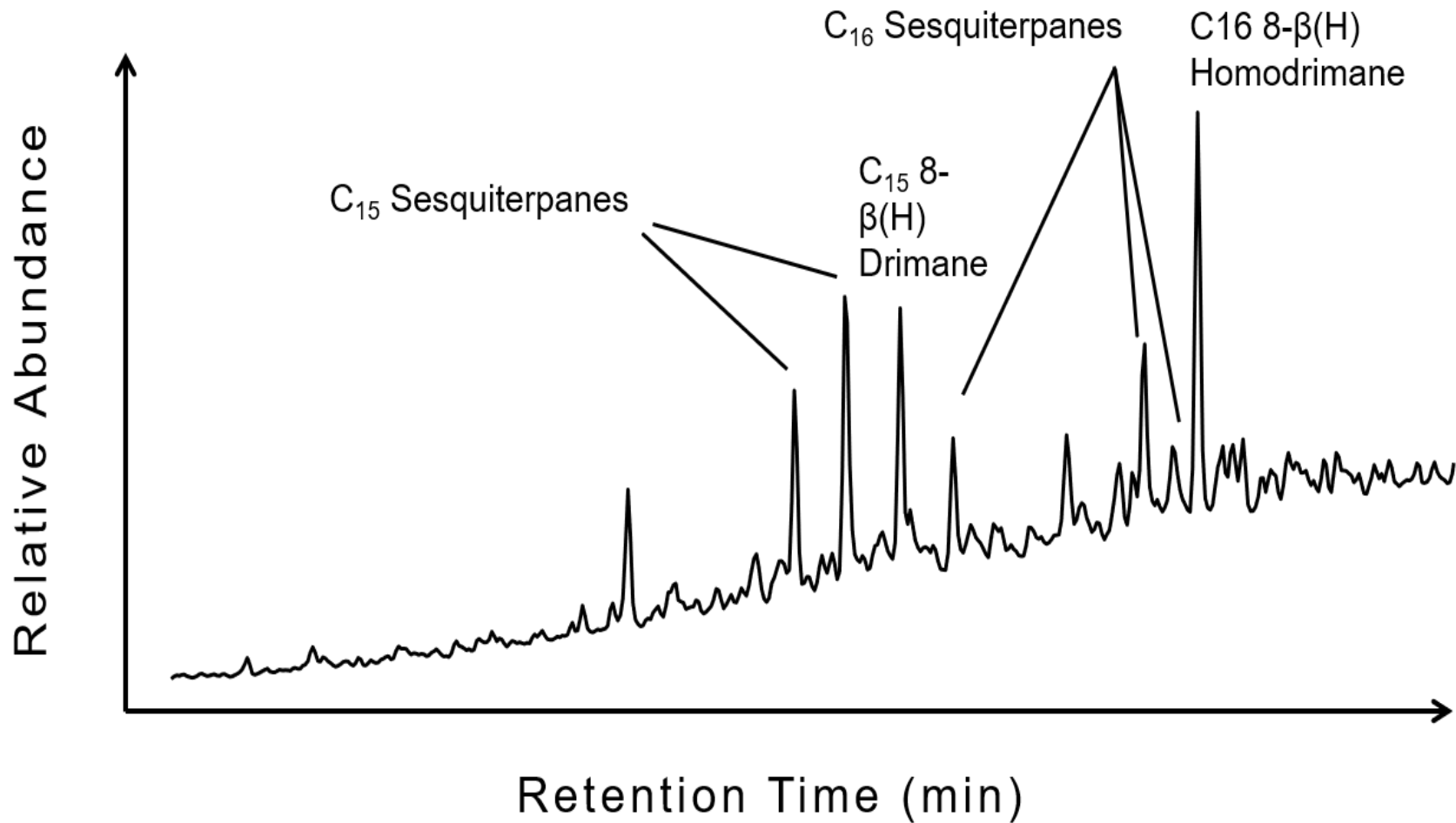


Figure 23. Partial fragmentogram of m/z 123 showing sesquiterpene distribution. Compounds are denoted on fragmentogram. Note absence of eudesmane.

7.2.2.2. *Terpanes*

Terpanes are compounds commonly used for correlation, biodegradation, maturity, migration, organic matter input, and depositional environment assessments (Moldowan et al., 1983; Philp and Gilbert, 1986; Weston et al., 1989; Peters et al., 1990; de Grande et al., 1993; Revill et al., 1994; Meijun et al., 2014; Tao et al., 2015). However, this investigation is primarily concerned with paleo-environmental reconstruction and thus focuses on the relationship between changes in terpane distributions, depositional environment, and organic matter. Aiding in the strict depositional interpretation of these ratios are the inherent properties of the source rock itself. The effects of migration on the biomarker compositions are negligible in a continuous section of unfractured nano-porous source rock. Furthermore, the 160 ft. section of core is roughly the same maturity and within the late oil generation window. Terpane ratio were compared to the maturity assessment to ensure that the depositional interpretation was not influenced by the small scale maturity variability observed in the previous section. Lastly, the effects of biodegradation are largely constrained to oils (Connan et al., 1980; Goodwin et al., 1983; Connan, 1984). However, evidence of biodegradation has been reported in source rock extracts, although it remains unclear if it is a result of migrated non-indigenous oil or some form of in-situ bacterial reworking during and immediately after deposition (paleo-biodegradation) (Noble et al., 1985; Peters et al., 2005). The abundance of *n*-alkanes in the samples of this current study suggests samples are not affected by biodegradation, however, extensive bioturbation was observed. Therefore, terpanes distribution will be compared to ichnological data.

Terpanes are separated from the branched and cyclic portion of the saturate fraction into families based on number of rings they possess. The tricyclic, tetracyclic, and pentacyclic (hopanes) terpanes, respectively, were all examined in this study. Terpanes were determined using GCMS and single ion monitoring of the ion at m/z 191. Compounds that were identified are indicated on representative m/z 191 fragmentograms shown in Figure 24 and corresponding identities are listed in Table 5. Selected terpane ratios and their respective values are found in Table 6. Notably, the terpane gammacerane, a compound characteristic of hypersaline systems with pronounced water column stratification, is absent. The absence of gammacerane, coupled with ichnological and trace metal evidence of episodic suboxia, and Pr/Ph values centered around one, suggest that water column stratification, and associated anoxia, did not occur.

The terpane distributions do not change substantially as a function of depth, suggesting that paleoceanographic conditions, source material, and lithology did not change significantly throughout deposition, but rather slightly fluctuated (see Appendix D). This is consistent with the overall low concentrations of trace metals associated with anoxia and Pr/Ph values centered around 1. In general, the terpanes display a bimodal distribution, with abundant tricyclic terpanes relative to hopanes. Small fluctuations in the tricyclic, tetracyclic, and pentacyclic terpanes will be rigorously assessed in the following sections.

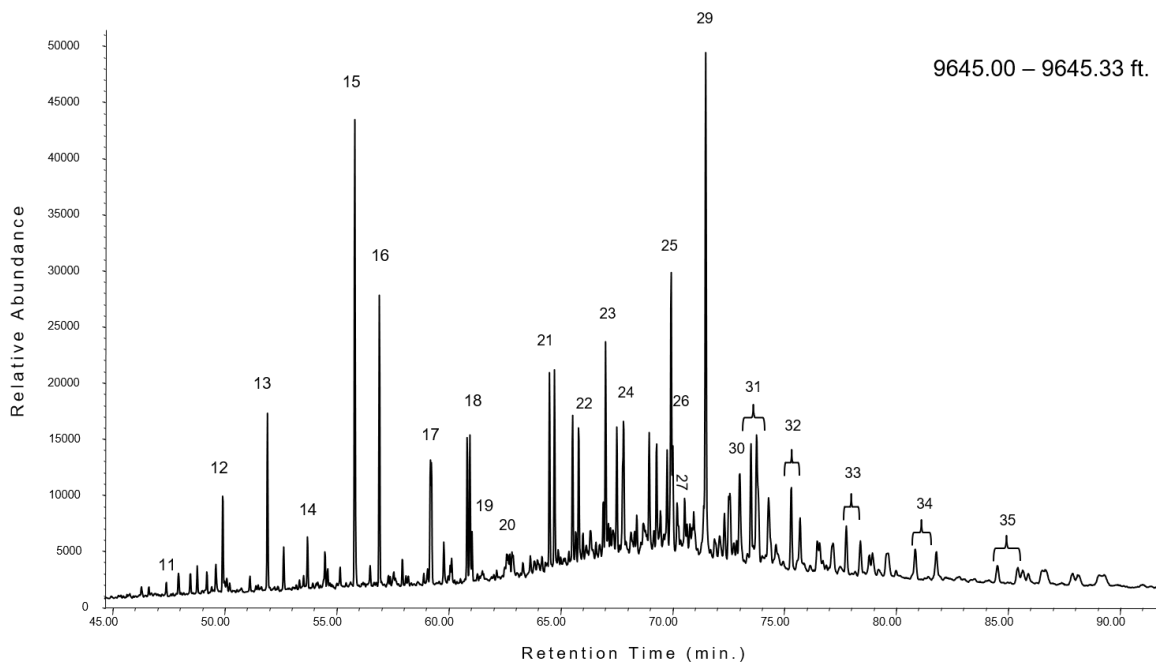
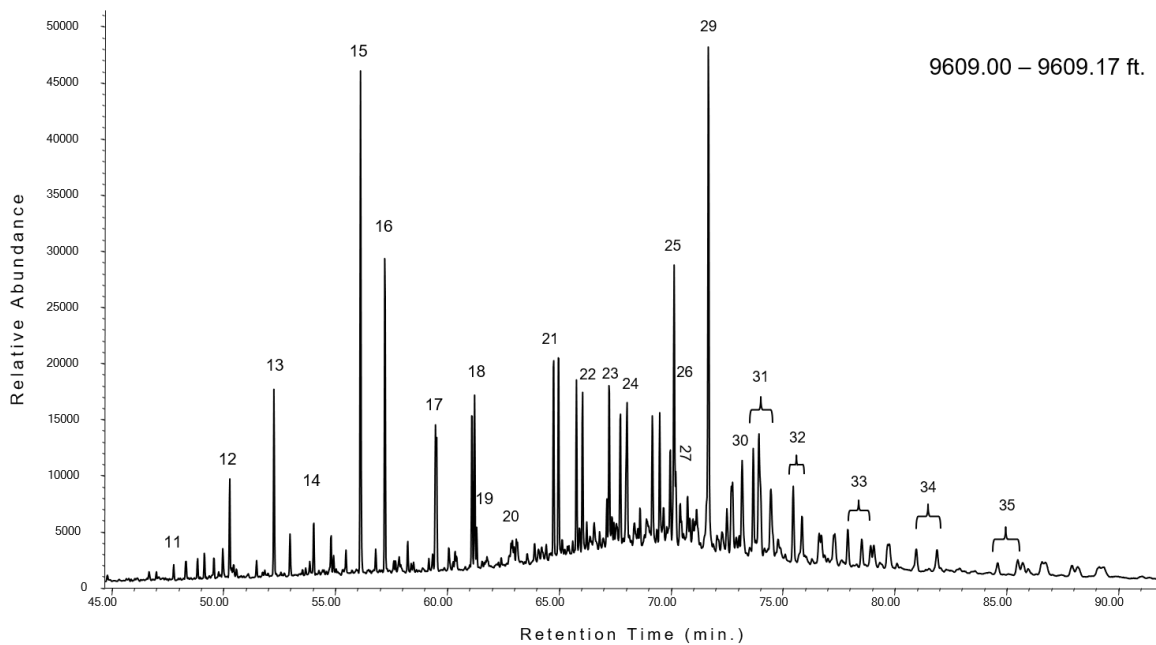


Figure 24. Partial fragmentogram of m/z 191 ion showing terpane distributions for two different samples. Sample taken from 9609.00 – 9609.17 ft. (top) and 9645.00 – 9645.33 ft. (bottom). Peaks are identified in Table 3. Note $17\alpha(H)$, $21\beta(H)$ Homohopane $22R$ coelutes with unknown tricyclic terpane

Table 5. Terpane compound Identification (m/z 191)

Peak Number	Compound
11	C ₁₉ Tricyclic Terpane
12	C ₂₀ Tricyclic Terpane
13	C ₂₁ Tricyclic Terpane
14	C ₂₂ Tricyclic Terpane
15	C ₂₃ Tricyclic Terpane
16	C ₂₄ Tricyclic Terpane
17	C ₂₅ Tricyclic Terpane
18	C ₂₆ Tricyclic Terpane (22S + 22R)
19	C ₂₄ Tetracyclic Terpane
20	C ₂₇ Tricyclic Terpane (22S + 22R)
21	C ₂₈ Tricyclic Terpane (22S + 22R)
22	C ₂₉ Tricyclic Terpane (22S + 22R)
23	17 α -Trisnorhopane (C ₂₇ Ts)
24	18 α -Trisnorhopane (C ₂₇ Tm)
25	Norhopane
26	Norneohopane (C ₂₉ Ts)
27	C ₃₀ Diahopane (C ₃₀ D)
28	17 β (H), 21 α (H) Moretane
29	17 α (H), 21 β (H) Hopane
30	17 β (H), 21 α (H) Moretane
31	17 α (H), 21 β (H) Homohopane (22S+22R*)
32	17 α (H), 21 β (H) Bishomohopane (22S+22R)
33	17 α (H), 21 β (H) Trishomohopane (22S+22R)
34	17 α (H), 21 β (H) Tetrakishomohopane (22S+22R)
35	17 α (H), 21 β (H) Petakishomohopane (22S+22R)

Table 6. Selected terpene biomarker ratios for Wolfcamp B3 and B2 samples.

Core Depth (ft.)	C ₁₉ /C ₂₃ TT	C ₂₀ /C ₂₃ TT	C ₂₃ TT / (C ₂₃ TT + C ₃₀ H)	C ₂₆ /C ₂₅ TT	C ₂₄ Tet / C ₂₆ TT	C ₂₈ +C ₂₉ TT / C ₃₀ H	C ₂₉ /C ₃₀ H	C ₃₀ D / 29 Ts	Ts / (Ts/Tm)	C ₃₁ S / (S+R)	C ₃₂ S / (S+R)	C ₃₅ /C ₃₄ HH
9543.10	0.03	0.19	0.44	1.31	0.16	1.11	0.55	0.80	0.43	0.46	0.66	0.61
9569.50	0.03	0.20	0.46	1.03	0.19	1.14	0.51	0.91	0.44	0.43	0.67	0.58
9577.10	0.03	0.19	0.45	1.38	0.18	1.32	0.51	0.98	0.41	0.43	0.61	0.65
9585.20	0.03	0.19	0.44	0.98	0.19	1.17	0.54	0.96	0.43	0.43	0.65	0.67
9593.20	0.03	0.19	0.42	1.03	0.18	1.05	0.51	0.84	0.45	0.42	0.67	0.68
9601.40	0.03	0.19	0.43	1.37	0.18	1.11	0.50	1.11	0.43	0.45	0.65	0.55
9609.10	0.03	0.19	0.43	1.38	0.18	1.17	0.55	1.15	0.43	0.40	0.66	0.6
9617.10	0.04	0.17	0.42	1.37	0.18	1.08	0.49	1.02	0.49	0.43	0.63	0.63
9625.10	0.04	0.18	0.42	1.03	0.22	0.98	0.43	0.81	0.54	0.44	0.65	0.47
9633.10	0.04	0.18	0.40	1.17	0.22	0.96	0.43	0.93	0.51	0.46	0.68	0.43
9641.10	0.04	0.18	0.38	0.99	0.20	0.87	0.43	0.86	0.54	0.46	0.67	0.53
9645.20	0.03	0.20	0.42	1.26	0.25	1.04	0.54	0.72	0.48	0.41	0.67	0.67
9653.30	0.02	0.16	0.41	1.02	0.28	0.88	0.45	0.90	0.55	0.47	0.65	0.64
9657.15	0.04	0.17	0.42	0.96	0.23	0.93	0.52	0.81	0.54	0.44	0.67	0.52
9665.20	0.04	0.19	0.41	1.32	0.30	0.98	0.43	0.83	0.56	0.44	0.65	0.55
9673.20	0.03	0.18	0.39	1.03	0.24	0.93	0.47	0.87	0.59	0.46	0.66	0.54
9681.10	0.04	0.15	0.38	1.03	0.29	0.85	0.37	0.68	0.61	0.49	0.67	0.45
9689.10	0.04	0.18	0.37	1.04	0.24	0.94	0.40	0.69	0.58	0.45	0.60	0.61
9697.20	0.04	0.17	0.36	1.02	0.31	0.85	0.47	0.87	0.61	0.48	0.60	0.51

7.2.2.2.1. Tricyclic Terpanes

Tricyclic terpanes begin at C₁₉ and extend out to at least C₅₄, although the higher members of the series beyond C₂₉ are often occluded by the hopanes, which begin to appear at the same retention time (Moldowan et al., 1983; de Grande et al., 1993; Peters, 2000; Tao et al., 2015). Although tricyclic terpanes are pervasive in both source rock extracts and oils, their specific biological precursors and diagenetic pathways are diverse and enigmatic. Many tricyclic terpanes (TT) are believed to be derived from regular C₃₀ isoprenoids originating from prokaryotic bacterial membranes (Ourisson et al., 1982; Aquino Neto et al., 1983). However, high concentrations of tricyclic terpanes have been found in *Tasmanites* rich rocks, suggesting that the primitive marine algae may be their biological precursor as well (Aquino Neto et al., 1983; Volkman et al., 1989; Azevedo et al., 1992; de Grande et al., 1993; Revill et al., 1994). In particular, the abundances of the C₂₈ and C₂₉ TT relative to the C₃₀ hopane, the dominant terpane in marine siliciclastic settings, are examined in order to observe changes in the organic matter input of the marine algae *Tasmanites* (C₂₈+C₂₉ TT/C₃₀ Hopane). However, hopanes begin to thermally degrade earlier than tricyclic terpanes, causing the ratio of tricyclic terpanes to hopanes to increase as a function of maturity (Farrimond et al., 1999; Tao et al., 2015). Caution should be taken when interpreting changes in tricyclic terpane to hopane ratios, particularly in the later stages of oil generation, since they may not be reflecting changes in the organic matter input alone.

Both C₁₉ and C₂₀ tricyclic terpanes are thought to be derived from diterpenoids produced from vascular plants (Reed, 1977; Simoneit, 1977; Barnes and Barnes, 1983; Palmer, 1984; Noble et al., 1986; Zumberge, 1987; Peters et al., 1993). Their abundance

relative to the C₂₃ tricyclic terpane, a strong marine indicator, is thought to reflect changes in the organic matter source over time (C₁₉/C₂₃ TT, C₂₀/C₂₃ TT) (Ourisson et al., 1982; Peters et al., 1993; Tao et al., 2015). However, structural dissimilarities between diterpenoids and the tricyclic terpanes in the homologues series have been observed, while different precursors altogether, such as the marine algae *Tasmanites*, have been proposed, limiting the utility of the C₁₉₋₂₀ TT as plant matter indicators (Simoneit et al., 1990; Greenwood and George, 1999). Furthermore, it has been suggested that the relative abundances of the C₁₉ and C₂₀ TT may differ from one another due to changes in oxicity and microbial degradation (Cassani and Eglinton, 1991; Cuny et al., 2011; French et al., 2014; Cheng et al., 2016; Pan et al., 2017).

The ratio of the C₂₆ to the C₂₅ tricyclic terpane (C₂₆/C₂₅ TT) is thought to reflect the salinity of the system (Burwood et al., 1992; Hanson et al., 2000). Values greater than 1 are associated with less saline, freshwater, typical of lacustrine systems, whereas values less than one are associated with more saline, marine environments (Hanson et al., 2000; Tao et al., 2015).

Tricyclic terpane biomarker ratios were plotted as a function of depth and compared to the working sequence stratigraphic model (Figure 25). First, the C₂₀/C₂₃ TT and C₂₀/C₂₃ TT ratio, their discrepancies, and their source material and redox implications will be discussed. Then, fluctuations in the salinity of the system will be assessed using the C₂₆/C₂₅ TT ratio. Finally, the C₂₈+C₂₉ TT / C₃₀ Hopane ratio will be discussed and compared to petrographic evidence of *Tasmanites*.

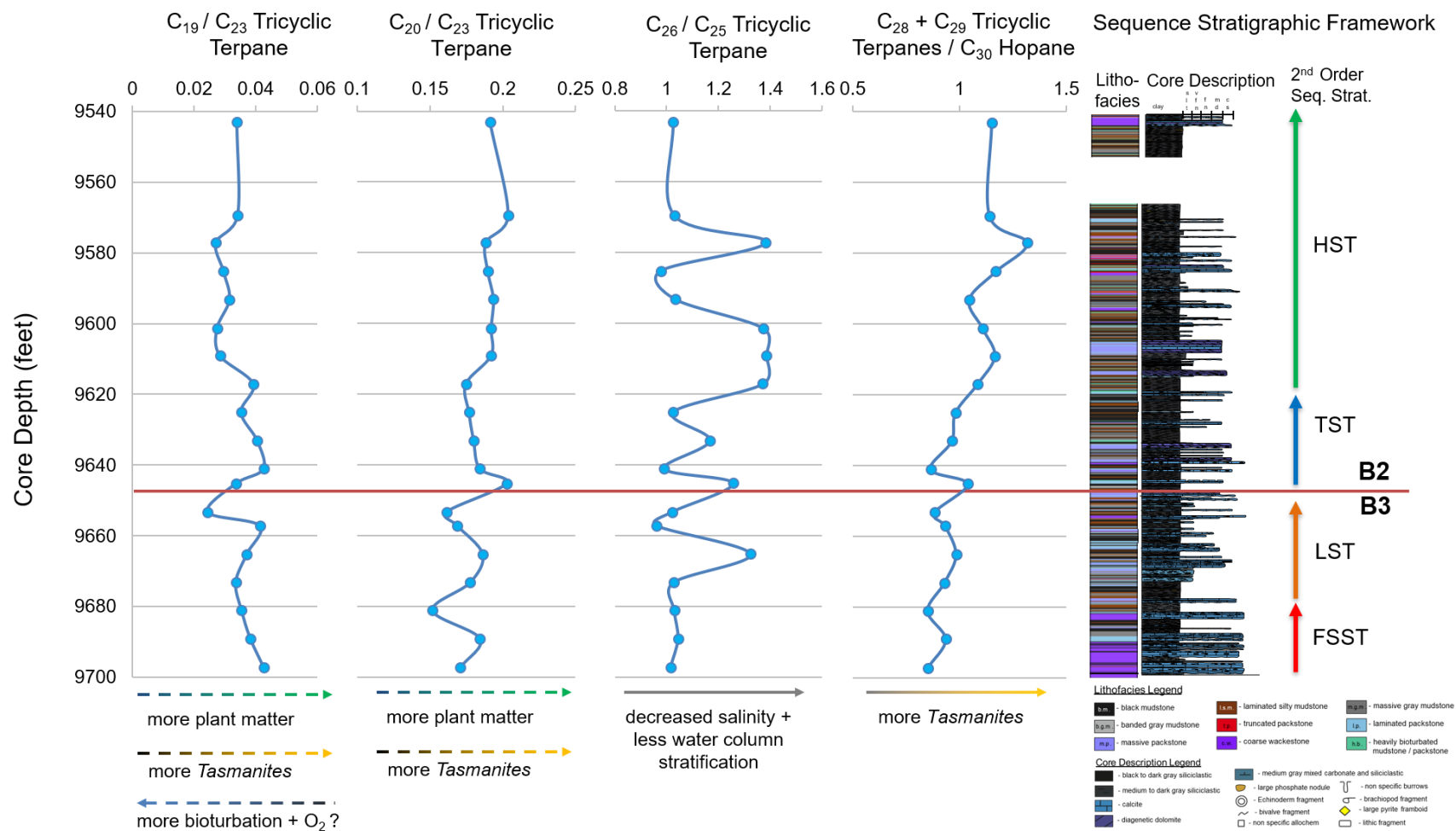


Figure 25. Tricyclic terpene depth plots. Ratios from left to right: C_{19}/C_{23} , C_{20}/C_{23} , and C_{26}/C_{25} tricyclic terpanes and $(C_{28}+C_{29}$ tricyclic terpanes)/ C_{30} hopane. Arrows indicate environmental factors and source material precursors thought to influence the biomarker ratios and how. Stippled arrows indicate lower confidence interpretations of those controls that exert less influence on their respective biomarker ratios.

7.2.2.2.1.1. C₁₉₋₂₀ and C₂₃ Tricyclic Terpanes

The C₁₉/C₂₃ and C₂₀/C₂₃ TT ratios' averages are 0.04 and 0.18, respectively. These low values are consistent with a predominately marine depositional setting with little terrigenous plant matter input (Tao et al., 2015). Both the C₁₉/C₂₃ TT and C₂₀/C₂₃ TT ratio values vary little throughout the core (0.02-0.04, 0.15-0.20, respectively) and in all but 2 samples, C₂₀ TT abundances are one order of magnitude greater than C₁₉ TT. Furthermore, the two ratios do not track each other well as a function of depth, often decoupling at important sequence stratigraphic intervals. However, the overall C₂₀ and C₂₃ TT values and ranges as well as the C₁₉/C₂₃ and C₂₀/C₂₃ TT ratio depth plot discrepancies are consistent with previous Wolfcamp Formation studies (Salisbury, 2014). This implies that there may be factors other than plant matter input influencing the relative abundances of C₁₉ and C₂₀ TT in the Wolfcamp Formation. Although other useful organic matter source and paleoredox information can be extracted from the C₁₉/C₂₃ TT and C₂₀/C₂₃ TT ratios, little confidence can be placed in these paleoenvironmental interpretations due to the analytical uncertainty surrounding such low concentrations, particularly in the case of the C₁₉ TT.

Beginning at 9697 ft., the C₁₉/C₂₃ TT ratio progressively decrease from 0.04 to 0.03 by 9673 ft., just above the FSST – LST boundary, before increasing again to 0.04 by 9657 ft., towards the late middle LST. The C₁₉/C₂₃ TT values then drop off to 0.02 by 9653 ft., equivalent to the end of the LST. The change in C₁₉/C₂₃ TT over this depth interval are thought to weakly reflect changes in the plant matter input with a potential redox overprint. However, TAR values show large influxes of terrigenous material over different sequence stratigraphic intervals, particularly the FSST-LST transition and at the onset of the TST.

Elevated C_{19}/C_{23} TT values during the early FSST and late middle LST may therefore reflect influxes of terrestrial material that were subject to less bioturbation and microbial oxidation (French et al., 2014; Cheng et al., 2016). Increased bioturbation during the late early LST combined with low HI values, interpreted as more terrestrially prone organic matter, during the early FSST and late middle LST support the C_{19}/C_{23} TT interpretation. The drop in C_{19}/C_{23} TT at the very end of the LST poses a greater problem for the organic matter source and redox indicator interpretation since HI values at this depth suggest an increase in terrigenous contribution to the organic matter, and there is a marked absence in bioturbation. Interestingly however, the CPI and OEP values, although centered around 1 due to maturation, exhibit similar depth patterns to the C_{19}/C_{23} TT ratio. Given that a slight odd over even predominance in is thought to reflect more terrigenous, the agreement of the of the CPI, OEP, and C_{19}/C_{23} TT depth plots suggests that the later may reflect plant matter input.

The C_{20}/C_{23} TT ratio exhibits a different depth compared to the C_{19}/C_{23} TT ratio over the Wolfcamp B3, with elevated values (~ 0.18) center around 9681.1 and 9665.2 ft. However, the C_{20}/C_{23} TT looks markedly similar to that of the $C_{28}+C_{29}$ TT/ C_{30} Hopane ratio depth plot, indicating that it may reflect marine algae input of *Tasmanites* more so than that of plant matter during the FSST and LST. The depositional and paleoceanographic significance of increase *Tasmanites* algal input is expanded upon in a later section.

The C_{19}/C_{23} TT and C_{20}/C_{23} TT depth plots track each other fairly well for the remainder of the core, with the exception of the early and middle HST (~ 9609 - 9585 ft. 2928.8 - 2921.5 ft.). At the onset of the TST (~ 9645.2 ft.; 2939.9 m), both the C_{19}/C_{23} TT

and C_{20}/C_{23} TT ratios increase suggesting a potential increase in plant and algal contribution to the OM, respectively. Beginning at 9641.1 ft. (2938.6 m), both the C_{19}/C_{23} TT and C_{20}/C_{23} TT ratios begin to decrease and continue to do so for the remainder of the TST, suggesting a decrease in plant matter material as sea level rises. It is also at this depth that the C_{20}/C_{23} TT and $C_{28}+C_{29}$ TT/ C_{30} Hopane ratios become notably decoupled, suggesting that for that the C_{20}/C_{23} TT ratio may not be entirely reflecting marine algae input during Wolfcamp B2 deposition. However, the geochemical controls by which the C_{20}/C_{23} TT ratio reflects plant matter versus marine algal contribution to the OM remains unknown. Elevated Pr/Ph values and increased bioturbation suggest increased oxicity during Wolfcamp B2 deposition may be playing a role, however, this is highly speculative. Regardless of the cause, beginning around 9609 ft. (2928.8 m), or the interpreted onset of the HST, the C_{19}/C_{23} TT ratio exhibits an initial decrease while the C_{20}/C_{23} TT ratio exhibits an initial increase. In both cases, the values remain relatively constant throughout the early and middle HST, signifying a relatively constant influx of plant material throughout this time. However, it remains unclear if the constant influx of higher plant matter observed in the HST is a relative decrease or increase from the previous TST. Both the C_{19}/C_{23} TT and C_{20}/C_{23} TT ratios increase at the very end of the HST suggesting an increase in plant matter input towards the end of Wolfcamp B2 deposition.

Overall, the ambiguity surrounding the diterpenoid precursor to C_{19} and C_{20} TT make high resolution paleoenvironmental reconstruction based on these compounds difficult, but, the agreement of both proxies, amongst other geochemical source material parameters, gives us a general understanding of the system during Wolfcamp B3 and B2 deposition. That being said, there is most likely an influx of terrestrial material towards the

end of the middle LST, before a decrease at the very end of the LST. Both proxies as well as TAR values suggest an initial influx of terrestrial plant matter at the onset of the TST, which decreases as the TST proceeds. The HST can generally be characterized as having a relatively constant influx of plant material with small oscillations therein. This cryptic relationship between redox conditions and humic and fulvic acids, potential derived from higher plant matter, will be examined in greater detail later on.

7.2.2.2.1.2. C₂₅₋₂₆ Tricyclic Terpanes

The ratio of the C₂₆ to the C₂₅ the tricyclic terpane (C₂₆ / C₂₅ TT) is thought to reflect salinity (Burwood et al., 1992; Hanson et al., 2000). Values greater than one are associated with less saline, typical freshwater systems, whereas values less than one are associated with more saline, marine environments (Hanson et al., 2000; Tao et al., 2015). The C₂₆ / C₂₅ TT ratio values ranged from 0.96 -1.38, with an average 1.12, suggesting a non-saline or weakly saline environment throughout Wolfcamp B3 and B2 deposition. At first glance, the notion of a significant amount of freshwater in the marine setting of the Wolfcampian Permian Basin is somewhat surprising. However, if one considers the abundance of sediment gravity flows observed throughout the core, and the entrained oxygenated water therein, the notion becomes more reasonable. The C₂₆ / C₂₅ TT ratio as a function of depth is plotted next to the working sequence stratigraphic framework and core description in Figure 25.

Throughout the FSST, the C₂₆ / C₂₅ TT values remain relatively constant, (0.96-1.38), averaging 1.03, indicating a weakly saline setting. However, it is important to note that in relative terms, the FSST exhibits the most consistently low values throughout the

core. Each sequence stratigraphic tract contains samples with C_{26} / C_{25} TT values lower than the FSST average, however, they do not stay that low for more than 16 ft. This suggests that paleogeographic conditions were relatively stable and saline during the FSST and initial parts LST. The lack of variation in the relatively low C_{26} / C_{25} TT ratio provides geochemical evidence for sedimentological theory debris flows, characteristic of the FSST, do not entrain as much water as their more turbiditic counterparts. It is not until the middle of the LST, at 9665 ft. (2945.9 m), that there is a dramatic increase in the C_{26} / C_{25} TT ratio, jumping to 1.32. Although the sample taken at 9665 ft. (2945.9 m) is mainly comprised of siliciclastic material, the influence of numerous underlying and overlying calciturbidites, containing mainly laminated packstones, cannot be overlooked. It is thought that the series of calciturbidites beginning at around 9670 ft. (2947.4 m) were bringing in oxygenated waters to the distal part of the basin. The C_{26} / C_{25} TT ratio goes further to suggest that this oxygenated water was also less saline. Furthermore, the influx of freshwater correlates with the increase in terrigenous plant matter indicated by the C_{20} / C_{23} TT ratio. This increase in both tricyclic terpane ratios centered around the series of calciturbidites in the LST compared to the ratios decoupling around the rather isolated calciturbidite package in the FSST (9697 ft.; 2955.6 m) is also telling. The increase in the C_{26} / C_{25} TT ratio for the former suggests that a threshold number of calciturbidites is necessary to geochemically record the change in salinity of system. Both the calciturbidite intervals, in the FSST and LST, brought in more terrigenous material than their debritic counterparts, however, only the higher frequency calciturbidites of the LST manage to record the changes in salinity, a trend that will be further highlighted in the highstand. Towards the end of the LST, the C_{26} / C_{25} TT ratio drops significantly to 0.96 at 9657 ft.

(2943.5 m), the lowest in the entire core. The C_{26} / C_{25} TT ratio increases only slightly to 1.02 by 9653 ft. (2942.2 m), suggesting that towards the end of the LST, palaeoceanographic conditions remained relatively saline.

Overall, the salinity during the TST is more dynamic than previous sequence stratigraphic tracts. The onset of the TST is marked by an increase in the C_{26} / C_{25} TT ratio, jumping to 1.26 by 9645 ft. (2939.8 m). The laminated packstone at this depth has also be marked by an influx of terrigenous material brought in by the calcareous flow event, as well as a rapid drop in sulfur content. However, the Pr/Ph value at 9645 ft. does not reflect the influx of oxygenated freshwater that other geochemical parameters suggest, highlighting the insensitivity of Pr/Ph to relatively small fluctuations in depositional redox conditions. It also important to reiterate that particularly for intermediate values in mature samples, Pr/Ph values often times also reflect diagenetic redox conditions and source material (Rashid and Leonard, 1973; ten Haven et al., 1987; Sinninghe Damsté et al., 1995). The C_{26} / C_{25} TT ratio then decreases to 0.99 at 9641 ft. (2938.6 m), only to increase to 1.67 by 9633 ft. (2936.1 m). This oscillation in the C_{26} / C_{25} TT ratio exemplifies the influence calcareous sediment gravity flows, with the stratigraphically lower sample being deposited before a series of small calciturbidites with and the stratigraphically higher, heavily bioturbated sample after. The TST ends with a drop in the C_{26} / C_{25} TT ratio to 1.03 by 9625 ft. (2933.7 m). Although there is a decrease in the C_{26} / C_{25} TT ratio within the *mfz*, the C_{26} / C_{25} TT value is neither the lowest exhibited throughout the core, nor even within the TST, suggesting that even at the sea level high, high salinity, and the associated water column stratification, had not been developed.

The onset of the highstand is marked by sharp increase in the C_{26} / C_{25} TT ratio ($\Delta C_{26} / C_{25}$ TT = 0.33), with a value of 1.37 at 9617 ft. (2931.3 m). The C_{26} / C_{25} TT ratio remains relatively constant over the next 16 ft. ($\Delta C_{26} / C_{25}$ TT = 0.33), with the highest value throughout the entire core of 1.39 centered around 9609 ft. (2928.8 m). An influx of freshwater agrees with the sedimentological, ichnological, and geochemical interpretation of a more well-oxygenated highstand. Interestingly, there is a notable decrease in the C_{26} / C_{25} TT ratio beginning around 9593 ft. (2923.9 m), dropping to 1.03, and remaining relatively low (C_{26} / C_{25} TT = 0.98) until 9585 ft. This departure from the relatively high C_{26} / C_{25} TT values of the early HST comes at a somewhat stratigraphically significant position – the first observance of the truncated packstones. Although individual oscillations between Pr/Ph are difficult to solely attribute to changes in depositional redox, particularly for intermediate values, confidence can be placed in the redox interpretations for the overall trends. Generally, the Pr/Ph values increase throughout the core, and remain relatively high during the HST, suggesting an overall oxygenation of the system. Furthermore, low sulfur content and increase bioturbation support the oxygenated HST interpretation. For the previous sequence stratigraphic intervals, oxygenation has coincided with freshwater influxes, however, this relationship does not appear to hold up in the upper highstand. The inferred decoupling of oxygenation and freshwater input is thought to most likely be attributed to either a nested 4th order cycle or the development of contourites.

Ambiguities concerning a potential 3rd order cycle within the 2nd order HST was first mentioned when developing the initial sequence stratigraphic framework. This inferred 3rd order cycle coincidentally begins around the same depth as the drop in the

C₂₆ / C₂₅ TT values, at 9590 ft. (2923 m). It is entirely plausible that the 3rd order cycle, beginning with an FSST, would cause a decrease in the freshwater input, similar to that observed by the 2nd order FSST approximately 100 ft. (3.5 m) further down section. However, changes in salinity become increasingly harder to reconcile with the effect of a nested 3rd order cycle in another sequence stratigraphic intervals, mostly because of sampling limitation. The C₂₆ / C₂₅ TT ratio increases to 1.35 by 9577 ft. (2919.1 m), hypothetically interpreted as the 3rd order LST within the 2nd order HST. Although it is difficult, if not scientifically improper, to characterize an interval solely off a single sample, the decrease in salinity during this questionable 3rd order LST is somewhat problematic. Although geochemical evidence suggests that the LST, particularly the latter portion of the LST, is characterized by relatively more anoxic, saline conditions, calciturbidites can still bring in enough oxygenated fresh water to leave a mark on the geochemical record. Therefore, this more freshwater prone 3rd order LST may be an isolated incident similar to that observed in the middle of the 2nd order LST. The sample taken at 9577 ft. (2919.1 m) is also interpreted as a heavily bioturbated lithofacies, leaving open the possibility that a series of small flow events capped by an abundance of bioturbation is more closely associated with event deposits rather than background palaeoceanographic conditions during a sea level low. With only one sample taken over potential 3rd order LST, any interpretation is tenuous at best. The same sampling issue arises during the potential 3rd order transgression. The C₂₆ / C₂₅ TT ratio decreases to 1.03 at 9569.5 ft. (2916.8 m), suggesting more saline conditions during the potential 3rd order transgression. Although this is consistent with conventional sequence stratigraphic theory, which would support the claim of a geochemical signal for a 3rd order cycle, the previous 2nd order

transgression proved to be markedly more dynamic. Once again, palaeoceanographic analysis of hypothetical 3rd order transgression, and its potential variability, is limited by the sampling density.

The decrease in the C_{26} / C_{25} TT ratio beginning at 9653 ft. (2942.2 m) can also be interpreted as the development of contour currents. Bottom water currents, while oxygenating, are inherently denser, and more saline. Therefore, the interpretation of the truncated packstones as contourites, rather than tempestites, reconciles the increase in salinity with more persistent oxygenating conditions. Conversely, tempestites are more typically associated with a decrease in salinity since storms tend to increase the amount of freshwater run off. Furthermore, the increase salinity towards the end of the middle HST suggests that potential greenhouse conditions, typical of the late Permian, may not be playing a significant palaeoceanographic role during Wolfcamp B2 deposition. Waning icehouse conditions, and the associated increase in storm activity, would likely cause a decrease in salinity, not increase. Therefore, the decrease in the C_{26} / C_{25} TT ratio from 9593 – 9585 ft. (2923.9 - 2921.5 m) is mostly likely reflecting the temporary development of contouring currents rather than tempestites or a 3rd order sequence cycle. Although the tempestites are sedimentologically plausible, the organic geochemistry suggests that they are most likely not the culprits. However, a 3rd order sequence cycle cannot be entirely ruled out but is hindered as an acceptable interpretation due to sampling limitations of such a high-frequency, small scaled event. The increase in the C_{26} / C_{25} TT ratio to 1.38 at 9577 ft. (2919.1 m) is therefore considered a return to typical highstand conditions. The highly bioturbated sample is associated with an increase in freshwater input associated with the sediment gravity flows characteristic of the highstand. The last

two samples are somewhat problematic to the working sequence stratigraphic model. The C_{26} / C_{25} TT ratio decreases to 1.03 by 9569.5 ft. (2916.8 m) and remains relatively constant ($\Delta C_{26} / C_{25}$ TT < 0.01) for the remainder of the core. These low values suggest an increase in salinity at the end of the highstand. From a purely sedimentological perspective, the decrease in freshwater input is intuitive. The end of the highstand is marked by a decrease in frequency of sediment gravity flows which in turn would decrease the amount of freshwater in the system. Although the sample at 9569 ft. (2916.6 m) is as laminated packstone, it is somewhat isolated and a measurable increase in the C_{26} / C_{25} TT ratio is not expected. However, the sulfur content at 9569.5 ft. (2916.8 m) is relatively low ($S < 2$ wt. %) before jumping significantly by 9543 ft. ($S = 6.69$ wt. %). The decrease in sulfur by 9543 ft. coupled with a notable decrease in bioturbation over the same interval suggests that the end of the HST may have been more oxygen limited than earlier in the HST. Therefore, it is reasonable to suggest that a decrease in salinity had to be established prior to the development of relatively more anoxic conditions. Unfortunately, due to the significant underlying core gap and subsequent missing section, potential parasequence postulation must be forgone.

7.2.2.2.1.3. *C₂₈₋₂₉ Tricyclic Terpanes*

Tasmanites were petrographically observed in the more argillaceous petrographic microfacies, warranting a geochemical evaluation of marine algae input. The ratio of the sum of the C_{28} and C_{29} tricyclic terpanes relative to the C_{30} hopane ($(C_{28}+C_{29}$ TT) / C_{30} H) is used to evaluate the degree of *Tasmanites* input. Although it is often the case to use a multi-proxy approach for paleoenvironmental reconstruction efforts, inorganic

geochemical evidence supporting changes in the *Tasmanites* contribution to the organic matter is temporarily omitted for a more rigorous investigation later on. Changes in the $(C_{28}+C_{29} \text{ TT}) / C_{30} \text{ H}$ ratio were plotted as a function of depth and summarized in the tricyclic terpane plots of Figure 25.

Overall, the $(C_{28}+C_{29} \text{ TT}) / C_{30} \text{ H}$ ratio shows decreases as one moves up section, indicating a progressive increase in the marine algae contribution to the organic matter over time. This increase is consistent with the sequence stratigraphic interpretation and overall sea level rise. Confidence can be placed in this interpretation since a maturity overprint would preferentially degrade the hopanes, causing the ratio to increase as a function of depth, which is the inverse of the relationship observed. The $(C_{28}+C_{29} \text{ TT}) / C_{30} \text{ H}$ ratio average is 1.02, with a minimum of 0.85 at the bottom of the core and a maximum at 1.32 toward the end of the highstand. Minor fluctuation in the $(C_{28}+C_{29} \text{ TT}) / C_{30} \text{ H}$ ratio occur at sequence stratigraphically important intervals and coincide with other tricyclic terpane ratio fluctuations. The $(C_{28}+C_{29} \text{ TT}) / C_{30} \text{ H}$ ratio most closely tracks the $C_{26} / C_{25} \text{ TT}$ ratio as function of depth. Although the magnitude of changes exhibited by the $(C_{28}+C_{29} \text{ TT}) / C_{30} \text{ H}$ ratio are smaller than of the $C_{26} / C_{25} \text{ TT}$, their agreement is extremely geochemically significant, particularly for paleoenvironmental reconstruction efforts. *Tasmanites* are thought to inhabit low salinity marine to brackish lacustrine environments in high paleolatitudes, thriving on nutrient influxes which cause their algal blooms (Parke and Hartog-Adams, 1965; Ackman et al., 1970; Calver et al., 1984; Revill et al., 1994). Although they are thought to dominate shallow water marine environments, their abundance in a deeper base of slope setting is most likely facilitated by the oxygenated freshwater entrained in the abundant sediment gravity flows. The influxes of

less saline water as a function of the frequency of sediment gravity flows within a sequence stratigraphic framework were rigorously examined in the previous section and will not be elaborated on in this section. However, certain discrepancies, and their palaeoceanographic significance, will be.

During the FSST, around 9689 ft. (2953.2 m), the $(C_{28}+C_{29} \text{ TT}) / C_{30} \text{ H}$ ratio shows a relatively larger increase than the negligible increase in the $C_{26} / C_{25} \text{ TT}$ ratio. Although the associated turbiditic flow probably contained both oxygenated freshwater, the decrease in salinity appears to have equilibrated to the more persistent saline and oxygen limited background conditions quite quickly. This re-equilibration of redox conditions most likely only left geochemical evidence of the short lived *Tasmanites* algal bloom, which was readily preserved. The last discrepancy between the $(C_{28}+C_{29} \text{ TT}) / C_{30} \text{ H}$ and $C_{26} / C_{25} \text{ TT}$ ratios of paleoenvironmental significance occurs during the latter part TST (9633 – 9625 ft.; 9633 - 2933.7 m). The $(C_{28}+C_{29} \text{ TT}) / C_{30} \text{ H}$ ratio suggests a gradual increase in the contribution of *Tasmanites* to the organic matter throughout the TST, beginning at 9641 ft. (2938.6 m) while the $C_{26} / C_{25} \text{ TT}$ ratio suggests a major influx of freshwater of at 9633 ft., which then decreases at 9625 ft. (2933.7 m), within the interpreted *mfz*. The overall relationship between the $(C_{28}+C_{29} \text{ TT}) / C_{30} \text{ H}$ and $C_{26} / C_{25} \text{ TT}$ ratios suggests that pulses of freshwater are linked to an increase in the abundance of *Tasmanites*, suggesting an inherently “productivity” based relationship. However, the importance of preservation is highlighted by the relationship of the two ratios in the more oxygen limited FSST. Therefore, the small increase in the $(C_{28}+C_{29} \text{ TT}) / C_{30} \text{ H}$ ratio at 9633 ft. (2936.1 m) is thought to reflect a boost in productivity due to an influx of freshwater at the same time. In contrast, the slight increase in the $(C_{28}+C_{29} \text{ TT}) / C_{30} \text{ H}$ ratio, just 8 ft. (2.4 m)

further up section, is thought to reflect better preservation due more saline, oxygen limited conditions. Aside from the discrepancies observed in the FSST and the *m/z*, which are thought to reflect palaeoceanographic conditions more favorable for preservation, the $(C_{28}+C_{29} \text{ TT}) / C_{30} \text{ H}$ and $C_{26}/C_{25} \text{ TT}$ ratios track each other very well. This unique relationship between freshwater influxes and algal blooms further supports the notion of an overall weakly suboxic system, heavily influenced by the geochemical implications of sediment gravity flows, particularly in the more oxygenated HST.

7.2.2.2.2. Tetracyclic and Pentacyclic Terpanes

Tetracyclic terpanes are thought to originate by thermal or microbial degradation of a precursor hopane or hopanoid, although an independent bacterial biosynthetic pathway may exist (Grice et al., 2001; Peters et al., 2005). The C_{24} tetracyclic terpane ($C_{24} \text{ Tet}$) is commonly associated with carbonate and anoxic to evaporitic source rock settings (Palacas et al., 1984; Connan et al., 1986; Connan and Dessort, 1987; Clark and Philp, 1989). Furthermore, caution should be taken when utilizing tetracyclic terpane to hopane ratios for paleoenvironmental reconstruction interpretations since tetracyclic terpanes are thought to be more resistant to biodegradation and thermal degradation than hopanes (Aquino Neto et al., 1983).

Pentacyclic terpanes, or hopanes, are thought to originate from the membranes of prokaryotic organisms, such as bacteria, and higher plant matter, but are absent in eukaryotic algae (Ourisson et al., 1987). Bacterially derived compounds are ubiquitous in all oils and sedimentary rocks, suggesting that they are the most abundant source of organic matter on Earth (Ourisson and Albrecht, 1992). The ratio of the C_{29} to the C_{30}

hopane (C_{29} / C_{30} hopane) is used to distinguish lithology, and to a lesser degree, redox conditions. The C_{29} / C_{30} hopane values can be used as a scale for carbonate richness, with higher values indicating more carbonate, and when values are greater than one, indicate both anoxia and a carbonate-rich environment (Connan et al., 1986).

The $C_{31} - C_{35}$ extended hopanes, or homohopanes, are also thought to originate from hopanoids common in prokaryotic microorganism, such as bacteria (Ourisson et al., 1979 and 1987; Rohmer et al., 1984). The relative distributions of the $C_{31} - C_{35}$ 17α $22S$ and $22R$ homohopanes are used as an indicator of lithology and redox conditions during deposition. In particular, elevated amounts of C_{35} homohopane indicate anoxic carbonate deposition (Boon et al., 1979; Connan et al., 1986; Mello et al., 1988; ten Haven et al., 1988; Clark and Philp, 1989). However, ambiguity still exists as to degree to which the ratios reflect lithology or redox conditions (Peters et al., 2005). Peters et al. (2005) argued for a stricter, more redox dependent, interpretation of the C_{35} homohopane, citing evidence of high abundances of the C_{35} homohopane in some anoxic marine clay-rich sediments. Both the Homohopane Index ($C_{35} / (C_{31} - C_{35})$ HH) and the simpler C_{35} to C_{34} homohopane ratio (C_{35} / C_{34} HH) can be used to decipher depositional environment, although only latter is used in this investigation. Typically, resinous coaly source rock extracts have a C_{35} / C_{34} HH ratio value less than 0.6, lower than the typical marine, carbonate or clastic, source rock (Peters et al., 2005). Conversely, extracts and oils from marine carbonate source rocks typically have a C_{35} / C_{34} homohopane ratio value greater than 0.8 combined with a C_{29} / C_{30} hopane ratio value greater than 0.6. Regardless of lithology, C_{35} / C_{34} HH values > 1 indicate anoxic depiction, regardless of lithology (Peters et al., 2005).

Rearranged hopanes, such as the norneohopanes or diahopanes, are believed to provide valuable information about the redox conditions during deposition and early diagenesis (Farrimond and TelnAES, 1996; Peters et al., 2005). Although there have been many studies regarding the depositional significance of 17 α (H)-diahopane (also referred as C₃₀ diahopane or C₃₀ D), their origin and significance is still disputed (Jiang et al., 2018). The occurrence of rearranged hopanes were originally attributed to land plant sources after they were found in coals and terrigenous oils (Philp and Gilbert, 1986). However, their isotopic similarity to regular hopanes suggest a similar bacterial origin (Moldowan et al., 1991; Peters et al., 2005). Alternatively, marine red algae has been proposed as a potential precursor (Zhang et al., 2007 and 2009). The most widely accepted interpretation of the presence of 17 α (H)-diahopane is the hopane rearrangement facilitated by clay-rich, brackish water environments under suboxic to oxic conditions during deposition and early diagenesis (Moldowan et al., 1991; Farrimond and TelnAES, 1996; Peters et al., 2005; Zhang et al., 2009; Jiang et al., 2018). Conversely, 18 α (H)-30-norneohopane (C₂₉ Ts) is thought to have a similar geochemical character as Ts and is widespread in crude oils (Moldowan et al., 1991; Peters et al., 2005). Therefore, the ratio of 17 α (H)-diahopane to 18 α (H)-30-norneohopane (C₃₀ D / C₂₉ Ts) reflects both in lithology and redox conditions, where higher values suggest more clay and oxygenated conditions. Aside from depositional controls on the C₃₀ D/ C₂₉ Ts ratio, higher values can also reflect higher maturity since C₃₀ D is more thermally stable than C₂₉ Ts (Horstad et al., 1990; Kolaczowska et al., 1990).

Strict paleoenvironmental reconstruction is imbedded by the influence of both depositional redox conditions and lithology on tetracyclic and pentacyclic terpane

abundances. Anoxia, salinity, and carbonate content are often conflated with the C_{29} / C_{30} H, C_{35} / C_{34} HH, and the C_{24} Tet/ C_{30} H ratios. Likewise, oxygenation and clay content often pull biomarker ratios in the same direction, such as with the C_{30}^* / C_{29} Ts ratio. Although lithology and redox controls typically work in concert with one another in many systems, the Wolfcampian Permian Basin appears to be a notable exception.

Prior sedimentological and geochemical assessments within this study have suggested that increases in carbonate content is usually by means of oxygenating sediment gravity flows. Conversely, much of the siliciclastic deposition is by means of hemipelagic to pelagic sedimentation under more oxygen limiting conditions or by weakly oxidizing dilute siliciclastic sediment gravity flows. Therefore, the relationship between lithology and redox conditions in a mixed carbonate siliciclastic system limits the utility of tetracyclic terpanes and hopanes for paleoenvironmental reconstruction. Therefore, depositional environment interpretations utilizing tetracyclic terpane and hopane biomarker ratios as a function of depth will be tenuous, since they often conflict. Interpretations will be supported by other geochemical, ichnological, and sedimentological data. The tetracyclic terpane and hopane biomarker ratios are plotted as a function of depth along with the core description and working sequence stratigraphic framework in Figure 26.

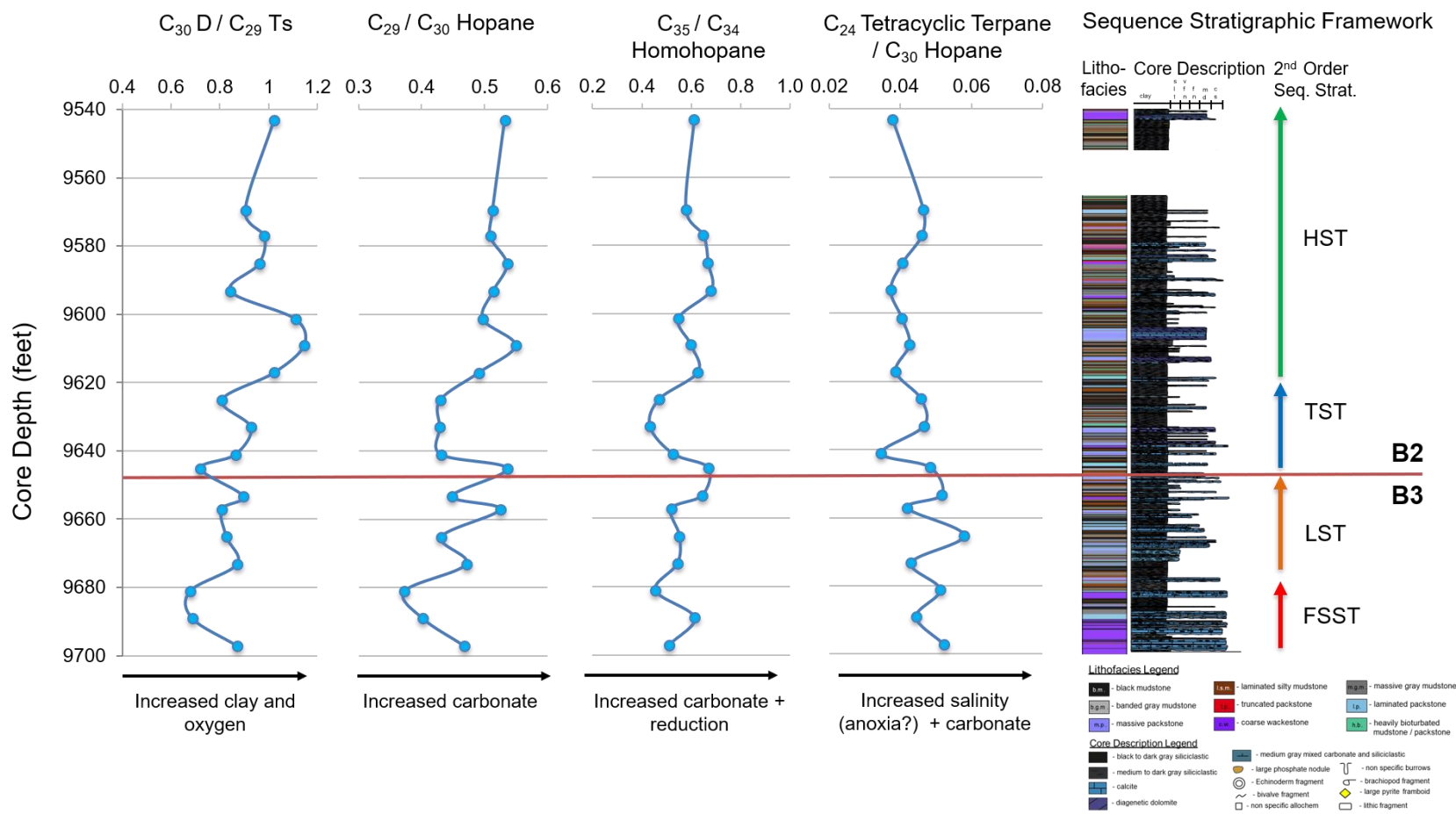


Figure 26. Tetracyclic and pentacyclic terpane ratios plotted as a function of depth. From left to right: C_{30}^*/C_{29} Ts, C_{29}/C_{30} Hopane, C_{35}/C_{34} Homohopane, and the C_{24} Tetracyclic / C_{30} Hopane. Arrows below depth plot indicate controls on biomarker ratio and the direction it pulls the value. The sequence stratigraphic framework, including the lithofacies and core description are shown for reference.

7.2.2.2.1. C₃₀ Diahopane and C₂₉ TS

Intermediate values for the C₃₀ D / C₂₉ Ts ratio (0.68 – 1.15) suggest suboxic deposition (Peters et al., 2005). Overall, the C₃₀ D / C₂₉ Ts ratio increases up section, suggesting increasingly oxygenated redox conditions as a function of time (Figure 26). However, attempting to parse out individual fluctuations and attributing them to oxygenation events proves difficult due the destructive lithologic signal interference. The decreasing C₃₀ D / C₂₉ Ts values during the FSST are intuitive and supported by low bioturbation, sulfur, Pr / Ph, and C₂₆ / C₂₅TT values. The C₃₀ D / C₂₉ Ts ratio then increases to 0.87 by 9673 ft. (2948.3 m), sequence stratigraphically equivalent to the onset of the LST. The C₃₀ D / C₂₉ Ts ratio then gradually decreases over the next 16 ft. (Δ C₃₀ D / C₂₉ Ts = 0.06), until slightly increasing again to 0.90 at the end of the LST (9653 ft.; 2942.2 m). The increased oxicity during the early to middle LST relative to the FSST has been supported by other geochemical parameters. However, ichnological, inorganic geochemical, and tricyclic terpane biomarker data suggests that the end of the LST is relatively more oxygen limited. Thus, the minor increase in the C₃₀ D / C₂₉ Ts ratio observed at 9657 ft. is thought to reflect the relative increase in siliciclastic material towards the end of the LST rather than an increase in oxygen.

The onset of the TST is lithologically marked by the observance of a laminated packstone at 9645 ft. The decrease in C₃₀ D / C₂₉ Ts ratio at this same depth therefore thought to reflect the decrease in clay rather than oxygen. The increase in the C₃₀ D / C₂₉ Ts ratio observed in the middle TST (9641 – 9633 ft.; 2938.6 - 2936.1 m) is thought to reflect an increase in oxygen rather than an increase in clay since given the abundance of calciturbidites over this interval and the calcareous nature of the samples themselves.

Similarly, the decrease in the $C_{30} D / C_{29} Ts$ ratio to 0.81 at the end of the TST reflects the decrease in oxygen since the sample, and most of the stratigraphic section in the *mfz*, is comprised of siliciclastic material. This redox interpretation is supported by the ichnological data, Pr/Ph values, and the $C_{26} / C_{25} TT$ ratio. However, it is important to note that the consistent decrease in sulfur throughout the entire TST continues into the *mfz*, contradicting several other redox parameters, including the $C_{30} D / C_{29} Ts$.

The beginning of the HST is marked by a progressive increase in the $C_{30} D / C_{29} Ts$ ratio, maxing out at 1.15 at a depth of 9609 ft. (2928.8 m). These relatively high $C_{30} D / C_{29} Ts$ values are in fact the highest observed throughout the core yet come from an stratigraphic interval characterized by abundant calciturbidites. This seeming contradiction between the geochemistry and the sedimentology exemplifies the conflicting variables that control the ratio itself. Sedimentological, ichnological, and previous biomarker data indicate that these calcareous flows oxygenated the systems. Therefore, the high $C_{30} D / C_{29} Ts$ values observed in the early highstand are thought to reflect an increase in oxygen in the system rather than an increase in argillaceous material. The $C_{30} D / C_{29} Ts$ ratio decrease to 0.84 before progressively increasing to 0.98 by 9577 ft. (2919.1 m), stratigraphically equivalent to where the truncated packstones are observed. This slight increase in the $C_{30} D / C_{29} Ts$ ratio is thought to reflect the development of oxygenating contouring currents. The $C_{30}^* / C_{29} Ts$ then decrease to 0.91 by 9569.5 (2916.8 m) ft., the same depth where an isolated calciturbidite is observed. This isolated sediment gravity flow, unlike its higher frequency counterparts, most likely did not oxygenate the system. Therefore, the decrease in the $C_{30} D / C_{29} Ts$ at 9569.5 ft. (2916.8 m) reflects a decrease in the amount of clay. Lastly, the increase in the $C_{30} D /$

C₂₉ Ts ratio to 1.02 at the top of the core is thought to reflect both the increase in clay content and the overall oxygenated highstand. Although one would expect the coupling of argillaceous material and oxygenation to constructively interfere and produce C₃₀ D / C₂₉ Ts values higher than those observed in the early HST, ichnological data suggests that there is a slight decrease in the amount of oxygen towards the very end of the highstand, producing this relatively intermediate C₃₀ D / C₂₉ Ts value.

7.2.2.2.2. C₂₉₋₃₀ Hopanes

All C₂₉ / C₃₀ hopane ratio values are less than one, indicating an overall siliciclastic, clay-rich source rock. Given known suboxic conditions, changes in the C₂₉ / C₃₀ hopane ratio are interpreted to reflect changes in the carbonate content. However, caution should be taken when interpreting increases in the C₂₉ / C₃₀ hopane ratio as increases in the carbonate content for C₂₉ / C₃₀ hopane ratio values are < 1 (Riva et al., 1988). The C₂₉ / C₃₀ hopane ratio ranges from 0.52 to 0.68 with an average of 0.60. The C₂₉ / C₃₀ hopane ratio generally increases up section, suggesting an overall increase in the carbonate content, differing from the previous sedimentological and inorganic geochemical assessment (Figure 26). Furthermore, individual C₂₉ / C₃₀ hopane fluctuations within the overall trend do not appear to reflect changes in carbonate content well. The C₂₉ / C₃₀ hopane ratio progressively decreases throughout the FSST, omitting the increase in calcareous material from the calciturbidite in at 9689 ft. (2953.2 m). The C₂₉ / C₃₀ hopane ratio over the LST is very dynamic, oscillating on average 0.07. However, these oscillations do not coincide with any lithologic changes, in fact often conflict them. The Wolfcamp B3-B2 and LST-TST boundary is marked by a thick calcareous bed, which may

be reflected in the increase of the C_{29} / C_{30} hopane ratio to 0.54 at 9645 ft. (2939.8 m). The subsequent drop in the C_{29} / C_{30} hopane ratio to 0.43 at 9641 (2938.6 m) underestimates the amount of carbonate toward the bottom of the TST. However, the C_{29} / C_{30} hopane ratio remains relatively low and consistent throughout the TST ($\Delta C_{29} / C_{30}$ hopane < 0.01), at least in part accurately reflecting the decrease in carbonate material towards the end of the TST. Interestingly, the C_{29} / C_{30} hopane ratio more accurately reflects the carbonate content in the highstand, exhibiting higher values centered around 9609 and 9585 ft. (2928.8 and 2921.5 m). The former coincides with an increase in the C_{30}^* / C_{29} Ts ratio over the interval, suggesting that the calciturbidites were bringing in oxygenated water as well. Although C_{29} / C_{30} hopane values less than one theoretically only reflect carbonate content, potential redox influence on the ratio were investigated in order to attempt to reconcile the disparity between the C_{29} / C_{30} hopane ratio and lithology, Unfortunately, higher C_{29} / C_{30} hopane ratios that could potentially reflect more anoxic conditions often coincided with more oxygenated intervals.

7.2.2.2.3. C_{34-35} Homohopanes

All C_{35} / C_{34} HH ratio values are less than 1, suggesting that anoxic conditions did not occur throughout Wolfcamp B3 and B2 deposition, an assertion consistent with ichnological and geochemical assessments. Under the guidelines proposed by Peters et al. in 2005, those C_{35} / C_{34} HH values <0.6 reflect siliciclastic marine deposition under more suboxic conditions while values >0.8 reflect carbonate deposition under slightly more anoxic conditions. The C_{35} / C_{34} HH ratio values range from 0.43 – 0.68, with an average of 0.57. These intermediate C_{35} / C_{34} HH ratio values indicate a predominately

suboxic siliciclastic deposition with varying amounts of calcareous material. Changes in the C_{35} / C_{34} HH ratio is thought to most accurately reflect changes in carbonate content, a finding that will later be expanded on later. Interestingly, individual fluctuations in redox conditions do not seem to affect the C_{35} / C_{34} HH ratio, since carbonate packages with elevated C_{35} / C_{34} HH values are typically induced more oxic conditions. Changes in the C_{35} / C_{34} HH ratio as a function of depth are depicted in Figure 26.

Overall, the C_{35} / C_{34} HH values do not show a simple depth trend but rather fluctuates at sequence stratigraphically significant intervals. The FSST is characterized by a small increase in the C_{35} / C_{34} HH ratio to 0.61, centered around 9689 ft. (2953.2 m), which most likely reflects the change from less calcareous debrites to more calcareous calciturbidites. The C_{35} / C_{34} HH then decrease to 0.45 at 9689 ft. (2953.2 m), representing the slight increase in siliciclastic material at the FSST – LST transition. The progressive yet slight increase in the C_{35} / C_{34} HH ratio to 0.55 at 9665 ft. (2945.9 m) accurately reflects increase in calcareous material observed in the early and middle LST. The slight decrease in the C_{35} / C_{34} HH ratio at 9657 ft. (2943.5 m) reflects the slight increase in siliciclastic towards the end of the LST. The C_{35} / C_{34} HH ratio then increases to 0.64 at 9653 ft. (2942.2 m) remaining relatively constant ($\Delta C_{35} / C_{34}$ HH = 0.03) through 9645 ft. (2939.8 m). This most likely reflects the thick carbonate package at the LST – TST boundary as well as the calciturbidite overlying them. However, the elevated value at 9653 ft. (2942.2 m) may also be influenced by the relatively more anoxic conditions at the end of the LST, since the sample at this depth is more clay rich than other calciturbidites.

The C_{35} / C_{34} HH ratio progressively decreases ($\Delta C_{35} / C_{34}$ HH = - 0.24) over the course of the TST (9645 - 9633 ft.; 2939.8 - 2936.1 m), consistent with the overall

sedimentological assessment of the TST. However, the C_{35} / C_{34} HH taper off relatively quickly, somewhat under emphasizes the amount of calcareous material deposited in the early LST. It is entirely plausible that the relatively more oxic conditions during the early and middle TST amplified the decrease in the C_{35} / C_{34} HH values, although sampling bias cannot be ruled out. The C_{35} / C_{34} HH ratio then slightly increases ($\Delta C_{35} / C_{34}$ HH = 0.05) to 0.47 by the end of the TST (9625 ft.; 2933.7 m). The *mfz* is characterized slightly more anoxic conditions yet significant increase in the clay content. Therefore, this negligible increase in the C_{35} / C_{34} HH ratio may be reflecting the constructive interference of two conflicting biomarker ratio controls. Constructive signal interference is observed during the early HST as well. The onset of the HST is marked by an increase in the amount of calcareous material, particularly around 9609 ft. (2928.8 m). Although the C_{35} / C_{34} HH ratio initially increases to 0.63 at the onset HST ($\Delta C_{35} / C_{34}$ HH = 0.16), it declines slightly to 0.6 by 9609 ft. (2928.8 m), even though the amount of carbonate increases. The constructive signal interference can be slightly deconvoluted by comparing it to the $C_{30} D / C_{29} Ts$ and C_{29} / C_{30} hopane ratios, both of which show an increase at 9609 ft (2928.8 m). The latter suggests there is an increase in calcareous material, which agrees with the sedimentology, while the former suggests there is an increase in the amount of oxygen in the system, which is supported by the increase in bioturbation over the same interval. This combination of both calcareous material and relatively more oxygenated conditions produced the intermediate C_{35} / C_{34} HH value observed at 9609 ft. (2928.8 m). The C_{35} / C_{34} HH ratio decreases to 0.55 by 9601 ft. (2926.4 m), reflecting an increase in the clay content. The C_{35} / C_{34} HH ratio then increases to 0.68 by 9593 ft. (2923.9 m) and remains relatively constant until 9577 ft. The increase in the C_{35} / C_{34} HH ratio coincides

with elevated C_{29} / C_{30} hopane values, suggesting an increase in the carbonate content, which is sedimentologically supported by the truncated packstones. Furthermore, the elevated $C_{30} D / C_{29} Ts$ value observed up section (9577 ft.; 2919.1 m) coincides with the slight decrease in the C_{35} / C_{34} HH ratio, suggesting that the relatively more oxygenated conditions may have reduced the C_{35} / C_{34} HH ratio even further. The C_{35} / C_{34} HH ratio then decreases to 0.58 by 9569.5 ft. (2916.8 m), potentially reflecting an increase in clay towards the end of the HST. The slight increase in the C_{35} / C_{34} HH ratio at 9543 ft. ($\Delta C_{35} / C_{34} HH = 0.03$) most likely reflects the more reducing conditions towards the very end of the HST, as suggested by the decrease in bioturbation after the core gap decrease in bioturbation after the core gap.

7.2.2.2.4. C_{24} Tetracyclic Terpene

Although the core is considered uniformly mature, the increase in the $C_{24} Tet / C_{30} H$ values as a function of depth may be reflecting the preferential thermal degradation of the C_{30} hopane relative to the more thermally stable tetracyclics, particularly since the absolute values of the ratio in this study are very small. Therefore, the preferential thermal degradation of the hopanes may limit the $C_{24} Tet / C_{30} H$ ratio's utility as a paleoredox and lithology indicator. However, it is important to point out that tricyclic terpanes are also more thermally stable than hopanes, yet the $(C_{28} + C_{29} TT) / C_{30}$ hopane ratio decreases as a function of depth, suggesting that the C_{30} hopane has not thermally degraded to any appreciable degree. This increases our confidence in the $C_{24} Tet / C_{30} H$ depth trend, although the ratio itself is still susceptible to the same destructive inferences of two conflicting ratio variables – carbonate content and salinity.

The C₂₄ Tet / C₃₀ H ratio values are low and do not vary much, ranging from 0.04 –0.06, with an average of 0.05. High concentrations of C₂₄ Tet are thought to reflect more evaporitic carbonate deposition rather than simply carbonate deposition, particularly when the abundance of the tetracyclics is greater than that of the tricyclics (Aquino Neto et al., 1981; Connan et al., 1986; Clark and Philp, 1989). The low C₂₄ Tet / C₃₀ H ratio values suggest that the Wolfcamp B3 and B2 was not deposited under anoxic conditions and has a significant siliciclastic component (Hanson et al., 2000; Tao et al., 2015). The overall low concentrations of C₂₄ Tet coupled with the higher abundance of tricyclic terpanes suggest that the increases in the C₂₄ Tet / C₃₀ H ratio may not reflect changes in salinity. The lack of gammacerane and relatively high C₂₆ / C₂₅ TT values throughout the core casts further doubt on oscillations in the generally low C₂₄ Tet / C₃₀ H reflecting changes in salinity.

Overall, the C₂₄ Tet / C₃₀ H ratio decreases up section, suggesting either a decrease in the carbonate content or salinity over time (Figure 26). This overall decrease in carbonate content is at odds with the C₂₉/C₃₀ hopane and C₃₅/C₃₄ HH biomarker ratio interpretations, but somewhat consistent with the C₃₀ D / C₂₉ Ts ratio and sedimentological and XRF derived calcium data. However, in absolute terms the C₂₄ Tet / C₃₀ H ratio varies very little throughout the core, suggesting no significant changes in the carbonate content through time. Increases in the C₂₆/ C₂₅ TT ratio, a freshwater input indicator, were compared to the C₂₄ Tet / C₃₀ H ratio to see if high C₂₄ Tet / C₃₀ H coincided with low C₂₆ / C₂₅ TT ratio values. Interestingly, increases in C₂₆ / C₂₅ TT correlates with increases in the C₂₄ Tet / C₃₀ H ratio at various depths (9665, 9645, 9633, 9609, and 9557 ft.; 2945.9, 2939.8, 2936.1, 2928.8, and 2913 m), suggesting that at these depths the C₂₄ Tet / C₃₀ H

ratio definitively does not reflect increases in salinity. The coupling of these two ratios suggests that the C_{24} Tet / C_{30} H ratio mainly reflects changes in carbonate content and that increases in carbonate content are often coupled with influxes of freshwater, probably by means of entrained fluid in the calcareous turbidity currents. This claim is further supported by increases in the C_{35} / C_{34} HH at the same depths. Conversely, when the C_{26} / C_{25} TT and C_{24} Tet / C_{30} H are decoupled, increases in the C_{24} Tet / C_{30} H ratio generally reflect increases in salinity, such as those observed at the end of the LST (9653 ft.; 2913 m) and the *mfz* (9625 ft.; 2933.7 m). Although the majority of biomarker ratios plotted as a function of depth are described from bottom to top in order to fully understand the changes in the paleoenvironment over time, the various controls on the C_{24} Tet / C_{30} H ratio and low measured values somewhat limit the utility of this practice.

7.2.2.3. Steranes

Steranes were identified using GCMS and single ion monitoring of the ion at m/z 217. A representative m/z 217 fragmentogram is shown in Figure 27 and the identity of the labeled peaks are listed in Table 7. Selected sterane ratios and their respective values are found in

Table 8. Steranes are derived from sterols, which are vital components to all eukaryotic cells (Volkman, 2003). Sterols are believed to reflect organic matter derived from specific ecological systems (Huang and Meinschein, 1979). There are four main families of sterols with differing carbon numbers, C_{27} , C_{28} , C_{29} , and C_{30} . The C_{27} sterols are believed to be primarily derived from marine phytoplankton and are indicators of red

algae. The C₂₈ sterols are dominant in green algae, which are common in lacustrine environments. The C₂₉ sterols were initially thought to be derived from terrestrial plant

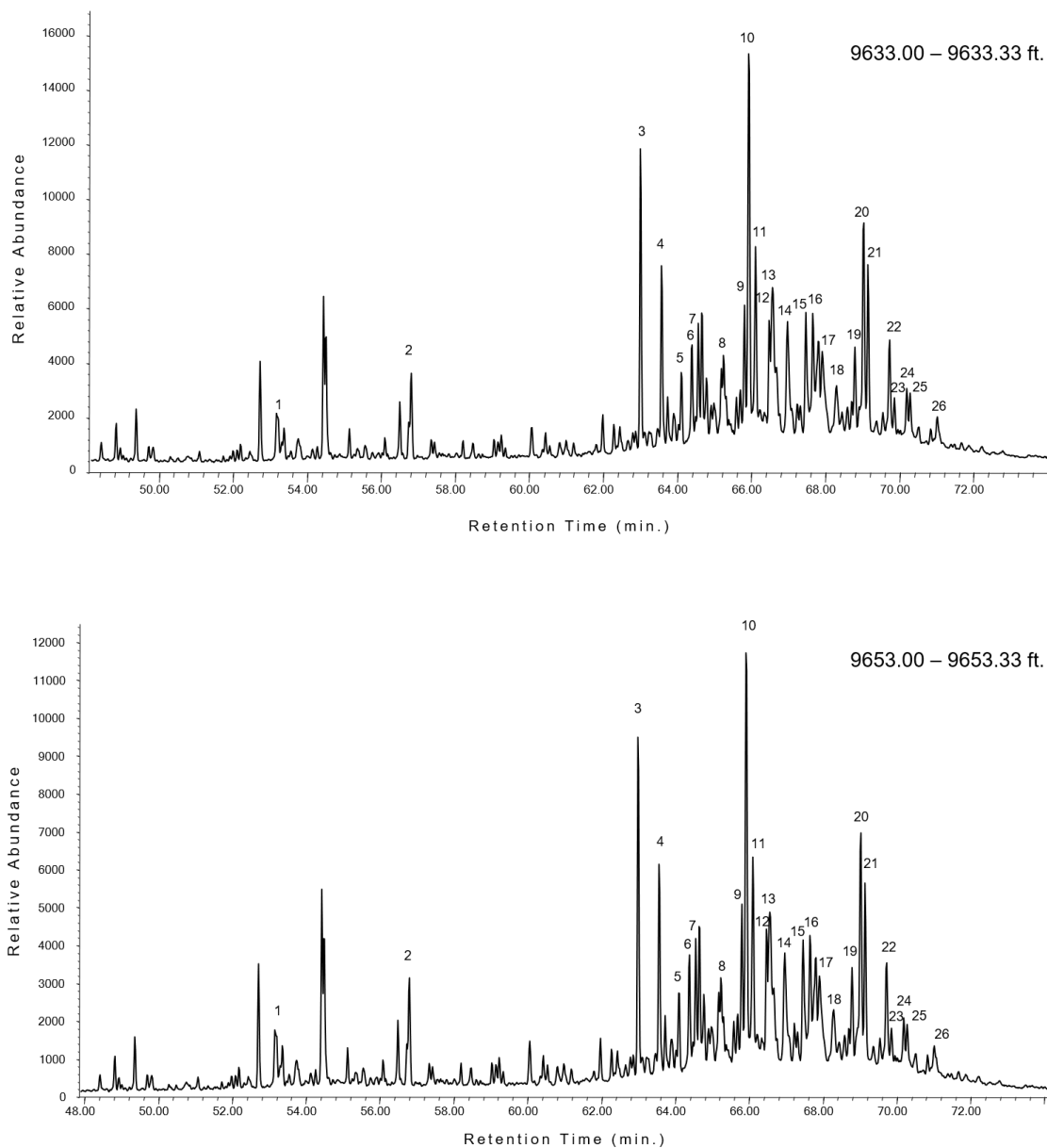


Figure 27. Partial fragmentograms of *m/z* 217 showing differing sterane distributions in samples taken from 9633.00 – 9633.33 ft. (top) and 9653.00 – 9653.33 ft. (bottom). Identification of labelled peaks are listed in Table 7.

Table 7. Sterane compound identification (m/z 217)

Peak	Compound
1	5 α (H), 14 α (H), 17 β (H) Pregnane
2	5 α (H), 14 α (H), 17 β (H) Homopregnane
3	13 β (H), 17 α (H) Diacholestane (20S)
4	13 β (H), 17 α (H) Diacholestane (20R)
5	13 α (H), 17 β (H) Diacholestane (20S)
6	13 α (H), 17 β (H) Diacholestane (20R)
7	24-methyl-13 β (H), 17 α (H) Diacholestane (20S)
8	24-methyl-13 β (H), 17 α (H) Diacholestane (20R)
9	5 α (H), 14 α (H), 17 α (H) Cholestane (20S) + C ₂₈ 24-methyl-13 α (H), 17 β (H) Diacholestane (20S)
10	5 α (H), 14 β (H), 17 β (H) Cholestane (20R) + C ₂₈ 24-ethyl-13 β (H), 17 α (H) Diacholestane (20S)
11	5 α (H), 14 β (H), 17 β (H) Cholestane (20S) + C ₂₈ 24-Methyl-13 α (H), 17 β (H) Diacholestane (20R)
12	5 α (H), 14 α (H), 17 α (H) Cholestane (20R)
13	24-ethyl-13 β (H), 17 α (H) Diacholestane (20R)
14	24-ethyl-13 α (H), 17 β (H) Diacholestane (20S) + C ₃₀ 24-propyl-13 β (H), 17 α (H) Diacholestane (20S)
15	5 α (H), 14 α (H), 17 α (H) Cholestane (20S) + C ₂₉ 24-methyl-13 α (H), 17 β (H) Diacholestane (20S)
16	24-methyl-5 α (H), 14 β (H), 17 β (H) Cholestane (20R)
17	24-methyl-5 α (H), 14 β (H), 17 β (H) Cholestane (20S)
18	24-methyl-5 α (H), 14 α (H), 17 α (H) Cholestane (20R)
19	24-ethyl-5 α (H), 14 α (H), 17 α (H) Cholestane (20S)
20	24-ethyl-5 α (H), 14 β (H), 17 β (H) Cholestane (20R) + C ₃₀ 24-propyl-13 α (H), 17 β (H), Dicholestane (20R)
21	24-ethyl-5 α (H), 14 β (H), 17 β (H) Cholestane (20S)
22	24-ethyl-5 α (H), 14 α (H), 17 α (H) Cholestane (20R)
23	24-propyl-5 α (H), 14 α (H), 17 α (H) Cholestane (20S)
24	24-propyl-5 α (H), 14 β (H), 17 β (H) Cholestane (20R)
25	24-propyl-5 α (H), 14 β (H), 17 β (H) Cholestane (20S)
26	24-propyl-5 α (H), 14 α (H), 17 α (H) Cholestane (20R)

Table 8. Selected sterane biomarker ratios for Wolfcamp B3 and B2 samples.

Core Depth (ft.)	ΣC_{27-30} regular steranes / ΣC_{29-33} hopanes	C_{27} Regular Steranes (f)	C_{28} Regular Steranes (f)	C_{29} Regular Steranes (f)	$C_{30}/(\Sigma C_{27-30})$ steranes	ΣC_{27-29} diacholestane/ ΣC_{27-29} reg steranes	$(C_{27}\alpha\alpha\alpha SR + C_{27}\alpha\beta\beta SR) / (C_{29}\alpha\alpha\alpha SR + C_{29}\alpha\beta\beta SR)$ steranes	$C_{29} 20\alpha\alpha\alpha S / (20\alpha\alpha\alpha S + 20\alpha\alpha\alpha R)$ sterane
9543.10	0.79	0.44	0.21	0.62	0.15	0.54	1.79	0.46
9569.50	0.79	0.46	0.21	0.62	0.15	0.54	1.62	0.48
9577.10	0.81	0.45	0.21	0.62	0.15	0.55	1.52	0.48
9585.20	0.76	0.44	0.21	0.62	0.15	0.56	1.57	0.48
9593.20	0.76	0.43	0.22	0.61	0.17	0.57	1.39	0.41
9601.40	0.78	0.44	0.22	0.61	0.16	0.56	1.40	0.48
9609.10	0.76	0.44	0.21	0.63	0.15	0.57	1.36	0.48
9617.10	0.75	0.45	0.21	0.61	0.16	0.62	1.36	0.47
9625.10	0.74	0.45	0.21	0.61	0.15	0.60	1.33	0.43
9633.10	0.71	0.46	0.21	0.61	0.17	0.64	1.27	0.46
9641.10	0.75	0.45	0.20	0.63	0.15	0.59	1.27	0.46
9645.20	0.98	0.47	0.20	0.63	0.15	0.59	1.26	0.44
9653.30	0.76	0.42	0.25	0.57	0.13	0.52	1.28	0.32
9657.15	0.72	0.47	0.21	0.59	0.15	0.60	1.32	0.43
9665.20	0.72	0.47	0.23	0.56	0.16	0.63	1.35	0.44
9673.20	0.66	0.48	0.23	0.57	0.15	0.63	1.34	0.46
9681.10	0.66	0.50	0.22	0.56	0.15	0.65	1.36	0.44
9689.10	0.61	0.48	0.21	0.59	0.16	0.66	1.57	0.47
9697.20	0.57	0.48	0.22	0.57	0.16	0.68	1.65	0.52

matter, but were later show to also be found in brown and green algae. (Huang and Meinschein, 1979; Moldowan et al., 1985; Volkman, 1986) . The relative proportions of the C₂₇ – C₂₉ sterols provides valuable insight into the specific biological precursors of the organic matter itself. Unfortunately, steranes often lose this specificity during their diagenetic conversion from sterols. However, plotting the relative proportion the C₂₇, C₂₈, and C₂₉ regular steranes is common practice in most organic geochemical investigations, providing useful information of organic matter source and depositional environment. The distribution C₂₇ – C₂₉ regular sterane distributions for the Wolfcamp B3 and B2 are summarized in Figure 28. Overall, the C₂₇ – C₂₉ regular steranes have a narrow distribution with values consistent with an open marine depositional environment with potentially some lacustrine influence. This is consistent with the tricyclic terpane distributions, which indicates influxes of freshwater and *Tasmanites* algal blooms. diacholestane/ C₂₇-C₂₉ regular steranes ratio are plotted as a function of depth in Figure 29. Overall, C₃₀ / ΣC₂₇₋₃₀ steranes ratio ranged from 0.12 to 0.17, indicating a significant contribution of marine algae to the organic matter. There is no clear C₃₀ / ΣC₂₇₋₃₀ steranes depth trend, but significant shifts did occur at sequence stratigraphically significant positions. The C₃₀ / ΣC₂₇₋₃₀ steranes ratio remains relatively constant over FSST, slightly decreasing into the LST (Δ C₃₀ / ΣC₂₇₋₃₀ steranes = - 0.01). However, the C₃₀ / ΣC₂₇₋₃₀ steranes ratio then increases from 0.15 at 9673 ft. (2948.3 m) to 0.16 at 9665 ft. (2945.9 m). This increase in the C₃₀ / ΣC₂₇₋₃₀ steranes ratio suggests that there is an increase in the marine algae contribution as the LST progresses. This interpreted increase in the marine algae contribution is supported by an increase in the (C₂₈ + C₂₉ TT) / C₃₀ H ratio, which indicates an increase in *Tasmanites*.

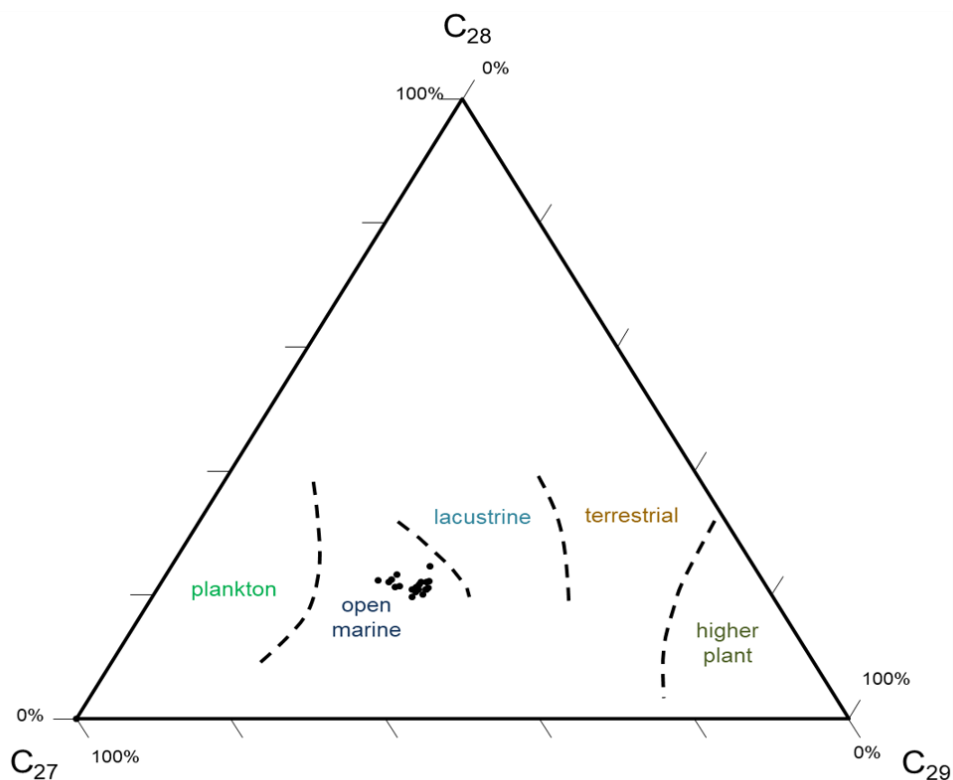


Figure 28. Ternary diagram for C₂₇, C₂₈, and C₂₉ regular sterane distribution Based on original diagram produced by Huang and Meinschein, 1979 for sterol distributions from different depositional environments.

The C₃₀ steranes have been linked to *Chrysophyte* marine algae (Moldowan et al., 1990) and the relative proportion of C₃₀ steranes to C₂₇₋₂₉ steranes (C₃₀ / C₂₇₋₃₀ steranes) is indicative of algal marine input. Values greater than 0.04 (or 4%) indicate significant marine contribution (Hays et al., 2012). Diacholestanes are rearranged regular cholestanes formed via a clay catalyzed redox reaction (Rubinstein et al., 1975; van Kaam-Peters et al., 1998). Therefore, the ratio of clay rearranged diacholestanes relative to regular steranes (C₂₇₋₂₉ diacholestane/ C₂₇₋₂₉ regular steranes) indicates a relative increase in clay and oxygen. Both the C₃₀ / C₂₇₋₃₀ steranes and C₂₇₋₂₉ diacholestane/ C₂₇₋₂₉ regular steranes ratio are plotted as a function of depth in Figure 29.

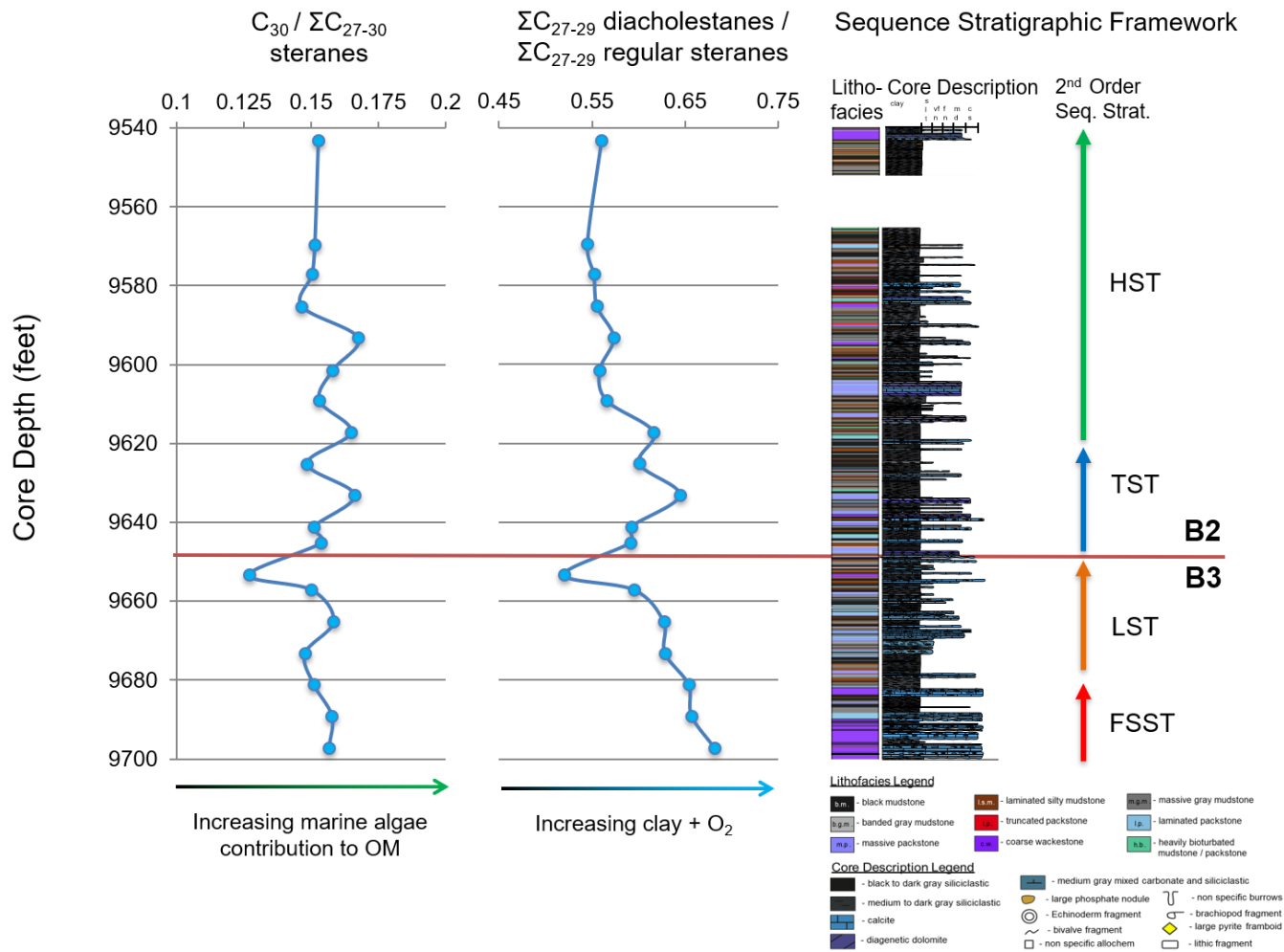


Figure 29. Sterane depth plots. From left to right: $C_{30}/\Sigma C_{27-30}$ steranes indicating marine algae input, ΣC_{27-29} diacholestanes/ ΣC_{27-29} regular steranes, reflecting changes in clay content and redox conditions, and the sequence stratigraphic framework for reference. Arrows below biomarker depth plots indicate factors controlling ratios and how.

However, the $(C_{28} + C_{29} \text{ TT}) / C_{30} \text{ H}$ ratio increase begins earlier on in the LST and does not appear to be as large of an increase as the one depicted by the C_{30} / C_{27-30} steranes ratio. Furthermore, the increase in C_{30} / C_{27-30} steranes ratio contradicts the HI and $C_{20} \text{ TT}$ data, which suggest an increase in terrestrial plant matter input during the middle LST. The disagreement between the different parameters decreases our confidence in higher plant matter source interpretation for the middle to late LST. The $C_{30} / \Sigma C_{27-30}$ steranes ratio then decreases to 0.13 by 9653 ft. (2942.2 m), ($\Delta C_{30} / \Sigma C_{27-30}$ steranes = -0.03), suggesting a relatively rapid decrease in marine algae toward the end of the LST, consistent with decrease in the $(C_{28} + C_{29} \text{ TT}) / C_{30} \text{ H}$ *Tasmanites* indicator.

The $C_{30} / \Sigma C_{27-30}$ steranes ratio increases after the onset of the TST, reaching a value of 0.17 by 9633 ft. (2936.1 m)., right below the *mfz*. The $C_{30} / \Sigma C_{27-30}$ steranes ratio then decreases slightly to 0.15 by 9625 ft. (2933.7 m), counterintuitively indicating a decrease in marine algae at the sea level maximum. However, the sample at 9625 ft. (2933.7 m) was taken from a silty laminated mudstone, which differs from the black mudstone primarily observed throughout the *mfz*. Hence the slight decrease in the $C_{30} / \Sigma C_{27-30}$ steranes ratio may be reflecting a decrease in marine algae contribution within a more proximally source event deposit rather than a change in predominate organic matter source during the overall sea level maximum.

. The $C_{30} / \Sigma C_{27-30}$ steranes ratio then increases again slightly to 0.17 at the onset of the HST before decreasing again to 0.15 by 9609 ft (2928.8 m). The $C_{30} / \Sigma C_{27-30}$ steranes ratio then increase to 0.17 by 9593 ft (2923.9 m). This increase occurs after the first occurrence of the truncated packstones, which are tentatively interpreted as either storm deposits or contourites, suggesting that the influx of proximal nutrients or

development of basin wide nutrient rich currents may have spurred these marine algal blooms. The $C_{30} / \Sigma C_{27-30}$ steranes ratio decreases to 0.15, where it remains relatively constant for the remainder of the core. Overall, the $C_{30} / \Sigma C_{27-30}$ steranes ratio decreases at sequence stratigraphic intervals that are interpreted to represent more anoxic conditions. Interestingly, the $C_{30} / \Sigma C_{27-30}$ steranes ratio tracks $\Sigma C_{27-C_{29}}$ diacholestane/ $\Sigma C_{27-C_{29}}$ regular steranes ratio quite well, further suggesting increases in marine algae under more oxic conditions.

The $\Sigma C_{27-C_{29}}$ diacholestanes/ $\Sigma C_{27-C_{29}}$ regular steranes ratio ranges from 0.52 - 0.68, with an average value of 0.60, suggesting a significant degree of sterane rearrangement, consistent with suboxic deposition. Overall, the $\Sigma C_{27-C_{29}}$ diacholestanes/ $\Sigma C_{27-C_{29}}$ regular steranes ratio decreases up section, indicating either an overall increase in carbonate content or increasingly reducing conditions over time. The latter is inconsistent with almost all the sedimentologic, ichnologic, and organic and inorganic geochemical data and thus does not seem like a reasonable interpretation. Therefore, the overall decrease of this ratio is interpreted as an increase in the amount of carbonate over time, consistent with the overall increase in the C_{29} / C_{30} hopane ratio. Although the overall $C_{27-C_{29}}$ diacholestane/ $C_{27-C_{29}}$ regular steranes ratio appears to more closely follow lithology, individual fluctuations in the ratio are thought to more closely reflect changes in redox conditions. The $\Sigma C_{27-C_{29}}$ diacholestane/ $\Sigma C_{27-C_{29}}$ regular steranes ratio decreases throughout the FSST and LST, reaching the lowest value observed throughout the core at the end of the LST.

The ratio then progressively increases throughout the TST, reaching one of the highest values observed throughout the core, 0.65, by 9633 ft (2936.1 m). This increase

in the $\Sigma C_{27-C_{29}}$ diacholestanes/ $\Sigma C_{27-C_{29}}$ regular steranes ratio suggests the development of more oxygenated conditions as sea level rose. However, the ratio decreases to 0.60 at 9635 ft. (2936.7 m), a depth interpreted to represent the *mfz*, suggesting the development of slightly more reducing conditions during sea level maxima, although not to the same degree that was experienced in the more stagnant LST.

The $\Sigma C_{27-C_{29}}$ diacholestanes/ $\Sigma C_{27-C_{29}}$ regular steranes ratio then increases slightly to 0.62 at a depth of 9617 ft. (2931.3 m). The sample taken at this depth was highly bioturbated, which is consistent with increased oxicity. The decrease in the $\Sigma C_{27-C_{29}}$ diacholestanes/ $\Sigma C_{27-C_{29}}$ regular steranes ratio from 9609 – 9601 ft. (2928.8 - 2926.4 m) appears to reflect the increase in carbonate content over the associated increase in oxygen brought down by the turbiditic flow itself. The $\Sigma C_{27-C_{29}}$ diacholestanes/ $\Sigma C_{27-C_{29}}$ regular steranes ratio then increases to 0.57 at 9593 ft. (2923.9 m) before decreasing to 0.56 by 9585 ft. (2921.5 m). The $\Sigma C_{27-C_{29}}$ diacholestanes/ $\Sigma C_{27-C_{29}}$ regular steranes ratio remains relatively constant before lightly increasing again at the end of the core, most likely reflecting an increase in clay at the very end of the HST. Interestingly, the $\Sigma C_{27-C_{29}}$ diacholestanes/ $\Sigma C_{27-C_{29}}$ regular steranes depth trend differs greatly from the clay-catalyzed, rearranged hopane ratio ($C_{30} D / C_{29} Ts$), which conversely appears to track redox conditions overall, with minor fluctuations reflecting lithologic changes.

8. Integrated Organic - Inorganic Geochemistry

8.1. Theoretical Refinement of Organic - Inorganic Geochemical Comparisons

Suboxia throughout the Wolfcamp B3 and B2 deposition, with small fluctuations to relatively more anoxic or oxic conditions has been established through a multiproxy approach to paleoredox reconstruction. Sedimentological and petrographic data reflects a highly heterogenous source rock, with depositional conditions that varied substantial over 2-inch sections. Furthermore, during weakly anoxic conditions, trace metals indicative of anoxia may be more variably distributed amongst the sediment in accordance to upward diffusing pathways between the sediment and the overlying water column. Since organic geochemical samples often represented more than 2 inches of deposition, individual, 2 inch evenly spaced XRF data points did not accurately reflect organic geochemical changes. Therefore, an inorganic interval averaging technique was developed to more accurately compare inorganic and organic geochemical data. Since the largest organic geochemical sample was approximately 6 inches thick, XRF data was averaged over 6 inches to more accurately reflect the organic geochemical samples. Furthermore, TOC data was collected on the other, thicker slab (butt end) of the core, inherently limiting a 1:1 depth comparison of the inorganic and TOC data. Therefore, inorganic geochemical data averaged over 6 inches was compared to TOC and biomarker data at the closest depth. This technique proved successful for inorganic geochemical comparisons with both biomarker and TOC data, which is imperative to better understanding the role of preservation and productivity in TOC richness.

8.1.1. Mo and Paleoredox Proxy - TOC Covariance

Molybdenum (Mo) concentrations (ppm) are often plotted against TOC in order to better understand paleoceanographic conditions, particularly anoxia and euxinia, and its role in organic matter preservation (Algeo and Lyons, 2006; Tribovillard et al., 2006, 2008, 2012; Gilleaudeau and Kah, 2013; Baumgardner et al., 2014; Turner and Slatt, 2016). Molybdenum concentrations averaged over 6 inch intervals are cross plotted with TOC (wt. %) in Figure 30.

Even with the aid of the interval averaging, Mo does not correlate well with TOC ($R^2 = 0.24$), indicating overall suboxia during Wolfcamp B3 and B2 deposition. However, when the data is segregated by sequence stratigraphic tracts, trends begin to appear. In particular, Mo correlates extremely well with TOC over the FSST and LST ($R^2 = 0.94$), although the sample size is limited. This high correlation value not only suggests that relatively more anoxic conditions persisted during the FSST and LST compared to the TST and HST, but that preservation is the dominant control for TOC richness during the FSST and LST. This interpretation of more persistent oxygen limited conditions during the FSST and LST is supported by both ichnological and biomarker data. Therefore, TOC values from samples in the Wolfcamp B3 may co-vary better with anoxia and euxinia trace proxies. Combining these two principles, Mo values averaged over 6 inch intervals were plotted against TOC values. There does not appear to be a clear relationship between Mo and TOC during the HST, suggesting that more oxygenated conditions persisted in

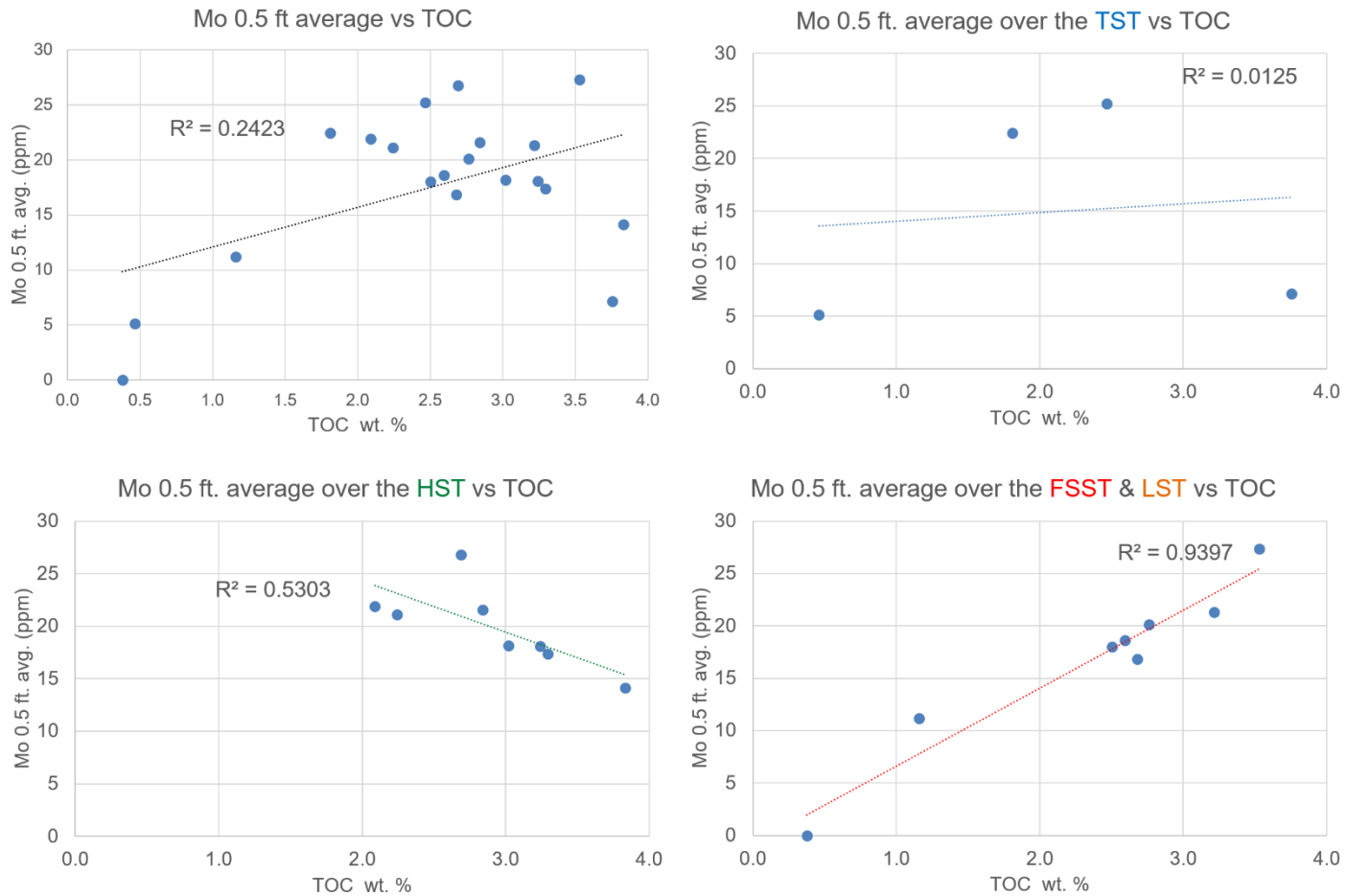


Figure 30. Half-foot averaged molybdenum (Mo) concentration cross plotted with corresponding TOC wt.% for the Wolfcamp B2 and B3 samples, segregated by 2nd order sequence stratigraphic position. From top to bottom, left to right: all samples; samples taken from the interpreted HST (marked in green); samples taken from the interpreted TST (marked in blue); and samples taken from the interpreted FSST and LST (marked in red and orange, respectively). Note varying correlation values.

the highstand, an interpretation that is supported by a significant increase in bioturbation at the onset and of the HST and the occurrence of the at the end of the HST.

8.1.2.Ni and Redox Sensitive Organometallic Proxy - TOC

Covariance

Nickel (Ni) concentrations (ppm) are often plotted against TOC (wt.%) to better understand paleoceanographic conditions and organic matter source material, in particular the relationship between suboxia and humic and fulvic acids in organometallic complexing (Tribovillard et al., 2006 and 2008). Nickel concentrations averaged over a half foot interval are cross plotted with TOC (wt. %) in Figure 31.

Overall, Ni correlates better with TOC than Mo, but still show a relatively weak positive linear relationship (Ni $R^2 = 0.39$; Mo $R^2 = 0.24$). The Ni – TOC data was segregated by interpreted 2nd order sequence stratigraphic tracts, revealing more significant geochemical trends. Nickel and TOC exhibit a very strong linear relationship over the TST ($R^2 = 0.98$) compared to any other point in time. This strong correlation suggests that conditions were more oxygenated during the TST than during the LST and FSST ($R^2 = 0.49$). However, Ni concentrations are influenced by redox conditions as well as humic and fulvic acid availability in the water column. Hence, the stronger correlation between Ni and

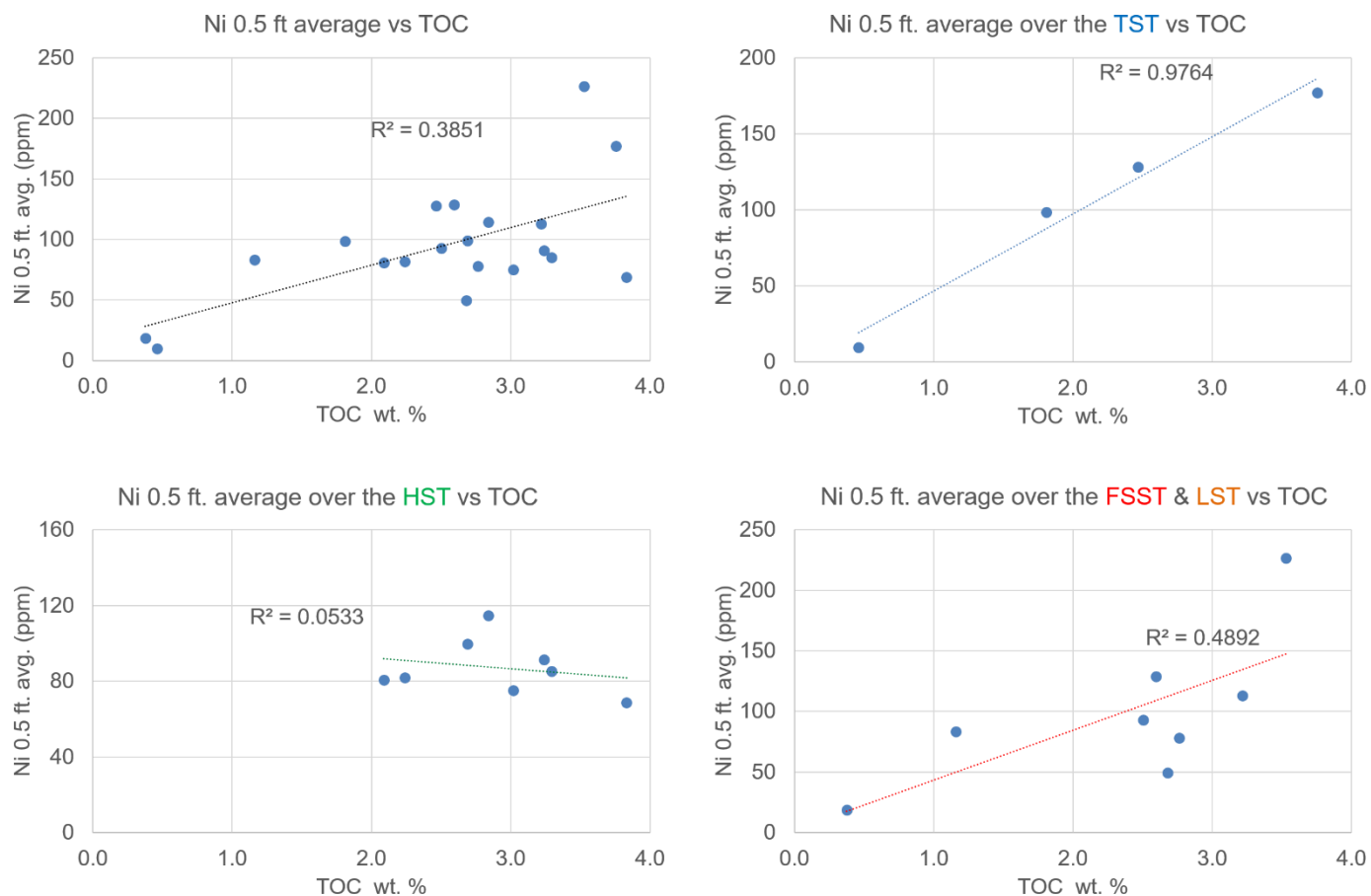


Figure 31. Half-foot averaged molybdenum (Ni) concentration cross plotted with corresponding TOC wt.% for the Wolfcamp B2 and B3 samples, segregated by 2nd order sequence stratigraphic position. From top to bottom, left to right: all samples; samples taken from the interpreted HST (marked in green); samples taken from the interpreted TST (marked in blue); and samples taken from the interpreted FSST and TST (marked in red and orange, respectively). Note varying correlation values and absolute ppm concentrations relative to Mo.

TOC during the TST may be reflecting an increase in plant matter contribution, microbial degradation by-products, or increased contribution from some forms of marine algae (Hatcher and Orem, 1986; Münster and Chróst, 1990; Tribovillard et al., 2006). Organic matter source-specific biomarkers help resolve this ambiguity and are investigated in the following section. Whatever the source may be, there appears to be an increase in the overall amount of organic matter during the relatively more suboxic TST, indicating that paleo-productivity played a larger role in the development of TOC richness during the TST. Although there should be a theoretical increase in the amount of plant matter delivered to distal parts of the basin during the HST due to shoreline progradation in mixed carbonate-siliciclastic shelves, more oxic conditions most likely limited Ni incorporation into sediments, creating the dispersed Ni – TOC data observed over the HST.

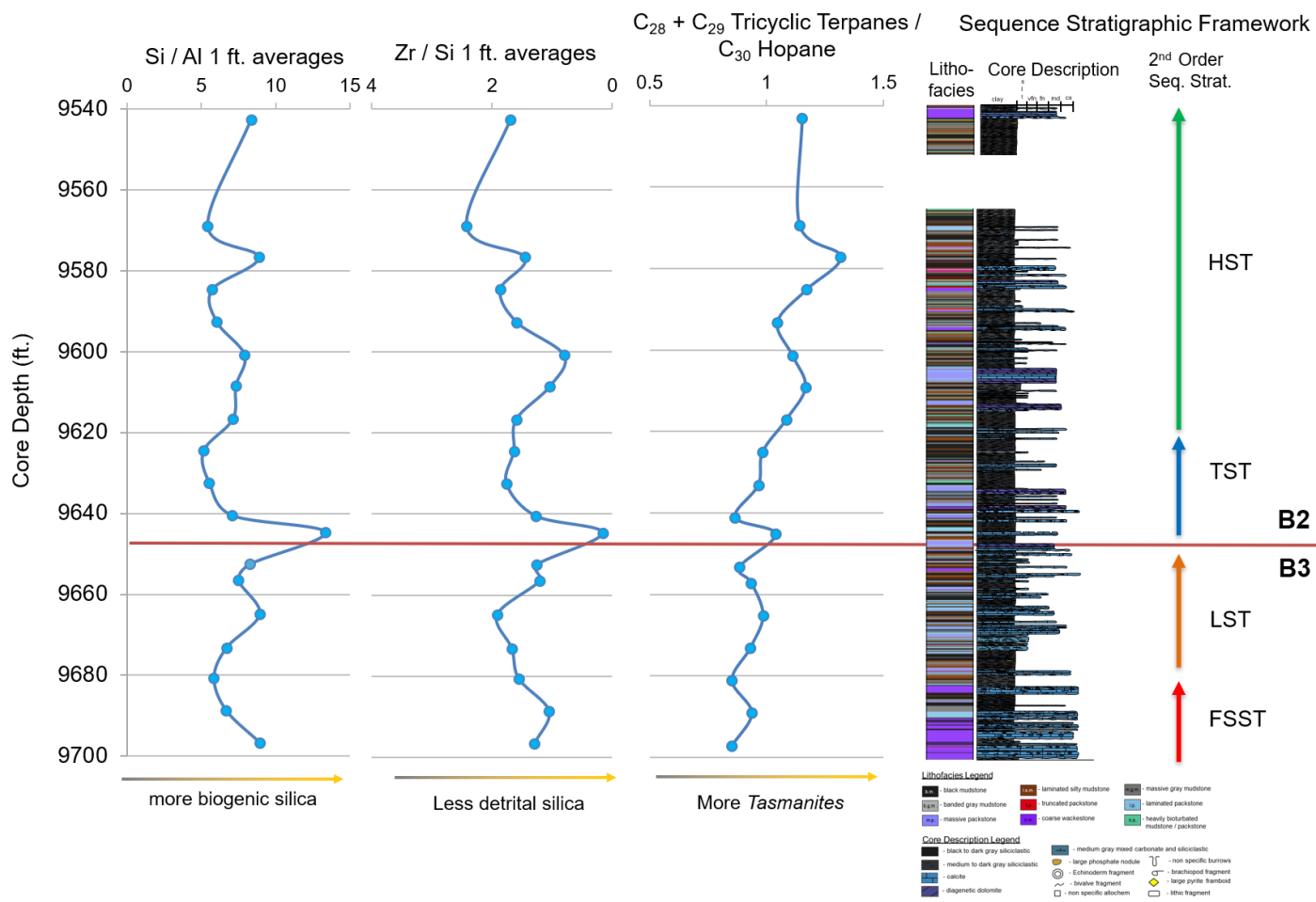
8.2. Novel biomarker-elemental proxy correlations

8.2.1. Biogenic Silica and *Tasmanites* Biomarker Ratio

It has been well documented that *Tasmanites*-rich rocks are enriched in higher carbon numbered tricyclic terpanes (Volkman et al., 1989; Greenwood et al., 2000; Vigran et al., 2008). Since siliceous *Tasmanites* were observed petrographically, they are thought to contribute to the biogenic silica fraction in the Wolfcamp B3 and B2. Biogenic silica was assessed in two ways – the conventional enrichment factor approach of Si / Al, as well as slightly more indirect proxy, the relative enrichment of Zr / Si. Since Al enrichment factors can vary dramatically with Ca abundance, a second proxy was used to check for this inherent pitfall when working in a mixed carbonate-siliciclastic

environment. Low Zr / Si values should indicate non-detrital Si, potentially biogenic. Silica (Si) and zirconium (Zr) concentrations (wt. %, and ppm respectively) averaged over 6 inch interval are plotted against the $(C_{28} + C_{29} TT) / C_{30} H$ biomarker ratio in Figure 32. Both inorganic biogenic silica proxies track the *Tasmanites* biomarker indicator well. The sequence stratigraphic implications of changes in the abundance of *Tasmanites* is explained in detail in the previous organic geochemical section. Thus, the focus of this section is to compare the inorganic and organic geochemical proxies for biogenic silica.

Interestingly, Zr / Si values correlated better with the $(C_{28} + C_{29} TT) / C_{30} H$ ratio over the FSST, particularly for the laminated packstone samples. This suggests that the Zr / Si ratio may be less influenced by changes in the Ca abundance. However, the $(C_{28} + C_{29} TT) / C_{30} H$ ratio begins to increase earlier than either the inorganic ratios would suggest. The decoupling of the biomarker and Zr / Si ratios over the LST may be reflecting the increase in detrital siliciclastic material during reciprocal sedimentation. Although all the ratios indicate an increase in the amount of biogenic silica at the onset of the TST, the inorganic ratios appear to over estimate the amount of biogenic silica, particularly the Si / Al ratio, which is more influenced by increases in Ca. This increase in Ca, with a reciprocal decrease in Al values, can cause an over estimation in the amount of biogenic silica, further highlighting enrichment factors issues in mixed carbonate siliciclastic systems. Overall, the $(C_{28} + C_{29} TT) / C_{30} H$ ratio increases up section,



S

Figure 32. Inorganic and organic biogenic silica indicators. From left to right: Si / Al averaged over 0.5 ft., Zr / Si averaged over 0.5 ft. with axis reversed to indicate non-detrital Si, and $(C_{28} + C_{29}$ tricyclic terpanes) / C_{30} hopane, an organic geochemical indicator for the silica rich marine algae *Tasmanites*. Sequence stratigraphic framework on right for reference.

while the inorganic ratios do not show a similar overall depth trend. This upward decoupling is interpreted as an overall increase in the amount of clay towards the end of the HST which may be suppressing the inorganic biogenic silica signal.

8.2.2. Organometallic Trace Metal and Plant Matter Biomarker

Ratios

As previously stated, Ni forms organic metallic complexes with humic and fulvic acids and is hence an indicator of both redox conditions and OM fluxes into the system. The C_{19} / C_{23} TT ratios is also thought to reflect relative changes in terrestrial plant matter contribution and redox conditions more so than the C_{20} / C_{23} TT ratio. Therefore, the C_{19} / C_{23} TT ratio is thought to reflect increases the relative anoxia as well as terrigenous plant matter contribution to the OM.

Both the Ni concentrations averaged over 6 inch intervals and the C_{19} / C_{23} TT ratio were plotted as a function of depth in Figure 33. Overall the two ratios track each other fairly well, particularly over the LST – TST transition. However, Ni is thought to more strongly reflect redox conditions relative to C_{19} / C_{23} TT given its relative increase at two sequence stratigraphically significant locations: 1) the FSST – LST transition and 2) the middle and late TST. The discrepancy at the *mfz* further highlights the slightly more reducing conditions towards the end of the TST, relative to higher energy and more oxygenated conditions associated with the initiation of sea level rise. However, it is also possible that the Ni concentrations are reflecting an increase in humic acids from other marine algae which may have

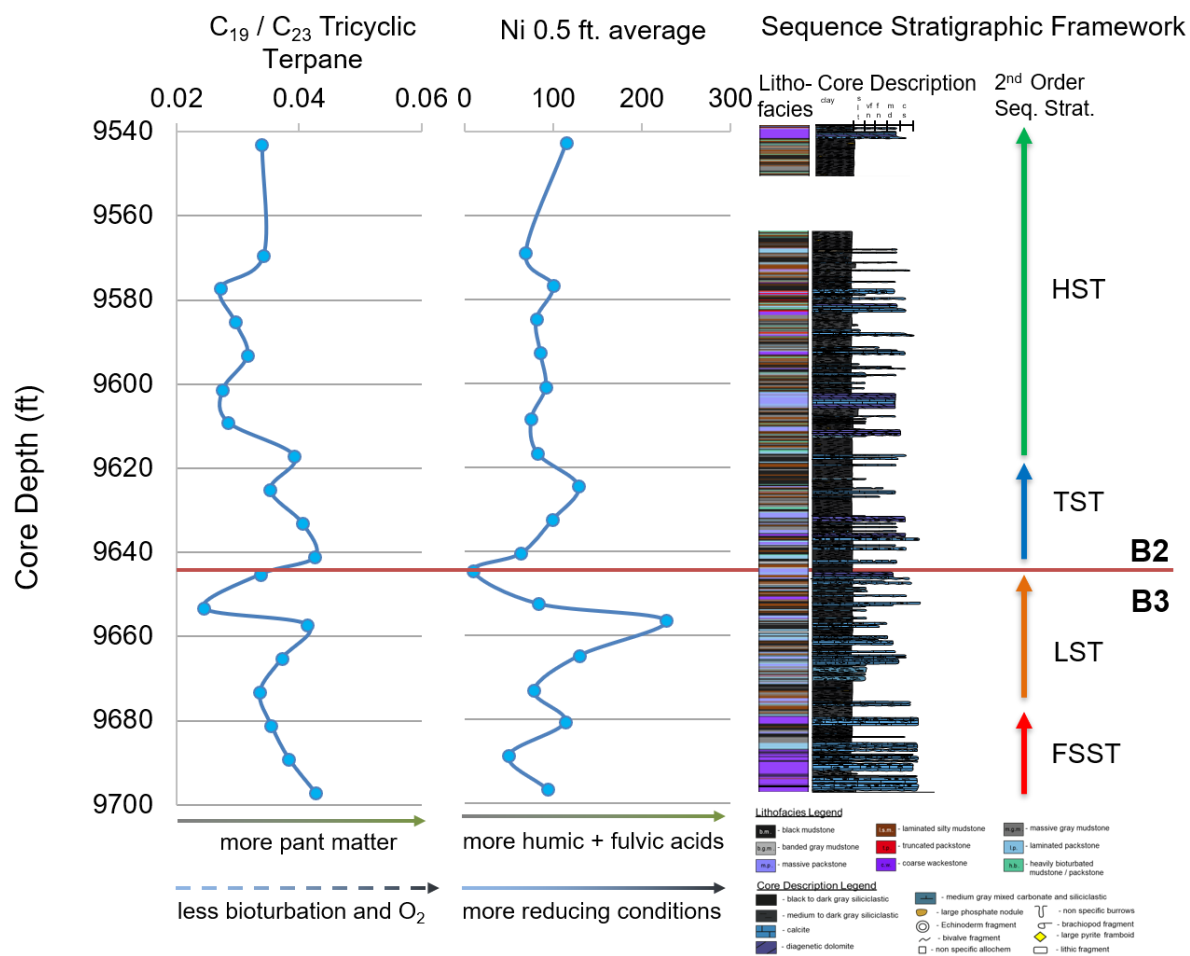


Figure 33. Organic and inorganic redox sensitive plant matter indicators. C_{19} / C_{23} tricyclic terpene ratio (left) compared to averaged Ni concentrations averaged over 0.5 ft. (ppm) (right). Controls on relative abundances indicated by arrows below respective Ni depth plots, tenuous interpretations in stippled arrows. Sequence stratigraphic framework on far right for reference.

been more ubiquitous at the sea level maximum (Nissenbaum and Kaplan, 1972; Hedges and Oades, 1997).

8.2.3. Ca Elemental Abundance and the Homohopane Index

In the early terpane analysis, certain biomarker ratios more closely related to either anoxia or carbonate content, such as Pr/Ph or C_{29}/C_{30} hopane ratios respectively, were compared to the C_{35} / C_{34} HH ratio. The C_{35} / C_{34} HH ratio more closely tracked pure carbonate content indicators, such as C_{29}/C_{30} hopane, which suggests that changes in the C_{35} / C_{34} HH ratio more closely reflect changes in the carbonate content rather than redox conditions. In order to further investigate this relationship, the Ca content (wt.%) averaged over 6 inch intervals and the C_{35} / C_{34} HH ratio are plotted as function of depth in Figure 34. Both geochemical depth plots tracked each other well, further supporting a predominately carbonate content control on the C_{35} / C_{34} HH ratio. This observation is interesting, if not geochemically counterintuitive, because during Wolfcamp B3 and B2 deposition carbonate content and relative anoxia are inversely related: generally, the more carbonate material, the less anoxic the environment. This however is sedimentologically and ichnologically intuitive because oxygenating calcareous sediment gravity flows were the dominant mechanism for carbonate deposition in the Wolfcamp B3 and B2. Although the geochemical specificities and mechanisms that would cause the C_{35} / C_{34} HH ratio to be primarily controlled by carbonate content rather than both carbonate content and anoxia remains unknown, this unique relationship is clearly observed. Since all the C_{35} / C_{34} HH

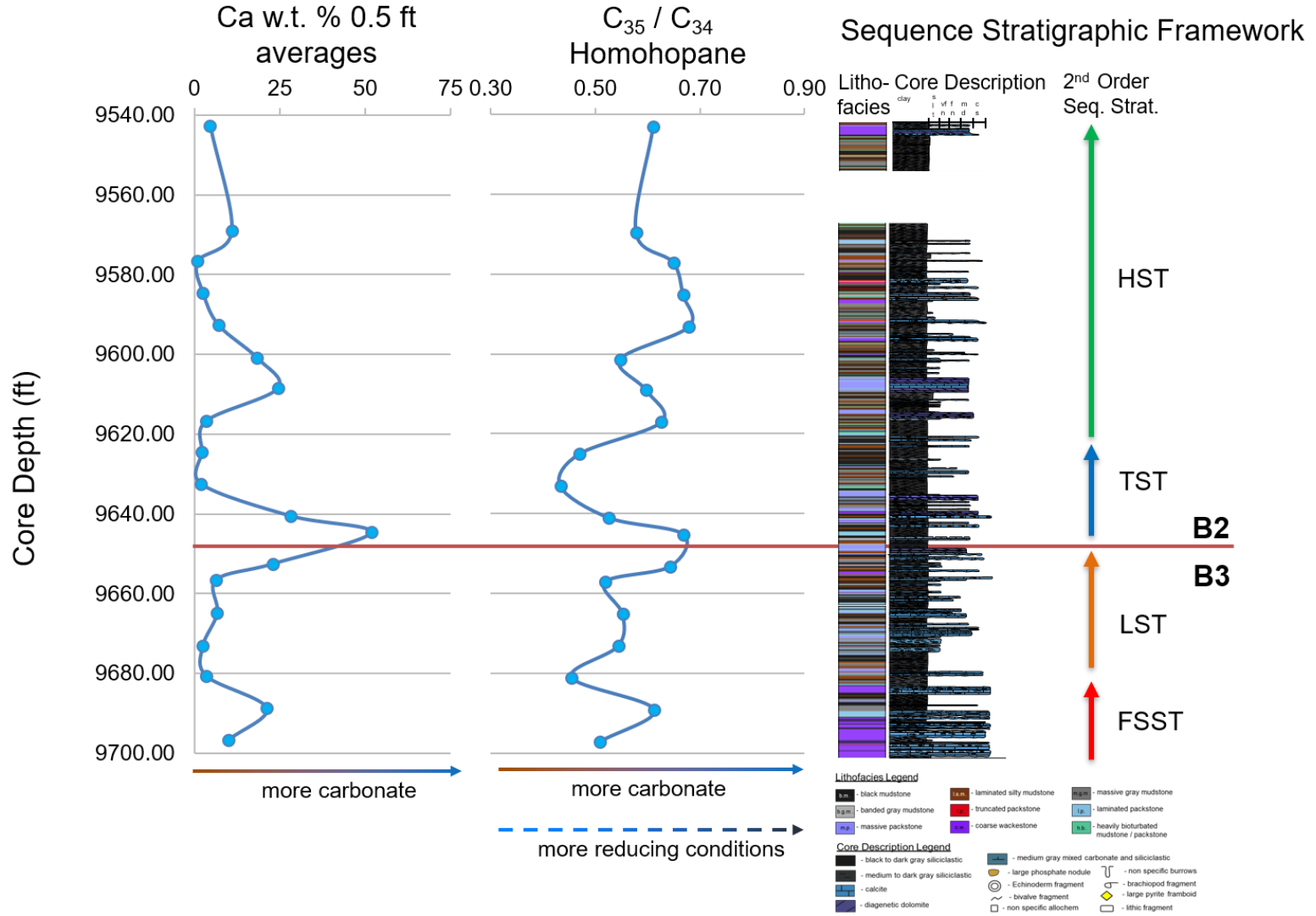


Figure 34. Inorganic and organic carbonate indicators. Calcium abundance averaged over 0.5 ft (w.t%) on the left and C_{35} / C_{34} homohopane ratio on right. Controls on relative abundances indicated by arrows below respective depth plots, with more minor controls in stippled arrows. Working sequence stratigraphic framework on far right for reference.

ratio values are <1 , it is hypothesized that the C_{35} / C_{34} HH ratio more closely reflects carbonate content in overall more suboxic conditions. The two carbonate parameters track each other fairly well, however, discrepancies between the C_{35} / C_{34} HH ratio and the Ca wt. % are observed. These discrepancies are thought reflect the limitations of the interval averaging technique, particularly over 9577 – 9593 ft. This interval is dominated by thin bedded calcareous beds (< 6 inches thick), and although individual XRF data points accurately reflect the Ca content, once averaged out over a half foot interval, their Ca signal is greatly reduced. This happened to a lesser degree over the early to middle LST. However, the interval averaging technique more accurately reflects changes in the C_{35} / C_{34} HH ratio than a 1:1 comparison alone, suggesting that the technique itself, although useful, needs refinement.

9. Conclusions

The assessment of subtle fluctuations in redox conditions proved to be very cryptic for the suboxic Wolfcamp B3 and B2 intervals on the edge of slope setting of the Midland Basin. A deep sedimentological understanding of the core was necessary to build a working sequence stratigraphic framework and contextualize the geochemical data. Larger overall trends in redox conditions typically associated with sequence stratigraphic interpretations were sometimes occluded by the redox fluctuations associated with the entrained oxygenated waters of sediment gravity flows. However, sediment gravity flow types and frequency were generally dependent on the changes in energy associated with sea level fall and rise. Large-scale sequence stratigraphic trends in redox conditions were consistent between the vast multi-proxy approach and are as follows: (1) relatively more

anoxic conditions persisted during Wolfcamp B3, or during the FSST and LST and (2) relatively more oxic conditions persisted during Wolfcamp B2, or TST and HST, deposition. However, it cannot be understated that these relative changes in redox fall within the larger context of general suboxia. As observed from this study, there is at no point any clear, well established anoxia. Furthermore, the LST, and to some degree the FSST, demonstrate more anoxic conditions than the interpreted *mfz*. The generalization that sea level highs are marked by water column stratification and more anoxic conditions does not apply for the Wolfcampian B3 and B2 deposition at this location.

Calcareous sediment gravity flows are interpreted to have brought oxygenated waters to the distal parts of the basin. This relationship is best observed by the established ichnological relationships with turbidites. This argument was further supported by both inorganic and organic geochemical proxies. The variations in degrees of suboxia proved useful in identifying what was the dominant control on many of the multivariable biomarker redox proxy ratios. Terrigenous plant matter was the dominant contributor to the OM during more reducing conditions, while marine algae was the dominant contributor during more oxic conditions. Furthermore, a clear relationship between freshwater influxes and *Tasmanites* algal blooms was established. Overall, heavily bioturbated and truncated packstone lithofacies correlated well with more oxygenated highstand conditions. These relationships are summarized in Figure 35.

Potential subtle parasequence variations towards the top of the Wolfcamp B2 interval were not interpreted in the geochemical data. This either reflects the limited vertical resolution of organic geochemical techniques or established that the redox fluctuations associated with the parasequence were either too subtle or nonexistent.

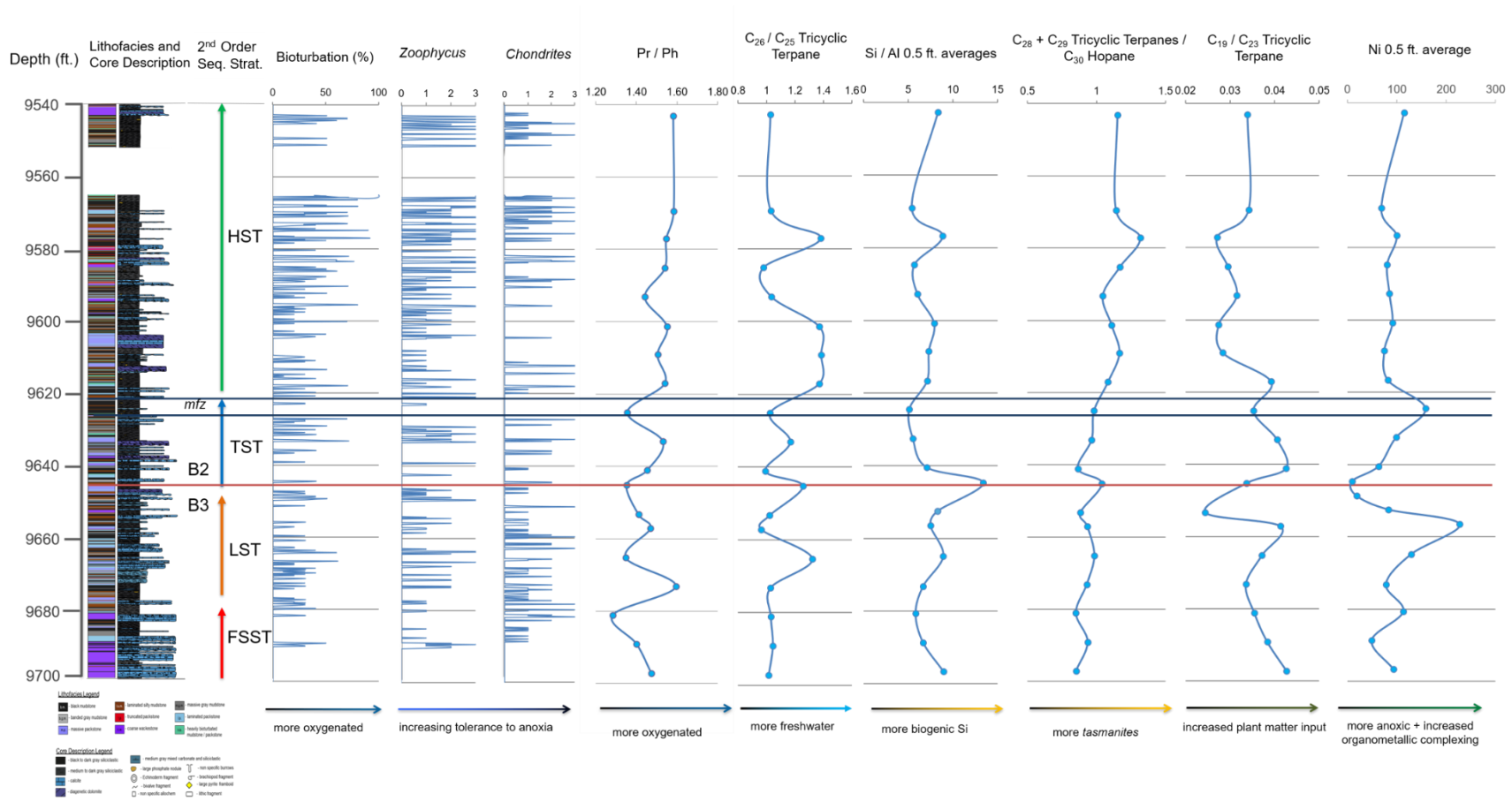


Figure 35. Summary figure showing changes in sedimentology, ichnology, inorganic geochemistry, and organic geochemistry in a sequence stratigraphic framework. From left to right: lithofacies log; core description; 2nd order sequence stratigraphic interpretation; total bioturbation; *Zoophycus* ichnofossil; *Chondrites* ichnofossil; Pr/ Ph; C₂₆/C₂₅ TT; Si / Al averaged over 0.5 ft.; (C₂₈ + C₂₉ TT) / C₃₀ hopane; C₁₉ / C₂₃ TT; and Ni concentrations averaged over 0.5 ft

Therefore, the preferred interpretation is that the series of truncated packstones towards the top of the B2 interval are most likely contourites or storm deposits reflecting highstand conditions rather than a drop in relative sea level. Aside from findings concerning fluctuations in redox condition due to sea level change or oxygenated sediment gravity flows, which appear to be relatively intertwined, novel refinements to trace metal – TOC proxies proved valuable. Interval averaging techniques helped bridge the gap between theoretical organic-inorganic geochemical relationships and observed ones.

10. Future Work

Although the core was rigorously analyzed using various redox proxies, a comprehensive diagenetic history was not established. Hence the potential effects of diagenesis on observed changes in redox conditions were not investigated. All redox proxies were assumed to reflect conditions at or near the sediment water interface at the time of deposition. Unfortunately, petrographic analysis established that much of the core experienced complex multistage diagenesis. This limitation of the study should be further investigated since many diagenetic fluid fronts have oxidizing potential. Pyrite framboid dimensional analysis could help aid in discerning reducing conditions during later abiotic diagenesis versus microbially induced reducing conditions in the pore waters of near surface sediments. The development of a more mathematically based, systematic approach to calculating the frequency of calciturbidites could allow for a more quantitative assessment of the interplay between oxygenation and sediment gravity flows. X-ray diffraction (XRD) analysis could expand our understanding of the incorporation of certain elements into mineral phases, particularly Fe in ferroan dolomite, which could shed light

on geochemical conditions farther up slope. Further application of the interval averaging approach to the previously disregarded enrichment factor technique have allowed for a more robust use of the inorganic geochemical data. Although visualizing the major and trace metal compositions of each lithofacies proved valuable for the purpose of this study, a more in-depth look into changes in trace metal fluctuations as a function of time would have helped parse out palaeoceanographic changes independent of certain lithologies or sedimentary textures.

A more in-depth investigation into organic geochemical evidence for microbial degradation, particularly when compared to the ichnological data as a function of depth, would shed light on potential geochemical evidence for bioturbation induced paleo-biodegradation. Analysis of the aromatic fraction for plant matter indicators, such as polyaromatic hydrocarbons (PAH) like retene, trimethylnaphthalenes (TMN), and dibenzofuran (DBF), could help refine our understanding of the fluctuation in terrigenous plant input over time. Further analysis of a single core however will only expand ones understanding of Wolfcamp B3 and B2 deposition at one discrete point along the base of slope setting. To fully understand the changes of redox conditions for the formation, other nearby cores should be examined. This would shed light on the redox condition fluctuations along turbidity current channel axial and lateral transects. As of now it is not fully understood if observed changes in redox conditions are truly attributable to more regional sequence stratigraphic model, or simply a localized avulsion of a submarine channel complex.

References

- Abbott, G. D., and J. R. Maxwell, 1988, Kinetics of the aromatisation of rearranged ring-C monoaromatic steroid hydrocarbons: *Organic Geochemistry*, v. 13, no. 4–6, p. 881–885.
- Achterberg, E. P., C. M. G. Van Den Berg, M. Boussemart, and W. Davison, 1997, Speciation and cycling of trace metals in Esthwaite Water: A productive English lake with seasonal deep-water anoxia: *Geochimica et Cosmochimica Acta*, v. 61, no. 24, p. 5233–5253.
- Ackman, R. G., R. F. Addison, S. N. Hooper, and A. Prakash, 1970, Halosphaera viridis: Fatty Acid Composition and Taxonomical Relationships: *Journal of the Fisheries Research Board of Canada*, v. 27, no. 2, p. 251–255.
- Adams, J. E., 1965, Stratigraphic-Tectonic Development of Delaware Basin: *AAPG Bulletin*, v. 49, no. 11, p. 2140–2148.
- Ainaji, N. S., 2013, Permian Basin Tectonics - SEPM Strata: <<http://www.sepmstrata.org/page.aspx?&pageid=137&2>> (accessed October 5, 2017).
- Albrecht, P., M. Vandenbroucke, and M. Mandeng, 1975, Geochemical studies on the organic matter from the Douala Basin (Cameroon)-I. Evolution of the extractable organic matter and the formation of petroleum: *Geochimica et Cosmochimica Acta*, v. 40, no. 7, p. 791–799.
- Alexander, R., R. Kagi, and R. Noble, 1983, Identification of the bicyclic sesquiterpenes drimane and eudesmane in petroleum: *Journal of the Chemical Society, Chemical Communications*, no. 5, p. 226–228.
- Algeo, T. J., D. L. Hoffman, J. B. Maynard, M. M. Joachimski, J. C. Hower, and W. L. Watney, 1997, Environmental Reconstruction of Anoxic Marine Systems: Core Black Shales of Upper Pennsylvanian Midcontinent Cyclothems: p. 103–147.
- Algeo, T. J., and T. W. Lyons, 2006, Mo-total organic carbon covariation in modern anoxic marine environments: Implications for analysis of paleoredox and paleohydrographic conditions: *Paleoceanography*, v. 21, no. 1, p. 1–23.
- Algeo, T. J., and J. B. Maynard, 2004, Trace-element behavior and redox facies in core shales of Upper Pennsylvanian Kansas-type cyclothems: *Chemical Geology*, v. 206, no. 3–4, p. 289–318.
- Algeo, T. J., J. L. Morford, and A. Cruse, 2012, Reprint of: New Applications of Trace Metals as Proxies in Marine Paleoenvironments: *Chemical Geology*, v. 324–325, p. 1–5.

- Algeo, T. J., L. Schwark, and J. C. Hower, 2004, High-resolution geochemistry and sequence stratigraphy of the Hushpuckney Shale (Swope Formation, eastern Kansas): Implications for climato-environmental dynamics of the Late Pennsylvanian Midcontinent Seaway: *Chemical Geology*, v. 206, no. 3–4, p. 259–288.
- Amy, L. A., J. Peakall, and P. J. Talling, 2005, Density- and viscosity-stratified gravity currents: Insight from laboratory experiments and implications for submarine flow deposits: *Sedimentary Geology*, v. 179, no. 1–2, p. 5–29.
- Andresen, N., J. J. G. Reijmer, and A. W. Droxler, 2003, Timing and distribution of calciturbidites around a deeply submerged carbonate platform in a seismically active setting (Pedro Bank, Northern Nicaragua Rise, Caribbean Sea): *International Journal of Earth Sciences*, v. 92, no. 4, p. 573–592.
- Aquino Neto, F. R., J. M. Trendel, A. Restle, Albrecht P., and Connan J., 1981, Occurrence and formation of tricyclic and tetracyclic terpanes in sediments and petroleum, *in* M. Bjorøy, P. Albrecht, and C. Cornford, eds., *Advances in Organic Geochemistry 1981*: J. Wiley and Sons, p. 659–667.
- Aquino Neto, F. R., J. M. Trendel, A. Restle, and J. Connan, 1983, Occurrence and formation of tricyclic and tetracyclic terpanes in sediments and petroleum, *in* M. Bjorøy, P. Albrecht, and C. Cornford, eds., *Advances in Organic Geochemistry 1981*: Wiley, p. 659–676.
- Ashckenazi-Polivoda, S., Y. Edelman-Furstenberg, A. Almogi-Labin, and C. Benjamini, 2010, Characterization of lowest oxygen environments within ancient upwelling environments: Benthic foraminifera assemblages: *Palaeogeography, Palaeoclimatology, Palaeoecology*, v. 289, no. 1–4, p. 134–144.
- Azevedo, D. A., F. R. Aquino Neto, B. R. T. Simoneit, and A. C. Pinto, 1992, Novel series of tricyclic aromatic terpanes characterized in Tasmanian tasmanite: *Organic Geochemistry*, v. 18, no. 1, p. 9–16.
- Banerjee, A., A. K. Sinha, A. K. Jain, N. J. Thomas, K. N. Misra, and K. Chandra, 1998, A mathematical representation of Rock-Eval hydrogen index vs Tmax profiles: *Organic Geochemistry*, v. 28, no. 1–2, p. 43–55.
- Barnes, M. A., and W. C. Barnes, 1983, Oxic and anoxic diagenesis of diterpenes in lacustrine sediments, *in* M. Bjorøy, P. Albrecht, and C. Cornford, eds., *Advances in Organic Geochemistry 1981*: Wiley, p. 289–298.
- Baumgardner, R. W., H. S. Hamlin, and H. D. Rowe, 2014, High-Resolution Core Studies of Wolfcamp/Leonard Basinal Facies, Southern Midland Basin, Texas: *AAPG Search and Discovery*, v. 10607, no. 10607, p. 1–4.
- Blumer, M., R. R. L. Guillard, and T. Chase, 1971, Hydrocarbons of marine phytoplankton: *Marine Biology*, v. 8, no. 3, p. 183–89.

- Blumer, M., M. M. Mullin, and D. W. Thomas, 1963, Pristane in Zooplankton: *Science*, v. 140, no. 3570, p. 974.
- Blumer, M., and W. D. Snyder, 1965, Isoprenoid Hydrocarbons in Recent Sediments: Presence of Pristane and Probable Absence of Phytane: *Science*, v. 150, no. 3703, p. 1588–1589.
- Boon, J. J., W. I. C. Rijpstra, F. De Lange, J. W. De Leeuw, M. Yoshioka, and Y. Shimizu, 1979, Black Sea sterol—a molecular fossil for dinoflagellate blooms: *Nature*, v. 277, no. 5692, p. 125–127.
- Bourbonniere, R. A., and P. A. Meyers, 1996, Sedimentary geolipid records of historical changes in the watersheds and productivities of Lakes Ontario and Erie: *Limnology and Oceanography*, v. 41, no. 2, p. 352–359.
- Breit, G. N., and R. B. Wanty, 1991, Vanadium accumulation in carbonaceous rocks: A review of geochemical controls during deposition and diagenesis: *Chemical Geology*, v. 91, no. 2, p. 83–97.
- Bromley, R. G., and A. A. Ekdale, 1984, Chondrites: A Trace Fossil Indicator of Anoxia in Sediments: *Science*, v. 224, no. 4651, p. 872–874.
- Brooks, J. D., K. Gould, and J. W. Smith, 1969, Isoprenoid Hydrocarbons in Coal and Petroleum: *Nature*, v. 222, no. 5190, p. 257–259.
- Brown, L. F., and W. L. Fisher, 1977, Seismic-Stratigraphic Interpretation of Depositional Systems: Examples from Brazilian Rift and Pull-Apart Basins, *in* *Seismic Stratigraphy—Applications to Hydrocarbon Exploration: American Association of Petroleum Geologists Memoir 26: AAPG Special Volumes*, p. 213–248.
- Burwood, R., P. Leplat, B. Mycke, and J. Paulet, 1992, Rifted margin source rock deposition: a carbon isotope and biomarker study of a West African lower cretaceous “Lacustrine” section: *Organic Geochemistry*, v. 19, no. 1–3, p. 41–52.
- Calver, C. R., M. J. Clarke, and M. Truswell, 1984, The stratigraphy of a Late Palaeozoic borehole section in Douglas River, eastern Tasmania: a synthesis of marine macro-invertebrate and palynological data, *in* *Papers and Proceedings of the Royal Society of Tasmania*: p. 137–161.
- Calvert, S. E., and T. F. Pedersen, 1993, Geochemistry of Recent oxic and anoxic marine sediments: Implications for the geological record: *Marine Geology*, v. 113, no. 1–2, p. 67–88.
- Cassani, F., and G. Eglinton, 1991, Organic geochemistry of Venezuelan extra-heavy crude oils 2. Molecular assessment of biodegradation: *Chemical Geology*, v. 91, no. 4, p. 315–333.

- Cheng, X., D. Hou, C. Xu, and F. Wang, 2016, Biodegradation of tricyclic terpanes in crude oils from the Bohai Bay Basin: *Organic Geochemistry*, v. 101, p. 11–21.
- Cheng, M., C. Li, L. Zhou, and S. C. Xie, 2015, Mo marine geochemistry and reconstruction of ancient ocean redox states: *Science China Earth Sciences*, v. 58, no. 12, p. 2123–2133.
- Clark, J. P., and R. P. Philp, 1989, Geochemical Characterization of Evaporite and Carbonate Depositional Environments and Correlation of Associated Crude Oils in the Black Creek Basin, Alberta: *Bulletin of Canadian Petroleum Geology*, v. 37, no. 4, p. 401–416.
- Connan, J., 1984, Biodegradation of crude oils in reservoirs, *in* J. Brooks, and D. H. Welte, eds., *Advances in Petroleum Geochemistry*: London, Associated Press, p. 298–335.
- Connan, J., 1974, Time-Temperature Relation in Oil Genesis: *American Association Petroleum Geologists Bulletin*, v. 56, no. 10, p. 2068–2071.
- Connan, J., J. Bouroulllec, D. Dessort, and P. Albrecht, 1986, The microbial input in carbonate-anhydrite facies of a sabkha palaeoenvironment from Guatemala: A molecular approach: *Organic Geochemistry*, v. 10, no. 1–3, p. 29–50.
- Connan, J., and A. M. Cassou, 1980, Properties of gases and petroleum liquids derived from terrestrial kerogen at various maturation levels: *Geochimica et Cosmochimica Acta*, v. 44, no. 1, p. 1–23.
- Connan, J., and D. Dessort, 1987, Novel family of hexacyclic hopanoid alkanes (C32-C35) occurring in sediments and oils from anoxic paleoenvironments: *Organic Geochemistry*, v. 11, no. 2, p. 103–113.
- Connan, J., A. Restle, and P. Albrecht, 1980, Biodegradation of crude oil in the Aquitaine basin: *Physics and Chemistry of the Earth*, v. 12, p. 1–17.
- Corn, R. M., 2017, Trace Metals in Seawater: p. 1–21: <<https://www.chem.uci.edu/~unicorn/M3LC/handouts/Seawater.pdf>>.
- Cortez III, M., 2012, Chemostratigraphy, Paleooceanography, and Sequence Stratigraphy of the Pennsylvanian – Permian Section in the Midland Basin of West Texas, With Focus on the Wolfcamp Formation: The University of Texas at Arlington, 1–107 p.
- Cranwell, P. A., 1973, Chain-length distribution of n-alkanes from lake sediments in relation to post-glacial environmental change: *Freshwater Biology*, v. 3, p. 259–265.
- Cranwell, P. A., G. Eglinton, and N. Robinson, 1987, Lipids of aquatic organisms as potential contributors to lacustrine sediments-II: *Organic Geochemistry*, v. 11, no. 6, p. 513–527.

- Crevello, P. D., and W. Schlager, 1980, Carbonate Debris Sheets and Turbidites, Exuma Sound, Bahamas: *Journal of Sedimentary Research*, v. Vol. 50, no. 4, p. 1121–1147.
- Crusius, J., and J. Thomson, 2000, Comparative behavior of authigenic Re, U, and Mo during reoxidation and subsequent long-term burial in marine sediments: *Geochimica et Cosmochimica Acta*, v. 64, no. 13, p. 2233–2242.
- Cullen, J. J., and T. Tyrell, 1999, Oceanography: iron, nitrogen and phosphorus in the ocean: *Nature*, v. 402, no. November, p. 2098.
- Cuny, P., C. Cravo-Laureau, V. Grossi, and F. Gilbert, 2011, Biodegradation of Hydrocarbons in Bioturbated Marine Sediments, *in* A.-I. Koukkou, ed., *Microbial Bioremediation of Non-metals: Current Research*: Norfolk, Caister Academic Press, p. 55–89.
- D'Alessandro, A., A. A. Ekdale, and M. Sonnino, 1986, Sedimentologic significance of turbidite ichnofacies in the Saraceno Formation ((Eocene)), southern Italy: *Journal of Sedimentary Research*, v. 56, no. 2, p. 294–306.
- Dartiguelongue, C., F. Behar, H. Budzinski, G. Scacchi, and P. M. Marquaire, 2005, Thermal stability of dibenzothiophene in closed system pyrolysis: Experimental study and kinetic modelling: *Organic Geochemistry*, v. 37, no. 1, p. 98–116.
- Didyk, B. M., B. R. T. Simoneit, S. C. Brassell, and G. Eglinton, 1978, Organic geochemical indicators of palaeoenvironmental conditions of sedimentation: *Nature*, v. 272, no. 5650, p. 216–222.
- DiMichele, W. A., D. S. Chaney, W. J. Nelson, S. G. Lucas, C. V. Looy, K. Quick, and W. Jun, 2007, A low diversity, seasonal tropical landscape dominated by conifers and peltasperms: Early Permian Abo Formation, New Mexico: *Review of Palaeobotany and Palynology*, v. 145, no. 3–4, p. 249–273.
- Dunham, R. J., 1962, Classification of Carbonate Rocks According to Depositional Textures, *in* W. E. Ham, ed., *AAPG Memoir 1: Classification of Carbonate Rocks--A Symposium*: AAPG, p. 108–121.
- Ece, O. I., 1990, Geochemistry and occurrence of authigenetic phosphate nodules from the Desmoinesian cyclic Exello epeiric sea of the Midcontinent, USA: *Marine and Petroleum Geology*, v. 7, no. 3, p. 298–312.
- Eglinton, G., and R. J. Hamilton, 1967, Leaf epicuticular waxes: *Science*, v. 156, no. 3780, p. 1322–1335.
- Einsele, G., 1996, Event deposits: the role of sediment supply and relative sea-level changes—overview: *Sedimentary Geology*, v. 104, no. 1–4, p. 11–37.
- Einsele, G., and A. Seilacher, 1982, Paleogeographic significance of tempestites and

- periodites, *in* Cyclic and event stratification; symposium.: Berlin, Heidelberg, Springer Berlin Heidelberg, p. 531–536.
- Ekdale, A. A., 1985, Paleoeology of the marine endobenthos: *Palaeogeography, Palaeoclimatology, Palaeoecology*, v. 50, no. 1, p. 63–81.
- Ekdale, A. A., R. G. Bromley, and D. B. Loope, 2007, Ichnofacies of an Erg: A Climactically Influenced Trace Fossil Association in the Jurassic Navajo Sandstone, Southern Utah, USA, *in* Trace Fossils: Concepts, Problems, Prospects: p. 562–574.
- Ekdale, A. A., and T. R. Mason, 1988, Characteristic trace fossils associations in oxygen-poor sedimentary environments: *Geology*, v. 16, p. 720–723.
- Ekdale, A. A., L. N. Muller, and M. T. Novak, 1984, Quantitative ichnology of modern pelagic deposits in the abyssal Atlantic: *Palaeogeography, Palaeoclimatology, Palaeoecology*, v. 45, no. 2, p. 189–223.
- Elser, J. J., M. E. S. Bracken, E. E. Cleland, D. S. Gruner, W. S. Harpole, H. Hillebrand, J. T. Ngai, E. W. Seabloom, J. B. Shurin, and J. E. Smith, 2007, Global analysis of nitrogen and phosphorus limitation of primary producers in freshwater, marine and terrestrial ecosystems: *Ecology Letters*, v. 10, no. 12, p. 1135–1142.
- Ewing, T. E., 2013, Subsidence and Uplift History of the West Texas Basin and its (Post-Paleozoic) Margins: *AAPG Search and Discovery*, v. 30272, no. 30272, p. 1–25.
- Farrimond, P., J. C. Bevan, and A. N. Bishop, 1999, Tricyclic terpane maturity parameters: response to heating by an igneous intrusion: *Organic Geochemistry*, v. 30, no. 8, p. 1011–1019.
- Farrimond, P., and N. Telnæs, 1996, Three series of rearranged hopanes in Toarcian sediments (northern Italy): *Organic Geochemistry*, v. 25, no. 3–4, p. 165–177.
- Feret, F. R., H. Hamouche, and Y. Boissonneault, 2003, Spectral Interference in X-ray Fluorescence Analysis of Common Material: *Advances in X-ray Analysis*, v. 46, p. 381–387.
- Flaig, W., 1972, Biochemical factors in coal formation, *in* H. R. Gaertner, and H. Wehner, eds., *Advances in Organic Geochemistry*: Oxford-Braunschweig: Pergamon Press, p. 197–232.
- Flaig, W., 1966, Chemistry of humic substances, *in* *The Use of Isotopes in Soil Organic Matter Studies*: Oxford: Pergamon Press, p. 103–127.
- Follmi, K. B., 1996, The phosphorus cycle, phosphogenesis and marine phosphate-rich deposits: *Earth-Science Reviews*, v. 40, no. 1–2, p. 55–124.

- Follmi, K. B., and K. A. Grimm, 1990, Doomed pioneers: gravity-flow deposition and bioturbation in marine oxygen-deficient environments: *Geology*, v. 18, no. 11, p. 1069–1072.
- French, K. L., J. Sepúlveda, J. Trabucho-Alexandre, D. R. Gröcke, and R. E. Summons, 2014, Organic geochemistry of the early Toarcian oceanic anoxic event in Hawsker Bottoms, Yorkshire, England: *Earth and Planetary Science Letters*, v. 390, p. 116–127.
- Frey, R. W., S. G. Pemberton, and T. D. A. Saunders, 1990, Ichnofacies and bathymetry: A passive relationship: *Journal of Paleontology*, v. 64, no. 1, p. 155–158.
- Frey, R. W., and A. Seilacher, 1980, Uniformity in marine invertebrate ichnology: *Lethaia*, v. 13, no. 3, p. 183–207.
- Fu, Q., 2011, Wolfcamp Platform Carbonate and Basinal Facies in the Midland Basin, *in* SEPM Permian Basin Section Presentation.
- Garrison, R. E., 1990, Pelagic and hemipelagic sedimentary rocks as source and reservoir rock: *Pacific Section SEPM*, v. 66, p. 123–149.
- Gaswirth, S. B., 2017, Assessment of Continuous Oil Resources in the Wolfcamp Shale of the Midland Basin, Permian Basin Province, Texas, 2016, Open File-Report 2017–1013: 14 p. p.
- Gentzis, T., F. Goodarzi, and L. R. Snowdon, 1993, Variation of maturity indicators (optical and Rock-Eval) with respect to organic matter type and matrix lithology: an example from Melville Island, Canadian Arctic Archipelago: *Marine and Petroleum Geology*, v. 10, no. 5, p. 507–513.
- Gianniny, G. L., and J. A. T. Simo, 1996, Implications of Unfilled Accommodation Space for Sequence Stratigraphy on Mixed Carbonate-Siliciclastic Platforms: An Example from the Lower Desmoinesian (Middle Pennsylvanian), Southwestern Paradox Basin, Utah, *in* Paleozoic Systems of the Rocky Mountain Region: Rocky Mountain Section (SEPM), p. 213–234.
- Giger, W., C. Schaffner, and S. G. Wakeham, 1980, Aliphatic and olefinic hydrocarbons in recent sediments of Greifensee, Switzerland: *Geochimica et Cosmochimica Acta*, v. 44, no. 1, p. 119–129.
- Gilleaudeau, G. J., and L. C. Kah, 2013, Oceanic molybdenum drawdown by epeiric sea expansion in the Mesoproterozoic: *Chemical Geology*, v. 356, p. 21–37.
- Gingras, M. K., J. A. MacEachern, and S. E. Dashtgard, 2011, Process ichnology and the elucidation of physico-chemical stress: *Sedimentary Geology*, v. 237, no. 3–4, p. 115–134.

- Goodwin, N. S., P. J. D. Park, and A. P. Rawlinson, 1983, Crude oil biodegradation under simulated and natural conditions, *in* M. Bjorøy, P. Albrecht, and C. Cornford, eds., *Advances in Organic Geochemistry 1981*: Wiley, p. 650–658.
- Goossens, H., J. W. de Leeuw, P. A. Schenck, and S. C. Brassell, 1984, Tocopherols as likely precursors of pristane in ancient sediments and crude oils: *Nature*, v. 312, no. 5993, p. 440–442.
- Grammer, G. M., and R. N. Ginsburg, 1992, Highstand versus lowstand deposition on carbonate platform margins: insight from Quaternary foreslopes in the Bahamas: *Marine Geology*, v. 103, no. 1–3, p. 125–136.
- de Grande, S. M. B., F. R. Aquino Neto, and M. R. Mello, 1993, Extended tricyclic terpanes in sediments and petroleum: *Organic Geochemistry*, v. 20, no. 7, p. 1039–1047.
- Greenwood, P. F., K. R. Arouri, and S. C. George, 2000, Tricyclic terpenoid composition of tasmanites kerogen as determined by pyrolysis GC-MS: *Geochimica et Cosmochimica Acta*, v. 64, no. 7, p. 1249–1263.
- Greenwood, P., and S. George, 1999, Mass spectral characteristics of C19 and C20 tricyclic terpanes detected in Latrobe Tasmanite oil shale: *European Journal of Mass Spectrometry*, v. 5, no. 1, p. 221.
- Grice, K., M. Audino, C. J. Boreham, R. Alexander, and R. I. Kagi, 2001, Distributions and stable carbon isotopic compositions of biomarkers in torbanites from different palaeogeographical locations: *Organic Geochemistry*, v. 32, no. 10, p. 1195–1210.
- Grice, K., C. Cao, G. D. Love, M. E. Böttcher, R. J. Twitchett, E. Grosjean, R. E. Summons, S. C. Turgeon, W. Dunning, and Y. Jin, 2005, Photic Zone Euxinia during the Permian-Triassic Superanoxic Event: *Science*, v. 307, no. 5710, p. 706–709.
- Hallworth, M. A., J. C. Phillips, H. E. Huppert, and R. S. J. Sparks, 1993, Entrainment in turbulent gravity currents: *Nature*, v. 362, p. 829–831.
- Handford, C. R., 1981, *Sedimentology and Genetic Stratigraphy of Dean and Spraberry Formations (Permian), Midland Basin, Texas*: AAPG Bulletin, p. 1602–1616.
- Hanson, A. D., S. C. Zhang, J. M. Moldowan, D. G. Liang, and B. M. Zhang, 2000, *Molecular Organic Geochemistry of the Tarim Basin, Northwest China 1*: AAPG Bulletin, v. 84, no. 8, p. 1109–1128.
- Haq, B. U., and S. R. Schutter, 2008, A Chronology of Paleozoic Sea-Level Changes: *Science*, v. 322, no. 5898, p. 64–68.
- Hatch, J. R., and J. S. Leventhal, 1992, Relationship between inferred redox potential of the depositional environment and geochemistry of the Upper Pennsylvanian

- (Missourian) Stark Shale Member of the Dennis Limestone, Wabaunsee County, Kansas, U.S.A.: *Chemical Geology*, v. 99, no. 1–3, p. 65–82.
- Hatcher, P. G., and W. H. Orem, 1986, Structural Interrelationships among Humic Substances in Marine and Estuarine Sediments, *in* *Organic Marine Geochemistry ACS Symposium Series*: p. 142–157.
- Haughton, P. D. W., S. P. Barker, and W. D. McCaffrey, 2003, “Linked” debrites in sand-rich turbidite systems - Origin and significance: *Sedimentology*, v. 50, no. 3, p. 459–482.
- Haughton, P. D. W., C. Davis, W. D. McCaffrey, and S. P. Barker, 2009, Hybrid sediment gravity flow deposits - Classification, origin and significance: *Marine and Petroleum Geology*, v. 26, no. 10, p. 1900–1918.
- ten Haven, H. L., J. W. de Leeuw, J. Rullkötter, and J. S. S. Damsté, 1987, Restricted utility of the pristane/phytane ratio as a palaeoenvironmental indicator: *Nature*, v. 330, no. 6149, p. 641–643.
- ten Haven, H. L., J. W. de Leeuw, J. S. Sinninghe Damsté, P. A. Schenck, S. E. Palmer, and J. E. Zumberge, 1988, Application of biological markers in the recognition of palaeohypersaline environments, *in* A. J. Fleet, K. Kelts, and M. R. Talbot, eds., *Geological Society Special Publication No. 40: Lacustrine Source Rocks*: London, Geological Society of London, p. 123–130.
- Hays, L. E., T. Beatty, C. M. Henderson, G. D. Love, and R. E. Summons, 2007, Evidence for photic zone euxinia through the end-Permian mass extinction in the Panthalassic Ocean (Peace River Basin, Western Canada): *Palaeoworld*, v. 16, no. 1–3, p. 39–50.
- Hays, L. E., K. Grice, C. B. Foster, and R. E. Summons, 2012, Biomarker and isotopic trends in a Permian–Triassic sedimentary section at Kap Stosch, Greenland: *Organic Geochemistry*, v. 43, p. 67–82.
- Hedges, J. I., R. G. Keil, and R. Benner, 1997, What happens to terrestrial organic matter in the ocean? *Organic Geochemistry*, v. 27, no. 5–6, p. 195–212.
- Hedges, J. ., and J. . Oades, 1997, Comparative organic geochemistries of soils and marine sediments: *Organic Geochemistry*, v. 27, no. 7–8, p. 319–361.
- Helz, G. R., B. E. Erickson, and T. P. Vorlicek, 2014, Stabilities of thiomolybdate complexes of iron; implications for retention of essential trace elements (Fe, Cu, Mo) in sulfidic waters: *Metallomics*, v. 6, no. 6, p. 1131–1140.
- Hemmesch, N. T., N. B. Harris, C. A. Mnich, and D. Selby, 2014, A sequence-stratigraphic framework for the Upper Devonian Woodford Shale, Permian Basin, west Texas: *AAPG Bulletin*, v. 98, no. 1, p. 23–47.

- Hine, A. C., 2001, Advances in carbonate sequence stratigraphy: Application to reservoirs, outcrops, and models: *Eos, Transactions American Geophysical Union*, v. 82, no. 2, p. 18–18.
- Horstad, I., S. R. Larter, H. Dypvik, P. Aagaard, A. M. Bjørnvik, P. E. Johansen, and S. Eriksen, 1990, Degradation and maturity controls on oil field petroleum column heterogeneity in the Gullfaks field, Norwegian North Sea: *Organic Geochemistry*, v. 16, no. 1–3, p. 497–510.
- Huang, W.-Y., and W. G. Meinschein, 1979, Sterols as ecological indicators: *Geochimica et Cosmochimica Acta*, v. 43, no. 5, p. 739–745.
- Huerta-Diaz, M. A., and J. W. Morse, 1992, Pyritization of trace metals in anoxic marine sediments: *Geochimica et Cosmochimica Acta*, v. 56, no. 7, p. 2681–2702.
- Hunt, D., and M. E. Tucker, 1992, Stranded parasequences and the forced regressive wedge systems tract: deposition during base-level fall: *Sedimentary Geology*, v. 81, no. 1–2, p. 1–9.
- Ikeda, M., M. Bôle, and P. O. Baumgartner, 2016, Orbital-scale changes in redox condition and biogenic silica/detrital fluxes of the Middle Jurassic Radiolarite in Tethys (Sogno, Lombardy, N-Italy): Possible link with glaciation? *Palaeogeography, Palaeoclimatology, Palaeoecology*, v. 457, p. 247–257.
- Ito, M., A. Ishigaki, T. Nishikawa, and T. Saito, 2001, Temporal variation in the wavelength of hummocky cross-stratification: Implications for storm intensity through Mesozoic and Cenozoic: *Geology*, v. 29, no. 1, p. 87–89.
- Jacobson, S. R., J. R. Hatch, S. C. Teerman, and R. A. Askin, 1988, Middle Ordovician organic matter assemblages and their effect on Ordovician-derived oils: *AAPG Bulletin*.
- James, N. P., and I. G. Macintyre, 1985, Carbonate Depositional Environments – Modern and Ancient. Part 1: Reefs-Zonation, Depositional Facies, Diagenesis.: *Colorado School of Mines Quarterly*, v. 80, no. 03, p. 70.
- Jarvis, I., 1992, Sedimentology, geochemistry and origin of phosphatic chalks: the Upper Cretaceous deposits of NW Europe: *Sedimentology*, v. 39, no. 1, p. 55–97.
- Jiang, L., S. C. George, and M. Zhang, 2018, The occurrence and distribution of rearranged hopanes in crude oils from the Lishu Depression, Songliao Basin, China: *Organic Geochemistry*, v. 115, p. 205–219.
- van Kaam-Peters, H. M. ., J. Köster, S. J. van der Gaast, M. Dekker, J. W. de Leeuw, and J. S. Sinninghe Damsté, 1998, The effect of clay minerals on diasterane/sterane ratios: *Geochimica et Cosmochimica Acta*, v. 62, no. 17, p. 2923–2929.

- Keller, G. R., J. M. Hills, and R. Djeddi, 1980, New Mexico Geological Society A regional geological and geophysical study of the Delaware Basin, New Mexico and west Texas Annual NMGS Fall Field Conference Guidebooks: Trans Pecos Region (West Texas), v. 308, p. 105–111.
- Kendall, C. G. S. C., and W. Schlager, 1981, Carbonates and relative changes in sea level: *Marine Geology*, v. 44, no. 1–2, p. 181–212.
- Kidder, D. L., and D. H. Erwin, 2001, Secular Distribution of Biogenic Silica through the Phanerozoic: Comparison of Silica-Replaced Fossils and Bedded Cherts at the Series Level: *The Journal of Geology*, v. 109, no. 4, p. 509–522.
- Kolaczowska, E., N.-E. Slougui, D. S. Watt, R. E. Maruca, and J. Michael Moldowan, 1990, Thermodynamic stability of various alkylated, dealkylated and rearranged 17 α - and 17 β -hopane isomers using molecular mechanics calculations: *Organic Geochemistry*, v. 16, no. 4–6, p. 1033–1038.
- Kottlowski, F. E., and W. J. Stewart, 1970, The Wolfcampian Joyita uplift in central New Mexico, *in* State Bureau of Mines and Mineral Resources. Memoir 23.: State Bureau of Mines and Mineral Resources Memoir 23, p. 500–511.
- Kozur, H. W., K. Krainer, and H. Mostler, 1996, Ichnology and sedimentology of the early Permian deep-water deposits from the Lercara-Roccapalumba area (Western Sicily, Italy): *Facies*, v. 34, no. 1, p. 123–150.
- van Krevelen, D. W., 1961, Coal--typology, chemistry, physics, constitution: Amsterdam, Netherlands, Elsevier Scientific Pub. Co., 1–514 p.
- Kuenen, P. H., 1957, Sole Markings of Graded Graywake Beds: *The Journal of Geology*, v. 65, no. 3, p. 231–258.
- Kupecz, J. A., 1974, Depositional Setting, Sequence Stratigraphy, Diagenesis, and Reservoir Potential of a Mixed-Lithology, Upwelling Deposit: Upper Triassic Shublik Formation, Prudhoe Bay, Alaska: *AAPG Bulletin*, v. 79, no. 9, p. 1301–1319.
- Li, M., T. G. Wang, B. R. T. Simoneit, S. Shi, L. Zhang, and F. Yang, 2012, Qualitative and quantitative analysis of dibenzothiophene, its methylated homologues, and benzonaphthothiophenes in crude oils, coal, and sediment extracts: *Journal of Chromatography A*, v. 1233, p. 126–136.
- Li, F., H. Zhang, X. Jing, and X. Cheng, 2017, Paleoenvironmental analysis of the ichnogenus *Zoophycos* in the Lower Devonian tempestite sediments of the Longmenshan area, Sichuan, China: *Palaeogeography, Palaeoclimatology, Palaeoecology*, v. 465, p. 156–167.
- Lowe, D. R., 1979, Sediment gravity flows; their classification and some problems of application to natural flows and deposits: *Geology of continental slopes*, v. 27, p. 75–82.

- Lowe, D. R., and M. Guy, 2000, Slurry-flow deposits in the Britannia Formation (Lower Cretaceous), North Sea: A new perspective on the turbidity current and debris flow problem: *Sedimentology*, v. 47, no. 1, p. 31–70.
- MacEachern, J. A., K. L. Bann, M. K. Gingras, J.-P. Zonneveld, S. E. Dashtgard, and S. G. Pemberton, 2012, The Ichnofacies Paradigm: Developments in *Sedimentology*, v. 64, p. 103–138.
- Markello, J., R. B. Koepnick, L. E. Waite, and J. F. Collins, 2011, The Carbonate Analogs Through Time (CATT) Hypothesis and the Global Atlas of Carbonate Fields—A Systematic and Predictive Look at Phanerozoic Carbonate Systems, *in* Controls on Carbonate Platform and Reef Development: SEPM (Society for Sedimentary Geology), p. 15–45.
- Marzi, R., B. E. Torkelson, and R. K. Olson, 1993, A revised carbon preference index: *Organic Geochemistry*, v. 20, no. 8, p. 1303–1306.
- Mazzullo, L., 1995, Permian Stratigraphy and Facies, Permian Basin (Texas-New Mexico) and Adjoining Areas in the Pangea Supercontinent United States, *in* The Permian of Northern Pangea: Berlin, Heidelberg, Springer Berlin Heidelberg, p. 41–60.
- McLaughlin, P. I., C. E. Brett, S. L. Taha McLaughlin, and S. R. Cornell, 2004, High-resolution sequence stratigraphy of a mixed carbonate-siliciclastic, cratonic ramp (Upper Ordovician; Kentucky-Ohio, USA): Insights into the relative influence of eustasy and tectonics through analysis of facies gradients, *in* *Palaeogeography, Palaeoclimatology, Palaeoecology*: p. 267–294.
- McManus, J., W. M. Berelson, G. P. Klinkhammer, D. E. Hammond, and C. Holm, 2005, Authigenic uranium: Relationship to oxygen penetration depth and organic carbon rain: *Geochimica et Cosmochimica Acta*, v. 69, no. 1, p. 95–108.
- McManus, J., W. M. Berelson, S. Severmann, R. L. Poulson, D. E. Hammond, G. P. Klinkhammer, and C. Holm, 2006, Molybdenum and uranium geochemistry in continental margin sediments: Paleoproxy potential: *Geochimica et Cosmochimica Acta*, v. 70, no. 18, p. 4643–4662.
- Meijun, L., T. G. Wang, S. Shengbao, Z. Lei, and F. Ronghui, 2014, Oil maturity assessment using maturity indicators based on methylated dibenzothiophenes: *Petroleum Sciences*, v. 11, no. 234–246.
- Mello, M. R., P. C. Gaglianone, S. C. Brassell, and J. R. Maxwell, 1988, Geochemical and biological marker assessment of depositional environments using Brazilian offshore oils: *Marine and Petroleum Geology*, v. 5, no. 3, p. 205–223.
- Meyers, P. A., 1997, Organic geochemical proxies of paleoceanographic, paleolimnologic, and paleoclimatic processes, *in* *Organic Geochemistry: Pergamon*, p. 213–250.

- Miceli Romero, A. A., T. Nguyen, and R. P. Philp, 2018, Organic geochemistry of the Eagle Ford Group in Texas: AAPG Bulletin, v. 102, no. 7, p. 1379–1412.
- Miller, M. F., 1991, Morphology and Paleoenvironmental Distribution of Paleozoic Spirophyton and Zoophycos: Implications for the Zoophycos Ichnofacies: PALAIOS, v. 6, no. 4, p. 410.
- Minter, N. J., L. A. Buatois, and M. G. Mángano, 2016, The Conceptual and Methodological Tools of Ichnology, *in* The Trace-Fossil Record of Major Evolutionary Events: Springer, Dordrecht, p. 1–26.
- Moldowan, J. M., F. J. Fago, R. M. K. Carlson, D. C. Young, G. an Duvne, J. Clardy, M. Schoell, C. T. Pillinger, and D. S. Watt, 1991, Rearranged hopanes in sediments and petroleum: Geochimica et Cosmochimica Acta, v. 55, no. 11, p. 3333–3353.
- Moldowan, J. M., F. J. Fago, C. Y. Lee, S. R. Jacobson, D. S. Watt, N.-E. Slougui, A. Jeganathan, and D. C. Young, 1990, Sedimentary 24-n-Propylcholestanes, Molecular Fossils Diagnostic of Marine Algae: Science, v. 247, no. 4940, p. 309–312.
- Moldowan, J. M., W. K. Seifert, and E. J. Gallegos, 1983, Identification of an extended series of tricyclic terpanes in petroleum: Geochimica et Cosmochimica Acta, v. 47, no. 8, p. 1531–1534.
- Moldowan, J. M., W. K. Seifert, and E. J. Gallegos, 1985, Relationship Between Petroleum Composition and Depositional Environment of Petroleum Source Rocks: AAPG Bulletin, v. 69, no. 8, p. 1255–1268.
- Molina, J. M., P. A. Ruiz-Ortiz, and J. A. Vera, 1997, Calcareous tempestites in pelagic facies (Jurassic, Betic Cordilleras, Southern Spain): Sedimentary Geology, v. 109, no. 1–2, p. 95–109.
- Monaco, P., F. J. Rodríguez-Tovar, and A. Uchman, 2012, Ichnological Analysis of Lateral Environmental Heterogeneity within the Bonarelli Level (Uppermost Cenomanian) in the Classical Localities Near Gubbio, Central Apennines, Italy: PALAIOS, v. 27, no. 1, p. 48–54.
- Moore, C. H., 2002, Carbonate Reservoirs Porosity Evolution and Diagenesis in a Sequence Stratigraphic Framework: 1295–1296 p.
- Morse, J. W., and G. W. Luther, 1999, Chemical influences on trace metal-sulfide interactions in anoxic sediments: Geochimica et Cosmochimica Acta, v. 63, no. 19–20, p. 3373–3378.
- Muehlberger, W. R., and P. W. Dickerson, 1989, A tectonic history of Trans-Pecos Texas: Structure and Stratigraphy of Trans-Pecos Texas: El Paso to Guadalupe Mountains and Big Bend July 20-29, 1989, p. 35–54.

- Münster, U., and R. J. Chróst, 1990, Origin, Composition, and Microbial Utilization of Dissolved Organic Matter, *in* J. Overbeck, and R. J. Chróst, eds., *Aquatic Microbial Ecology - Biochemical and Molecular Approaches*: New York, NY, Springer, p. 8–46.
- Murphy, R., 2015, Depositional systems interpretation of early Permian mixed siliciclastics and carbonates, Midland Basin, Texas: Indiana University, 1–99 p.
- Neal, D. L. O., 2015, Chemostratigraphic and Depositional Characterization of the Niobrara Formation, Cemex Quarry, Lyons, CO: Colorado School of Mines, 26–33 p.
- Nissenbaum, A., and I. R. Kaplan, 1972, Chemical and Isotopic Evidence for the In Situ Origin of Marine Humic Substrates: *Limnology and Oceanography*, v. 17, no. 4, p. 570–582.
- Noble, R., R. Alexander, and R. I. Kagi, 1985, The occurrence of bisnorhopane, trisnorhopane and 25-norhopanes as free hydrocarbons in some Australian shales: *Organic Geochemistry*, v. 8, no. 2, p. 171–176.
- Noble, R. A., R. Alexander, R. I. Kagi, and J. K. Nox, 1986, Identification of some diterpenoid hydrocarbons in petroleum: *Organic Geochemistry*, v. 10, no. 4–6, p. 825–829.
- Okin, G. S. et al., 2011, Impacts of atmospheric nutrient deposition on marine productivity: Roles of nitrogen, phosphorus, and iron: *Global Biogeochemical Cycles*, v. 25, no. 2, p. 1–10.
- Okiongbo, K. S., A. C. Aplin, and S. R. Larter, 2005, Changes in Type II Kerogen Density as a Function of Maturity: Evidence from the Kimmeridge Clay Formation: *Energy and Fuels*, v. 19, p. 2495–2499.
- Olivero, D., 1996, Zoophycos distribution and sequence stratigraphy. Examples from the Jurassic and Cretaceous deposits of southeastern France: *Palaeogeography, Palaeoclimatology, Palaeoecology*, v. 123, no. 1–4, p. 273–287.
- Osleger, D. A., and I. P. Montañez, 1996, Cross-platform architecture of a sequence boundary in mixed siliciclastic-carbonate lithofacies, Middle Cambrian, southern Great Basin, USA: *Sedimentology*, v. 43, no. 2, p. 197–217.
- Ourisson, G., and P. Albrecht, 1992, Hopanoids. 1. Geohopanoids: the most abundant natural products on Earth? *Accounts of Chemical Research*, v. 25, no. 9, p. 398–402.
- Ourisson, G., P. Albrecht, and M. Rohmer, 1982, Predictive microbial biochemistry - from molecular fossils to procaryotic membranes: *Trends in Biochemical Sciences*, v. 7, no. 7, p. 236–239.

- Ourisson, G., P. Albrecht, and M. Rohmer, 1979, The Hopanoids: palaeochemistry and biochemistry of a group of natural products: *Pure and Applied Chemistry*, v. 51, no. 4, p. 709–729.
- Ourisson, G., M. Rohmer, and K. Poralla, 1987, Prokaryotic Hopanoids and other Polyterpenoid Sterol Surrogates: *Annual Review of Microbiology*, v. 41, no. 1, p. 301–333.
- Ozalas, K., C. E. Savrda, and R. R. Fullerton, 1994, Bioturbated oxygenation-event beds in siliceous facies: Monterey Formation (Miocene), California: *Palaeogeography, Palaeoclimatology, Palaeoecology*, v. 112, no. 1–2, p. 63–83.
- Palacas, J. G., D. E. Anders, and J. D. King, 1984, South Florida Basin-A Prime Example of Carbonate Source Rocks of Petroleum, *in* J. G. Palacas, ed., *AAPG Special Publication 18: Petroleum Geochemistry and Source Rock Potential of Carbonate Rocks*: p. 71–96.
- Palmer, S. E., 1984, Hydrocarbon Source Potential of Organic Facies of the Lacustrine Elko Formation (Eocene/Oligocene), Northeast Nevada, *in* *Hydrocarbon Source Rocks of the Greater Rocky Mountain Region: Denver, Colorado*, Rocky Mountain Association of Geologists, p. 491–511.
- Pan, S., B. Horsfield, C. Zou, Z. Yang, and D. Gao, 2017, Statistical analysis as a tool for assisting geochemical interpretation of the Upper Triassic Yanchang Formation, Ordos Basin, Central China: *International Journal of Coal Geology*, v. 173, p. 51–64.
- Parke, M., and I. Den Hartog-Adams, 1965, Three species of Halosphaera: *Journal of the Marine Biological Association of the United Kingdom*, v. 45, no. 02, p. 537.
- Pemberton, S. G., and R. W. Frey, 1982, Trace Fossil Nomenclature and the Planolites-Palaeophycus Dilemma: *Journal of Paleontology*, v. 56, no. 4, p. 843–881.
- Pemberton, S. G., and J. A. MacEachern, 2005, Significance of Ichnofossils to Applied Stratigraphy, *in* *Applied Stratigraphy*: Springer Netherlands, p. 279–300.
- Peters, K. E., 2000, Petroleum tricyclic terpanes: Predicted physicochemical behavior from molecular mechanics calculations: *Organic Geochemistry*, v. 31, no. 6, p. 497–507.
- Peters, K. E., J. M. Moldowan, and P. Sudararaman, 1990, Effects of hydrous pyrolysis on biomarker thermal maturity parameters: Monterey Phosphatic and Siliceous members: *Organic Geochemistry*, v. 15, no. 3, p. 249–265.
- Peters, K. E., C. Walters, Clifford, and J. M. Moldowan, 1993, *The Biomarker Guide - Volume 1*: Cambridge University Press, 1–498 p.
- Peters, K. E., C. Walters, Clifford, and J. M. Moldowan, 2005, *The Biomarker Guide -*

Volume 2: Cambridge University Press, 475–1155 p.

- Phillips, C., D. McIlroy, and T. Elliott, 2011, Ichnological characterization of Eocene/Oligocene turbidites from the Gres d'Annot Basin, French Alps, SE France: *Palaeogeography, Palaeoclimatology, Palaeoecology*, v. 300, no. 1–4, p. 67–83.
- Philp, R. P., and T. D. Gilbert, 1986, Biomarker distributions in Australian oils predominantly derived from terrigenous source material: *Organic Geochemistry*, v. 10, no. 1–3, p. 73–84.
- Philp, R. P., T. D. Gilbert, and J. Friedrich, 1981, Bicyclic sesquiterpenoids and diterpenoids in Australian crude oils: *Geochimica et Cosmochimica Acta*, v. 45, no. 7, p. 1173–1180.
- Powell, T. G., and D. M. McKirdy, 1973, Relationship between Ratio of Pristane to Phytane, Crude Oil Composition and Geological Environment in Australia: *Nature Physical Science*, v. 243, no. 124, p. 37–39.
- Prochnow, S. J., and G. Hinterlong, 2014, Pennsylvanian and Wolfcampian Sequence Stratigraphy Using FMI and Log Analysis on the Western Edge of the Midland Basin : A Tool for Guiding Well Completions: Midland, TX, Poster Adapted from AAPG 2014 Southwest Section Annual Convention.
- Racka, M., L. Marynowski, P. Filipiak, M. Sobstel, A. Piszczowska, and D. P. G. Bond, 2010, Anoxic Annulata Events in the Late Famennian of the Holy Cross Mountains (Southern Poland): Geochemical and palaeontological record: *Palaeogeography, Palaeoclimatology, Palaeoecology*, v. 297, no. 3–4, p. 549–575.
- Rashid, M. A., and J. D. Leonard, 1973, Modifications in the solubility and precipitation behavior of various metals as a result of their interaction with sedimentary humic acid: *Chemical Geology*, v. 11, no. 2, p. 89–97.
- Reed, W. E., 1977, Molecular compositions of weathered petroleum and comparison with its possible source: *Geochimica et Cosmochimica Acta*, v. 41, no. 2, p. 237–247.
- Revill, A. T., J. K. Volkman, T. O'Leary, R. E. Summons, C. J. Boreham, M. R. Banks, and K. Denwer, 1994, Hydrocarbon biomarkers, thermal maturity, and depositional setting of tasmanite oil shales from Tasmania, Australia: *Geochimica et Cosmochimica Acta*, v. 58, no. 18, p. 3803–3822.
- Risatti, J. B., S. J. Rowland, D. A. Yon, and J. R. Maxwell, 1984, Stereochemical studies of acyclic isoprenoids—XII. Lipids of methanogenic bacteria and possible contributions to sediments: *Organic Geochemistry*, v. 6, p. 93–104.
- Riva, A., P. G. Caccialanza, and F. Quagliarioli, 1988, Recognition of 18 β (H)oleanane in several crudes and Tertiary-Upper Cretaceous sediments. Definition of a new maturity parameter: *Organic Geochemistry*, v. 13, no. 4–6, p. 671–675.

- Roe, K. K., W. C. Burnett, K. H. Kim, and M. J. Beers, 1982, Excess protactinium in phosphate nodules from a coastal upwelling zone: *Earth and Planetary Science Letters*, v. 60, no. 1, p. 39–46.
- Rohmer, M., P. Bouvier-Nave, and G. Ourisson, 1984, Distribution of Hopanoid Triterpenes in Prokaryotes: *Microbiology*, v. 130, no. 5, p. 1137–1150.
- Romero, A. M., and R. P. Philp, 2012, Organic geochemistry of the Woodford Shale, southeastern Oklahoma: How variable can shales be? *AAPG Bulletin*, v. 96, no. 3, p. 493–517.
- Ross, C. A., 1963, Standard Wolfcampian Series (Permian), Glass Mountains, Texas: *Geologic Society of America Memoir* 88, 1–230 p.
- Ross, C. A., and J. R. P. Ross, 1995, Permian Sequence Stratigraphy, *in* *The Permian of Northern Pangea*: Berlin, Heidelberg, Springer Berlin Heidelberg, p. 98–123.
- Rubinstein, I., O. Sieskind, and P. Albrecht, 1975, Rearranged sterenes in a shale: occurrence and simulated formation: *Journal of the Chemical Society, Perkin Transactions 1*, v. 0, no. 19, p. 1833.
- Rygel, M. C., C. R. Fielding, T. D. Frank, and L. P. Birgenheier, 2008, The Magnitude of Late Paleozoic Glacioeustatic Fluctuations: A Synthesis: *Journal of Sedimentary Research*, v. 78, no. 8, p. 500–511.
- Sageman, B. B., 1996, Lowstand tempestites: Depositional model for Cretaceous skeletal limestones, Western Interior basin: *Geology*, v. 24, no. 10, p. 888–892.
- Salisbury, M. N., 2014, Depositional setting of the Wolfcamp Formation, Midland Basin, Texas, using organic geochemistry: *The University of Oklahoma*, 1–81 p.
- Sarg, J. F., 1988, Carbonate sequence stratigraphy, *in* D. Nummedal, O. H. Pilkey, and J. D. Howard, eds., *SEPM Special Publication: Sea-Level Changes - An Integrated Approach*: SEPM, p. 155–181.
- Savrda, C. E., and D. J. Bottjer, 1986, Trace-fossil Model for Reconstruction of Paleooxygenation in Bottom Waters: *Geology*, v. 14, no. 1, p. 3–6.
- Schnitzer, M., 1977, Recent findings on the characterization of humic substances extracted from soils from widely differing climatic zones, *in* *Soil organic matter studies*: International Atomic Energy Agency (IAEA), p. 117–131.
- Schultz, R. B., and S. M. Rimmer, 2004, Geochemistry of organic-rich shales: new perspectives: *Chemical Geology*, v. 206, no. 3–4, p. 163–165.
- Scotese, C. R., R. K. Bambach, C. Barton, R. Van der Voo, A. M. Ziegler, R. Van Der Voo, and A. M. Ziegler, 1979, Paleozoic Base Maps: *The Journal of Geology*, v. 87, no. 3, p. 217–277.

- Scott, C., and T. W. Lyons, 2012, Contrasting molybdenum cycling and isotopic properties in euxinic versus non-euxinic sediments and sedimentary rocks: Refining the paleoproxies: *Chemical Geology*, v. 324–325, p. 19–27.
- Seilacher, A., 1967, Bathymetry of trace fossils: *Marine Geology*, v. 5, no. 5, p. 413–428.
- Seilacher, A., 1977, Chapter 11 Evolution of Trace Fossil Communities: Developments in Palaeontology and Stratigraphy, v. 5, p. 359–376.
- Seilacher, A., 1962, Paleontological Studies on Turbidite Sedimentation and Erosion: *The Journal of Geology*, v. 70, no. 2, p. 227–234.
- Seilacher, A., 2007, Trace fossils analysis: Berlin, Heidelberg, Springer Berlin Heidelberg, 1–226 p.
- Simoneit, B. R. ., 1977, Diterpenoid compounds and other lipids in deep-sea sediments and their geochemical significance: *Geochimica et Cosmochimica Acta*, v. 41, no. 4, p. 463–476.
- Simoneit, B. R. T., R. N. Leif, F. Radler de Aquino Neto, D. Almeida Azevedo, A. C. Pinto, and P. Albrecht, 1990, On the presence of tricyclic terpane hydrocarbons in permian tasmanite algae: *Naturwissenschaften*, v. 77, no. 8, p. 380–383.
- Sinninghe Damsté, J. S., F. Kenig, M. P. Koopmans, J. Köster, S. Schouten, J. M. Hayes, and J. W. de Leeuw, 1995, Evidence for gammacerane as an indicator of water column stratification: *Geochimica et Cosmochimica Acta*, v. 59, no. 9, p. 1895–1900.
- Smith, S. V., 1984, Phosphorus Versus Nitrogen Limitation in the Marine-Environment: *Limnology and Oceanography*, v. 29, no. 6, p. 1149–1160.
- Snowdon, L. R., 1995, Rock-Eval Tmax Suppression: Documentation and Amelioration: *AAPG Bulletin*, v. 79, no. 9, p. 1337–1348.
- Sofer, Z., 1984, Stable carbon isotope composition of crude oils: Application to source depositional Environments and petroleum Alteration: *AAPG Bulletin*, v. 68, no. 1, p. 31–49.
- Stanley, D. J., 1993, Model for turbidite-to-contourite continuum and multiple process transport in deep marine settings: examples in the rock record: *Sedimentary Geology*, v. 82, no. 1–4, p. 241–255.
- Sumner, E. J., P. J. Talling, L. A. Amy, R. B. Wynn, C. J. Stevenson, and M. Frenz, 2012, Facies architecture of individual basin-plain turbidites: Comparison with existing models and implications for flow processes: *Sedimentology*, v. 59, no. 6, p. 1850–1887.

- Sur, S., 2009, An integrated sedimentological and geochemical study to test the possible links between late paleozoic climate change, atmospheric dust influx, and primary productivity in the Horseshoe Atoll, West Texas: ProQuest, 1–128 p.
- Swain, F. M., 1961, Limnology and Amino-Acid Content of Some Lake Deposits in Minnesota, Montana, Nevada, and Louisiana: GSA Bulletin, v. 72, no. 4, p. 519–545.
- Swanson, V. E., 1961, Geology and geochemistry of uranium in marine black shales: a review: USGS Professional Paper, v. 365– C, p. 67–112.
- Sweeney, R. E., and I. R. Kaplan, 1973, Pyrite Framboid Formation; Laboratory Synthesis and Marine Sediments: Economic Geology, v. 68, no. 5, p. 618–634.
- Sweetman, S. C., and A. N. Insole, 2010, The plant debris beds of the Early Cretaceous (Barremian) Wessex Formation of the Isle of Wight, southern England: Their genesis and palaeontological significance: Palaeogeography, Palaeoclimatology, Palaeoecology, v. 292, no. 3–4, p. 409–424.
- Talling, P. J., 2014, On the triggers, resulting flow types and frequencies of subaqueous sediment density flows in different settings: Marine Geology, v. 352, p. 155–182.
- Talling, P. J., D. G. Masson, E. J. Sumner, and G. Malgesini, 2012, Subaqueous sediment density flows: Depositional processes and deposit types: Sedimentology, v. 59, no. 7, p. 1937–2003.
- Tao, S., C. Wang, J. Du, L. Liu, and Z. Chen, 2015, Geochemical application of tricyclic and tetracyclic terpanes biomarkers in crude oils of NW China: Marine and Petroleum Geology, v. 67, p. 460–467.
- Taylor, A., R. Goldring, and S. Gowland, 2003, Analysis and application of ichnofabrics: Earth-Science Reviews, v. 60, no. 3–4, p. 227–259.
- Tegelaar, E. W., R. M. Matthezing, J. B. H. Jansen, B. Horsfield, and J. W. De Leeuw, 1989, Possible origin of n-alkanes in high-wax crude oils: Nature, v. 342, no. 6249, p. 529–531.
- Tissot, B. P., and D. H. Welte, 1978, Petroleum Formation and Occurrence: A New Approach to Oil and Gas Exploration: Berlin, Heidelberg, Springer-Verlag, 1–669 p.
- Trela, W., 2008, Sedimentary and microbial record of the Middle/Late Ordovician phosphogenetic episode in the northern Holy Cross Mountains, Poland: Sedimentary Geology, v. 203, no. 1–2, p. 131–142.
- Tribouillard, N., T. J. Algeo, F. Baudin, and A. Riboulleau, 2012, Analysis of marine environmental conditions based on molybdenum-uranium covariation-Applications to Mesozoic paleoceanography: Chemical Geology, v. 324–325, p. 46–58.

- Tribovillard, N., T. J. Algeo, T. W. Lyons, and A. Riboulleau, 2006, Trace metals as paleoredox and paleoproductivity proxies: An update: *Chemical Geology*, v. 232, no. 1–2, p. 12–32.
- Tribovillard, N., V. Bout-Roumazielles, T. J. Algeo, T. W. Lyons, T. Sionneau, J. C. Montero-Serrano, A. Riboulleau, and F. Baudin, 2008, Paleodepositional conditions in the Orca Basin as inferred from organic matter and trace metal contents: *Marine Geology*, v. 254, no. 1–2, p. 62–72.
- Tribovillard, N., A. Riboulleau, T. W. Lyons, and F. Baudin, 2004, Enhanced trapping of molybdenum by sulfurized marine organic matter of marine origin in Mesozoic limestones and shales: *Chemical Geology*, v. 213, no. 4, p. 385–401.
- Turner, B. W., 2015, *Mudrock Chemostratigraphy: Theory, Techniques, Applications, Case Studies, and Cautionary Tales*, in *University of Oklahoma Guest Lecture*.
- Turner, B. W., and R. M. Slatt, 2016, Assessing bottom water anoxia within the Late Devonian Woodford Shale in the Arkoma Basin, southern Oklahoma: *Marine and Petroleum Geology*, v. 78, p. 536–546.
- Uchman, A., 2009, The *Ophiomorpha rudis* ichnosubfacies of the *Nereites* ichnofacies: Characteristics and constraints: *Palaeogeography, Palaeoclimatology, Palaeoecology*, v. 276, no. 1–4, p. 107–119.
- Uchman, A., 2003, Trends in diversity, frequency and complexity of graphoglyptid trace fossils: evolutionary and palaeoenvironmental aspects: *Palaeogeography, Palaeoclimatology, Palaeoecology*, v. 192, no. 1–4, p. 123–142.
- Uchman, A., K. Bak, and F. J. Rodríguez-Tovar, 2008, Ichnological record of deep-sea palaeoenvironmental changes around the Oceanic Anoxic Event 2 (Cenomanian-Turonian boundary): An example from the Barnasiówka section, Polish Outer Carpathians: *Palaeogeography, Palaeoclimatology, Palaeoecology*, v. 262, no. 1–2, p. 61–71.
- Uchman, A., and A. Wetzel, 2011, *Deep-Sea Ichnology: The Relationships Between Depositional Environment and Endobenthic Organisms: Developments in Sedimentology*, v. 63, p. 517–556.
- Vecsei, A., and D. G. K. Sanders, 1997, Sea-level highstand and lowstand shedding related to shelf margin aggradation and emersion, Upper Eocene-Oligocene of Maiella carbonate platform, Italy: *Sedimentary Geology*, v. 112, no. 3–4, p. 219–234.
- Vigran, J. O., A. Mørk, A. W. Forsberg, H. M. Weiss, and W. Weitschat, 2008, *Tasmanites* algae-contributors to the Middle Triassic hydrocarbon source rocks of Svalbard and the Barents Shelf: *Polar Research*, v. 27, no. 3, p. 360–371.
- Volkman, J. K., 1986, A review of sterol markers for marine and terrigenous organic

- matter: *Organic Geochemistry*, v. 9, no. 2, p. 83–99.
- Volkman, J., 2003, Sterols in microorganisms: *Applied Microbiology and Biotechnology*, v. 60, no. 5, p. 495–506.
- Volkman, J. K., M. R. Banks, K. Denwer, and F. R. Aquino Neto, 1989, Biomarker composition and depositional setting of Tasmanite oil shale: 14th Intl. Mtg. On Organic Geochemistry, Poster presentation.
- Volkman, J. K., and J. R. Maxwell, 1986, Acyclic Isoprenoids as Biological Markers, *in* R. B. Johns, ed., *Biological Markers in the Sedimentary Record*: Amsterdam, Elsevier, p. 1–42.
- Vorlicek, T. P., M. D. Kahn, Y. Kasuya, and G. R. Helz, 2004, Capture of molybdenum in pyrite-forming sediments: role of ligand-induced reduction by polysulfides: *Geochimica et Cosmochimica Acta*, v. 68, no. 3, p. 547–556.
- Waite, L., M. McGlue, T. Reed, and O. Woodruff, 2015, Preliminary analysis of Wolfcamp D basinal cyclothems, Midland Basin, west Texas, *in* *Carboniferous-Permian Sedimentology and Sequence Stratigraphy of the Midcontinent: In Memory of Darwin R. Boardman II: Geological Society of America Abstracts with Programs*. Vol. 47, No. 1, p.47.
- Wang, H. Da, and R. P. Philp, 1997, Geochemical Study of Potential Source Rocks and Crude Oils in the Anadarko Basin, Oklahoma: *AAPG Bulletin*, v. 81, no. 2, p. 249–275.
- Werne, J. P., D. J. Hollander, T. W. Lyons, and J. S. Sinninghe Damste, 2004, Organic sulfur biogeochemistry: Recent advances and future research directions: *Geological Society of America Special Paper*, no. 379, p. 135–150.
- Weston, R. J., R. P. Philp, C. M. Sheppard, and A. D. Woolhouse, 1989, Sesquiterpanes, diterpanes and other higher terpanes in oils from the Taranaki basin of New Zealand: *Organic Geochemistry*, v. 14, no. 4, p. 405–421.
- Wetzel, A., 1984, Bioturbation in deep-sea fine-grained sediments: influence of sediment texture, turbidite frequency and rates of environmental change: *Geological Society, London, Special Publications*, v. 15, no. June 2007, p. 595–608.
- Wetzel, A., and A. Uchman, 1998, Deep-Sea Benthic Food Content Recorded by Ichnofabrics : A Conceptual Model Based on Observations from Paleogene Flysch , Carpathians, Poland: *PALAIOS*, v. 13, no. 6, p. 533–546.
- Wickard, A. K., 2016, A Diagenetic Study of the Wolfcamp Shale in the Midland Basin, West Texas: The University of Oklahoma, 1–72 p.
- Wilkin, R. T., and H. L. Barnes, 1997, Formation processes of framboidal pyrite:

Geochimica et Cosmochimica Acta, v. 61, no. 2, p. 323–339.

Wilmsen, M., 2000, Evolution and demise of a mid-Cretaceous carbonate shelf: The Altamira Limestones (Cenomanian) of northern Cantabria (Spain): *Sedimentary Geology*, v. 133, no. 3–4, p. 195–226.

Wilson, J. L., 1967, Cyclic and Reciprocal Sedimentation in Vigilian Strata of Southern New Mexico: *GSA Bulletin*, v. 78, no. July, p. 805–818.

Zecchin, M., and O. Catuneanu, 2017, High-resolution sequence stratigraphy of clastic shelves VI: Mixed siliciclastic-carbonate systems: *Marine and Petroleum Geology*, v. 88, p. 712–723.













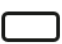
Zhang, W., H. Yang, L. Hou, and F. Liu, 2009, Distribution and geological significance of 17 α (H)-diahopanes from different hydrocarbon source rocks of Yanchang Formation in Ordos Basin: *Science in China Series D: Earth Sciences Ordos Basin. Sci China Ser D-Earth Sci*, v. 52, no. 7, p. 965–974.

Zhang, S., B. Zhang, L. Bian, Z. Jin, D. Wang, and J. Chen, 2007, The Xiamaling oil shale generated through Rhodophyta over 800 Ma ago: *Science in China Series D: Earth Sciences*, v. 50, no. 4, p. 527–535.






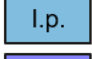
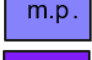

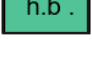
Zumberge, J. E., 1987, Prediction of source rock characteristics based on terpane biomarkers in crude oils: A multivariate statistical approach: *Geochimica et Cosmochimica Acta*, v. 51, no. 6, p. 1625–1637.

Appendix A. Core Photos, Core Description, and Lithofacies




Core Description Legend

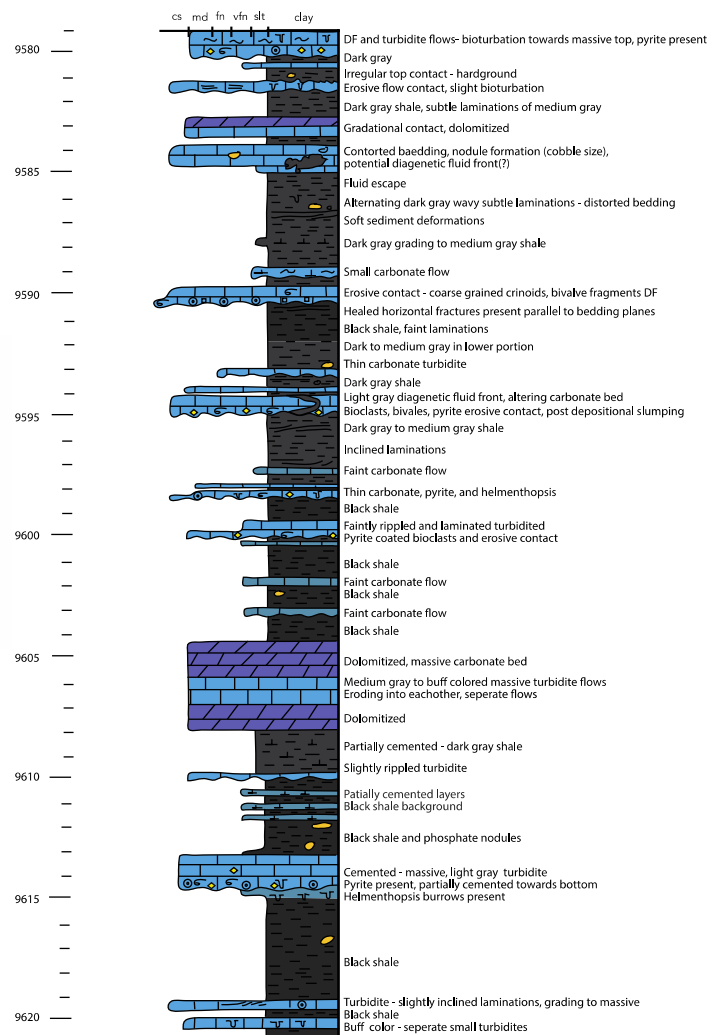
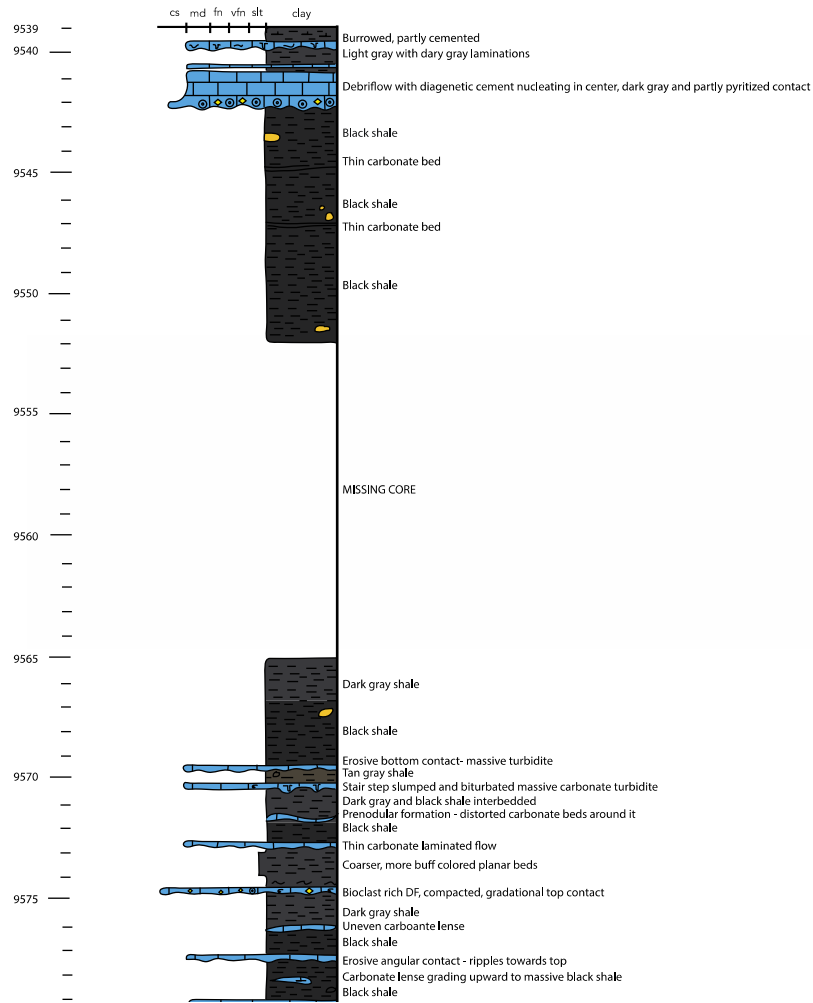
	- diagenetic dolomite
	- calcite
	- medium gray mixed carbonate and siliciclastic
	- black to dark gray siliciclastic
	- medium to dark gray siliciclastic
	- large phosphate nodule
	- non specific burrows
	- echinoderm fragment
	- brachiopod fragment
	- bivalve fragment
	- large pyrite framboid
	- non specific allochem
	- lithic fragment

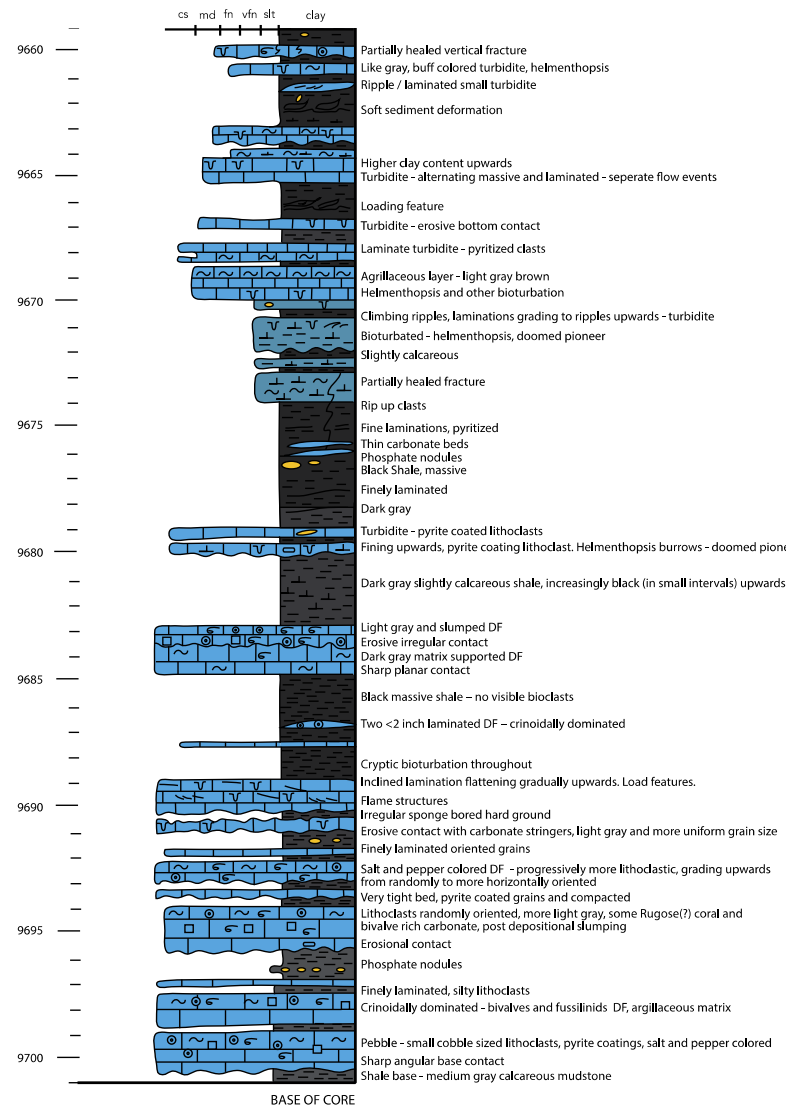
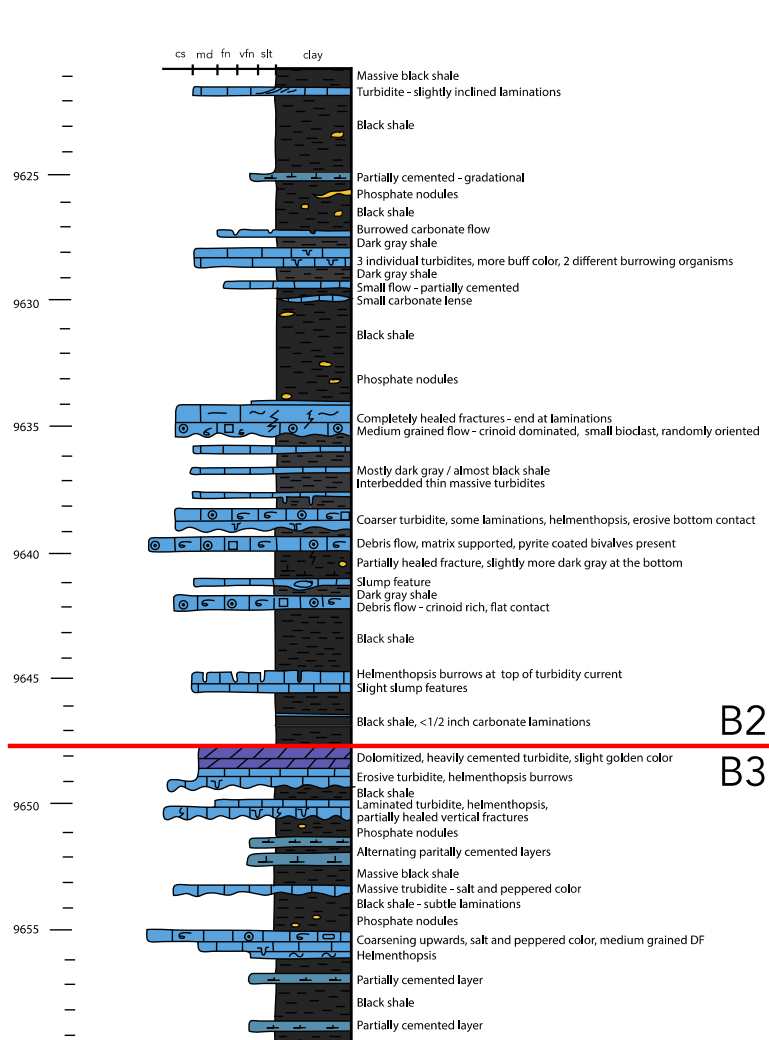
Lithofacies Legend

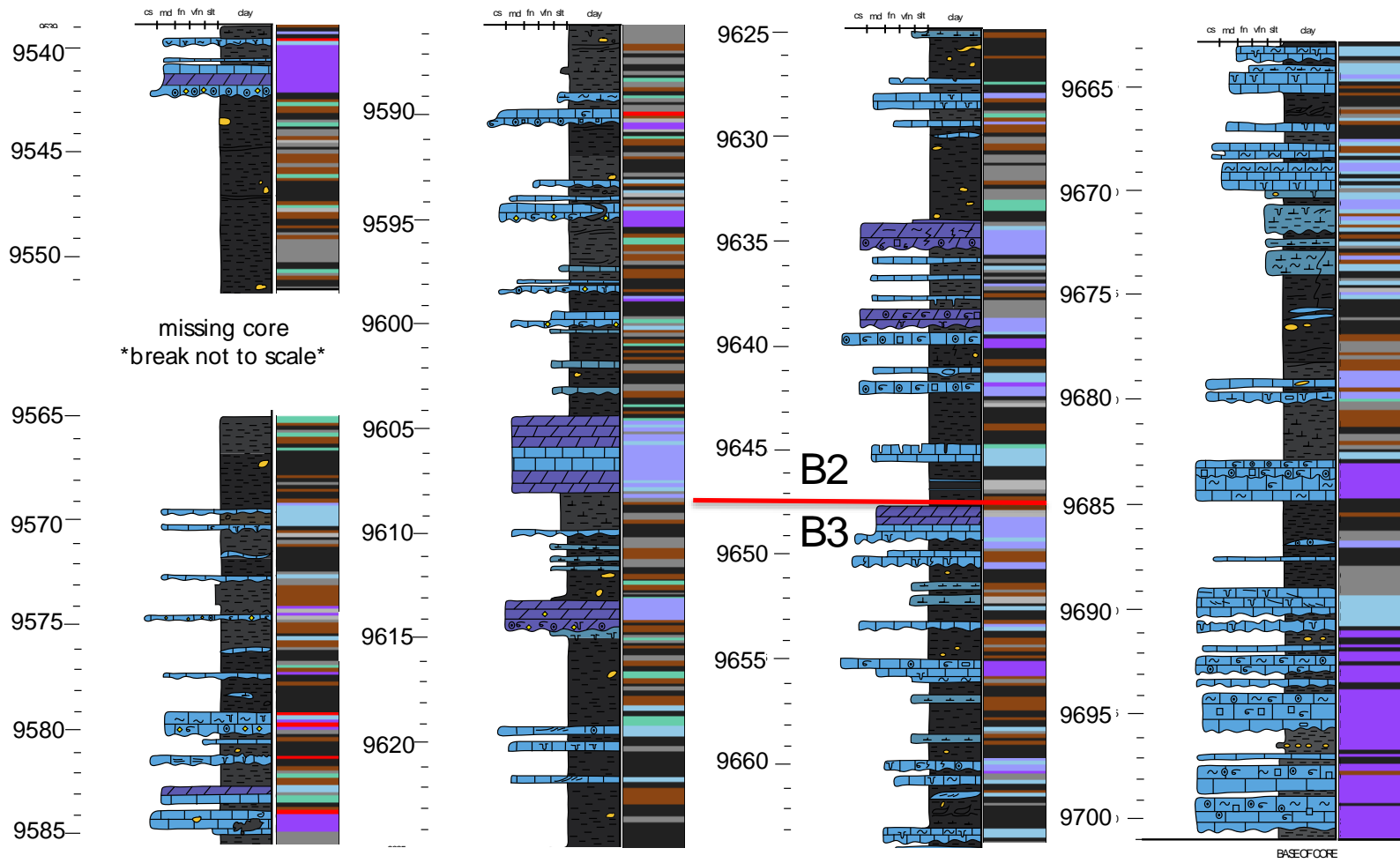
	b.m.	- black mudstone
	l.s.m.	- laminated silty mudstone
	m.g.m.	- massive gray mudstone
	b.g.m.	- banded gray mudstone
	t.p.	- truncated packstone
	l.p.	- laminated packstone
	m.p.	- massive packstone
	c.w.	- coarse wackestone
	h.b.	- heavily bioturbated mudstone / packstone

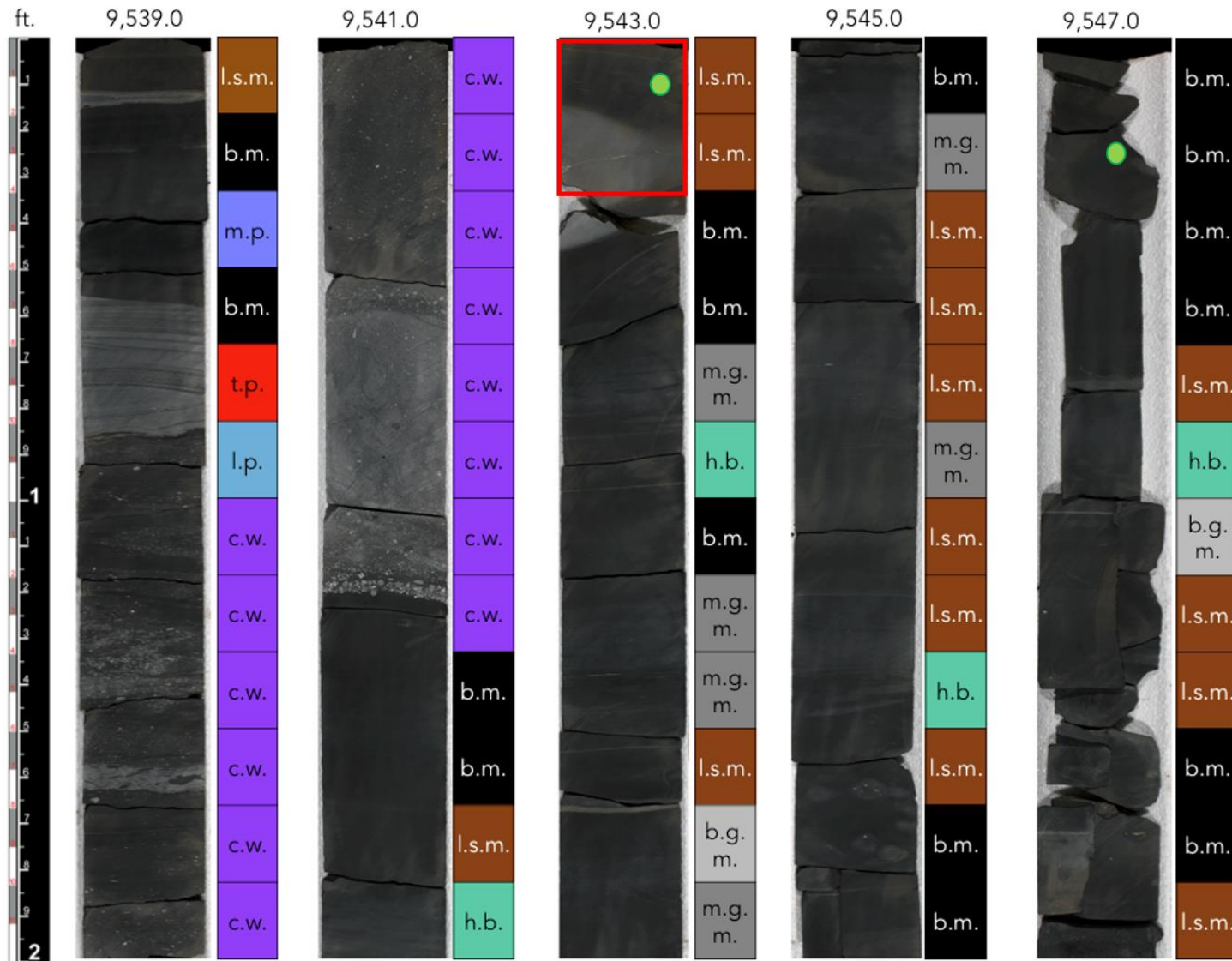
Sample Type Legend

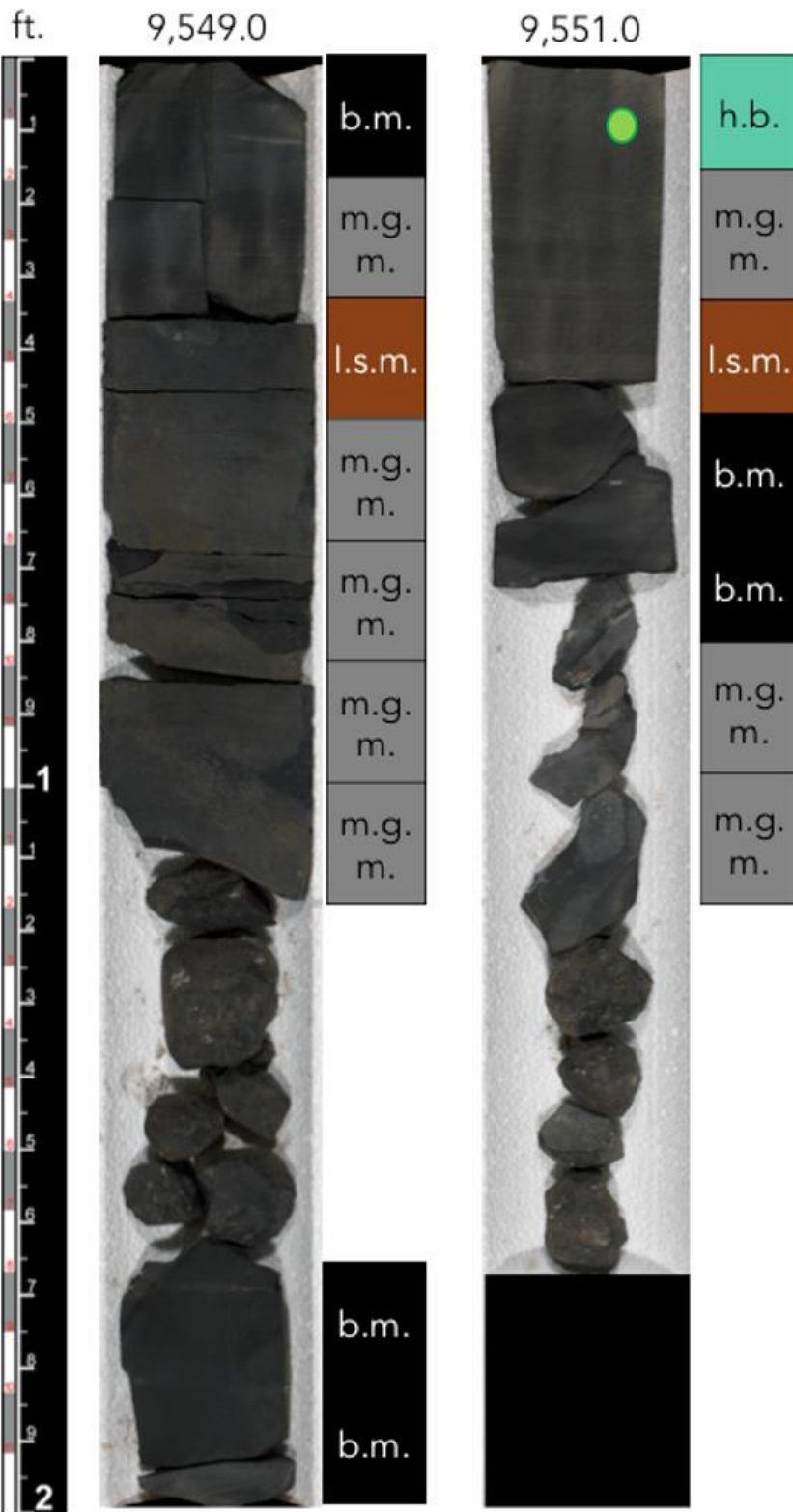
	- biomarker sample
	- thin section sample
	- TOC sample

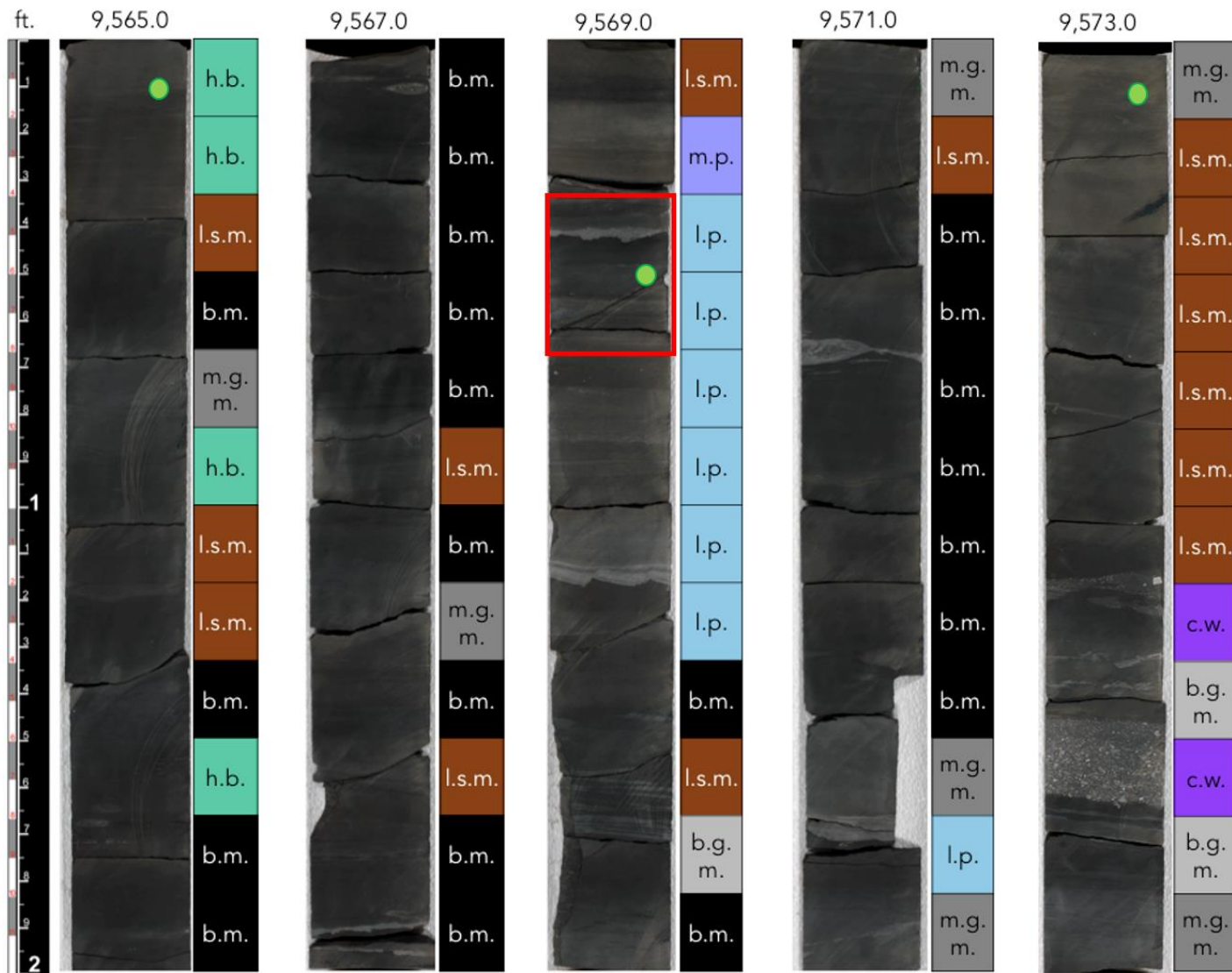


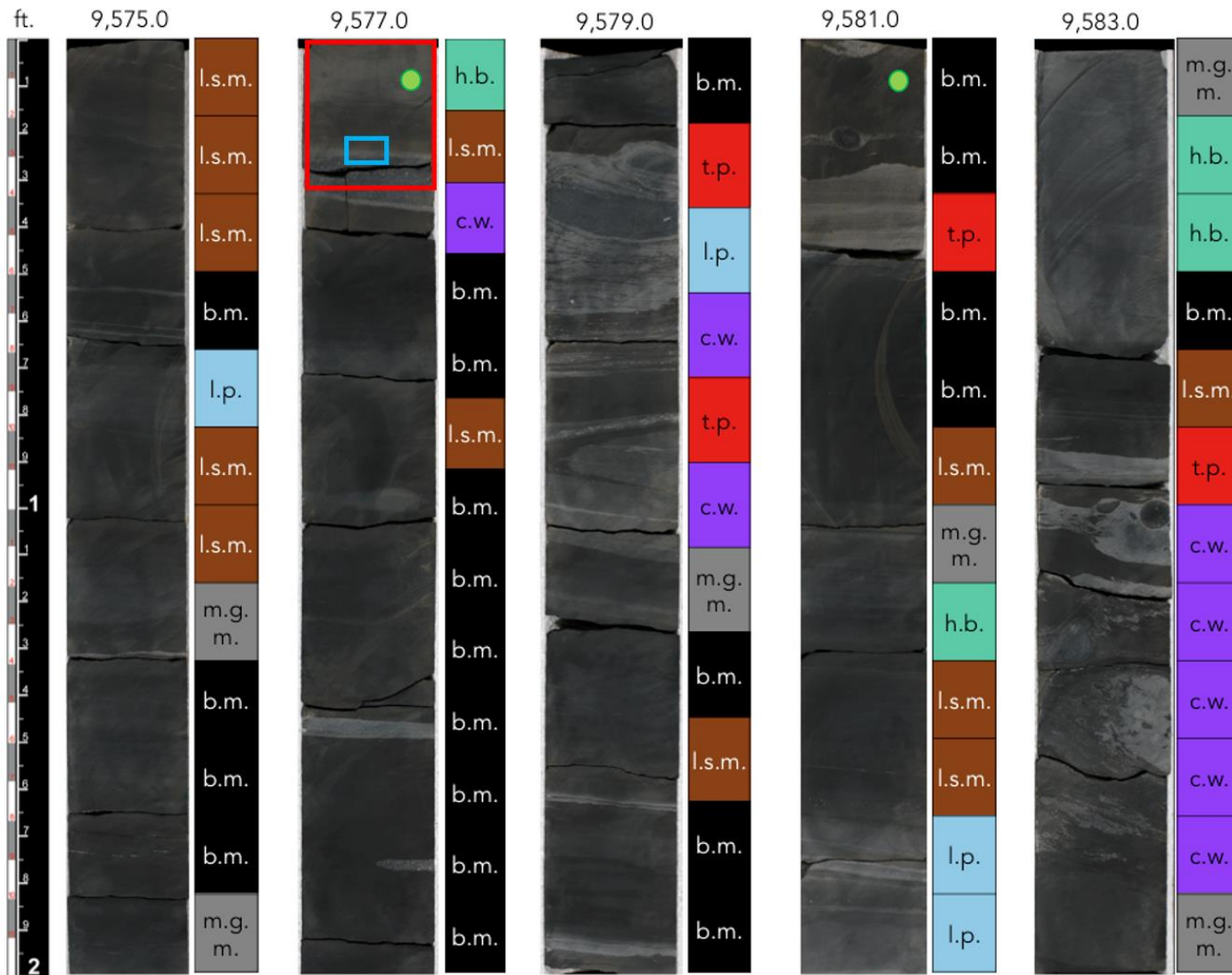


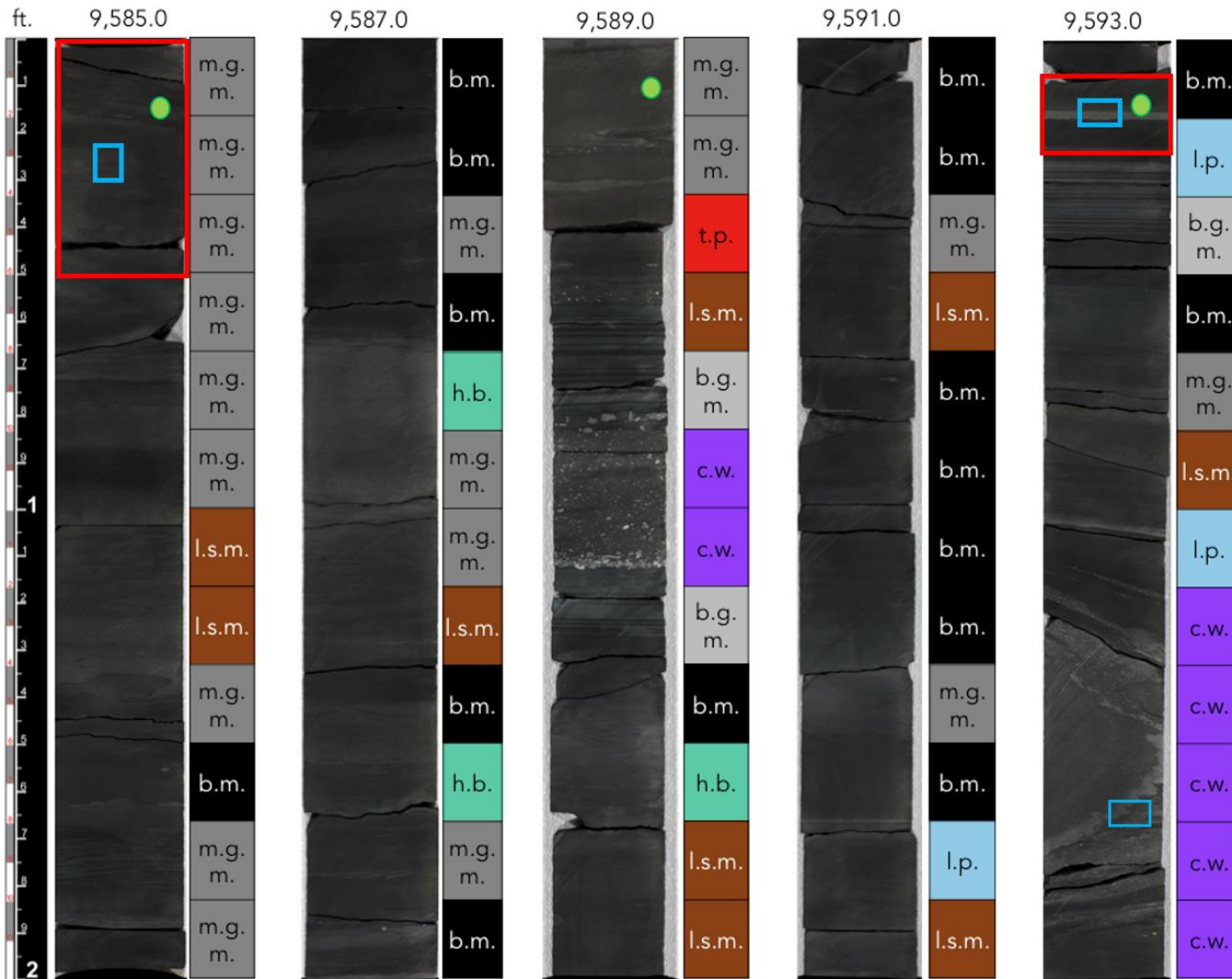


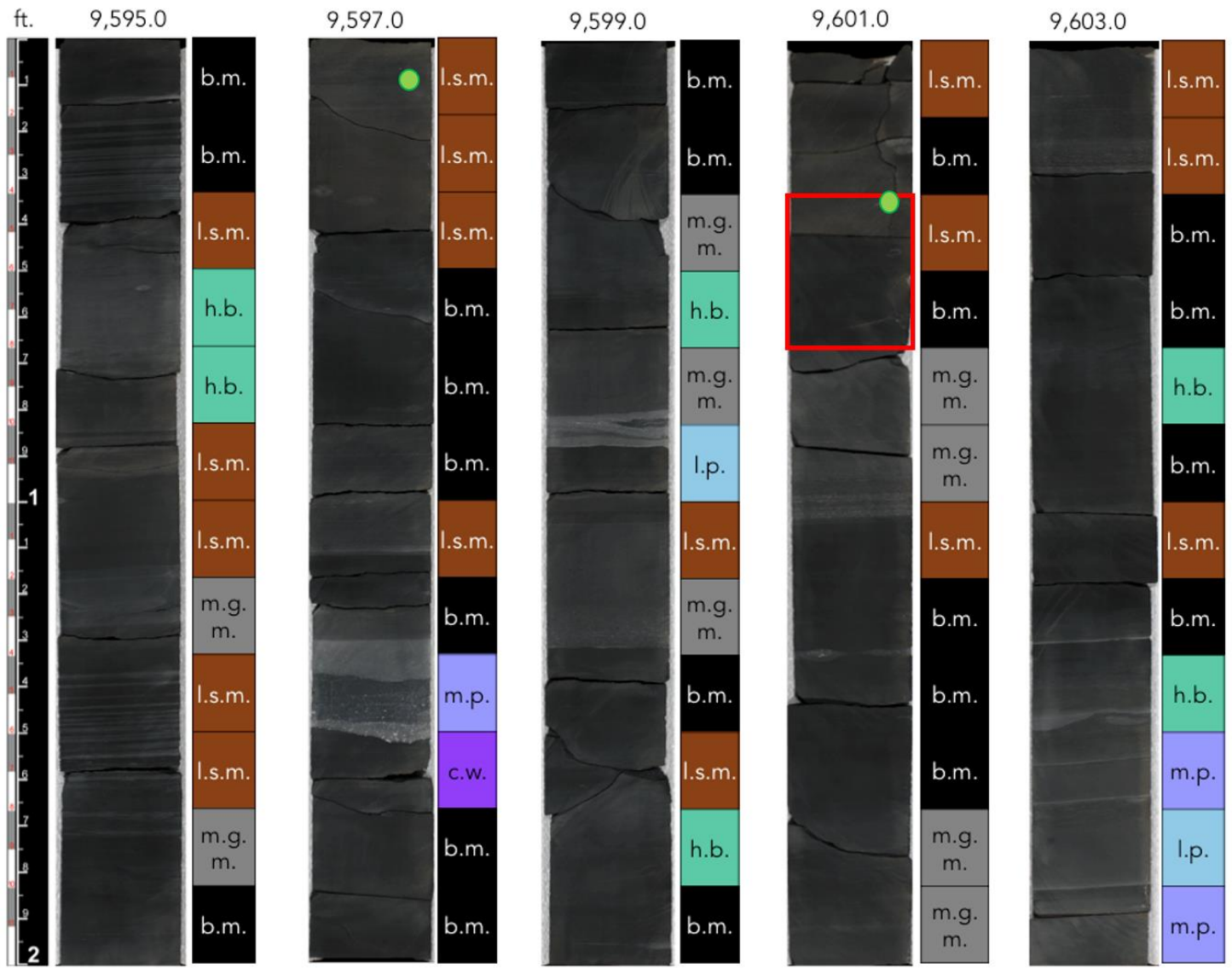


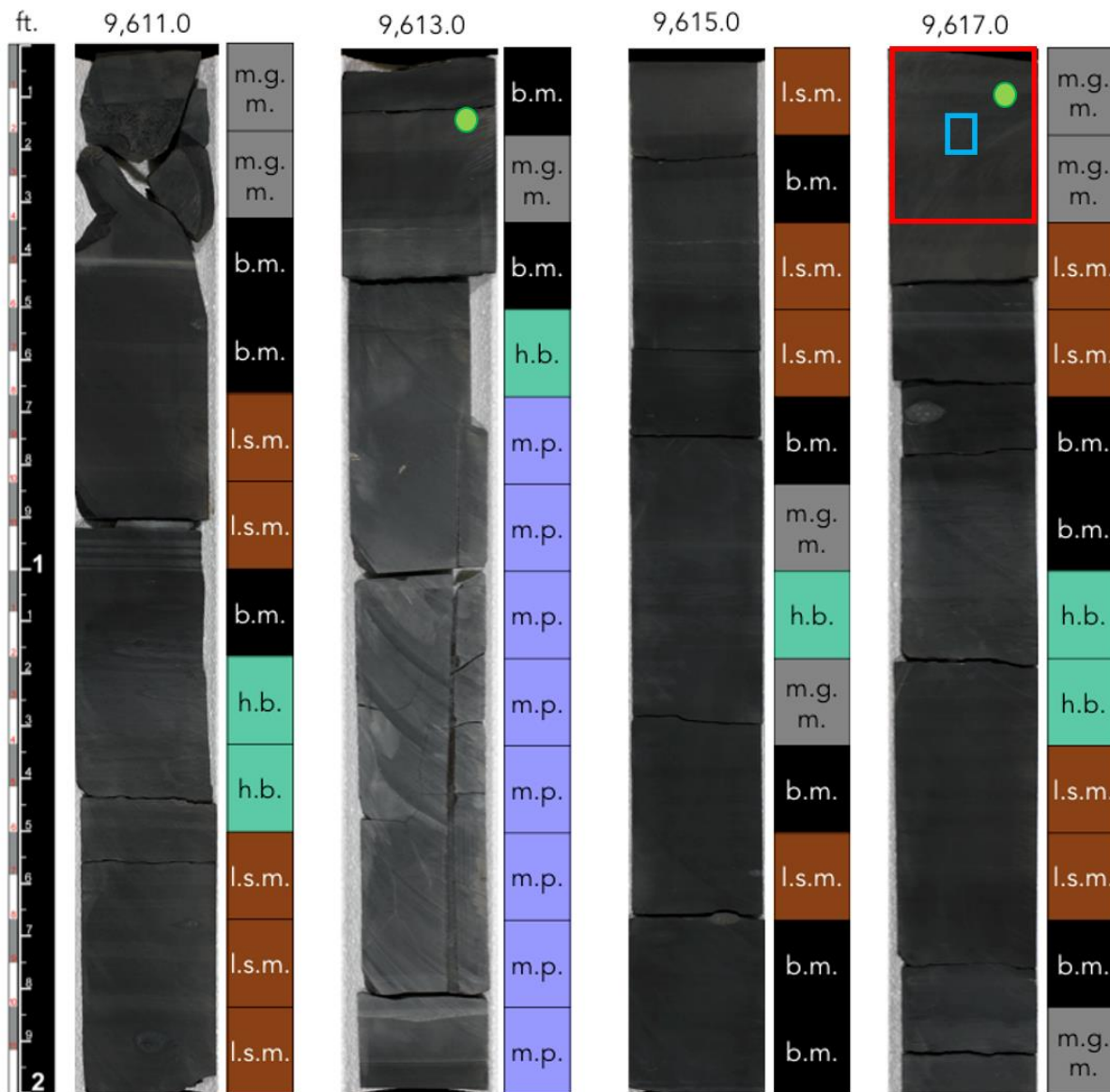


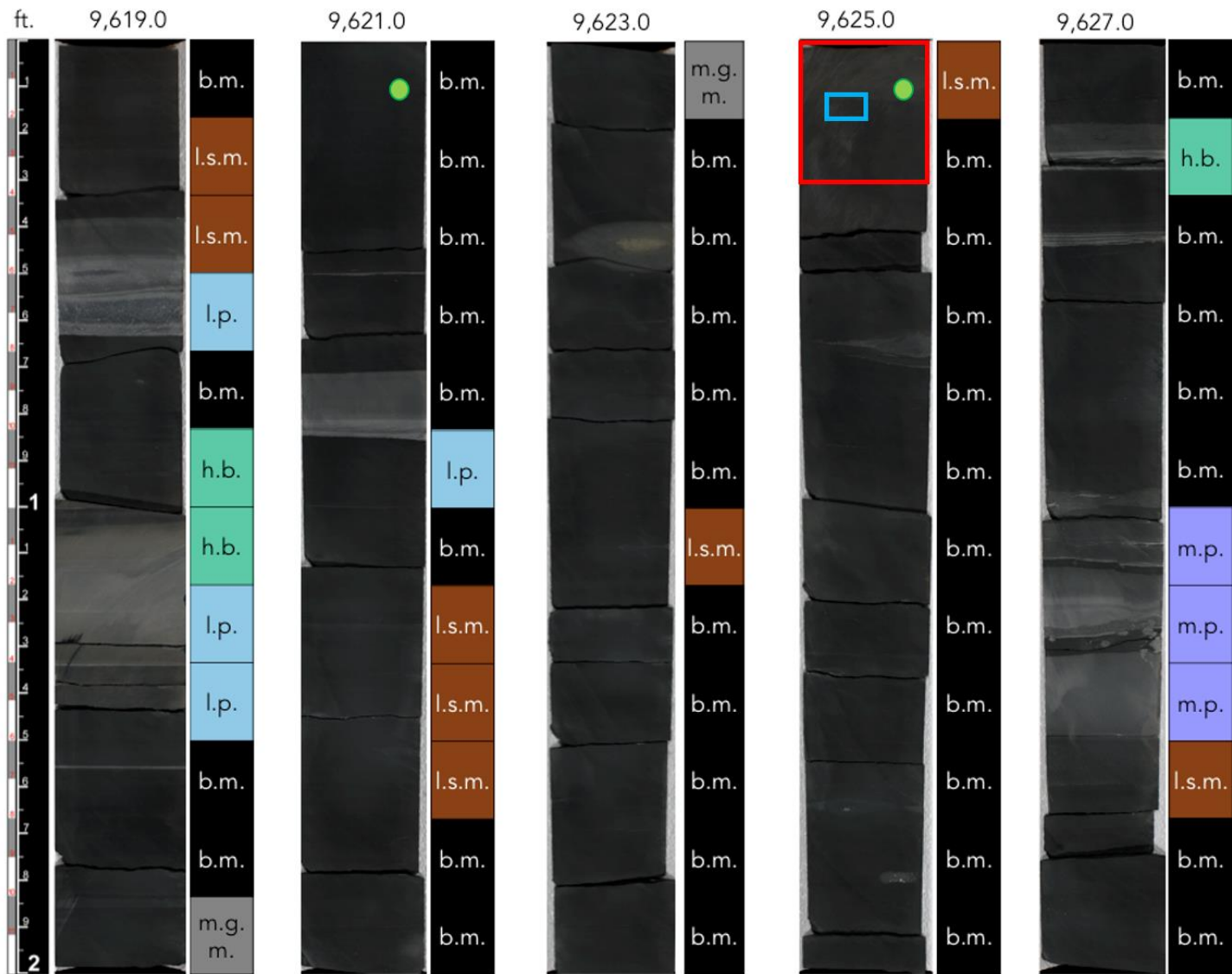


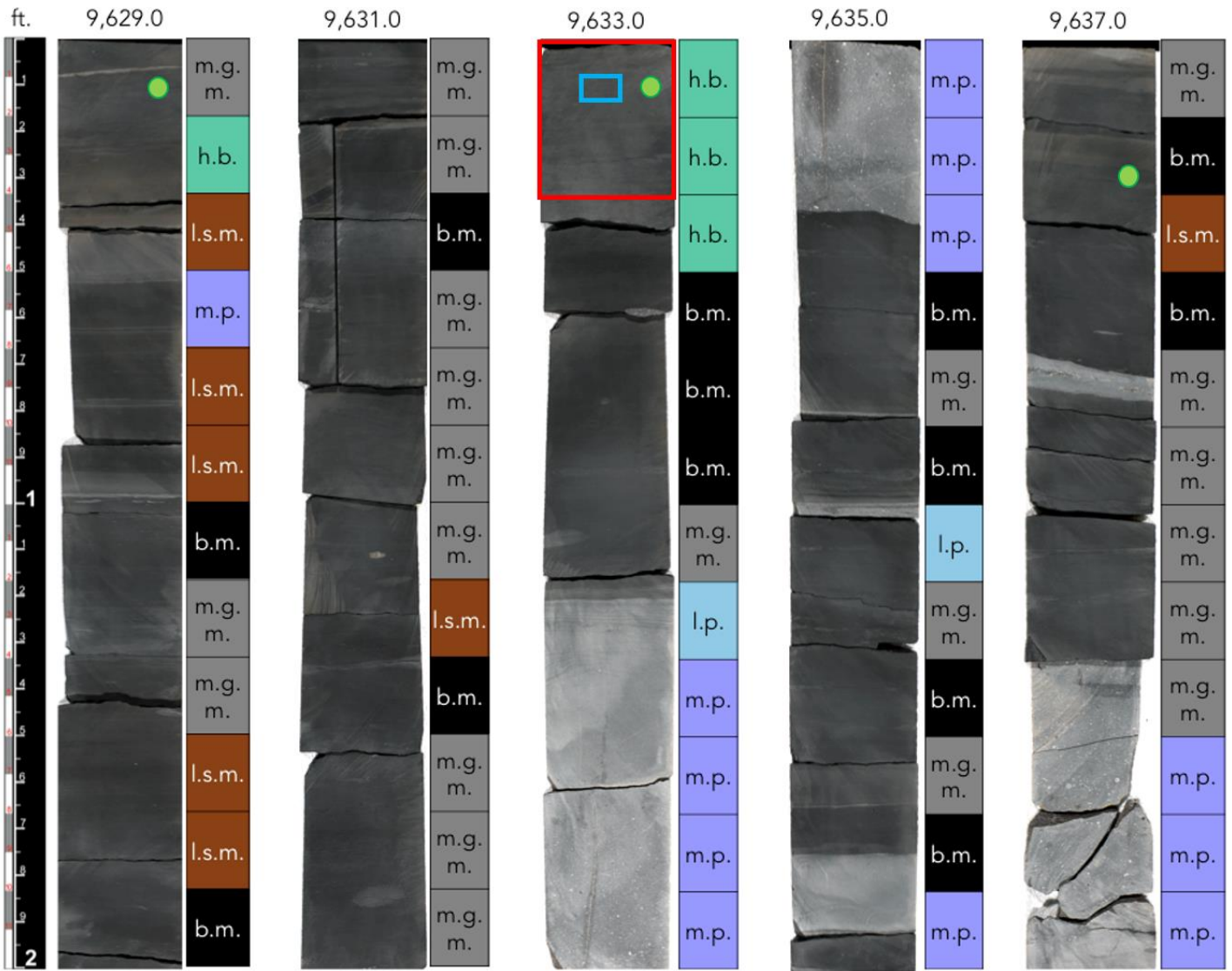


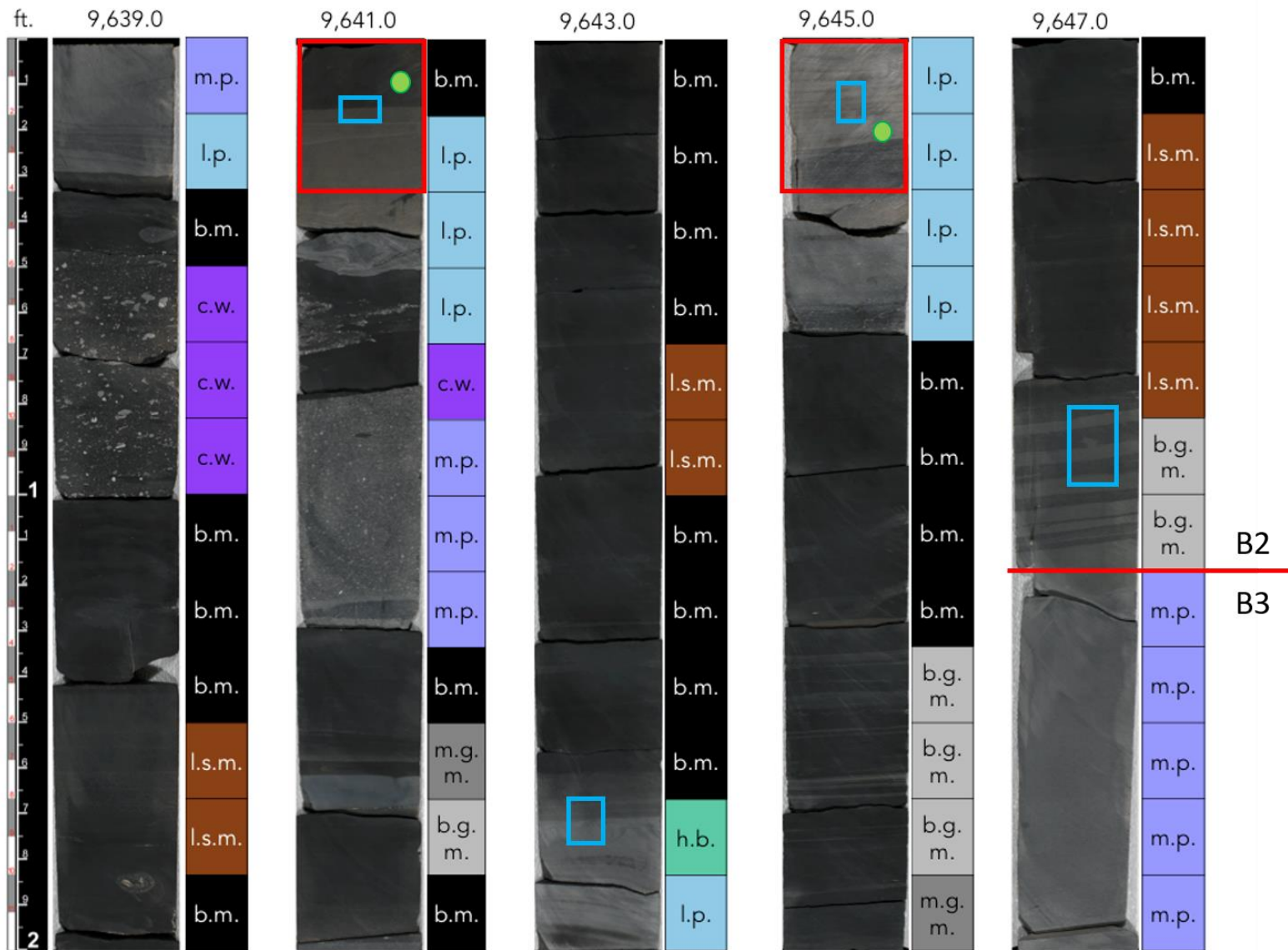


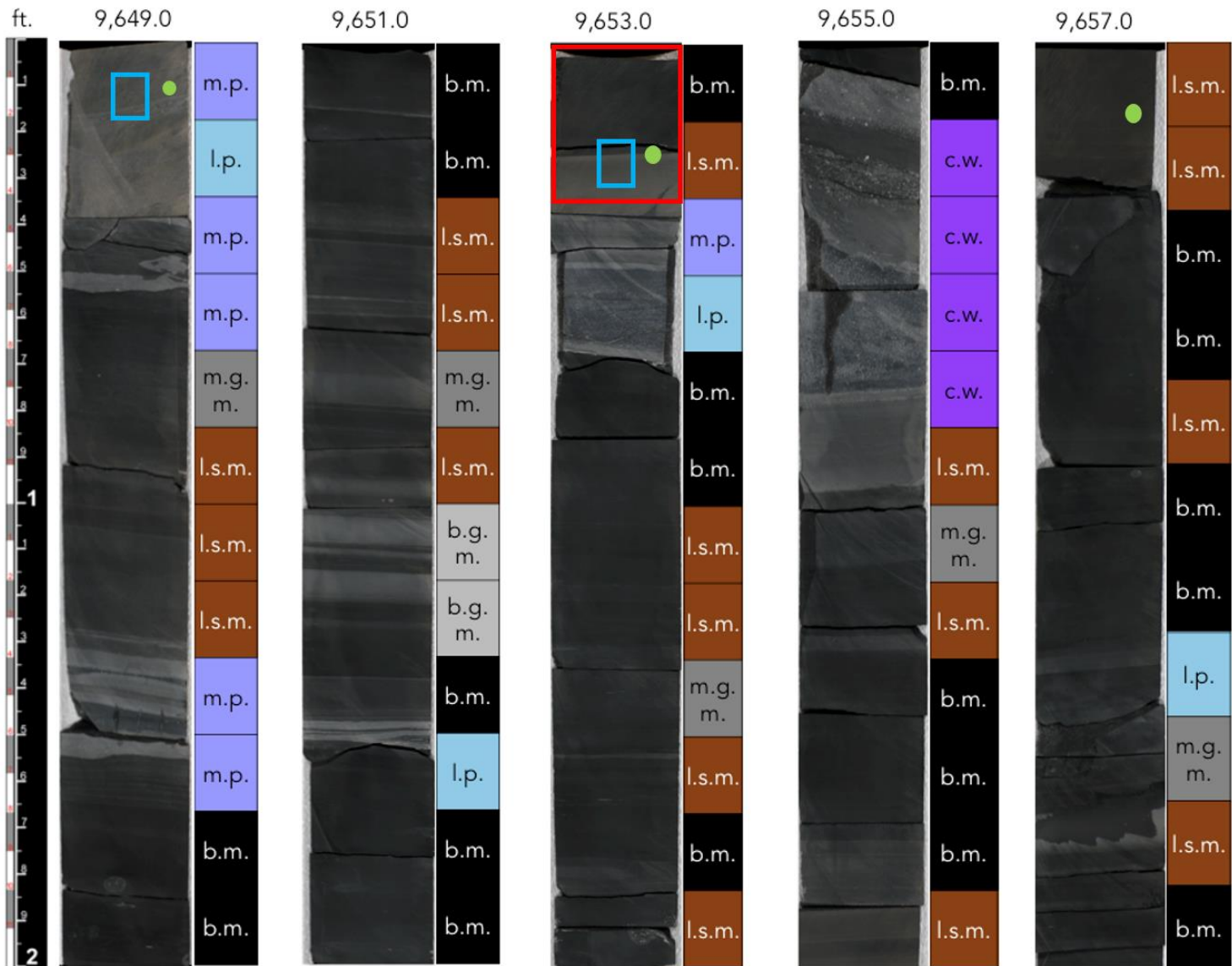


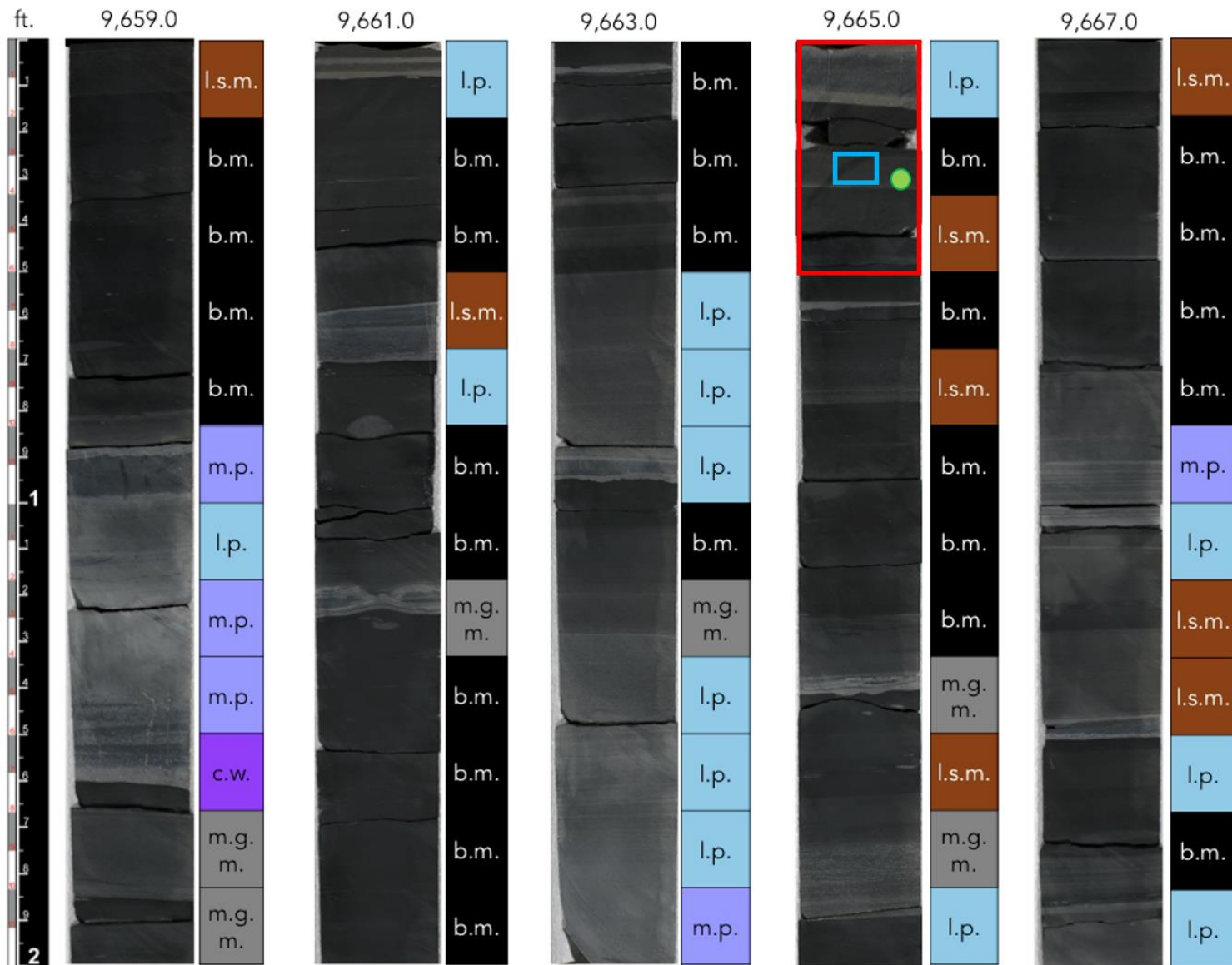


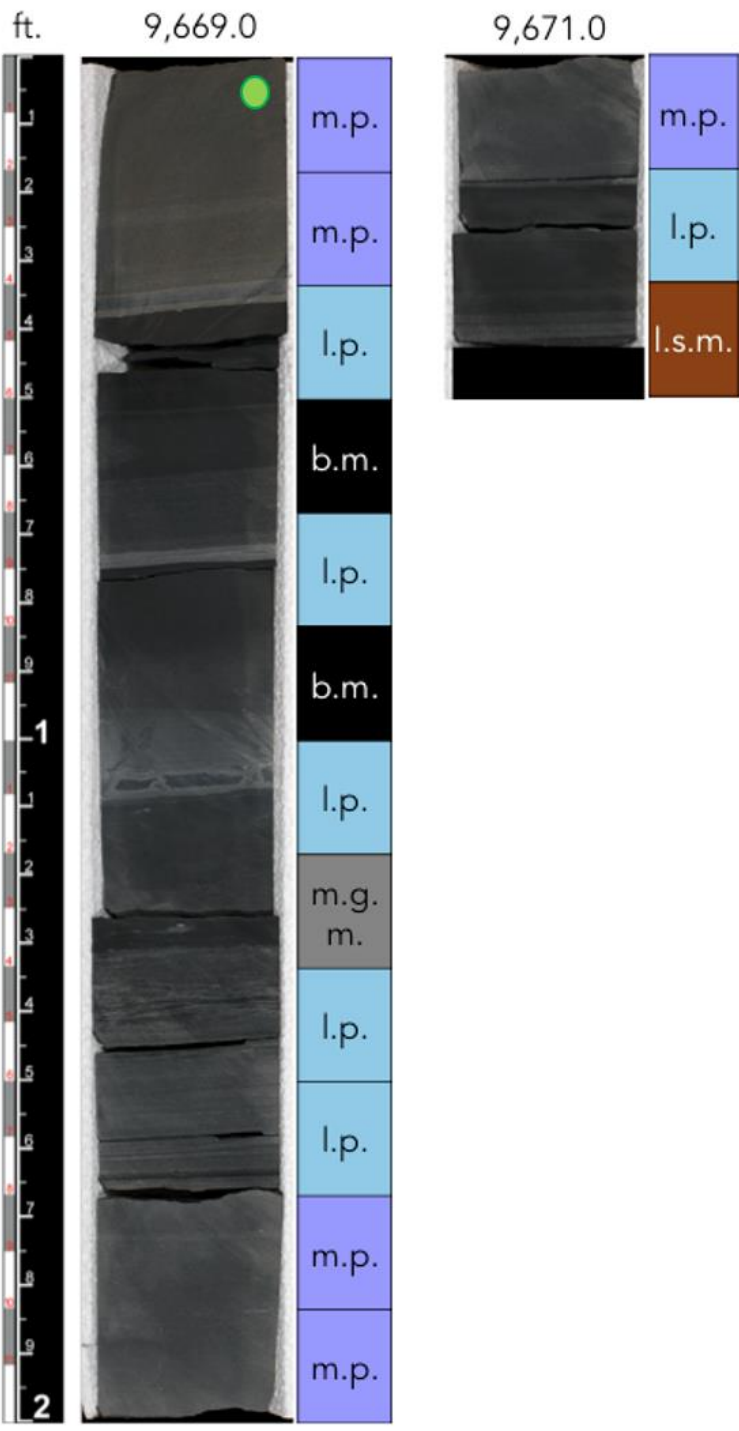


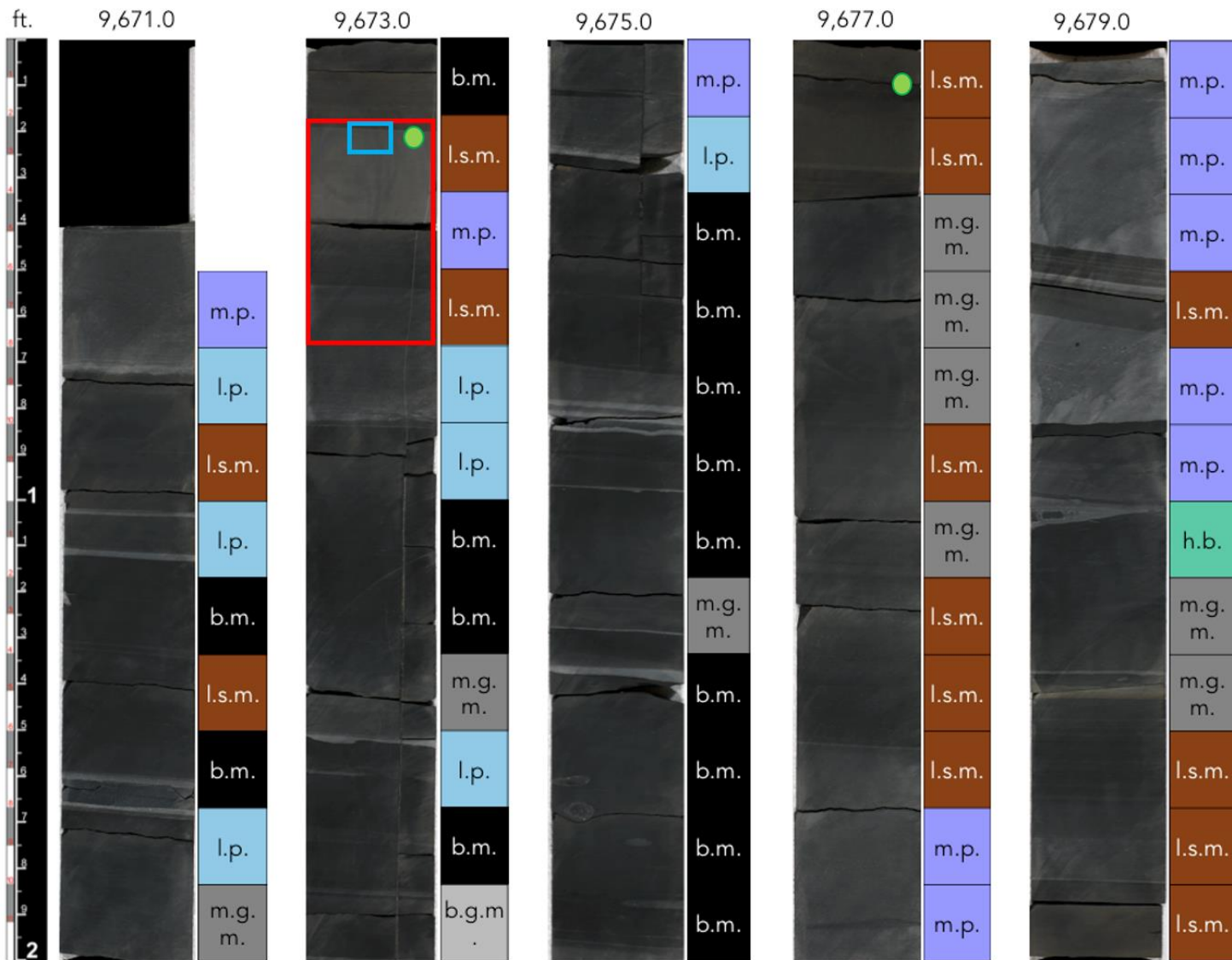


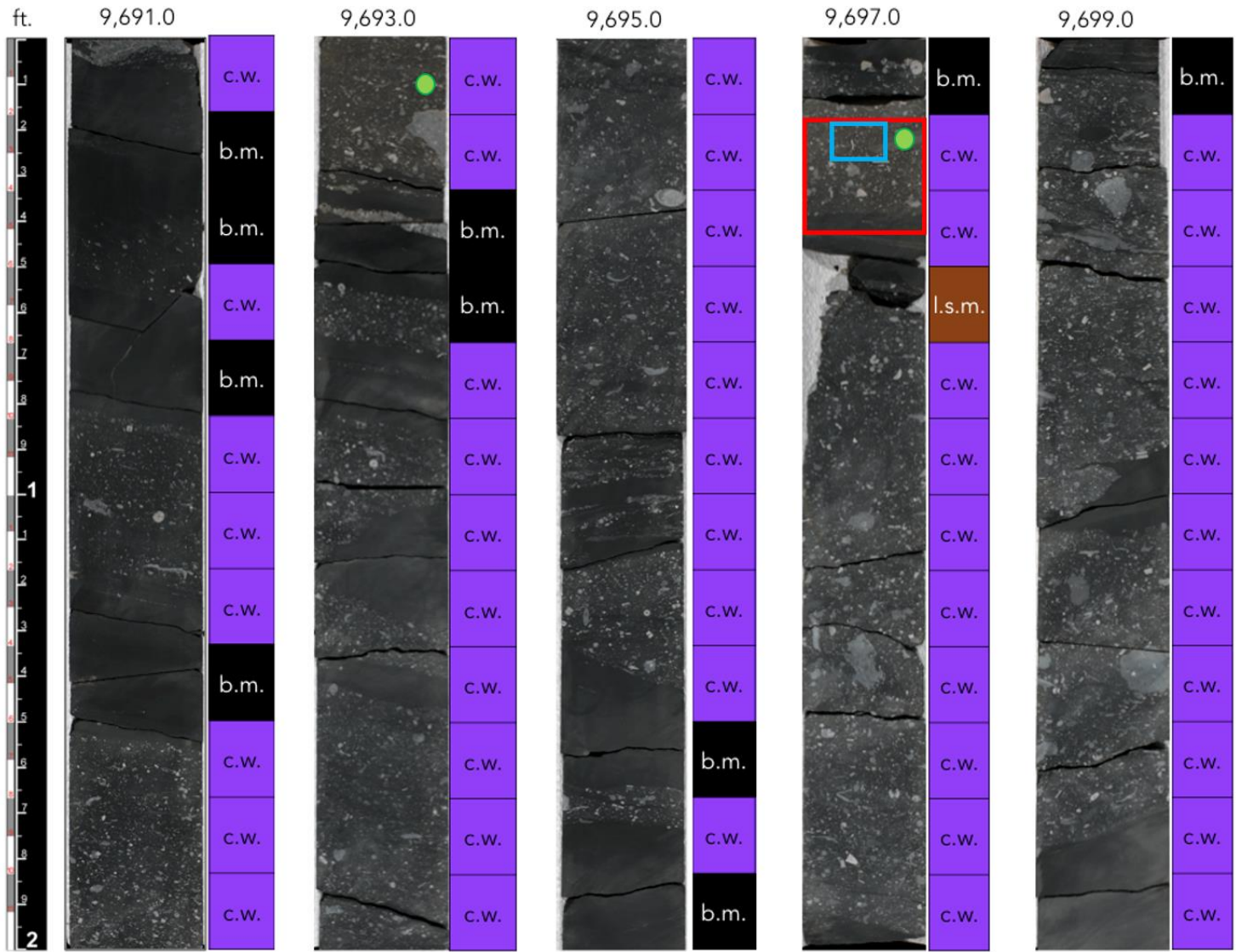












Appendix B. Petrography

Sample Depth (ft)	Petrographic microfacies					
	Faintly laminated silty mudstone	Bioturbated silty mudstone	Well sorted carbonate packstone	Mixed carbonate siliciclastic wackestone	Non-laminated mudstone	Poorly sorted coarse packstone
9577.17	X		X			
9585.17		X				
9593.17	X		X	X		
9594.66				X		
9617.17	X					
9625.17					X	
9633.17		X				
9641.17				X	X	
9644.67			X	X		
9645.17			X			
9647.84		X				
9649.17			X			
9653.17	X		X	X		
9657.17	X					
9665.34	X					
9673.17	X			X		
9681.17	X			X		
9683.17						X
9689.17			X			
9690.84			X			
9697.17						X



Figure 36. Sample Depth: 9577.17 ft. (A) Thin section: 3 distinct layers based on lithologic alternation observed: 1) clay laminated carbonate packstone with contorted pyrite bed. Dolomite below pyrite contact. Laminated finer grained carbonate above. Slightly dipping laminations/ cross stratification, 2) faintly laminated mudstone, 3) laminated and bioturbated siltstone – horizontal burrows create discontinuities in horizontal laminae.

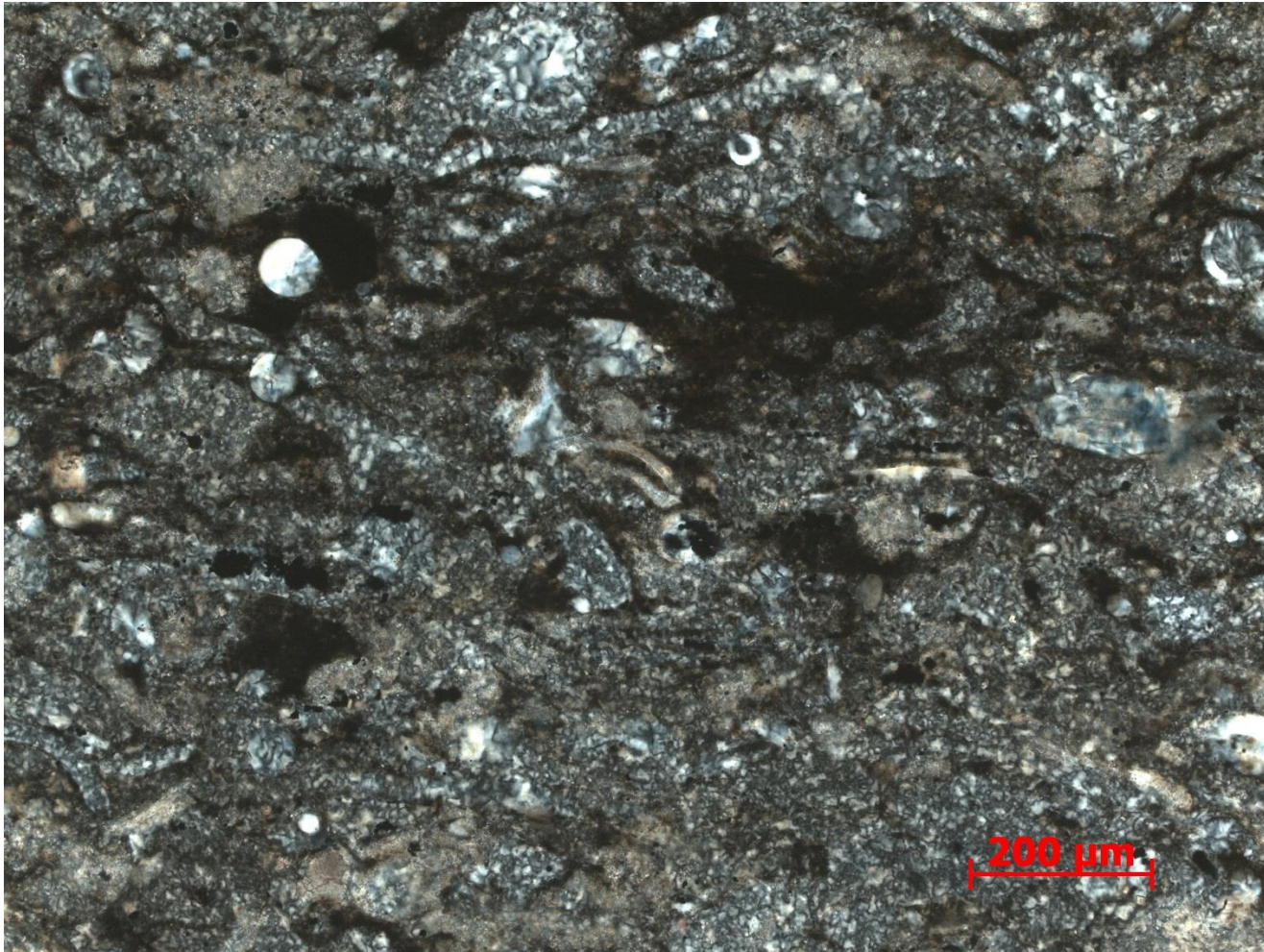


Figure 37. Sample Depth: 9577.17 ft. 10 x PPL – Partial micritization (stippled texture) and dolomitization (equant beige crystals) of grains and amorphous silica replacement of allochems. Clay and organic material laminations.

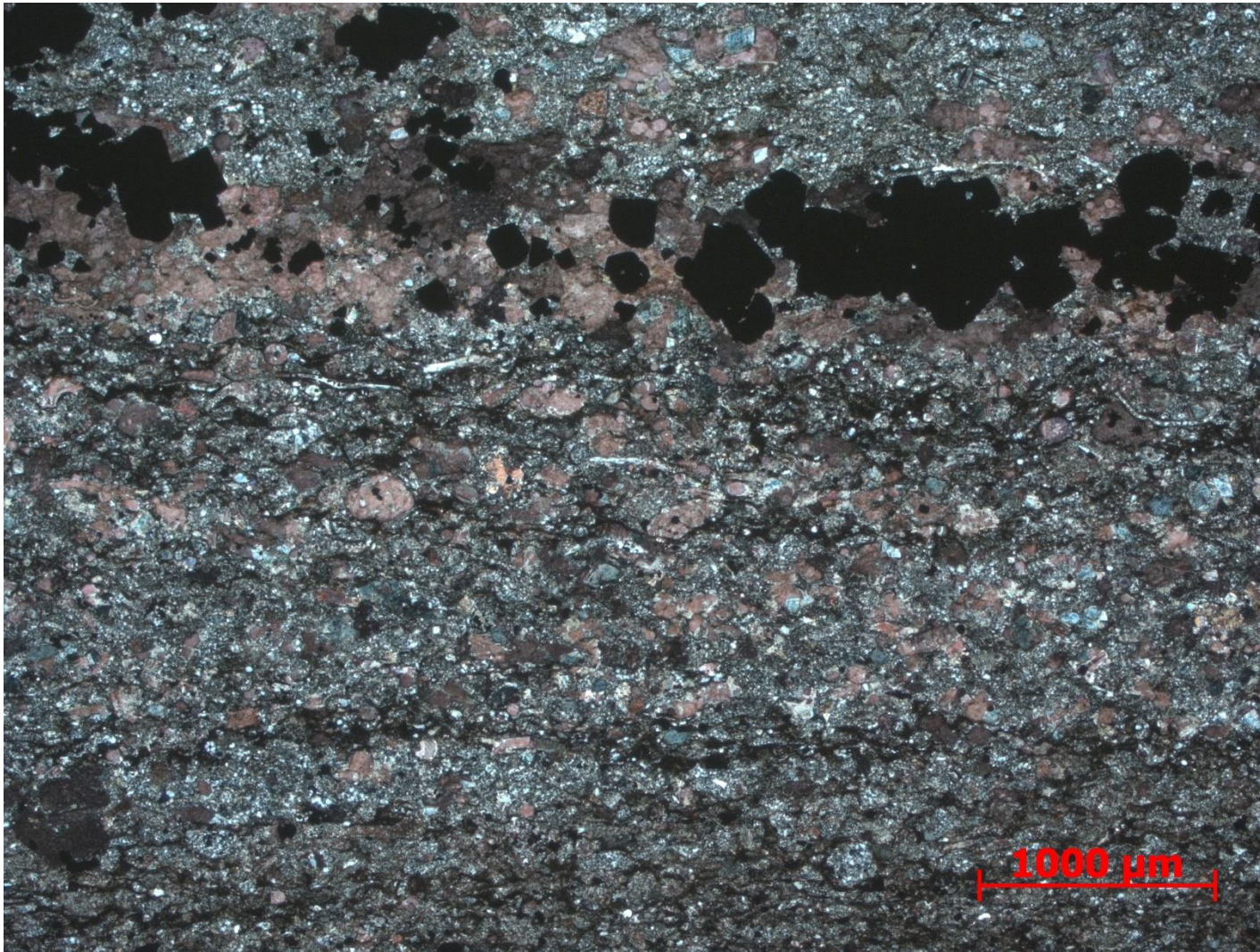


Figure 38. Sample Depth: 9577.17 ft. 2.5 XPL – Skeletal fragments include small bivalves, echinoderms spines, and radiolaria. Allochem grain boundary dissolution from cement overprint. Large euhedral pyrite framboids, most likely formed during later diagenesis. Diffuse laminations composed of clay rip up fragments. Ferroan dolomite intergranular cement, rarely large rhombic crystals overprinting entire grains. Allochems predominately calcite, some abrasion and rounding. Elongate allochems aligned.

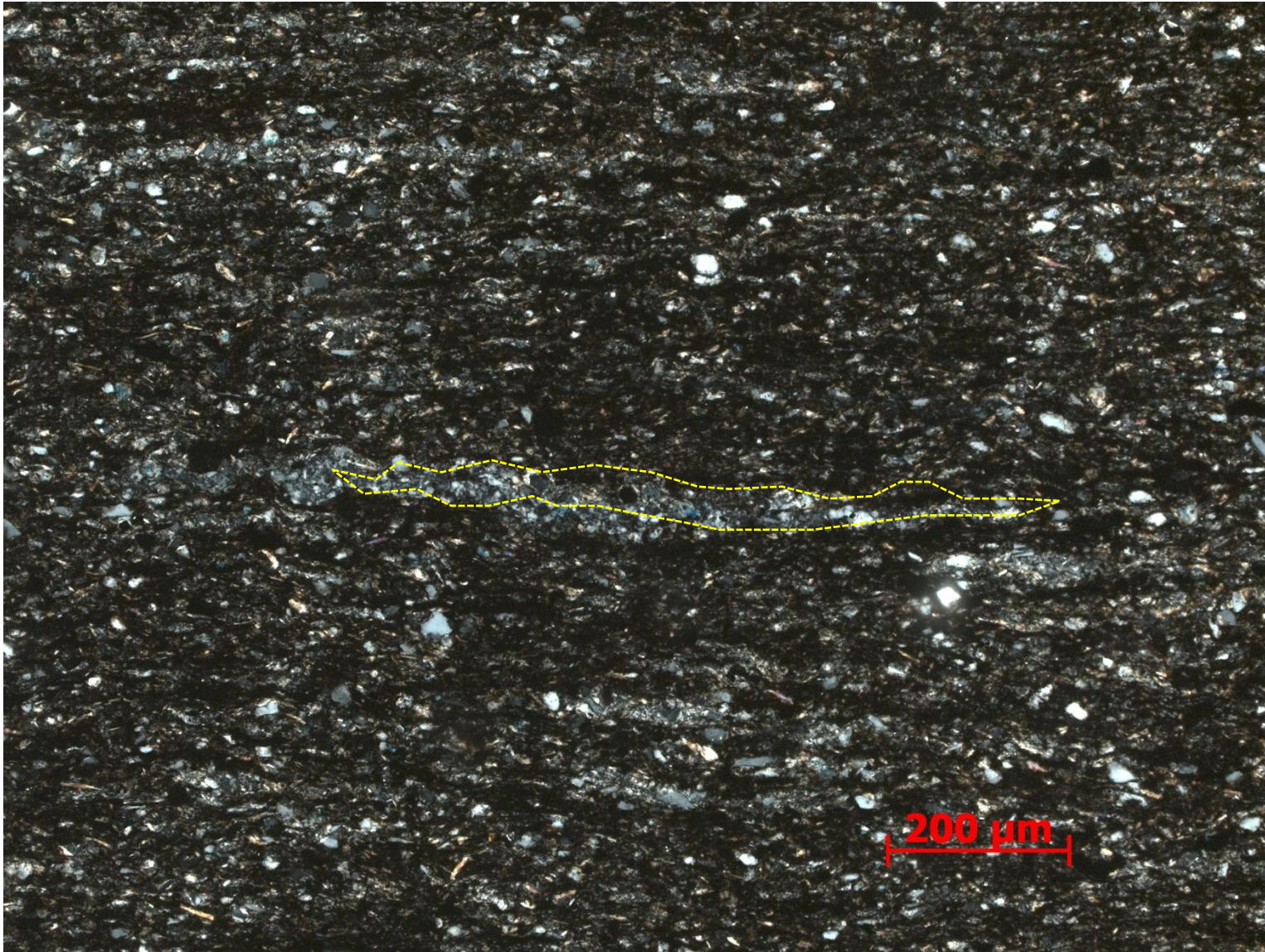


Figure 39. Sample Depth: 9577.17 ft. 10x XPL – Agglutinated foram, outlined in yellow, with incorporated detrital quartz and replacive dolomitized grains



Figure 40. Sample Depth: 9577.17 ft. 2.5x PPL – Large unidentified horizontal burrow: Cleaner silt inside burrow



Figure 41. Sample depth: 9585.17 ft. Light brown silt sized detrital quartz matrix. Discontinuous and inclined laminations of darker brown clays and some lighter tan carbonate material. Churned texture. Small ripples observed. Diffuse areas of cleaner sediment absent of clay, most likely horizontal burrows. Moderately sorted. Radiolaria are sparse and only allochems observed.

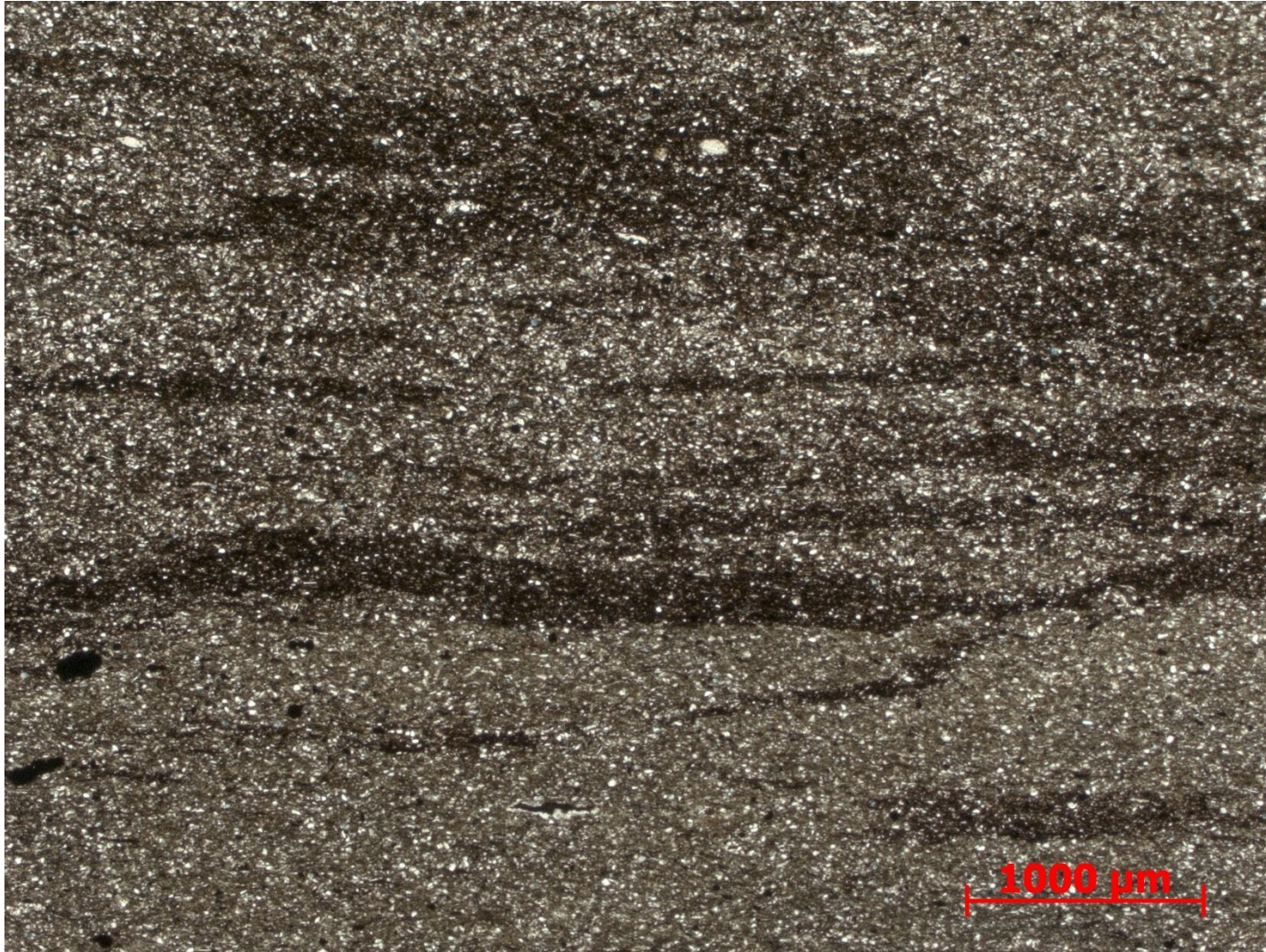


Figure 42. Sample depth: 9585.17 ft. 2.5x PPL – Bands of cleaner sediment, interpreted as horizontal burrows. Organic rich clay laminations distorted and discontinuous.

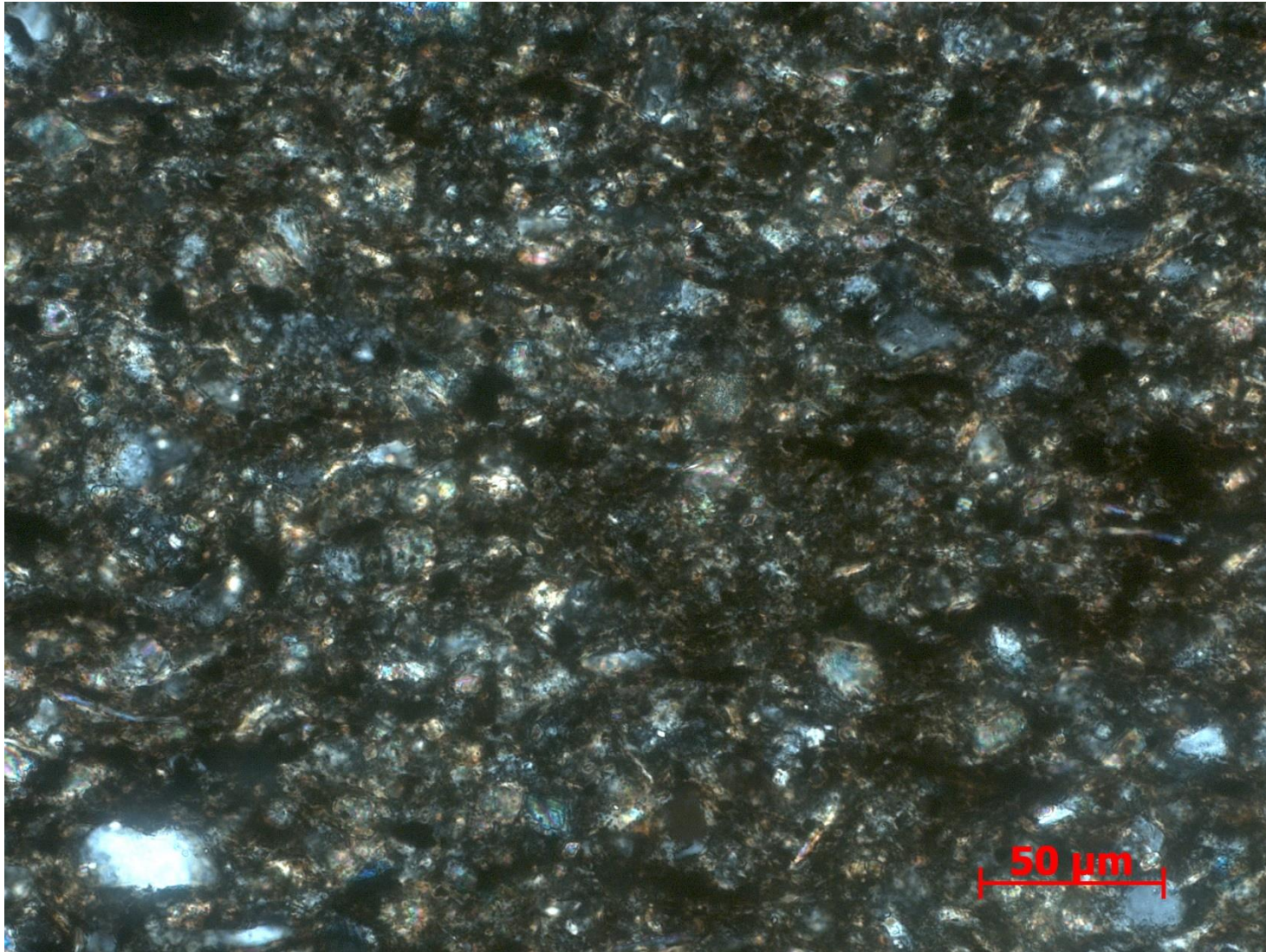


Figure 43. Sample depth: 9585.17 ft. 40 x XPL – Magnification of matrix – Abundant subrounded detrital quartz with elongate micas. Micrite present but in very low quantities. Deformed clay and organic matter.

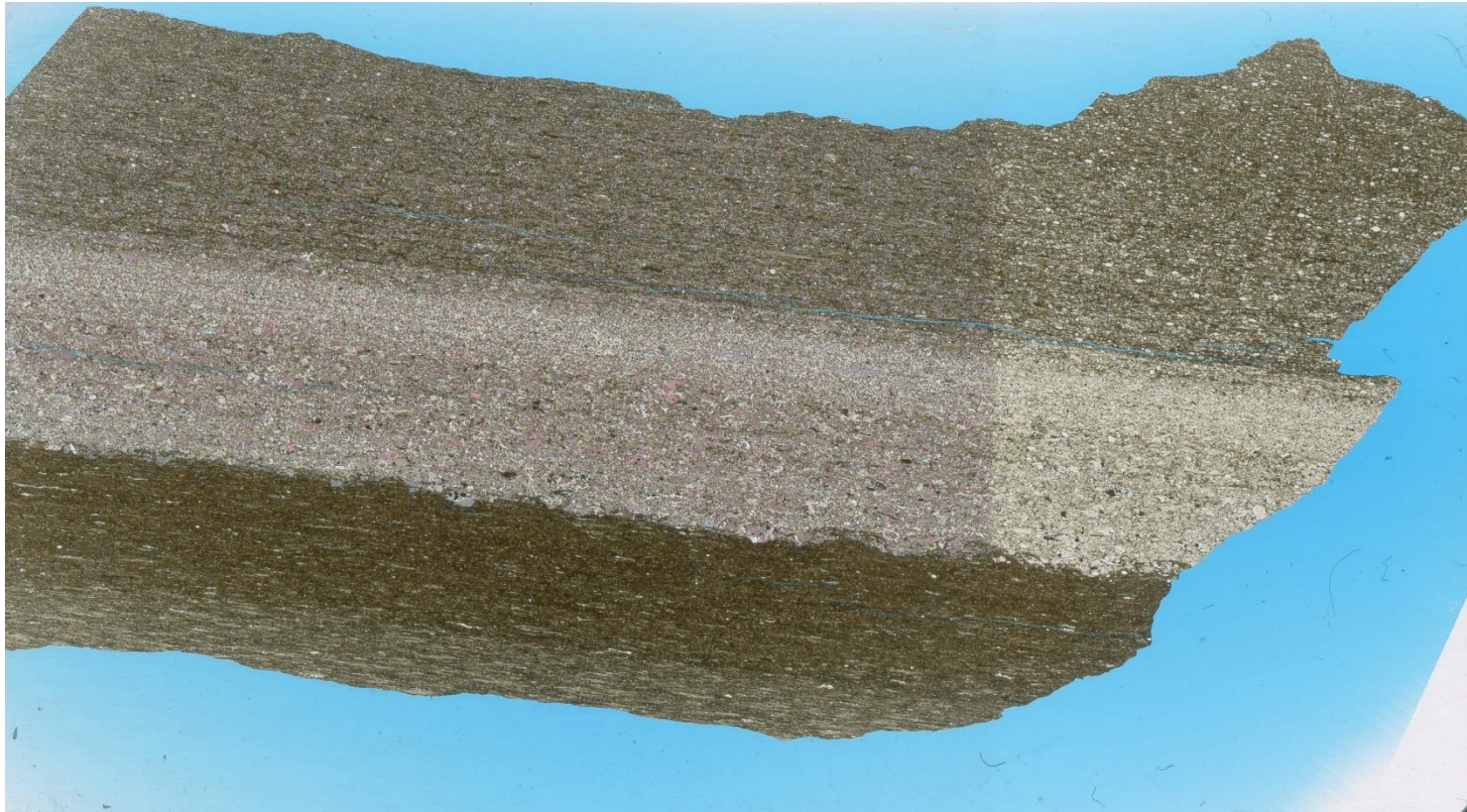


Figure 44. Sample Depth: 9593.17 ft. Mineralogically and texturally can be separated into 3 distinct layers, listed from top to bottom, Mineralogy: (1) clays, OM, detrital quartz (2) minimal clay, calcite replacement and org. calcareous fossil fragments, silica replacement and pore cement, oxides (3) detrital quartz, siliceous radiolaria and calc. replacement of radiolaria, clays. Texture: (1) lower almost entirely detrital part begins with abundant bioturbation which gradually decreases upwards until the contact with the carbonate flow. OM content increases upwards as well although not very present. (2) Carbonate flow – heavy diagenetic alteration, carbonate skeletal fragments abundant and diverse, although hard to see original fauna over abrasion from transport + dissolution of edges and internal structure, silica replacement prevalent and abundant, not totally cemented but present as silica; (3) upper mixed part shows abundant bioturbation and calcareous replacement of radiolaria, detrital quartz present, larger grain size compared to (1) Bioturbation: small horizontal burrows in (1) and (3), Fauna: (1) agglutinated forams, radiolaria abundant (2) bivalves, echinoderm spines, skeletal fragments hard to identify due to replacement (3) radiolaria (calc replacement), echinoderm spines, sponge spicules, agglutinated foram rare to absent, skeletal fragments from flow.

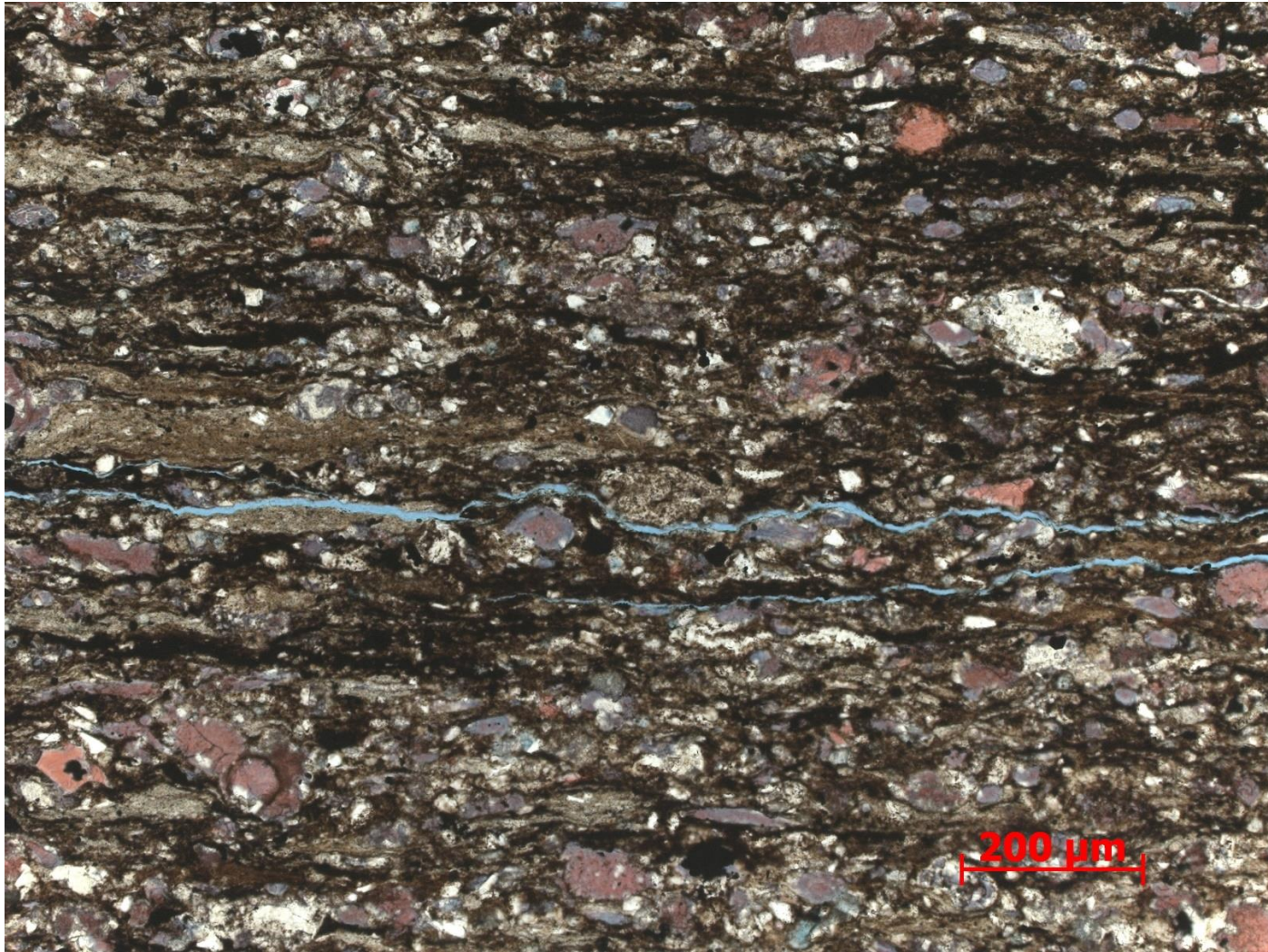


Figure 45. Sample Depth: 9593.17 ft. 10 x PPL – Top third of thin section (3) – Silt and detrital quartz grains intermixed with carbonate grains and allochems. Small silt lithoclasts also exhibit elongated shape. Note zonation of ferroan dolomite. Calcite center of carbonate grains, ferroan dolomitization of edges. Abraded dolomite indicated potential dolomitization before transport. Radiolaria, sponge spicule, and agglutinated foram present.



Figure 46. Sample Depth: 9593.17 ft. 10x XPL – Middle portion (2) – Various cement types and textures visible. Equant and sparry silica cement with low (light to dark gray) birefringence and optical relief. Dissolution and grain edge growth of dolomite visible – small un-abraded rhombohedra crystals. Sometimes bladed.

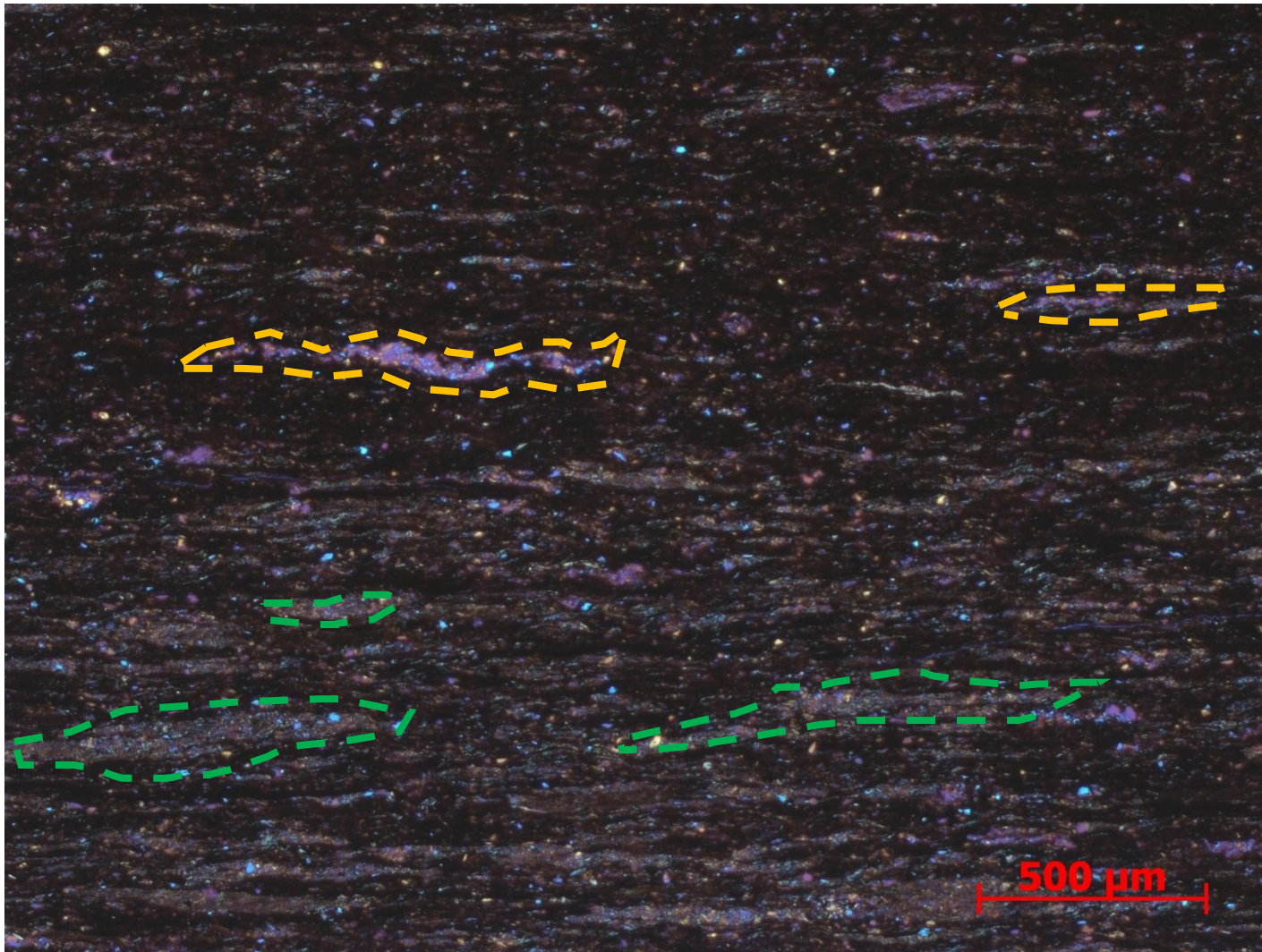


Figure 47. Sample Depth: 9593.17 ft. 5x XPL with gypsum plate – Bottom third of thin section (1) – small elongated horizontal burrows parallel to bedding (750 μm), cleaner sediment in interior of burrow. Bioturbation decreasing upwards. Organic material and clay content increasing upwards. Agglutinated forams (700 – 500 μm) present towards top, absent when bioturbation is abundant. Agglutinated forams (orange stippled line) distinguishable from burrows (green stippled line) via the larger well sorted interlocking quartz grains (no silt or clay).

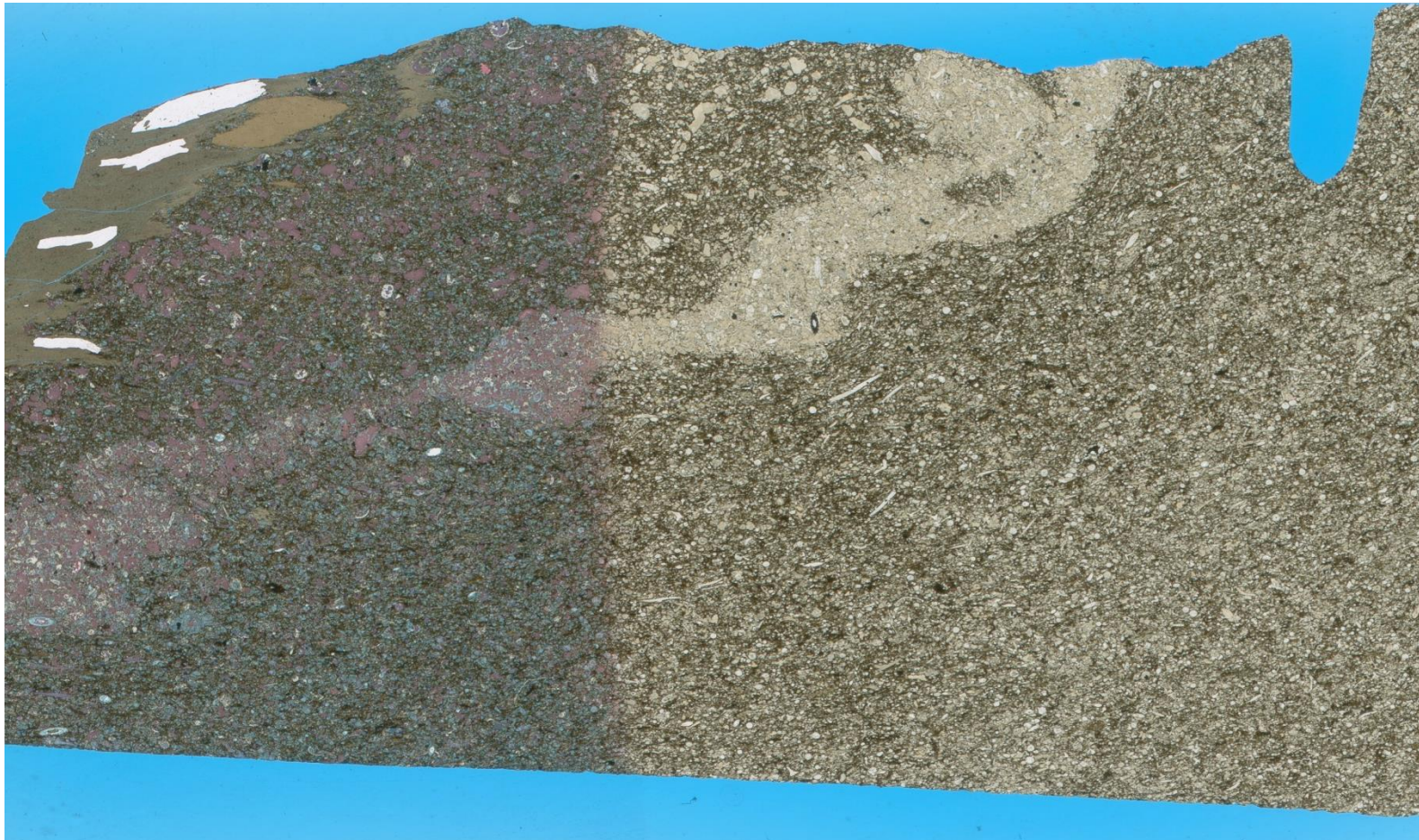


Figure 48. Sample Depth: 9594.66 ft. Mineralogy: argillaceous (potentially phosphatic) rip up clast, clay matrix, calcareous shell fragments, calcite replacement and cement in diagenetic band (abundant), dolomite replacement of skeletal material (minimal), ferroan dolomite replacement (abundant). Texture: shale rip up clasts, diagenetic alteration "band" w/ heavy calcite replacement and cement – edge dissolution difficult to see fauna and regular "white" dolomite replacement; lots of ferroan dolomite replacement, shale matrix (<25%); more ferroan dolomite outside of diagenetic alteration or fluid front, random grain orientation and skeletal fragment assemblage + abrasion indicate transport of material. No bioturbation. Fauna: echinoderm spine fragments, sponge spicules, abraded shell and lithoclast fragments, bivalve shells fragments

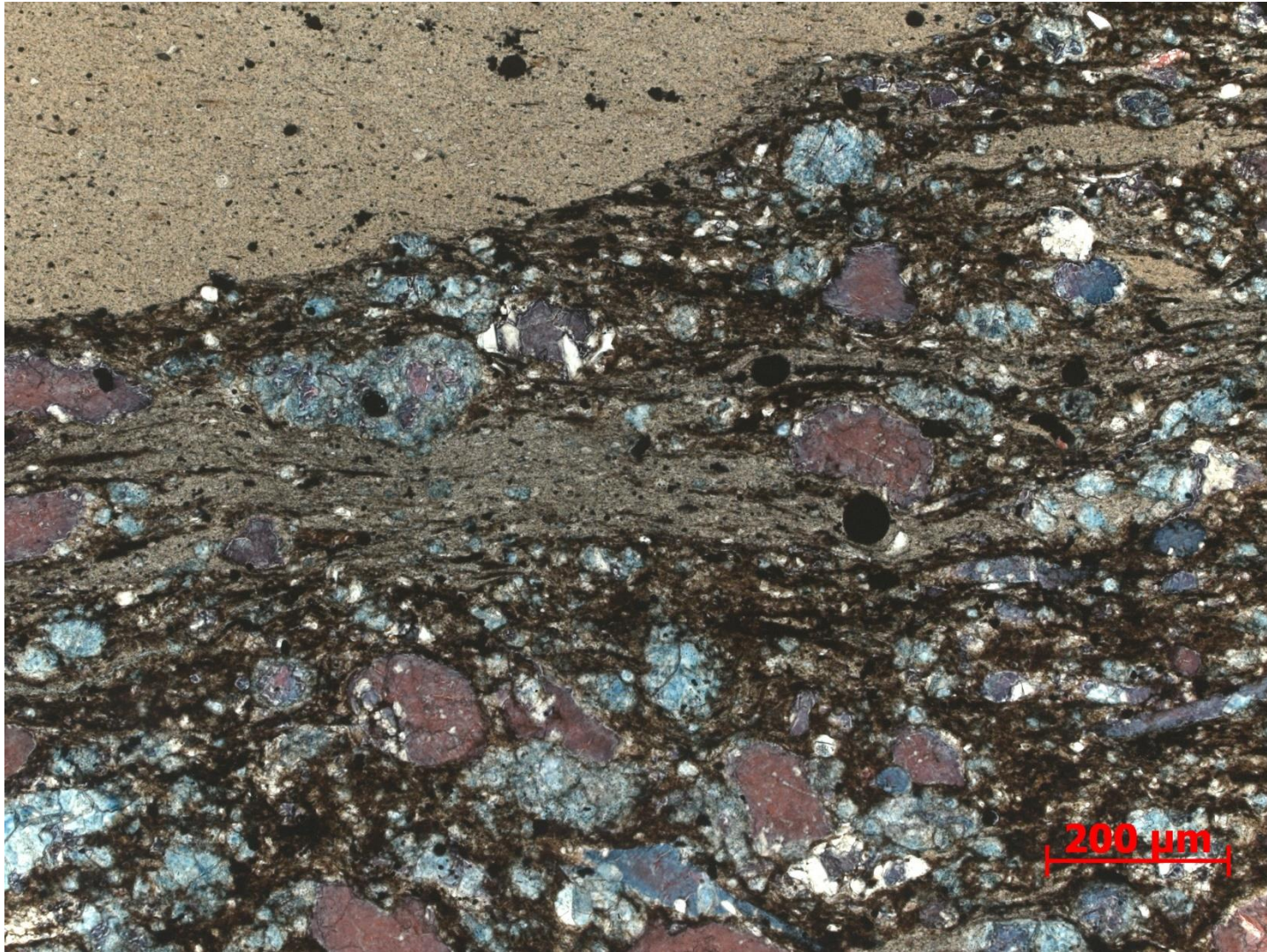


Figure 49. Sample Depth: 9594.66 ft. 10x PPL – Large rounded, elongated silty lithoclast in top left. Original allochems difficult to distinguish due to ferroan dolomite replacement and dissolution of internal skeletal structure. Non-ferroan dolomite . Ferroan dolomite replacement either limited to grain edges or complete. Matrix composed of clays, relatively free of silt size particle. Wide grain size distribution.

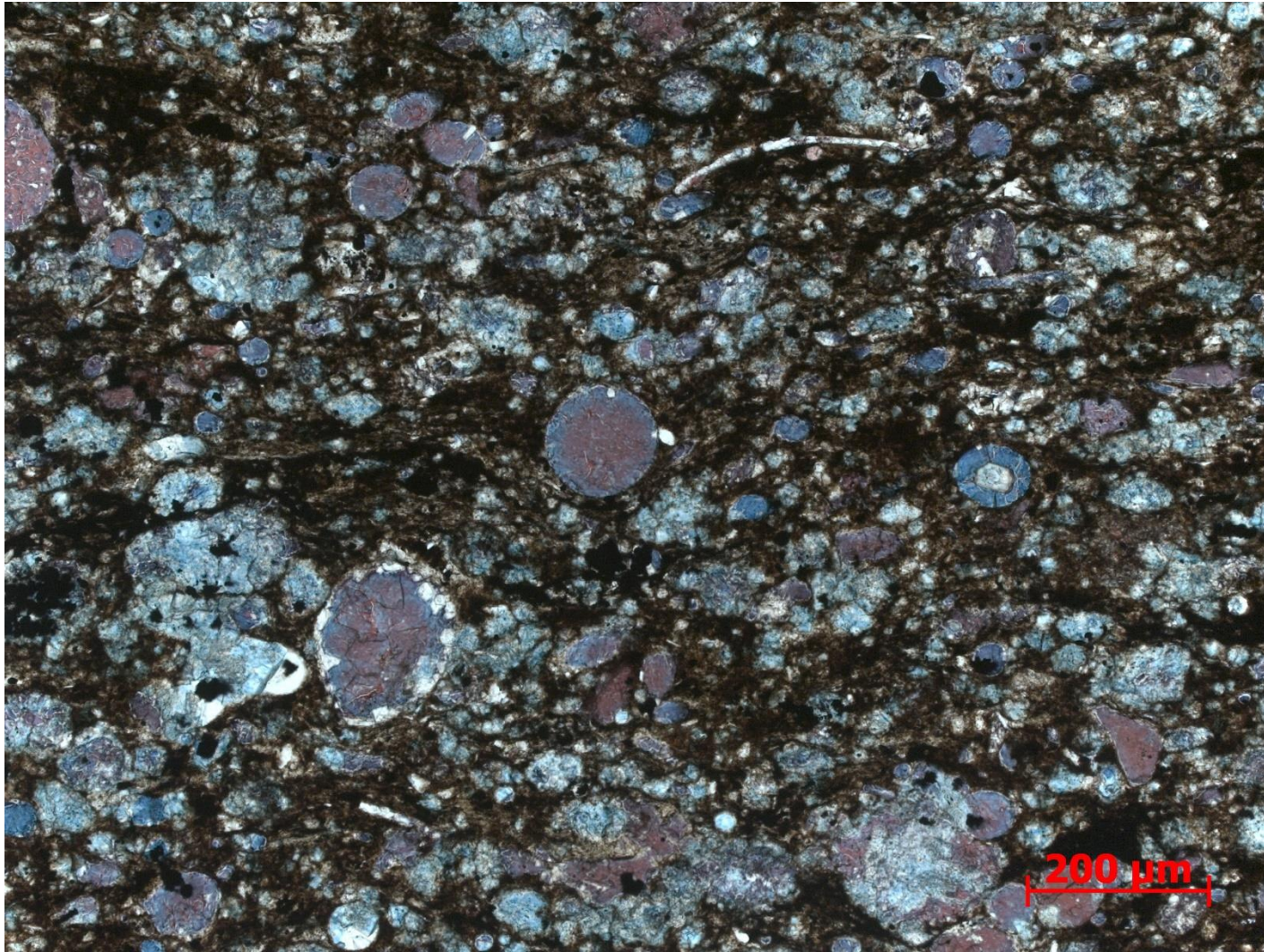


Figure 50. Sample Depth: 9594.66 ft. 10x PPL – Cement zonation: Calcite in center of allochems (original mineralogy?), ferroan dolomite towards grain edge, and less often pure dolomite on edge. Carbonate material equally mixed with siliciclastic clay and organic material. Silt sized particles and detrital quartz absent.



Figure 51. Sample Depth: 9617.17 ft. Mineralogy – clays, detrital qtz, pyrite, OM, minor Fe-dolomite replacement, no calcite present. Texture – faint planar laminations, disrupted by bioturbation. Bioturbation - Faint vertical bioturbation into more organic rich material, coarser grains inside burrow. Horizontal bioturbation, coarser slit sized particles in burrow, OM depletion inside relative to matrix, cleaner (abundant). Homogenous matrix composition of very fine detrital quartz (sand?) and silt. Minimal clay material. Macroscopic lobe like horizontal burrows with clean infill. Discontinuous laminations of fine sediment. White grains are quartz silt particles and *Tasmanties*.

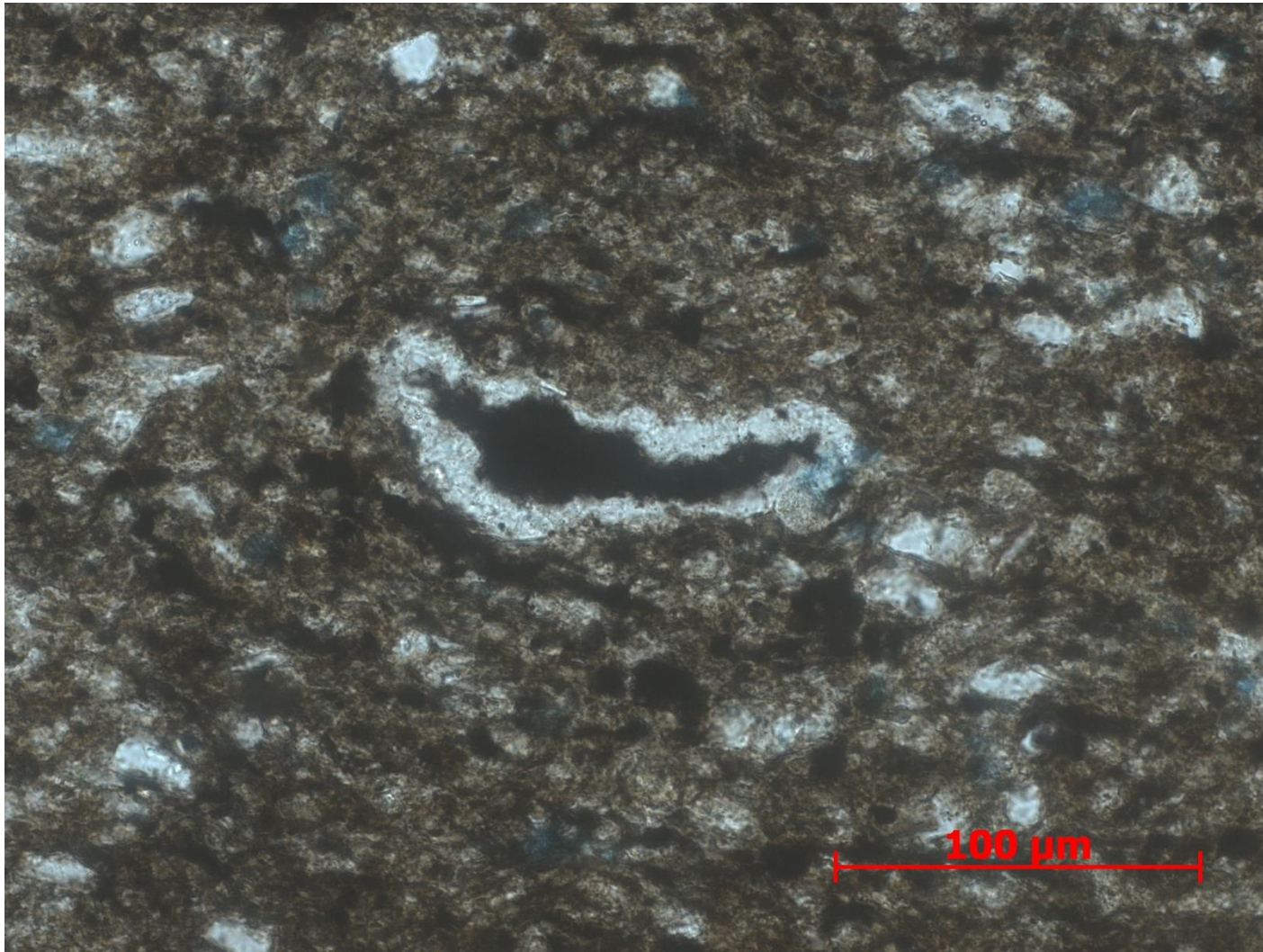


Figure 52. Sample Depth: 9617.17 ft. 40x PPL – Compressed *tasmanites* with organic matter infill. Silty matrix with detrital quartz. Oxides present. Ferroan dolomitization of some grains and edge of *tasmanites*.

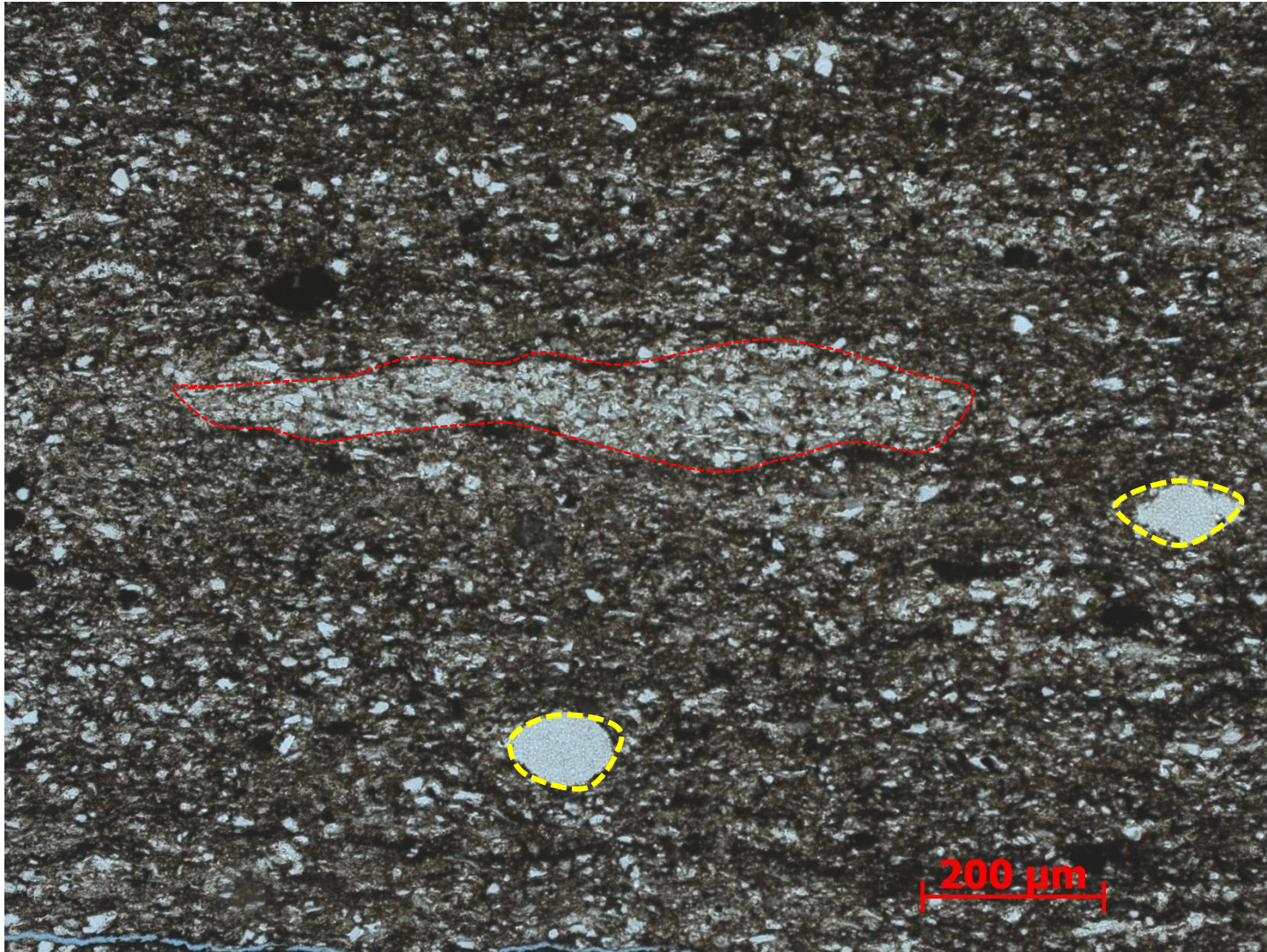


Figure 53. Sample Depth: 9617.17 ft. 10x PPL – 600 μm horizontal burrow outlined in red with cleaner sediment on inside. Radiolaria in yellow, $\sim 75 \mu\text{m}$ long. No visible carbonate (dolomite and calcite). Clay and organic material in wavy discontinuous laminations.

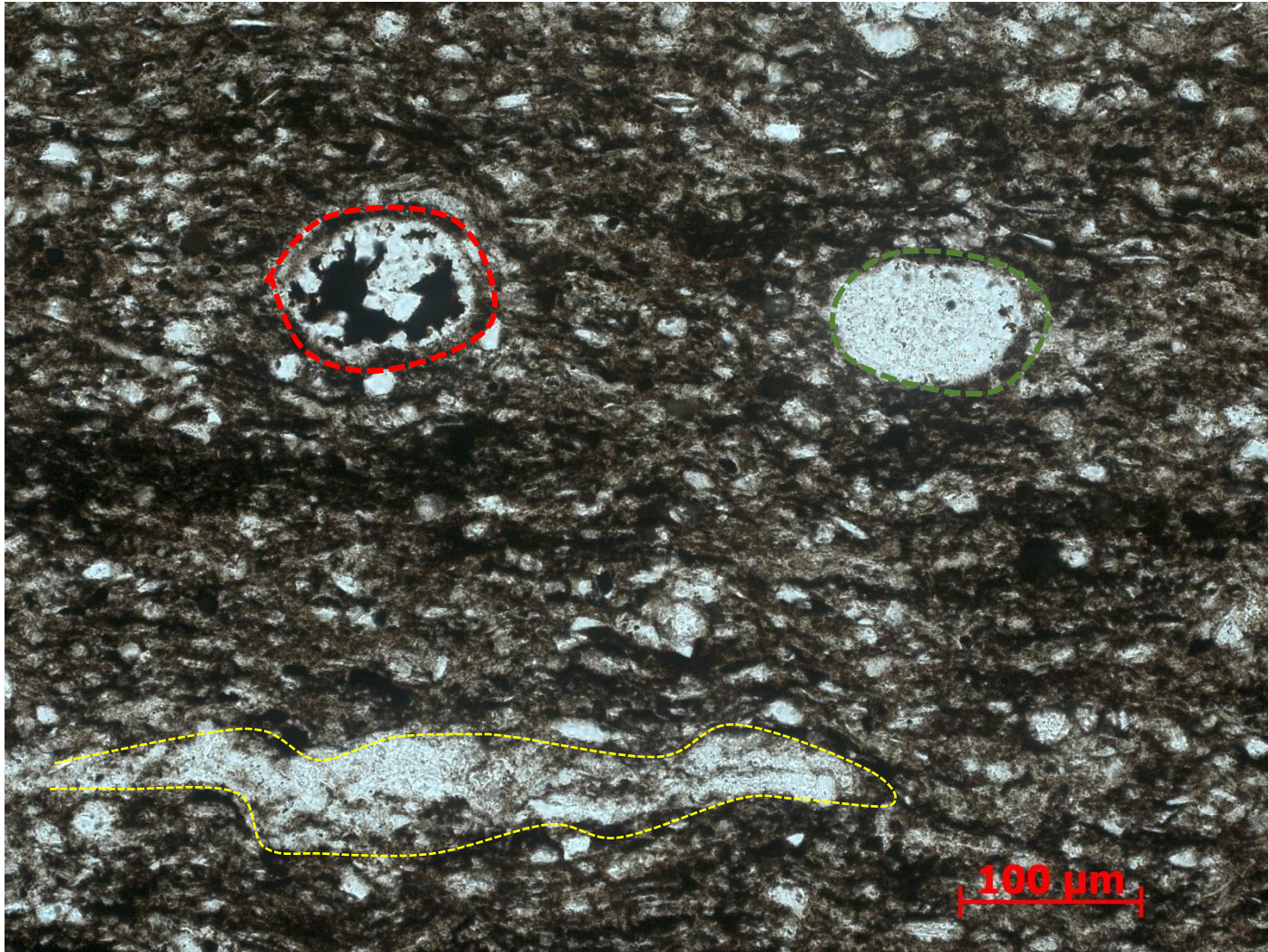


Figure 54. Sample Depth: 9617.17 ft. 20x PPL – Radiolaria with organic matter infill outlined in red. Bladed calcite crystals growing from grain edge towards center of radiolaria. Other radiolaria with partially preserved internal structure, outlined in orange. Evidence of compaction due to elongation in direction of bedding plane of ideally circular radiolaria. Partial dissolution of edges. Compacted agglutinated foram in bottom left outlined in yellow. Mostly detrital quartz silt with some finer clays present in discontinuous laminations with organic material (center left).

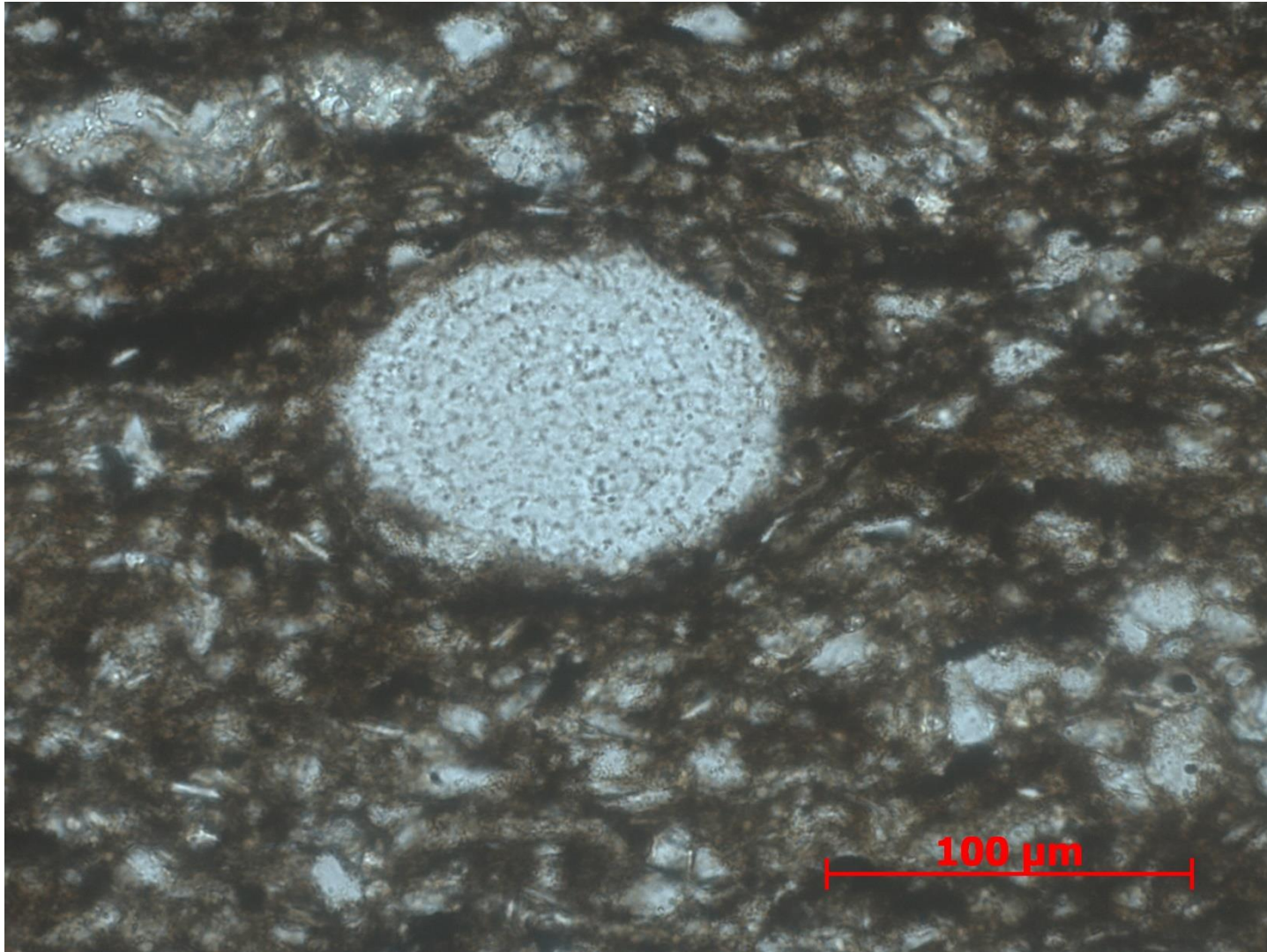


Figure 55. Sample Depth: 9617.17 ft. 40x PPL – Radiolaria with concentric internal structure still preserved. Partial grain edge dissolution, Matrix composed of detrital quartz silt with minor clay component.

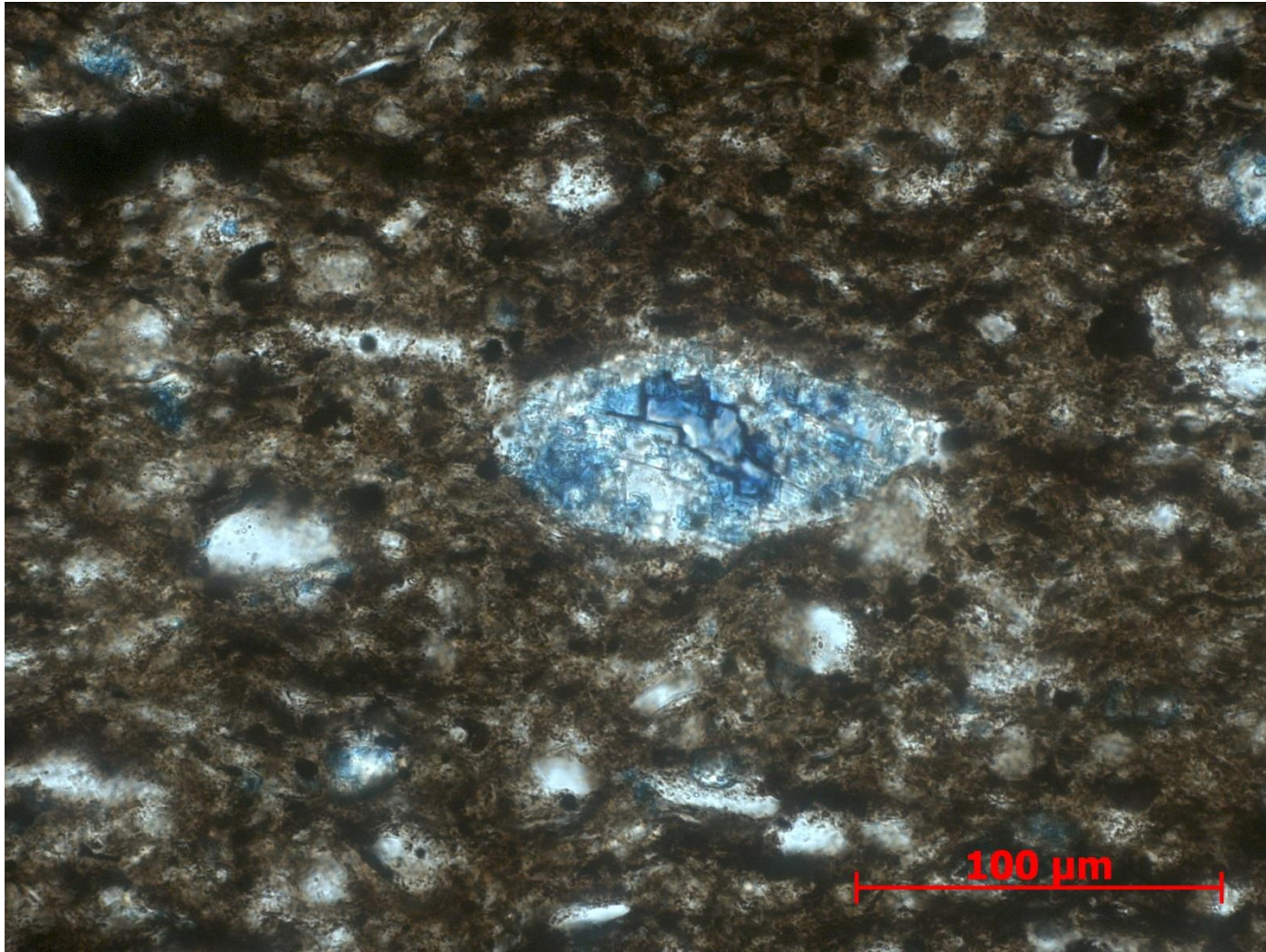


Figure 56. Sample Depth: 9617.17 ft. 40x PPL – Partial ferroan dolomite replacement of compacted radiolaria. High optic relief of rhombohedra, blue dye indicating ferroan dolomite. Primary internal structure of radiolaria destroyed. Silt and detrital quartz matrix also exhibit partial dolomitization.

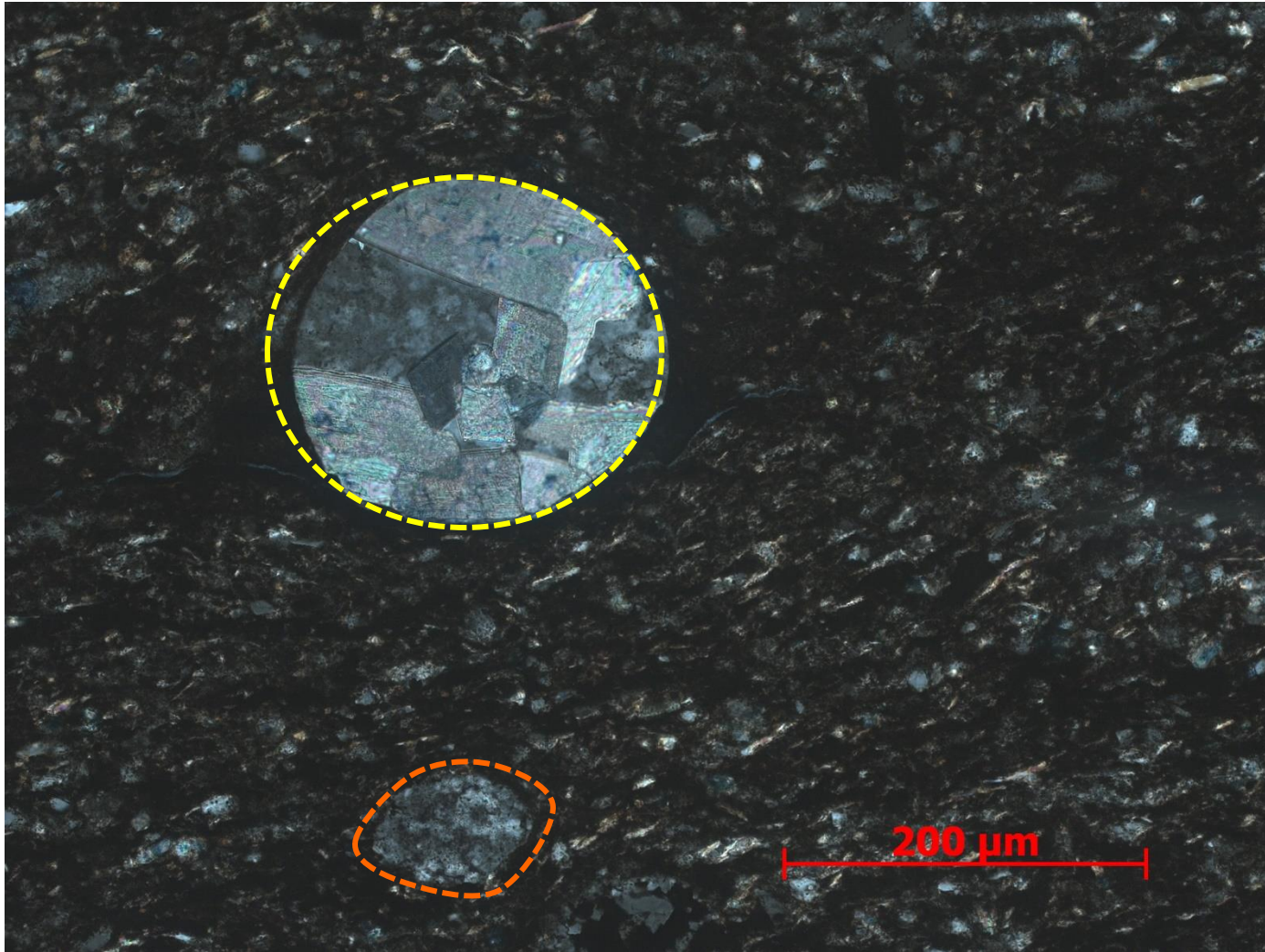


Figure 57. Sample Depth: 9617.17 ft. 20x XPL – Sparry equant calcite replaced echinoderm spine cross-section outlined in yellow. Clays and detrital quartz wrapping around (?) echinoderm spine. Siliceous radiolaria ~ 100 um below in orange. Internal structure and texture still preserved. Detrital quartz, elongated micas and sponge spicule fragments visible.

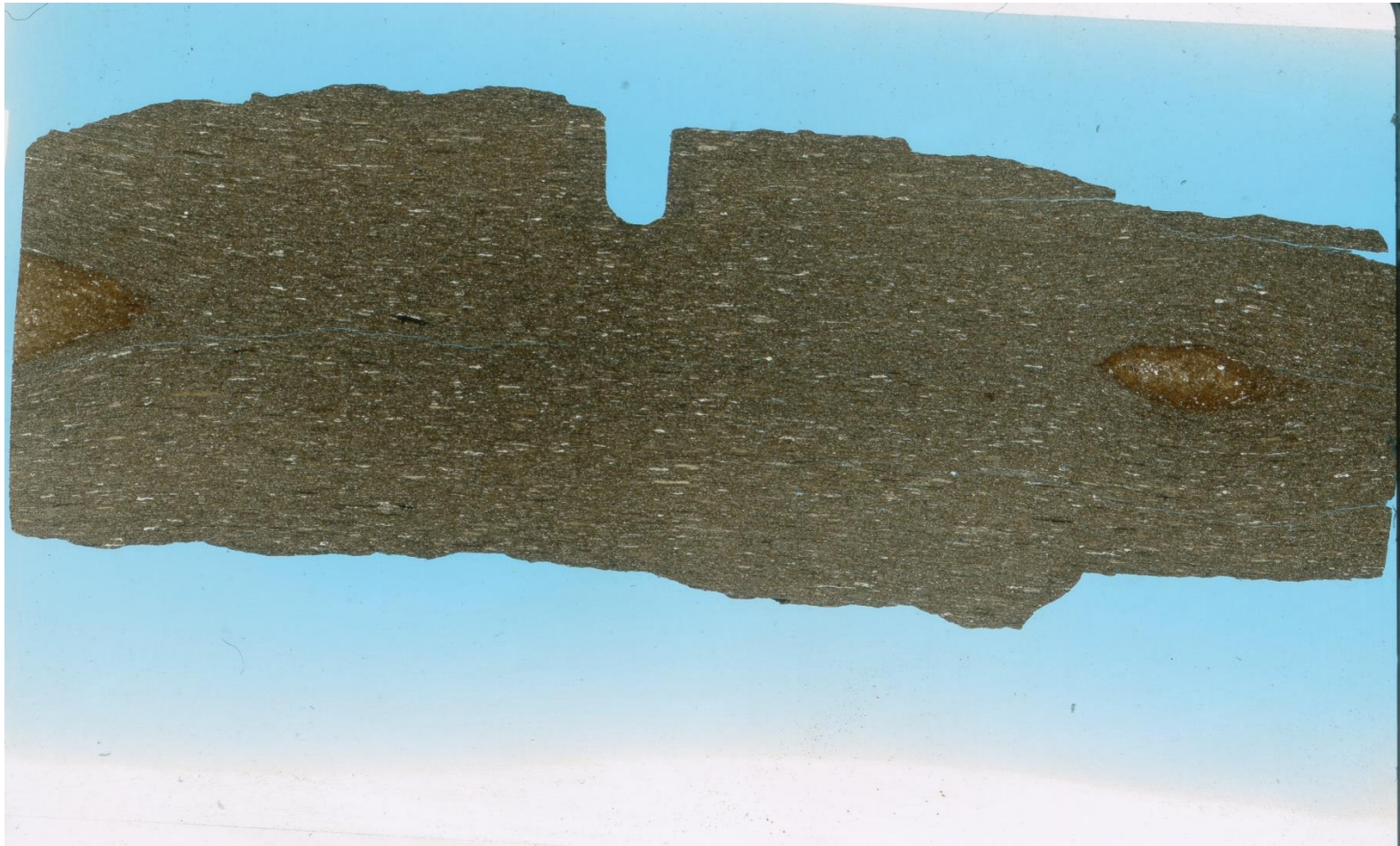


Figure 58. Sample Depth: 9625.17 ft. Mineralogy –small dolomite replacement, little calcite present, mostly as small fragments in matrix, detrital subrounded quartz, clays and micas, OM high. Texture – subtle planar bedding of clays. Bioturbation - Small horizontal burrows (abundant), 2 macroscopic horizontal burrows, filled with siliceous shell fragments. Fauna – tasmanites, partially compressed, OM matter infill, siliceous (few), radiolaria, very few almost absent, abundant agglutinated forams.



Figure 59. Sample Depth: 9625.17 ft. 20x PPL – Compacted tasmanites ~400 um with clay infill. Detrital silt and clay matrix. Partial ferroan dolomite replacement of siliceous grains.

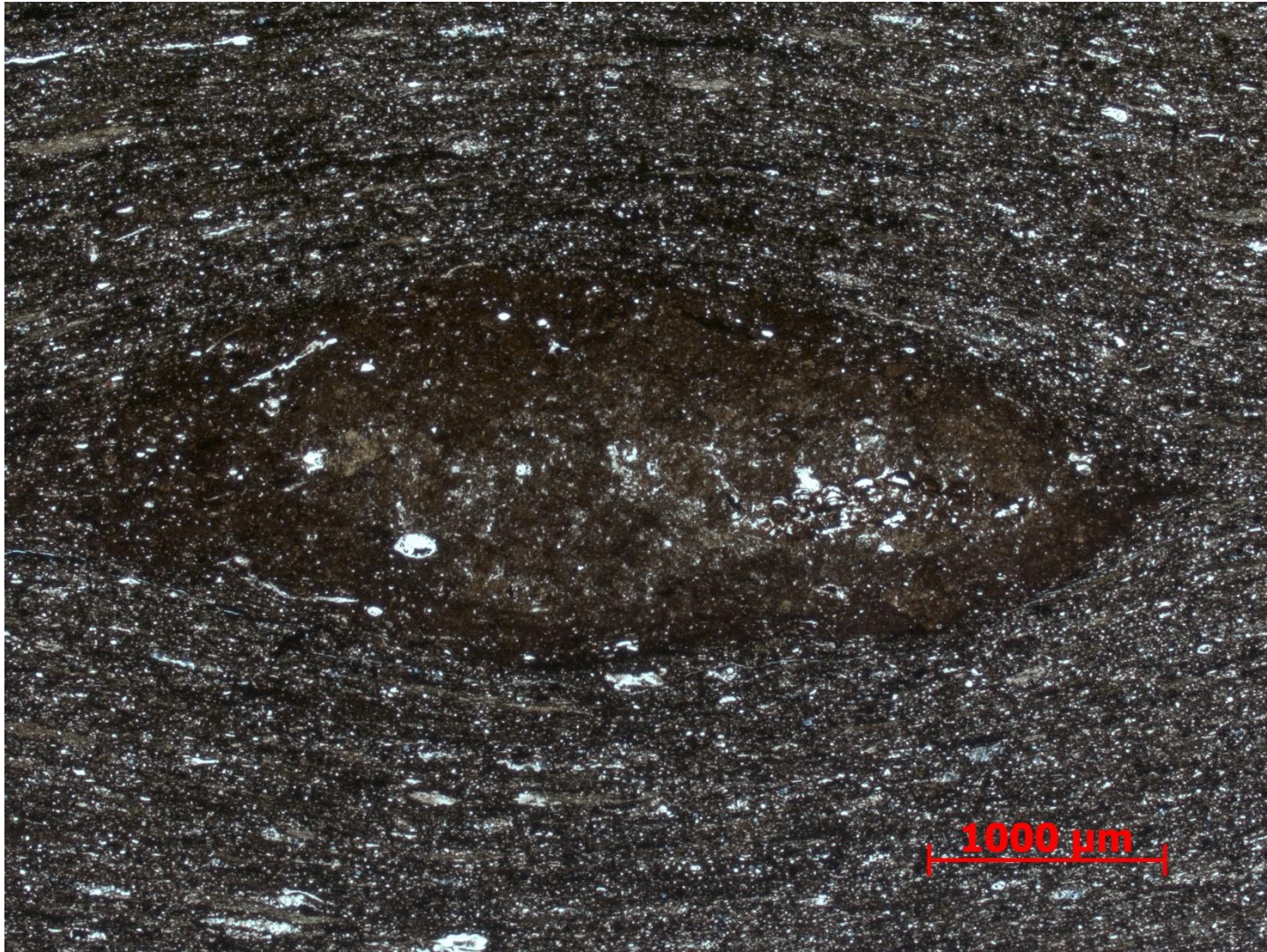


Figure 60. Sample Depth: 9625.17 ft. 2.5 x PPL of large horizontal burrow? macroscopically observed in thin section.

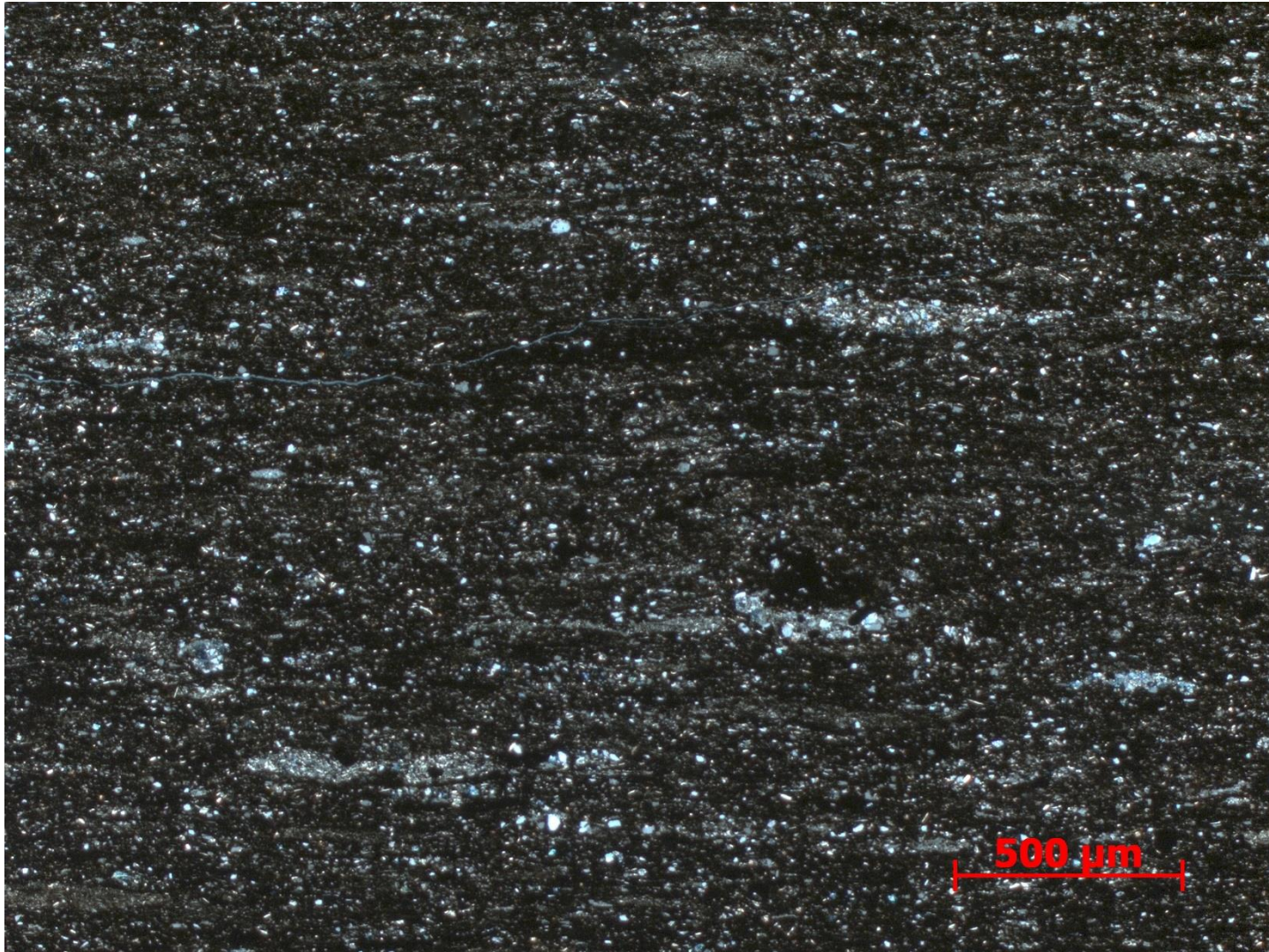


Figure 61. Sample Depth: 9625.17 ft. 5x XPL – Matrix dominated by clay and organic matter dominate. Small 500 nm horizontal burrows infilled with cleaner sediment – partial dolomite replacement visible in burrows. Unlaminated detrital quartz, no evident grain orientation or flow direction, lacks evidence of event deposit



Figure 62. Sample Depth: 9633.17 ft. Mineralogy – lots of detrital quartz and clay, no carbonate, faint dolomite replacement, little OM. Heavily bioturbated, disruption of original lamination. Sub-horizontal burrows defined by cleaner sediment with small lithic fragments. Original sedimentary structures destroyed by bioturbation. Almost entirely silt and detrital quartz. Light brown in color

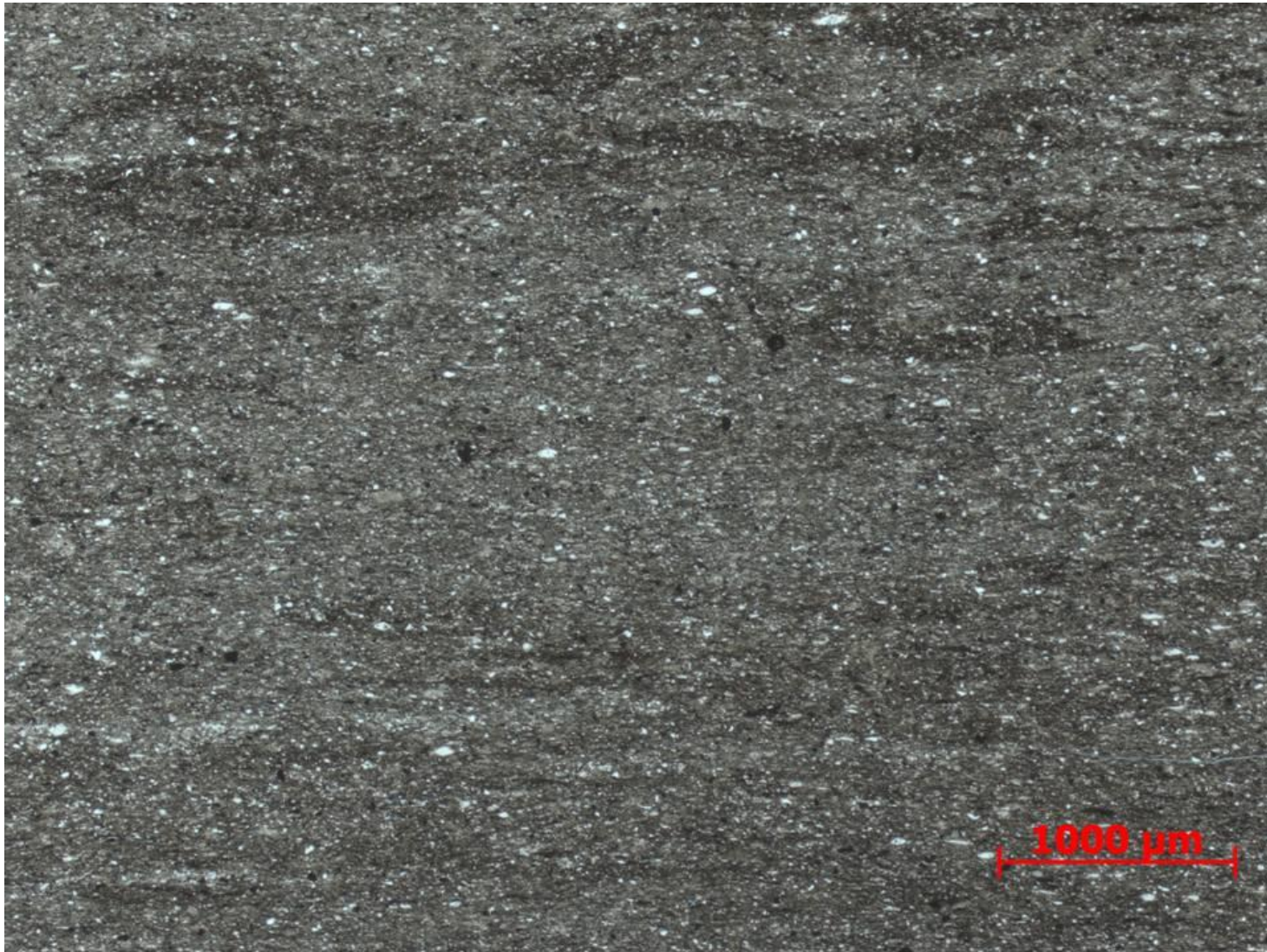


Figure 63. Sample Depth: 9633.17 ft. 2.5x PPL – Clay rich wavy lenses and discontinuous sub-horizontal laminations are unbioturbated portions. Majority of original depositional fabric lost. Minor oxides present. Well rounded detrital quartz, elongated / compacted along bedding plane.



Figure 64. Sample Depth: 9641.17 ft. Mineralogy: (3) argillaceous portion - clay matrix, OM rich, detrital quartz abundant, minimal ferroan dolomite replacement, no calcite (1 & 2) calcareous flows – calcareous skeletal fragments, minor OM, oxides (maybe pyrite?). Texture: calcareous flow (1) – coarser grained, larger skeletal fragments more abundant, less clay, coarse contact marking beginning of flow? normal grading. calcareous flow (2) – finer grained, less and smaller skeletal fragments, less clay, micrite matrix? coarse contact marking beginning of flow? normal grading. (1) argillaceous dominant – horizontal parallel orientation of agglutinated fauna and burrows, very fine grained clay, OM in planar lamination under, more abundant right below calcareous flows (may be a function of too thin of a TS towards bottom). Bioturbation: calcareous flow (2) – vertical burrows, cleaner, finer grained material, dendritic downwards pattern (3) argillaceous dominant – silt/ cleaner, coarser sediment horizontal burrows. Fauna: argillaceous portion (3) - agglutinated forams (abundant), *Tasmanites*. calcareous flows (1 & 2) – echinoderm spines, micritized radiolaria?, undifferentiated skeletal fragments – calcite replacement obliterating internal structure, sub rounded to rounded from transport, lithic fragments – sub rounded, rare siliceous radiolaria

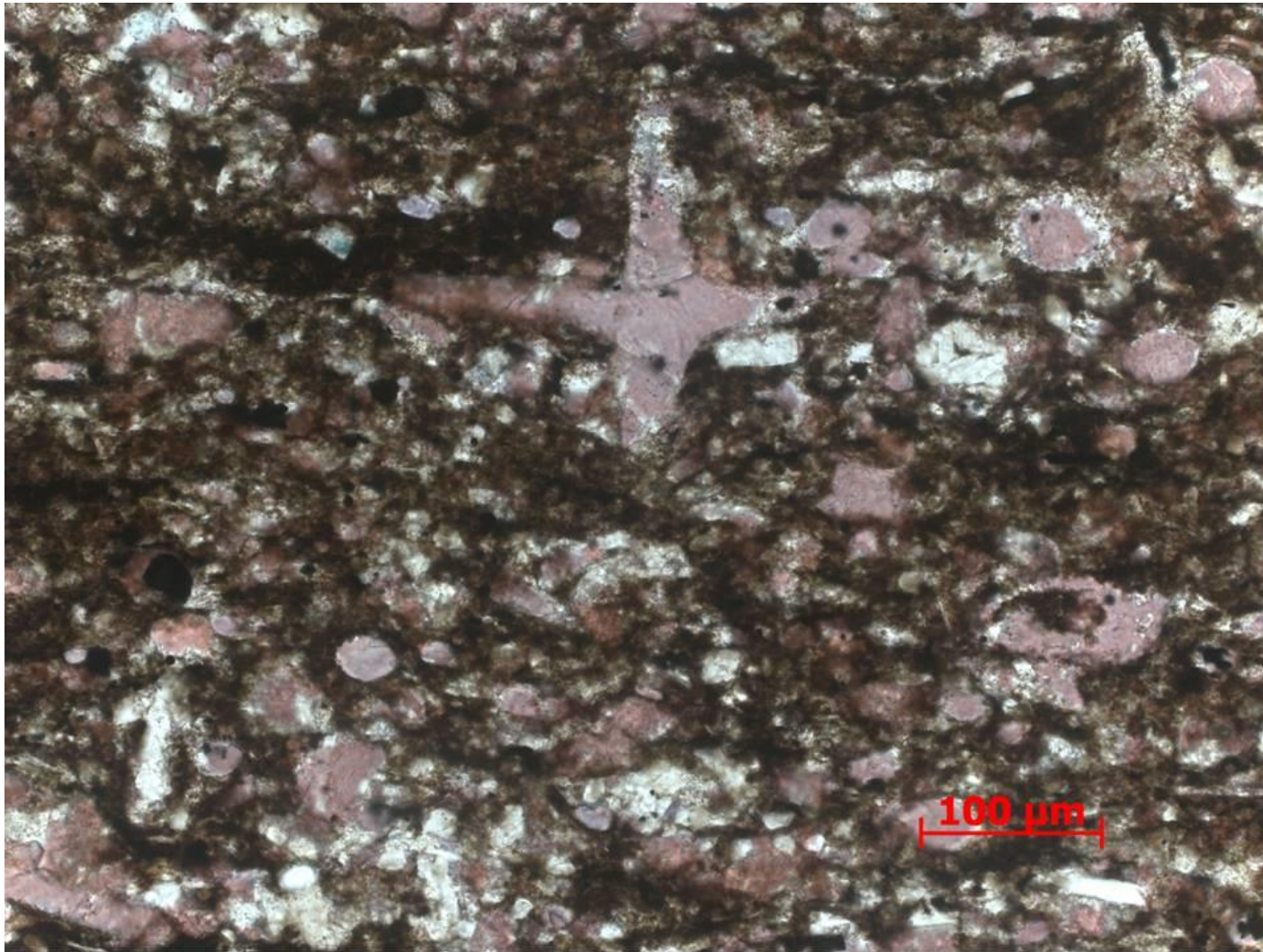


Figure 65. Sample Depth: 9641.17 ft. 20x PPL – Bottom 1/3 of slide. Packed biomicrite - Cross-section of calcareous sponge spicule 200 μm across with diagnostic “t” shape. Well rounded, abraded calcareous fragments - echinoderm spines and radiolaria(?). Difficult to identify skeletal remains due to extensive abrasion. Partial dolomitization of entire grains and grain edges. Ferroan dolomite present but in trace quantities. Cement present but not heavy due to amount of clays / micrite present.

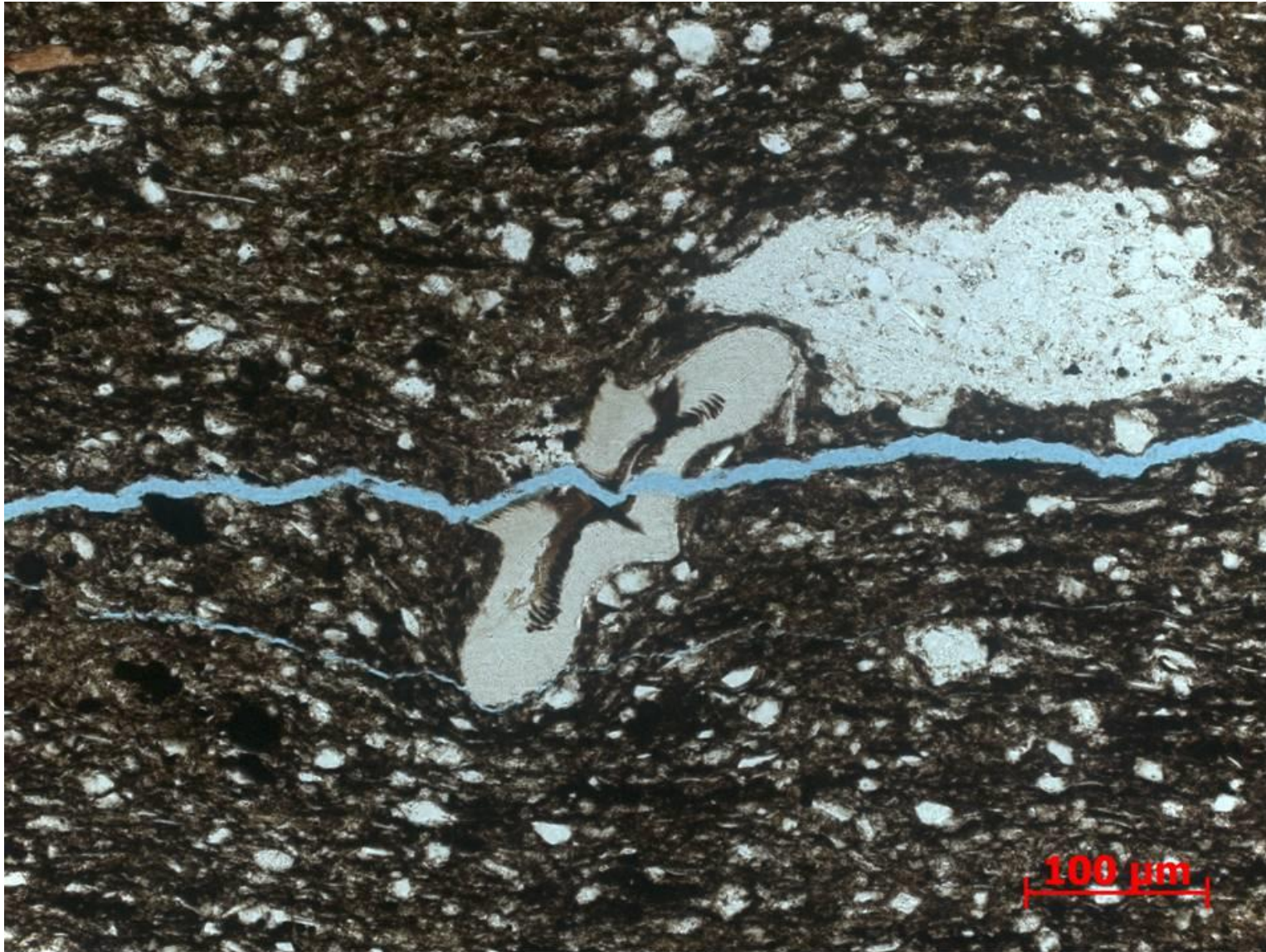


Figure 66. Sample Depth: 9641.17 ft. 20x PPL – Top 1/3 of thin section. 200 μm *Tasmanites* infilled with organic matter adjacent to detrital quartz lithoclast. Matrix rich in clay and organic material. Subrounded to well rounded, silt-sized, and elongate detrital quartz.

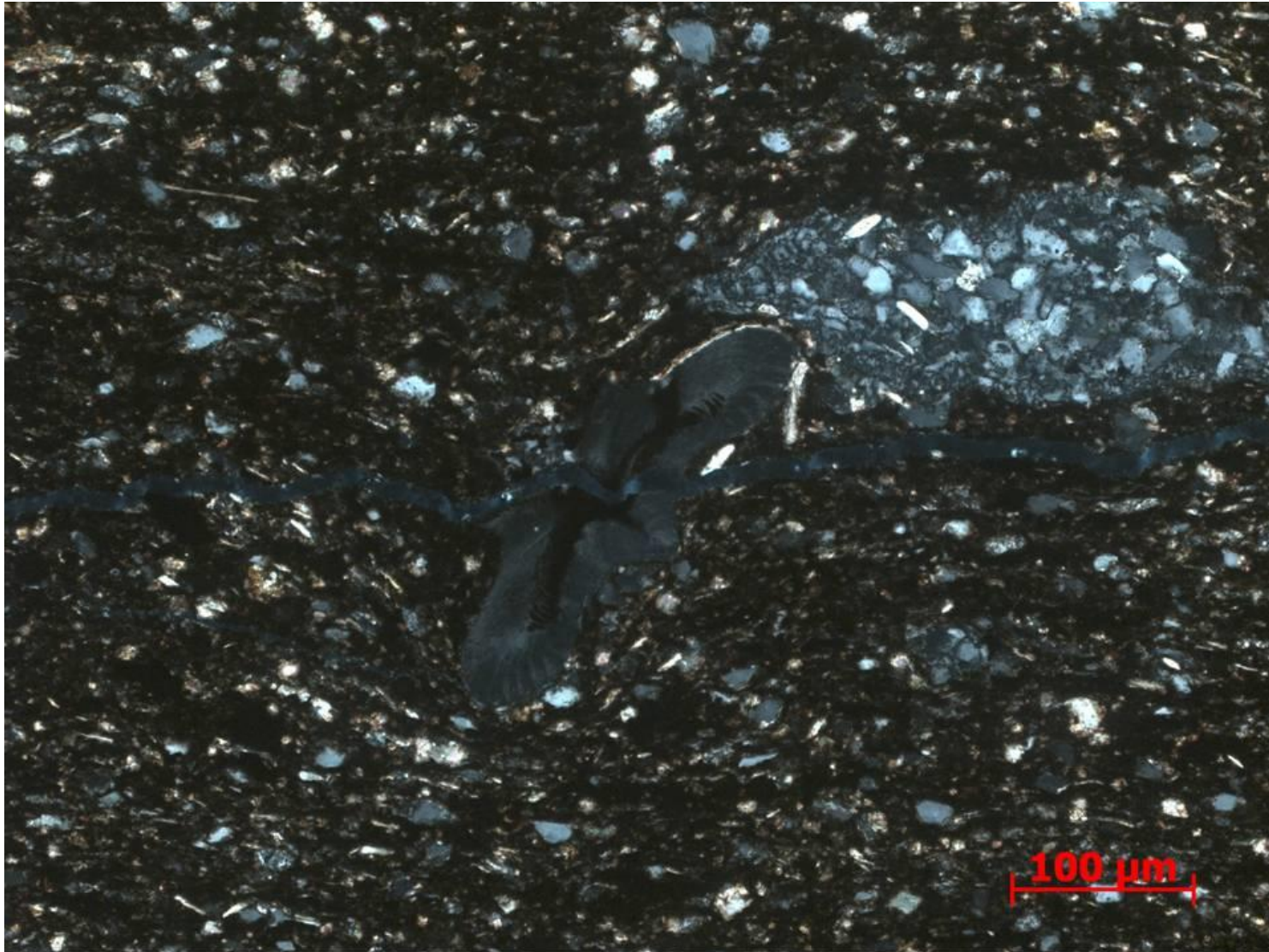


Figure 67. Sample Depth: 9641.17 ft. 20x XPL – Cross-polarized version of previous photograph. Adjacent lithoclast (?) comprised of mainly detrital quartz and equant feldspars. Tasmanites comprised of amorphous silica/ chert. Matrix comprised of detrital fine grained silt sized quartzs, clays (elongate micas visible), and organic matter.



Figure 68. Sample Depth: 9641.17 ft. 10x PPL - Top 1/3 of thin section. Large agglutinated foram (~800 μm) in same detrital quartz, clay, and organic matter rich matrix. Ferroan dolomite replacement of some detrital quartz grains and radiolaria.

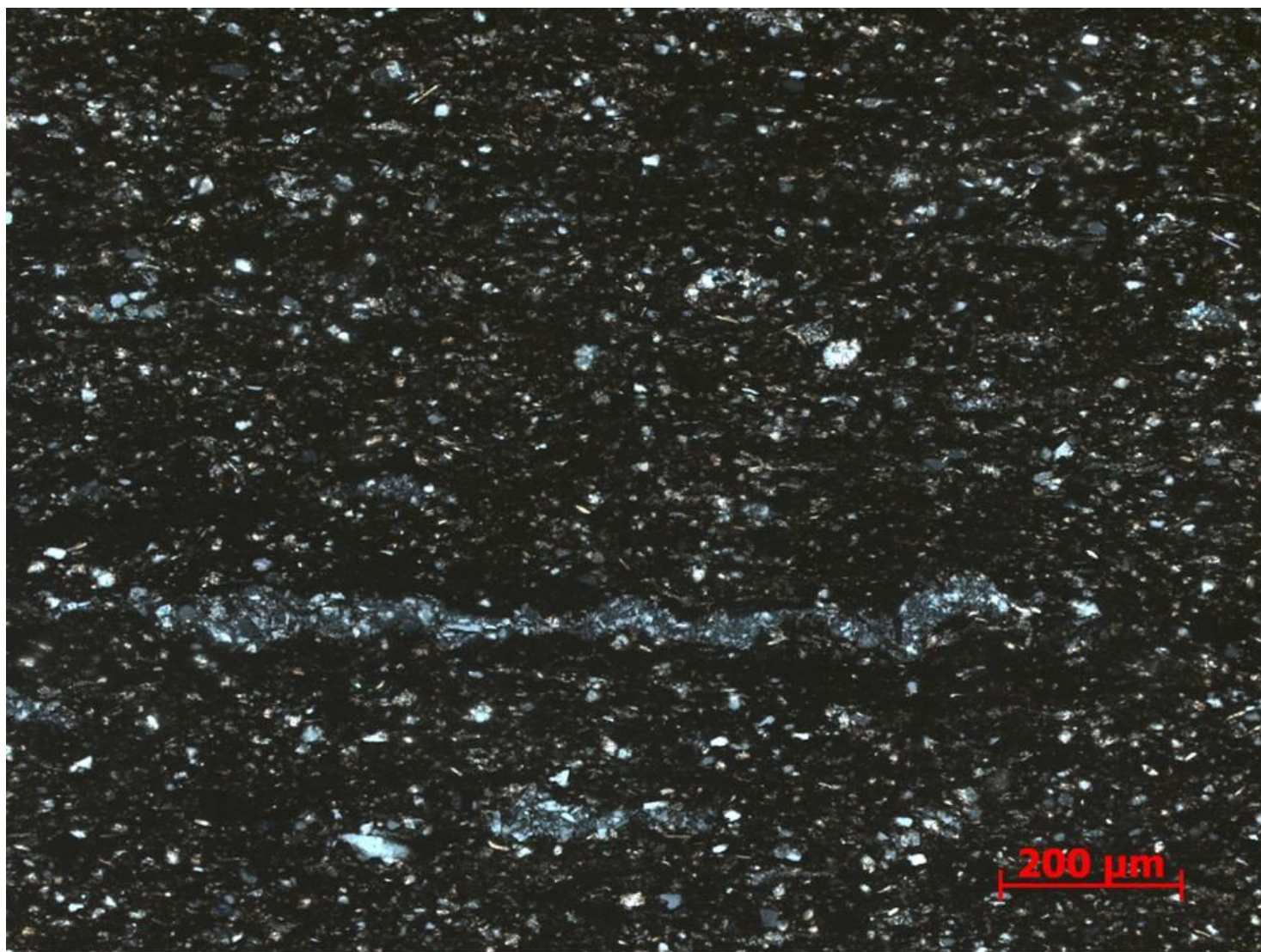


Figure 69. Sample Depth: 9641.17 ft. 10x XPL - Cross-polarized version of previous photograph. Agglutinated foram composition visible: grain to grain contact of subrounded detrital quartz. Differentiated from *tasmanites* via scale and crystal structure (or lack there of) of silica.



Figure 70. Sample Depth: 9641.17 ft. 2.5x PPL - Middle 1/3 of thin section, second calcareous flow event. More clay particles in second flow event relative to bottom 1/3 of thin section. Faint vertical, dendritic burrows (?) or potentially fluid escape or dewatering structures. Reverse grading visible – coarser towards top of event. Well rounded undifferentiated carbonate skeletal fragments.



Figure 71. Sample Depth: 9644.67 ft. Mineralogy – Carbonate flow: highly cemented, predominately calcite, but some random banding of dolomite – diagenetic front? OM present towards bottom of flow as discontinuous bands. No quartz. Small pyrite crystals Non calcareous flow? – increased clay content, decreased grain size. Diagenetic replacement of fragments however matrix not cemented like flow below, no visible quartz although diagenetic replacement of detrital grains possible. Texture – Carbonate flow below visible – highly diagenetically altered – about 2 faint flows above main flow (scan entire TS to see), coarsening upwards, better sorting with no fines upwards, more prevalent dolomitization Less calcareous flow on top? – micritic but definitely more arg. Clay present, more OM present Bioturbation: Faint bioturbation / horizontal burrows towards top above carbonate flow – different grain size inside burrow? Fauna – very diagenetically altered– difficult to pinpoint fauna but multichambered forams, high diversity, echinoderm spines, brachiopod shell fragments; other more clay rich flow? above has diagenetically alter clasts but brachiopod shells, echinoderm spines visible.



Figure 72. Sample Depth: 9644.67 ft. 2.5x XPL – Banded portion in upper half of thin section. Matrix composed of small abraded, subrounded calcareous lithoclasts, detrital quartz, and clays with ferroan dolomite replacement cement. Distorted discontinuous clay lamination in center. Small oxides prevalent.

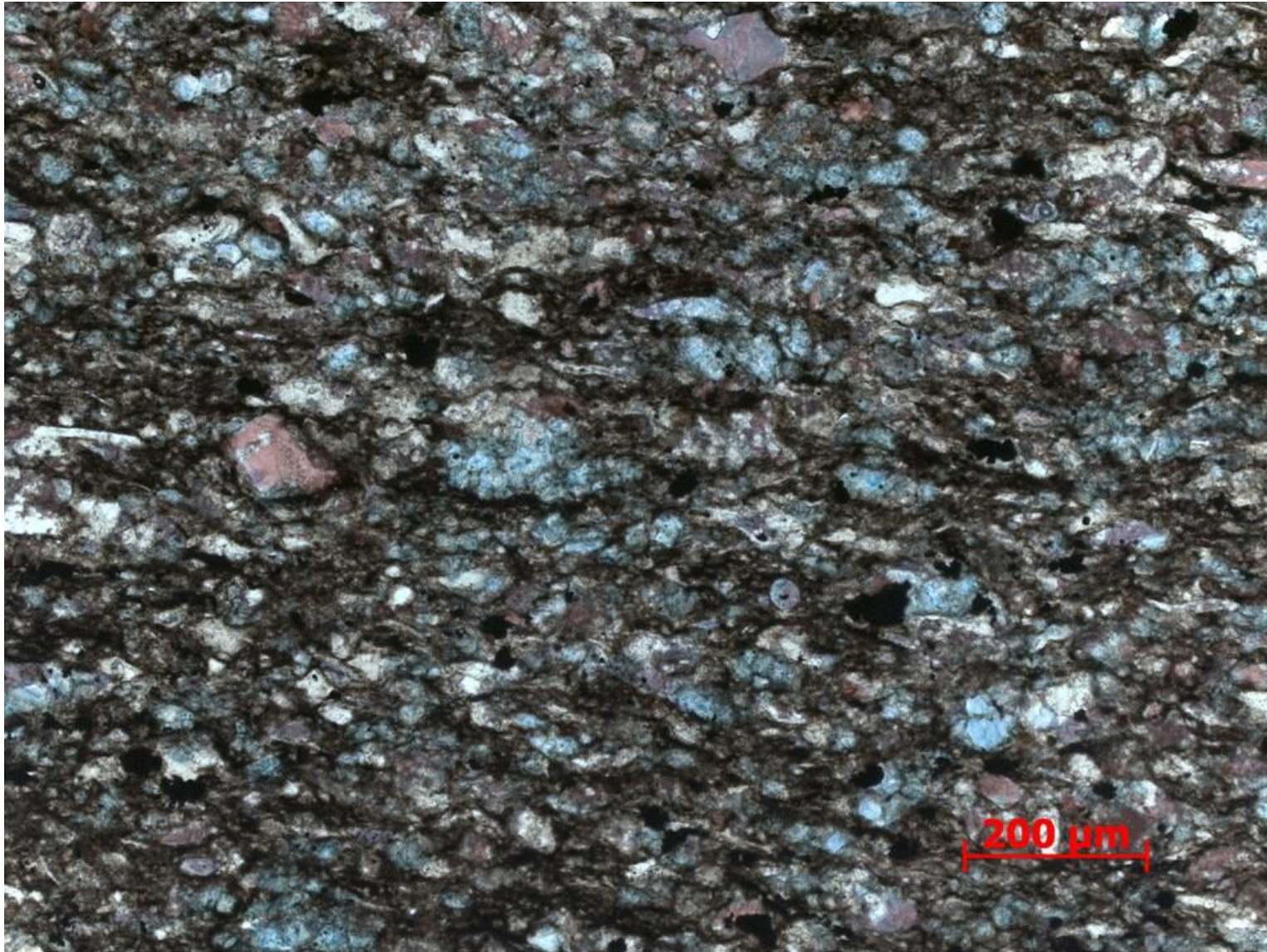


Figure 73. Sample Depth: 9644.67 ft. 10x PPL – Magnified laminated upper portion of thin section – Carbonate (dolomite, calcite and ferroan dolomite) allochems and silt sized lithoclasts mud supported. Grain boundary dissolution extensive, difficult to identify certain allochems with minor exceptions – dolomitized 100 um foram in center.



Figure 74. Sample Depth: 9644.67 ft. 2.5x XPL – Contact between calcareous lower half of thin section and upper mixed siliciclastic and carbonate portion. Inclined discontinuous clay laminations. Small clay rip ups and oxides present to lower degree in bottom portion. Clays limiting the extent of matrix cement in upper portion.

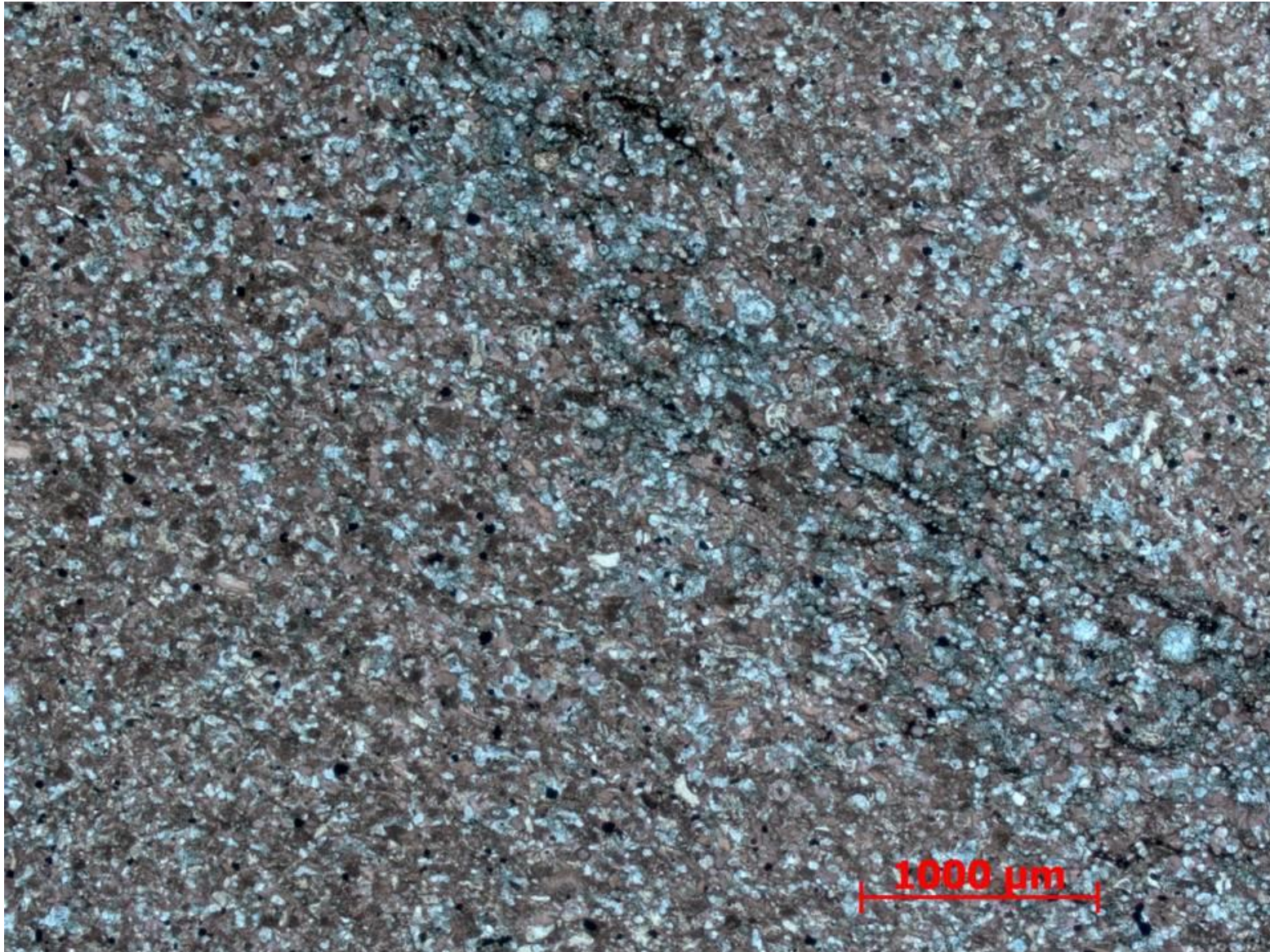


Figure 75. Sample Depth: 9644.67 ft. 2.5x PPL – Extensive ferroan dolomite intergranular and replacive cement band / fluid front in blue stain along mixed carbonate (dolomite, calcite and ferroan dolomite) allochems.



Figure 76. Sample Depth: 9645.17 ft. Mineralogy – highly cemented, predominately dolomite interclast infill (blue), calcite intraclast are cement, lots of dissolution on shell fragment edges, hard to identify fauna and taxa, very little OM present but visible, no clays visible, very little to absent. Texture – Clay laminations visible macroscopically. Grains and skeletal fragments very difficult to distinguished – diagenetic overprint, randomly oriented grains and shell fragments, evidence of transport, well sorted. Bioturbation: none. Fauna – multichambered forams, high diversity, echinoderm spines, brachiopod shell fragments

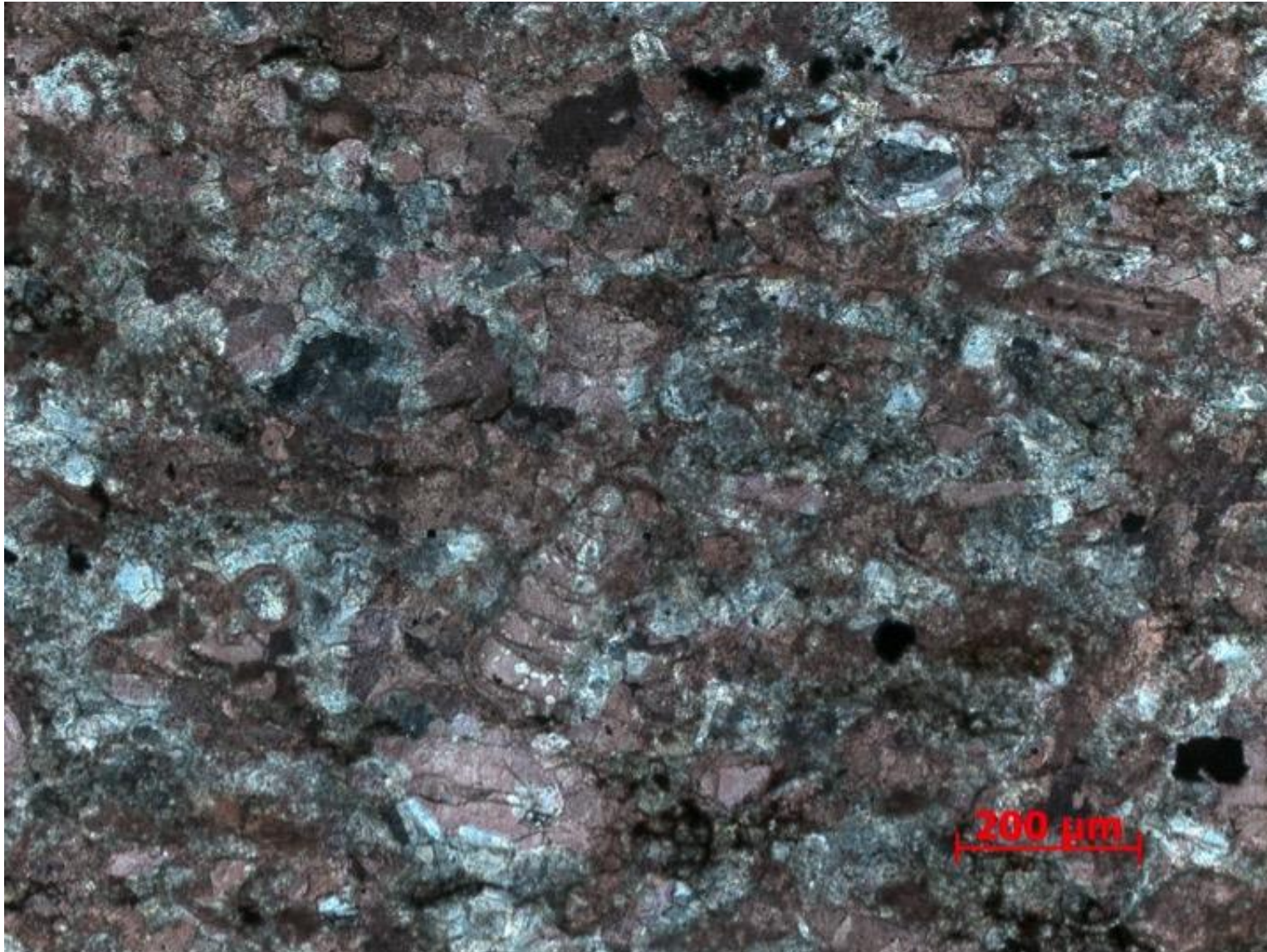


Figure 77. Sample Depth: 9645.17 ft. 10x XPL – Heavy intergranular, equant sparry predominately ferroan dolomite cement. Allochem identification difficult due to heavy grain boundary dissolution. Multichamber forams and echinoderm spines visible. Small angular oxides and potential organic material. Minor amounts of mud – packstone to poorly washed packed biosparite

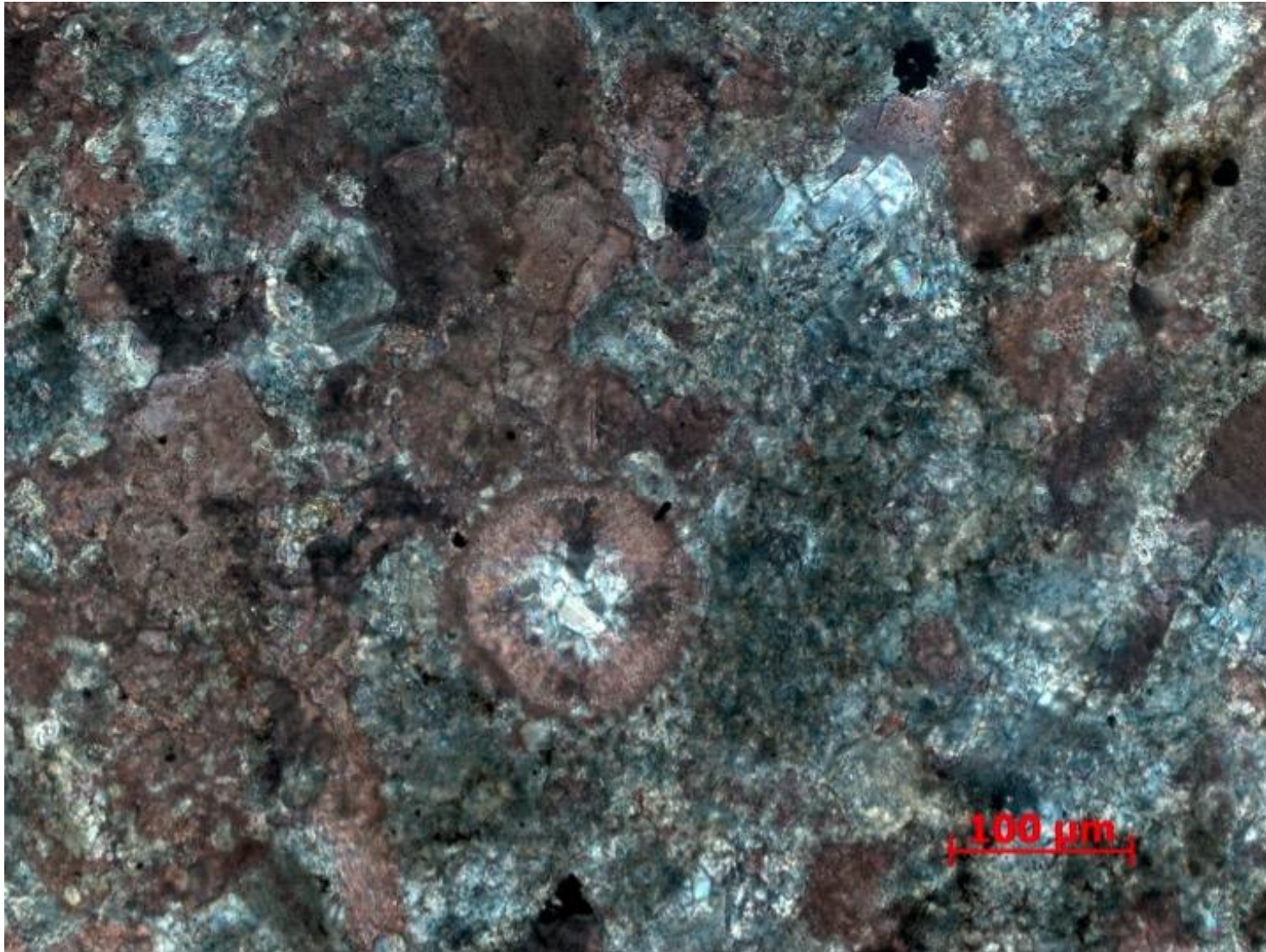


Figure 78. Sample Depth: 9645.17 ft. 20x XPL – Aragonite ooid (“maltese cross” / aragonite extinction pattern) with late rhombic intragranular ferroan dolomite cement in center – potentially long transport distance. Heavy grain edge dissolution and replacive cement – difficult to distinguish allochems. Calcite and ferroan dolomite cement.

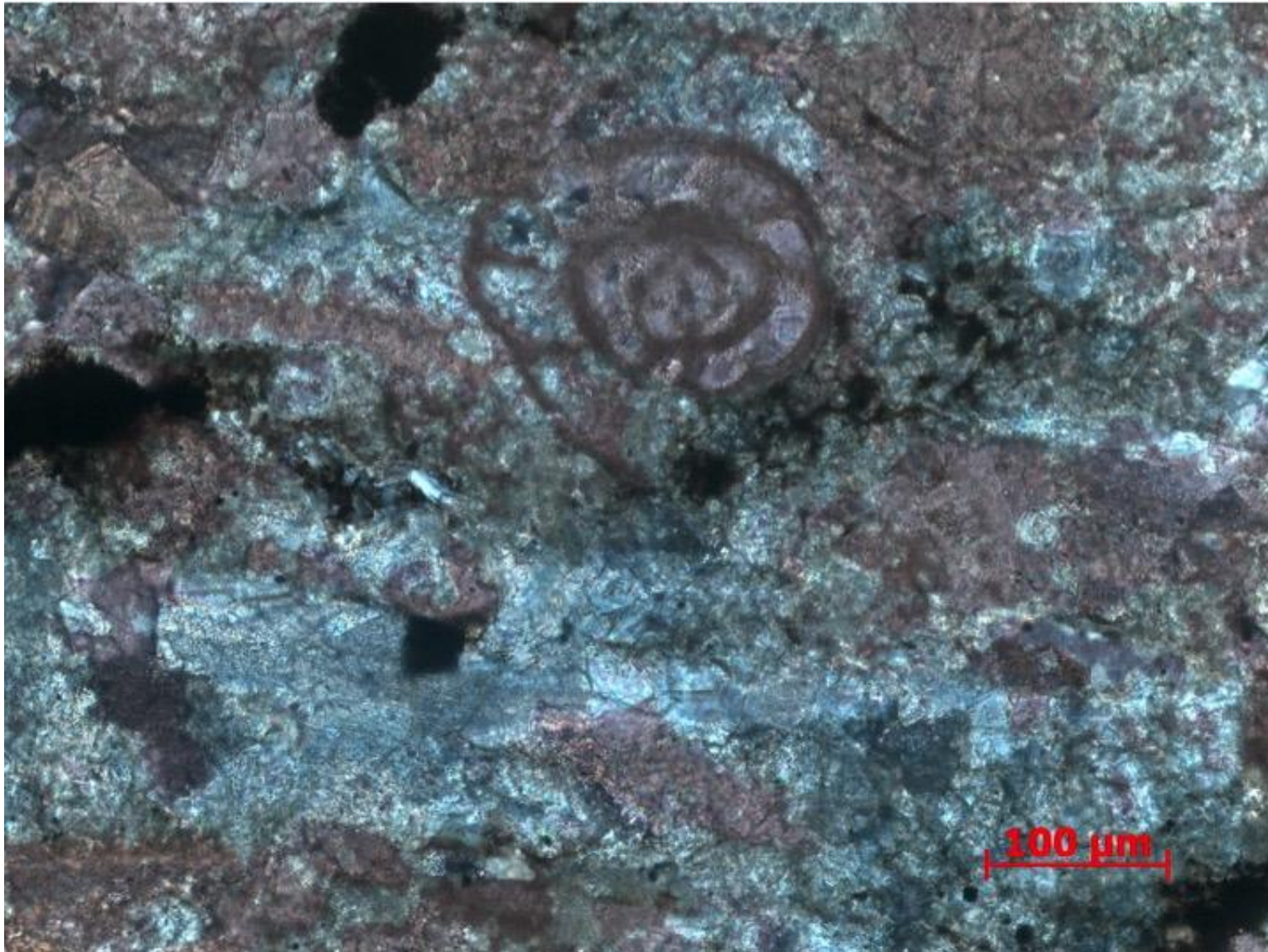


Figure 79. Sample Depth: 9645.17 ft. 20x XPL – Calcite foram with sparry ferroan dolomite and calcite intragranular cement in chamber interior. Grain boundary dissolution pervasive. Heavily cemented, much of primary fabric destroyed besides partial allochem preservation. Amorphous oxides present, no distinct framboids visible.



Figure 80. Sample Depth: 9647.84 ft. Mineralogy: volcanic ash converted to some clay mineral? Dolomite and calcite replacement, minor clay and OM, oxides, minor quartz component. Texture: banded clay/volcanic ash – grain on grain contact due to alteration, silty interbeds. Bioturbation: potential horizontal burrows in non (ash?) banded areas, coarser grained on inside. From ash beds into silt rich finer grained material, vertical burrows?? Or fluid escape – unknown since both extending up and down. Fauna: radiolaria (diagenetically altered – ferroan dolomite mostly

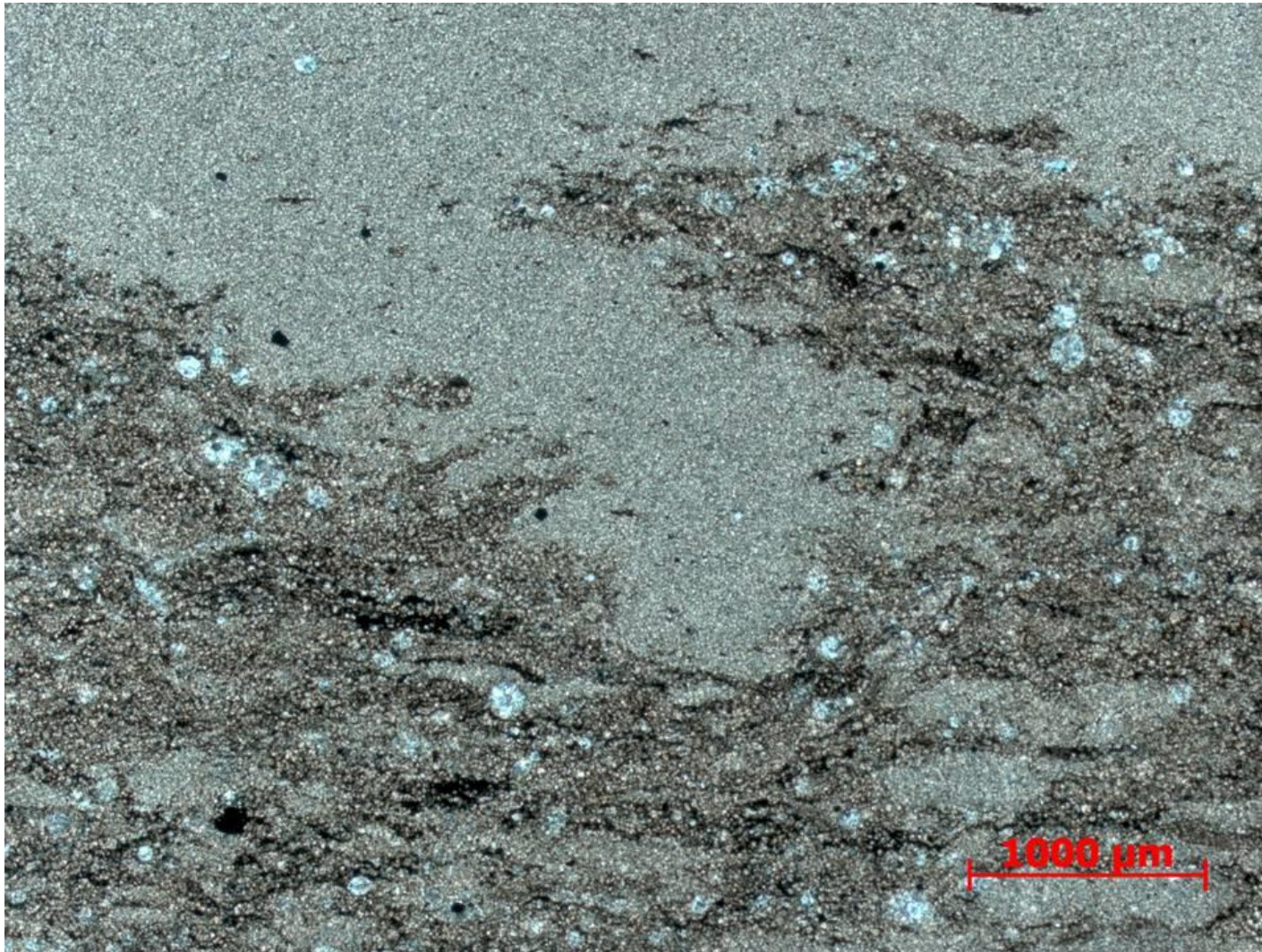


Figure 81. Sample Depth: 9647.84 ft. 2.5x XPL – potentially vertical burrow or downward fluid escape structure(?) interpreted from upward direction of other vertical perturbation from band well-sorted fine-grained material (see previous full thin section scan). Cleaner, homogeneous grains in bands light tan bands. Darker brown bands consist of more heterogenous matrix – clay rip ups and high clay content in matrix. Ferroan dolomite replace radiolaria and other rounded skeletal fragment allochems. Partial isolated portions of homogeneous cleaner material, ~ 1000 um in width.

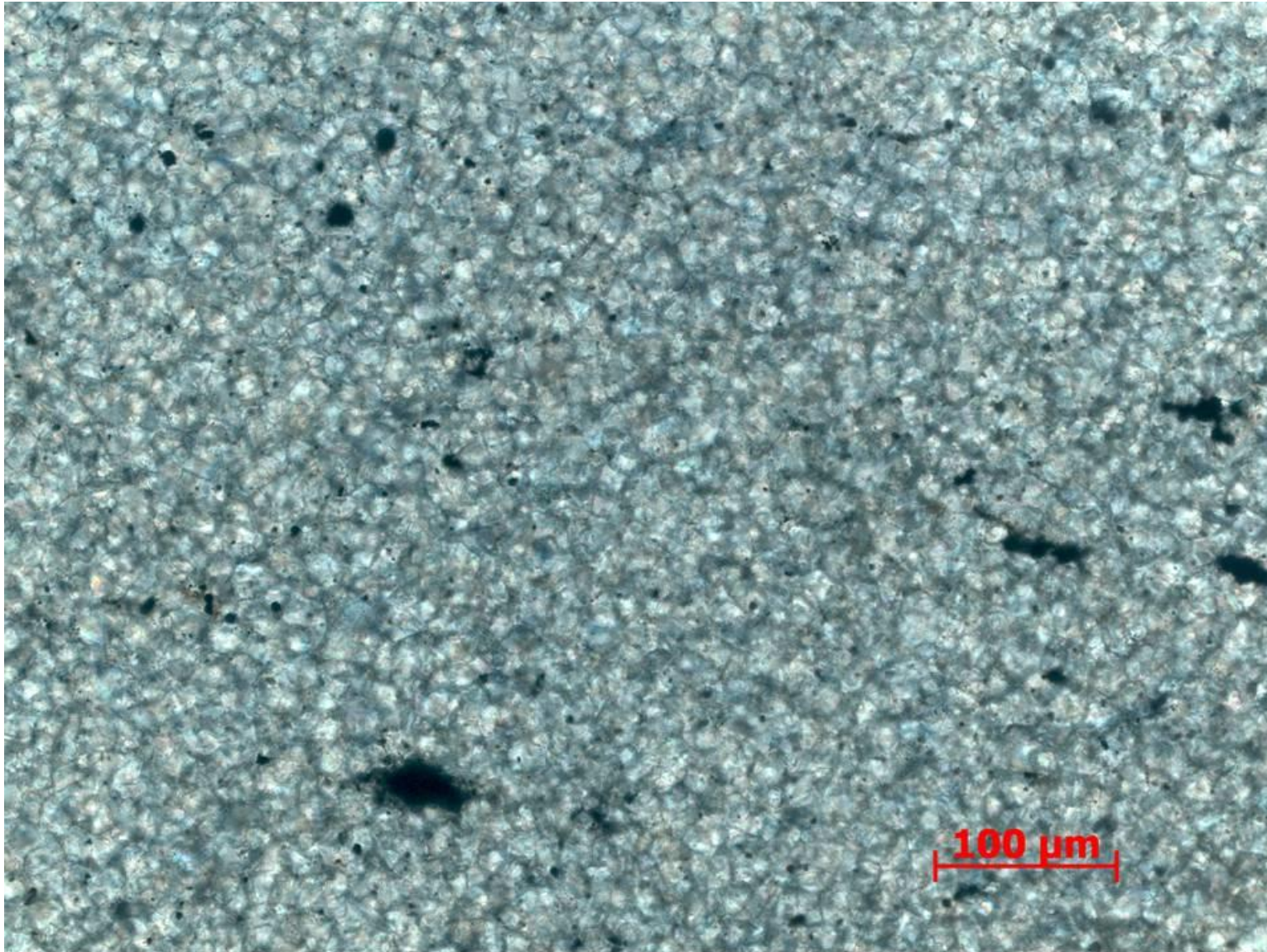


Figure 82. Sample Depth: 9647.84 ft. 20x XPL – Light brown homogenous cleaner band. Potentially alteration of some volcanic ashes or silts? Completely cemented with dolomite and ferroan dolomite. Partial grain boundary dissolution.



Figure 83. Sample Depth: 9647.84 ft. 10x XPL – Dark brown heterogeneous bands. Intergranular ferroan dolomite cement more pervasive. Clay and organic material in matrix. Interlocking ferroan dolomite replaced(?) grains.

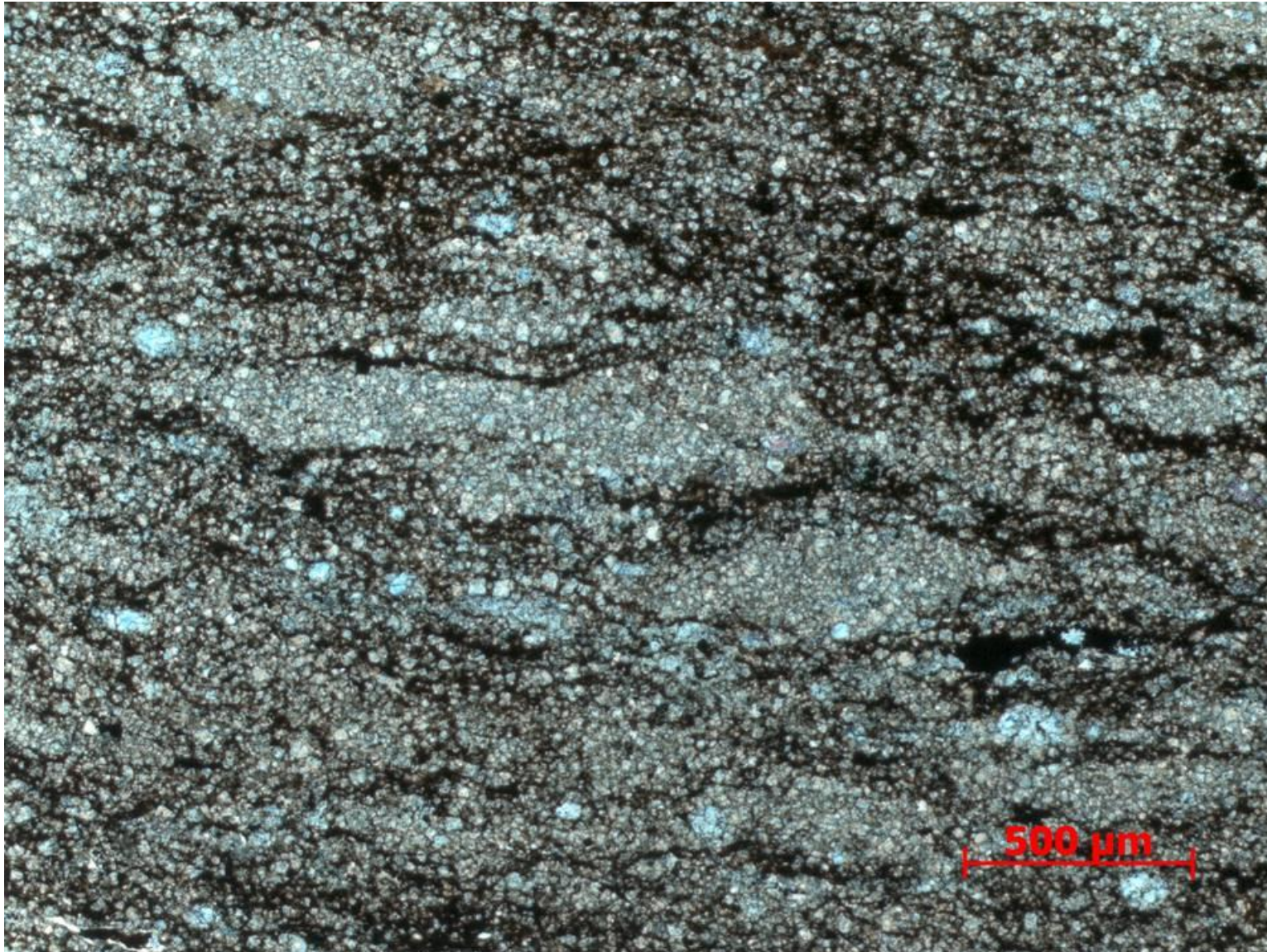


Figure 84. Sample Depth: 9647.84 ft. 5x XPL – ~1000 μm lobes (probably lithoclasts but potentially unidentifiable horizontal burrows) of cleaner homogenous grains (as visible in light brown bands) mixed in with dark brown clay and organic rich material. Ferroan dolomite replacive cement more apparent in darker brown bands.



Figure 85. Sample Depth: 9649.17 ft. Mineralogy: Ferroan dolomite (white), calcite (pink), clays (brown), and micrite cements. Bottom quarter mostly comprised of calcite and ferroan dolomite. Upper portion contains more clays and rounded and elongate peloids? Contact between Lower quarter and upper portion relatively diffuse. Upper portion grains exhibit planar to subplanar inclinations, Grain boundaries diffuse due to heavy cementation / diagenetic overprint.

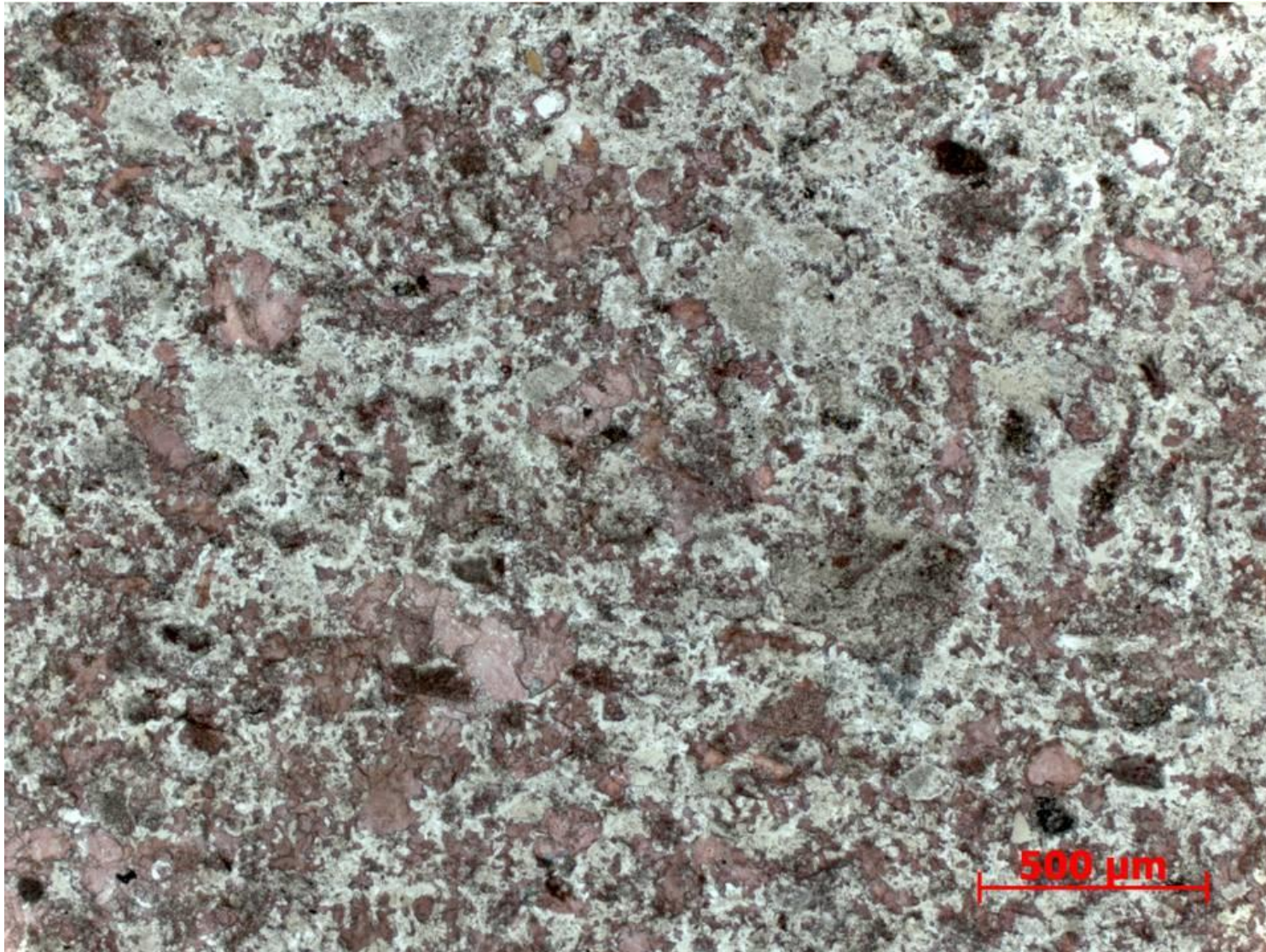


Figure 86. Sample Depth: 9649.17 ft. 5x PPL – Lighter colored bottom $\frac{1}{4}$ of thin section. Heavy ferroan dolomite cementation (white) overprinting original fabric. Allochem grain boundaries diffuse and overprinted, difficult to discern allochem types and origins. Sub rounded to rounded peloids (?) present but not abundant. Random grain orientation.

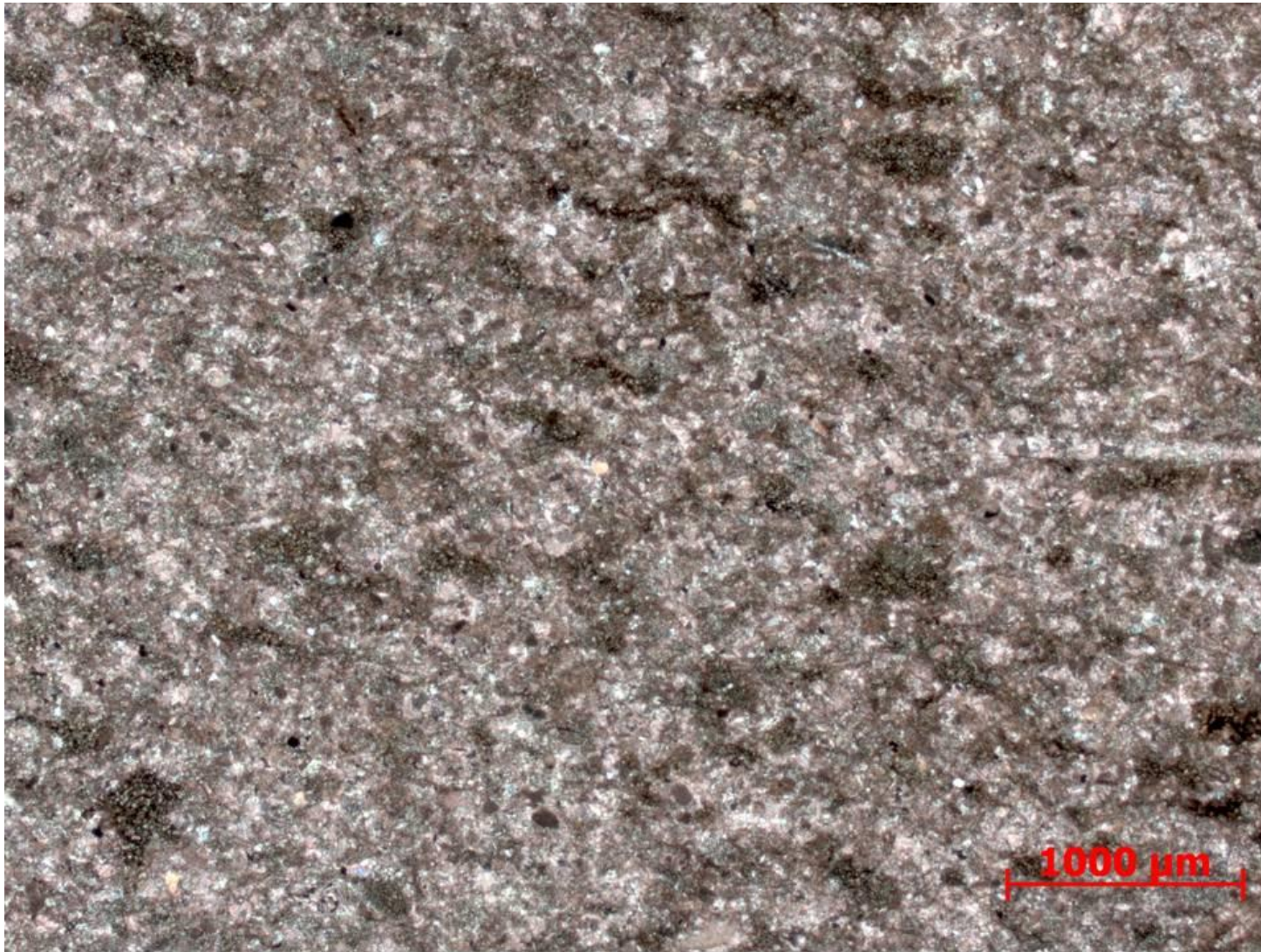


Figure 87. Sample Depth: 9649.17 ft. 2.5x PPL – Darker colored upper $\frac{3}{4}$ of thin section. Echinoderm spines on right of image. Abundant possible peloids or rounded rip up clasts with organic matter and clay. Significantly more clay than bottom $\frac{1}{4}$ of thin section.

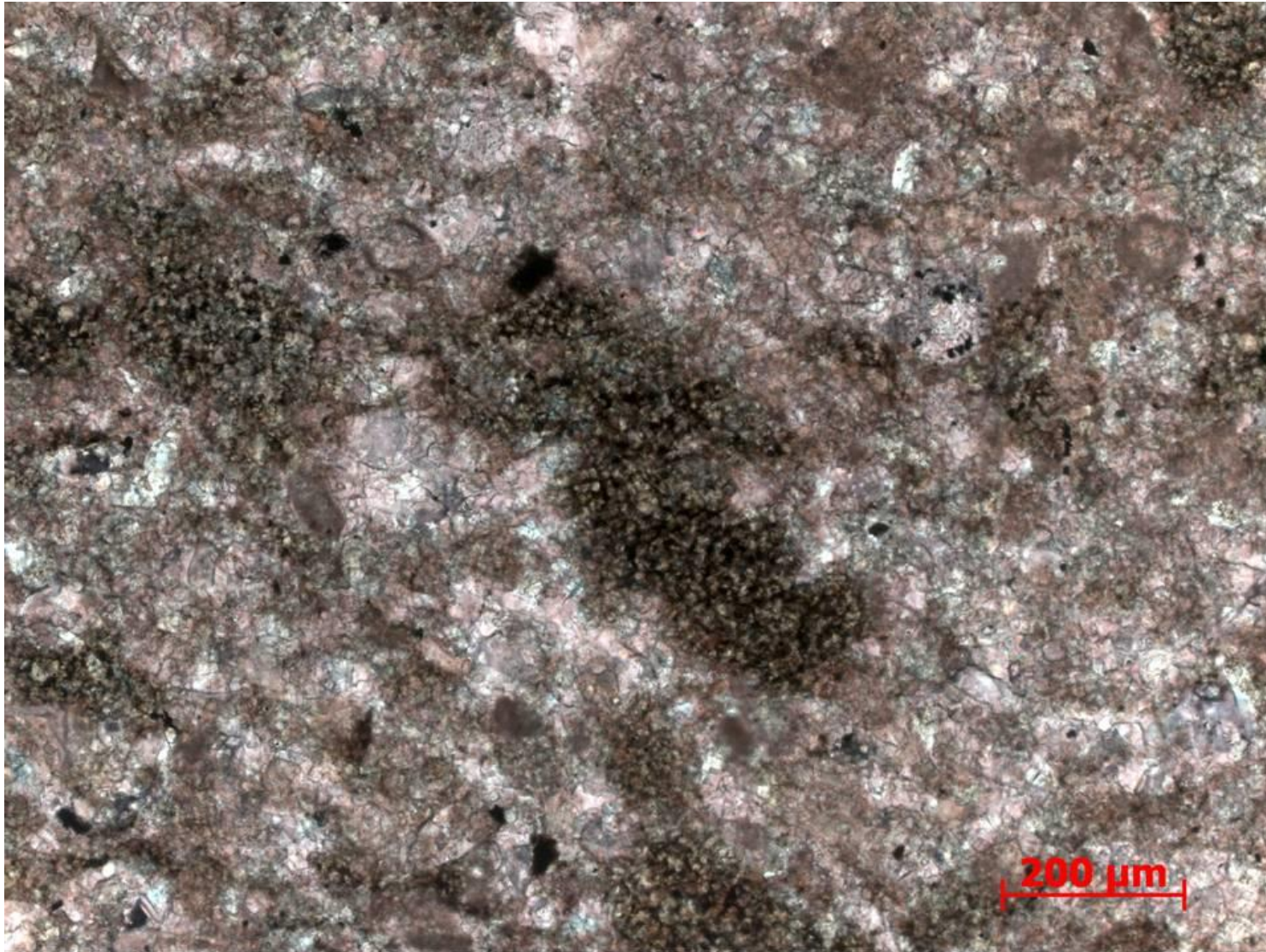


Figure 88. Sample Depth: 9649.17 ft. 10x PPL – Darker colored upper $\frac{3}{4}$ of thin section. Large diffuse grains, potentially peloids. Micritized internal structure and abundant organic matter. Calcite and ferroan dolomite interparticle cements. Allochems are readily distinguishable due to heavy diagenetic overprint.



Figure 89. Sample Depth: 9649.17 ft. 40x PPL – Darker colored upper $\frac{3}{4}$ of thin section. Approximately 110 μm diameter radiolaria with partially preserved intimal structure. Calcite mineralogy with some ferroan dolomite overprint. Diffuse edges due to cementation. Matrix overprinted with cement. Diffuse brown areas may reflect original peloids that were cemented over. Stippled internal texture of some allochems may reflect partial grain dissolution and internal porosity.



Figure 90. Sample Depth: 9653.17 ft. Mineralogy: Bottom portion: matrix micritic (or patchy carbonate cement?) with very little clays, some OM discontinuous fragments calcareous shell fragments with grain dissolution, cement overprint. Partially dolomitize fragments. Top portion: clay matrix and dolomite lithic fragments and *Tasmanites*. Texture – changes from predominately calcareous with clay content present, abundant shell fragments to clay and OM dominant - somewhat sharp contact towards (non-erosive). For calcareous portion – calcareous shell fragments increase towards top, changes from random orientation to parallel laminations of fragments as you go upwards. Bioturbation: n/a Fauna: Top siliciclastic portion – *Tasmanites* Bottom portion – radiolaria – internal structure obliterated by diagenetic overprint, brachiopod shell fragments (small)

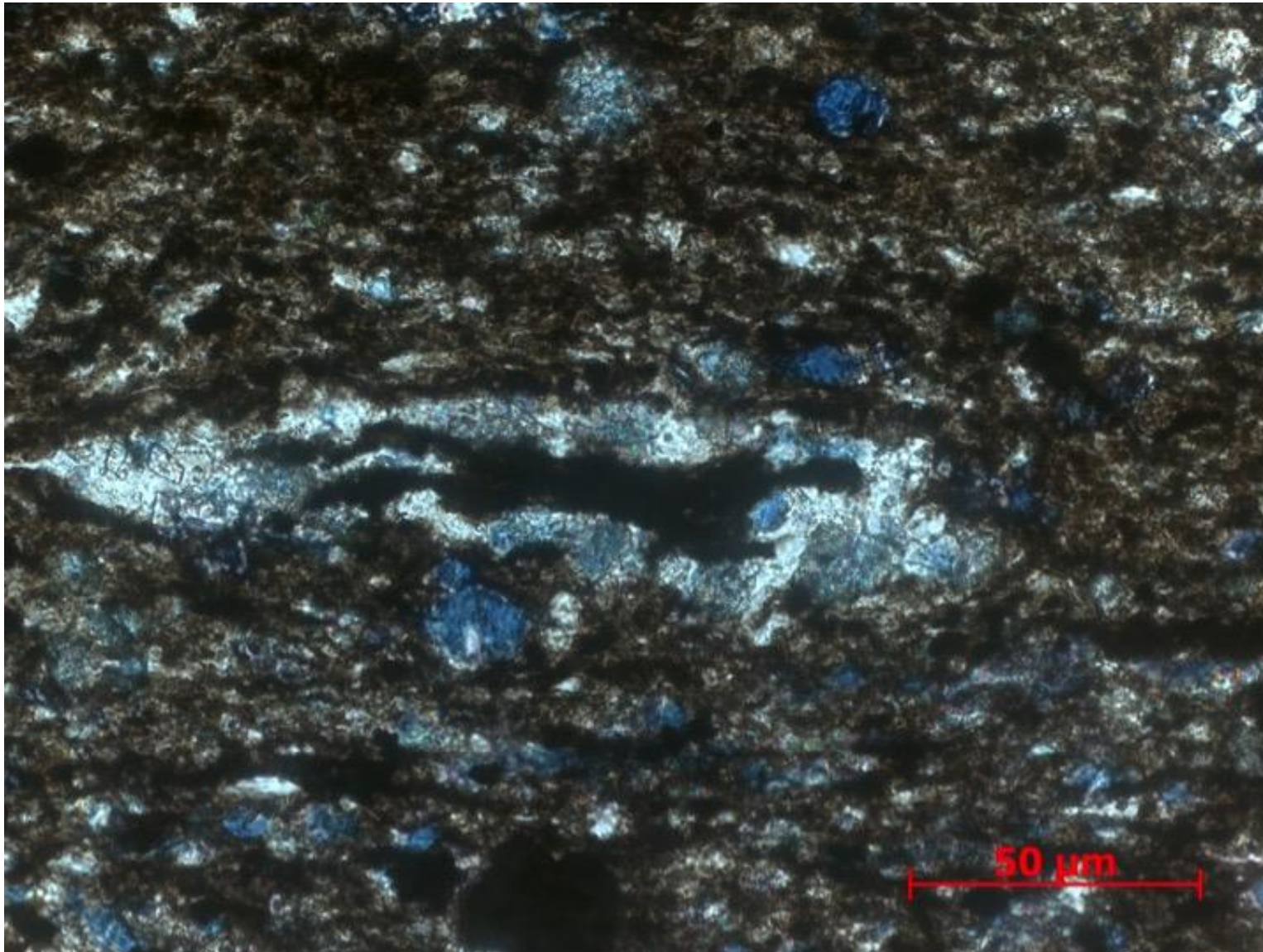


Figure 91. Sample Depth: 9653.17 ft. 40x XPL – Dark brown top 1/5 of thin section. Small 150 um tasmanites with organic matter infill. Original silica algal wall partially replaced by ferroan dolomite (blue). Detrital silt-sized quartz and clay matrix. Abundant oxides. Ferroan dolomite replacement of detrital quartz grains.

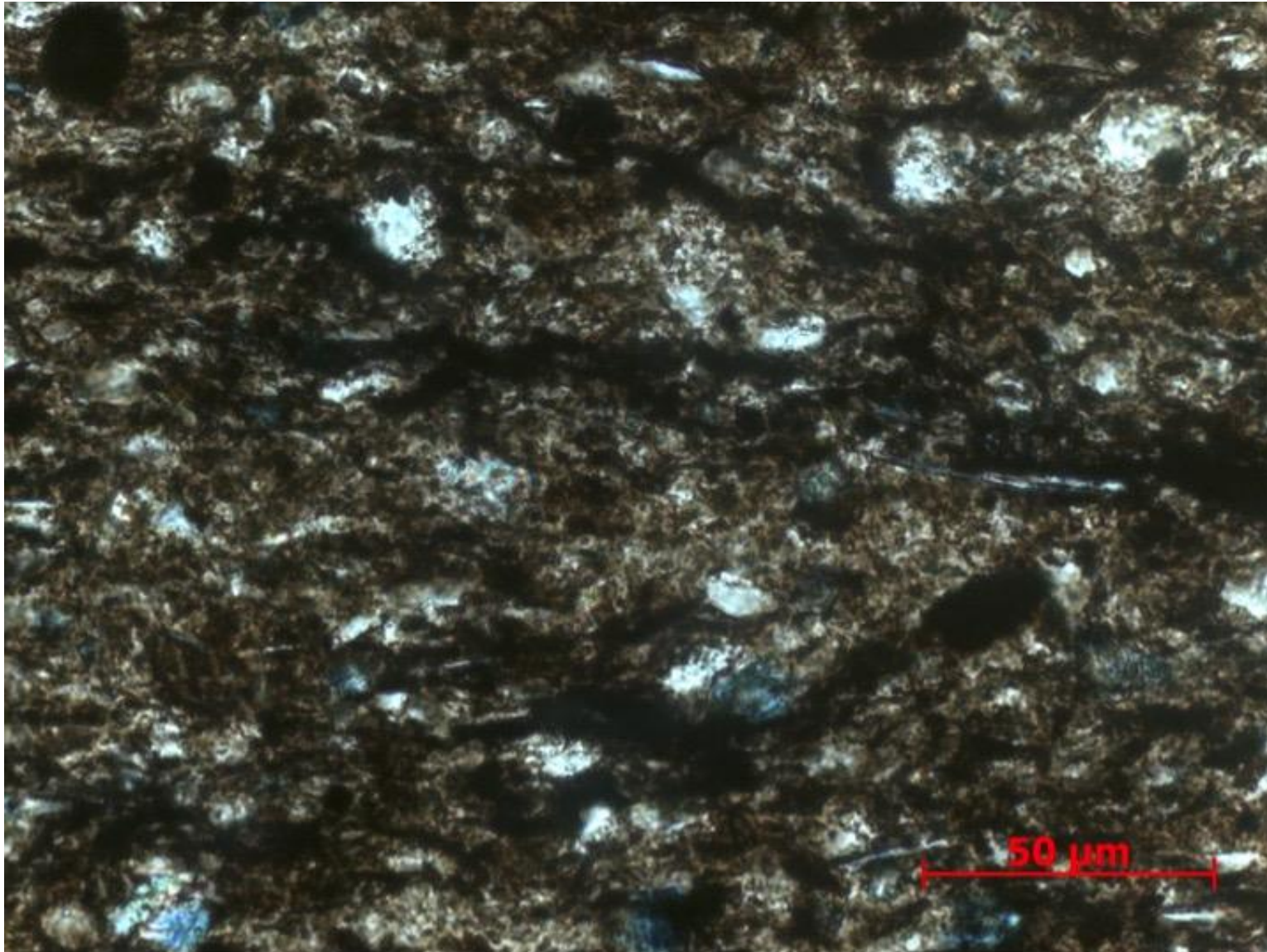


Figure 92. Sample Depth: 9653.17 ft. 64x XPL – 64x magnification of matrix of top 1/5 of thin section. Fine silt sized detrital quartz and clays (elongate micas visible) both diagenetically altered. Ferroan dolomite cement. Black organic matter (?) visible. Diagenetically altered sponge spicules ~ 50 μm .

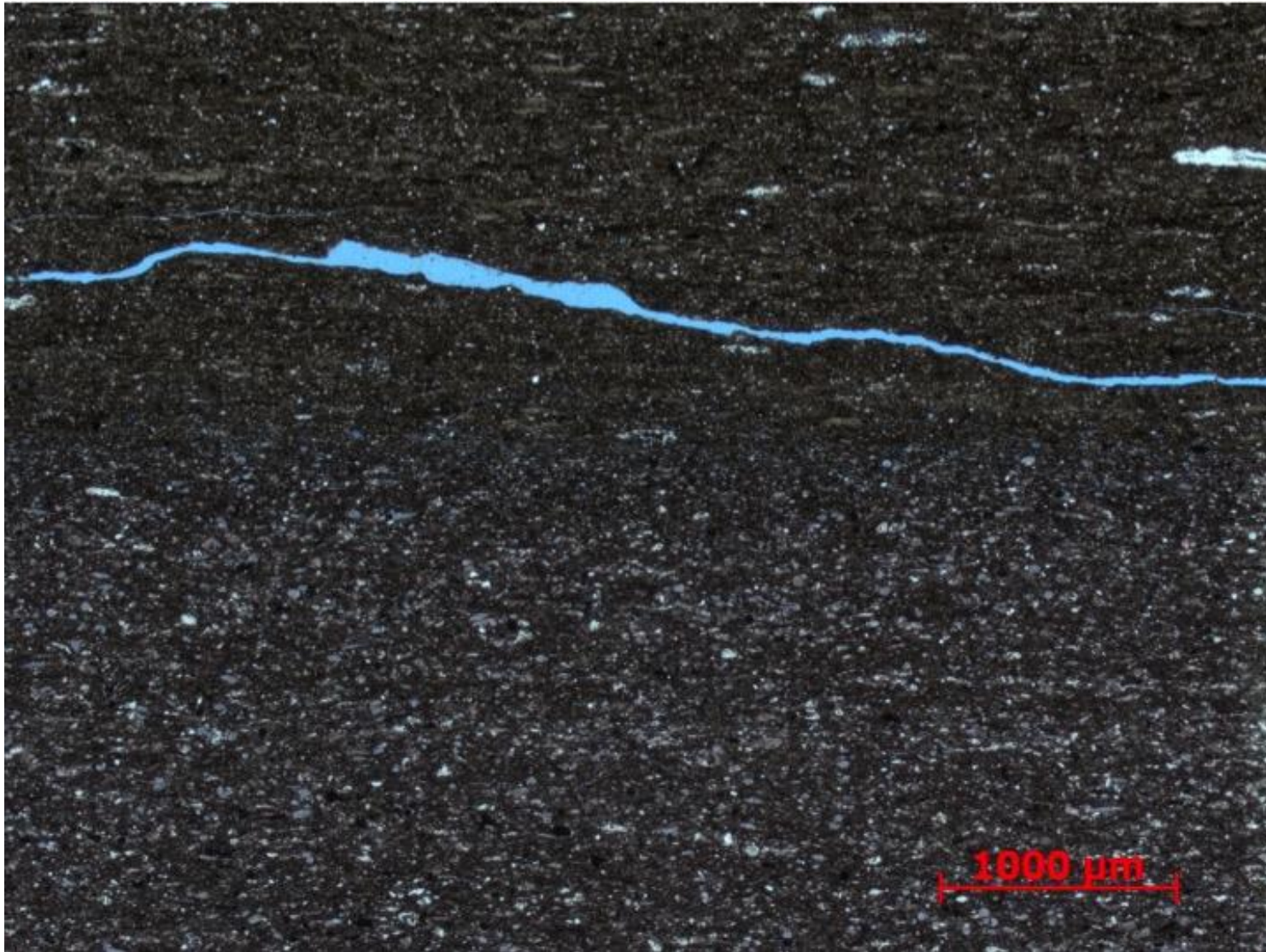


Figure 93. Sample Depth: 9653.17 ft. 2.5x PPL – Gradational contact between carbonate rich bottom 4/5th of slide and top siliciclastic rich 1/5th of slide. Coarser carbonate allochems exhibit faint laminations. Small cleaner silt sized horizontal burrows ~300 um in length.

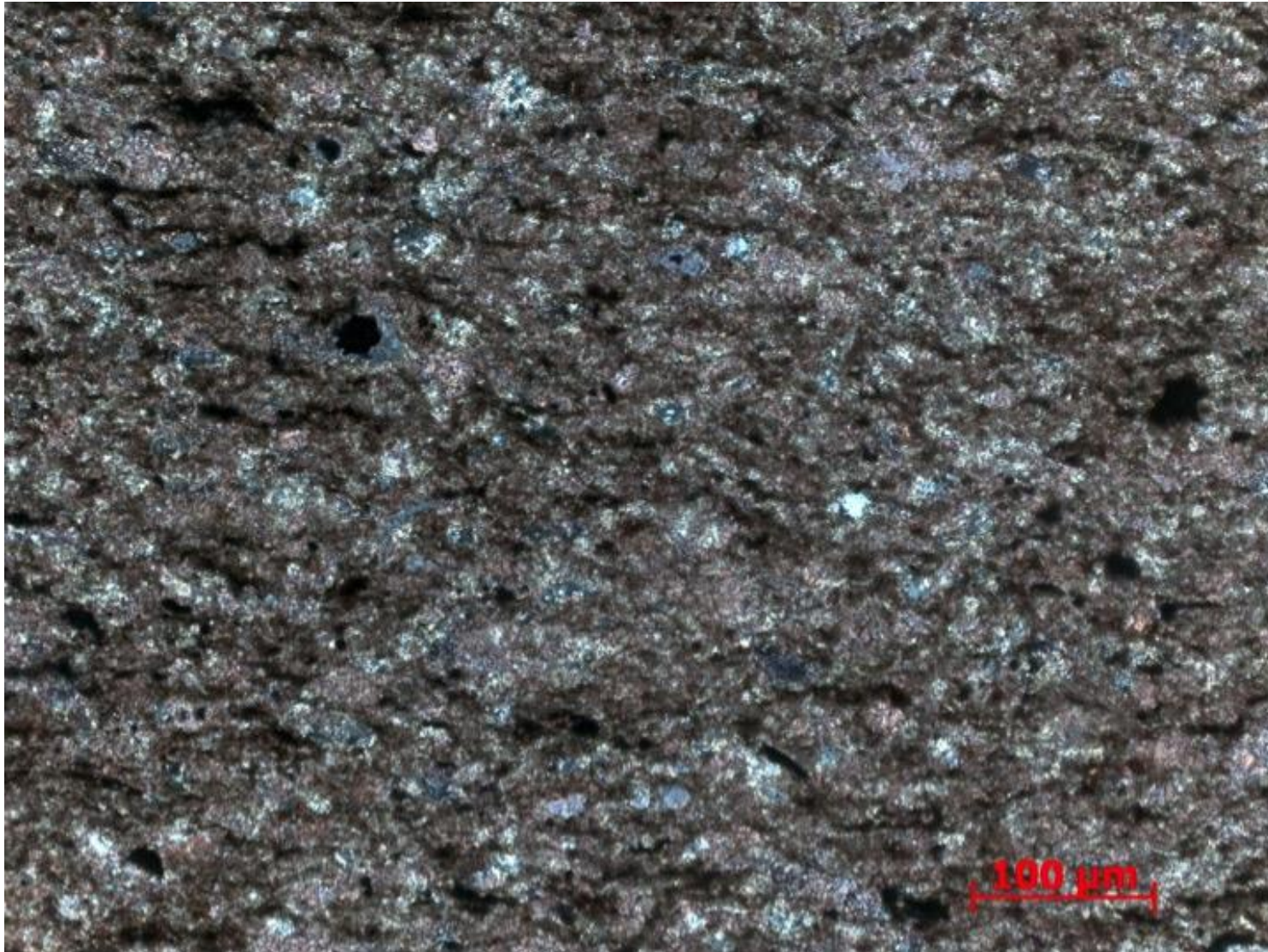


Figure 94. Sample Depth: 9653.17 ft. 20x XPL – Bottom 4/5 of thin section. Replacive dolomite, ferroan dolomite, and calcite present. Allochems very difficult to identify due to grain boundary dissolution. Clay rip up clasts <50 μm in length comprising 30% of matrix. Mostly carbonate allochem grain to grain contact.

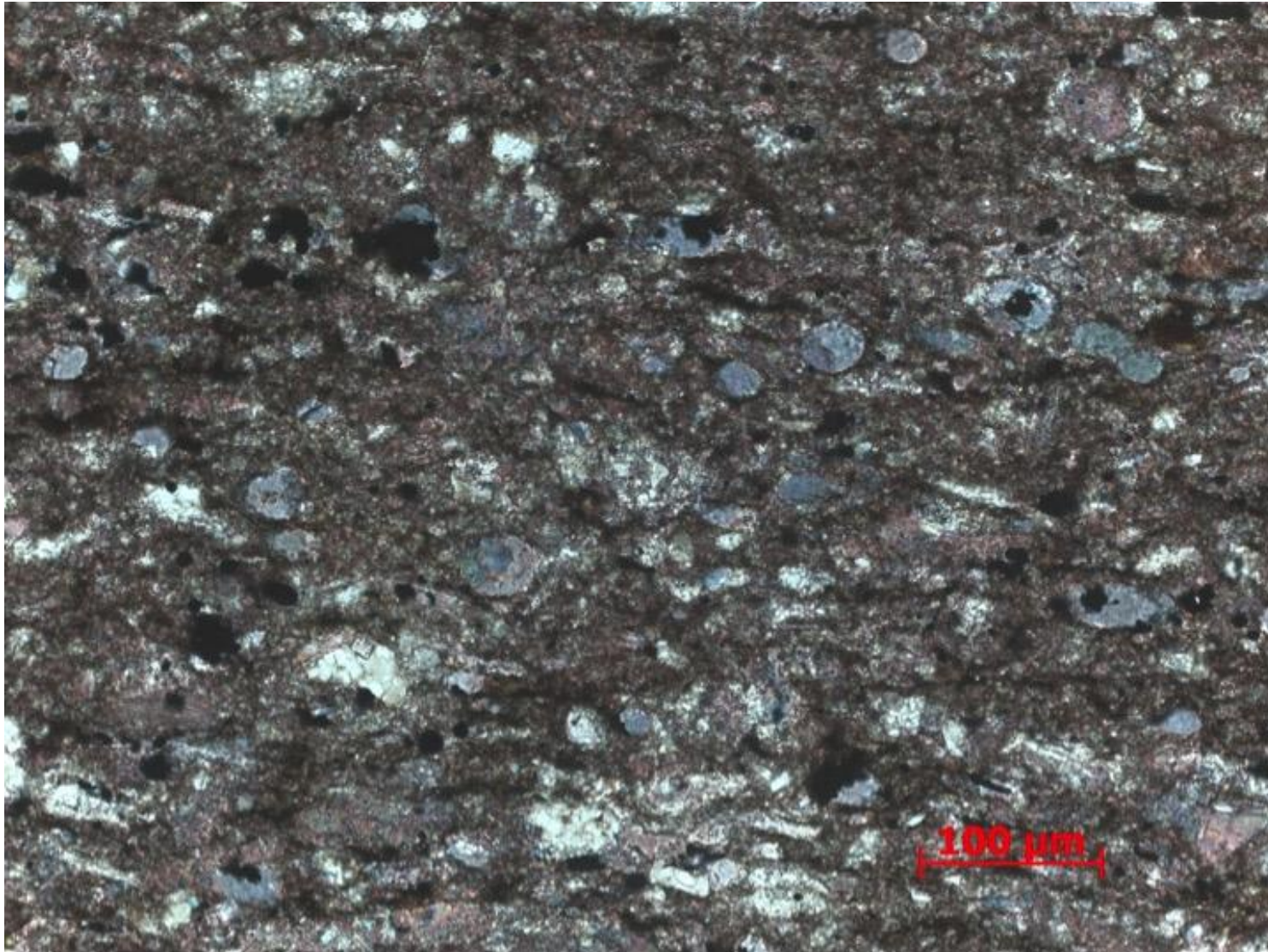


Figure 95. Sample Depth: 9653.17 ft. 20x XPL – Ferroan dolomite replacement of 50 um radiolaria pervasive. Dolomite, calcite, and ferroan dolomite replacive cement. Ferroan and regular dolomite restricted to intragranular replacement. Heavy intergranular calcite cement with partial micritization of smaller allochems.



Figure 96. Sample Depth: 9657.17 ft. Mineralogy: minimal calcite, mostly clay and detrital quartz, faint dolomite replacement, abundant OM. Texture: faint banding, prevalent laminations, normal grading (check orientation), OM predominantly. Bioturbation: horizontal burrows towards top. Fauna: agglutinated foram (abundant), *Tasmanites* (present)



Figure 97. Sample Depth: 9657.17 ft. 2.5x PPL - Upper portion of thin section. Silty and clay rich matrix with some discontinuous organic rich laminae. Clean sub-horizontal burrow >1000 um long. Compacted tasmanites abundant.



Figure 98. Sample Depth: 9657.17 ft. 2.5x PPL – Agglutinated foram (500 μm), elongated clay rip ups ($\sim 600 \mu\text{m}$), and detrital quartz dominant in matrix before laminations. Thin laminations of detrital quartz indicating flow event. Clay content decreases and small oxides and detrital quartz increase after laminations. Band of reddish brown has more bimodal grain size distribution. Finer reddish mud more homogenous and generally less detrital quartz.

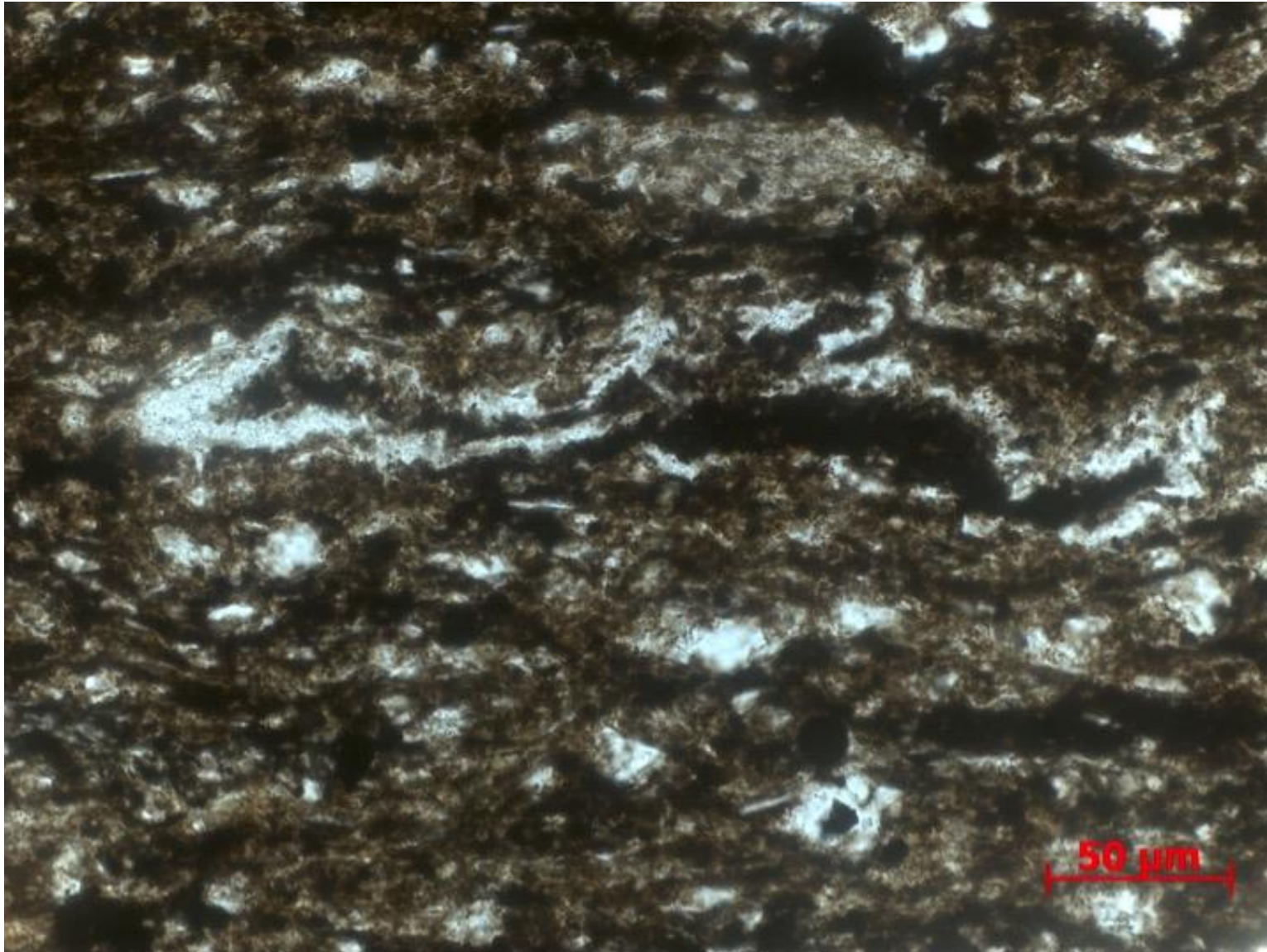


Figure 99. Sample Depth: 9657.17 ft. 40x PPL – Algal wall of ~250 *Tasmanites* partially destroyed / abscessed. Internal organic matter partially expelled. Abundant silt sized detrital quartz. Moderate amount of clays. Oxides present. Silty 100 um lithoclast above tasmanites.

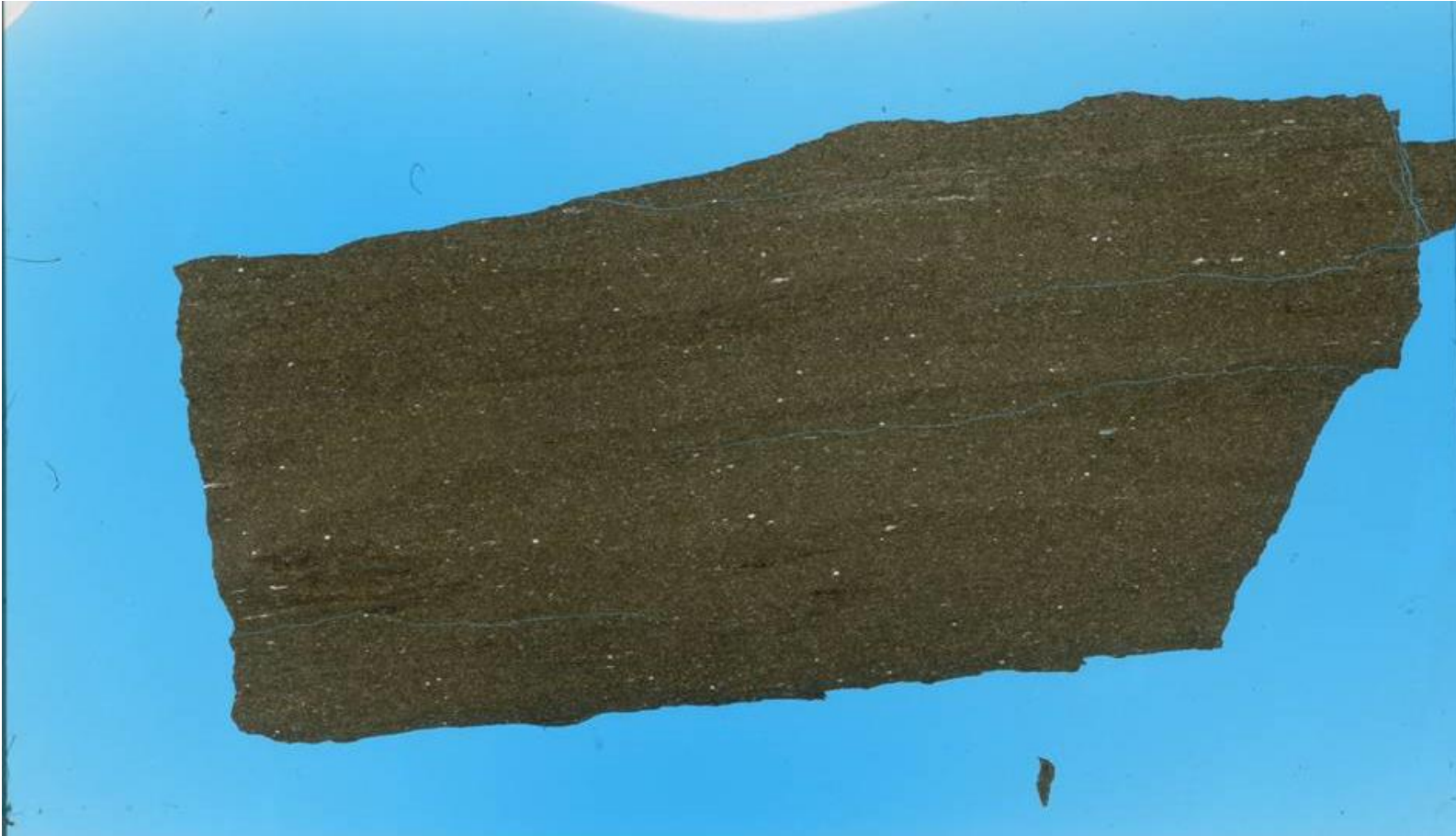


Figure 100. Sample Depth: 9665.34 ft. Mineralogy: minimal calcite, minimal dolomite replacement mostly clay and abundant detrital quartz, OM present. Texture: almost no lamination, some potential horizontal macroscopic burrows, may have removed OM. OM patchy but abundant, may not be evenly distributed due to selective bioturbation. Faint irregular bands of cleaner sediment – potential macroscopic horizontal burrows or soft sediment deformation of original banding. Mainly silt and clay sized particles. Isolated patch of clay rip ups and organics on center left indicate that area not entirely churned / bioturbated. Bioturbation: large but sparse horizontal burrows visible, visibly cleaner inside burrow – coarser grained and less OM inside - created patchy OM distribution. Fauna: radiolarian (present) *Tasmanites* (sparse/ few)

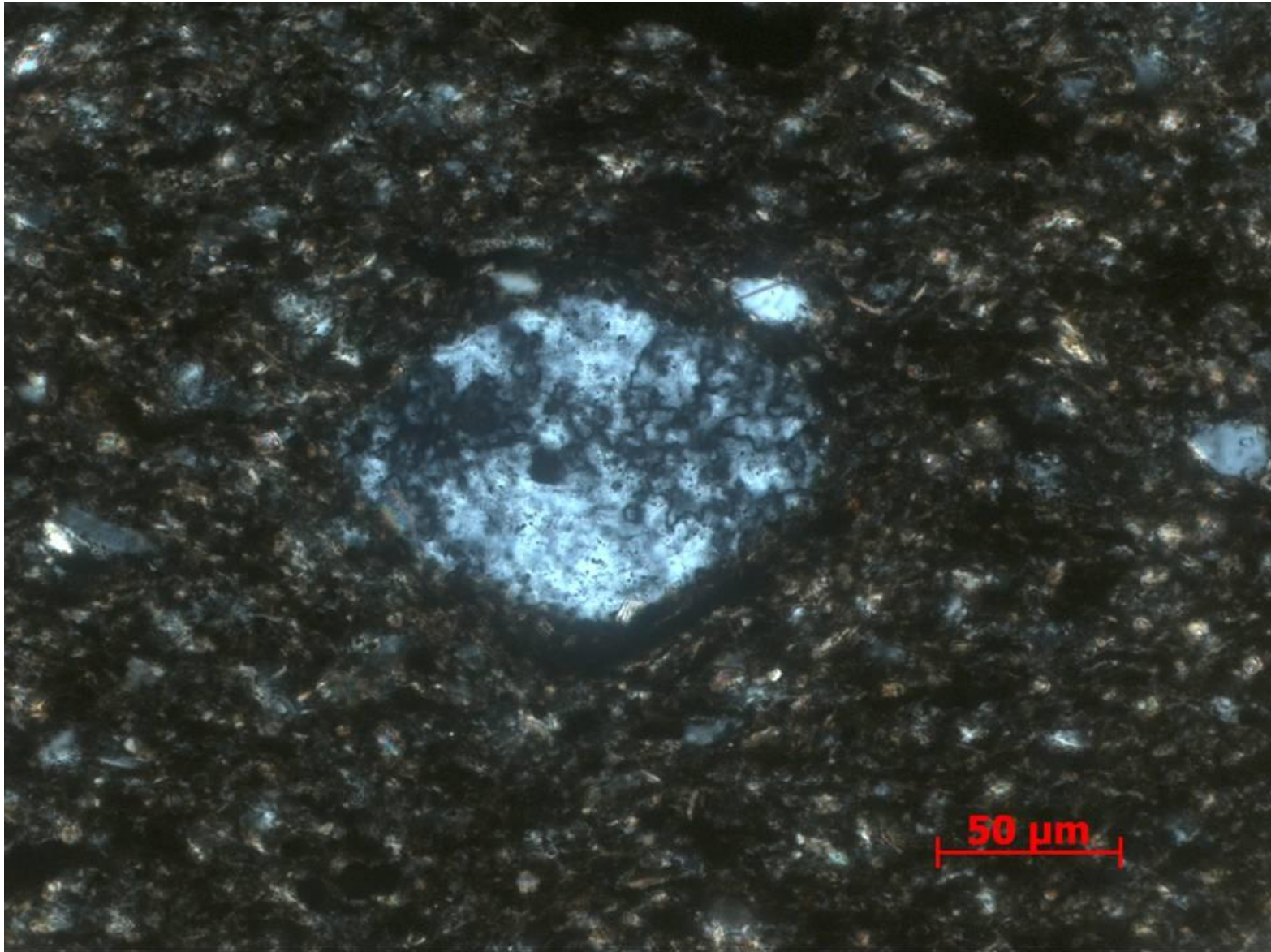


Figure 101. Sample Depth: 9665.34 ft. 40x XPL – Slightly compressed and deformed along bedding plane siliceous radiolaria in silt sized detrital quartz, clay fragments, and organics rich matrix.



Figure 102. Sample Depth: 9665.34 ft. 2.5x XPL – Partially ferroan dolomite replacement of scattered radiolaria. ~ 1000 um long clay fragments horizontally oriented. Mostly detrital silt sized quartz and clay particles.

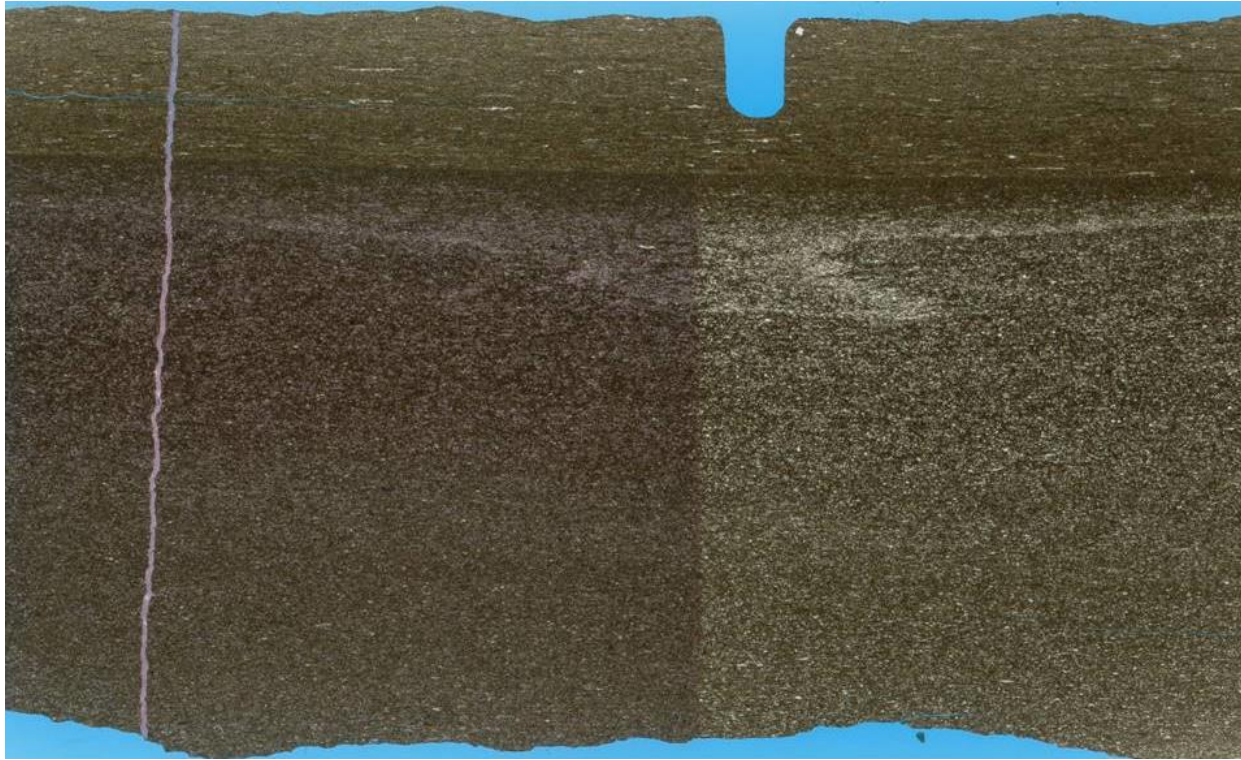


Figure 103. Sample Depth: 9673.17 ft. Mineralogy: lots of calcite (shell fragments and in cement of lower flow), can see it as diagenetic overprint, lose a lot of texture, minimal to absent dolomite throughout. Texture: separated into flow events – lower an potentially upper. Lower flow event – calcareous, calcareous shell fragments (see fauna) in clay (not micrite?) matrix. Dissolution along edges of shell and lithic fragments – diagenetic calcite replacement prevalent, coarsening upwards flow – more chaotic and randomly oriented towards the bottom with more laminations and larger shell fragments towards top/ detrital (silt sized) quartz still present. Clay content decreasing upwards but more OM? Rare silica replacement of radiolaria .Upper section – silt sized, detrital quartz content increases significantly, although grain size decreases. Considerably less clay. Not laminations. Bioturbation: no visible bioturbation in lower flow, upper silty less calc – some silty small horizontal burrows potentially? Fauna: Lower carbonate flow: echinoderm spines (very abundant), benthic multichamber forams, brachiopod shell fragments, echinoderm spines?, siliceous radiolaria (rare). Upper siliceous – calcareous shell fragments absent – agglutinated forams?



Figure 104. Sample Depth: 9673.17 ft. 2.5x PPL – Gradational contact between calcareous lower portion and silty siliciclastic upper portion. Lower calcareous portion has bimodal grain size distribution, more heterogeneous. Calcite allochems in clay and organic matter rich matrix. Very little detrital quartz or silt sized particles. Upper siliciclastic portion shows a relative decrease in clay and organic fraction and an increase in detrital quartz (very fine grained sand to silt sized). Tasmanites and agglutinated forams relatively abundant. Vertical calcite vein exhibiting beef texture.

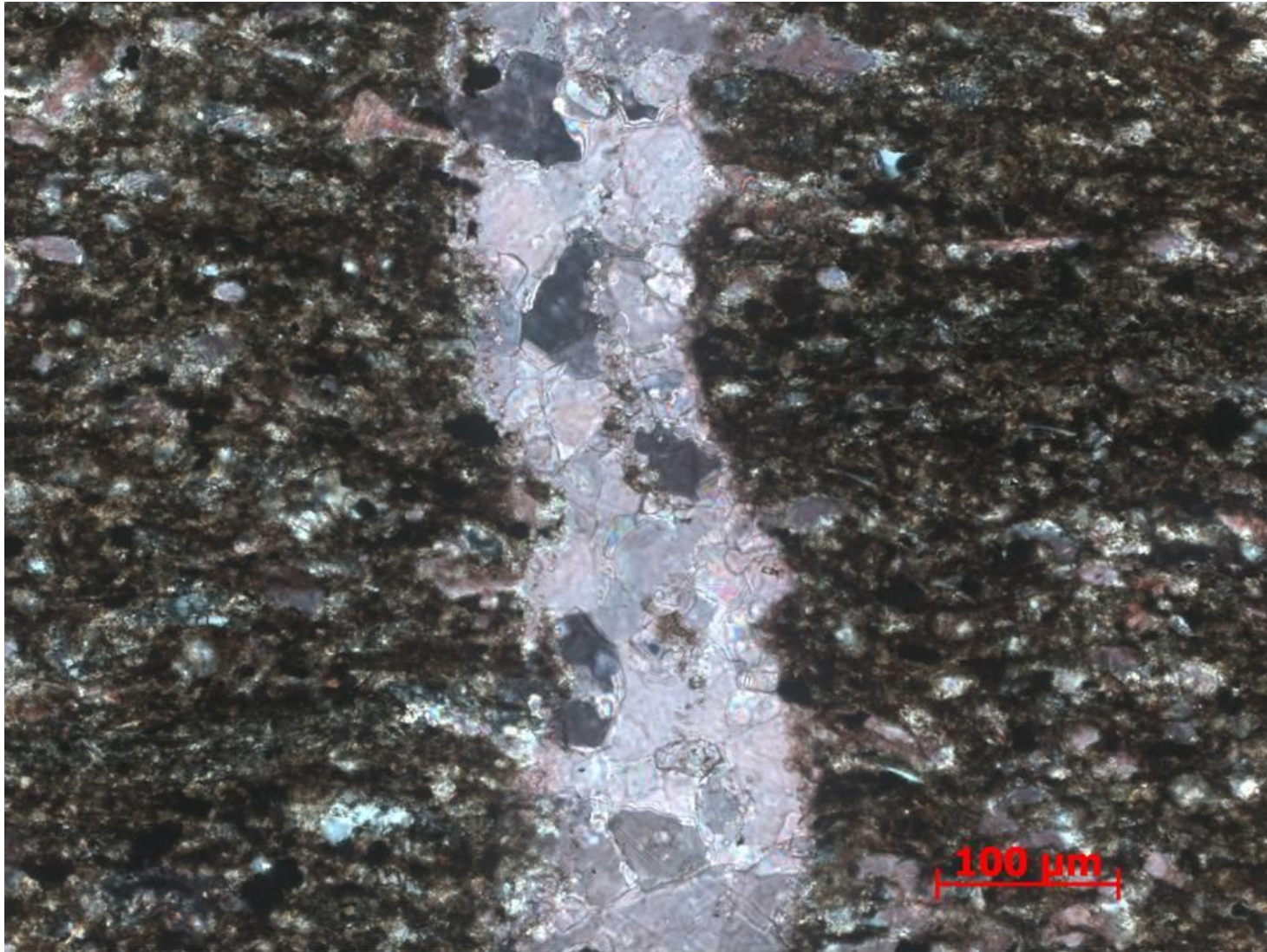


Figure 105. Sample Depth: 9673.17 ft. 20x XPL – Calcite vein in lower calcareous portion. Large (30 -100 μm) interlocking equant calcite grains. Infilled and cemented fracture – evidence of diagenetic fluid. Matrix abundant in clays, opaque oxides, and diagenetically altered carbonate allochem: echinoderm spines (very abundant), and brachiopod shell fragments. Partial and complete ferroan dolomite replacement observed in purple and blue staining respectively.



Figure 106. Sample Depth: 9673.17 ft. 2.5x XPL – Gradational contact between lower carbonate rich portion and upper siliciclastic portion. Coarsening upwards within carbonate rich portion – reverse grading. Carbonate rich portion with more clays and organics compared to upper siliciclastic



Figure 107. Sample Depth: 9673.17 ft. 20x XPL – Calcite multichamber foraminifera (~140 µm) exhibiting grain boundary dissolution. Some remaining organic matter in internal skeletal structure with fibrous calcite infilling cement. Rounded and elongated cherty lithoclast (potentially compressed tasmanites ?) ~120 µm. Abundant abraded undifferentiated skeletal fragments (20-50 µm). Oxides and clays inhibiting grain to grain contact of carbonate allochems.

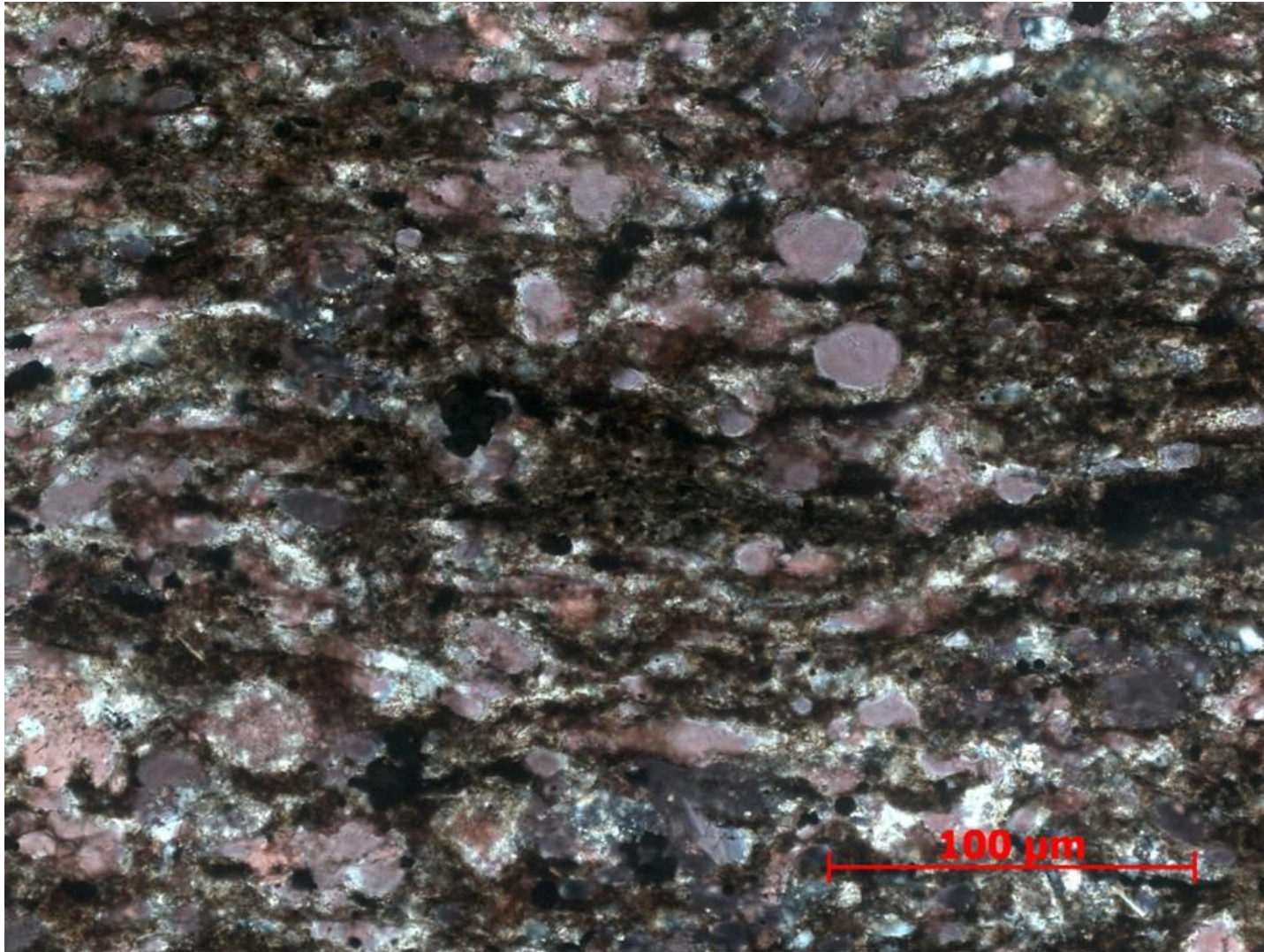


Figure 108. Sample Depth: 9673.17 ft. 20x XPL – Bivalve fragment, cross-sectional view of echinoderms spines. Extensive grain boundary dissolution. Partial intergranular calcite and silica cement? Intragranular replacive cement limited to calcite and ferroan dolomite. 20 um amalgamation of undifferentiated oxides. Clay rich in organic matter in discontinuous wavy planar laminations.

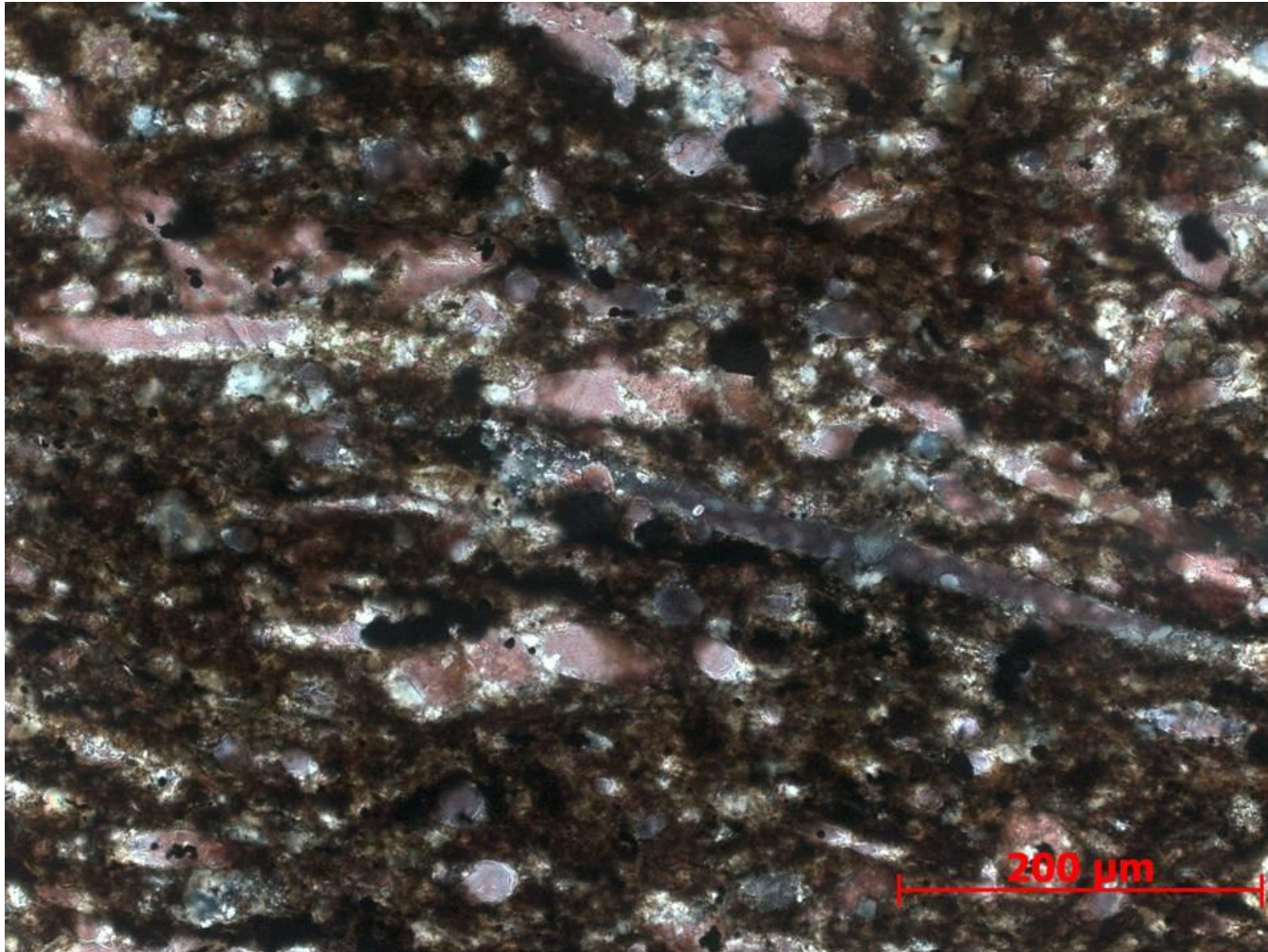


Figure 109. Sample Depth: 9673.17 ft. 20x XPL – Brachiopod fragments ~400 μm long exhibiting grain boundary dissolution and partial micritization. Lower right brachiopod shell fragment shows partial ferroan dolomitization. Upper left brachiopod fragment shows partial micritization in center (stippled brown texture) and only calcite replacement. Background matrix includes skeletal fragments such as cross-sectional cut of echinoderm spines <40 μm and small less abundant radiolara (?)

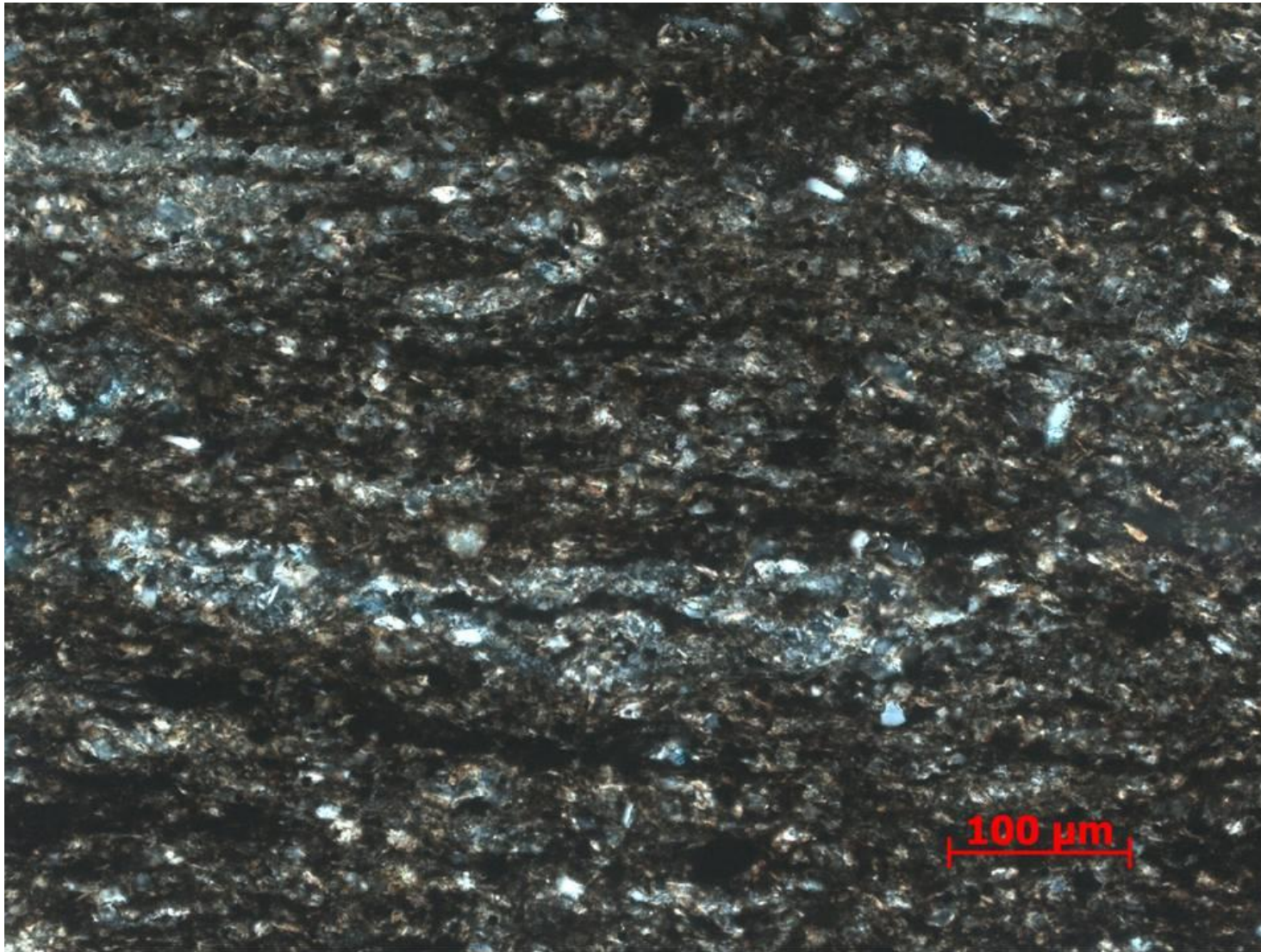


Figure 110. Sample Depth: 9673.17 ft. 20x XPL – Silica and ferroan dolomite agglutinated foram (tasmanites?) ~300 um – aggregated detrital original and replaced quartz grains with organic material in center. Minor ferroan dolomite replacement. Silt sized detrital quartz particles.

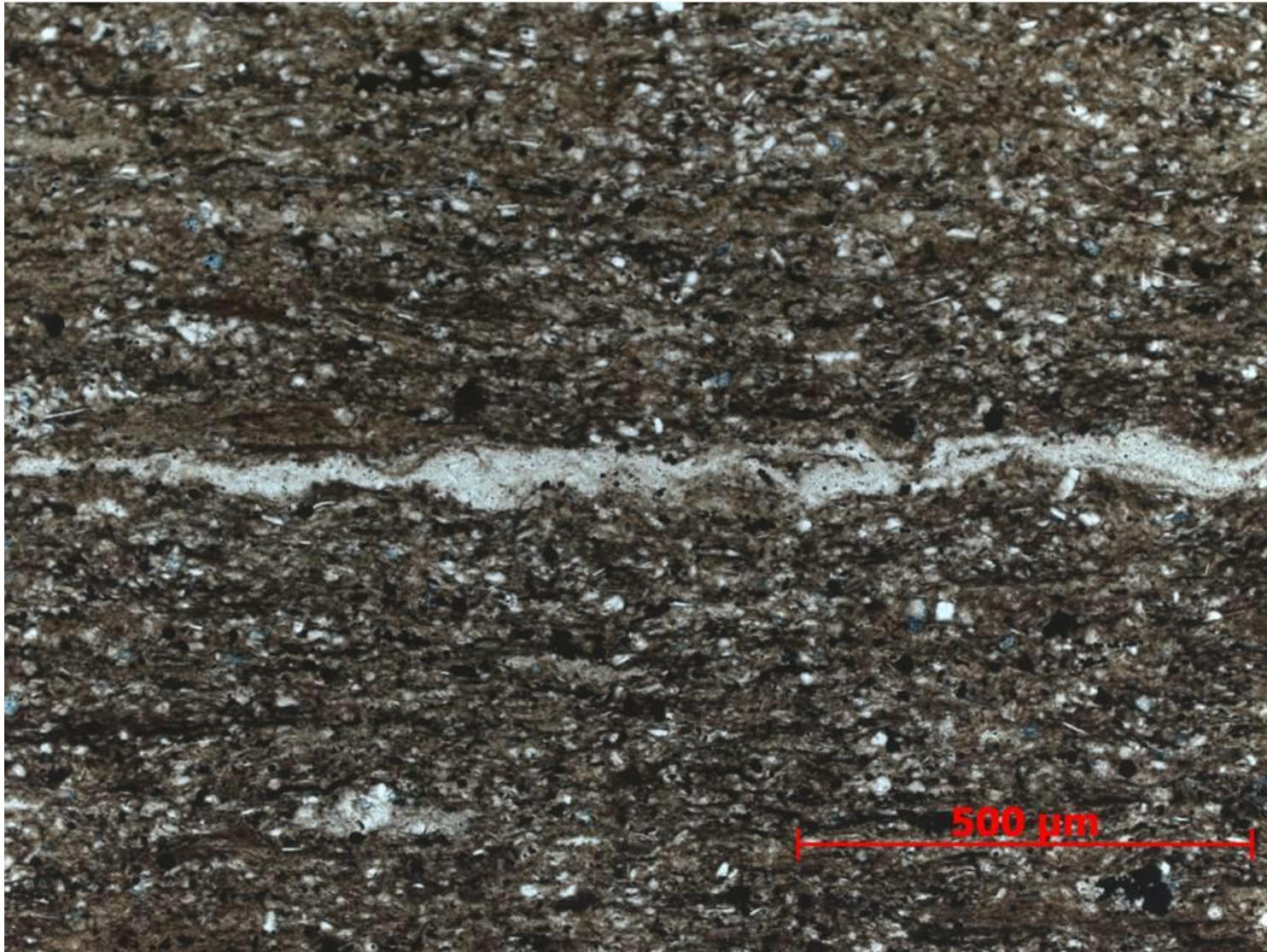


Figure 111. Sample Depth: 9673.17 ft. 10x PPL – Agglutinated foram >1000 um in detrital silt sized quartz matrix. Minor ferroan dolomite replace of some quartz grains. Less clay relative to silt. Abundant oxides.

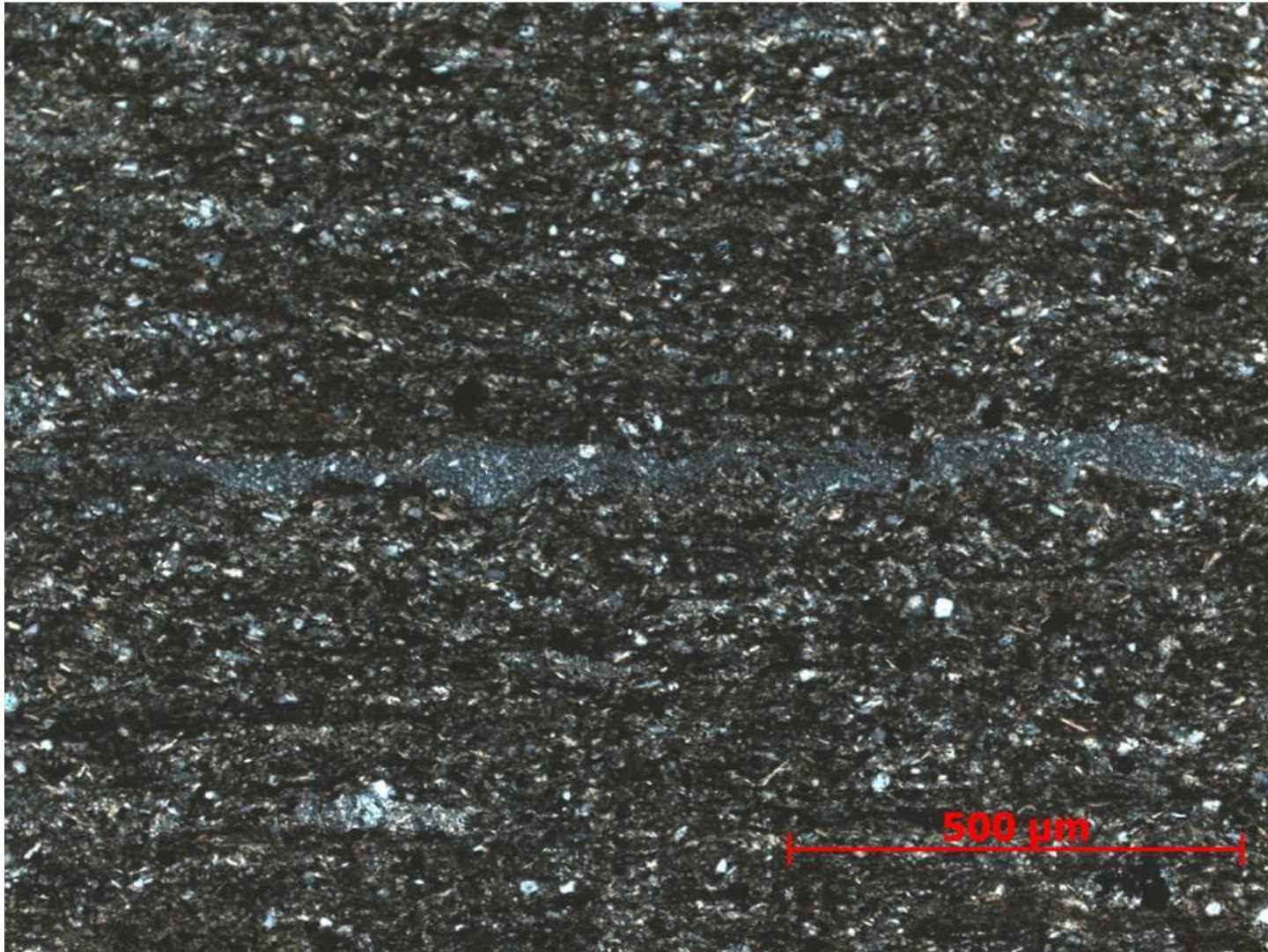


Figure 112. Sample Depth: 9673.17 ft. 10x XPL – Agglutinated foram in previous figure in cross polarized light 0 showing previously aggregated detrital quartz crystals replaced by microcrystalline quartz cement. Abundant detrital quartz in matrix.

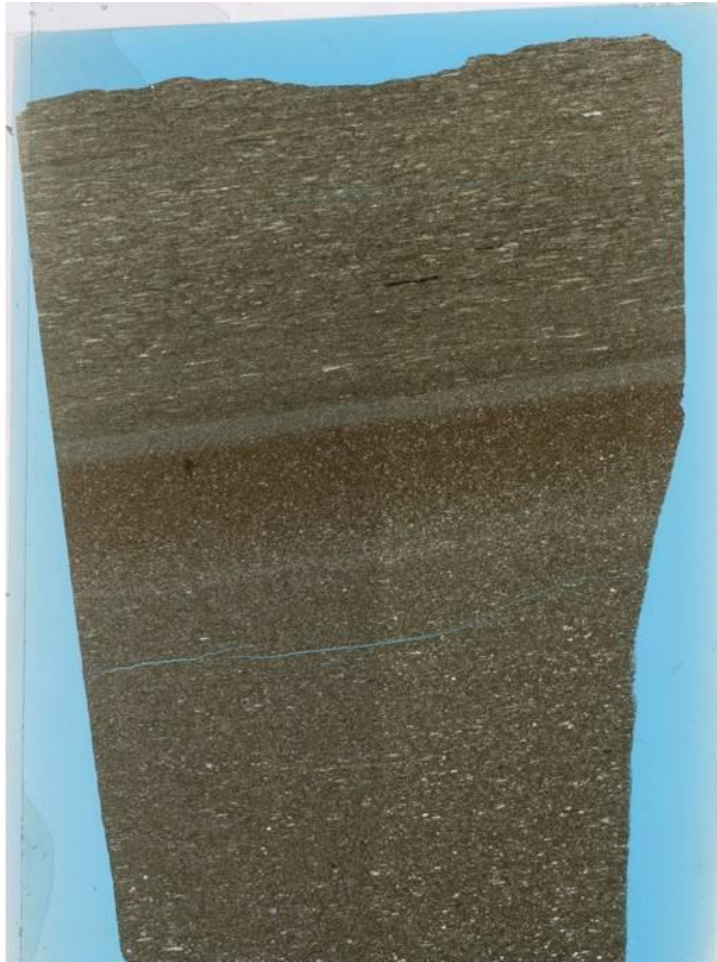


Figure 113. Sample Depth: 9681.17 ft. Mineralogy: calcite shell fragments in heavily clay matrix so minimal actual calcite, some dolomite replacement in both fractions. detrital quartz in separate event in minor clay. no calcite above. OM in detrital fraction. Texture: contact between faint calcareous flow event(s?) and more detrital event, with planar orientation. Random orientation of grains shell fragments in calc flows with initial increase in reddish clay content then increasing detrital grains concentration (relative to clay fraction) towards detrital event. Calc flows have more clay, detrital portion has more detrital quartz and less clay, OM in detrital fraction, discontinuous OM lams. Bioturbation: potential small horizontal burrows in detrital fraction, none on calcareous flow events? Fauna: Mainly calc flows - echinoderm spines, brachiopod shells, agglutinated forams (siliceous still), well rounded lithic fragments, ooids, crinoid button? Heavy replacement and dissolution on edges – hard to identify. Detrital fraction – agglutinated foram



Figure 114. Sample Depth: 9681.17 ft. 2.5x XPL – Abundant small (~700 μm) horizontal burrows in topmost portion of thin section. Silt sized detrital quartz and organics.

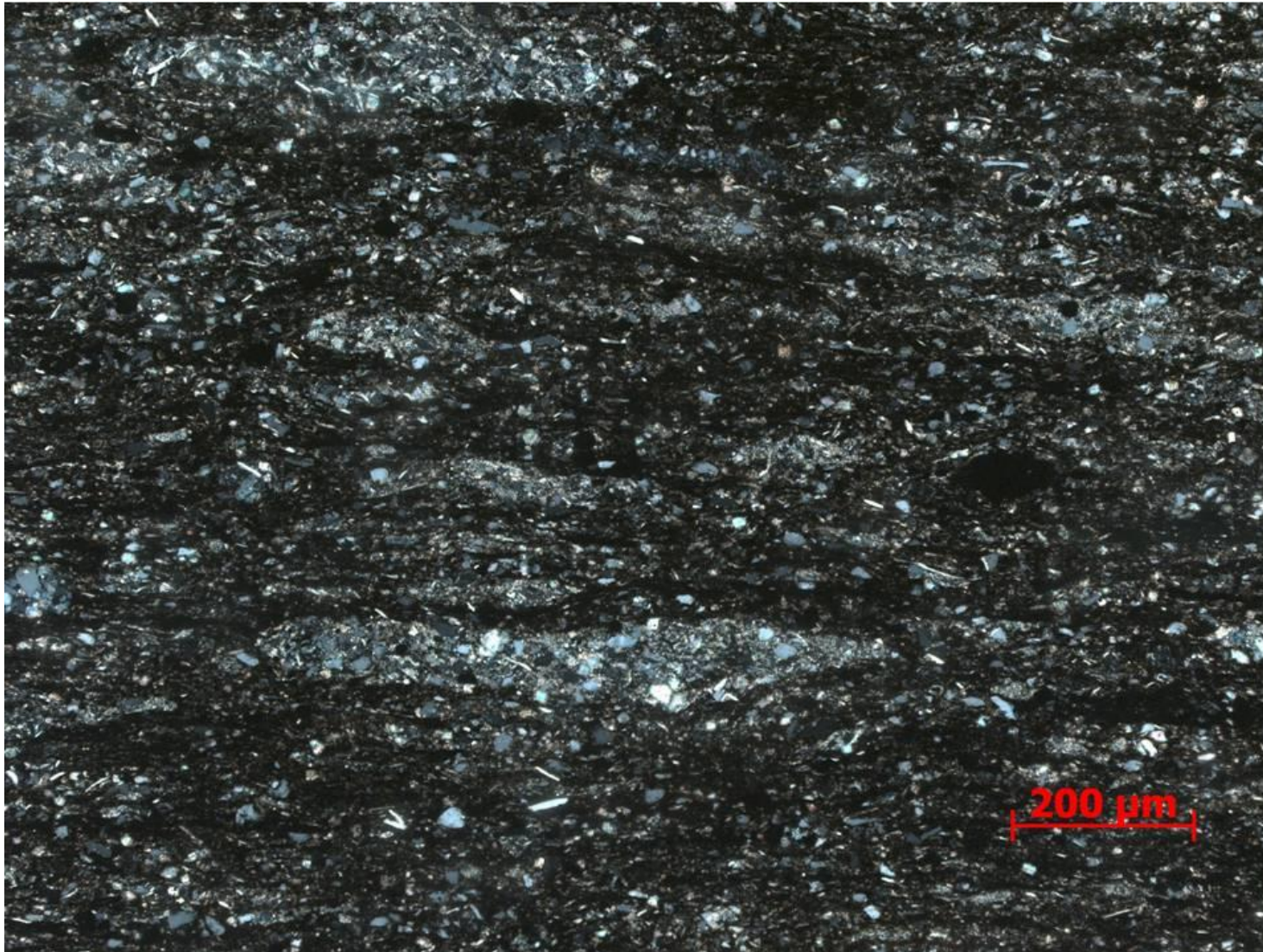


Figure 115. Sample Depth: 9681.17 ft. 10x XPL – Abundant horizontal burrows (?) or agglutinated forams of varied sizes <700 um long. Cleaner coarser grained quartz infill compared to matrix. Muddy matrix with organics and oxides.

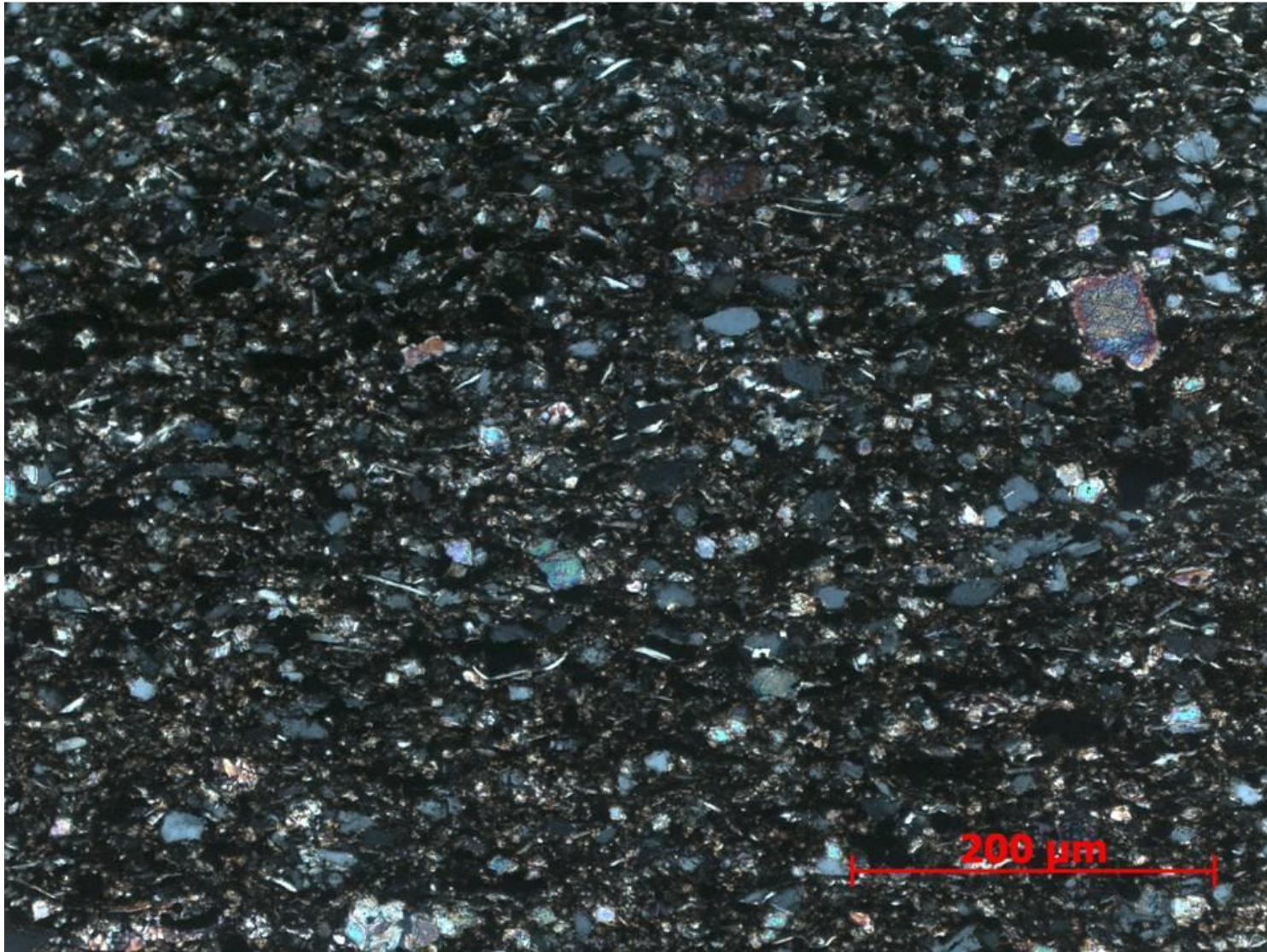


Figure 116. Sample Depth: 9681.17 ft . 20x XPL – 20x magnification of silty matrix in bioturbated portion. Elongate micas present but minor matrix component. Detrital quartz dominant mineralogy. Oxides and organics abundant, No evident grain orientation, somewhat chaotic. Sparse carbonate allochems.

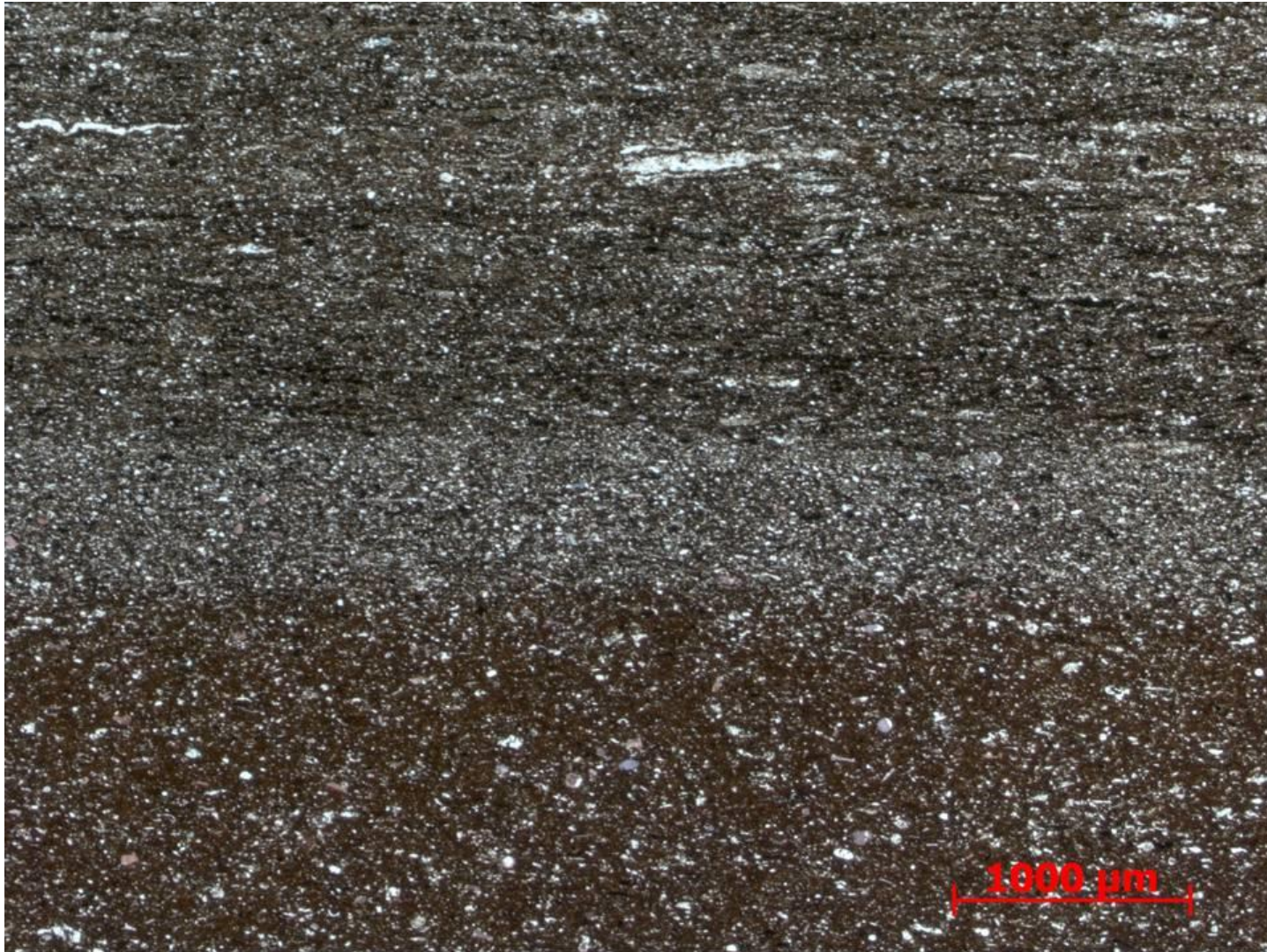


Figure 117. Sample Depth: 9681.17 ft 2.5x XPL – Description from top to bottom: (1) carbonate (mostly calcite) allochems in red brown clay matrix, bimodal grain size distribution (2) 0.05 cm band of detrital silt sized quarts almost entirely absent of clay (3) Reddish brown silt sized detrital quartz grains mixed with clay and oxides. Relatively more clays than (2) but less than (3). Agglutinated forams and horizontal burrows abundant

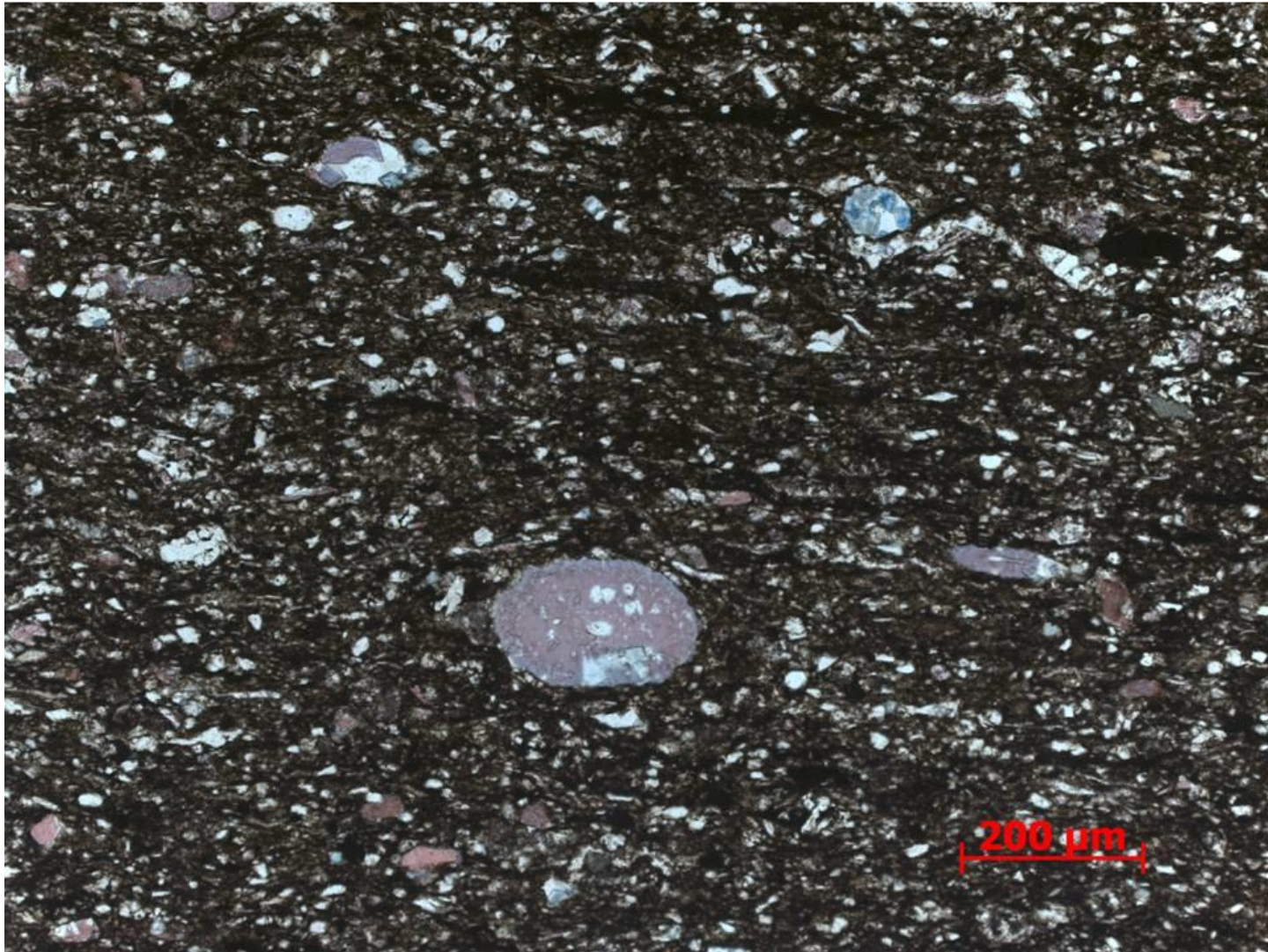


Figure 118. Sample Depth: 9681.17 ft. 2.5x. 10x PPL -10x magnification of carbonate and clay matrix below reddish brown band. Cross-section view of calcite echinoderm spine exhibiting partial ferroan dolomitization. Ferroan dolomite replacement of radiolaria in top right quadrant. Clay dominated matrix with some small detrital quartz grains.

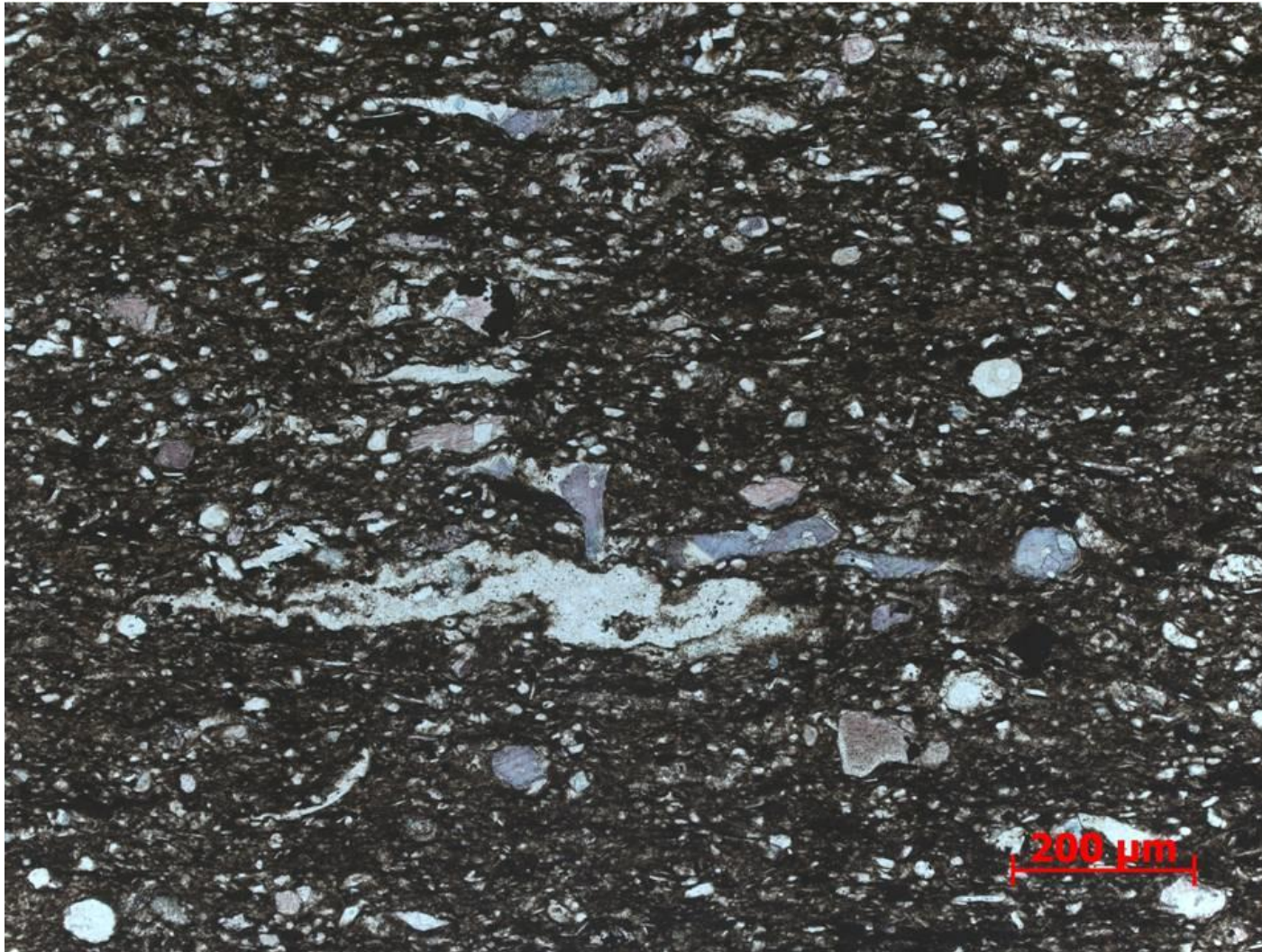


Figure 119. Sample Depth: 9681.17 ft. 10x PPL – Compressed and deformed agglutinated foram(?) approximately 400 um long. Allochems include echinoderm spine and bivalve fragments. Abraded carbonate lithoclasts are well rounded. Clay rich matrix with minimal detrital quartz. Partial ferroan dolomite replacement.

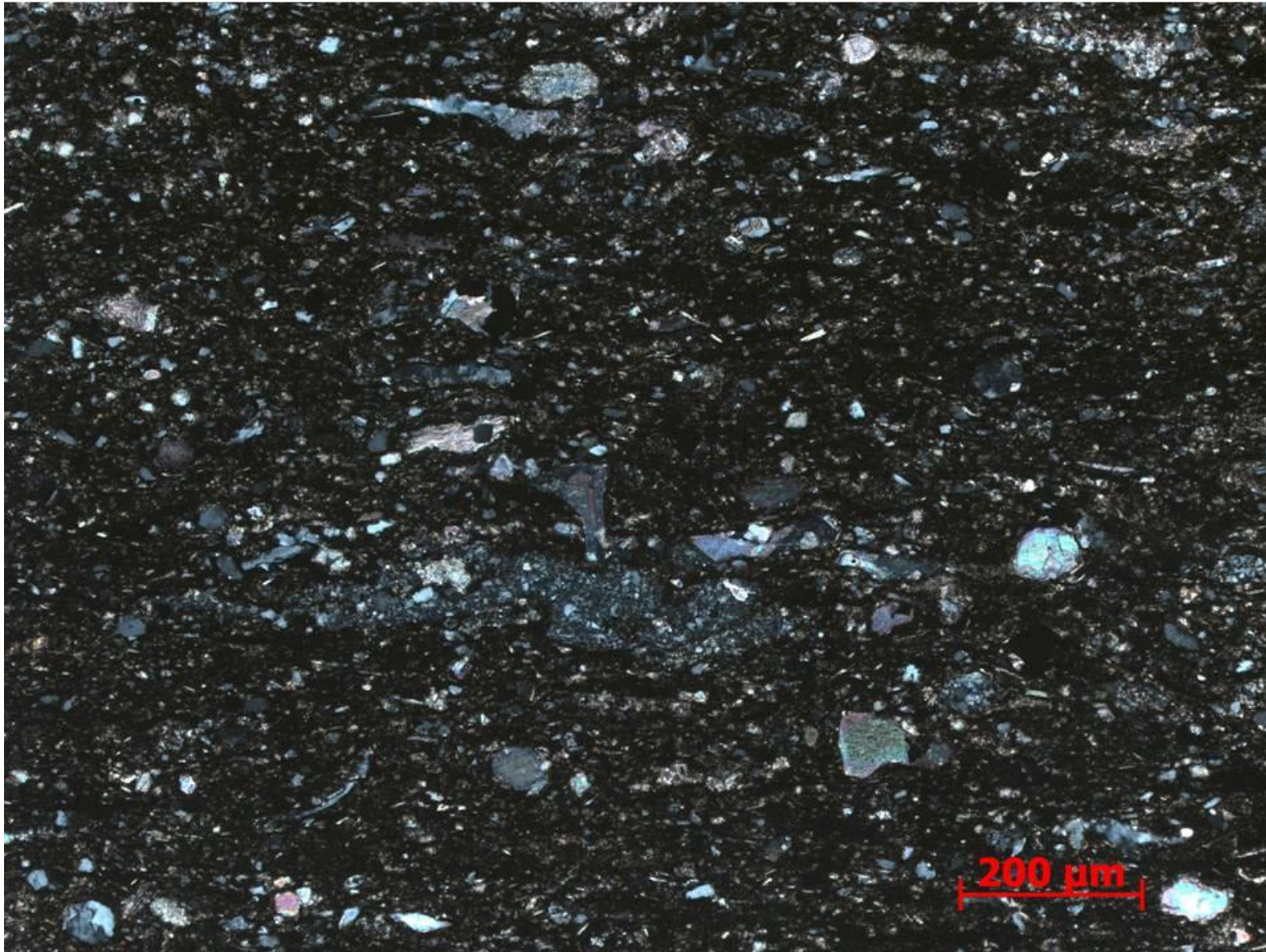


Figure 120. Sample Depth: 9681.17 ft. 10x XPL - 100 um brachiopod shell fragment exhibiting feather calcite texture. Individual detrital silt grains in agglutinated foram visible. Echinoderm spine (long and short axial cross-sectional view) and bivalve fragments. Minimal silt sized detrital quartz in matrix.



Figure 121. Sample Depth: 9683.17 ft. Mineralogy: calcite and clays matrix, minor silica replacement – no ferroan dolomite or regular dolomite visible, no visible detrital quartz. Texture: packstone, large skeletal fragments randomly oriented and subrounded, large lithic fragments of aggregated skeletal material, subrounded clay rip up clasts, high energy debris flow, differential compaction visible. Bioturbation: n/a. Fauna: large multichamber forams, echinoderm shell / plate fragments, echinoderm spines, brachiopods, bivalves, bryozoan, complex assemblage of large fossil fragments - diversity

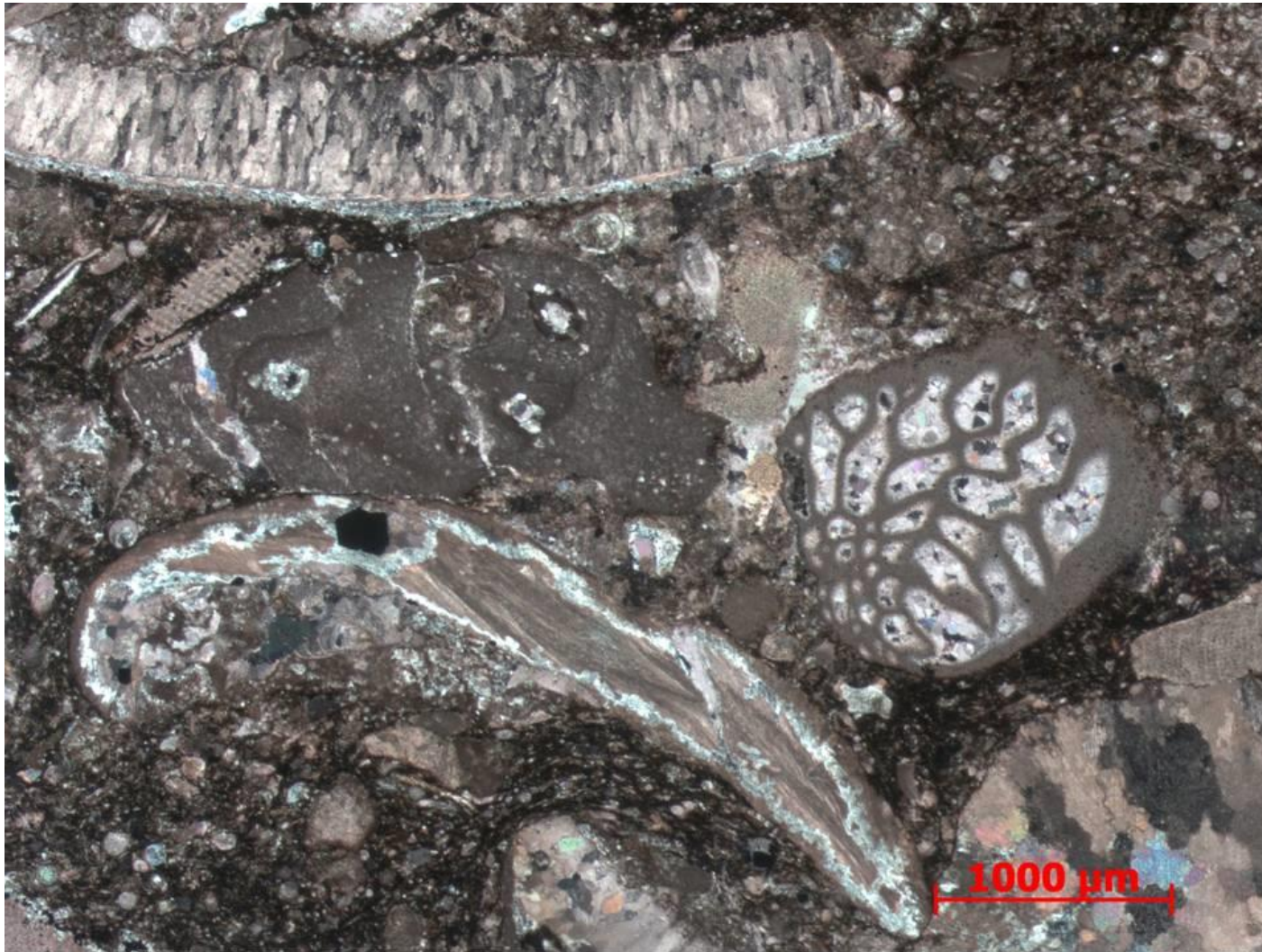


Figure 122. Sample Depth: 9683.17' ft. 2.5x XPL – Brachiopod (bivalve?) (3500 μm length) with partially preserved internal original feather texture. Partial replacive sparry calcite cement. Multichamber foram (1500 μm) with sparry calcite cement infill in internal void. Partial micritization of internal foram structure. Large 2000 μm lithoclast – small cross-sectional cut of echinoderm spine inside. Small (500 μm) echinoderm shell fragment. Partial intergranular / inter-allochem cement between foram and dark gray lithoclast. Carbonate, mostly calcite mud, matrix with small well rounded carbonate clast. No visible ferroan dolomite. Very chaotic shell fragment orientation and no visible sediment size grading.

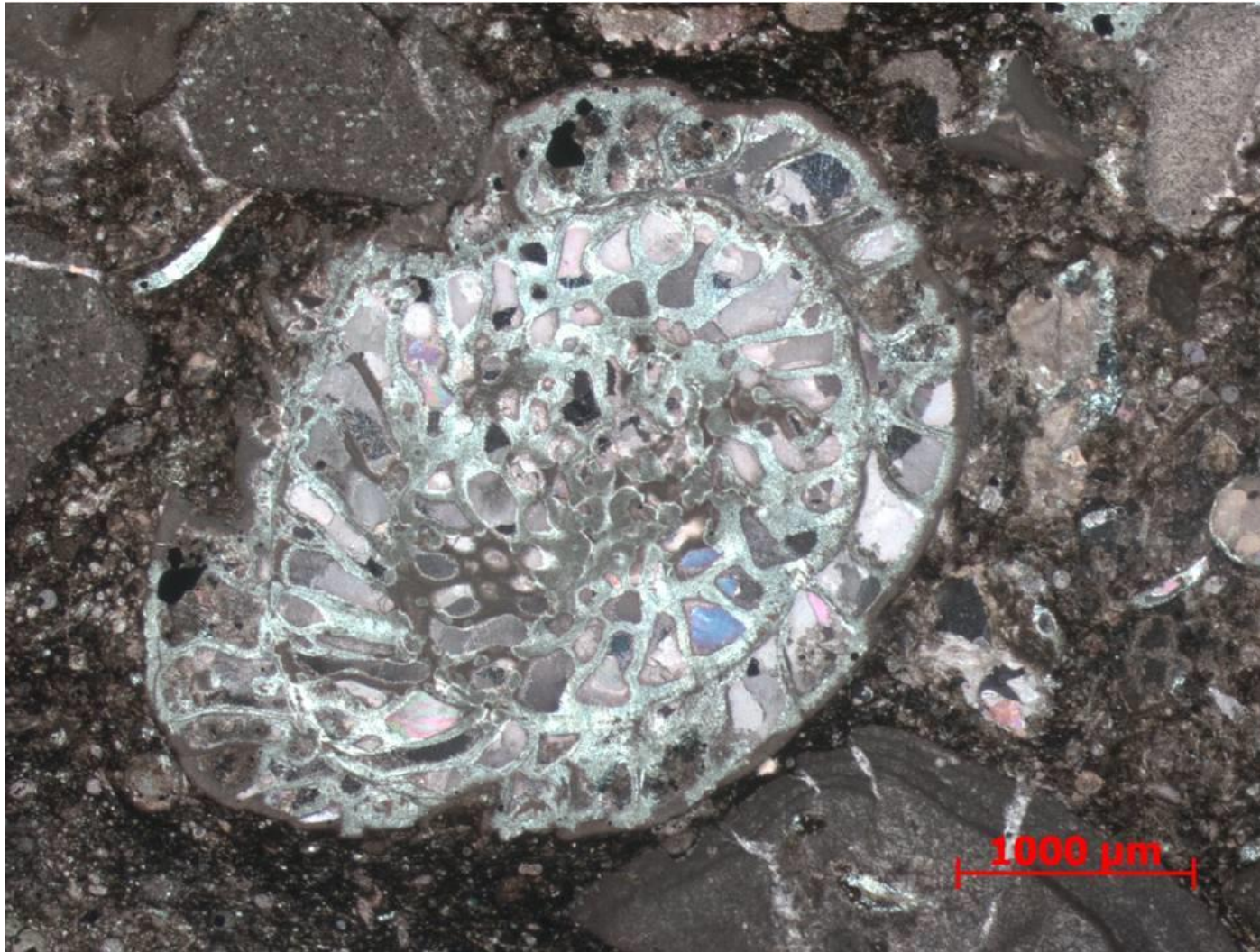


Figure 123. Sample Depth: 9683.17' ft. 2.5x XPL – Brachiopod (bivalve?) (3500 µm length) with partially preserved internal original feather texture. Partial replacive sparry calcite cement. Multichamber foram (1500 µm) with sparry calcite cement infill in internal void. Partial micritization of internal foram structure. Large 2000 µm lithoclast – small cross-sectional cut of echinoderm spine inside. Small (500 µm) echinoderm shell fragment. Partial intergranular / inter-allochem cement between foram and dark gray lithoclast. Carbonate, mostly calcite mud, matrix with small well rounded carbonate clast. No visible ferroan dolomite. Very chaotic shell fragment orientation and no visible sediment size grading.

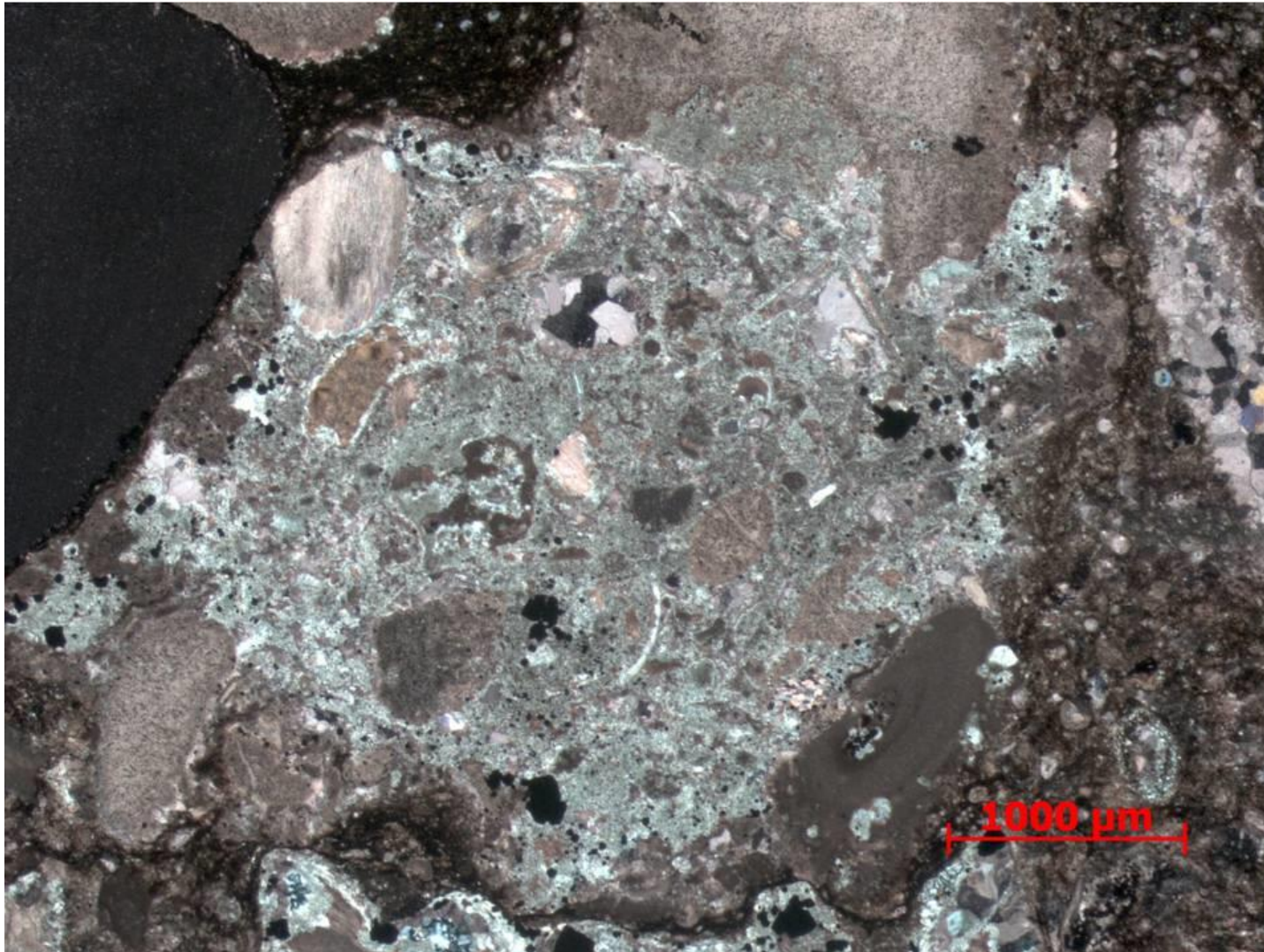


Figure 124. Sample Depth: 9683.17' ft. 2.5x XPL – Large light gray (4000 μm) angular lithoclast composed of well-rounded lithic fragments (200 – 1100 μm). Large well rounded black mud clast to immediate left. Small amorphous oxides. Well rounded carbonate silt sized grains in matrix with organic material.

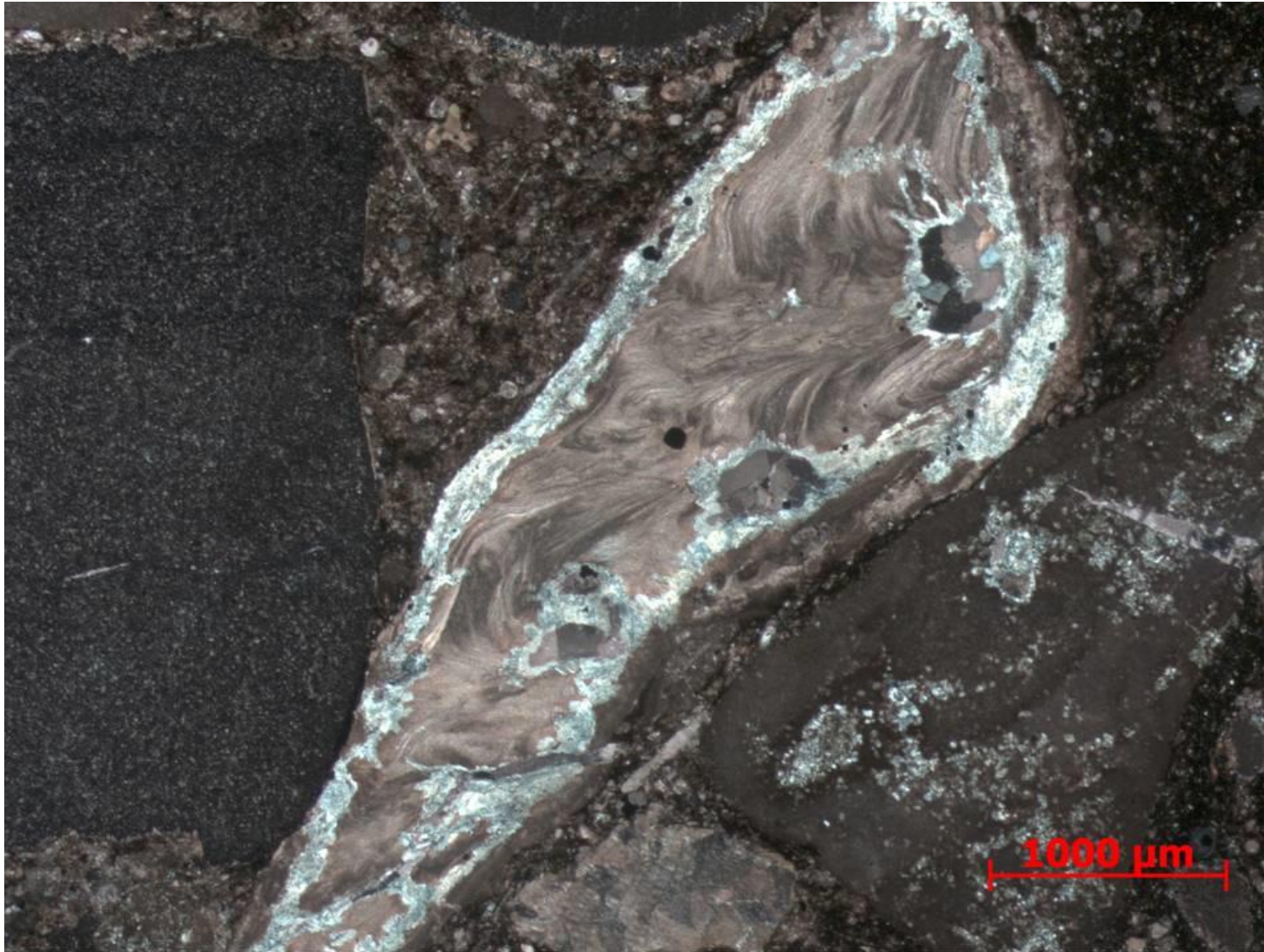


Figure 125. Sample Depth: 9683.17' ft. 2.5x XPL – Calcite brachiopod shell fragment showing original corrugated / feathery texture. Allochem boundary showing sparry calcite replacement. Dark gray echinoderm fragment with uniform extinction pattern (crinoid stem fragment). Heterogeneous and compartmentalized carbonate matrix grain size: coarser between echinoderm and brachiopod, organic lean; finer and more organic rich to the right of brachiopod.



Figure 126. Sample Depth: 9683.17' ft. 2.5x PPL – (1) Large bryozoan (3000 μm) fragment. Mud infill of internal void space. (2) Partially visible carbonate lithoclast comprised of angular lithic shards (3) Allochem of unknown origin showing heavily abraded spine edges or saw tooth grain boundary. Calcite twinning visible – uniform calcite replacement. Potential semicircle halo of now replace internal structure,



Figure 127. Sample Depth: 9689.17 ft. Mineralogy: calcite dominant (over 80%), dolomite cement towards top ferro and regular, clay and OM together, although not abundant (~30%). Texture: carbonate turbidite, heavily cemented over, clay and OM in inclined lamination indicating flow direction? Poorly sorted, faunal diversity, large lithic fragments, dissolved edges. Bioturbation: none visible. Fauna: brachiopod shells (abundant), multichamber forams (present), radiolaria (rare), deformed calcareous fragments (abundant)



Figure 128. Sample Depth: 9689.17 ft. 5x XPL – Grain boundary dissolution of well rounded large (600 μm) calcite echinoderm fragment with continuous optical extinction. Crinoid, bivalve, brachiopod, and echinoderm shell fragments. Mostly replacive intragranular calcite cement with minor intergranular silica cement. Euhedral pyrite and other small amorphous oxides present. Isolated selective oxide replacement visible. Mottled texture showing partial micritization. Very well cemented with abundant grain boundary dissolution. Overall poorly sorted.

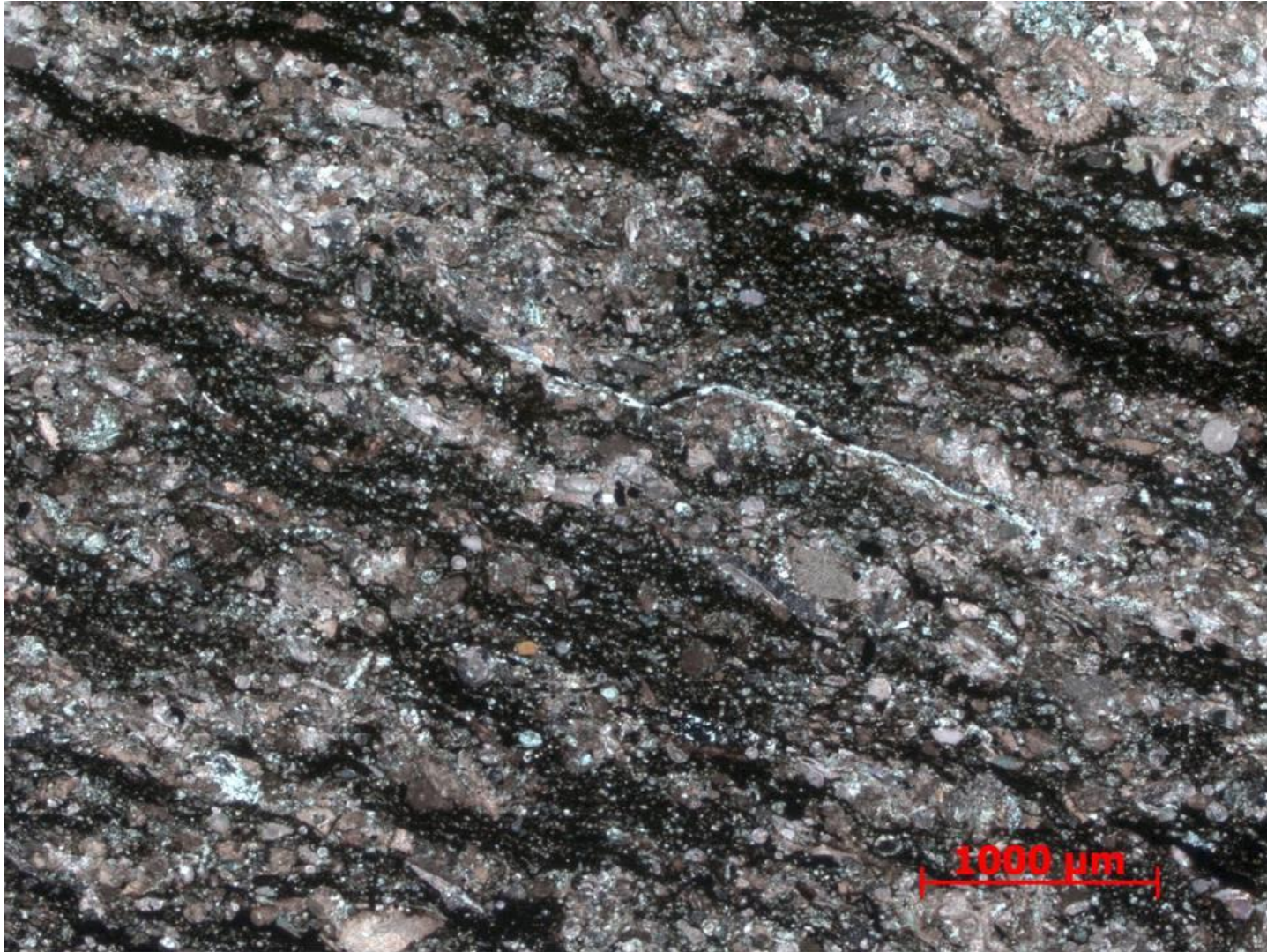


Figure 129. Sample Depth: 9689.17 ft. 2.5x XPL – 2.5x magnification of inclined discontinuous clay laminations composed of diffuse rip up clasts. Calcite lithoclasts and allochems well cemented compared to clay fragments. Moderately well sorted along laminations relative to more grainstone (devoid of mud) portions previously seen.

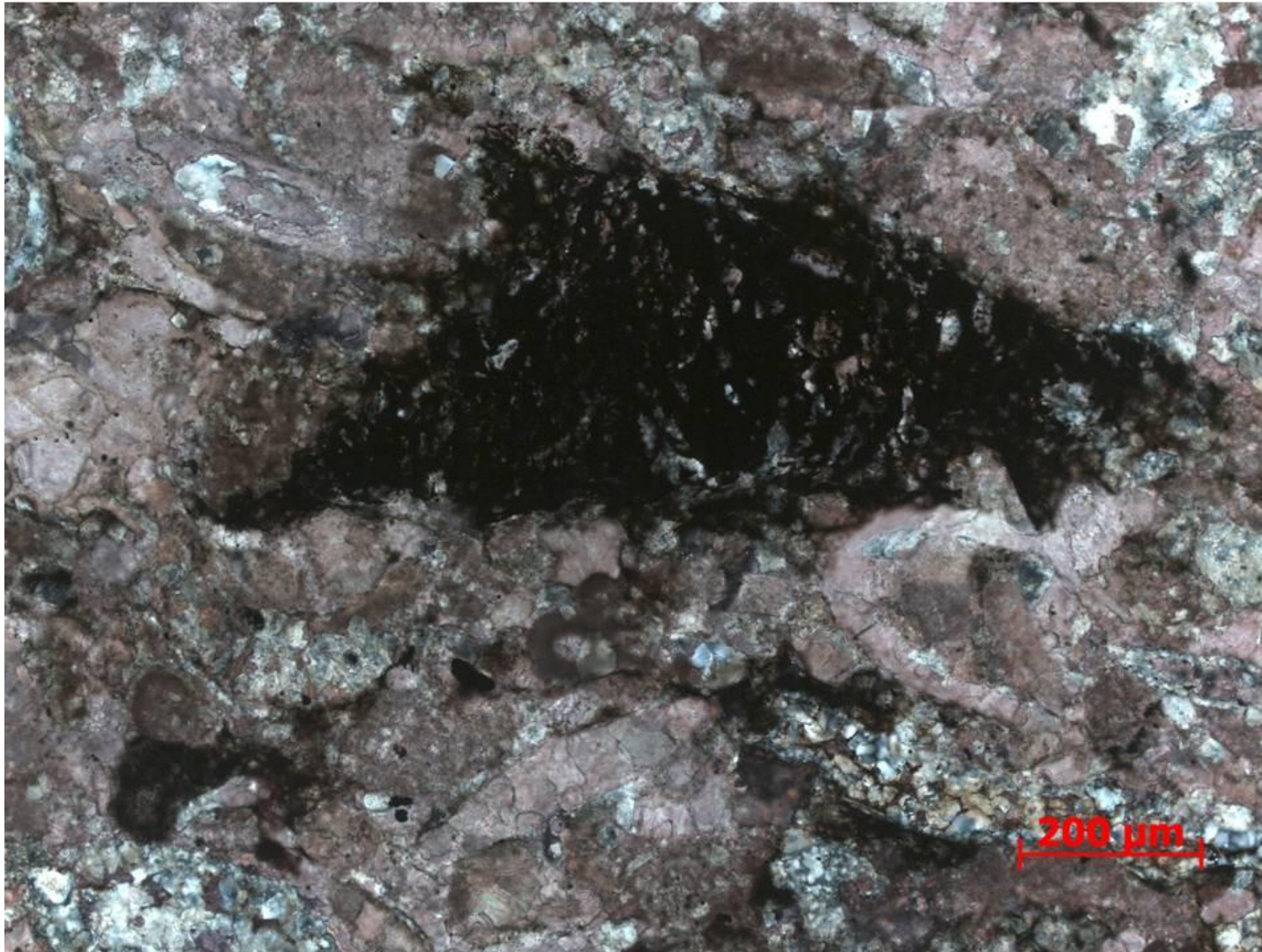


Figure 130. Sample Depth: 9689.17 ft. 10x XPL – 10x magnification of isolated clay rip up within clay lamination. Abundant organic matter inferred from oil staining. Mixed calcite and silica cement. Intra- vs inter- granular cement specificity difficult to discern due to extensive grain boundary dissolution

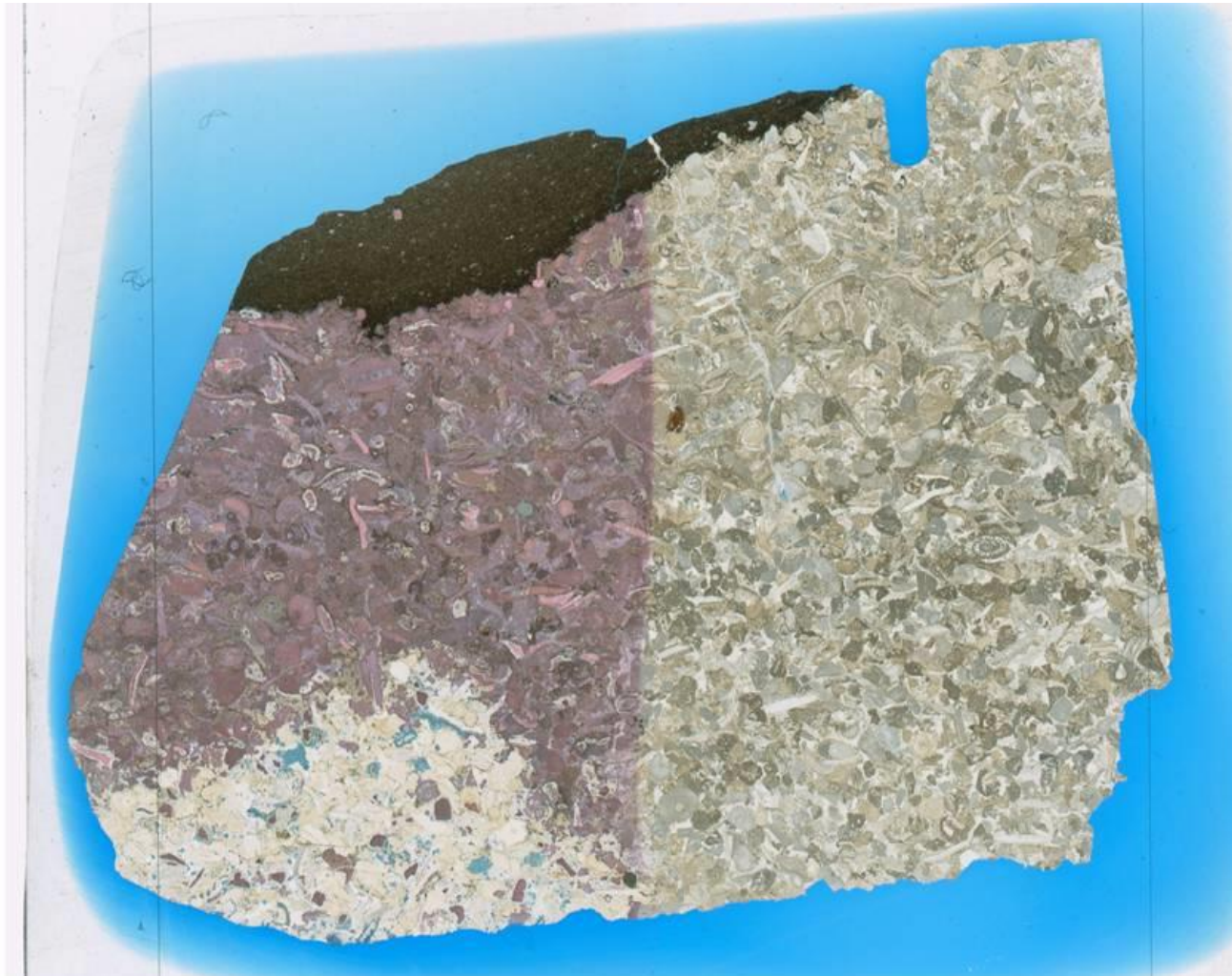


Figure 131. Sample Depth: 9690.84 ft. Mineralogy: within grain flow - calcite, no clay or OM visible, ferroan dolomite rhombs (not really replacement following skeletal fragments, just overprint?) quartz cement and replacement (some microcrystalline and chalcedony); above grain flow - clay and OM dominant, very little to absent detrital quartz, quartz present in agglutinated foram. Texture: white pore space near bottom indicating silica (microcrystalline) cement, patchy, mostly calcite cement towards top of low, grain to grain contact visible - grainstone, very well cemented, above grain flow, very clay rich, little detrital quartz, quartz present in agglutinated foram. Bioturbation: no bores or /burrows. Fauna: echinoderm shell fragments and spines, large forams, gastropods, brachiopods, bivalves, all skeletal material, no lithic fragments.

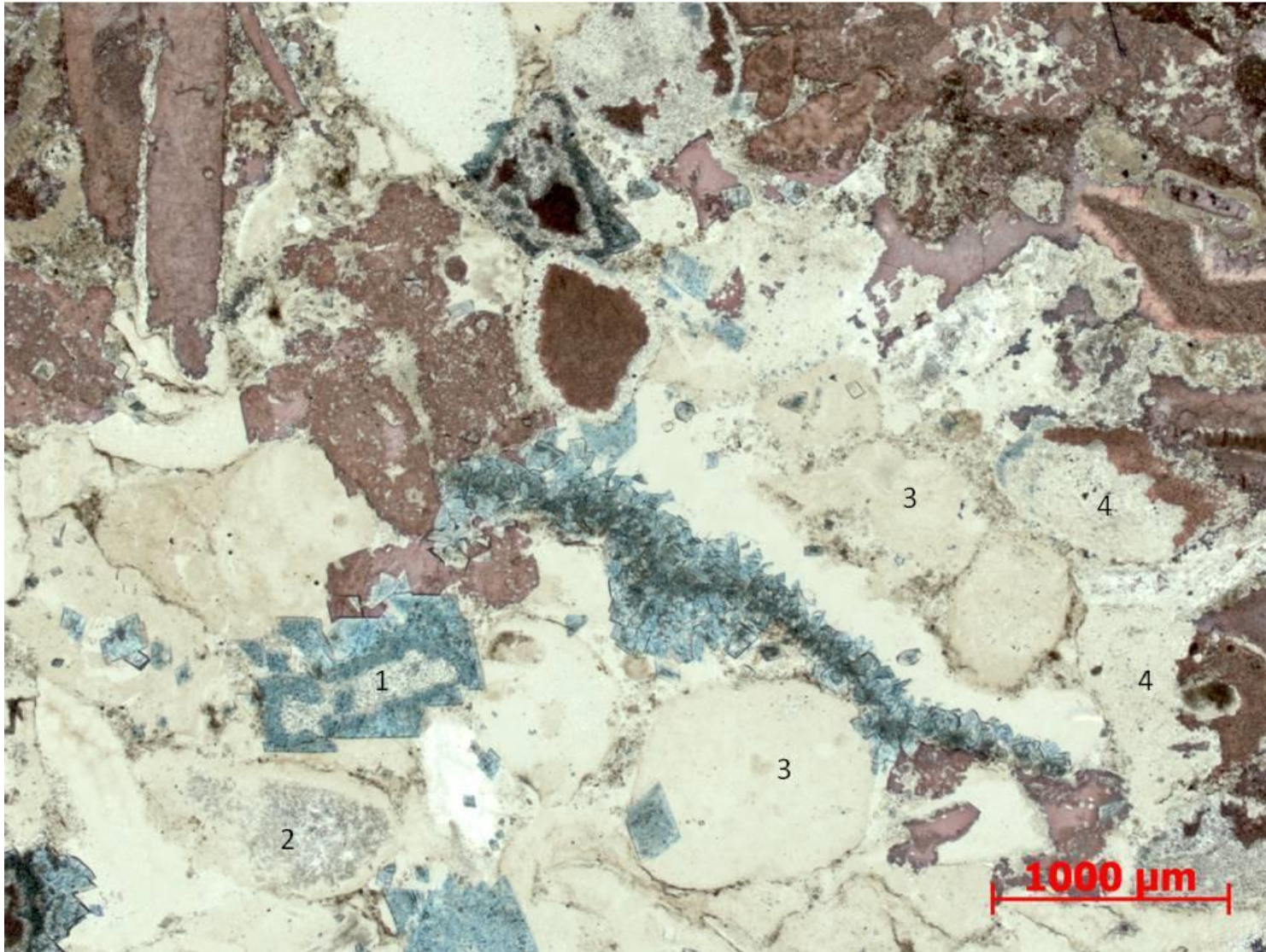


Figure 132. Sample Depth: 9690.84 ft. 2.5x PPL – Rounded and subrounded calcite allochems. (1) Replacive ferroan dolomite and overgrowth of previously dolomitized allochem. (2) Non ferroan dolomite allochem with edge replacive cement, most likely silica. (3) Complete silica overgrowth on silica replaced allochems (4) Partial silica replacement of previously carbonate allochems. Most likely multiple diagenetic fluid fronts recorded complex diagenetic history or fluid front.



Figure 133. Sample Depth: 9690.84 ft. 2.5x XPL – Abundant dark gray stippled with white intergranular and replacive intragranular microcrystalline quartz cement – (1) halos of previous grain boundaries prior to silica cement overprint visible. (2) Calcite grain exhibiting calcite cement overgrowth. (3) Indiscriminate replacive ferroan dolomite with individual rhombs approximately 200 μm . (4) Intergranular pore filling ferroan dolomite cement (5) Original calcite allochems with intergranular non ferroan dolomite and calcite cement.

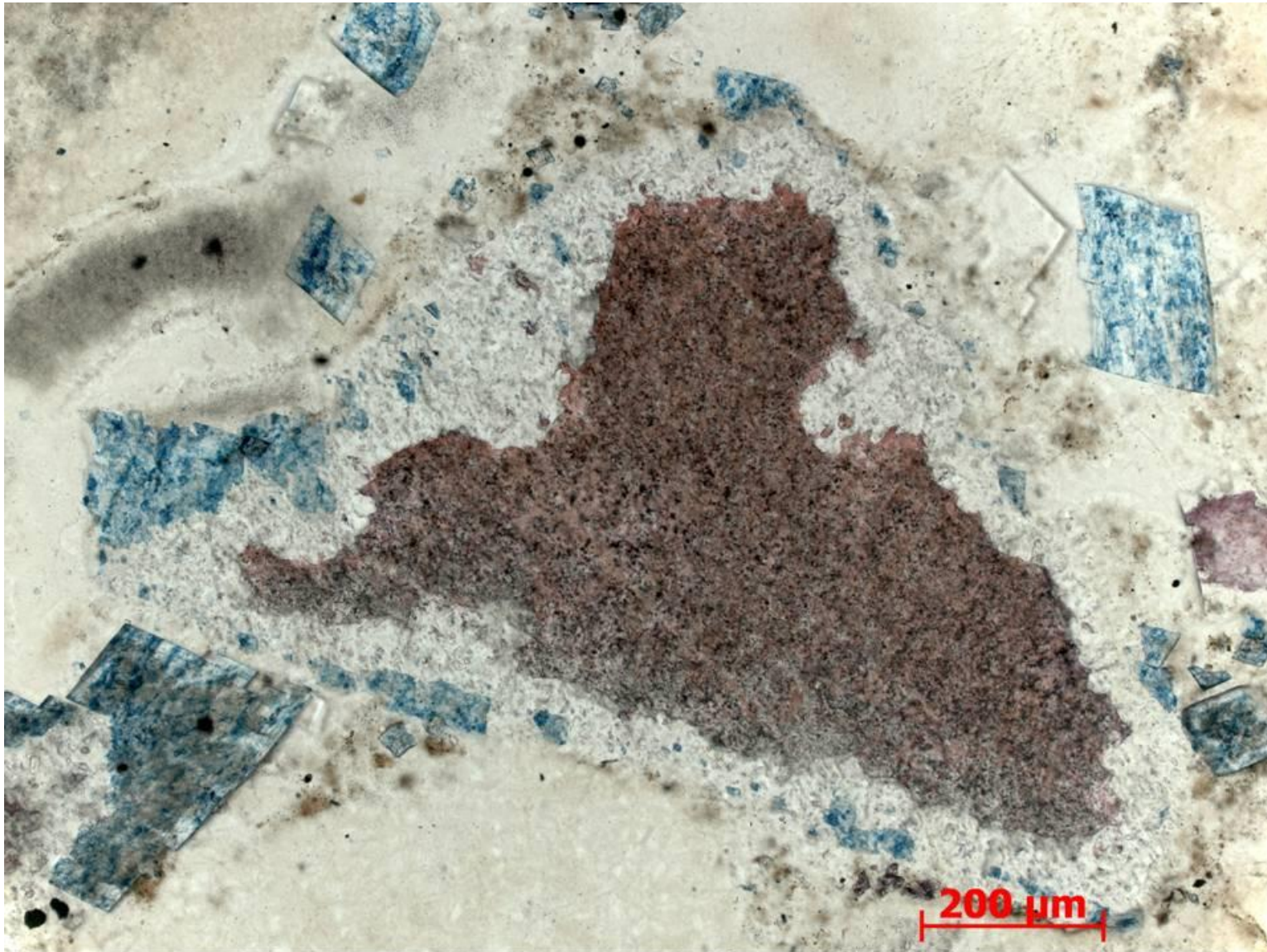


Figure 134. Sample Depth: 9690.84 ft. 10x PPL – Different carbonate forms all exhibit higher optical relief than surrounding silica / chert cement. Very well defined dolomite rhomb, mainly indiscriminate replacement.

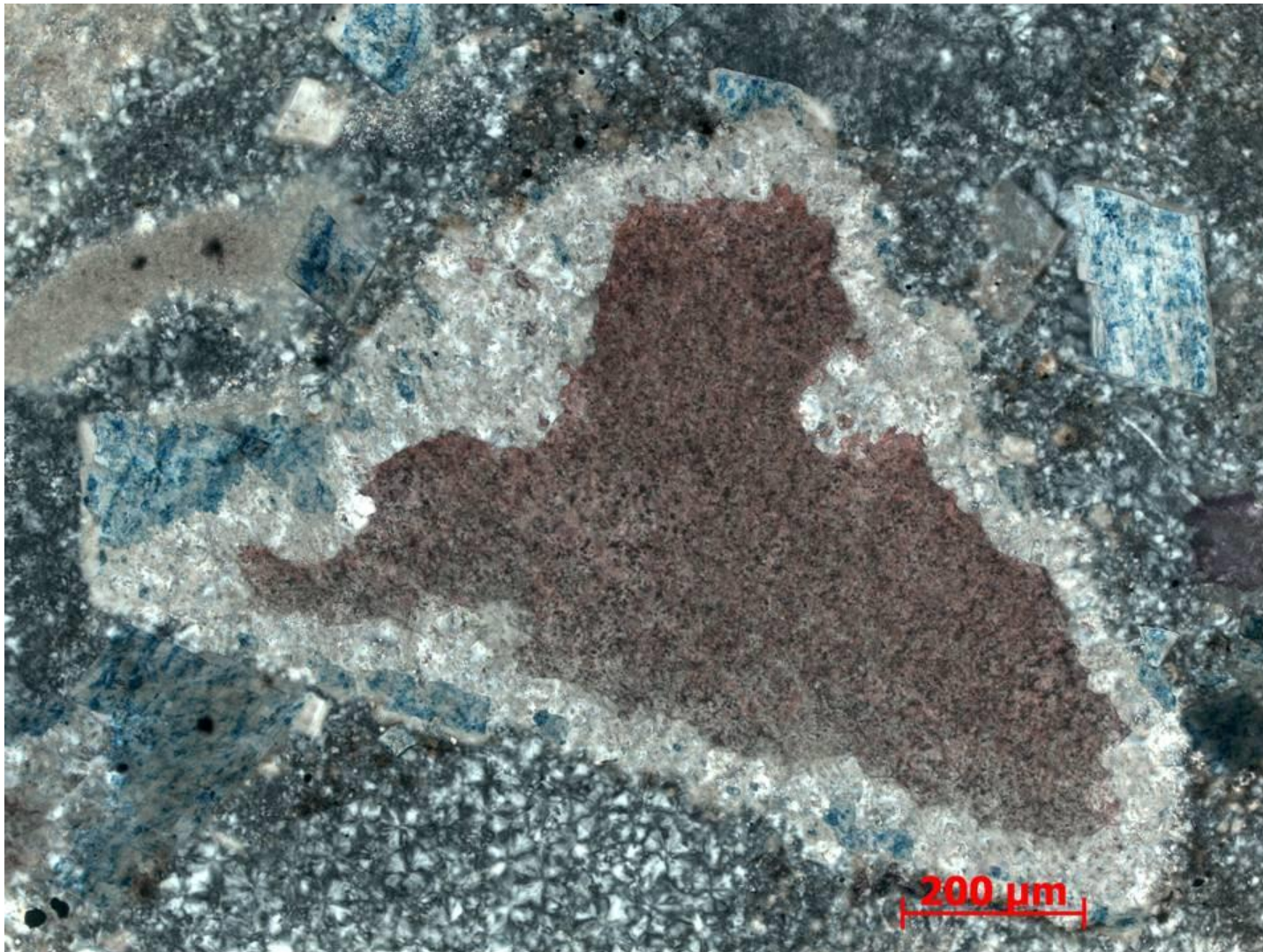


Figure 135. Sample Depth: 9690.84 ft. 10x XPL – Multiple cement types and zonation visible. Mottled calcite grain interior with dolomitized rim. Non ferroan dolomite gray white rim high optical relief. Edge dolomite rhombohedrals small and poorly defined. Either replacive or showing syntaxial growth off of central calcite allochem. Replacive ferroan dolomite over dolomite overgrowth and randomly within intergranular cement. Large ferroan rhombs (> 200 um long). Microcrystalline quartz cement surrounding majority of carbonate allochem – note low birefringence and undulose extinction.

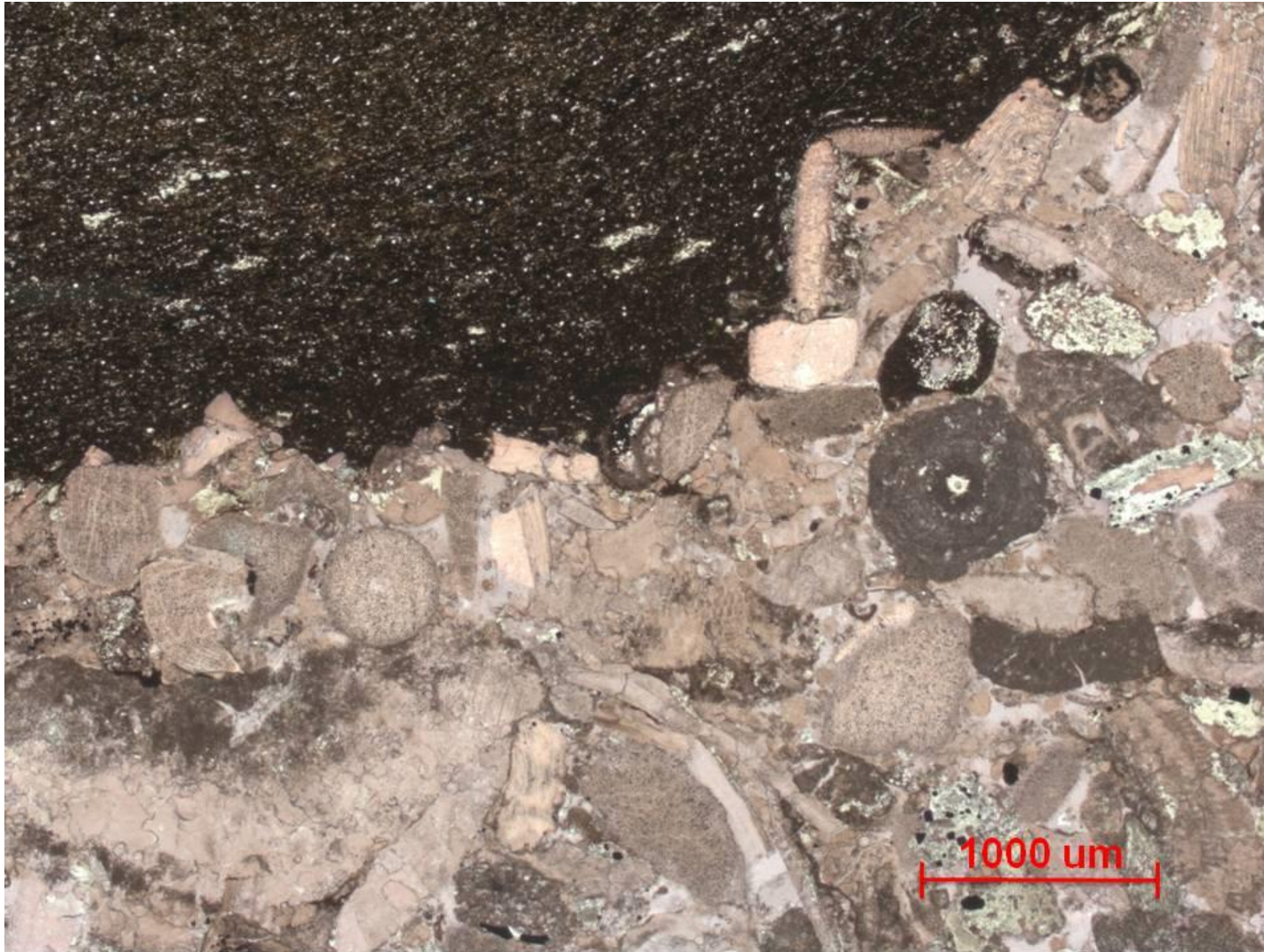


Figure 136. Sample Depth: 9690.84 ft. 2.5x PPL – Contact between calcareous portion and overlying argillaceous section. Lower calcareous portion, predominately calcite (red from staining), well cemented grainstone, lacking mud entirely. Randomly oriented moderately sorted sub angular carbonate allochems. Argillaceous portion above fine grained with minimal detrital quartz, primarily clays. White 200 μm long tasmanites.



Figure 137. Sample Depth: 9697.17 ft. Mineralogy: little dolomitization, calcareous lithic and shell fragments, clay matrix, small detrital quartz grains (very rarely in matrix), microcrystalline quartz abundant in chert in fossil fragments, large clay and micrite lithic fragment present. Texture: large rounded lithic fragments – visible intraclasts – well rounded, longer transport distance?? Fine grained matrix, matrix dominated, clasts and fragments rarely have grain contact. No bioturbation. Allochems- bryozoan, echinoderms, brachiopods, large multi-chamber forams (diverse assemblage), indistinguishable fossil fragments

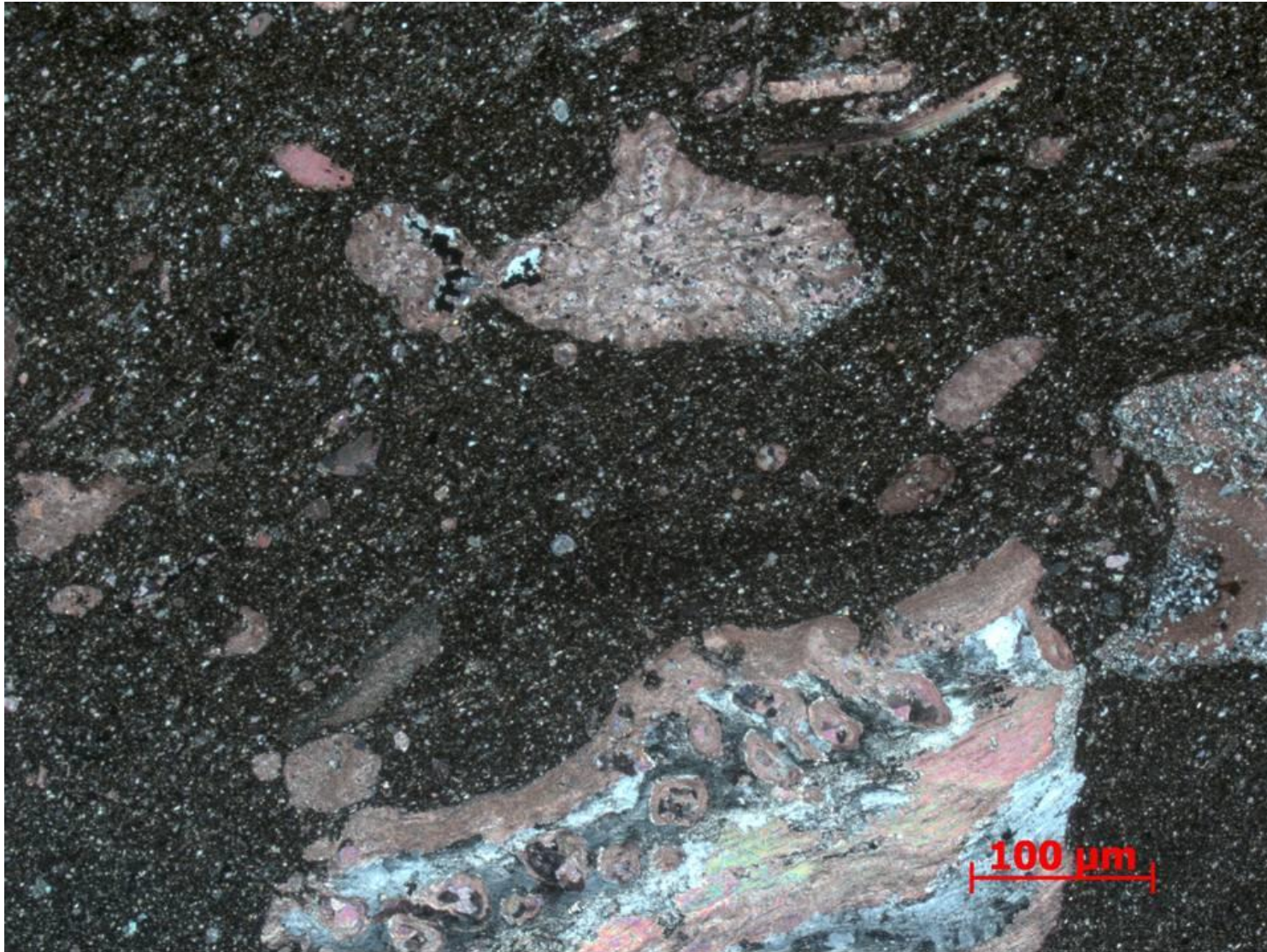


Figure 138. Sample Depth: 9697.17 ft. 10x XPL - Longitudinal section of calcite pseudopunctate (small 30 μm circular openings for spines) brachiopod shell fragment (~250 μm wide and >300 μm). Partial microcrystalline replacive cement aligning to original feathery internal structure. 150 μm long bryozoa fragment with some silica cement along edge, internally void cement primarily equant sparry calcite. Elongate subangular to spherical subrounded carbonate allochems. Matrix primarily clay rich with minor detrital quartz fraction.



Figure 139. Sample Depth: 9697.17 ft. 20x XPL – 20x magnification of bryozoan from previous slide: Bryozoan with calcite infill in void space. Original calcite mesh structure preserved. (1) Partial organic matter infill of void space with surrounding silica cement (2) Partial silica overgrowth and allochem coating.

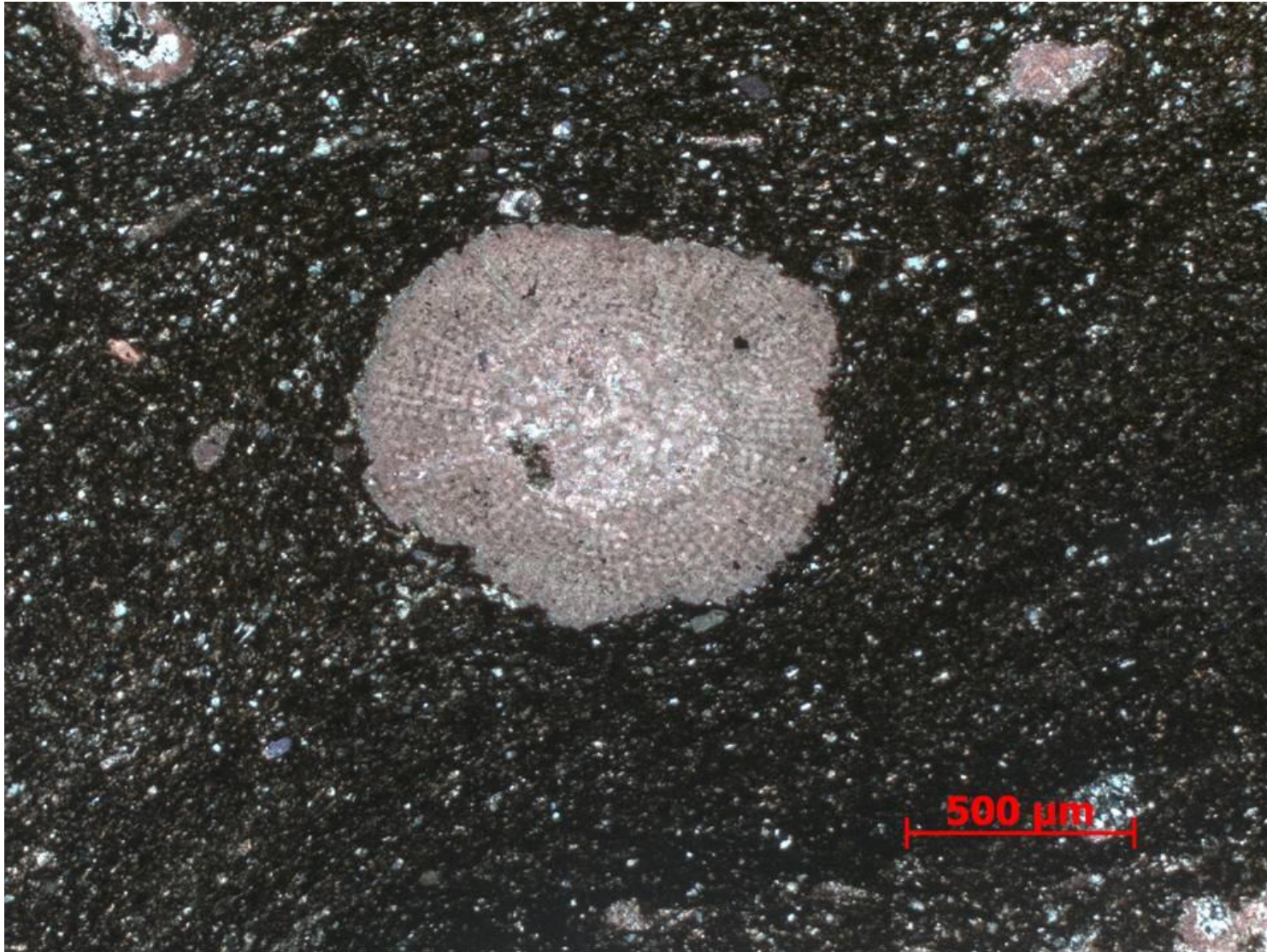


Figure 140. Sample Depth: 9697.17 ft. 5x XPL – 700 um well rounded calcite echinoderm fragment, potentially abraded spine. Radiating mesh texture preserved. Matrix composed of mainly clay size particles with minor mix of rounded fine silt sized undifferentiated carbonate clasts and detrital quartz.

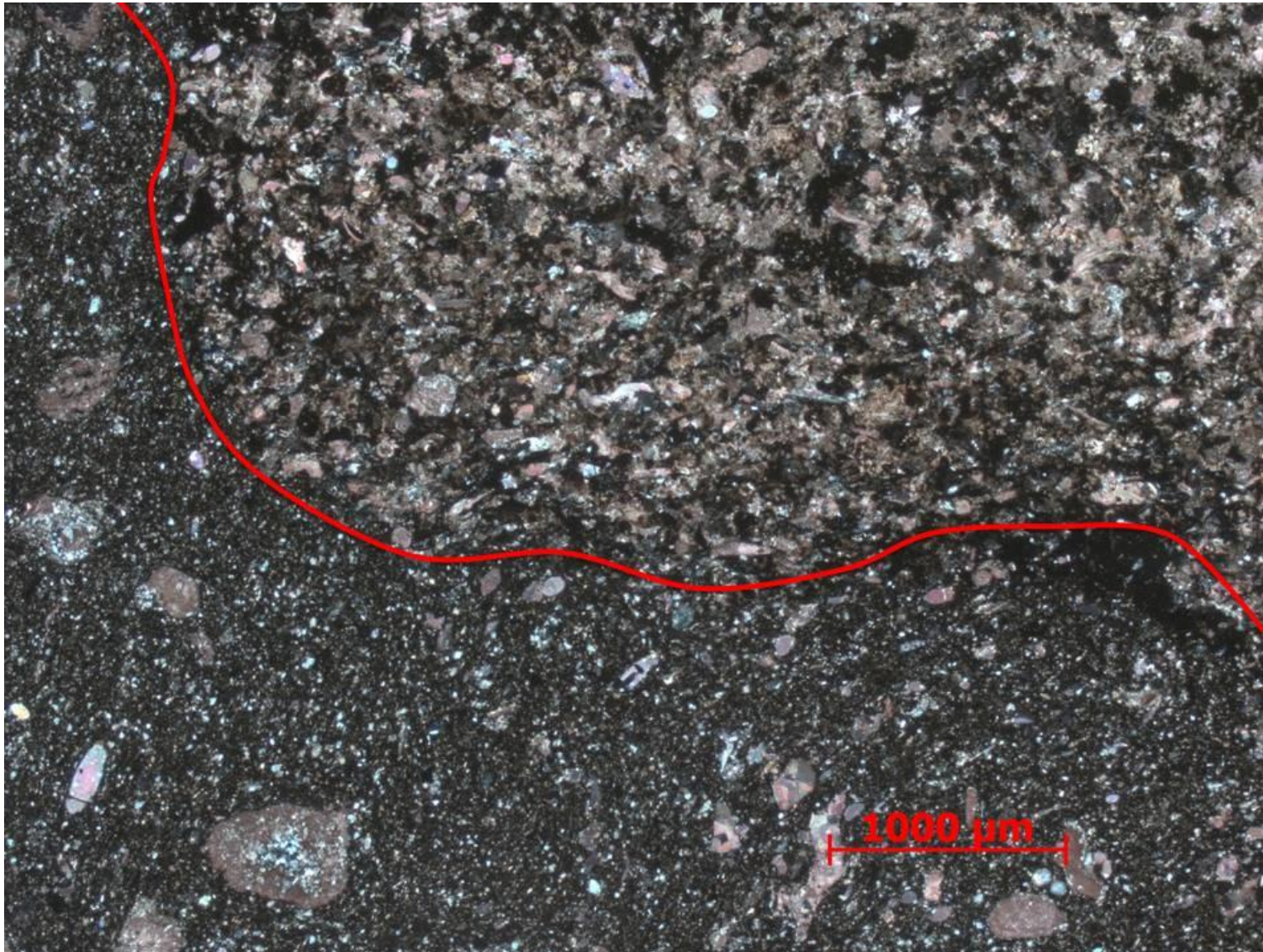


Figure 141. Sample Depth: 9697.17 ft. 2.5x XPL – Contact between subrounded carbonate fragment lithoclast composed of clay and carbonate skeletal fragments. Organic material in clay fragments of lithoclast more so than matrix. Matrix coarser grained with more detrital quartz than clay fragments within lithoclasts. Partial micritization of carbonate allochems within lithoclast visible – mottled texture.

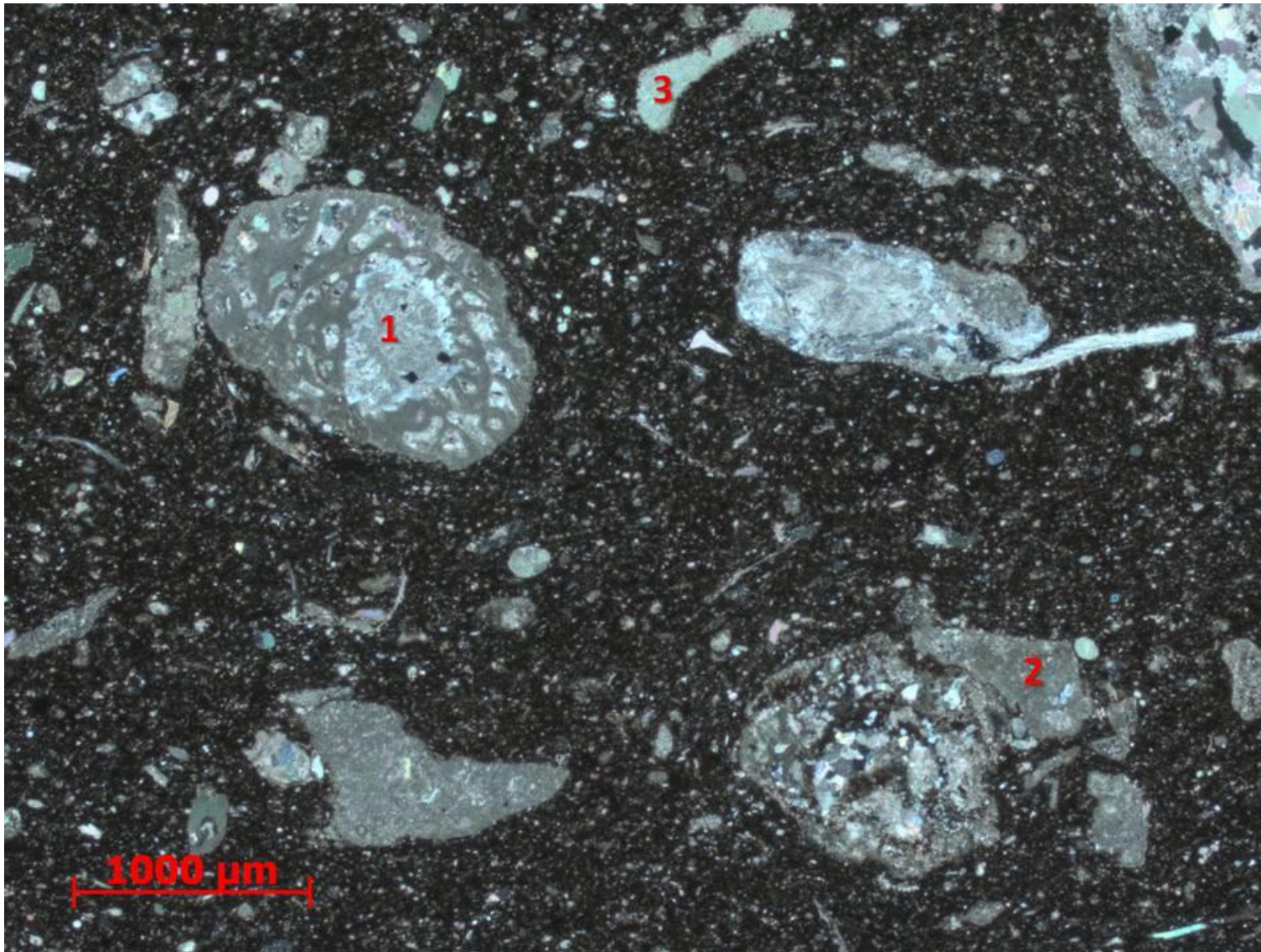


Figure 142. Sample Depth: 9697.17 ft. 2.5x XPL – (non-stained half of thin section) (1) Large multichamber foram (1000 um long) with high birefringence calcite chamber infill. Clay matrix with silt sized allochthonous carbonate and detrital quartz clasts. (2) Shattered multi-chamber foram with sparry calcite infill – indicating high energy environment. (3) Echinoderm spine fragment

Appendix C. Inorganic Geochemistry

Major and Minor Elements at TOC Data Points – Major elements expressed in weight percent %

DEPTH (FT.)	AL%	CA%	FE%	K%	MG%	MN%	NA%	P%	SI%	S%	TOC	S1	S2	S3	TMAX	HI	OI
9539.17	13.79	1.69	4.80	4.97	1.42	0.06	0.92	0.08	67.65	2.55	2.45	2.13	5.42	0.35	450	221.13	14.28
9543.17	10.50	2.35	5.33	3.80	1.88	0.06	0.78	0.19	66.63	6.69	2.84	3.41	7.24	0.24	449	255.02	8.45
9547.17	9.98	3.41	4.24	3.65	0.57	0.06	0.94	0.12	69.32	6.09	3.48	4.60	9.34	0.19	451	268.47	5.46
9551.17	0.00	11.88	0.72	0.00	2.11	0.02	0.00	76.56	8.70	0.00	3.79	2.03	3.42	0.44	445	90.29	11.62
9565.17	8.85	2.26	3.42	3.08	1.03	0.06	0.96	0.10	76.38	2.48	3.80	2.32	3.37	0.31	445	88.61	8.15
9569.50	12.40	2.85	5.04	4.28	0.60	0.06	1.13	0.09	68.78	2.81	3.83	3.22	8.40	0.50	450	219.21	13.05
9573.17	10.96	1.55	4.11	3.96	1.06	0.06	0.95	0.10	72.64	2.62	1.76	1.79	3.58	0.39	448	203.06	22.12
9577.17	10.60	0.64	4.04	3.89	1.09	0.06	0.87	0.10	74.19	2.72	2.69	2.22	4.53	0.33	449	168.40	12.27
9581.17	11.14	1.95	5.15	3.96	1.76	0.05	0.77	0.12	69.54	3.72	3.43	4.70	9.43	0.28	450	275.33	8.18
9585.17	10.46	2.28	4.19	3.75	1.81	0.06	0.79	0.11	71.89	2.82	2.09	1.68	3.59	0.41	445	171.85	19.63
9589.17	18.58	5.89	8.66	6.45	2.47	0.05	0.90	0.28	48.29	6.56	1.99	2.70	6.27	0.36	450	314.92	18.08
9593.17	8.99	6.56	6.42	2.94	2.71	0.06	0.66	0.15	67.06	2.81	3.29	2.08	5.69	0.30	452	172.74	9.11
9597.17	11.47	1.56	5.49	4.30	1.40	0.06	0.87	0.09	69.74	3.31	3.25	1.56	3.23	0.30	447	99.26	9.22
9601.33	6.19	25.48	4.51	1.60	2.51	0.05	0.50	0.36	54.57	3.24	3.24	3.43	7.34	0.18	453	226.54	5.56
9605.17	1.48	72.42	4.31	0.30	11.87	0.06	0.58	0.00	7.90	0.73	1.02	1.00	1.86	0.45	445	183.07	44.29
9609.17	11.13	2.55	4.85	3.94	1.11	0.06	0.78	0.12	68.86	4.88	3.02	2.35	6.47	0.52	451	214.24	17.22
9613.17	1.91	58.06	10.63	0.45	16.55	0.10	0.83	0.00	10.12	0.75	3.32	2.66	7.60	0.70	451	229.12	21.10
9617.17	9.17	3.54	4.79	3.32	1.59	0.06	0.85	0.12	72.41	2.61	2.24	1.86	3.94	0.31	449	175.81	13.83
9621.17	1.42	55.75	3.36	0.16	3.11	0.05	0.45	0.44	32.16	2.75	0.64						
9625.17	14.05	1.05	5.77	5.12	0.83	0.06	1.10	0.07	66.35	3.52	2.47	2.00	4.73	0.32	449	191.89	12.98
9629.17	11.04	4.42	6.29	4.10	0.00	0.06	1.26	0.09	66.44	4.44	1.39	0.94	1.73	0.39	448	124.10	27.98
9631.17	11.46	2.96	6.35	4.00	1.76	0.05	0.71	0.14	65.37	5.38	1.81	1.03	2.45	0.37	449	135.43	20.45
9637.34	14.86	2.99	5.93	5.45	1.85	0.05	0.79	0.14	59.74	6.22	3.13	1.63	4.67	0.55	451	149.11	17.56
9641.17	9.93	3.20	4.57	3.58	1.86	0.06	0.79	0.17	67.69	6.37	3.76	3.34	9.29	0.24	453	247.40	6.39
9645.17	0.12	72.01	6.11	0.03	8.62	0.04	0.54	0.00	11.78	0.54	0.46						
9649.17	0.00	78.33	2.75	0.04	5.71	0.08	0.76	0.00	11.76	0.35	0.38						
9653.17	10.74	4.29	4.73	3.98	2.19	0.05	0.46	0.22	61.50	10.27	1.16	0.88	1.73	0.23	450	149.27	19.84
9657.17	5.35	11.08	5.26	2.53	2.87	0.05	0.36	7.44	58.76	5.21	3.53	2.59	6.23	0.32	452	176.59	9.07
9661.17	10.48	3.05	3.82	3.68	1.93	0.07	0.70	0.16	68.11	6.47	2.64	2.28	5.52	0.19	452	208.77	7.19

9665.34	9.17	8.42	4.01	3.39	1.12	0.07	0.94	0.12	67.84	3.39	2.60	1.63	3.94	0.55	450	151.83	21.19
9669.00	2.29	65.05	2.83	0.48	3.20	0.05	0.42	0.17	23.98	1.09	1.40	1.14	2.28	0.35	449	163.21	25.05
9673.17	10.61	2.69	4.42	3.50	1.11	0.06	0.88	0.12	71.10	3.73	2.76	2.10	5.30	0.39	449	191.82	14.12
9677.17	9.54	8.40	4.57	3.01	1.52	0.06	0.86	0.20	66.96	3.25	3.40	3.02	8.12	0.38	451	239.10	11.19
9681.17	11.93	5.39	5.48	3.99	1.90	0.06	0.87	0.14	63.92	4.34	3.22	2.83	8.39	0.44	448	260.88	13.68
9685.17	11.71	3.61	4.87	3.86	0.75	0.06	0.93	0.12	67.30	4.92	2.69	2.27	6.55	0.47	450	243.95	17.50
9689.17	9.23	19.69	5.87	2.90	2.00	0.06	0.89	0.19	55.31	2.41	2.68	1.73	4.54	0.58	453	169.47	21.65
9693.17	7.54	27.28	4.19	2.01	2.63	0.05	0.64	0.31	51.18	2.87	2.24	1.86	3.85	0.38	449	172.11	16.99
9697.17	7.05	13.29	4.00	2.02	1.13	0.07	0.99	0.22	68.03	1.98	2.50	2.09	4.15	0.56	445	165.80	22.37

Trace Element Concentrations at TOC Data Points – Trace elements expressed in parts per million (ppm)

DEPTH (FT.)	CO	CR	CU	MO	NI	RB	SR	TH	U	V	ZN	ZR	TOC	S1	S2	S3	TMAX	HI	OI
9539.17	10.35	221.21	51.64	22.82	161.31	122.65	105.81	7.98	0.00	84.80	348.21	112.50	2.45	2.13	5.42	0.35	450	221.13	14.28
9543.17	12.51	126.60	42.04	21.83	123.56	105.15	135.58	7.69	1.91	68.83	170.65	112.75	2.84	3.41	7.24	0.24	449	255.02	8.45
9547.17	10.54	62.90	23.17	19.75	91.43	102.14	141.73	7.46	7.29	78.37	59.29	116.61	3.48	4.60	9.34	0.19	451	268.47	5.46
9551.17	0.00	0.00	0.00	0.00	0.00	0.00	0.00	0.00	0.00	88.77	0.00	0.00	3.79	2.03	3.42	0.44	445	90.29	11.62
9565.17	9.62	39.64	28.86	19.98	80.99	99.32	143.17	7.84	0.00	71.81	178.49	104.65	3.80	2.32	3.37	0.31	445	88.61	8.15
9569.50	11.57	96.96	17.70	17.90	82.70	108.92	150.31	8.12	2.41	36.86	34.09	146.58	3.83	3.22	8.40	0.50	450	219.21	13.05
9573.17	10.52	92.73	7.93	16.39	68.19	111.53	148.86	8.05	9.15	58.52	27.96	146.36	1.76	1.79	3.58	0.39	448	203.06	22.12
9577.17	9.87	181.65	21.29	28.93	105.16	102.23	99.28	7.40	1.20	73.16	142.48	110.06	2.69	2.22	4.53	0.33	449	168.40	12.27
9581.17	10.42	169.16	13.61	27.53	92.88	104.07	110.18	6.87	0.00	122.01	78.18	107.15	3.43	4.70	9.43	0.28	450	275.33	8.18
9585.17	10.53	142.59	11.38	27.49	84.29	93.41	136.69	6.47	0.00	108.99	44.56	98.20	2.09	1.68	3.59	0.41	445	171.85	19.63
9589.17	20.20	189.67	20.53	10.57	62.95	166.92	423.53	11.56	6.28	0.00	48.89	91.08	1.99	2.70	6.27	0.36	450	314.92	18.08
9593.17	15.53	122.36	8.70	19.02	69.83	78.36	225.10	5.99	0.00	97.91	49.63	101.08	3.29	2.08	5.69	0.30	452	172.74	9.11
9597.17	10.75	207.34	16.48	22.05	107.58	124.90	135.86	8.65	6.47	87.69	144.67	99.90	3.25	1.56	3.23	0.30	447	99.26	9.22
9601.33	4.77	157.69	12.30	12.83	78.31	49.39	592.71	3.91	1.15	122.31	84.36	40.42	3.24	3.43	7.34	0.18	453	226.54	5.56
9605.17	5.59	33.13	0.00	0.00	23.69	9.94	862.14	2.46	8.38	64.01	0.00	19.18	1.02	1.00	1.86	0.45	445	183.07	44.29
9609.17	14.41	86.09	27.82	25.34	120.70	112.01	131.52	7.80	6.13	104.11	204.51	108.83	3.02	2.35	6.47	0.52	451	214.24	17.22
9613.17	7.19	78.34	0.00	0.00	13.71	3.77	574.45	2.48	0.00	102.72	3.45	26.66	3.32	2.66	7.60	0.70	451	229.12	21.10
9617.17	9.39	61.54	23.20	19.62	68.88	94.68	188.62	7.39	4.72	113.92	61.53	105.84	2.24	1.86	3.94	0.31	449	175.81	13.83

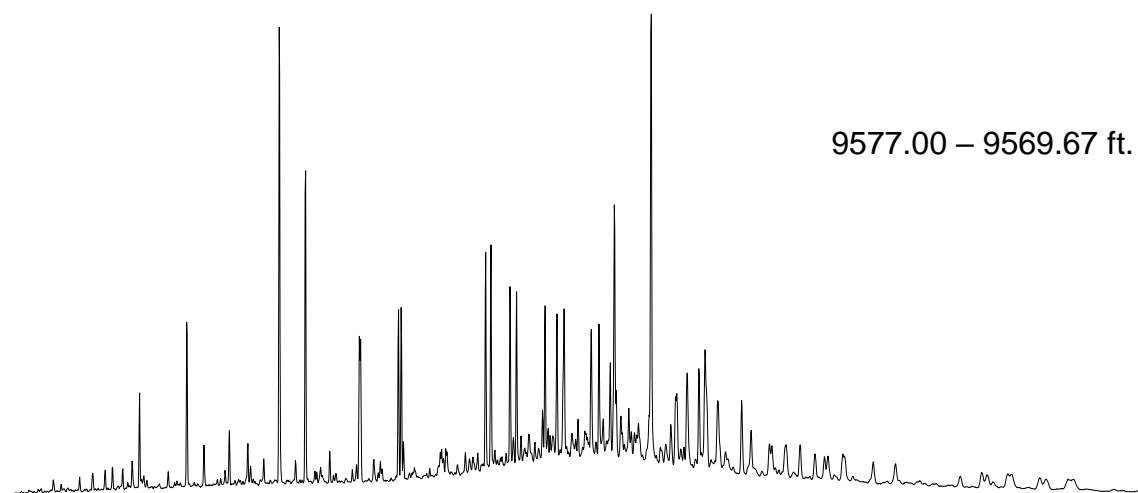
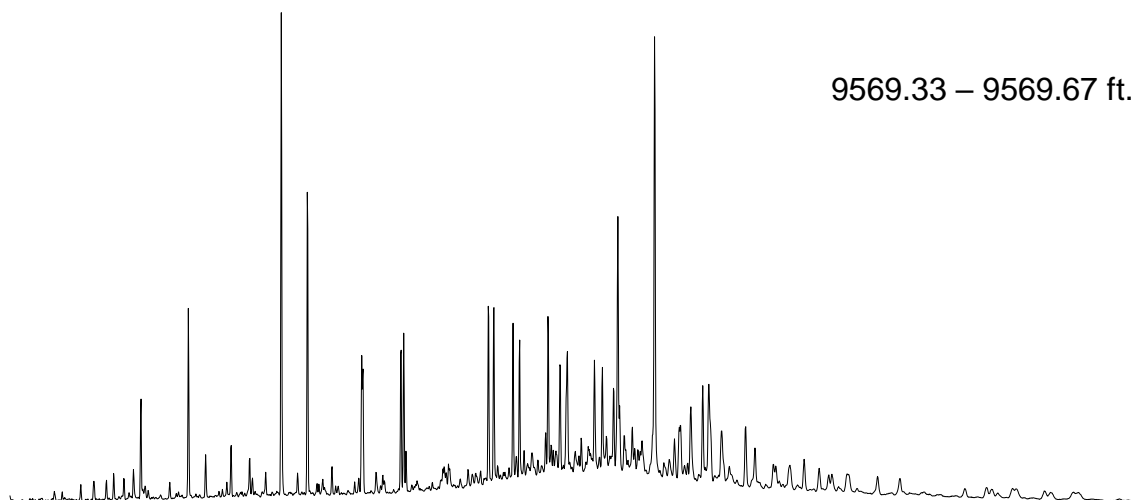
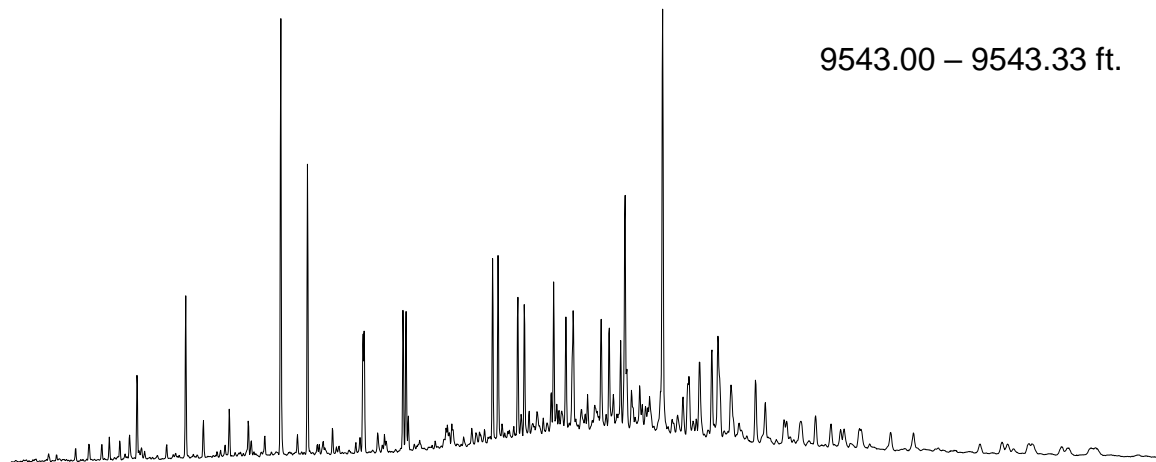
9621.17	6.92	45.58	25.88	0.00	36.11	12.30	2058.94	2.67	25.56	119.77	222.19	2.99	0.64						
9625.17	14.26	153.54	32.18	25.67	126.61	135.12	114.68	9.07	5.48	60.09	195.54	112.05	2.47	2.00	4.73	0.32	449	191.89	12.98
9629.17	14.62	177.58	26.55	27.57	106.75	107.75	127.21	7.36	4.46	65.42	110.34	94.86	1.39	0.94	1.73	0.39	448	124.10	27.98
9631.17	15.48	114.79	15.56	27.60	79.80	106.18	148.80	7.27	1.63	72.86	67.77	105.33	1.81	1.03	2.45	0.37	449	135.43	20.45
9637.34	13.90	90.09	34.86	19.90	120.17	159.60	225.47	11.28	2.59	19.71	167.14	120.24	3.13	1.63	4.67	0.55	451	149.11	17.56
9641.17	10.92	54.02	43.74	19.82	74.41	108.70	198.64	7.84	6.27	56.68	232.96	109.68	3.76	3.34	9.29	0.24	453	247.40	6.39
9645.17	5.53	63.87	0.00	0.00	13.92	0.00	1198.37	2.03	4.93	90.08	0.00	0.90	0.46						
9649.17	6.46	0.00	0.00	0.00	12.16	2.71	1218.29	2.01	14.20	73.54	0.00	6.54	0.38						
9653.17	11.68	95.44	33.14	22.35	114.39	123.00	209.58	9.36	0.00	67.43	181.06	98.30	1.16	0.88	1.73	0.23	450	149.27	19.84
9657.17	17.44	113.83	0.00	36.06	501.01	99.87	121.53	6.58	0.00	98.40	250.02	70.39	3.53	2.59	6.23	0.32	452	176.59	9.07
9661.17	10.26	78.47	42.07	25.29	99.12	115.39	204.62	8.49	8.01	77.13	153.96	96.73	2.64	2.28	5.52	0.19	452	208.77	7.19
9665.34	9.02	49.07	26.00	10.68	89.12	79.72	801.96	6.86	13.18	92.77	138.33	74.65	2.60	1.63	3.94	0.55	450	151.83	21.19
9669.00	6.16	73.00	12.18	0.00	37.21	10.19	819.94	2.92	5.15	90.94	57.11	22.05	1.40	1.14	2.28	0.35	449	163.21	25.05
9673.17	13.13	85.56	8.08	22.83	99.20	101.94	225.29	7.77	0.00	87.58	71.24	125.61	2.76	2.10	5.30	0.39	449	191.82	14.12
9677.17	10.94	61.11	26.11	19.00	111.54	82.81	309.34	6.12	5.80	91.84	124.98	98.76	3.40	3.02	8.12	0.38	451	239.10	11.19
9681.17	11.11	202.58	32.83	18.46	129.79	93.36	302.51	6.90	1.35	126.83	170.46	95.97	3.22	2.83	8.39	0.44	448	260.88	13.68
9685.17	13.14	147.17	38.27	21.67	127.69	117.25	147.92	8.34	9.70	84.20	209.96	113.08	2.69	2.27	6.55	0.47	450	243.95	17.50
9689.17	13.07	95.75	16.63	11.01	68.60	85.30	338.16	6.74	11.31	92.66	88.05	73.54	2.68	1.73	4.54	0.58	453	169.47	21.65
9693.17	9.88	83.47	18.16	10.19	71.53	60.25	428.91	5.30	4.57	80.65	73.76	73.79	2.24	1.86	3.85	0.38	449	172.11	16.99
9697.17	6.32	89.12	11.92	17.03	70.25	61.11	365.64	5.36	11.37	127.37	86.15	69.85	2.50	2.09	4.15	0.56	445	165.80	22.37

Appendix D. Biomarker fractions, m/z 191 and 217 chromatograms

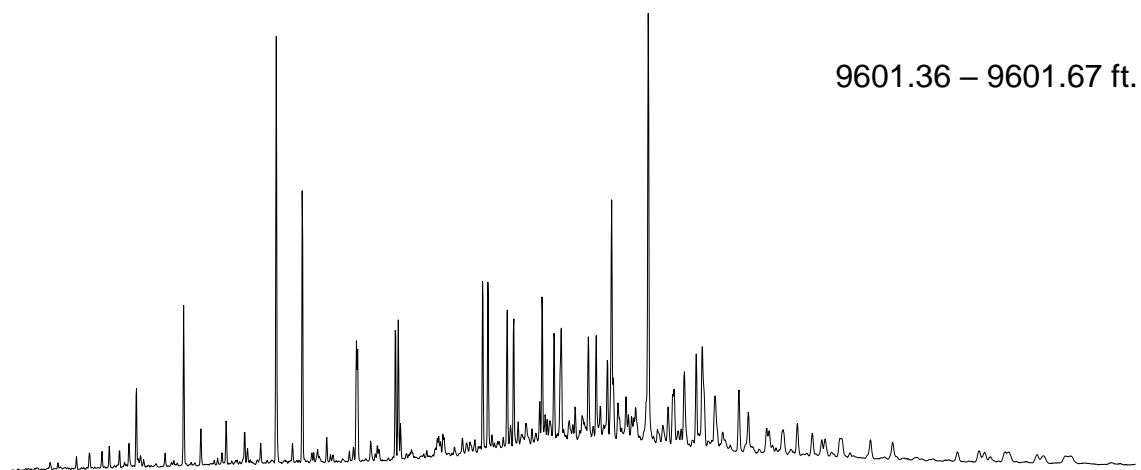
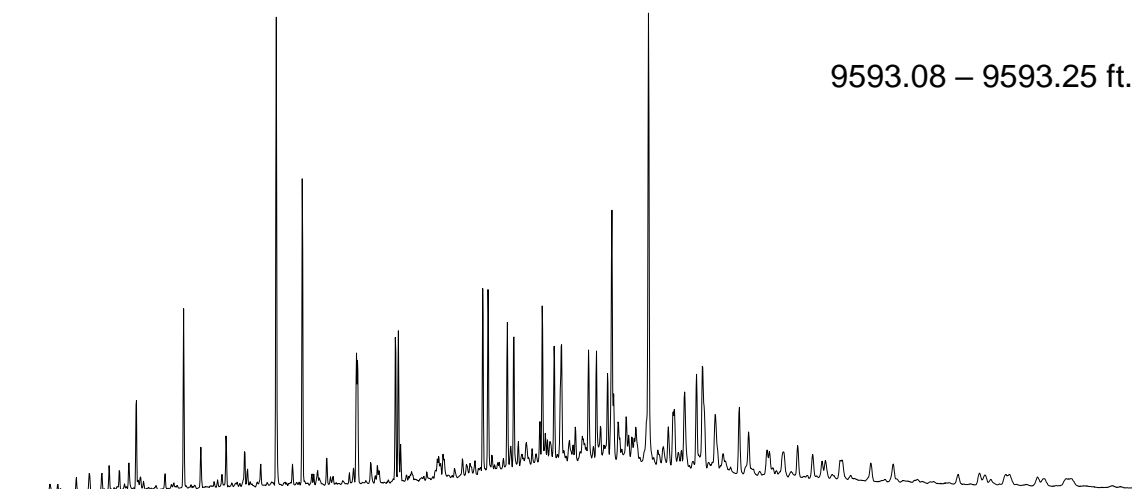
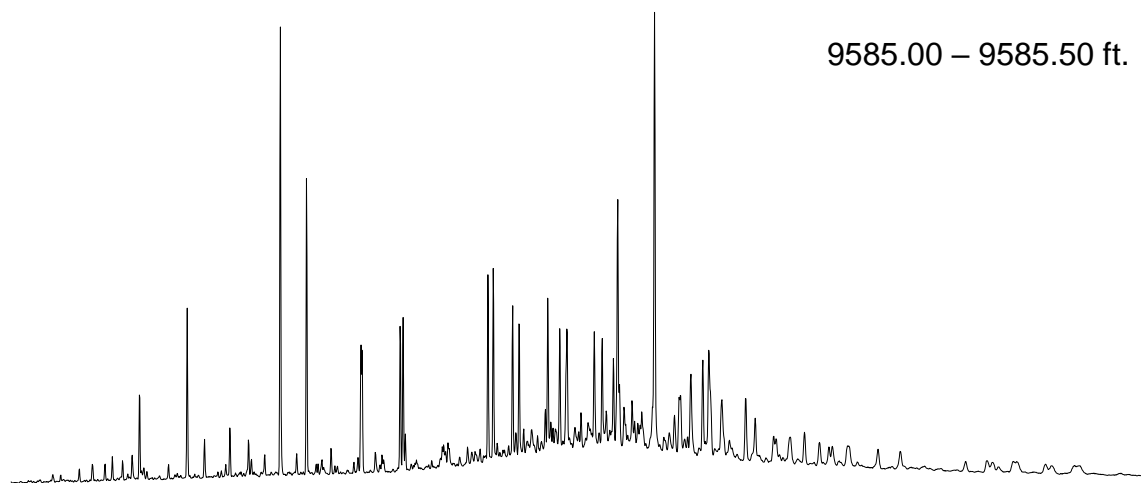
Sample Depth (ft.)		TOC depth (ft.)	TOC (wt. %)	Rock (g)	Total Extract (mg)	Maltene (% of total extract)	Asphaltene (% of total extract)	Saturate (% of maltene)	Aromatic (% of maltene)	Polars (% of maltene)
Top	Bottom									
9543.00	9543.33	9543.10	2.84	27.1	165.85	83.78	16.22	67.59	21.04	11.36
9569.33	9569.67	9569.50	3.83	28.2	185.24	82.86	17.14	64.04	24.54	11.41
9577.00	9577.33	9577.10	2.69	60.0	497.29	77.48	22.52	66.57	21.83	11.60
9585.00	9585.50	9585.20	2.09	36.4	269.97	85.68	14.32	61.27	27.18	11.55
9593.08	9593.25	9593.20	3.29	32.6	233.15	80.82	19.18	59.04	27.15	13.81
9601.36	9601.67	9601.40	3.24	13.0	94.16	85.43	14.57	61.17	28.46	10.38
9609.00	9609.17	9609.10	3.02	34.8	284.28	83.78	16.22	61.21	25.52	13.27
9617.00	9617.33	9617.10	2.24	55.5	384.57	89.88	10.12	63.63	25.25	11.12
9625.00	9625.17	9625.10	2.47	43.9	371.14	80.67	19.33	57.82	29.58	12.60
9633.00	9633.33	9633.10	1.81	43.0	242.84	80.29	19.71	64.38	22.94	12.68
9641.00	9641.33	9641.10	3.76	54.3	273.58	91.14	8.86	58.81	25.87	15.31
9645.00	9645.33	9645.20	0.46	38.5	31.87	65.52	34.48	65.63	23.85	10.52
9653.00	9653.33	9653.30	1.16	42.6	44.62	78.05	21.95	56.38	29.65	13.97
9657.00	9657.33	9657.15	3.53	36.4	290.81	82.07	17.93	56.67	30.73	12.60
9665.00	9665.42	9665.20	2.60	36.1	236.63	85.87	14.13	60.93	27.32	11.75

9673.20	9673.67	9673.20	2.76	17.5	127.67	84.52	15.48	63.00	25.75	11.25
9681.00	9681.25	9681.10	3.22	47.3	311.82	74.40	25.60	60.73	28.37	10.89
9689.00	9689.50	9689.10	2.68	24.2	19.01	69.93	30.07	65.30	25.07	9.63
9697.17	9697.42	9697.20	2.50	36.9	274.09	87.78	12.22	64.35	25.53	10.12

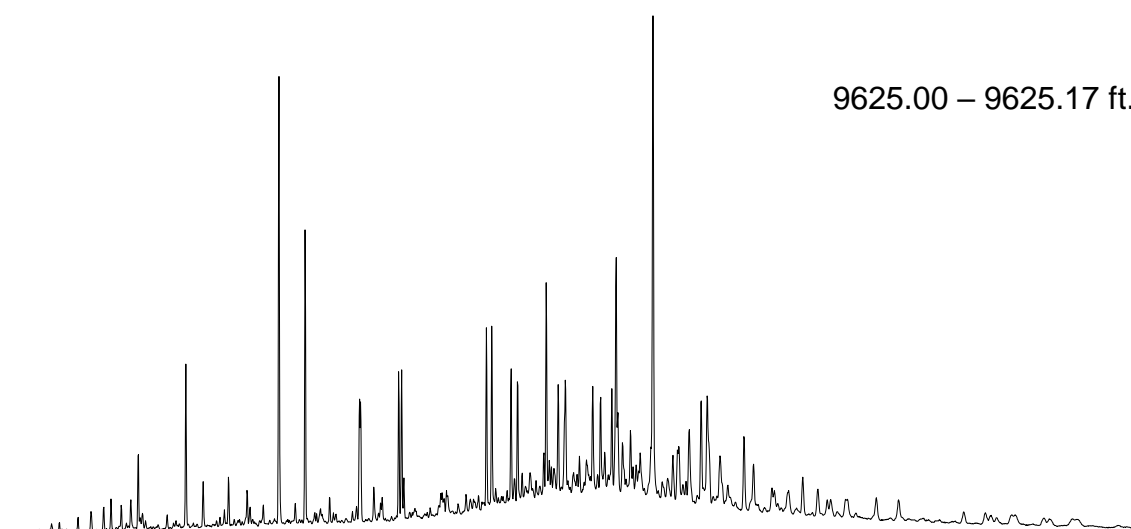
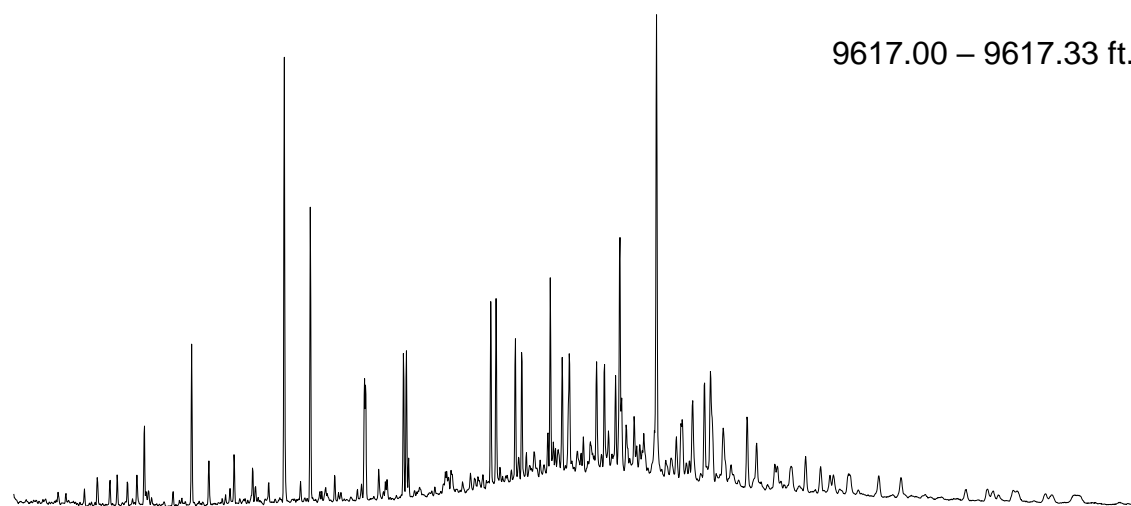
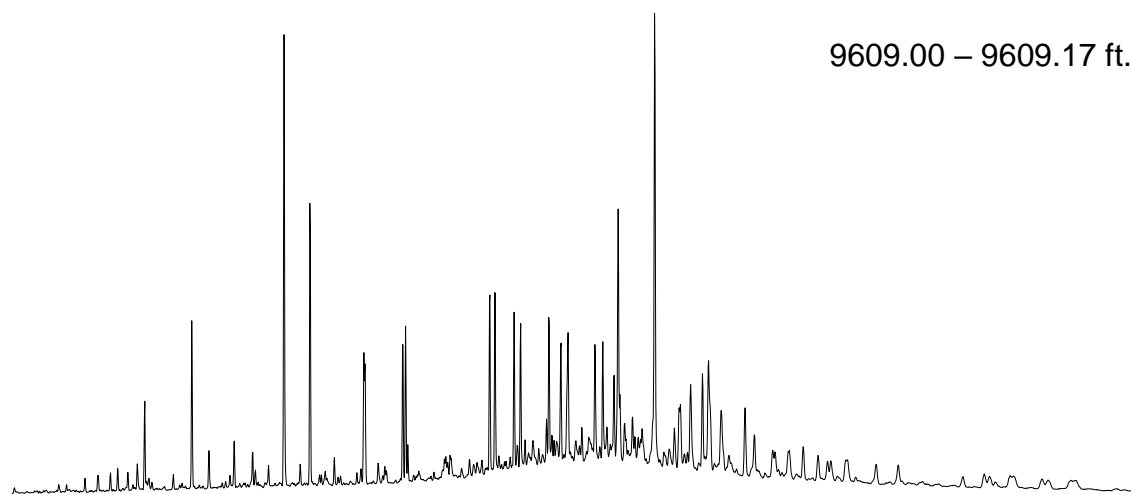
m/z 191 of branched and cyclic saturate fraction



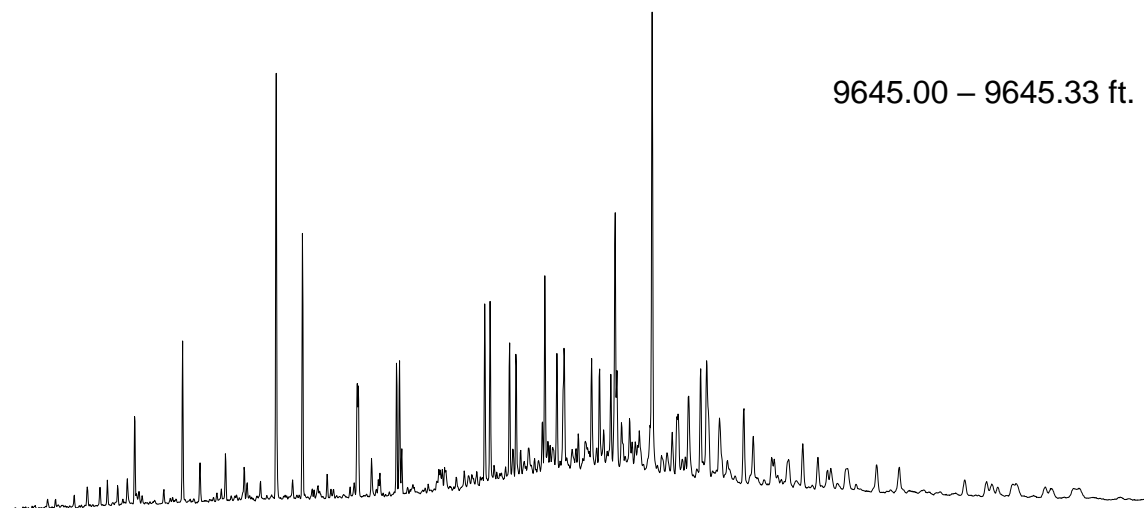
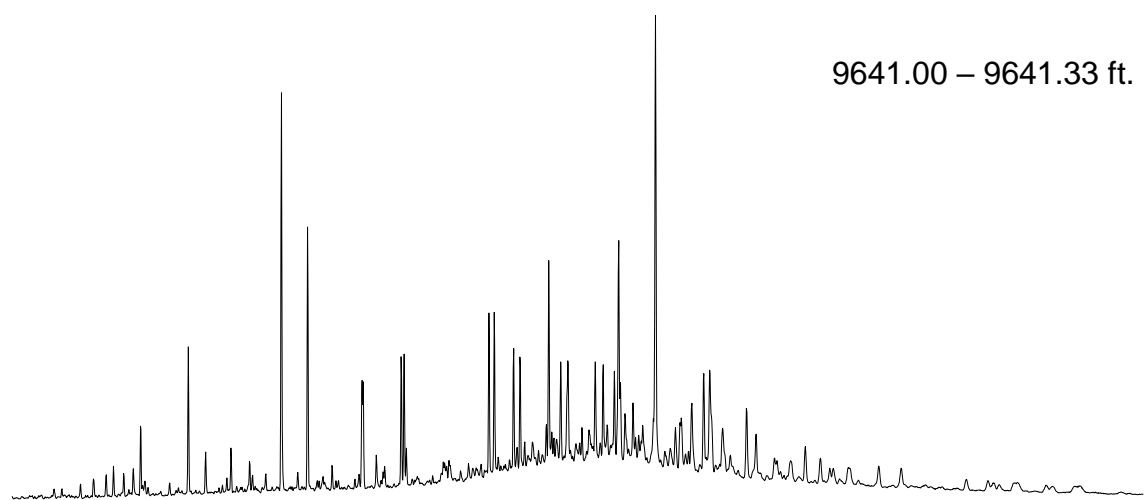
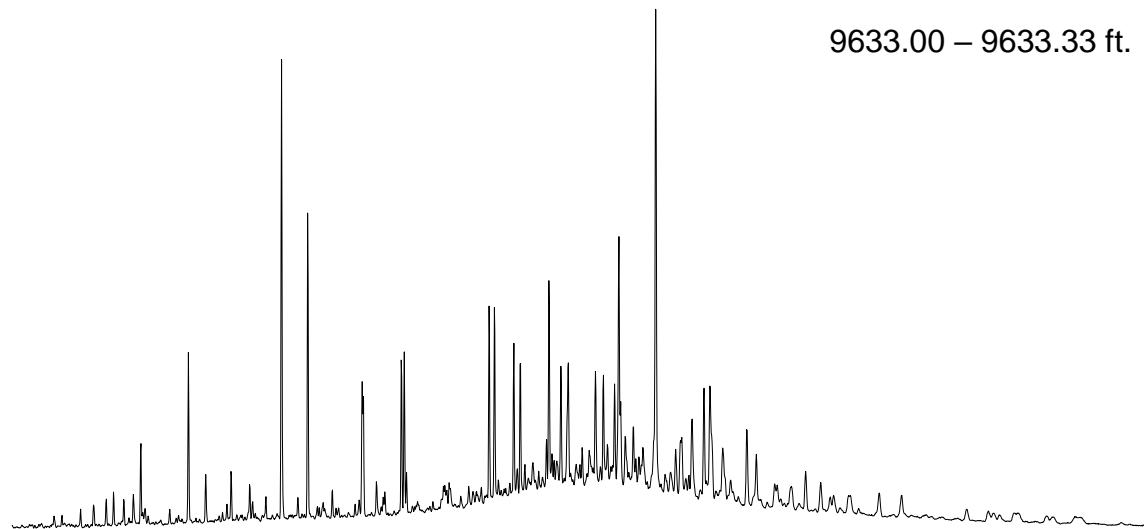
m/z 191 of branched and cyclic saturate fraction



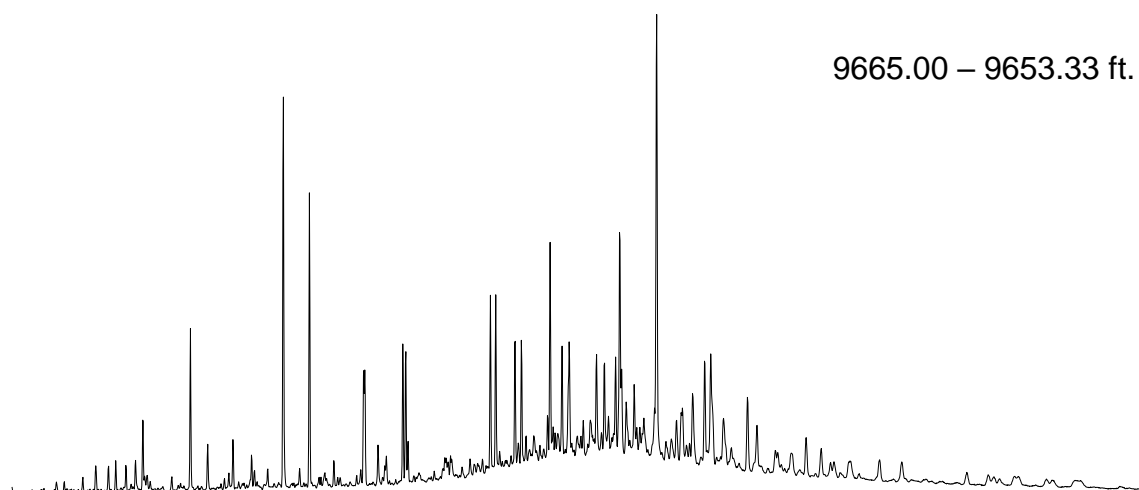
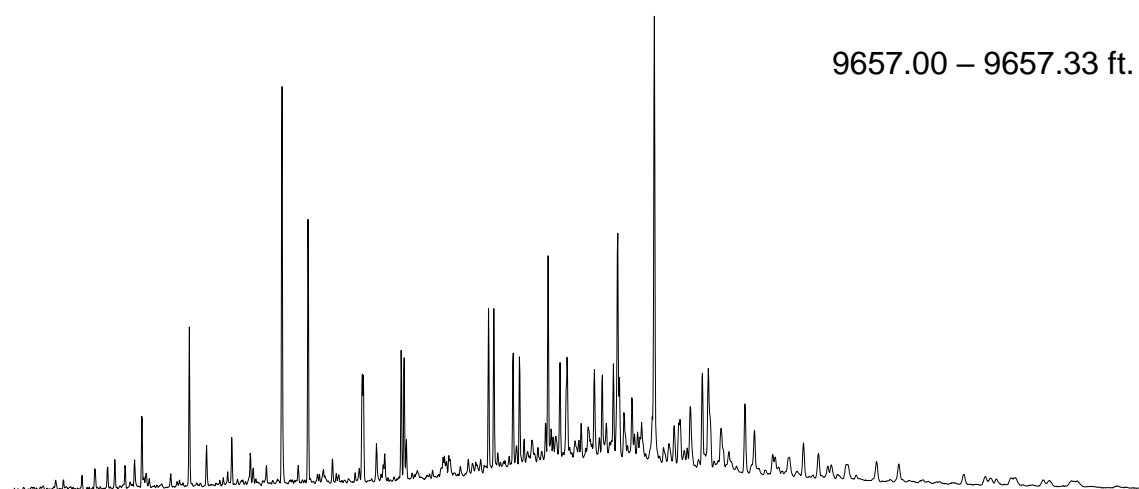
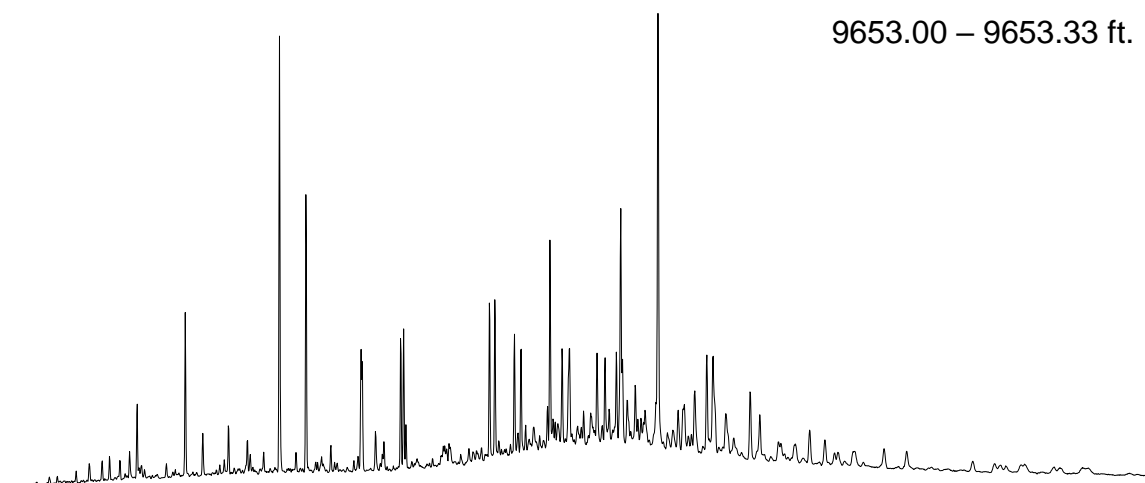
m/z 191 of branched and cyclic saturate fraction



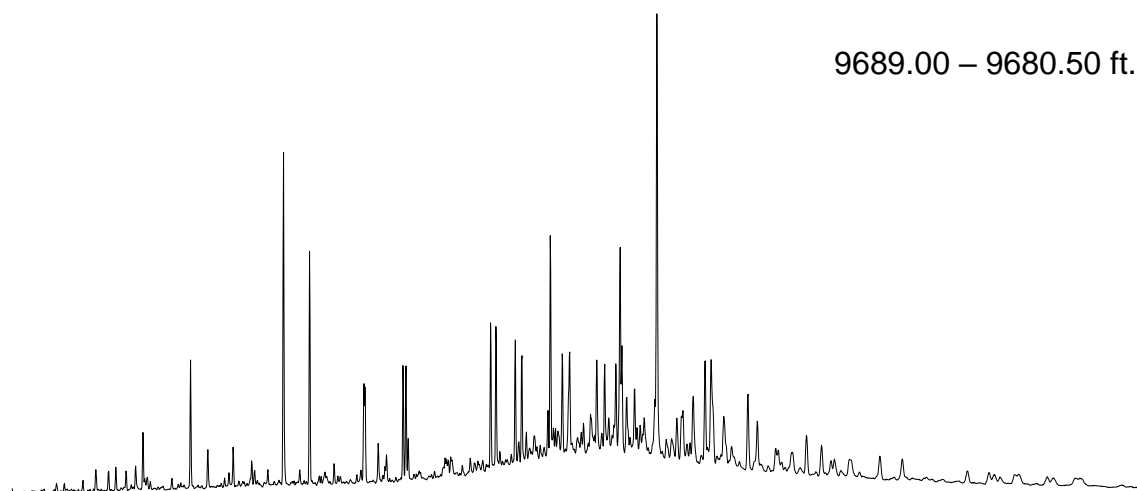
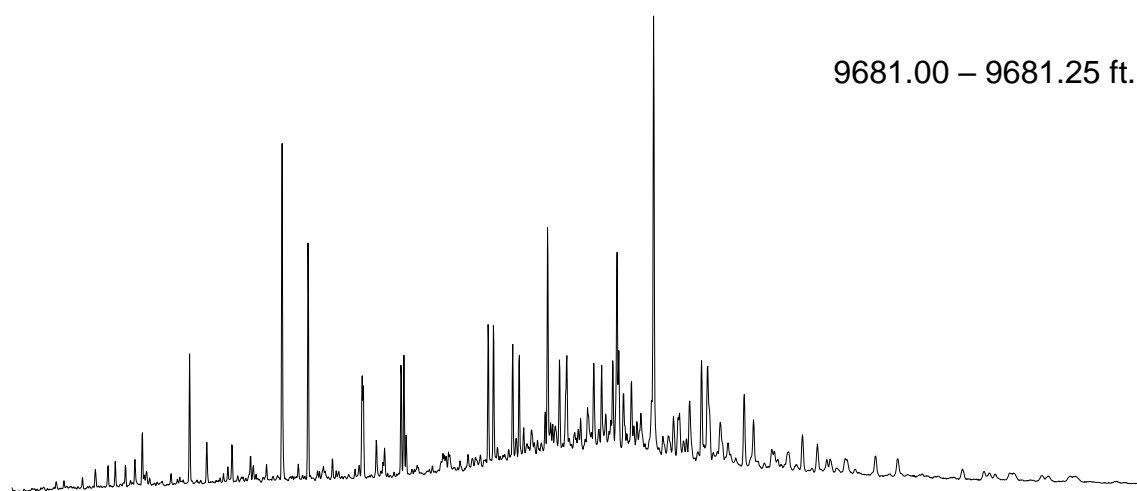
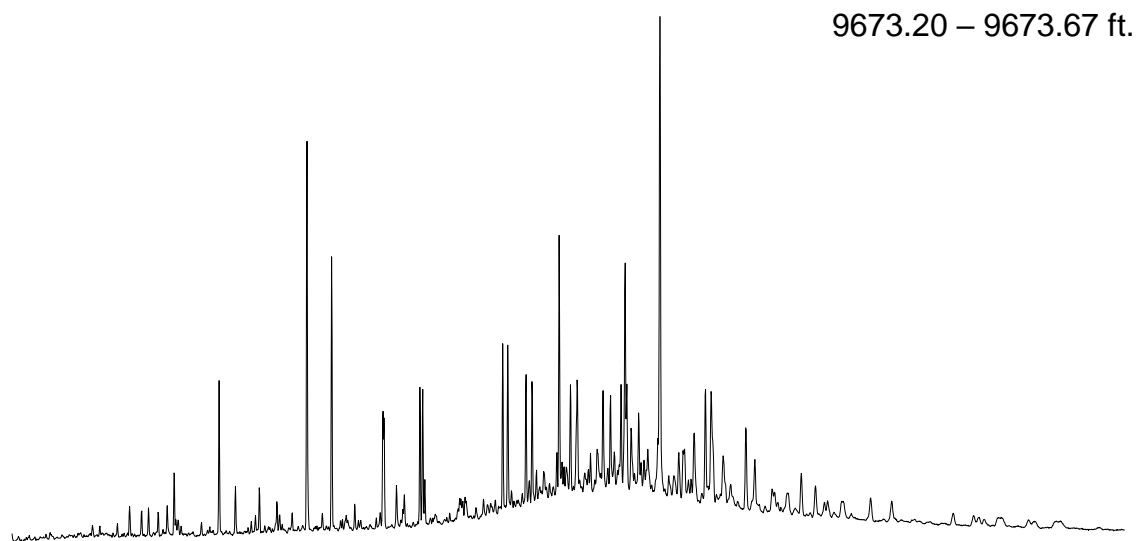
m/z 191 of branched and cyclic saturate fraction



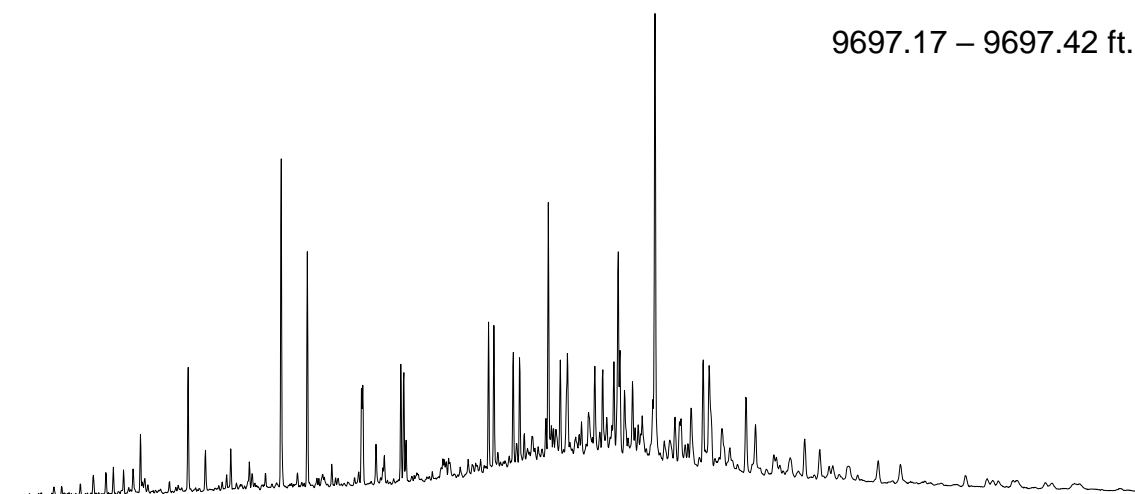
m/z 191 of branched and cyclic saturate fraction



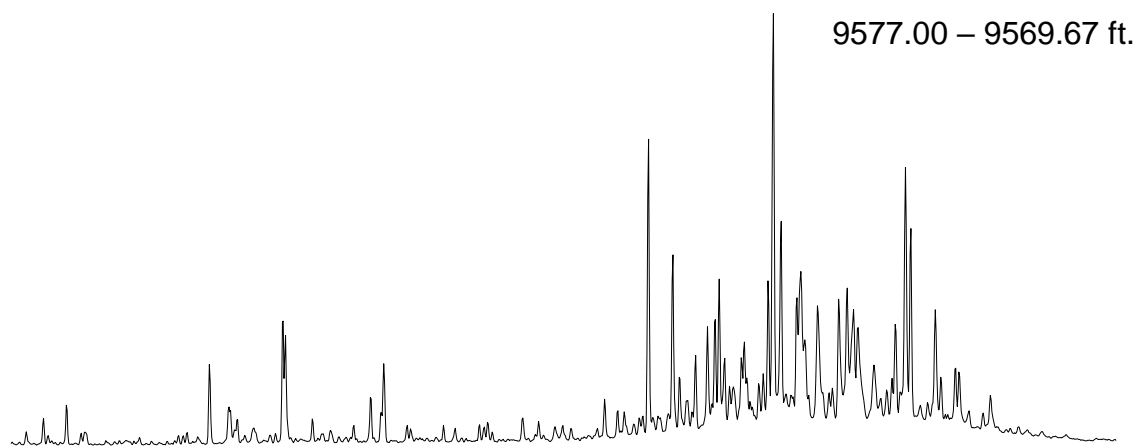
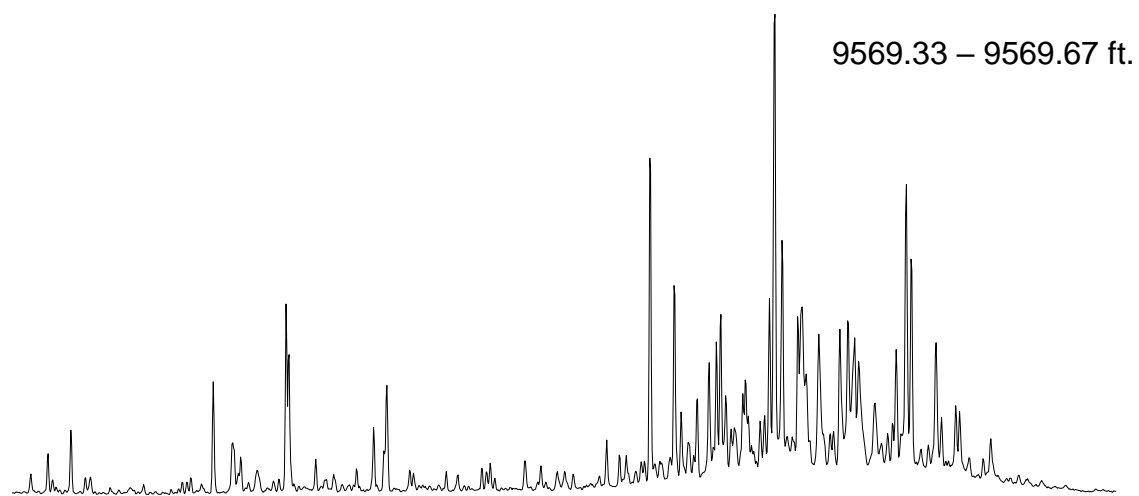
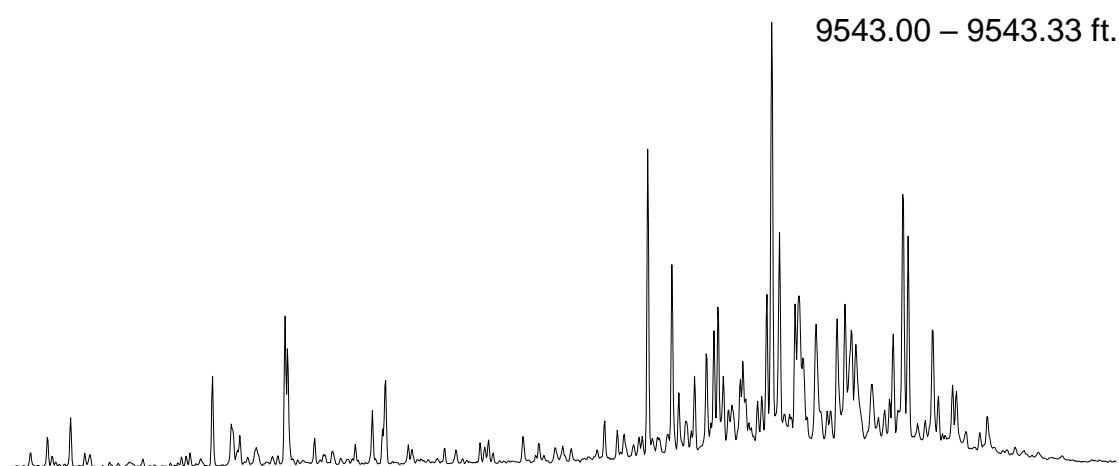
m/z 191 of branched and cyclic saturate fraction



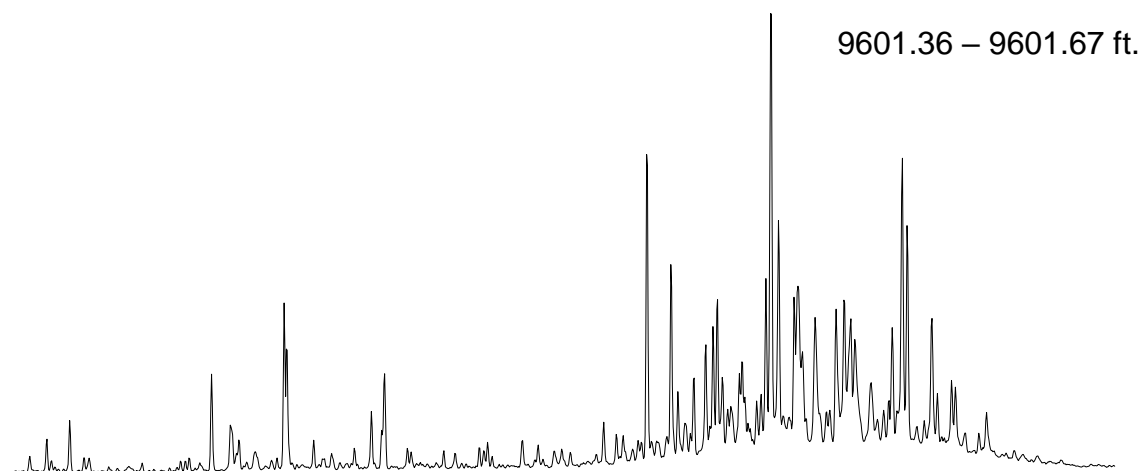
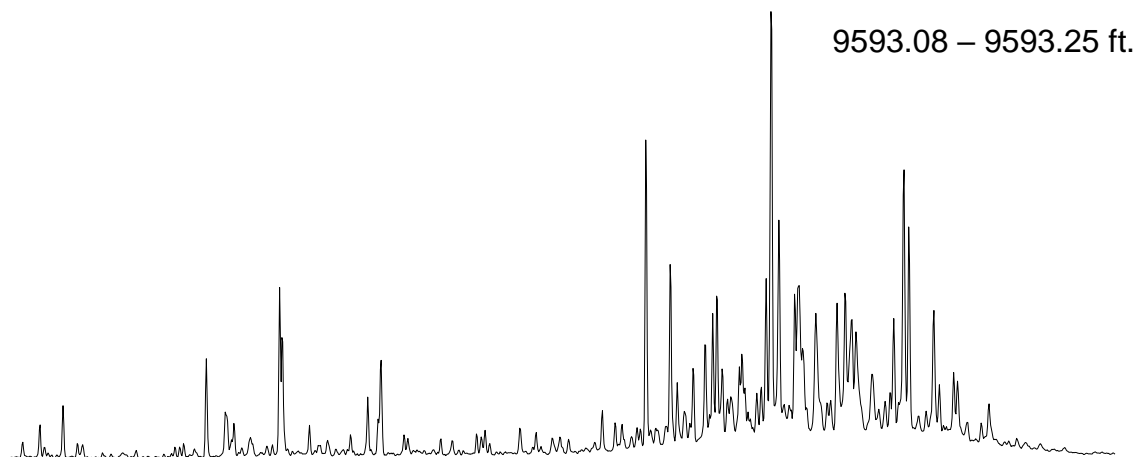
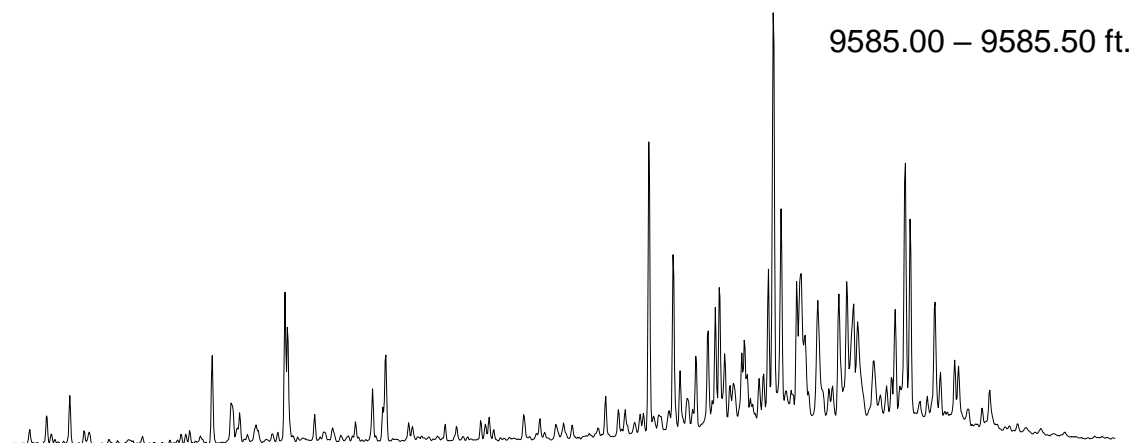
m/z 191 of branched and cyclic saturate fraction



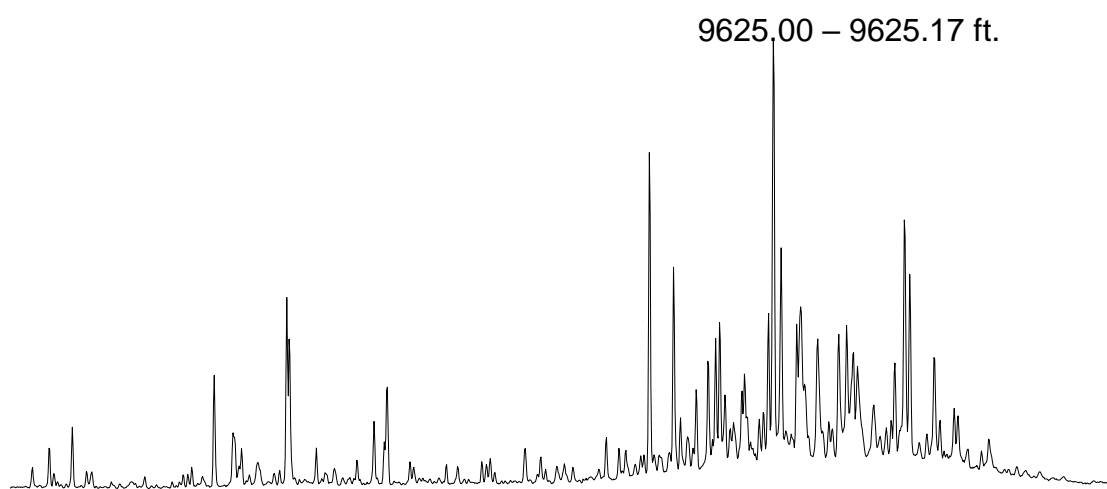
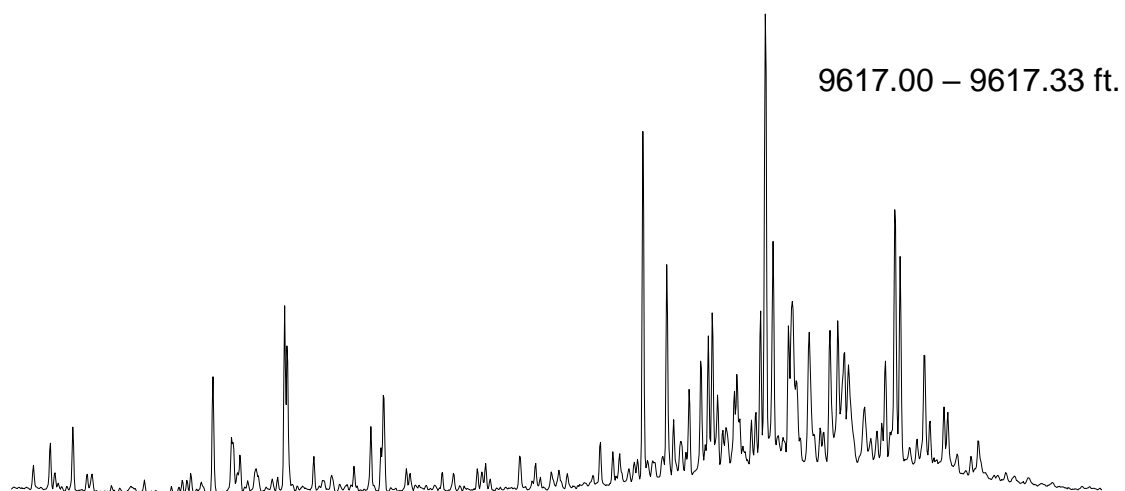
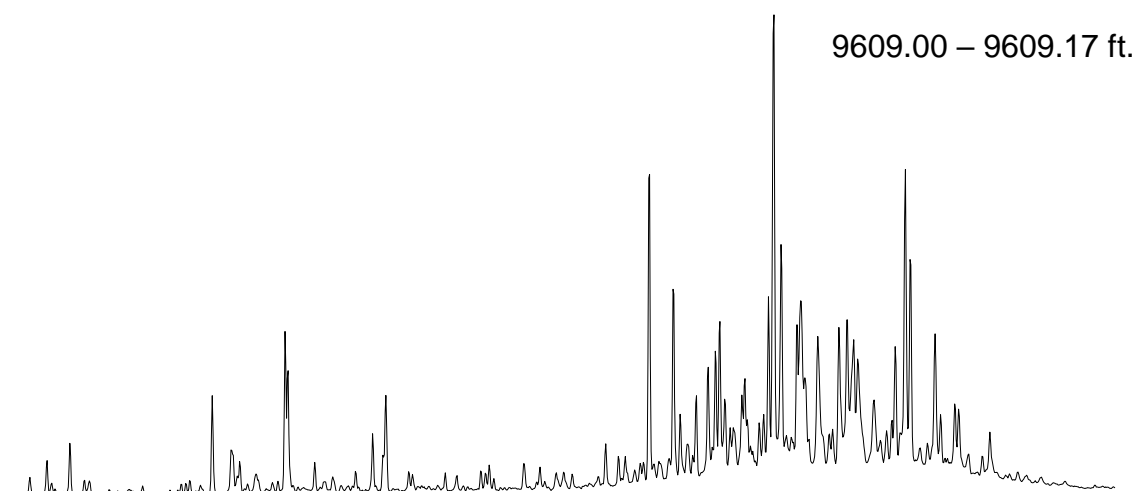
m/z 217 of branched and cyclic saturate fraction



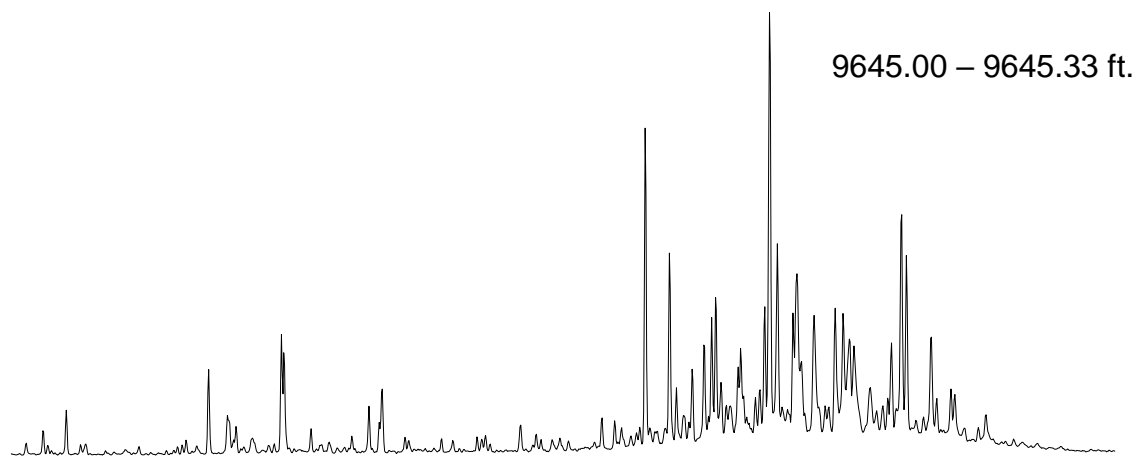
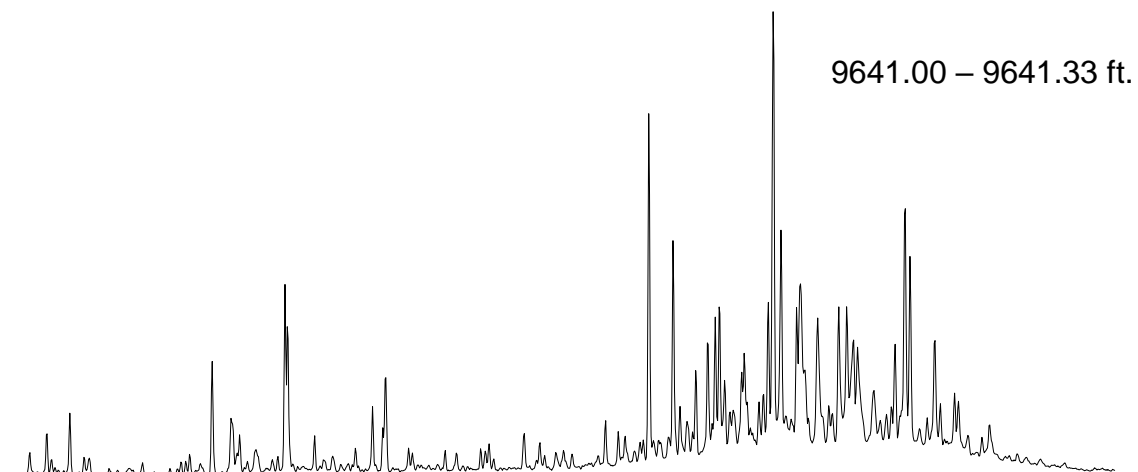
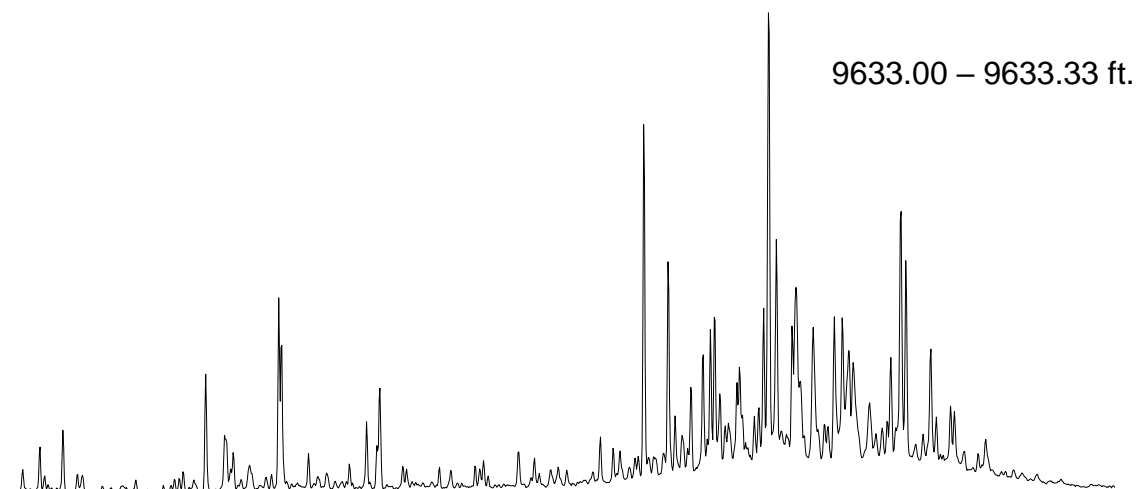
m/z 217 of branched and cyclic saturate fraction



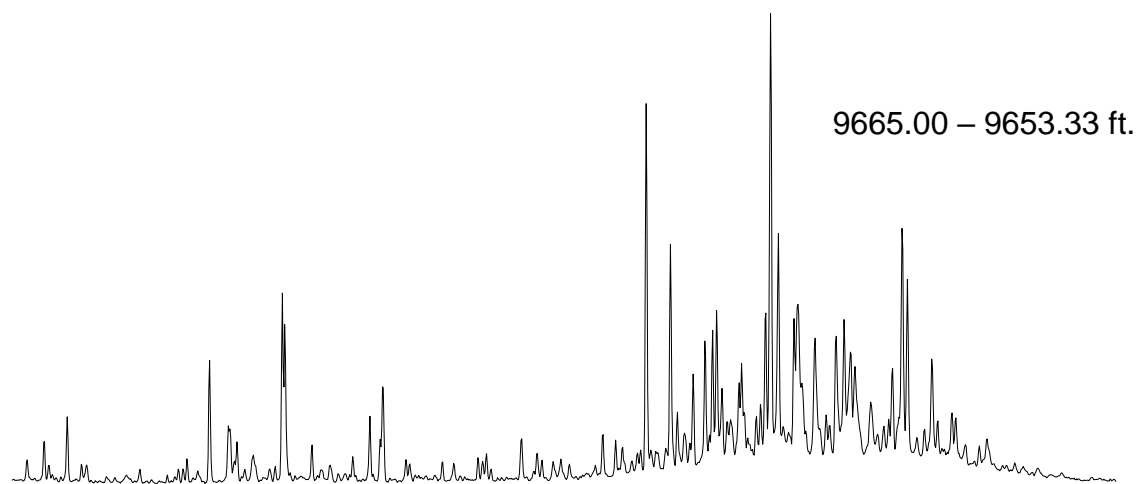
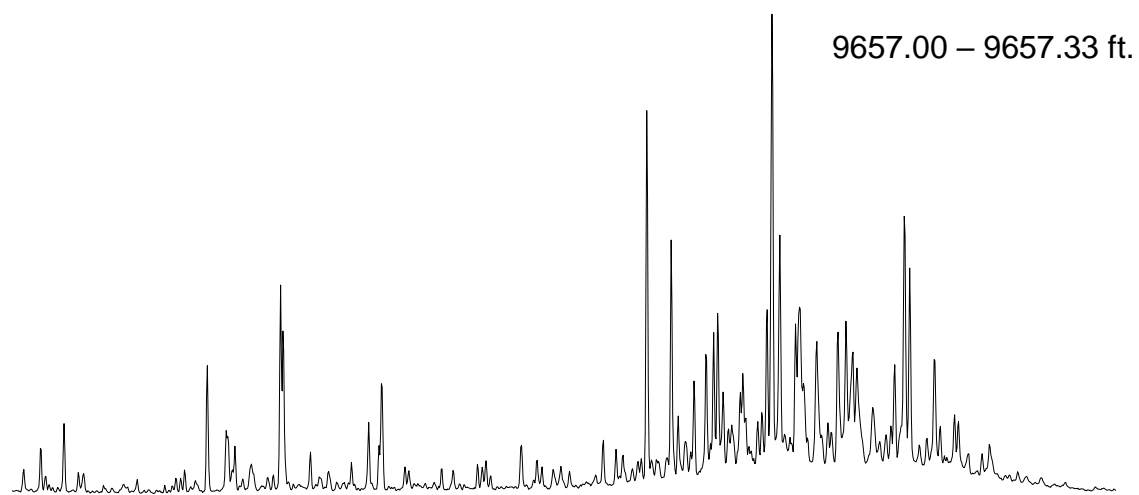
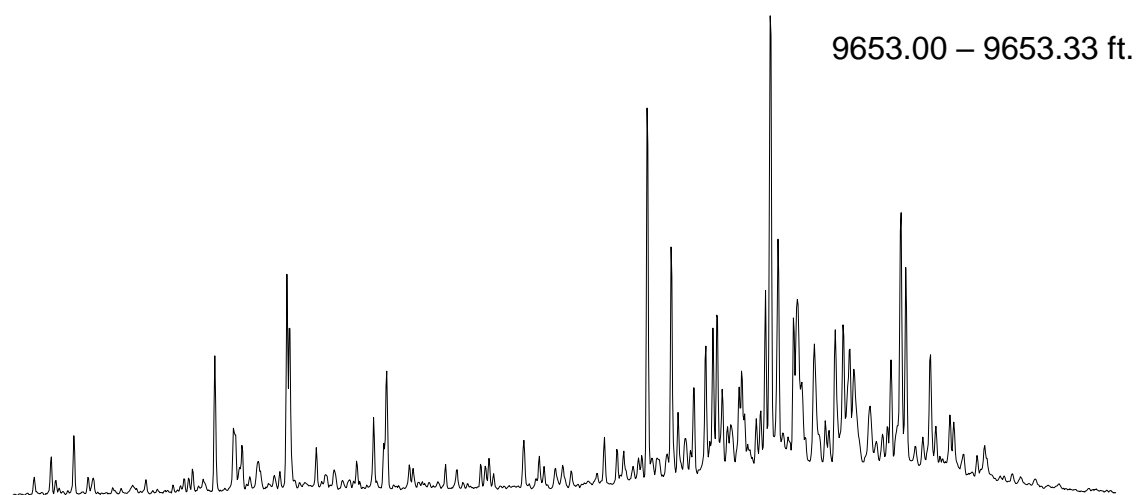
m/z 217 of branched and cyclic saturate fraction



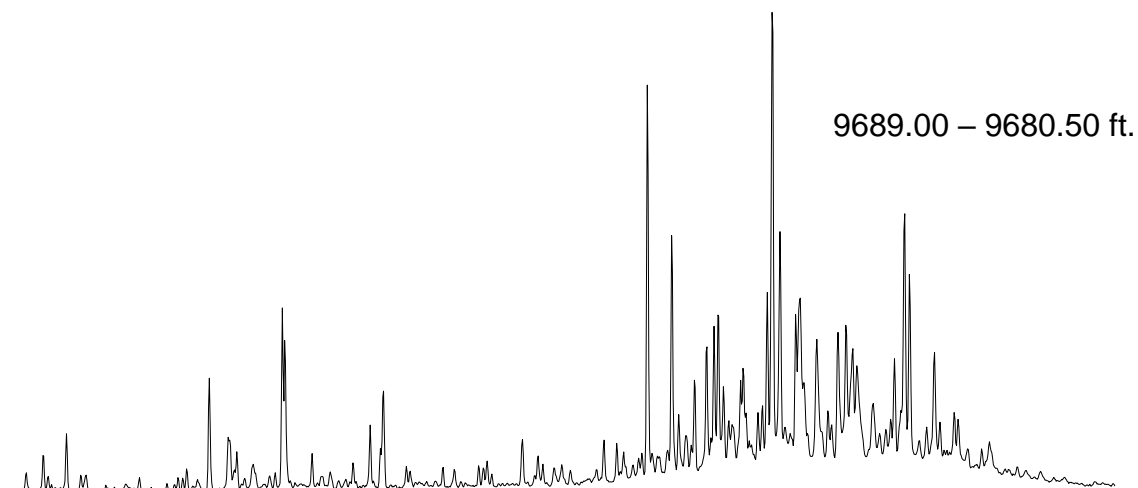
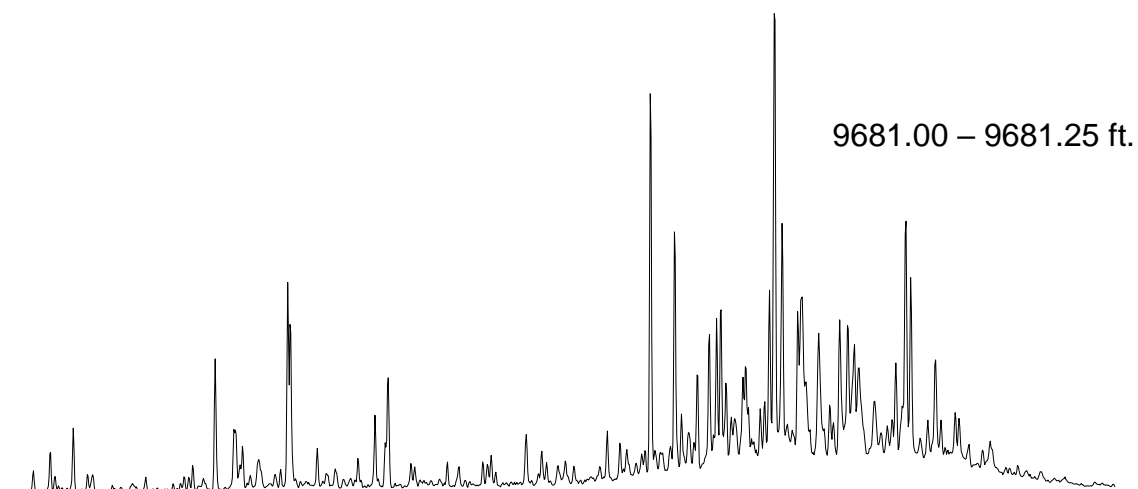
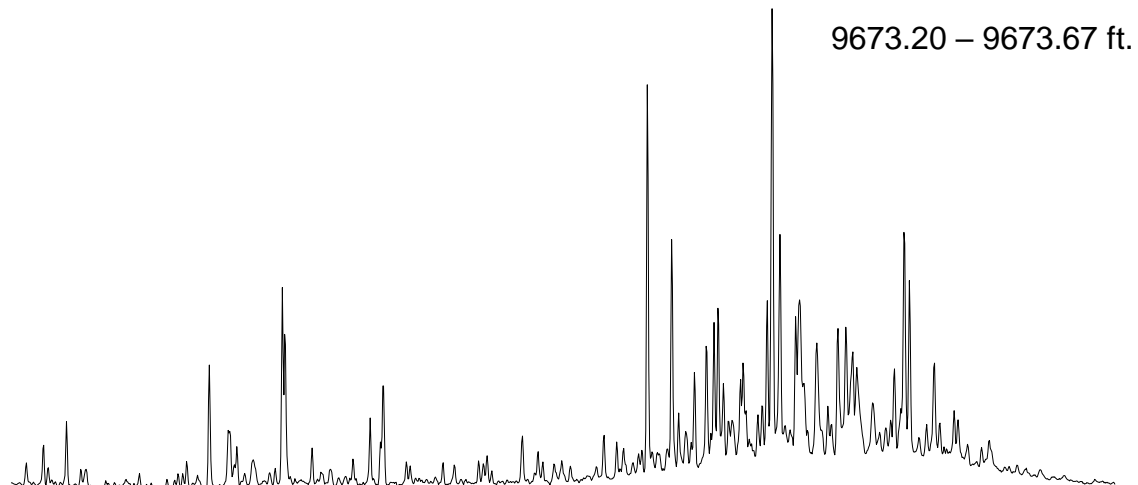
m/z 217 of branched and cyclic saturate fraction



m/z 217 of branched and cyclic saturate fraction



m/z 217 of branched and cyclic saturate fraction



m/z 217 of branched and cyclic saturate fraction

